eman ta zabal zazu

Universidad del País Vasco

Euskal Herriko Unibertsitatea

Novel surface engineering approaches for protein crystallization and structural insights into the enzymes of reverse transsulfuration from the human pathogens *Toxoplasma gondii* and *Pseudomonas aeruginosa.*

Carmen Fernández Rodríguez

2021

Thesis supervisors

Dr. Luis Alfonso Martínez de la Cruz and Dr. Iban Quintana

TEKNIKER and CIC bioGUNE funded this PhD fellowship. This research was supported by Spanish Ministerio de Ciencia e Innovación (MICINN), Grants PID2019-109055RB-I00 and AC19/00073, Spanish Ministry of Economy and Competitiveness Grants BFU2013-47531-R and BIOEF/EiTB MARATOIA BIO16/ER/035 (to Luis Alfonso Martínez de la Cruz). We thank MINECO for the Severo Ochoa Excellence Accreditation to CIC bioGUNE (SEV-2016-0644).

ABBREVIATIONS

The following list describes the meaning of various abbreviations and acronyms used throughout this thesis:

ACDP4: Ancient Domain Protein 4

ACE2: Angiotensin-converting enzyme 2

AD: Alzheimer disease

AdoHcy: S-adenosylhomocysteine

AdoMet: S-adenosylmethionine (SAM or SAMe)

AFM: Atomic Force Microscopy

ALS: Amyotrophic Lateral Sclerosis

***Am*CBS**: Cystathionine β-Synthase from *Apis mellifera*

Amp: ampicillin

AOAA: Aminooxyacetic acid

AR: Aspect Ratio

ARE: factor 2-Antioxidant Response Element

ATP: Adenosine Triphosphate

a.u.: Asymmetric Unit

AVG: L-aminoethoxyvinylglycine

BCA: β-cyano-L-alanine

BHMT: Betaine Homocysteine Methyltransferase

CA: Contact Angle

CAD: Computer Aided Design

CAT: catalase

CBL: Cystathionine β-Lyase

CCMs: Conditions with Crystalline Materials

CD: Circular Dichroism

***Ce*CBS**: Cystathionine β-Synthase from *Caenorhabditis elegans*

CGL: Cystathionine γ-Lyase

CGS: Cystathionine γ-Synthase

cNMP: Cyclic Nucleotide MonoPhosphate

CNS: Central nervous system

CNT: Classical Nucleation Theory

CPC: S-3-carboxpropyl-L-cysteine

Abbreviations

CS: Cysteine Synthase

CsdB: selenocysteine lyase

CSTNU: Cystathioninuria

Cth: Cystathionine

CV: Column Volume

CVB3: Coxsackie virus

CYMAL-3: 3-Cyclohexyl-1-Propyl-β-D-Maltoside

CYMAL-4: 4-Cyclohexyl-1-Butyl-β-D-Maltoside

Cys: Cysteine

CytBD: Cytochrome bd Complex

DLS: Diamond Light Source

***Dm*CBS**: Cystathionine β-Synthase from *Drosophila melanogaster*

DNA: Deoxyribonucleic acid

DTT: Dithiothreitol

EDTA: Ethylenediaminetetraacetic acid

ERK: Extracellular Signal-Regulated Kinase

Gm: Gentamycin

Gpx: Glutathionine Peroxidase

GSH: Glutathione

GYY4137: P-(4-Methoxyphenyl)-P-4-morpholinyl-phosphinodithioic acid

H_2S: Hydrogen Sulfide

HA: Hydroxylamine

HCC: Hepatocellular carcinoma

HCU: Homocystinuria

Hcys: Homocysteine

HD: Huntington´s disease

HEPES: 4-(2-hydroxyethyl)-1 piperazineethanesulfonic acid

HIV-1: Human Inmunodeficiency Virus

***h*MPV**: Human Metapneumovirus

Hs*CBS:* Cystathionine β-Synthase from *Homo sapiens*

***Hs*CGL:** Cystathionine γ-Lyase from *Homo sapiens*

***Hs*CNNM4**: Cyclin CBS domain divalent metal cation transport mediator 4 from *Homo sapiens*

ID: Identity

IMAC: Immobilized Metal Affinity Chromatography

IPTG: Isopropyl-β-D- thiogalactoside

Abbreviations

IRF-3: Interferon Regulatory Factor

IRI: Ischemia-Reperfusion Injury

K_{cat}/K_m: catalytic efficiency

K_{cat}: catalytic rate constant

K_D: Dissociation constant

K_i: Inhibition constant

K_m: Michaelis-Menten constant

KSHV: Kaposi sarcoma-associated herpesvirus

KTB: α-ketobutyrate

LA: Laser Ablation

LB: Luria-Bertani

LDH: Lactate Dehydrogenase

MAPK: Mitogen Activated Protein Kinase

MARV: Marburg virus

MAT: Methionine Adenosyltransferase

MDR: Multidrug Resistant

ME: Moth-eye

MES: 2-(N-morpholino)ethanesulfonic acid

Met: Methionine

MGL: methionine γ-lyase

MIPs: Molecular Imprinted Surfaces

MJ1004: CBS-domain protein from *Methanocaldococcus jannaschii*

MR: Molecular Replacement

MST: 3-mercaptopyruvate sulfurtransferase

MTHFR: methylenetetrahydrofolate reductase

MW: Molecular Weight

NaHS: sodium hydrosulphide

NASH: Non-Alcoholic Steatohepatitis

NCS: Non-Crystallographic Symmetry

NIL: Nanoimprint Lithography

NMDA: *N*-methyl-D-aspartate receptor

NN: Naomi´s Nucleant

Nr: Norfloxacin

Nrf2: Nuclear factor-erythroid 2 related factor 2

O/N: Overnight

Abbreviations

OAS: *O*-acetylserine

OASS: *O*-acetylserine sulfhydrylase

OASTL: *O*-acetyl-L-serine(thiol) lyase

OCBS: *O*-acetylserine-dependent CBS

OD: Optical Density

***Pa*CBS:** Cystathionine β-Synthase from *Pseudomonas aeruginosa*

***Pa*CGL**: Cystathionine γ-Lyase from *Pseudomonas aeruginosa*

PAG: DL-propargylglycine

PAGE: Polyacrylamide Gel Electrophoresis

PC: Polycarbonate

PCA: Principal Component Analysis

PCT: Pre-Crystallization Test

PD: Parkinson´s disease

PEG: Polyethylene glycol

pI: Isoelectric point

PLLA: Poly-L-Lactide

PLP: Pyridoxal 5'-phosphate

PMSF: Phenylmethylsulfonyl fluoride

PSU: Polysulfone

rmsd: Root Mean Square DeviationMD: Molecular Dinamics

RNA: Ribonucleic acid

RNS: Reactive Nitrogen Species

ROS: Reactive Oxygen Species

RP: Rapid Prototyping

RSV: Respiratory Syncytial Virus

S1 or S2: site 1 or site 2

SA: concentration first substrate

S_a: roughness

SAM: S-adenosylmethionine (AdoMet)

SARS-CoV-2: Severe acute respiratory syndrome coronavirus 2 (COVID-19)

SAT: Serine acetyltransferase

SB: concentration second substrate

***Sc*CBS**: Cystathionine β-Synthase from *Saccharomyces cerevisiae*

SDS: Sodium Dodecyl Sulphate

SDS-PAGE: Sodium dodecyl Sulfate Polyacrylamide Gel Electrophoresis

Abbreviations

SEM: Scanning Electron Microscope

Ser: Serine

SK: Shark-Skin

SOD: Superoxide Dismutase

SR-A: Scavenger Receptor class A

tBME: tert-butyl methyl ether

TCEP: tris (2-carboxyethyl)phosphine

TEV: Tobacco etch Virus

***Tg*CBS**: Cystathionine β-Synthase from *Toxoplasma gondii*

***Tg*CGL**: Cystathionine γ-Lyase from *Toxoplasma gondii*

Tm: melting temperature

TMPRSS2: transmembrane serine protease 2

TNF-α: tumor necrosis factor α

T-R2RNIL: Thermal roll to roll nanoimprint lithography

v/v: volume / volume

V_M: Matthews Volume

w/v: weight/volume

Wt: wild type

ε_{280}: Extinction coefficient

Θ: contact angle

ABSTRACT

ABSTRACT

This doctoral thesis, carried out in two Basque institutions of excellence, CIC-bioGUNE and Tekniker, has addressed a project divided in two complementary sections:

The first section, comprises Chapter I, and was mainly developed in the facilities of Tekniker and subsequently tested at CIC bioGUNE. Its aim was to develop an advanced polymeric material whose covering surface favors the nucleation and crystallization of proteins of great biomedical interest. Macromolecule crystallography is currently the most powerful technique for determining the three-dimensional structure of proteins at atomic resolution. However, despite its enormous level of technical development achieved, it is still limited by the great difficulty of obtaining crystals that, after exposure to X-rays, allow a high-resolution diffraction pattern from which the structure of the target protein can be elucidated. Even today, the crystallization process is a trial-and-error procedure that requires enormous experimental effort and high economic costs. This part of the thesis has focused on the development of multiscale surface topographies (micro and submicrometric) on polycarbonate that act as a heteronucleating agent that favors, enhances or induces the growth of protein crystals. The use of these polymers made it possible to improve the resolution of some of the crystals described in the following section.

The second section of the project, comprises Chapters II to IV, and was entirely developed at CIC-bioGUNE. Its main objective was the crystallographic characterization of the two enzymes of the reverse transsulfuration pathway from two human pathogens: *Toxoplasma gondii* and *Pseudomonas aeruginosa*. The transsulfuration pathway is a metabolic process involving the interconversion of homocysteine and cysteine via the intermediate cystathionine. The first enzyme in the pathway, cystathionine β-synthase, catalyzes the condensation of L-serine with L-homocysteine to form cystathionine. The second enzyme, cystathionine γ-lyase, hydrolyzes cystathionine yielding cysteine, α-ketobutyrate, and ammonium. Both enzymes catalyze alternative reactions leading to the biosynthesis of hydrogen sulfide (H_2S), a major gasotransmitter associated with numerous pathologies, including neurological disorders and various cancers. Recently, it has been shown that inactivation of these enzymes in multidrug-resistant bacteria and pathogenic organisms increases their sensitivity to oxidative stress and to a variety of antibiotics (in the case of bacteria). Therefore, the structural information obtained in this work is key to understand the implication of transsulfuration pathway in regulating the intracellular redox homeostasis in pathogens and will facilitate the rational structure-guided design of specific inhibitors.

GENERAL OVERVIEW

GENERAL OVERVIEW

The World Health Organization estimates, nearly 50,000 men, women, and children died every day from infectious diseases in 1996 (an estimated 17 million people per year)[1]. Today, diseases caused by bacteria, fungi, or parasites continue to challenge the health care system. In the ranking of the 10 leading causes of death worldwide reported by WHO in 2019, two were infectious or parasitic diseases. Deaths from lower respiratory infections (4th cause of death) and diarrheal diseases (8th cause of death) were estimated at 2.6 million and 1.5 million people, respectively.

Given their nature, infectious agents are evolutionarily dynamic, and the list of diseases they cause is constantly changing and growing. Even preexisting or established infectious diseases can reappear in different forms, such as the extensively multidrug-resistant bacterias [2,3] or emerging infectious diseases [4,5]. The emergence and spread of antimicrobial resistance (AMR) (https://www.who.int/news-room/fact-sheets/detail/antimicrobial-resistance) is increasing worldwide, with new mechanisms of resistance emerging that threaten the ability to treat common infectious diseases. A growing number of infections such as pneumonia, tuberculosis, gonorrhea, septicemia, and foodborne illness are becoming increasingly difficult, if not impossible, to treat as antibiotics become less effective. Remarkably, foodborne diseases represent a major problem health in the United States (U.S.). The Center for Disease Control and Prevention (CDC) expect that each year 31 pathogens acquired in US caused 9.4 million episodes foodborne illness, 55961 hospitalizations and 1351 deaths [6,7]. *Toxoplasma gondii*, causative agent of toxoplasmosis, is the second most common cause of death due to foodborne illness and the fourth leading cause of hospitalization in the middle 2000s at the United States [8]. The number of people infected is estimated over 8-22% in US and United Kingdom, while in Central America, South America and continental Europe estimated infection rates are even higher, ranging from 30% to 90% [9]. While toxoplasmosis is usually asymptomatic or causes only mild symptoms in immunocompetent individuals, it may cause severe diseases in immunocompromised patients. Infection in pregnancy may be even fatal to the fetus [10]. Moreover, multiple lines of evidence indicate that toxoplasmosis is related to a higher risk of many mental health disorders, including schizophrenia [11]. Despite intense efforts, effective vaccines are practically unavailable for humans and, consequently, chemotherapy represents the mainstay of disease control and treatment. However, recommended drugs require prolonged treatments and have high rates of toxic side effects. Moreover, the treatment has become complicated by the emergence of drug resistant parasites.

General Overview

On the other hand, especially alarming is the rapid proliferation of resistant bacteria known as "superbugs" that cause infections that cannot be treated with current antibiotics. It is estimated that by 2050, 10 million lives a year is at risk due to the AMR. *Pseudomonas aeruginosa* is a ubiquitous Gram-negative bacterium classified by the WHO as a critical priority on which to research, discover and develop new antibiotics. This opportunistic pathogen cause devastating infections in blood and lung (pneumonia), with an estimated 32 600 infections among hospitalized patients and 2700 estimated deaths in US [12]. *Pseudomonas aeruginosa* infections are generally treated with antibiotics. Unfortunately, infections caused by this bacteria are becoming increasingly difficult to treat in people exposed to healthcare facilities such as hospitals or nursing homes due to increasing antibiotic resistance [13].

Put all together, alternative therapies and new drugs are urgently needed. Recently, inhibition of endogenous H_2S production has emerged as one of the strategies against these pathogens [14–16]. Hydrogen sulfide plays a very important role as a protective agent against oxidative stress [17]. This function has been implicated in bacterial defense against reactive oxygen species (ROS) and antibiotic-induced oxidative damage [14]. This gasotransmitter is mainly produced within the transsulfuration pathway by two enzymes, namely cystathionine β-synthase (CBS) and cystathionine γ-lyase (CGL). Another enzyme related to cysteine catabolism, is 3-mercaptopyruvate sulfurtransferase which also produces H_2S, which will not be addressed in this thesis.

CHAPTER I

Improved success of protein crystallization with heterogeneous nucleating agents

1.1. INTRODUCTION

X-Ray crystallography, the most successful and widely used technique to determine the three-dimensional structure of macromolecules at high resolution, benefits from the ability of crystals to diffract X-rays. However, the crystallization process still is a trial-and-error and labor-intensive screening effort that represents the bottleneck of this method. In the face of so much uncertainty to obtain quality diffraction crystals, many authors have historically considered protein crystallization as an art [18,19]. The first stage in any crystallization process is *nucleation*, which requires overcoming an energy barrier to form an initial assembly or *primary nuclei*, where molecules become sorted following a bi- or three-dimensional pattern characteristic of a crystalline solid. Depending on the solution environment, this primary nuclei can either dissolve, or alternatively become stable thus forming a *critical nuclei* that continues growing to yield a large crystal.

1.1.1. Nucleation and nucleant agents.

In general, two different types of nucleation can be distinguished: The first one, known as *primary homogeneous nucleation* [20], is defined as a spontaneous formation of crystalline material from a previously crystal-free solution (**Fig. 1.1, A**). In the case of proteins, this random event is difficult to control and reproduce by the experimentalist due to the intrinsic characteristics of the biomolecules (irregular shape, surface charge distribution, dynamic properties, co-existence of oligomeric species) and depends on a wide variety of factors. Among them are the solution supersaturation level, temperature, pressure, pH, ionic strength, concentration of metal ions or precipitants, and the presence of traces of other molecules. All these factors may either induce and speed up the nucleation process, or alternatively prevent a successful outcome of the crystallization experiment. In probabilistic terms, nucleation always occur in supersaturated solutions, and never below the solubility curve (**Fig. 1.2**), where the nucleation probability is zero [21]. Between the extreme circumstances represented by the full solubility and the supersaturation condition, is the so-called *metastable zone,* where nucleation does not take place but growth of a pre-existing crystal is favored [22,23]. Importantly, the metastable zone varies for each particular protein in solution, what makes unpredictable the exact conditions in which a particular protein will nucleate. Frequently, too fast homogeneous nucleation causes unfavorable effects as the formation of a shower of small-sized crystals with poor diffraction capacity. The faster a crystal grows, the more defects it presents, and thus the poorer quality its diffraction pattern offers. High-quality protein crystals are

ideally grown at low supersaturation levels, where crystal growth is slow [24]. Thus, finding potential agents that favor nucleation at low saturation levels has been intensively pursued by the biomedical industry. To satisfy this demand, researchers have historically tried to exploit the potential of the second type of nucleation, known as *heterogeneous nucleation* [20], which starts at the surface of a solid foreign particle that acts as a seed (**Fig. 1.1**). These initiating surfaces, known as "*heterogeneous nucleants*" or "*heteronucleants*" [19,25,26], are thought to decrease the nucleation energy barrier and the time to obtain crystals, and require lower starting protein concentration to promote crystallization [21]. Growth of crystals on a heterogeneous surface may in turn promote the birth of new crystals in remote areas of the crystallization droplet (**Fig. 1.1, A**). This event is known as *Secondary homogeneous nucleation* and can occur at much lower supersaturation levels than primary nucleation (**Fig. 1.2**). Attrition, fracture caused by mechanical stress or fluid shear resulting in the separation of crystal surface clusters, have been proposed as possible causes of secondary nucleation [27,28].

A wide variety of materials have been tested as potential heteronucleants (**Fig. 1.1, B**), which can be classified in two well-distinguished classes:

(i) *Nanoscale heteronucleants*. The first group encompasses nanoscale structured surfaces showing topography templates that are either in the range of the hydration radius of the macromolecule to be crystallized [29], or match the lattice spacing of the target crystals (**Fig. 1.1, C**). The nanoscale heteronucleants are considered the most efficient agents to promote and enhance crystal growth via epitaxy, and have raised interest in the field of macromolecule crystallization[30–35]. This type of materials have important applications in biopharmaceutical bioseparation or biocrystallization processes, for example of monoclonal antibodies [36]. Among the used heterogeneous nucleants are complex thin films [18,26,37–39], chemically altered surfaces [40–44], carbon nanotubes [30,45], molecularly imprinted polymers (MIPs) [44], microgels [46–48] and three-dimensional nanotemplates [29] (**Fig. 1.1, B**). The weakness of nanoscale heteroagents lies in their specificity and their trend to work only for few specific molecular targets. Additionally, manufacturing of such nanostructural nucleants is not straightforward, leading to industrialization concerns.

(ii) *Microscale heteronucleants.* The second type of heteronucleants comprises materials whose surface contains pores, rugosities, or topographic motifs with dimensions that are closer to the micro- or submicrometric scale, thus significantly larger than the crystal lattice parameters (which range in the Angstroms and nanometers scale (1Å=10^{-10}m; 10^{-8}cm; 10^{-4}µM; 0.1 nm; 100 pm) [49]. Some examples

reported in the literature include dried seaweed [50], animal hairs [49], minerals [31,51–57] and carbon nanomaterials [30,45,58] (**Fig. 1.1, B**). Several theoretical models have tried to explain the impact of surface roughness on the crystallization of macromolecules [46,53,55,59–61], and generally conclude that roughness and porosity enhance the effective area producing an increase in the local concentration of the proteins in solution that favors nucleation in the valleys of the rough surface [50,62,63]. It has also been shown that surface hydrophobicity tuned by roughness modification processes [64], can enhance or alternatively hinder the interaction with a crystalline solution [65]. On the other hand, charged surfaces whose interfacial concentration of ions may cause electrostatic interactions with protein molecules of opposite charge may also enhance nucleation [37–40] (**Fig. 1.1, C**). In a recent study, Ye *et al.* demonstrated that protuberances, grooves and cavities with micrometer-scale sizes could serve as promising nucleation agents [66]. In this direction, some authors including ourselves, have recently investigated the effect of submicro- and micro-scaled surface features on the macromolecular crystallization [67,68].

Manufacturing of those submicro- and micro-scaled engineering surfaces count with the advantage of the enrolment of well-stablished high throughput microfabrication technologies, which enables the production of micro-patterned surfaces on flat flexible substrates as well as 3D-shaped components.

Although a priori less efficient than the nanoscale heteronucleants, the micro- or submicroscale heteroagents have shown very promising results on the crystallization of a wider variety of proteins, thus functioning much closer to the long-awaited *universal nucleants.*

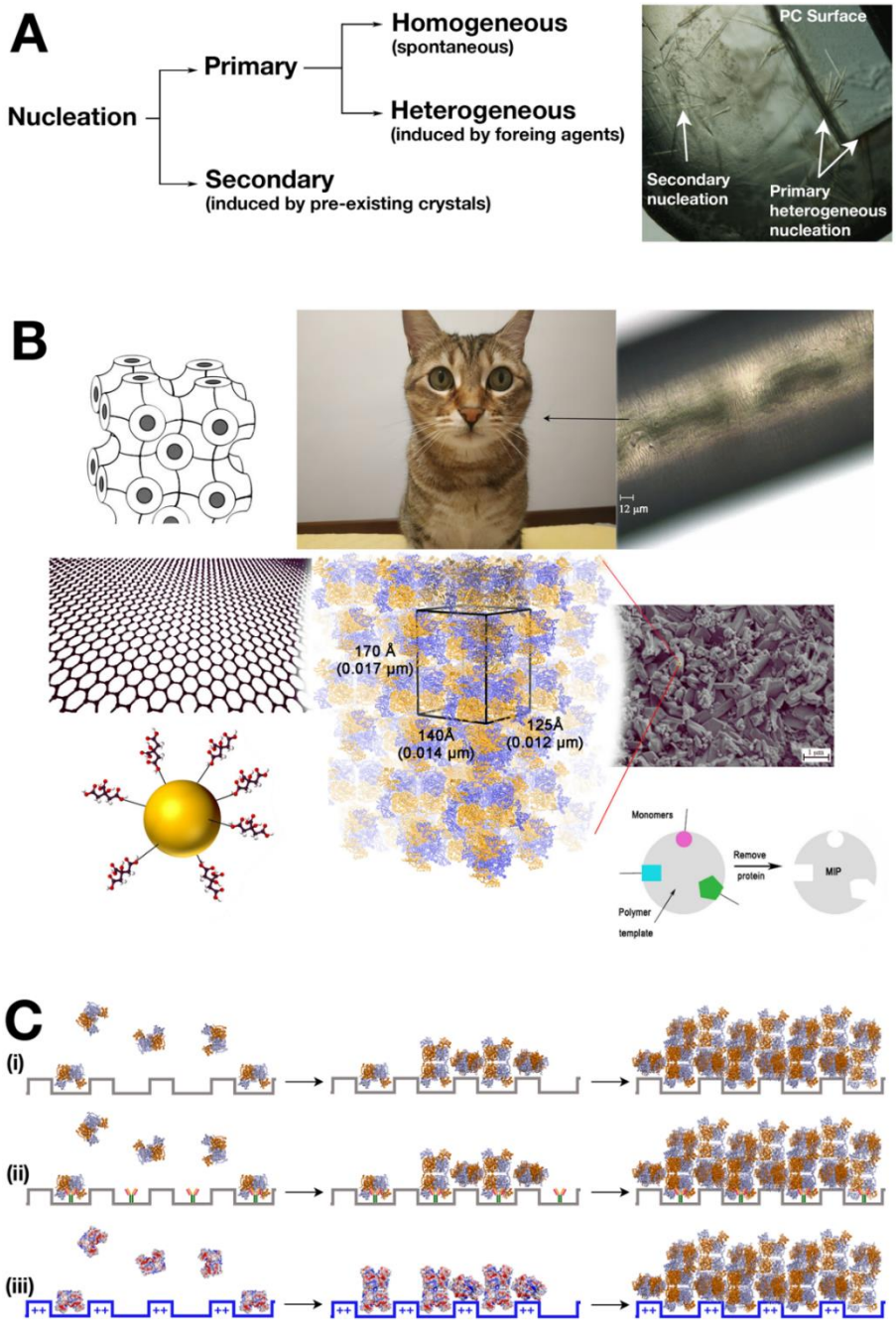

Figure 1.1. Nucleation agents. *(**A**) Nucleation types. (**B**) Representation of common heteronucleants used in protein crystalization: Microporous synthetic zeolites, carbon nanotubes, functionalized gold particles, animal hairs, porous/rugous minerals, and molecular imprinted surfaces (MIPs). The packing shown in the midle corresponds to that found in crystals of the human cystathionine β-synthase enzyme (HsCBS; PDB ID 4L0D)* [69]*. The dimensions of the unit cell and the corresponding size scales for the different materials are indicated for comparative purposes. HsCBS associates in tight dimers, whose subunits are colored in blue and orange, respectively. (**C**) Graphical representation of three different types of nanoscale nucleants: (i) surfaces with a geometrical distribution of cavities with size within the protein molecules scale; (i) Chemically functionalized nanosurfaces; and (iii) Surface with nanoscale charged cavities. The molecules represented are HsCBS dimers, colored according to their surface electrostatic potential. Positive and negative charges are colored in blue and red, respectively.*

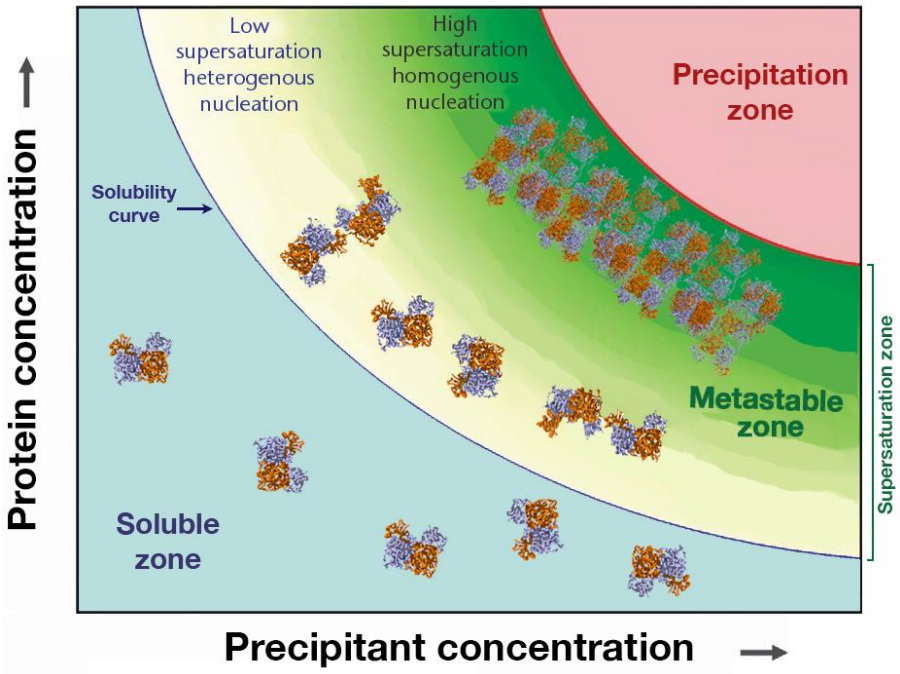

Figure 1.2. Phase Solubility diagram. *In undersaturated solutions, protein molecules are sorrounded by an extense solvation sphere that maintains them far away from each other. Upon increasing the protein or the precipitant concentration, molecules approximate to each other and start forming molecular clusters (low supersaturated zone) that keep growing and eventually become sorted in a regular arrangement (High supersaturated zone). Beyond certain concentration of the protein and/or the precipitant (precipitation curve, red line), proteins aggregate and precipitate.*

1.1.2. Fabrication of micro and nano- patterned heteronucleants for protein crystallization

As mentioned above, various materials have been employed as heteronucleants in recent research such as mineral substrates [70], chemically modified mica [41], bioglass [31,51], carbon-nanotube-based materials [30,58], nanoporous gold [71] or polymers [40,72–74]. The latter have shown highly promising in inducing protein nuclei, ranging from ionized gelatin films or silk fibers [40] to protein imprinted-polymers [44,74].

The success of polymers lies primarily in their manufacturability, enabling them to be modeled into a vast variety of products. By controlling their synthesis and processing, these materials can be designed and synthesized with a wide variety of chemical and mechanical properties [75]. Those properties can be optimized by selecting the appropriate monomer, additives, or processing conditions. Additionally, polymer degradation depends on their own physico-chemical properties, as well as the environmental conditions (temperature, pH). All these properties make them an ideal, chameleon-like material with numerous possible applications, not only as potential heteronucleants for protein crystallization: Biodegradable polymers are used as temporary barriers (artificial skin, surgical sutures), drug delivery, or temporary scaffolds (vascular grafts, orthopedic devices) [76]. Synthetic polymers show great potential in numerous fields, such as biomedical engineering [77], aerospace engineering [78], sensor fabrication [79] or as

thermal insulators. Their thermoplastic properties allow easy and reproducible production by conventional hot-melt processes. With the prior knowledge, these materials are a suitable aiding in the current research on heteronucleant manufacturing with the aim of finding an engineered device by easy-to-process, which expands structural knowledge of therapeutic targets and set the basis for drug-discovery by X-ray technique.

As mentioned earlier, the success of a large number of heteronucleants lies in the surface properties of the material, such as porosity, topography, or roughness [33,51,60,64]. Micro- and nanoscale surface patterns have a great impact on nucleation and promotion of protein crystals [31,45,51,66,80]. Many techniques have been investigated for the fabrication of micro- and nano-patterned polymeric surfaces. In the following, we will discuss those that allow the fabrication of patterns with controlled shape and size characteristics.

- Photolithography-based methods are processes in which geometric patterns from mold containing and inverse of the desired patterns are pressed onto a substrate to replicate the patterns via mechanical deformation [81]. There are two fundamental types of process: thermal NIL [82] and UV NIL. Currently, the most widely used is UV NIL in which the substrate is coated on the surface with a photosensitive organic polymer (photoresist) and exposed to UV light through a mask containing a specific pattern [83] (**Fig. 1.3**). This technique can be used to produce a wide range of patterns in the nanometer range with high resolution. However, it is an expensive process that requires clean rooms and expensive equipment.
- Rapid prototyping (RP) techniques are used to rapidly fabricate 3D components by deposition. RP is an additive process that is built up in layers step by step until the desired geometry is achieved. It consists of two steps: a virtual phase where the physical model is developed using 3D Computer Aided Design (CAD) [84]. Then, this model is cut into very thin layers (0.01 to 0.07 mm thick) and the manufacturing team uses this geometric data to build each layer in turn by adding and merging with the previous layer (**Fig. 1.3**). The main advantage is that the manufacturing process is very controlled. However, it is a long process that release high temperatures and toxic gases. Additionally, production of micro-scale features on the XY-plane is not straightforward. Another additive technology is the photo-polymerization based technique, which uses the photosensitivity of polymer resins to cure them and create 3D structures (**Fig. 1.3**). The major limitation is the availability of the raw material.

- Ultrashort-pulsed Laser Ablation is considered as universal tool for surface micro-structuring of a wide range of materials, from metals to biopolymers. Depending on the laser configuration, micro- and nano-scale structures can be produced on flat and 3D surfaces. The main advantage of this technology corresponds to the onset of the "cold" ablation process, which turns solid into plasma (material laser ablation), minimizing the thermal effects and without changing the properties of the material. Laser ablation is the process in which material is removed from a surface as a result of photo absorption. Laser photo absorption in polymers produces electronic excitation that is converted to heat and bond cleavage. This phenomenon triggers the ablation of the polymer by two main mechanisms: photochemical and photothermal ablation [85]. In photochemical ablation, the covalent bonds in the polymer chain are broken by the incident photons. Particularly, laser ablation of polymers with short wavelengths and ultrashort laser pulses is considered an example of photochemical ablation process [86]. While in the photothermal ablation, the incident energy is transfer to the lattice following a thermalization process (heat transfer), resulting in polymer bond breaking [87] (**Fig. 1.3**). The decomposition mechanisms of polymers under laser ablation depends on their method of synthesis [88]. In 2001, Serafetinides *et al*. reported that ultra-short laser pulses, such as picosecond and femtosecond pulses offer more advantages in terms of surface quality than the use of nanosecond and microsecond laser pulses. The main advantage is that the energy loss is minimized resulting in a high precision patterning without thermal damage of the surroundings [85]. In this context, it is worth to note the previous works of our group where picosecond laser micromachining technology were applied to poly-L-lactide (PLLA) (a biopolymer) to generate different microstructures (microgrooves and microcavities) that control cell growth and regeneration [86,89–92]. In those studies, the effects of laser wavelength, energy, and material microstructure were analyzed in detail, which provides a solid knowledge for further studies [92] including our own work.

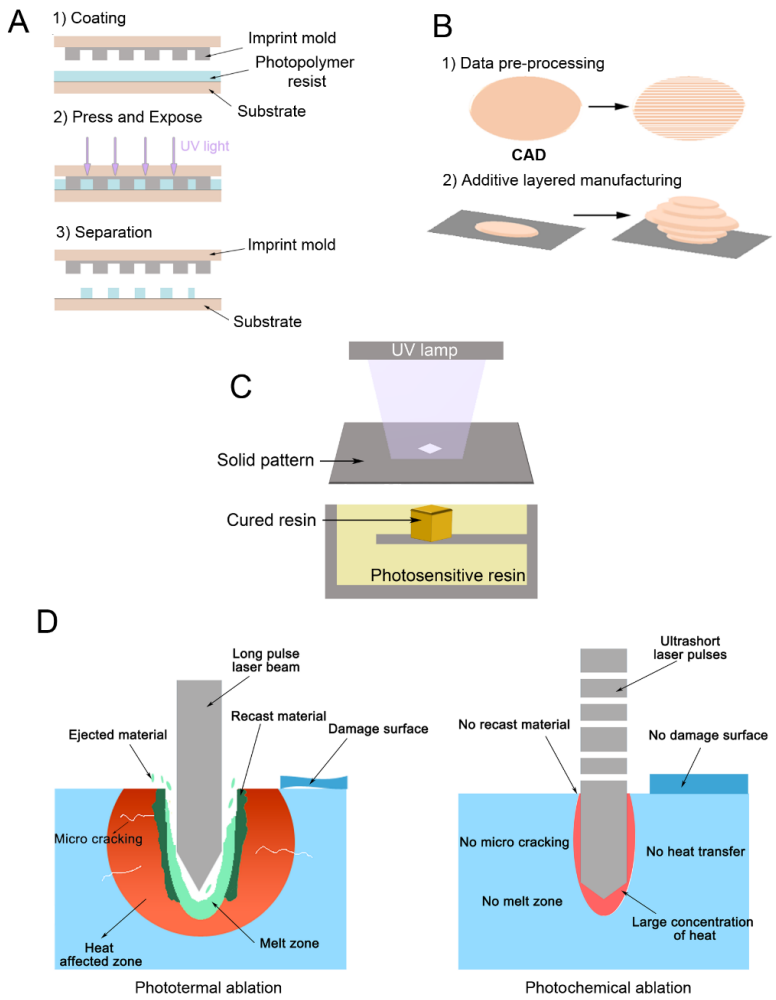

Figure 1.3. Fabrication techniques of micro and nano-patterns*. Scheme of (**A**) Nano-imprint lithography technique (figure adapted from [93], (**B**) rapid prototyping technique (figure taken from [94], (**C**) photopolymerization method (figure adapted from [95] and (D) laser ablation process (figure modified from [86,96]. Laser ablation process in polymers is decomposed in two major mechanisms; photothermal ablation (left) and photochemical ablation (right).*

1.1.3. Nucleation mechanisms.

It has been postulated that nucleation, thus the formation of initial crystals nuclei, may require the preexistence of unstable aggregates formed at low supersaturation levels. Such aggregates might be responsible to stabilize molecular clusters by nonspecific interactions and trigger the nucleation event [21]. Nevertheless, the mechanisms underlying this process still remain poorly understood. In the case of protein crystals, essentially two main theories have been proposed (**Fig. 1.4**):

(i) The first one, known as the *Classical Nucleation Theory* (CNT), assumes that fluctuations in the concentration within the protein solution result in the formation of small crystalline clusters that grow until they reach a critical size that makes the cluster stable (**Fig. 1.4**). The higher the saturation level, the smaller the clusters size is, and the higher is their number. Oppositely, low saturation levels favor the formation of fewer, larger clusters. Once formed, these critical nuclei keep adding individual molecules little by little until they become large crystals.

(ii) The second nucleation theory is known as the "("*Two-step nucleation model*") and proposes that nucleation takes place in two well-differentiated steps [97–101]. The first step consists in the formation of a

highly dense drop in which protein concentration is significantly higher than in the rest of the droplet. This step is limitant and is followed by a second step in which the crystal nuclei are born within this dense drop and grow to form a large crystal. Based on this theory, several authors have suggested that the heterogeneous agents do not neccesarily act by decreasing the nucleation energy barrier, but increasing protein concentration locally by adsorbing the protein molecules in the cavities and pores of their surface [101,102]. The increase in local concentration leads to the formation of tiny crystalline clusters that subsequently evolve into crystal nuclei that finally become large crystals (**Fig. 1.4**). The general idea behind this model is the formation of intermediate stages (clusters), which conceptually are equivalent to the reaction intermediates characteristic of an enzymatic reaction. An important aspect of the Two-steps theory is that it predicts the nucleation rate more realistically, and explains more convincingly the formation of crystalline nuclei from a liquid solution.

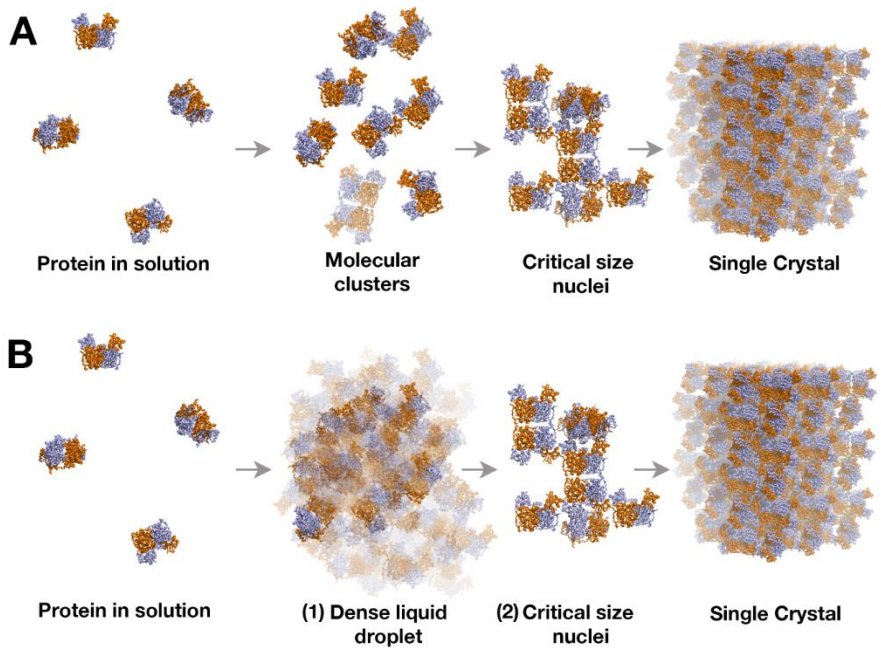

Figure 1.4. Main mechanisms proposed for protein crystallization. *(**A**) Classical Nucleation Theory (CNT), postulates the formation of molecular clusters by fluctuations in the protein concentration within the droplet. These clusters reach a critical size and become stable (critical nuclei) and then grow to become a large crystal. (**B**) The "Two-Steps mechanism", proposes two well-differentiated steps consisting in (1) formation of a dense liquid drop where protein is highly concentrated and (2) the formation of critical nuclei within the dense drop that subsequently grow little by little adding individual protein molecules, thus becoming a large crystal.*

1.2. HYPOTHESIS AND OBJECTIVES

The research developed in this chapter is based on the following hypothesis:

- Protein crystallization requires the formation of critical nuclei that subsequently grow little by little adding individual protein molecules, until a large crystal is formed. The nucleation process needs to overcome an energy barrier.
- Some materials known as heteronucleants may decrease such energy requirements.
- Surfaces containing micro- and submicrometric cavities, can promoted nucleation.
- Plastic polymers are ductile inert materials that can be easily molded, generating rough surfaces with micro- and submicrometric patterns, thus offering an excellent opportunity to developed new heteronucleants.

The chapter I of the present doctoral thesis focuses on the following objectives:

1. Design and development of multi-scaled dimensional patterns on two well-known thermoplastics: Polycarbonate (PC) and Polysulfone (PSU).

2. Correlation between manufacturing technologies selected (Nanoimprint Lithography and ultrashort pulsed laser ablation) and pattern quality based on microscopic characterization methods.

3. Correlation between pattern designs, materials, manufacturing technologies and crystallization outcomes considering different proteins. In this context, the polymer film must be adapted to the experimental requirements of the technique without losing the surface quality and the precision of the microstructures and promoting the crystallization of macromolecules.

4. Determination of design rules for the manufacturing of patterned polymeric heteronucleants that promote the crystallization of proteins of different nature.

5. Application of the developed technology in crystallization and determination of the three-dimensional structure of at least one protein of biomedical interest.

1.3. MATERIALS AND METHODS

1.3.1. Proteins expression and purification

1.3.1.1. *Hs*CNNM4$_{545\text{-}730}$

The CNNM4 construct containing the cNMP domain (Homo sapiens) includes residues 545 -730 and discards the last 45 residues of the protein, which belong to the potentially unstructured region. The construct was cloned into the pHis-parallel2 vector contributing a six-histidine tail at the N-terminal end, followed by a TEV protease recognition sequence using the same protocol described in [103]. The vector containing the protein of interest was transformed by heat shock using the competent *E. coli* BL21 (DE3) cell strain (Thermofisher). 10 ng of the vector was mixed with 50 µL of competent bacteria and the mixture was kept on ice for 30 minutes. The cells were then heat shocked at 315K for 42 seconds and then placed on ice for 2 minutes. Then, 500 µL of the medium previously tempered to 310K was added to Luria-Bertani (LB). Cells were shaken for 1 hour at 310K in an Excella E24R incubator (New Brunswick Scientific) and then centrifuged at 18 000 g for 1 minute in a Microfuge 22R centrifuge (Beckman Coulter) at 277K. The supernatant was discarded and the pellet containing the bacteria was seeded onto a LB agar plate containing 100 µg mL^{-1} ampicillin. The plates were incubated overnight at 310K in an oven. The next day, a pre-inoculum was prepared from a colony grown on the plate and allowed to grow overnight in 150 mL LB containing 100 µg mL^{-1} ampicillin at 310K with agitation. The pre-inoculum was then used to grow the protein on a large scale. For this purpose, 20 mL of the pre-inoculum was added per 2L of the previously autoclaved LB medium with a final concentration of 100 µg mL^{-1} ampicillin. Cultures were allowed to grow at 310K until an approximate optical density (OD_{600}) of 0.8 was reached as measured by a WPA Biowave C=8000 cell Density Metre spectrophotometer. Cultures were induced by addition of isopropyl-β-D-1-thiogalactopyranoside (IPTG) to a final concentration of 0.5 mM. The bacteria were allowed to grow overnight (O/N) at 293K. The next day, cultures were centrifuged in an Avanti J-26 XP centrifuge (Beckman Coulter) at 277K, 5053g for 20 minutes. The supernatant was discarded and the pellet was frozen at a temperature of 253K.

Protein purification started with bacterial lysis, in which the pellet was resuspended in lysis buffer (50 mM Tris pH 8, 300 mM NaCl, 1 mM dithiothreitol (DTT), 1 mM benzamidine, 0.1 mM Phenylmethylsulfonium Fluoride (PMSF), DNAse). After dissolution in the lysis buffer, the bacteria were sonicated with a Sonics Vibracell VCX500 Sonicator for 10 cycles of 15sec and 60% amplitude, always

cooling the lysate at 277K. Then, the cell lysate was clarified by ultracentrifugation at 186 009 g for 1 hour in an Optima L-90K ultracentrifuge (Beckman Coulter) with a 45Ti rotor (Beckman Coulter). The supernatant was recovered and loaded to immobilized nickel (Ni^{2+}) affinity chromatography (IMAC) using a His Trap HP 5 (Cytiva) connected to an AKTA-FPLC system previously equilibrated with 10 column volumes (CV) of buffer 50 mM Tris pH 8, 300 mM NaCl, 50 mM imidazole and 1 mM DTT, at 277K. The protein was eluted by applying a 20 CV gradient of elution buffer containing 50 mM Tris pH 8, 300 mM NaCl, 300 mM imidazole and 1 mM DTT. The presence of $CNNM4_{cNMP}$ was confirmed by SDS -PAGE (Section 1.3.2.1.). The construct was designed with a six-histidine tail at the N-terminal end and a TEV protease recognition site was inserted into the vector. To remove the histidine tail from the protein, 1 mg of TEV protease was used per 30 mg of target protein and dialyzed overnight at 277K against a buffer containing 50 mM Tris pH 8, 150 mM NaCl and 1 mM DTT. The next day, the protein was eluted in a second affinity chromatography equilibrated with 50 mM Tris pH 8, 300 mM NaCl, 50 mM imidazole and 1 mM DTT to separate $CNNM4_{cNMP}$ from the 6xHis tail proteolyzed by the TEV protease, which also contains a six-histidine tail. The volume of protein-containing solution that was not retained in the nickel column stationary phase was concentrated to approximately 2 mL by centrifugation at 3901g using an Amicon Ultra-15 10K (Milipore). The concentrated solution containing the target protein was injected onto a HiLoad 16/60 Superdex-75 molecular exclusion column (Cytiva) previously equilibrated in 20 mM HEPES pH 7.4, 200 mM NaCl and 1 mM DTT. Protein was eluted isocratically with a flow rate of 0.3 mL min^{-1} at 1 CV. The presence and purity of $CNNM4_{cNMP}$ was confirmed by SDS -PAGE and mass spectrometry. The purest fractions were selected for concentration on Amicon Ultra-15 10K and left at a concentration of 25 mg mL^{-1}.

1.3.1.2. *Hs*CBSΔ516-525

The cystathionine-β-synthase from human construct containing a deletion in region 516-525 was cloned into the pET28 vector according to the protocol described in [104] containing a six-histidine tail at the C-terminal end of the protein. The protein vector of interest was transformed into BL21- GOLD competent cells (DE3) according to the protocol described in previously section 1.3.1.1. A colony was grown with 150 mL LB containing 50 µg mL^{-1} kanamycin at 310K overnight. The culture was inoculated in four 5L Erlenmeyer flask (20 mL of inoculum were added in each flask) containing 2L of LB supplemented 0.1 mM ferric chloride ($FeCl_3$), 0.0025% pyridoxine-HCl, 0.001% thiamine-HCl, 0.3 mM δ-aminolevulinic acid and 50 µg mL^{-1} kanamycin. Cultures were allowed to grow at 310 K until OD_{600} of approximately 0.8 was reached, then they were induced with 0.5 mM IPTG and shaken overnight at 310K.

The pellet obtained by centrifugation of the cultures was placed in lysis buffer (50 mM Tris pH 8, 300 mM NaCl, 50 mM imidazole, 1 mM TCEP (tris (2-carboxyethyl)phosphine), 0.1 mM PMSF, 100x Triton (1x), 1 mM benzamidine and DNAse) and sonicated, keeping the sample on ice, following the same protocol as in section 1.3.1.1. Thereupon, the sample was ultracentrifuged at 186 009 g for 1 hour in an Optima L-90K ultracentrifuge (Beckman Coulter) with a 45Ti rotor (Beckman Coulter). The supernatant was injected onto a 5 mL HisTrap HP affinity column containing immobilized nickel (Ni^{2+}) (IMAC), taking advantage of the presence of a histidine tail previously equilibrated with10 CV of 50 mM Tris pH 8 buffer, 300 mM NaCl, 50 mM imidazole and 1 mM TCEP. Protein was eluted by applying a 20 CV gradient and using 50 mM Tris pH 8, 300 mM NaCl, 300 mM imidazole, and 1 mM TCEP buffer. The presence of *Hs*CBSΔ516-525 was confirmed by SDS-PAGE.

Fractions containing the protein of interest were pooled and injected onto a HiTrap Q HP anion exchange column (Cytiva) previously equilibrated with 10 CV of 50 mM HEPES pH 7.5 and 1mM TCEP and connected to an AKTA-FPLC at 277K. Impurities were removed while protein was retained on the column, the latter was eluted with buffer containing 50 mM HEPES pH 7.5, 1M NaCl and 1mM TCEP. The presence of *Hs*CBS was confirmed by SDS-PAGE. The protein was concentrated to 10 mL using Amicon Ultra-15 10K to prevent protein precipitation. Three HiLoad 16/600 Superdex-200 (Cytiva) molecular exclusion chromatographies were performed, previously equilibrated in 20 mM HEPES pH 7.4, 200 mM NaCl and 1 mM TCEP, and an isocratic flow rate of 1 CV at 0.3 mL min^{-1} was maintained. The presence of the protein of interest was confirmed by SDS -PAGE followed by mass spectrometry. The purest fractions were selected and concentrated to a concentration of 15 mg mL^{-1} using Amicon Ultra-15 30K. Aliquots were frozen by immersion in liquid nitrogen and stored at 193K.

1.3.1.3. MJ1004

The amplified DNA encoding MJ1004 protein was cloned into the pET101/D- TOPO vector (Invitrogen) and transformed into the Rosetta strain according to the protocol in section 1.3.1.1. The starter cultures were grown at 310K overnight in a flask containing 150 mL of LB supplemented with 100 µg mL^{-1} ampicillin and 25 µg mL^{-1} chloramphenicol. The protein growth was scaled up to 12L of LB distributed in six Erlenmeyer flask. Each flask contains 2L LB medium, 20 mL of starter culture, 100 µg mL^{-1} ampicillin and 25 µg mL^{-1} chloramphenicol.

Purification was performed in the following steps: 1) Bacterial lysate; the pellet was resuspended in a buffer containing 50 mM HEPES pH 7, 1 mM TCEP, 0.1 mM PMSF, 1 mM benzamidine and DNAsase and then sonicated, keeping the sample at 277K to avoid overheating the sample, following the same protocol as in section 1.3.1.1. The mixture was ultracentrifuged at 186 009 g for 1 hour at 277K using a 45 Ti rotor. 2) Anion exchange chromatography: the supernatant was injected onto a 5 mL HiTrap SP HP column previously equilibrated with 50 mM HEPES pH 7 and 1 mM TCEP buffer. Subsequently, the protein was eluted by applying a 20 CV gradient of buffer with 50 mM HEPES pH 7, 1 mM TCEP and 1M NaCl. The presence of the protein of interest was confirmed by SDS -PAGE followed by mass spectrometric analysis. Fractions were pooled and concentrated using an Amicon Ultra-10K. 3) Heat shock; since this is a hyperthermophilic protein, we heated the sample at 348K and centrifuge at 18 000g for 5 minutes. Impurities precipitated at the bottom of the Eppendorf and we removed the supernatant containing the target protein. 4) Molecular exclusion chromatography Hi Load 16/60 Superdex-75 (Ge Healthcare). The supernatant was filtered with a 0.22 µm filter and injected into the gel filtration column previously equilibrated with 50 mM HEPES pH 7, 200 mM NaCl and 1 mM TCEP. The sample was eluted isocratically at 1 CV. The presence and purity of MJ1004 was confirmed by SDS -PAGE and mass spectrometric analysis. The purest fractions were selected and concentrated using an Amicon Ultra-10K to a protein concentration of 37 mg mL^{-1}. Subsequently, the protein was aliquoted and stored at 193K until use.

The suitable concentration for the crystallization assays of each protein was decided after evaluating their solubility in testing solutions of the PCT Pre-crystallization Test from Hampton research (https://hamptonresearch.com/product-PCT-Pre-Crystallization-Test-10.html). The final concentration of the target proteins was 9.45 mg mL^{-1}, 13 mg mL^{-1} and 37 mg mL^{-1}, for *Hs*CNNM4$_{45-730}$, *Hs*CBSΔ516-525 and MJ1004 respectively.

1.3.2. Complementary techniques associated with protein purification

1.3.2.1. Protein electrophoresis

Analysis of the studied proteins in the different purification steps was confirmed by acrylamide gel electrophoresis in presence of sodium dodecyl sulphate (SDS-PAGE). Depending on the protein to be visualized, gels with a polyacrylamide percentage of 10 to 15% (w/v) were used. Samples were mixed with Laemmli loading buffer 2x (Bio-Rad) which contains 126 mM Tris-HCl pH 6.8, 20% glycerol, 4% SDS and 0.02% bromophenol blue. 10mM of 2-mercaptoethanol was added into the samples. The samples were

heated at 368 K during 5 minutes and centrifuged at 18 000 g at room temperature previously to be loaded into the gel. Precision Plus Protein ™ All Blue Standards (BIO-RAD) was used as molecular weight marker. Electrophoresis was performed at 200V with a standard running buffer (25 mM Tris, 190 mM glicine and 0.1% (w/v) SDS). Gels were stained with ProBlue Safe Stain@ (Giotto Biotech).

1.3.2.2. Determination of standard protein parameters

Standard protein parameters, such as the isoelectric point (pI), molecular weight (Mw), or extinction coefficient (ε_{280}) (**Table 1.1**) were determined using the online available ExPASy Bioinformatic Resource Portal (https://web.expasy.org/protparam/) [105].

Table 1.1. Number of aminoacid residues, molecular weight (Mw), pI and ε_{280} of the purified proteins

Protein	# of amino acids	Mw (Da)	pI	ε_{280} (M^{-1} cm^{-1})
C-*Hs*CBSΔ516-525	548	60522.4	6.19	54430
CNNM4$_{CNMP}$ (545-730)	186	20900	9.01	17880
MJ1004	214	24584.97	9.01	25440
***Tg*CBSΔ466-491**	488	53057.05	6.21	42400
***Tg*CGL**	417	45926.62	6.36	30370
***Tg*CGLN360S**	417	45899.59	6.36	30370

1.3.2.3. Determination of protein concentration

Purified protein concentration was determined by Nanodrop. This method calculates the concentration from the absorbance of the protein at 280 nm using its theoretical molar extinction coefficient provided by the ProtParam tool ExPASy Portal (**Table 1.1**). The extinction coefficient in an aqueous solution was calculated from aminoacids composition; number of tryptophanes (n_{Trp}), number of tyrosines (n_{Tyr}) and number of cysteines (n_{Cst}) (**Equation 1**).

$$E_{Prot} = (n_{Tyr}.\ \varepsilon_{Tyr}) + (n_{Trp}.\varepsilon_{Trp}) + (n_{Cst}.\varepsilon_{Cst}) \qquad \textbf{Equation 1}$$

Where at 280 nm ε_{Tyr}= 1490, ε_{Trp}= 5500 and ε_{Cst}= 125. The protein absorbance at 280 nm was measured using a Nanodrop and the protein concentration was determined by the Lambert-Beer Law (**Equation 2**):

$$Abs_{Prot} = \varepsilon_{Prot}.\ C.\ l \qquad \textbf{Equation 2}$$

1.3.2.4. Sequence comparison

The amino acid sequence of CBSs and CGLs across different organisms and the comparison with other members of the family of PLP dependent enzymes was done with Clustal Omega (https://www.ebi.ac.uk/Tools/msa/clustalo/). The graphic representation of sequence alignments was done with Chimera [106].

1.3.3. Protein crystallization

Taking into account the enormous difficulties encountered in previous studies to get the first positive crystallization hits of the three selected proteins, and to reduce the cost and time of the experiments, we focused our experimental approach on a commercial screen of solutions that yielded positive hits for the three target molecules, and from which optimal conditions were further tuned. The protein crystallization experiments were repeated three times for each of the model proteins and type of surface. All experiments were performed on the same day, with the same solutions, and subjected to the same external conditions. The crystallization scans were done using the PEG RX 1, 2 screen from Hampton Research Corp (REFs HR2-082 and HR2-084). The selection of this commercial screen is based on previous studies of our group showing that the buffered solutions are within the range of pH, precipitant and salt concentrations that yield well-diffracting crystals for the three analyzed proteins [104,107,108]. Crystallization drops were setup using the sitting-drop vapor-diffusion technique in 96-well MRC crystallization plates (Molecular Dimensions Ltd.). One prisma-shaped tablet of the corresponding surface (1000x500x200 micrometers) was placed manually in the seat of each plate with the help of fine-tip forceps. The precipitant solutions were subsequently dispensed in the reservoirs with the help of a TECAN Freedom EVo robot (Tecan Group Ltd.). Finally, 100 nL of protein solution at a fixed concentration were mixed with 100 nL of precipitant solution and placed in each well using a MOSQUITO liquid handling robot (TTP Labtech Ltd.). The resulting 200 nL drops were equilibrated over a reservoir volume of 50 µL at a constant temperature of 291K and covered entirely the surface tablets. The trays were sealed with ClearVue Sheets (Molecular Dimensions Ltd.). The presence of crystals was visually inspected using a MZ12.5 light stereomicroscope (Leica).

1.3.4. Manufacturing of patterned polycarbonate and polysulfone surfaces

Two high throughput manufacturing technologies: Thermal roll to roll nanoimprint lithography (T-R2RNIL) and Laser Ablation (LA) were considered for producing surface patterns on polycarbonate (PC) films (0.150 mm thickness) selected as substrate for protein crystallization. The PC film (Lexan 8010MC, 175 µm thickness) was provided by PTMTEC and surface patterning was performed on both sides of the film. T-R2RNIL process was carried out by a laboratory scale roll to roll imprinting machine, composed of a thermal module (R2R100UV_T Table, PTMTEC Oy). The imprinting speed was set to 0.08 m/min while temperature and pressure values were tuned to reach high-quality replication. Due to its Tg (around 150 °C), a temperature value and an imprinting force of 190°C and 5,000 N was applied, following the manufacturing parameters considered in our previous work [109]. Laser Ablation (LA) of PC sheets was carried out by means of a picosecond pulse Nd:YVO4 laser (RAPID: Lumera Laser), which is integrated in a micromachining workstation by 3D-Micromac. LA was carried out considering a laser wavelength of 355 nm, pulse energy of 7 µJ, frequency of 250KHz and laser scanning feed rate of 600 mm/s. The principal advantage of LA technology or "cold" ablation process, which turns solid into plasma, lies in minimizing the thermal effects without changing the properties of the material. The extreme intensities and short timescale at which ultrashort pulsed laser operate [110,111], allows contactless and single step process, and it is not require an expensive vacuum equipment. Laser technology was also applied to cut the PC films in the final dimensions used for the protein crystallization tests (1 x 0.5 mm^2).

Four different pattern geometries were manufactured for this work, covering the submicro- and micro-scale (see results section 1.4.1). In the case of T-R2RNIL, the pattern geometries of the nickel stamps (0.1 mm thickness) used for the replication process are the following: (i) *Shark-skin* (SS) (depth: 3 µm, width: 2 µm, pitch: 4 µm) mold (provided by Sharklet Technologies [*https://www.sharklet.com/*]; (ii) *Hexagonally ordered Moth-eye* (ME) shaped holes (provided by NIL Technology ApS [*https://www.nilt.com/*]) of 350 nm depth and 250 nm pitch; (iii) *Laser Grooves*: A hierarchical groove-pattern (25 µm width, 16 µm interdistance and 8 µm depth) was produced directly on the PC or the PSU substrate. This pattern contained micro and submicro-scale features as it has been reported in previous studies [89,112].

1.3.5. Stamps antisticking treatment.

The nickel stamp was treated by oxygen plasma and immersed for 2 h in a solution of perfluoro-octanephosphonate (Sigma-Aldrich) diluted in tert-Butyl methyl ether (tBME) (Sigma-Aldrich) to a concentration of 10 mg mL^{-1}. After that, the stamp was thoroughly rinsed with tBME and dried in a stream of nitrogen.

1.3.6. Characterization of Surface patterns

Surface patterns on PC surfaces were characterized by scanning electron microscopy SEM (Karl Zeiss XB1540, Jena, Germany), Atomic Force Microscopy AFM (Solver P-47 PRO, NT-MDT Spectrum Instruments, Moscow, Russia) and confocal microscopy (Sensofar SNEOX, Barcelona, Spain).

1.3.7. Interfacial energy (Contact angle) of the engineered surfaces

A goniometer (SURFTENS Universal, OEG GmbH, Frankfurt, Germany) was used to characterize the wettability properties of the patterned PC surfaces by measuring the contact angle (θ) of a protein crystallization solution (*Hs*CBS protein) droplet of 5 µL. After 1 min of stabilizing, a digital camera was used to record the shape of the droplet.

1.4. RESULTS

1.4.1. Surface Patterning and characterization of polycarbonate (PC) and polysulfone (PSU) heteronucleants.

In 2001, a pioneering work by Chayen *et al*. was first in bringing attention on the properties of porous materials as nucleation-inducing agents [51]. Since then, numerous studies have confirmed their findings [32,38,57]. However, the mechanisms underlying the heteronucleant-induced crystallization remain poorly understood [63]. Some authors have postulated that hydrophobic and rough surfaces showing topographic irregularities, facilitate the adsorption of molecules on their pores and crevices, thus favouring local concentration increases that in turn promote clustering and crystal growth [40,56,63].

Taking into account that thermoplastic polymers can be selected based on their optical transparency, manufacturability and aging resistant to a variety of external factor such as pH, temperature and UV radiation, we found reasonable to hypothesize that materials such as polycarbonate (PC) or polysulfone (PSU) might be attractive cost-effective and inert heteronucleants suitable for the buffered conditions commonly used in protein crystallization. PC is a durable transparent amorphous termoplastic known for its high chemical and impact resistance and advantageous optical properties (https://www.sciencedirect.com/topics/chemical-engineering/polycarbonate).

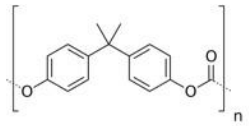

Polycarbonate (PC)

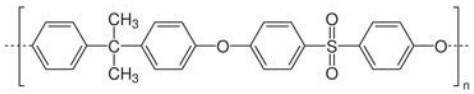

Polysulfone (PSU)

PSU shares many of the physicochemical properties of PC but shows a lower negative surface charge magnitude and slightly higher glass transition temperature (https://www.sciencedirect.com/topics/chemical-engineering/polysulfones) [113]. To confirm our hypothesis, we evaluated the effect of incorporating specifically designed patterned PC and PSU surfaces in vapour diffusion crystallization experiments for three challenging proteins. The outcomes were compared with parallel experiments obtained in (i) standard homogeneous conditions (absence of foreign agents); (ii) the presence of smooth (unpatterned) PC and PSU surfaces; and (iii) with the commercially available Naomi´s nucleant (NN, from now on) (www.moleculardimensions.com/products/nucleants-seeding-and-phasing-kits), which corresponds with a porous bioglass (shown in **Fig. 1.5, F**).

PC films were patterned considering five different topography designs, baptized as *Moth-eye (ME)*, *Shark-Skin (SK), Laser Ablated Grooves (LA), Ripples and Micropillars* (**Fig. 1.5, A** to **D**). The manufacturing technologies and protocols applied to the production of those surfaces are described in section 1.3.4. While the ME and SK topography were manufactured via NanoImprint Lithography (NIL) technique, considering industrially available stamps and optimizing the replication process on the polymer surface, the LA was directly patterned on the polymeric surface by considering the Laser Ablation technology.

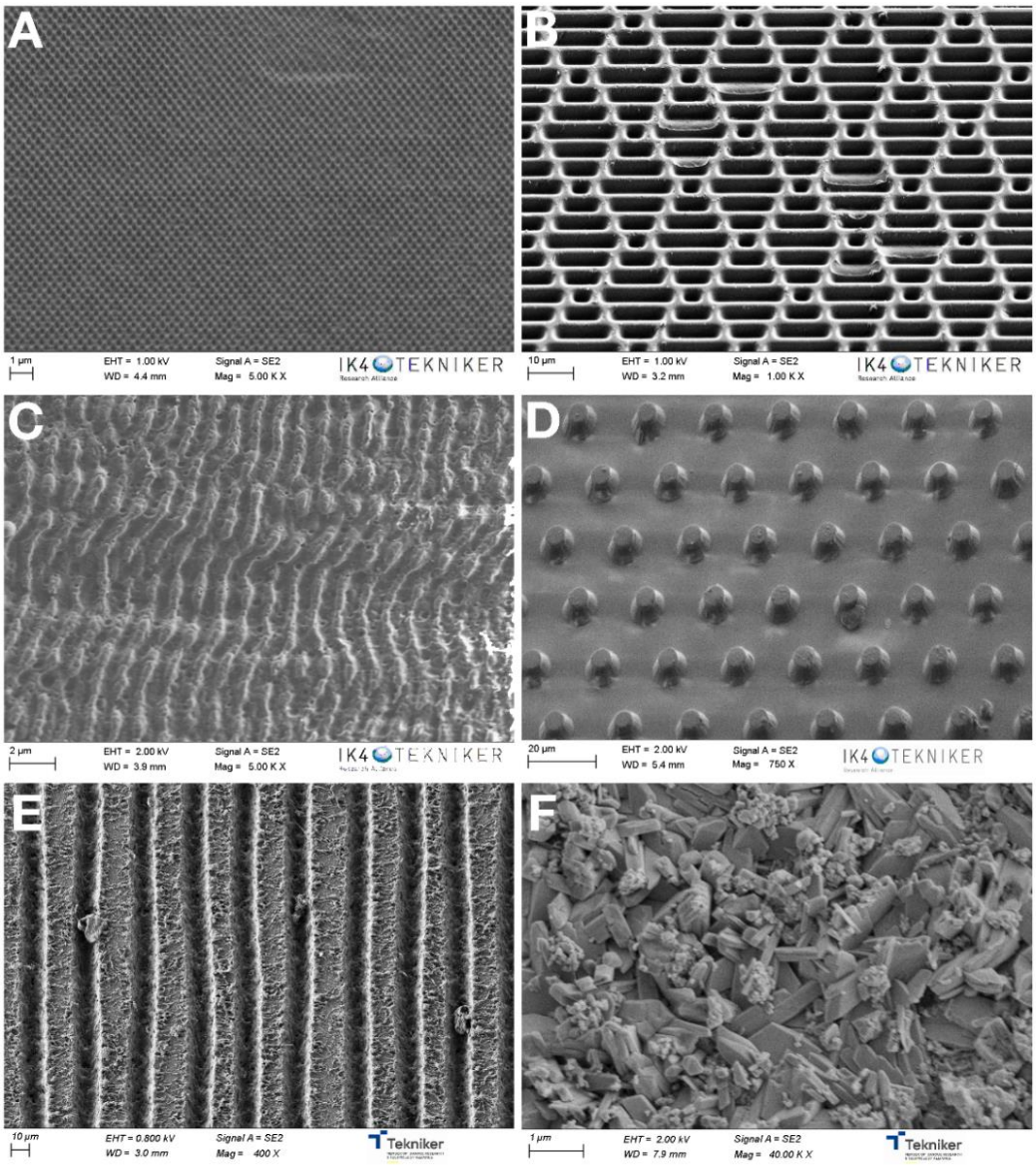

Figure 1.5. SEM characterization of PC patterned surfaces manufactured. *(**A**) Moth-eye (ME); (**B**) Shark-Skin (SK); (**C**) Ripples; (**D**) Micropillars; (**E**). Laser ablated grooves (LA); (**F**) Naomi´s Nucleant (NN).*

Before proceeding with crystallization experiments, we first characterized each of the patterned surfaces in terms of light transparency, hand ability and wettability, evaluating their suitability for standard vapour diffusion protein crystallization experiments. The main features we took into account were: the transparency under optical magnification with white light, the birefringence of the surface, the electrostatic properties in normal laboratory handling, the faculty to place with fine tweezers, and wettability considering a specific protein solution. The transparency of a surface is crucial to be able to evaluate the occurrence of crystalline nuclei when analyzing crystallization droplets under the microscope. On the other hand, a birefringent surface under white light makes the identification of possible microcrystals uncomfortable, due to the continuous emission of colored flashes when the crystallization boxes are manipulated under the microscope. In addition, due to the millimeter size of the droplets and tablets, a highly electrostatic surface also makes it very difficult to handle the tablets with tweezers. The same applies to a surface that is too soft, that is deformed or altered in topology when manipulated by the experimentalist. Finally, and due to the fact that crystallization is carried out by vapour diffusion experiments, thus a controlled evaporation of water from a drop, the hydrophobicity of the surface plays an important role in the evaporation rate, and consequently in the crystallization outcome.

The hydrophobicity of a particular surface can be measured in terms of its *wettability*, defined as the ease of spreading of liquid on a surface. This ability is directly related to the intermolecular forces between the phases in contact [114,115]. Typically, wettability can be estimated by contact angle measurements. The contact angle (θ) indicates the degree of wetting when a solid and liquid interact, and is defined as the angle formed by the intersection of the liquid-solid interface and the liquid-vapor interface (geometrically acquired by applying a tangent line from the contact point along the liquid-vapor interface in the droplet profile) [116] (**Fig. 1.6**). A complete spreading ideally surface shows a $\theta = 0°$. Good wetting, and incomplete wetting occur at values of $\theta < 90^o$ and $\theta = 90^o$, respectively. Thus, small contact angles ($\theta \ll 90°$) indicate wetting favorable surfaces, where the drop spreads on over a large area. In contrast, large contact angles ($\gg 90°$) indicate incomplete wetting, where the liquid beads on the surface, so the fluid barely contacts the surface. In the latter case the wetting of the surface is unfavorable so the fluid forms a compact liquid droplet. In general, surfaces with $\theta < 90^o$ are considered hydrophilic, while those with $\theta > 90^o$ are typical hydrophobic materials. Superhydrophobic surfaces show $\theta >> 150°$, and nonwetting occurs at $\theta > 180^o$.

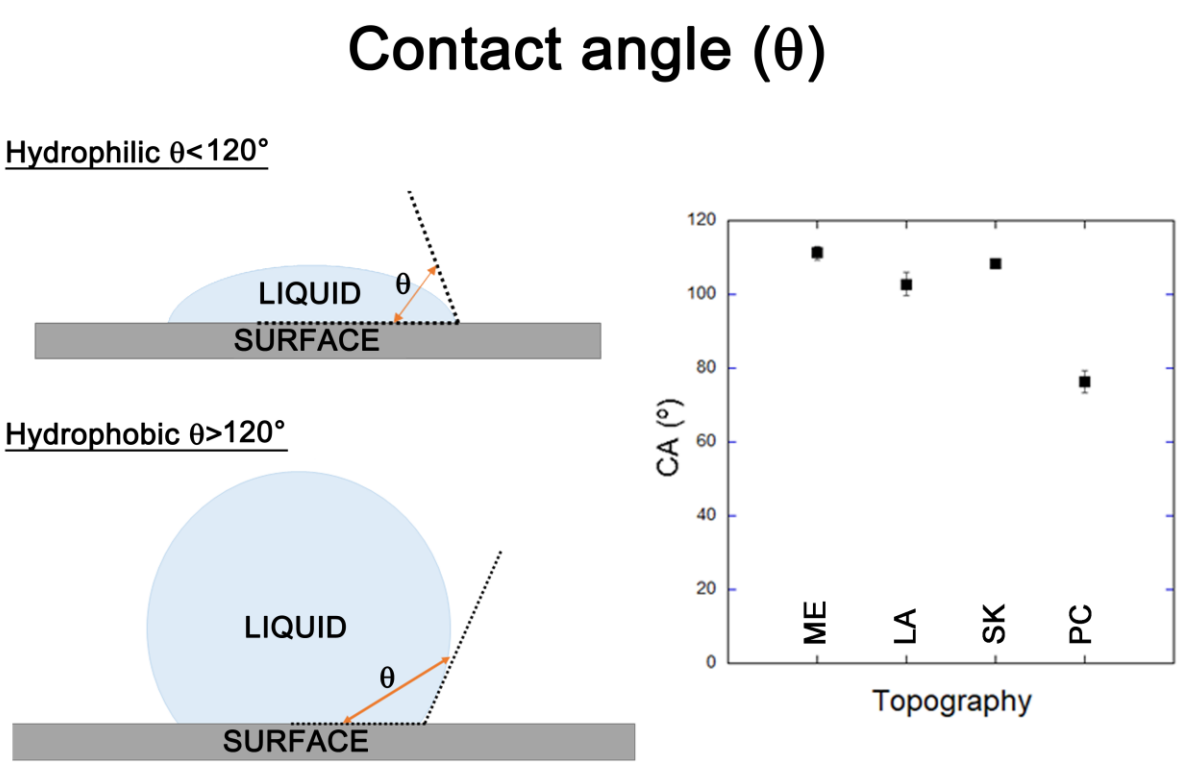

Figure 1.6. Wettability of the surfaces. *Contact angles (CA, θ) formed by liquid drops on the target surfaces were lower than 120º, but in the unprinted smooth polycarbonate film, which shows a contact angle =75º. θ values < 90º classify the films as hydrophilic. The liquid used to measure the values of contact angle was a protein solution of HsCBSΔ516-525 (13 mg mL^{-1}) in 20 mM HEPES pH 7.4, 200 mM NaCl and 1mM TCEP.*

Table 1.2. Contact angle of the imprinted surfaces.

Patterned surfaces	Measure contact angle (°)	Average contact angle (°)
Laser Ablated Grooves	107.5 104.5 96.6	102.9 ± 5.7
PC unpatterned	70.6 77.5 80.9	76.3 ± 5.3
Shark-Skin	108.5 105.8 110.5	108.3 ± 2.4
Moth-eye	114.6 111.1 108.1	111.3 ± 3.2

Two additional parameters used to describe the texture of a surface and its ability to interact with other materials or fluids, are the ***Roughness** (**Sa**)* and the ***Aspect Ratio** (**AR**)*. Any surface embodies a complex shape made of a series of peaks and troughs of varying heights, depths, and spacings. Surface roughness is defined as the shorter frequency of real surfaces relative to the troughs. Metrically, roughness is typically considered to be the high-frequency, short-wavelength component of a measured surface. Overall, roughness quantifies the deviations in the direction of a normal vector of the surface from its ideal form. The surface is considered ***rough*** if these deviations are large, while the surface is described as ***smooth*** if the deviations are small (**Fig. 1.7**).

On the other hand, the ***Aspect ratio** (**AR**)* of a solid surface is defined as the average ratio of the depth to the width of its protuberances and cavities (considering a homogeneously patterned surface) and it is related with topography (**Fig. 1.7**). The aspect ratio directly influences the wettability of the surface, and consequently the shape of a liquid drop deposited on it [65,117]. This is particularly important in protein crystallization, as the kinetics of water evaporation from a drop in a vapour diffusion experiment directly affects the nucleation event and the diffraction quality of the grown crystals.

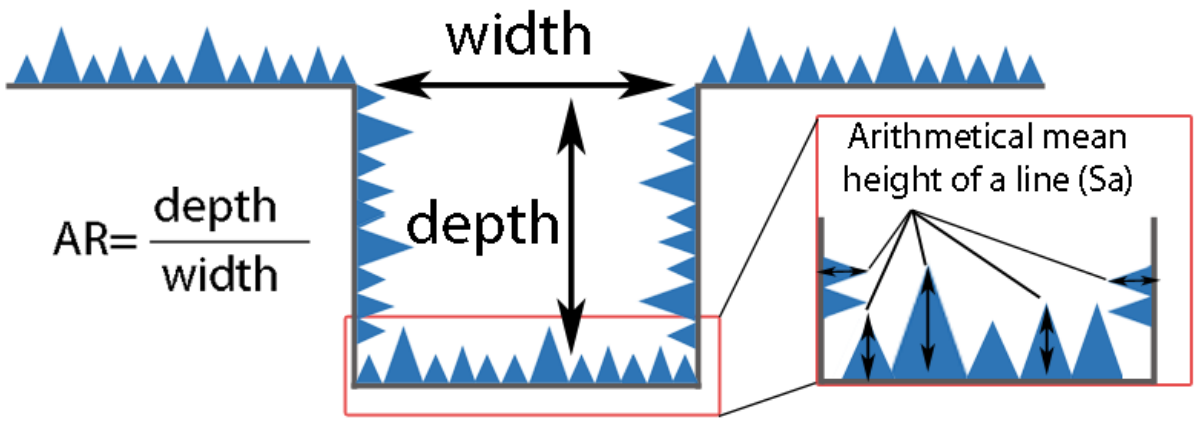

Figure 1.7. Descriptive scheme of the measurements of roughness (Sa) and aspect ratio (AR). *Line profile of a hypothetical patterned surface showing the geometric parameters such as depth and width (used to calculate the aspect ratio). The roughness of the tablet is represented with blue peaks, present along the whole surface. The region framed in red represents the roughness measured at the bottom of a cavity and is calculated from the average of the absolute heights values of the peaks. Note: roughness is determined by optical profilometry methods, corresponding to an isolated area of the surface.*

Accordingly, and aimed to broaden the characterization of our surfaces, we measured their roughness and aspect ratio (**Table 1.3**). The analysis confirmed the higher AR value was obtained for the SK topography. It should be noted that the roughness values for Moth-eye and Shark-skin are the same as PC unpatterned, because the same roughness values of this material and the stamp considered during the NIL replication process.

Table 1.3. Roughness and aspect ratio values of the patterned and unpatterned PC surfaces.

Patterned surfaces	Aspect ratio	Roughness
ME	0.05	Sa=11.83 nm
SK	1.64	Sa=11.83 nm
LA	0.30	Sa=0.10 µm
PC unpatterned	-	Sa=11.83 nm

1.4.1.1. Moth-eye Surface (ME)

The Moth-eye topography (**Fig. 1.5, A**), whose name is bioinspired from nature by its resemblance with the eyes of many insects, is a nanostructured repetitive array of cones (pillars) of different width and depth that can be described in terms of a hexagonal unit cell with **a-** and **b**-axis dimensions equal to the distance between the tip of two consecutive cones ("p" parameter in **Fig. 1.8**), and **c**-axis with the depth of each cone ("d" parameter in **Fig. 1.8**). In the insects, such array of nanostructures is formed by 200-300 nm sized pillars and provides exceptional optical performance by reducing the reflection while simultaneously enhancing night vision capability [118]. The excellent antireflection optical properties provided by this bio-mimetic pattern have contributed its widespread use for a wide variety of industrial purposes. Among the most common applications are laser systems, photovoltaics, LEDs, display screens, light emitting diodes (optic fibers), solar cells and antireflecting coatings (https://www.synopsys.com/photonic-solutions/product-applications/rsoft-optimization-nanostructured-moth-eye.html) [119–122]. Figure 1.8 shows the AFM (Atomic Force Microscopy) characterization of the ME replication patterned on the PC surface. The peak to peak distance was measured and reveals high x-y replicability, showing similar values than the ones provided by the NIL stamp manufacturer (p=0.26±0.022 µm) (Note: in this type of topography the values of pitch and width are identical, resulting in a w=0.26±0.022 µm). However the patterning transfer capability in the z-axis is very low (~4%: 12.64±1.04nm), which means that a proper optimization of the manufacturing process is required to reach higher replication of the stamp topography. However, this optimization has not been assessed in this work and the ME topography evaluated during the crystallization assays is the one

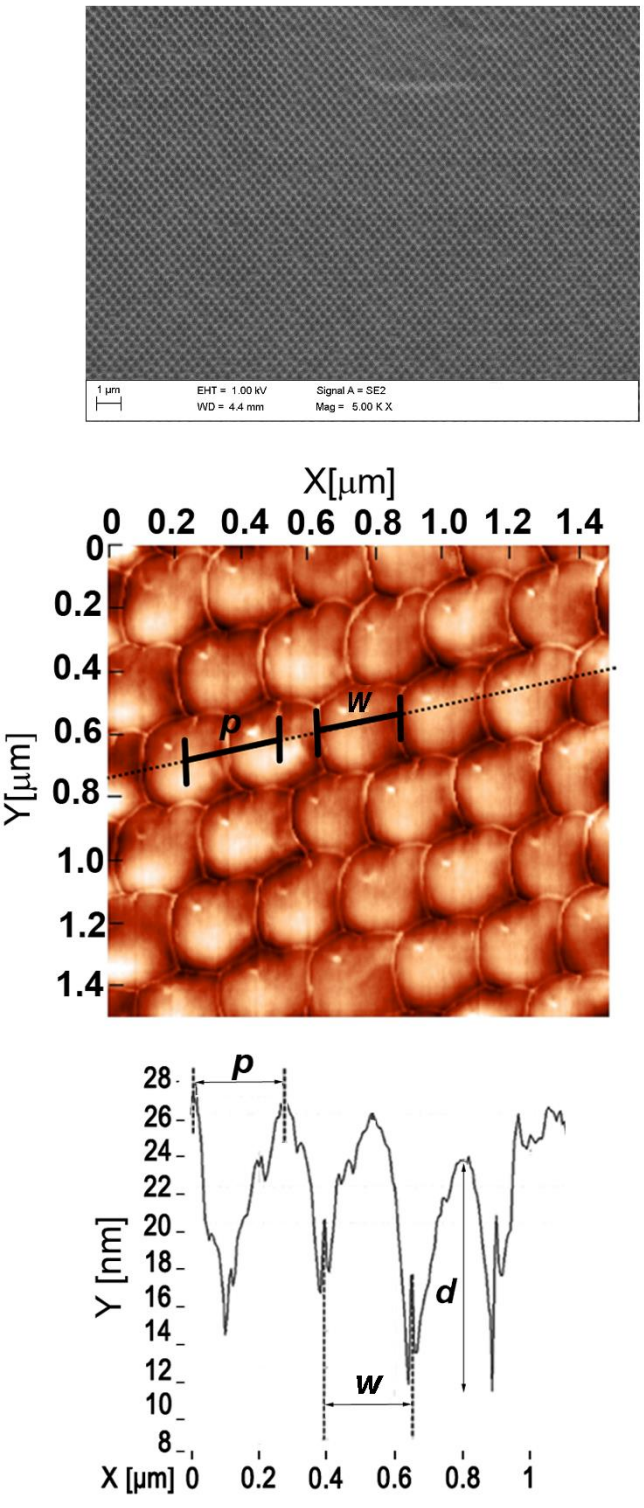

presented in Figure 1.8. The hydrophobicity (wettability) of the Moth-eye PC film, evaluated by measuring the contact angle of a water drop resting on the flat, horizontal surface, showed a contact angle of θ=111.3 $\pm$ 3.2 (**Fig. 1.6**), (**Table 1.2**), thus consistent with a hydrophobic surface. Importantly, the transparency of the Moth-eye PC surface under the white-light microscope was suitable for both, sitting- and hanging-drop vapour diffusion experiments (described in section 1.4.2.). Electrostatic properties were also considered appropriate for regular handling of the tablets with tweezers.

Figure 1.8. Moth-eye patterning. *(**Up**) SEM characterization of the Moth-eye polycarbonate surface. (**Middle**) AFM characterization (1.5x1.5 µm^2) of Moth-eye patterned PC surface. (**Bottom**) Line profile of selected region showing the geometrical parameters of the replicated features: pitch (p)= 0.26±0.022 µm, width (w)= 0.26±0.022 µm and depth (d)=12.64±1.04 nm.*

1.4.1.2. Shark-skin Surface (SK)

Shark-Skin terminology draws inspiration from the shape and pattern of the dermal denticles of sharskin, which presents milllions of microscopic features arranged in a peculiar diamond pattern (**Fig. 1.5, B**). Industrially, shark – skin patterned films are commerciallized by Sharklet Technologies (www.sharklet.com), being offered as an effective coating to prevent the formation of contaminating bacterial biofilms. This surface solution is also resistant to fouling organisms in the water including algae and barnacles. Structurally, this topography is made up of rhombic motifs (diamonds), divided inside by longitudinal cavities perpendicular to the longest axis. Figure 1.9 shows the Scanning Electron and optical confocal microscopic characterization of the replicated SK topography on the PC films used in our study. Values of depth (d=3.18±0.05 µm), width (w=1.95±0.24 µm) and pitch (p=3.95±0.1µm) are quite similar to the nominal ones reported by the NIL stamp manufacturer, which demonstrates the high transfer capability (x-y-z) of the NIL technology when micro-scaled features are considered. Similarly to the Moth-eye foil, the transparency and electrostatic properties were considered compatible with a regular handling by the experimentalist. The Shark-Skin film showed a contact angle of of θ=108.3 $\pm$ 2.4° (**Fig. 1.6**), (**Table 1.2**), consistent with a hydrophobic material.

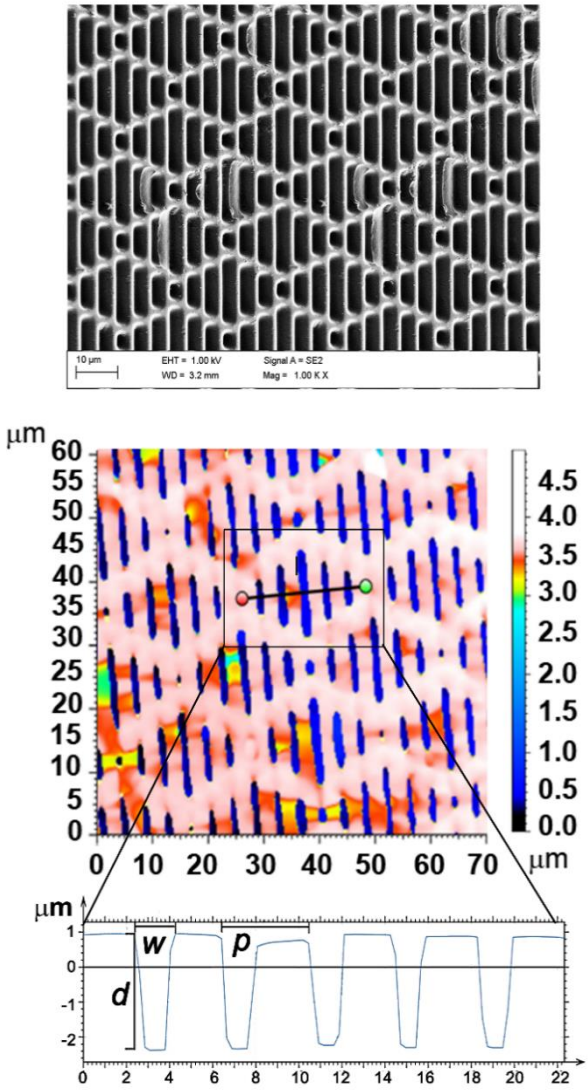

***Figure 1.9. Shark-Skin patterning**. (**Up**) SEM image of SK. (**Middle**) Confocal characterization of Shark-Skin patterned PC surface. (**Bottom**) Line profile of selected region showing the geometrical parameters of the replicated features: pitch (p)= 3.95±0.1µm, depth (d)=3.18±0.05 µm, width (w)= 1.95±0.24 µm.*

1.4.1.3. Ripples/Micropillars Surfaces

The next two PC imprinted surfaces that were evaluated as potential heteronucleants were baptized as *Ripples* and *Micropillars.* *Ripples*, mimics a regular sequence of waves with crests 0.5 µm in width, separated by valleys of approximately the same distance and depth (**Fig. 1.5, C** and **D**). The second surface, named as *Micropillars*, presented a hexagonal array of truncated-cones whose width ranged from 10 µm in the base to 5 µm in the vortex, separated from each other by approximately 20 µm. Prelliminary crystallization tests led us discard these two patterns due to different reasons. Ripples resulted highly opaque under the microscope once splitted in tablets, and thus impeded a user-friendly interpretation of hanging-drop crystallization outcomes. On the other hand, Micropillars did not yield significant crystallization outcomes when compared with controls in all preliminary crystallization assays, likely due to the lack of cavities in this imprinted film.

1.4.1.4. Laser Ablated Grooves (LA)

Based on the previous research works carried out by TEKNIKER in the field of cell-polymeric surface interaction as a function of the surface topography [86,89–92], a hierarchical (merging micro- and submicro-scale features) groove pattern was selected and manufactured on polymeric substrates (**Fig. 1.5, E**). Figure 1.10 shows the SEM and Confocal Microscopy characterization of the LA topography. As it was reported in previous publications, the remelted material ejected from the inner groove was deposited on both, the edges of the groove and the gaps between grooves. This effect contributes to the increment of the surface roughness (Sa=0.1 µm) compared to the one characteristic of the native (unpatterned) PC surface (Sa=0.012 µm), that might be enhance protein adhesion, triggers their crystallization. Another morphological aspect already reported in previous papers is the formation of micro-pores on the bottom surface of the grooves [91,92]. Based on the previous work as it was mentioned in the Introduction section, these features might also contribute to enhance the protein crystallization events. Pitch, width and depth values measured via confocal microscopy are indicated in the legend of the Figure 1.10. The wettability performance of this LA pattern has not shown significant differences (contact angle of θ=102.9 $\pm$ 5.7^{o}) (**Fig. 1.6**), (**Table 1.2**) compared to the one observed for ME and SK topographies.

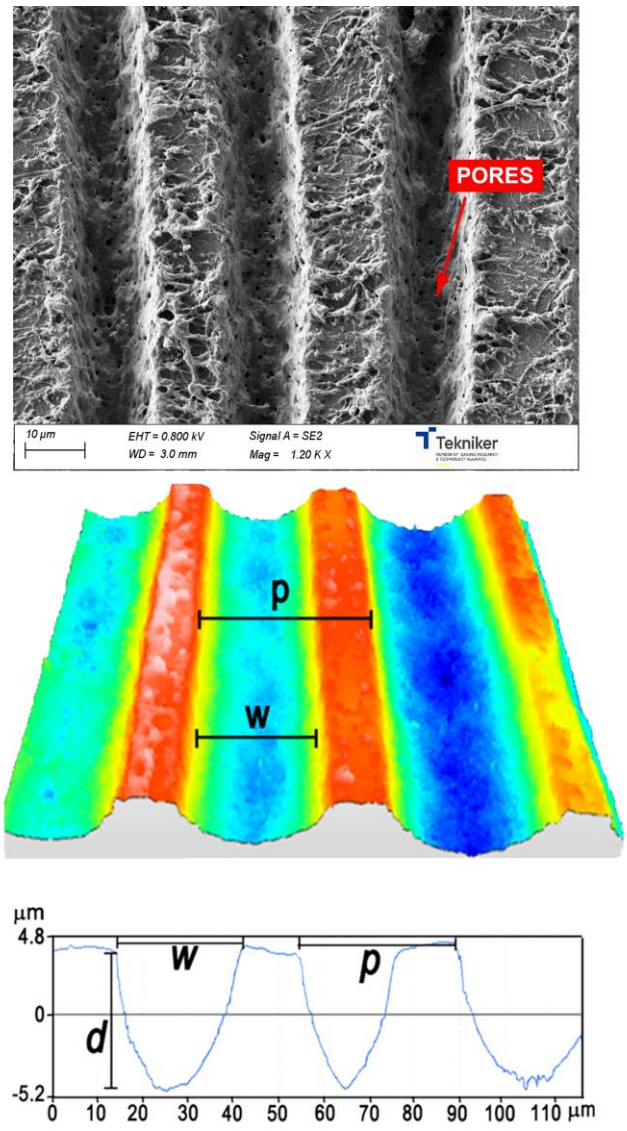

Figure 1.10. Laser Ablated patterning*. (**Up**) SEM image of LA pattern. Laser Ablation patterns on PC are characterized by hierarchical surface structures, showing micro- and submicro-scale features. The selected laser pulse energy, frequency and scanning feed rate led to pattern dimensions are indicated underneath. The presence of micropores is indicated by red arrow. (**Middle**) Confocal characterization of Shark-Skin patterned PC surface. (**Bottom**) Line profile of selected region showing the geometrical parameters of the pattern: pitch (p)= 39.8±0.27 µm, depth (d)= 8.04±0.25 µm, width (w)= 24.5±3.64 µm.*

1.4.1.5. Laser cutting of polymeric tablets

Polycarbonate (and Polysulfone) tablets used in the protein crystallization assays were patterned at both sides of the foil and, after that, small pieces (tablets from now on) were cut into the final dimension (1x0.5x0.15 mm^3) by using the same laser ablation technology that the one used for the production of the LA patterns. Hence, the resulting polymeric tablets contained two large opposite imprinted faces, and four side edges lacking any repetitive motif. However, far from being flat and smooth, these lateral sides showed bumps of plastic debris generated by the laser cut, which provide a non-negligible roughness, as well as high density of micropores.

Figure 1.11. and 1.12.C show the SEM image corresponding to the morphology of the laser cutting ditch produced during the manufacturing of the polymeric tables. The images shown the inhomogeneity on the surface topography of the crossed section as well as the presence of micropores (similar to the ones observed in the LA patterning) on the whole surface (**Fig. 1.11, B** *(up)*, corresponding to a zoom area indicated in **Fig. 1.11, B** (*bottom*)). The optical confocal microscopy characterization reveals an abrupt profile containing conical-shaped clefts between 1 and 10 µm wide, and a depth between 50 and 400 nm, as shown in Figure 1.12 and 1.13. The surface roughness parameter corresponding to the whole cross

section of the laser cutting ditch is Sa=1.83 µm, around 10 times higher than the values measured for the LA patterning and 100 times the values measured for the unpatterned PC.

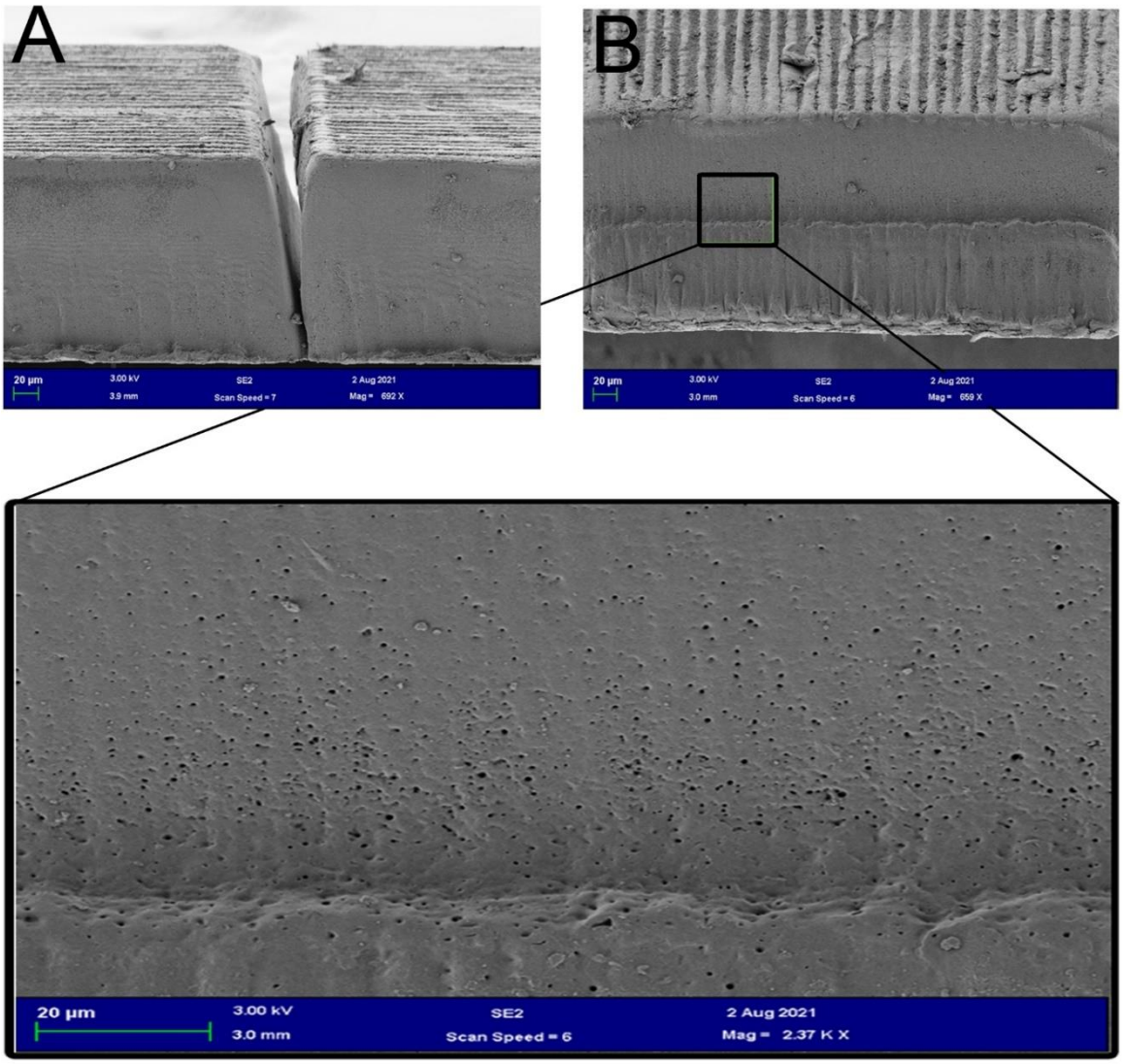

***Figure 1.11. SEM characterization of the laser cutting ditch on PC tables**. (**A**) Electron micrograph from the side of two tablets. (**B, up**) SEM characterization of the inhomogeneous region of the side, with the corresponding zoom view (**B, bottom**) showing the presence of micropores.*

A closer view further showed that the roughness is significantly higher at the edges. The rest of the face appears basically flat (**Fig. 1.12** and **1.13**)**.** As in the case of the LA pattern, the inhomogeneity on the surface topography of these edges of the polymer tablet, the higher values of their surface roughness and the presence of micropores might be contribute to enhance the protein crystallization events.

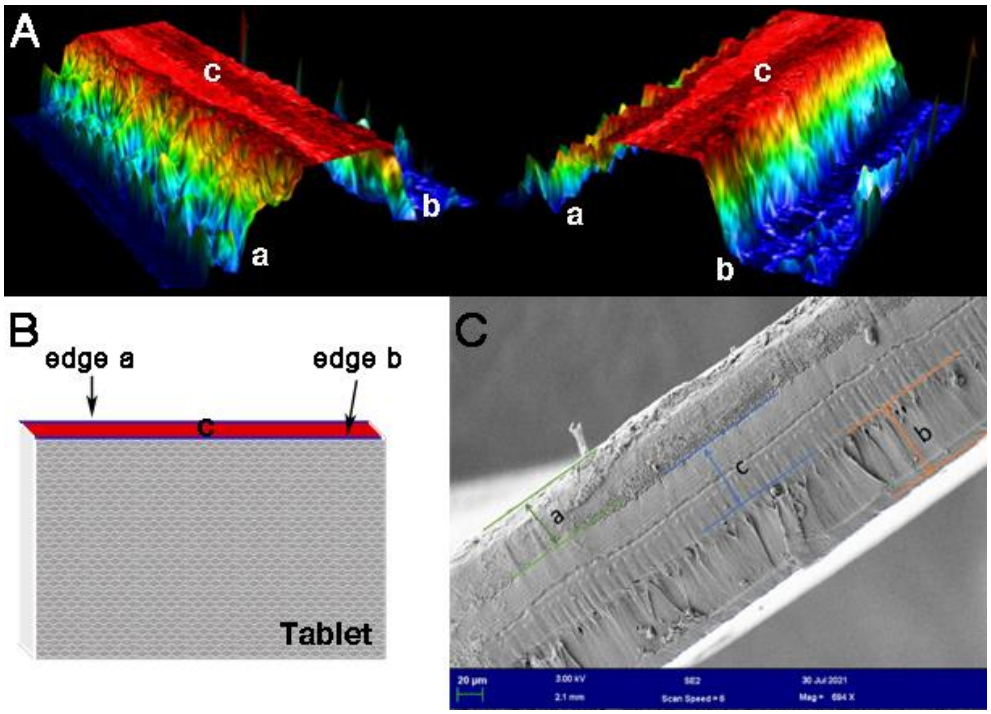

Figure 1.12. Profile of the tablet side face. *(**A**) Two different views of the tablet side face as seen by confocal microscopy. The edges "a" and "b" are colored in blue and green, respectively. The core of the face (c) is in red. (**B**) Representation of a tablet indicating the side face and its edges coloured with the criteria shown above. (**C**) SEM characterization of the edges "a", "b" and "c".*

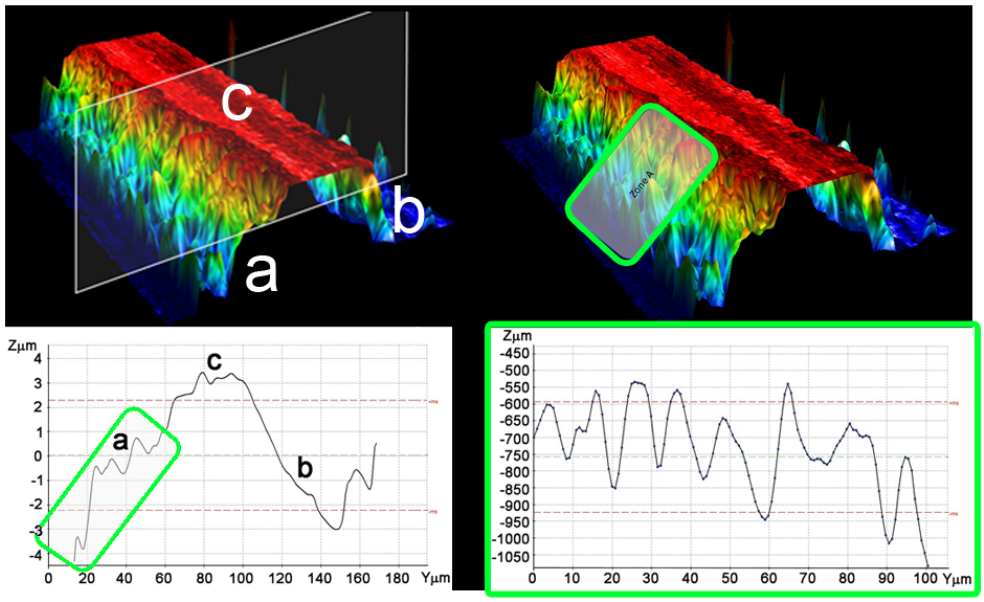

Figure 1.13. Profile of the tablet side face at a zone of the edge. *(**Left, up**) Section of the side face and (**left, bottom**) plot of its transversal profile. (**Right, up**) Confocal microscopy analysis of the pink squared zone "a". (**Right, bottom**) Zoom profile of the zone "a" green framed on the right and above.*

1.4.2. Experimental handling of imprinted surfaces in vapour diffusion crystallization assays.

Once the best candidate surfaces were selected, the next step was to adapt them for use in regular vapour diffusion crystallization experiments (excellent reviews on crystallization techniques can be found in [123,124]). For our purpose, two different strategies were followed:

(i) For the hanging-drop technique, the heteronucleant foil was cut in circles that were subsequently adhered to a commercial sheet prepared for automated dispensing of nanodroplets with a crystallization robot (https://store.sptlabtech.com/shop/product/4150-05600-viewdrop-ii-tm-96-well-plate-seals-for-hanging-drop-25-pack-114?category=93) (**Fig. 1.14**).

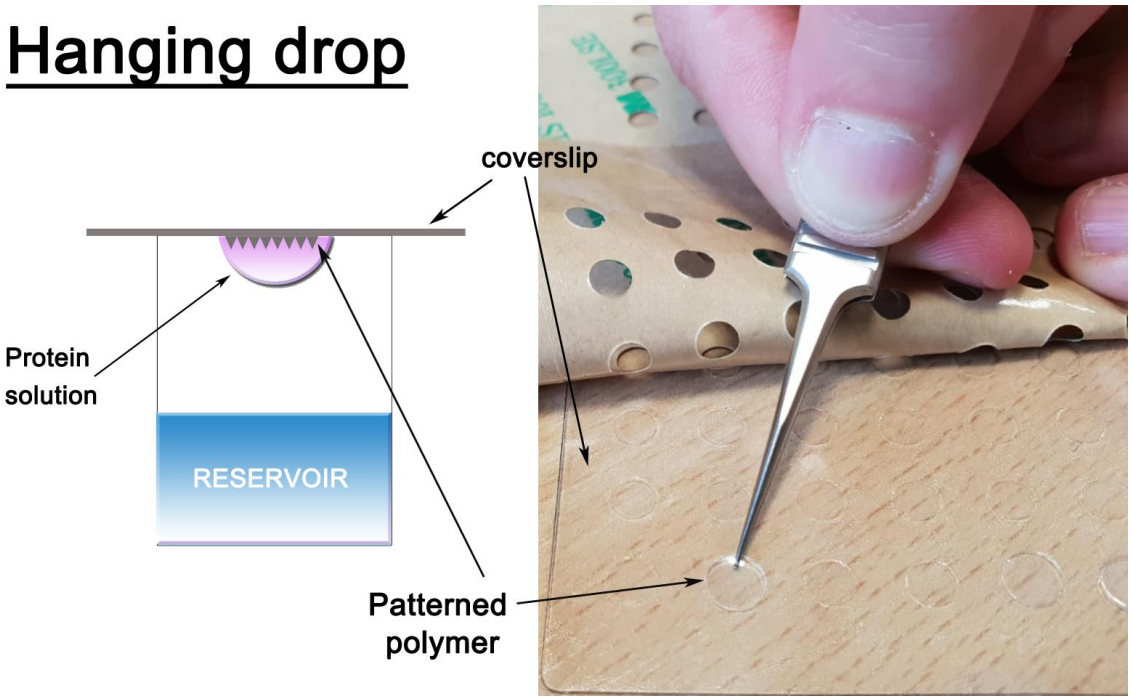

***Figure 1.14**. Experimental handling of patterned polymeric surfaces in hanging-drop crystallization assays.*

(ii) For the sitting drop technique, we fragmented the patterned foils into tiny tablets that could be deposited manually into the crystallization wells with the help of tweezers (**Fig. 1.15**). The size of the tablets was set according to the final volume of the crystallization drop, estimated to be 250 nanoliters, so that the tablet would be completely covered by the liquid dispensed automatically with the help of a crystallization robot (Mosquito from STP-Labtech, https://www.sptlabtech.com/products/liquid-handling/mosquito-crystal/).

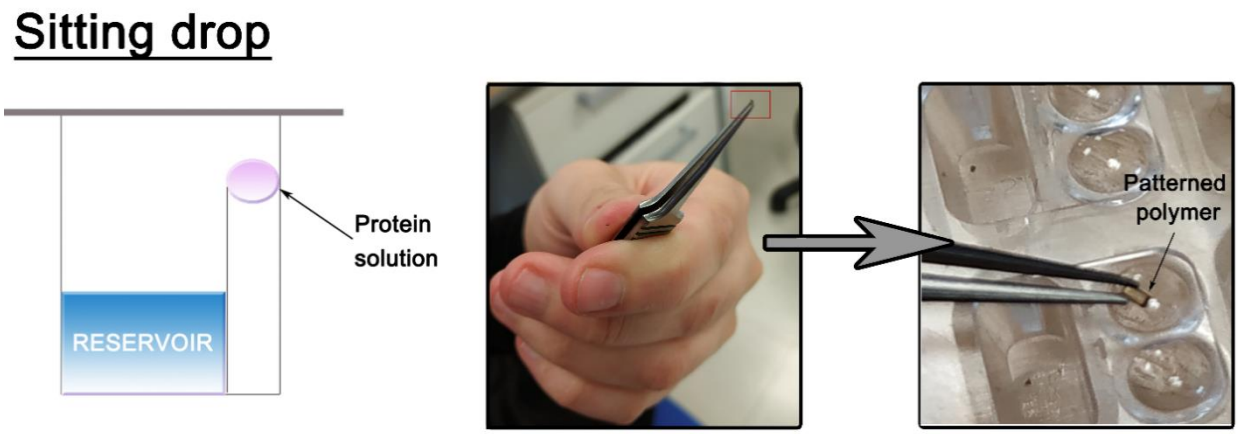

***Figure 1.15**. Experimental handling of patterned polymeric surfaces in Sitting-drop crystallization assays.*

1.4.3. Model proteins selected for the heterogeneous crystallization studies.

Three model proteins with different biological function, molecular weight, overall shape, surface electrostatic charge distribution and domain architecture, were selected as targets for the crystallization assays. All these molecules (**Fig. 1.16**) had posed an enormous challenge in past crystallization studies under homogeneous conditions [104,108,125], and share the common feature of including a so-called *Bateman module,* which has been widely studied by our laboratory [69] and others along the last decade [126]. Importantly, PEG RX 1,2 is one of the most commonly used screen in the early steps of the crystallization process,and so it was choosen for the evaluation of the imprinted surfaces. The proteins selected for our study were:

(i) A truncated construct (*Hs*CNNM4$_{545-730}$) containing the cytoplasmic Bateman module of the human magnesium transporter CNNM4 (residues 545-730; pI=6.41);

(ii) An engineered construct of human cystathionine β-synthase lacking residues 516-525 (*Hs*CBSΔ516-525, pI=9.01); and finally

(iii) Full-length protein MJ1004 from the archaea *Methanocaldocuccus jannaschii* (pI=9.01).

The Cyclin and CBS domain divalent metal cation transport mediator-4 (CNNM4), also known as Cyclin M4 or Ancient Domain Protein 4 (ACDP4), is the fourth member of the most recently identified proteins

involved in magnesium cation (Mg^{2+}) transport across the cell membranes. In humans, this family includes four integral membrane proteins (CNNM- 1 to 4) that show a strong homology to CorC, a bacterial magnesium/cobalt efflux protein [127]. The CNNMs show an expression pattern that varies significantly in different organs (https://www.proteinatlas.org/search/CNNM) [103,128,129]. For example, CNNM1 is mostly present in the brain and testis, while CNNM2 is detected in kidney and liver [127]. CNNM3 is ubiquitous and specially relevant in the heart [127]. CNNM4 is predominant in the brain, bone marrow, immune system, and very abundant in the intestinal tract [127,130]. The actual function of CNNM proteins still remains controversial [131–134]. CNNM4 is commonly considered as a basolateral Mg^{2+} extruder (likely a Na^{+}/Mg^{2+} exchanger) in the renal and intestinal epithelia [133,135].

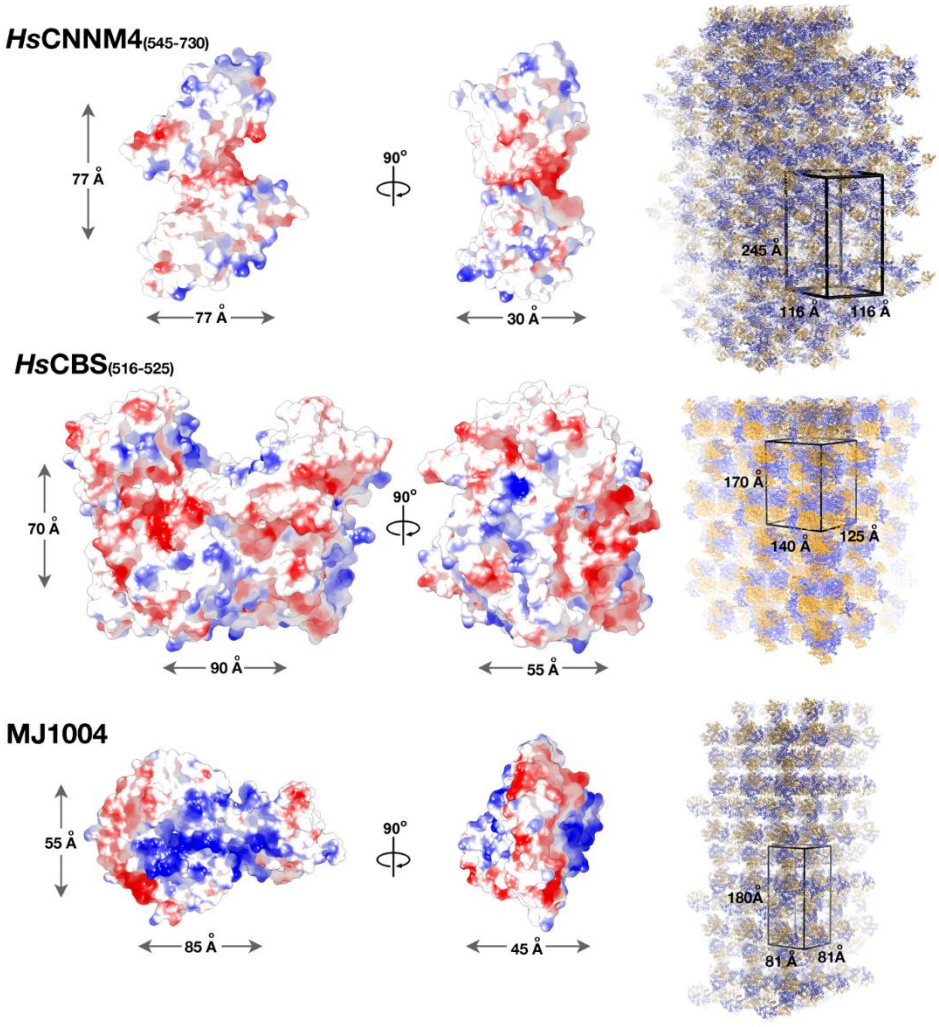

Figure 1.16. Target proteins used in the crystallization assays. *Surface representation of the electrostatic potential of each protein. Negative and positive charges are colored in red and blue, respectively. Neutral zones are colored in white. The three proteins exist as dimers in solution and in the crystals, whose the cells parameters and crystal packing are indicated on the right (the two complementary subunits of each dimer are colored in blue and orange, respectively). The approximate dimensions of each protein dimer, and of their crystals are indicated.*

However, some authors have alternatively proposed CNNMs as Mg^{2+} sensors [128] or homeostatic regulatory factors [131,136]. Yet, the key roles of CNNMs in maintaining Mg^{2+} homeostasis and in the development of Mg^{2+}-related pathologies are undoubted. Mutations in CNNM2 or CNNM4 cause recessively inherited dominant hypomagnesemia and renal Mg^{2+} wasting [128] or Jalili Syndrome, respectively [137–143]. Other disorders related to the altered activity of CNNMs include infertility [144,145], impaired brain development [146] along with neuropsychiatric disorders [147–150], and abnormal blood pressure levels [151]. Importantly, CNNM4 is involved in cancer progression [133,152] by associating with the highly oncogenic phosphatases of the regenerating liver (PRLs) and by promoting intracellular Mg^{2+} accumulation that favors tumor growth and metastasis [129,152,153]. Very recently, we have demonstrated that CNNM4 is overexpressed in non-alcoholic steatohepatitis (NASH) and promotes the export of Mg^{2+} from the liver. Importantly, the liver-specific silencing of Cnnm4 ameliorates NASH by reducing endoplasmic reticulum stress and promoting the activity of microsomal triglyceride transfer protein, highlighting CNNM4 as an attractive therapeutic target [154].

Cystathionine β-synthase (CBS), is the first enzyme of the reverse transsulfuration pathway, a metabolic pathway coupled to the methionine- and the folates- cycles, that allows the conversion of the essential amino acid methionine into L-cysteine (from now referred as cysteine), glutathione and other relevant molecules involved in maintaining the cellular redox balance. In mammals, this route represents the sole source of cysteine. An impaired CBS activity due to missence mutations in its amino acid sequence, results in classical homocystinuria (OMIM 236200), a rare, autosomal recessive inherited disorder that manifests clinically with cardiovascular, ocular and connective tissue disorders [155]. If untreated, classical homocystinuria can result in premature death caused by stroke or other thromboembolic events. On the other hand, hyperhomocysteinemia and abnormal levels of H_2S caused by an altered CBS activity, are also linked with liver diseases, including nonalcoholic steatohepatitis (NASH), cirrhosis or hepatocellular carcinoma (HCC) [156]. Several types of cancers have also been linked to a deficient activity of the CBS enzyme [157], as well as cognitive disorders that include Alzheimer disease and Schizophrenia [158]. The CBS enzyme, the transsulfuration pathway and the construct *Hs*CBSΔ516-525 are described in detail in Chapter II of this Tesis, and in references [69,159–161].

Finally, protein MJ1004 (UniProtKB/Swiss-Prot entry Q58410), is encoded by gene *mj1004* of the archaeon Methanocaldococcus jannaschii, and consists of a polypeptide chain of 214 amino acids with a molecular mass of 24 585 Da. Its sequence is formed by a CBS-domain pair (CBS1, residues 7–65; CBS2,

residues 69–129), an unknown region (residues 123–181) and a putative transmembrane region (residues 182–204) as predicted using *TMHMM2* (http://smart.embl-heidelberg.de/help/smart_glossary.shtml#TMHMM). MJ1004 is currently annotated as an uncharacterized hypothetical protein, whose crystallization conditions were reported in 2011 by Martinez-Cruz´s laboratory [108]. The crystal structure was elucidated by our laboratory and deposited in the protein databank under accession number 6H1W.

1.4.4. Crystallization assays in the presence of heteronucleants

Crystallization assays were setup at 291K in 96 well plates, following standard vapor diffusion methods. The experiments were done in triplicate and monitored along three weeks, after which they were considered finished. The imprinted surfaces were setup manually, before well solutions were added automatically with the help of a nanodispenser (Mosquito (STP LabTech). To avoid unnecesary delays in the assesment of results, we used a same set of buffered solutions in which the three target proteins could yield a certain percentage of crystals. We chose the commercial Screen PEG RX 1,2 from Hampton research (codes HR2-082, HR2-084, Hampton Research) which includes 96 aqueous solutions buffered at pH from 4 to 9, containing polyethylenglycols of molecular weight from 400 → 20,000 Da as precipitant agent (the concrete conditions per well are detailed in **Fig. 1.17**).

PEG variation

	1	2	3	4	5	6	7	8	9	10	11	12
A	200			300			400			550		
B	600			1 000			1 500			2 000		
C	Jeffamine			3 350			4 000			5 000		
D	6 000			8 000			10 000			20 000		
E	200					400				550		
F	550	1 000		1 500				2 000				3 350
G	3 350			4 000			5 000			6 000		
H	8 000			10 000				20 000				

pH Variation

	1	2	3	4	5	6	7	8	9	10	11	12
A	3.5	5.5	7.5	4.5	6.5	8.5	4.0	6.0	8.0	5.0	7.0	9.0
B	4.0	6.0	8.0	3.5	5.5	7.5	4.5	6.5	8.5	4.0	6.0	8.0
C	5.0	7.0	9.0	3.5	5.5	7.5	4.0	6.0	8.0	4.5	6.5	8.5
D	5.0	7.0	9.0	3.5	5.5	7.5	4.5	6.5	8.5	5.0	7.0	9.0
E	4.0	5.0	6.0	6.5	7.0	5.0	5.5	6.5	7.5	4.5	6.5	7.0
F	8.5	5.5	8.0	3.5	7.5	8.5	9.0	4.5	6.0	7.0	9.0	4.0
G	5.5	7.0	8.0	5.5	6.0	4.0	7.0	8.5	9.0	3.5	3.5	4.0
H	4.0	8.0	9.0	5.0	6.0	6.5	7.5	8.0	3.5	5.0	5.0	8.5

Precipitant + Buffer

Precipitant + Buffer + Aditive

Figure 1.17. Hampton Research Screen PEGRX1,2 *. Distribution of PEGs and pHs in the 96-well plate.*

A preliminary round of experiments using both, the hanging-drop and the sitting-drop approaches, led us conclude that outcomes from either technique barely differed from each other. However, visualization of the drops under the microscope was significantly poorer when using the hanging-drop approach. This fact, added to the significantly higher cost of the commercial adhesive tablets required for the hanging-drop setting (**Fig. 1.14**), as well as the longer time required to setup the experiments, led us discard this

latter technique for subsequent setups. Parallel experiments using the Naomi´s nucleant (NN), a commercially available mesoporous agent fabricated at the nanometric scale, were also carried out for comparison. Buffered solutions of the mother liquor lacking any protein were used as negative controls to discard false positives, cause c.a by salt crystals. The overall results obtained are summarized in **Figs. 1.18A** and **1.18B**.

To evaluate the nucleation effectivity of the different surfaces, we opted for a binary notation (positive/negative) in which the appearance of protein crystalline material (CCM) [58], either as primary or as secondary nuclei, was assigned as a positive hit in the corresponding drops. Neither the habit (large crystals, microcrystals, needles, spherules or microcrystalline clusters) nor the quality of the crystals were taken into account in the positive assignments. On the contrary, drops lacking CCMs or yielding salt crystals, were recorded as a negative result.

Within the positive hits, three different scenarios were envisaged:

(1) Formation of CCMs in absence of heteronucleant (homogenous nucleation).

(2) Formation of CCMs in presence of the unpatterned surface (heterogeneous nucleation).

(3) Formation of CCMs in presence of a patterned surface (ME, SK, LA)

(4) Formation of CCMs in the presence bioglass NN.

Taking into account the reluctancy of the target proteins to crystallize, an important aspect to assess the results was to make an estimation of the degree of reproducibility in the formation of crystals in each of the drops of the 96-well plate. In other words, what percentage of success was to be expected in each of the drops in homogeneous and in heterogeneous conditions for each of the proteins. To determine this, we performed triplicates of the PEGRX1,2 screen, and scored the results based on the positivity/negativity criteria described above (**Figs. 1.18A** and **1.18B**). As expected, the three proteins yielded crystals in several drops of the plate in the absence of heteronucleant (*blue* and *green* squares in **Fig. 1.18A**), thus confirming the PEG RX 1,2 screen as a suitable experimental framework. Importantly, we found that in homogeneous conditions, the number of new positive hits decreased in approximately 40% in each replicate, reaching only a 20% success rate at best after three trials. Based on these findings, we estimated that a formation of CCMs at least one time in a particular drop along the triplicate was a reasonable assessment to consider a certain condition (drop) as a positive hit.

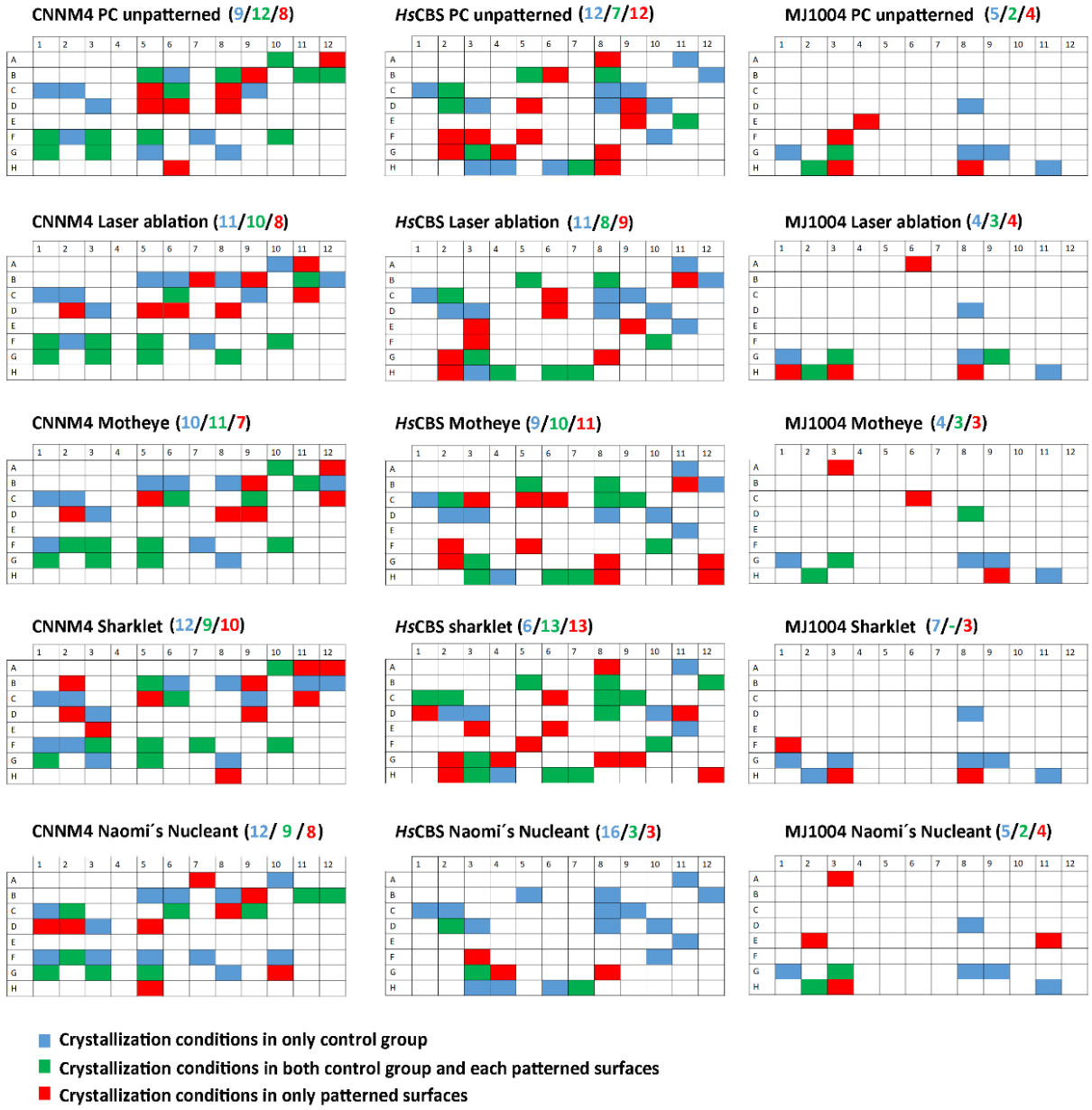

Figure 1.18A. Sitting-drop crystallization outcomes in the presence of the selected heteronucleants*. The figure summarizes those wells that yielded CCMs in at least one time in the triplicate experiment. The screen used is the PEGRX1,2 screen from Hampton Research. Blue squares indicate CCM growth only in the absence of heteronucleant; Green squares indicate CCM grown both, in the absence of heteronucleant and also in the presence of the corresponding PC-surface. Red boxes indicate CCM growth only in the presence of the corresponding PC-surface.*

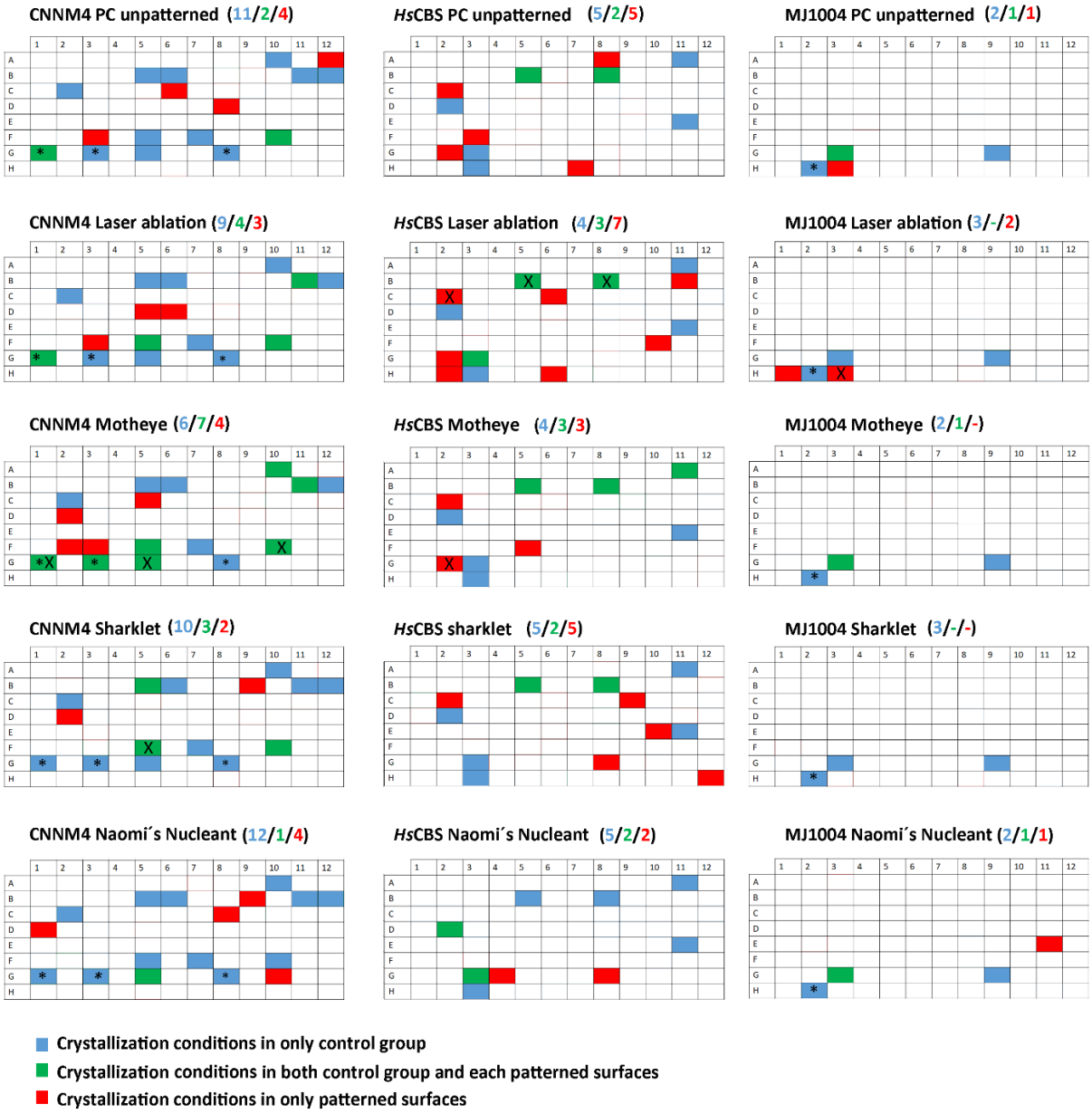

Figure 1.18B. Sitting-drop crystallization outcomes in the presence of the selective heteronucleants*. The figure summarizes those wells that yielded CCMs at least two times in the same conditions of crystallization in the triplicate experiment. The screen used is the PEGRX1,2 screen from Hampton Research. Blue squares indicate CCM growth only in the absence of heteronucleant; Green squares indicate CCM grown both, in the absence of heteronucleant and also in the presence of the corresponding PC-surface. Red boxes indicate CCM growth only in the presence of the corresponding PC-surface. Positive drops that yielded CCMs the three times in the triplicate experiment in homogenous conditions, or in the presence of a surface, are indicated with an asterisk and a cross, respectively.*

The previous analysis (**Fig. 1.18A**) suggested SK as the most efficient surface in *Hs*CNNM4$_{545-730}$ and *Hs*CBSΔ516-525, with a number of unique conditions against the control of 10 and 13, respectively (*red squares*, **Fig 1.18A**). Unexpectedly, the PC-unpatterned surface also increased the number of unique crystallization conditions (**Fig. 1.19**). This fact is related to both the material composition (polymer nature) and the surface characteristics of the laser cutting edge of the tablet. In order to isolate the effect of the surface pattern and the tablet edge on protein crystallization, we analyzed the number of unique CCMs conditions obtained with each patterned surface vs (i) controls (no tablet added), (ii) vs the PC-unpatterned tablets, and (iii) vs the control+PC-unpatterned surface (**Fig. 1.19**). The first of these values reflects the contribution of both, the patterning + the laser cut in nucleation versus the controls. The second, mostly reflects how a particular pattern (c.a SK, ME or LA) affects crystallization considering the unpatterned surface as a control. Finally, the third value shows the benefits of using each particular patterning (c.a SK, ME or LA) in a scenario where the "controls" are both, the unpatterned surface and the particular solution without any heteronucleant added.

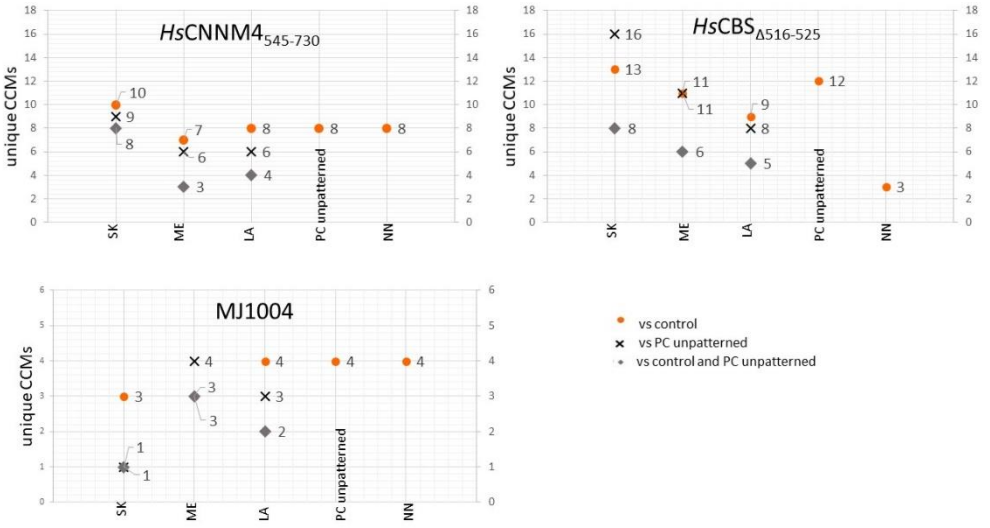

Figure 1.19. Unique crystallization conditions obtained for PC patterned surfaces. *The unique conditions obtained for a protein with a particular surface vs the control are shown in orange circles (corresponding to the red squares in Fig. 18A), vs the PC-unpatterned in black crosses and vs PC-unpatterned and control (grey diamonds.*

Next, we wanted to evaluate the effect of a change in surface charge density on the nucleation process. For this purpose, we produced laser patterned polysulfone (PSU) films and compared the results with those obtained with polycarbonate tablets. The two patterns selected for this study were (i) Unpatterned PSU, and (ii) Laser Ablation grooves tablets (PSU-LA). Similarly to the PC approach, the PSU tablets were fragmented in small tablets suitable for the sitting-drops setups. The results are summarized in **Figs 1.20A** and **1.20B**.

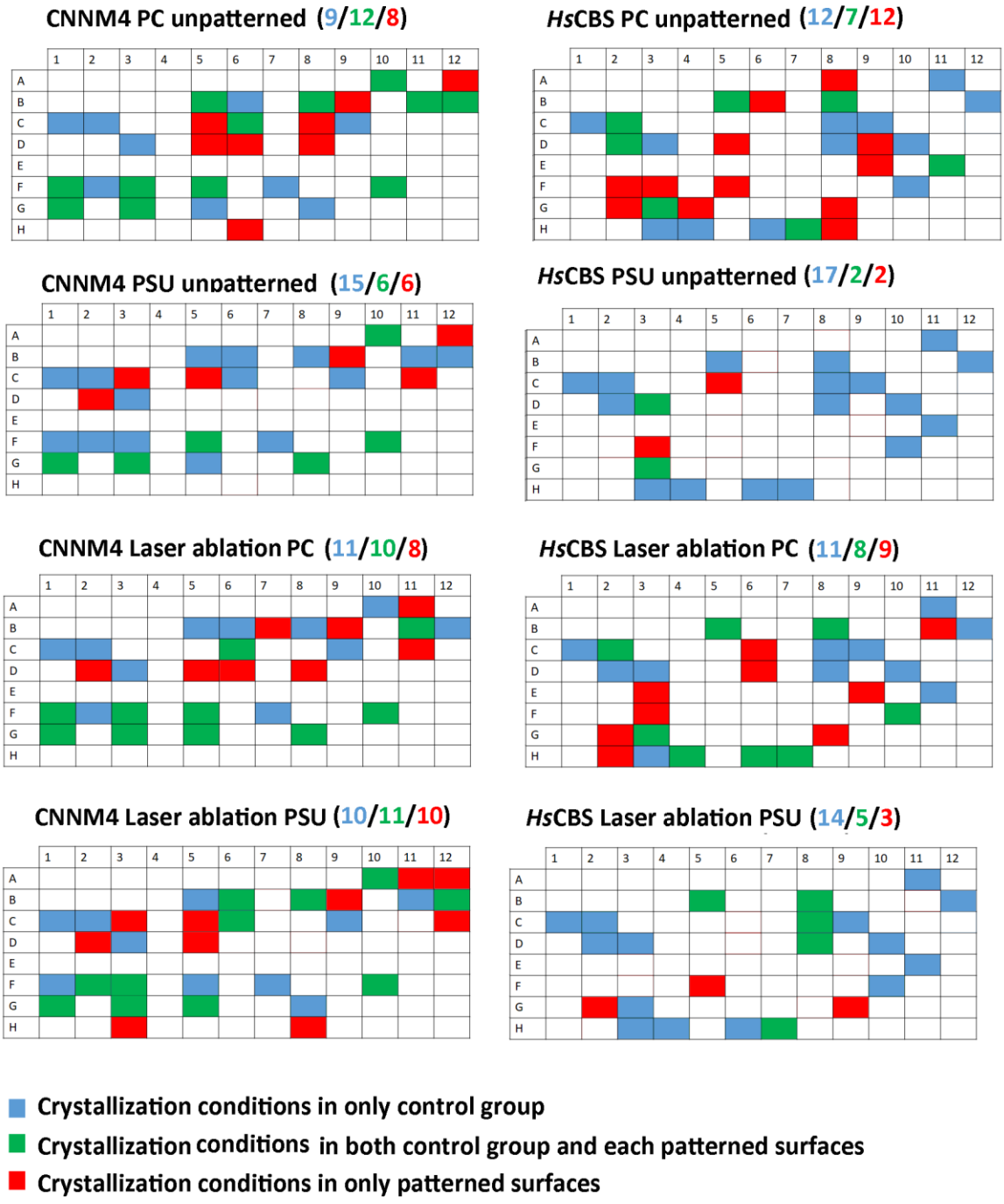

Figure 1.20A. Sitting-drop crystallization outcomes obtained in the presence of PC and PSU surfaces*. The figure summarizes those wells that yielded CCMs at least one time in the triplicate experiment. The screen used is the PEGRX1,2 screen from Hampton Research. Blue squares indicate CCM growth only in the absence of heteronucleant; Green squares indicate CCM grown both, in the absence of heteronucleant and also in the presence of the corresponding PC-surface. Red boxes indicate CCM growth only in the presence of the corresponding PC-surface.*

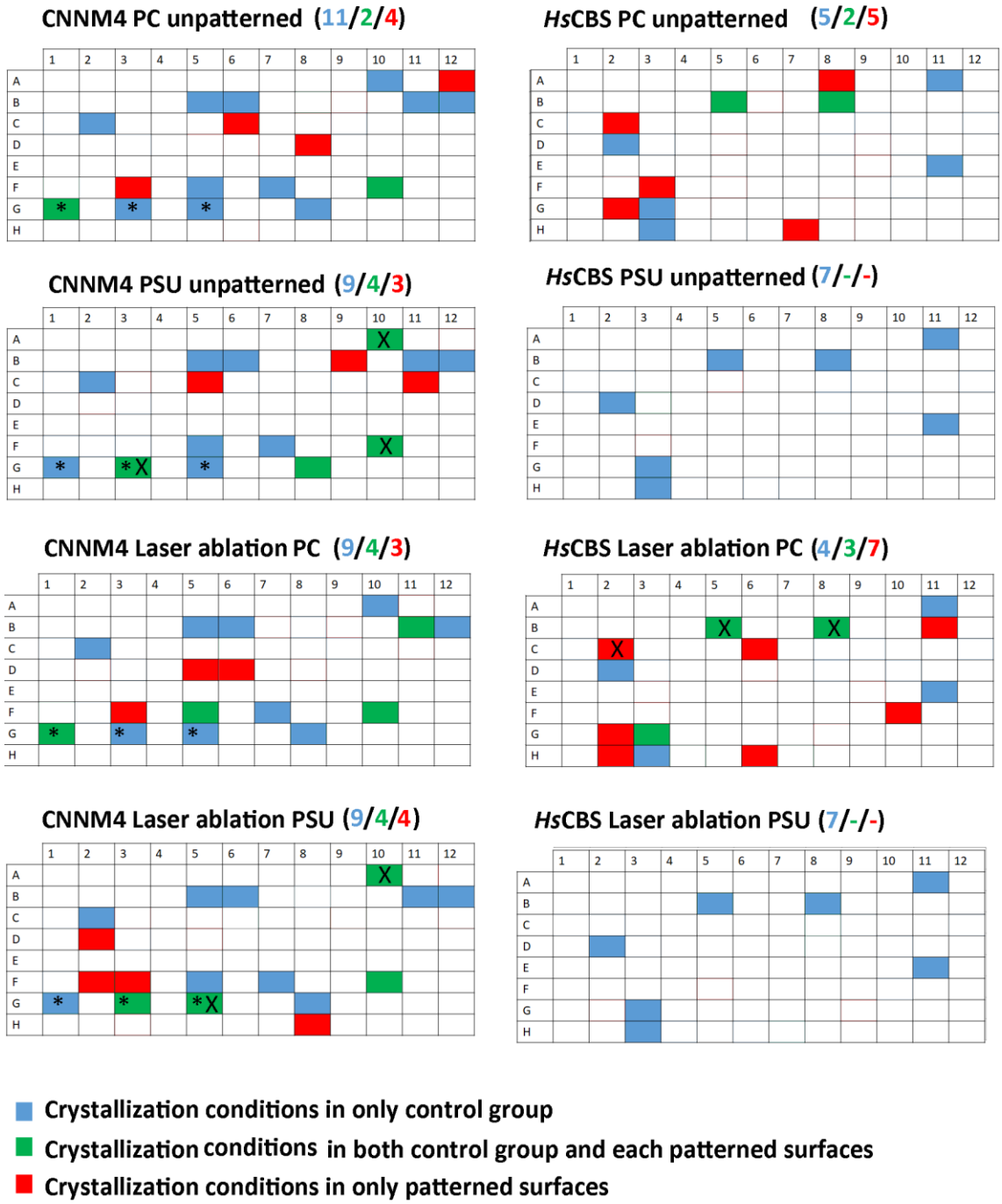

Figure 1.20B. Sitting-drop crystallization outcomes obtained in the presence of PC and PSU surfaces*. The figure summarizes those wells that have yielded CCMs at least two times in the triplicate experiment. The screen used is the PEGRX1,2 screen from Hampton Research. Blue squares indicate CCM growth only in the absence of heteronucleant; Green squares indicate CCM grown both, in the absence of heteronucleant and also in the presence of the corresponding PC-surface. Red boxes indicate CCM growth only in the presence of the corresponding PC-surface.Positive drops that yielded CCMs the three times in the triplicate experiment in homogenous conditions, or in the presence of a surface, are indicated with an asterisk and a cross, respectively.*

As previously described for the PC surfaces, we aimed to isolate the effect of the surface pattern and of the tablet edge on protein crystallization, analyzing the number of unique CCMs conditions obtained with the LA patterned surface vs (i) controls (no tablet added), (ii) vs the PSU-unpatterned tablets, and (iii) vs the control+PSU-unpatterned surface (**Fig. 1.21**). As a reminder, the orange circles show the effects of the patterning LA and the laser cut at the tablet edges vs the control. The black crosses indicate the effect of the LA pattern, independently of the effect of laser cut. Finally, the grey diamonds reflect the advantage of using LA pattern in a situation where the control are both, the homogeneous crystallization and the unpatterned surface.

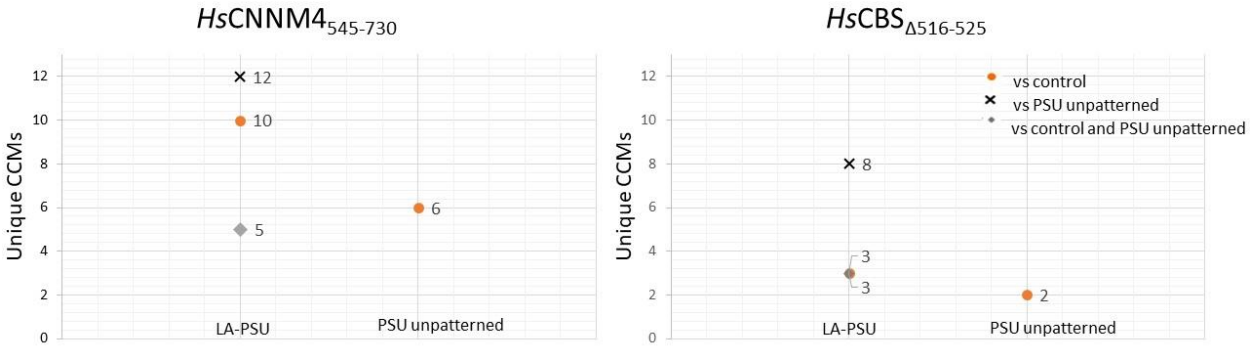

Figure 1.21. Unique crystallization conditions obtained for PSU patterned surface. *The number of unique conditions obtained for a protein with LA patterning vs the control are shown in orange circles (corresponding to the red squares in Fig. 20A), vs the PSU-unpatterned in black crosses and vs PSU-unpatterned and control in grey diamonds.*

Interestingly, in some cases we observed both, primary (originated on the surface) and secondary (arisen at any other location of the droplet) nucleation (**Fig. 1.22**), for both patterned and unpatterned tablet and regardless of the polymeric material employed (PC or PSU).

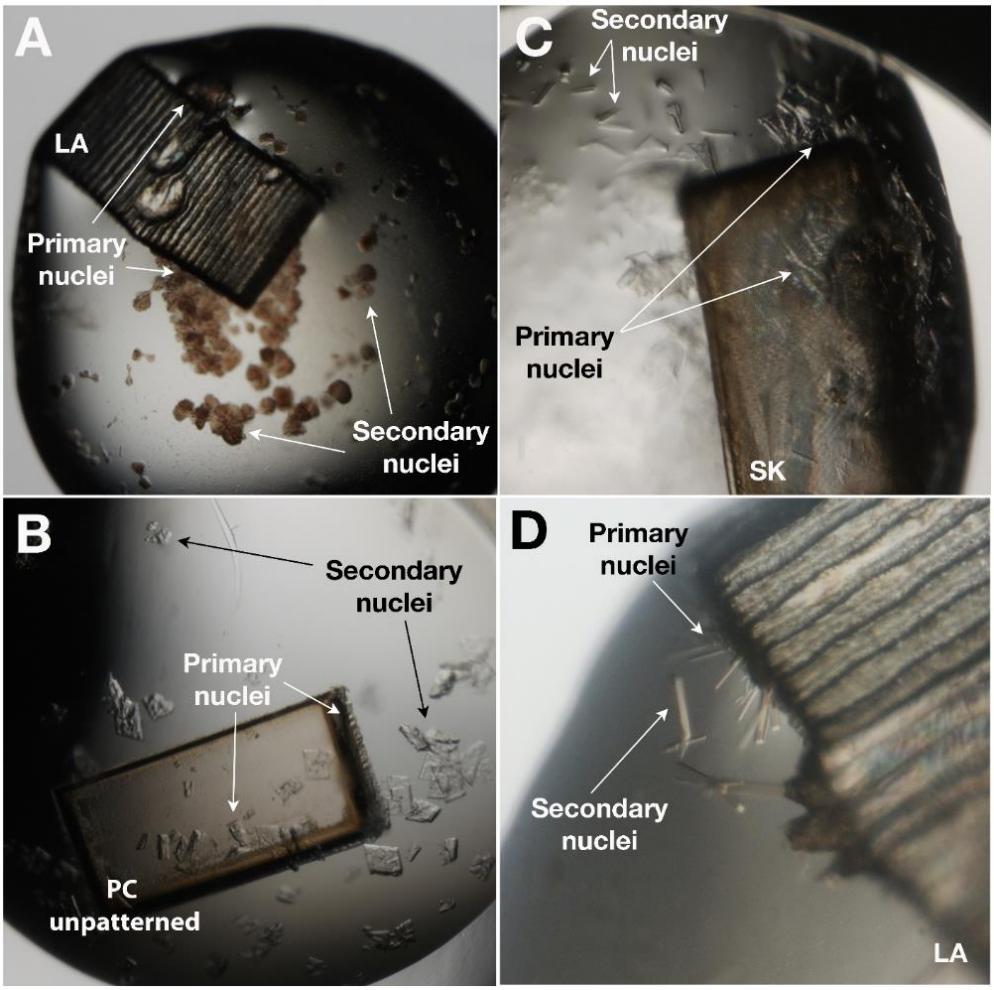

Figure 1.22. Primary and Secondary crystals obtained with PC surfaces. *Crystals of HsCBSΔ516-525 (**A, D**) and HsCNNM4$_{545-730}$ (**B, C**) in drops containing imprinted surfaces. LA=Laser Ablated Grooves; SK= Shark-skin. All experiments were carried out by using by sitting-drop vapour diffusion methods.*

Once carefully curated tables of "positive hits" were decided upon (results recovered in **Figs. 1.18A, 1.19, 1.20A and 1.21**), we proceeded to evaluate the results obtained with the corresponding patterned surfaces (heterogeneous conditions). Our main findings were:

(i) First, we found that all imprinted surfaces (ME, SK and LA) promoted *unique* crystallization hits, i.e growth of CCMs only took place in the presence of a particular patterned surface and for a concrete protein (*red* squares in **Fig. 1.18A** *and orange circles* **in Fig. 1.19**). These findings proved that each different pattern had a specific positive effect on nuclei formation. In our case, the most efficient surface was SK, which yielded the higher percentage of unique

conditions obtained from the whole set of surfaces, in two of the three proteins (*Hs*CNNM4$_{545-730}$ and *Hs*CBSΔ516-525) (**Figs. 1.18A** and **1.19**).

(ii) We also observed that the unpatterned PC surface not only promoted crystal growth, but intriguingly yielded a significant number of unique conditions (*red* squares in **Figs. 1.18A** and *orange circles* in **Fig. 1.19**) with respect to controls (8, 12 and 4, that represented an increment of 38%, 63% and 57% in the number of positive hits obtained in the control group for *Hs*CNNM4$_{545-730}$, *Hs*CBSΔ516-525 and MJ1004, respectively). A priori, this success was not attributable to any patterning.

(iii) SK is the most successfully topography to promote protein crystallization. As shown in **Fig. 1.19**, SK is the most efficient surface to favor nucleation both for proteins *Hs*CNNM4$_{545-730}$ and *Hs*CBSΔ516-525. The benefits of using this particular pattern design has been demonstrated by comparing the CCMs vs the control and the unpatterned surface. In contrast, protein MJ1004 behaves poorly than the other two proteins.

(iv) Notably, protein MJ1004 tends to crystallize in reservoir solutions containing 10-20% ethanol. However, the heteronucleants promoted new crystallization hits under conditions without alcoholic derivatives (c.a. A3, A6, C6, F1 or H8) (**Figs. 1.18A** and **1.19**).

(v) The surface charge of the polymeric material appears to have an effect on crystallization. As shown in **Figs. 1.20A** and **1.21**, PSU has a dramatic effect on promoting new crystallization hits in *Hs*CBSΔ516-525 (further details in section 1.4.4.2.). However, in *Hs*CNNM4 the number of positive hits is similar to those obtained with PC surfaces. Importantly, the LA topography promotes crystallization for proteins *Hs*CNNM4$_{545-730}$ and *Hs*CBSΔ516-525. As shown in **Fig. 1.21**, the advantages of using this pattern have been demonstrated by comparing the CCMs vs the PSU unpatterned surface (*black crosses* Fig. **1.21**)

(vi) Remarkably, in some drops we found two types of nucleation (primary and secondary) in the presence of a tablet (**Fig. 1.22**). The experimental need to leave the crystallization plates at rest without imaging them during the first week to avoid interfering with the experiment, made difficult determining what type of nucleation had occurred first. Nevertheless, these

findings suggested a possible migration of nuclei from the surfaces to remote locations of the droplet.

(vii) As just mention above, the nucleation in these experiments sometimes appeared in remote locations of the drop (**Fig. 1.22**), and were not necessarily accompanied by a primary crystal nucleated from the surface. We concluded that the simple inclusion of the tablet in the drop may have a drastic effect in terms of nucleation led by the roughness of the edge cutted by laser. As described in Chapter II, Section 2.4.7.1. of this thesis, **this type of event was found particularly relevant, not so much in crystal production, but in the diffraction quality of the resulting crystals.**

(viii) In some drops (see Chapter II, Section 2.4.7.1. describing crystals of *Toxoplasma gondii* CBS grown in the presence of *O*-acetylcysteine or cysteine), **the presence of a PC tablet was a sine qua non requisite to obtain good quality diffraction data**.

(ix) In general, we found that our patterned surfaces were more efficient in promoting nucleation of the target proteins than the commercial Naomi´s agent (**Fig. 1.18A**). Noteworthy, in *Hs*CBSΔ516-525, the presence of NN prevented nucleation in drops that normally yield crystals in the control and in the patterned surfaces (c.a. B5, C2, B8 or G3) (**Fig. 1.18A**). We also observed that the presence of NN in the crystallization of *Hs*CNNM4$_{545-730}$ and MJ1004 shows comparable results to the patterned surfaces.

(x) **Intriguingly, a significant number of crystals grew attached to the corners of the tablets, or emerged from their side faces (**see for example the crystals shown in **Fig. 1.23, D** and **H)**. An increment of the roughness value in this area, which is 10 and 30-fold higher than the values determined on LA and PC unpatterned, respectively, resemble to be behind this phenomena.

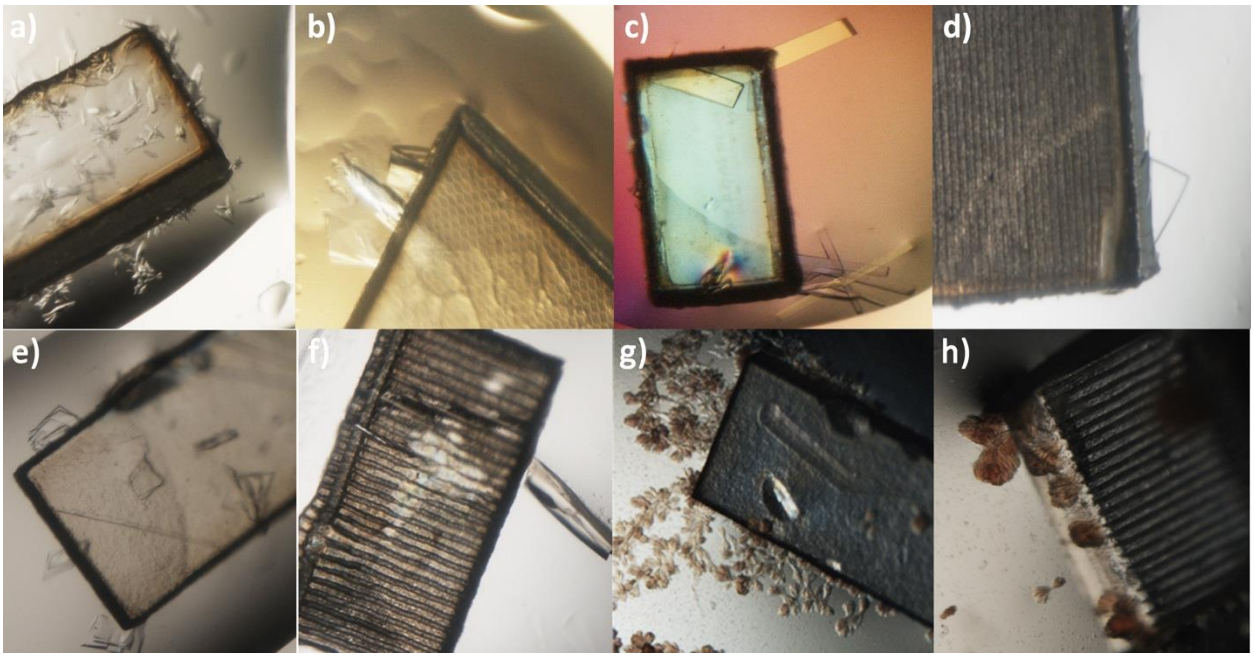

Figure 1.23. Nucleation at the side faces of the tablets. *The picture shows crystallization events occurred at the laser cut side edges of the different PC tablets in sitting-drop vapour diffusion experiments.* ***a****) CNNM4 at 11.54 mg/mL grown in 6% v/v Tacsimate pH 6.0, 0.1 M MES monohydrate pH 6.0, 25% w/v Polyethylene glycol 4,000 using PC unpatterned as heteronucleant;* ***b****) CNNM4 at 27 mg/mL grown in 0.15 M DL-Malic acid pH 7.0, 0.1 M Imidazole pH 7.0, 22% v/v Polyethylene glycol monomethyl ether 550 using Shark-skin as heteronucleant; c) MJ 1004 at 36 mg/mL grown in 2% v/v Tacsimate pH 7.0, 5% v/v 2-Propanol, 0.1 M Imidazole pH 7.0, 8% w/v Polyethylene glycol 3,350 using Moth-eye-PC as heteronucleant;* ***d****) CNNM4 at 9 mg/mL grown 0.1 M BICINE pH 8.5, 8% w/v Polyethylene glycol monomethyl ether 5,000 using Laser ablated-PC as heteronucleant;* ***e****) CNNM4 at 24.37 mg/mL grown in 0.2 M Ammonium citrate tribasic pH 7.0, 0.1 M Imidazole pH 7.0, 20% w/v Polyethylene glycol monomethyl ether 2,000 using PSU smooth as heteronucleant;* ***f****) CNNM4 at 24.37 mg/mL grown in 0.1 M Tris pH 8.0, 30% w/v Polyethylene glycol monomethyl ether 2,000 using Laser ablated-PSU as heteronucleant;* ***g****) HsCBS at 14 mg/mL grown in 12% PEG 5K, 0.1M Bicine pH= 8.5 and 0.3M sodium formate in hanging drop method using PSU smooth as heteronucleant;* ***h****) HsCBS at 14 mg/mL grown in 10% PEG 5K, 0.1M Bicine pH= 8.5 and 0.3M sodium formate in hanging drop method using Laser ablated-PSU as heteronucleant.*

Aimed to find a rationale for all these observations, we evaluated the crystallization outcome in the light of the different parameters described in section 1.4.1.

1.4.4.1. Effect of pH

A protein has its lowest solubility at its isoelectric point (pI). Without a net charge, the interaction of a protein with its surrounding water molecules is not favored, as the driving force of the interactions between the protein and its solvation sphere are electrostatic and H-bonds. Under this circumstances, the dissolved protein molecules trend to contact with the rest of proteins present in the solution, as protein-protein interactions may attract each other through Van der Waals or hydrophobic interactions that do

not involved charge. Accordingly, at the pI, protein-protein interactions and precipitation are more likely, and crystallization is frequently favored at pHs near the pI. Accordingly, a higher number of CCM positive hits in drops with a pH near the protein pI (**Table 1.4**) would have not been surprising. However, we found a broad distribution of CCMs across the plates, which led us conclude that a relationship between the solution pH and the protein pI could not be established in our study (see **Figs. 1.17, 1.18** and **1.20**).

***Table 1.4. Overall protein features**. Molecular weight (Mw) and Isoelectric point (pI) values of the target proteins.*

Protein	Mw (kDa)	pI
***Hs*CBSΔ516-525**	61.5	6.41
***Hs*CNNM4$_{545-730}$**	20.9	9.01
MJ1004	24.6	9.01

1.4.4.2. Effect of surface charge (PC vs PSU)

We next evaluated the effect of surface density charge on the crystallization outcomes. To that aim, PSU-unpatterned and PSU-Laser Ablation tablets were additionally tested (**Figs. 1.20A** and **1.20B**). At first glance, the most striking observation was that PSU drastically changed the scenario of crystallization conditions with respect to PC. For example, for *Hs*CNNM4$_{545-730}$ (see CNNM4 PSU unpatterned-panel in **Fig. 1.20A**) the conditions generating crystals in homogeneous conditions in the absence of any heteronucleant (sum of *blue*+*green* squares (15+6=21), in **Fig. 1.20A**), became reduced in 43% upon addition of the PSU-unpatterned film to a total of 12 hits (*green* + red squares (6+6)) (Note: notice that green squares also includes positive conditions yielding CCMs in the absence of heteronucleant). In the same conditions, polycarbonate (CNNM4 PC-unpatterned panel in **Fig. 1.20A**) reduced mildly the CCMs formation from 21 (sum of *blue*+*green* squares (9+12=21), to 20 positive hits (reduction of 5%) This trend was even more pronounced for *Hs*CBSΔ516-525, where the number of positive hits decreased from 19 (sum of *blue*+*green* squares (17+2=19), **Fig. 1.20A**) to 4 (green squares in *Hs*CBS-PSU unpatterned panel in **Fig. 1.20A**), a reduction of 79%. Using PC-unpatterned tablets, the number of CCMs was not reduced with respect to homogeneous crystallization, from 19 (blue and green squares, 12+7=19) to 19 (green and red squares) hits (0% reduction) (**Fig. 1.20A**).

No less significant was the change in the distribution of unique conditions (*red* squares, **Fig. 1.20A**) throughout the plate, which decreased from 8 (for PC unpatterned), to 6 (for PSU unpatterned) (10 %

reduction) in *Hs*CNNM4$_{545-730}$, and from 12 (PC unpatterned) to 2 (PSU unpatterned) (54% reduction) in *Hs*CBSΔ516-525.A similar trend was observed when using the PSU-LA patterning tablets with both, *Hs*CNNM4$_{545-730}$ and *Hs*CBSΔ516-525, not so much in the percentage of positive hits, but in their location on the 96-well plate (please see coordinates of *red* squares in **Fig. 1.20A**). Moreover, as mentioned earlier, the LA topography seems to have a positive effect in promoting unique CCMs (**Fig. 1.21**) compared to PSU unpatterned.

In summary, we concluded that unpatterned polysulfone surfaces cause a drastic effect on the crystallization outcome by reducing the number of positive hits. This overall effect is accompanied by the generation of new unique hits, well-differentiated from that exerted by equivalent polycarbonate tablets. These findings invite to use of PSU surfaces in vapour diffusion experiments where an excess of nucleation and the search of new crystallization conditions are needed. Further experiments and depth characterization (not developed in this thesis) will be required to determine the effects of patterning on PSU surfaces.

1.4.4.3. Effect of surface topography: Contact Angle, Roughness and Aspect ratio

We further evaluated whether topology parameters such as Contact Angle, Roughness and Aspect Ratio were linked to the crystallization success in terms of unique conditions vs the control (**Fig. 1.19** and **1.21**) (**Tables 1.2** and **1.3**)

Effect of roughness caused by Laser cut (tablet side faces)

Unexpected crystal growth on the side faces of the different types of tablets, including those corresponding to the PC-Unpatterned surface, support the idea already introduced previously that the laser cut might play a relevant role in the nucleation success. In fact, these observations encouraged us to design the LA pattern, which partially mimics the profile of such side faces in each groove. Confirming our expectations, we found that grooves generated on a polycarbonate surface become nucleation sites, (**Fig. 1.24**) while the plateaus remain free of crystalline material.

Strikingly, and despite the artificially created patterning present in the LA sheets, this was not the most successful pattern design (remember that the best results were achieved with SK and PC-unpatterned **Fig. 1.19**). Nevertheless, nucleation still occurred preferentially on the lateral faces of the tablets (**Fig. 1.23**), being especially abundant at the laser cutting edges (**Fig. 1.25**). We hypothesized that a possible explanation could be a larger exposed surface of the sides with respect to the grooves carved on the LA tablet. But, what characteristics did the side faces have that made them so effective in terms of nucleation? What features did the laser cutting add to the PC that might explain this effect?

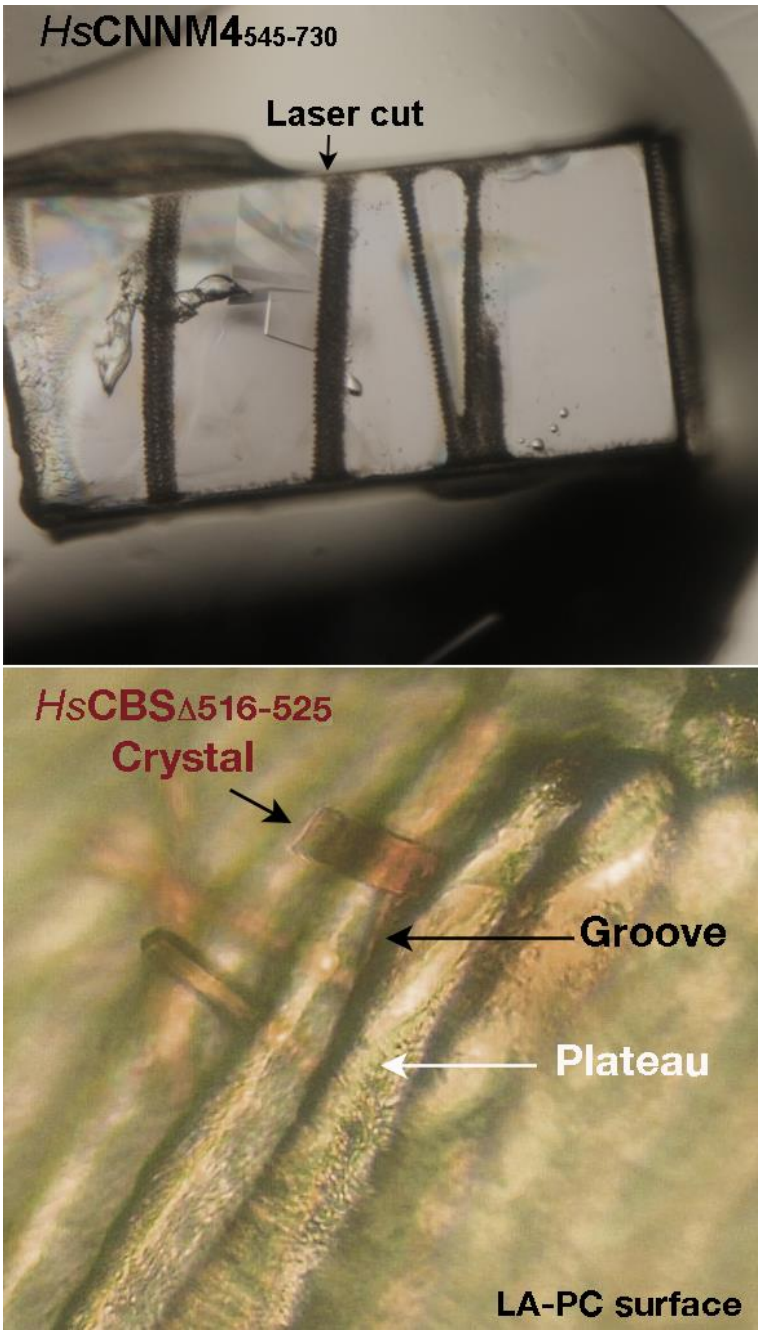

Aimed to answer these questions, we analyzed the profile of the tablet side faces, as well as the trace left by the laser beam along the cut. The images collected by confocal microscopy revealed an abrupt profile containing conical-shaped clefts between 1 and 10 μm wide, and a depth between 50 and 400 nm.

Figure 1.24. Nucleation at the grooves of the PC-LA tablet. *The picture shows crystals of HsCBSΔ516-525 grown on the grooves (dark lines) of the LA patterned polycarbonate surface.*

A closer view further showed that the roughness is significantly higher at the edges. The rest of the face appears basically flat (**Fig. 1.12** and **1.13**).

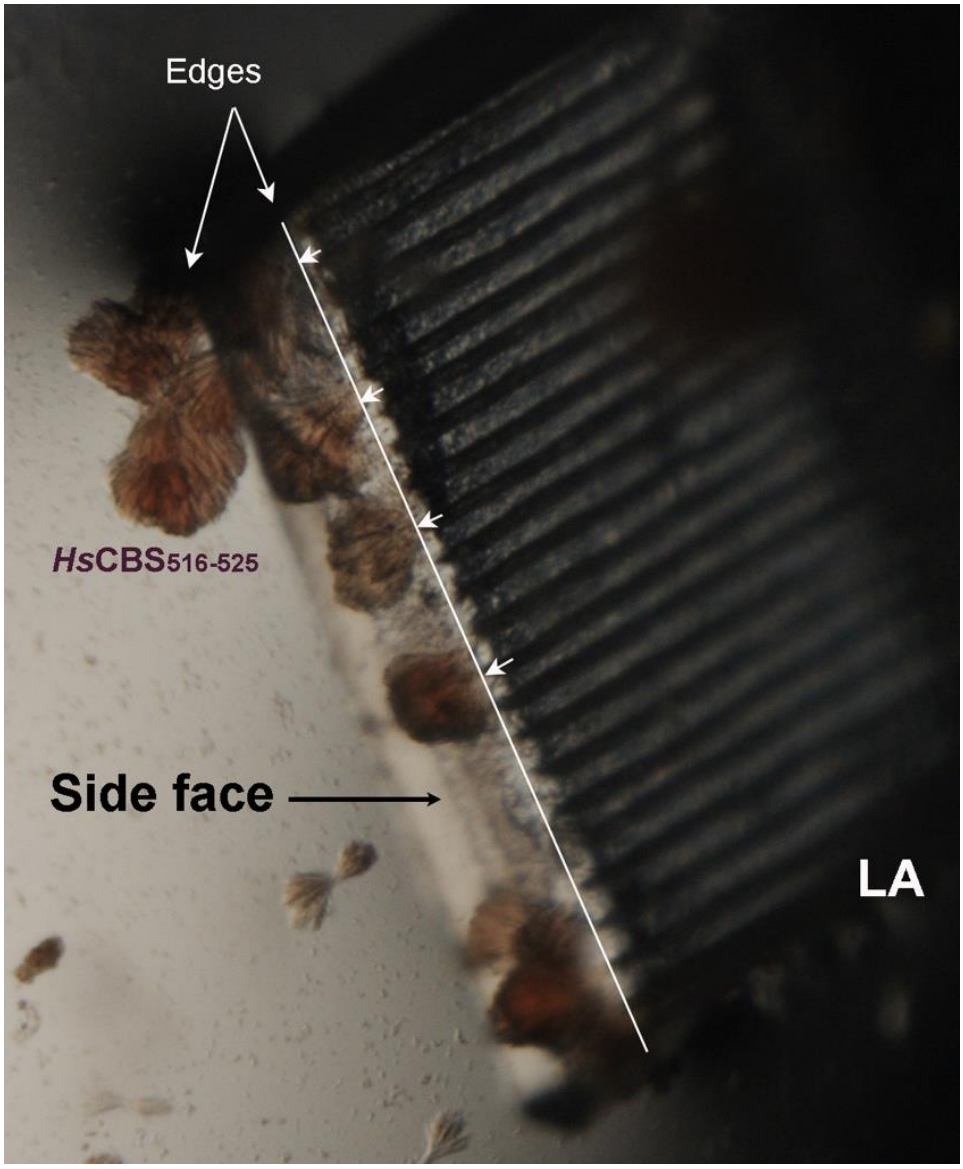

Figure 1.25. Nucleation at the tablet edges. *Crystals of HsCBSΔ516-525 grown at the edge of the LA tablet side faces. The edge line border is highlighted with a white line.*

1.5. DISCUSSION

Many attempts have been made for decades to find or develop agents (organic or inorganic materials) that promote the nucleation of proteins reluctant to crystallization. To this end, numerous studies have been conducted on how the chemistry and physics of such heteronucleating agents may affect and induce the crystallization process. Although different substances have been shown to be effective in protein crystallization, many of them are only efficient under certain conditions or for a scarce number of molecules, and thus can not be considered suitable for a "universal" use. In general, two main strategies have been devised for what a universal heteronucleant agent of biological macromolecules (such as proteins) should look like. Briefly stated, the first and most widely accepted approach, states that the heteronucleant should possess surface roughness or motifs that are on the size scale of the biological macromolecules to be crystallised, i.e., witin the nanometers range. These nanoscaled surfaces may or may not be chemically functionalized in various ways to vary their topology, charge, or affinity for the target macromolecules. The second approach, less studied and more controversial so far, postulates that the surface of the heteronucleant may similarly present topographical alterations (chemically functionalized or not), which do not necessarily need to be in the same metric range as the biological molecules, being in fact characterized by a much larger scale (micrometer to submicrometer range). These micro- and submicro- scaled surfaces have centered the focus of our research.

In an attempt to circumvent the crystallization barrier, or at least widen the success percentage, we have explored the effect of engineered polycarbonate (PC) plastic films, patterned considering different designs from the micro- to the submicro-scale, to create potential nucleation sites that promote the crystallization of proteins of a sparse nature (different size, shape, surface charge distribution, biological funtion, etc). The selection of polycarbonate (PC) as primary working material was based on its high stability and resilience to erosion under harsh conditions (changes in pH, acidity or basicity, degradation by chemicals, etc), and more importantly, its optical properties, transparency and ductility to be patterned through different imprinting techniques. This latter feature allowed us a rapid and cost-efficient modification of its surface geometry in three distinct designs, baptized as SK, LA, and ME (see **Table 1.3** and **Fig 1.5**). Not less important in the selection of PC was the fact that this polymer preserves its physico-chemical properties when is subject to laser micropatterning [162] and NIL [163] procedures.

Responding to our initial expectations, the three manufactured surfaces varied the response of the proteins to the commercial crystallization solution screens chosen for the study, suggesting a real and measurable (positive) impact of these materials on the nucleation process. However, we were surprised by two facts, a priori unexpected. The first was that the SK pattern, whose topography presents cavities of much larger size and depth than the rest, was the most efficient in promoting crystallization for two of the three proteins (*Hs*CBSΔ516-525 and *Hs*CNNM4$_{545-730}$) used in the study (**Fig. 1.19**). The second, even more striking, was that the unpatterned polycarbonate surface also acted as a crystallization inducer in a non-negligible number of droplets with respect to controls (absence of heteronucleant in the drop) (*red squares* in **Fig. 1.18A** and *orange circles* **Fig 1.19**). We found this fact very surprising, since the PC-unpatterned surface does not present any abrupt relief with cavities on the surface, even at the nanometer scale.

To try to understand the basis of the first strategy, we evaluate the possible role of the properties that usually determine the behavior of a surface, such as roughness, contact angle, chemical properties and relief.

The effect of the surface roughness of a nucleant agent on the crystallization efficiency is widely described in the literature [60,64,66], and has been linked with the induction time, as well as with the size and number of crystals. Our PC surfaces do not have the same structured pattern, but they do exhibit identical roughness values due to use of exactly the same stamp for the NIL replication process, in all Moth-eye, Shark-skin and PC-unpatterned films (**Table 1.3**).

Regarding the contact angle, we found that the surfaces enhanced their hydrophobicity with the patterning process with respect to the PC-unpatterned tablets, showing an increase in the contact angle value from 76.3° ± 5.3° (PC-unpatterned) to 102.9° ± 5.7°, 108.3° ± 2.4° and 111.3° ± 3.2° in LA, SK and ME, respectively (**Table 1.2**). Several studies have described that the hydrophobicity of a surface is strongly correlated with an improvement of the protein adsorption and a higher amount of protein crystals formed [164]. Our measured values of the contact angle, however, did not lead us to establish a clear link between an increase in the crystallization success on each particular pattern and their surface hydrophobicity. Accordingly, we concluded that the observed positive effects in the crystallization success (referred to the appearance of unique crystallization conditions) when using the SK tablets should be attributed to other parameters distinct from the roughness or the surface wettability.

As mentioned above, other factors may come into play to increase the nucleation efficiency of a particular heteroagent, such as its surface chemistry [46,165,166], and its geometry [33,167]. Our tests with PSU versus PC tabets indicated, indeed, a change in surface chemistry drastically modifies the crystallization outcome. In our case, this effect was manifested in a decrease in the number of positive hits (**Fig. 1.20A**). The geometry of a surface play an important role in promoting nucleation [33,167]. In our experimental setups, crystal growth improved upon increasing the Aspect Ratio of the patterns**.** For example, SK with a value far higher than those of ME and LA surfaces (35 and 5.5 times higher, respectively) (**Table 1.3**), yielded the best results. Interestingly, the shape of the surface patterning played also a role in the crystallization outcome. The ME and LA patterns are characterized by circular or linear shapes, lacking corners in their geometry, while SK has angular edges. These findings connect each particular pattern identity to angle-directed nucleation, and suggests that nucleation occurs more rapidly and easily on wedges than on flat surfaces, even when micro-scale patterns are considered [33,167].

As mentioned earlier, the second relevant result that caught our attention was the significantly high number of unique CCMs grown in the presence of the PC-unpatterned tablets (*red squares* in **Fig. 1.18A** and *orange circles* **Fig 1.19**). The crystalline growth obtained in these conditions, absent in the control experiments, was in itself an unexpected fact that could not be attributed to the topography of the tablet. In fact, this observation brought to light one of the discoveries that we consider, together with the one linked to the AR parameter, most relevant in our study. How can this crystallization outcome be explained?

A more careful analysis of the drops and of all images taken with the optical microscope, showed that a considerable number of crystals emerged from the edges of the PC-unpatterned tablets, there where the polycarbonate sheet had been cut with the picosecond pulsed laser beam to fragment the PC foil in small fragments that fit the dimensions of the crystallization wells (**Fig. 1.23**, **A, E** and **G**). Moreover, the characterization of the tablets side (**Figs. 1.12** and **1.13**) revealed significantly increased roughness values in comparison with those obtained for any of the designed patterns, (c.a around 10 times higher than that measured in LA, and 100 times higher than the values measured for the PC-unpatterned foil). Importantly, the characterization of the tablet edge revealed the presence of tiny pores (~ 0.5 -1 μm^2) randomly distributed all over the edge cut (**Fig. 1.11**). Similar pores, attributed to the ablation with picosecond pulsed laser had been previously reported in non-related studies [86,89–92], showing their effect in increasing platelet adhesion [92]. Reasonably, we observed the presence of these pores inside the grooves scarved in

the LA patterning tablets (**Fig. 1.10**). In agreement with these observations, crystal growth was also found inside the grooves generated on our LA patterning (**Fig. 1.24**). In 2018, Ortiz *et al.* demonstrated that the plateaus, which showed channels formed by the recast material, exerted the same effect as a proper groove, promoting cell confinement [91]. However we observed that our plateau remains free of crystalline material.

These data led us conclude that crystalline growth on the sides of the tablet was due to the increased effective rough surface area, which provide microscaled conical-shaped clefts that likely serve where supersaturation of protein result locally enhanced respect to the bulk solvent, thus promoting nuclei formation [62] (**Figs. 1.23** and **1.25**).

Taking into account that the diameter of each pore varies approximately between 500 nm-1 μm [89,92] (if a depth was estimated to have a similar value than the diameter and that the size of the target proteins is 100 Å for the largest one, (the dimension of each pore is 100 times larger than that of a protein), one can estimate that each pore may host 100x100x100=10^6 (1 Million) protein molecules. This value is tremendously larger than the sizes described as suitable for protein nucleation in the nanoscale-crystallization model (see the introduction section of this chapter), in which the protein is nanoconfined in a space with dimensions similar to its size (in a range between 3 to 21 nm) [51,168]. Of note, NN, the only heteronucleant available on the market [31,169], meets such nanoscale dimensional requirements, and yet the results obtained (**Figs. 1.18** and **1.19**) are the same (as it happens in *Hs*CNNM4$_{545\text{-}730}$) or worse (as with *Hs*CBSΔ516-525) than when using our polymeric heteronucleants. Thus, our data provide clear evidence that the protein molecules tends to crystallize in regions where these micropores are located (the edge of the tablet).

After this discovery, we revisited the location of the nascent crystals on the rest of the patterned surfaces (SK, ME and LA), and found that also in these cases nucleation took place (although not always) at the edge of the tablets (**Figs. 1.23** and **1.25**). The effective porous surface area (different on each pattern), and the double effect generated, on the one hand by each corresponding patterning, and on the other by the inevitable effect of laser cutting on the tablet edge, help explain the different nucleation success obtained with the polymeric surfaces studied.

Based on these data, we postulate that the micropores formed by the effect of the laser cut indeed serve as hot spots for nucleation that host highly dense protein microdrops, that in turn promote the formation of stable nuclei that are further converted into larger crystals (**Fig. 1.26**).

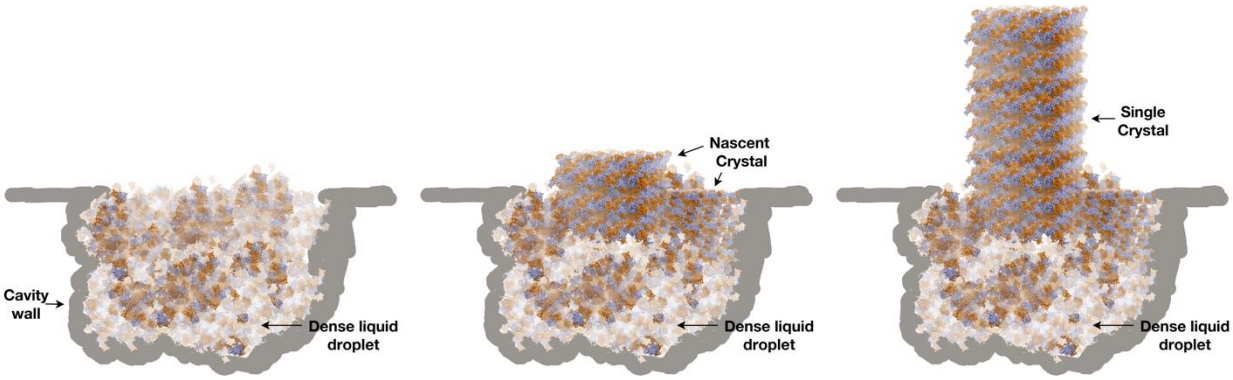

Figure 1.26. Proposed nucleation mechanism inside the cavities of the heteronucleant surfaces studied in this thesis. *Our findings are consistent with the two-step mechanism of nuclei formation. Cavities within the micrometer scale behave as hosts for highly (local) concentrated protein regions. This dense drops favour nuclei formation and stabilization of these nuclei, from which larger crystals are formed.*

1.6. CONCLUSIONS

1. NIL and ultrashort laser ablation technologies can been applied successfully on PC tablets to develop micro and submicrostructured surfaces.

2. Such patterned surfaces at the micro-scale can be used as promising heteronucleants in protein crystallization.

3. The Aspect Ratio of surfaces patterned within the microscale range emerges as the topographical parameter that most contributes to protein growth in patterned surfaces.

4. The high roughness combined with the random distribution of micropores at the laser cutting edges of the tablets, act as nucleation sites promoting a large number of new crystallization conditions.

5. A microstructured surface with pulsed laser cutting at the edges in polymeric materials resulted in more efficient crystallization of proteins of biomedical interest than controls and commercial products such as the Naomi´s Nucleant (NN).

CHAPTER II

Structural Characterization of Cystathionine β-synthase from *Toxoplasma gondii*

2.1. INTRODUCTION

2.1.1. Transsulfuration pathway

Sulfur is an essential element for all life forms, being the tenth most abundant element in the universe. It is a minor component in minerals, biological antioxidants, vitamins (such as biotin or thiamine), and it is a major constituent of proteins, where it is incorporated by the amino acids methionine (Met) and cysteine (Cys) [170–172]. Sulfur-containing amino acids are recognized to be some of the most potent modulators of lipid metabolism among amino acids [173]. In humans, methionine is an *essential amino acid* (thus, it cannot be endogenously synthesized) and therefore must be obtained from the diet. This amino acid not only acts as the initiating amino acid in the synthesis of proteins [174], but it is also one of the most important methyl group donors. In turn, cysteine is a derivative of methionine and plays an important role in protein synthesis, being a precursor of glutathione (GSH, an important antioxidant) and taurine (an organic compound widely distributed in animal tissues and involved in the formation of bile).

The transsulfuration (which means sulfur exchange, or sulfur-containing moiety exchange between two different compounds) is a metabolic route that, coupled to the methionine and the folates cycles, allows the interconversion of methionine (Met) and cysteine (Cys) through the intermediates homocysteine (Hcys) and L-cystathionine (from now referred as cystathionine) (Cth) [175] (**Fig. 2.1**). In evolutionary terms, transsulfuration includes two routes, the "forward" and the "reverse" pathways [176], which operate in opposite directions and may coexist in some species, or alternatively be present as a single and irreversible pathway in other organisms. The forward transsulfuration occurs in enteric bacteria [177], plants [178] and yeast [179] (**Fig. 2.1**) and enables the formation of Met from Cys. The thiol group of Cys is transferred to Hcys in two steps. Cys is first condensed with *O*-acetylhomoserine (or with *O*-succinylhomoserine) to form Cth and succinate in a reaction that is catalyzed by cystathionine γ-synthase (CGS) [180]. Cth is then cleaved by means of the β-elimination of the Hcys portion of the molecule leaving behind an unstable imino acid, which is attacked by water to form pyruvate and ammonia. This reaction is catalyzed the by cystathionine β-lyase enzyme (CBL) [181] (**Fig. 2.1**). In turn, the reverse transsulfuration permits the synthesis of Cys from Hcys, and operates in several organisms including mammals. In mammals, the reverse transsulfuration route represents the sole source of Cys biosynthesis from the essential amino acid Met and involves two distinct stages. The first step is catalyzed by the pyridoxal-5'-phosphate (PLP)-dependent cystathionine β-synthase enzyme (CBS, EC 4.2.1.22)[182], which condenses L-

serine (from now referred as serine) (Ser) and Hcys to generate Cth and H_2O in a β-replacement reaction (**Fig. 2.1**). CBS is mostly found in the liver [183,184], brain [185–188], kidney [189,190] and pancreas [191–193]. Other tissues express lower levels of CBS, such as endocrine tissues [194,195], digestive system [196–198], lungs [199–201], muscle and adipose and lymphoid tissues [202] and heart [203].

The second step of reverse transsulfuration is mediated by another PLP-dependent enzyme, cystathionine-γ-lyase (CGL, CSE or CTH, EC 4.4.1.1), that cleaves Cth into Cys, α-ketobutyrate and ammonia (NH_3) [204] (**Fig. 2.1**). The resulting Cys is further used in protein synthesis or in the biosynthesis of major cellular antioxidant glutathione [205] (**Fig. 2.1**). It is clear now that CGL shows high levels of expression in cardiovascular system [206–209], liver [210,211], kidney [212–214], pancreas [215,216], vascular smooth muscle cells [208,217,218], respiratory system [219,220] and prostate [221].

Historically, the relevance of the reverse transsulfuration pathway was mainly focused on its capacity to produce Cys, while consuming the toxic intermediate Hcys. However, new findings arised in the last years, have highlighted the no less important role played by this route in the endogenous production of H_2S, which has high physiological relevance. CBS, CGL (through its alternative reactions) (**Figs. 2.7** and **2.19**, respectively) and 3-mercaptopyruvate sulfurtransferase (MST) in concert with cysteine aminotransferase (CAT) are the three main enzymes responsible for the synthesis of this gassotransmitter. The reactivity of H_2S in biological systems is complex and permits to exert a wide variety of actions [194,207,222] which are described in more detail in Section 2.1.2.4.

Less evolved organisms such as bacteria [223,224], protozoans [225–229] and some plants [230,231], present an alternative way to obtain cysteine, the so-called *de novo pathway* [232] (**Fig. 2.1**). This route consists of two steps: In the first one, *O*-acetylserine (OAS) is formed by the condensation of serine with acetyl coenzyme A, a reaction catalysed by serine acetyltransferase (SAT). In parallel, inorganic sulfate is reduced to sulfide, then the latter is condensed to *O*-acetylserine to form cysteine in a reaction catalysed by *O*-acetylserine sulfhydrylase (OASS) in bacteria [233,234] or *O*-acetyl-L-serine(thiol)lyase (OASTL) in plants [235,236]. The association of SAT with OASS in bacteria, or OASTL in plants, results in an *O*-acetylserine (OAS)-regulated complex called "cysteine synthase" (CS) [177,237,238] (**Fig. 2.1**).

Recent studies have revealed that certain bacteria express enzymes that share features common between a CBS and an OASS [239–242]. These enzymes are referred to as *O*-acetylserine-dependent CBS (OCBS) and, beyond the canonical condensation of Ser with Hcys, are capable to use OAS (instead of Ser),

and exhibit OASS activity. However, other organisms lack either the forward or the reverse transsulfuration pathways, making de novo synthesis the main route to obtain cysteine. For example, some bacteria including *Salmonella enterica serovar Typhimurium* and *Escherichia coli*, unlike humans, can fix inorganic sulfate to produce cysteine [243,244] but they lack the reverse pathway and cannot use sulfur from methionine. On the contrary, humans lack the forward pathway and are auxotrophic for methionine, but are not for cysteine. Yeast can also incorporate inorganic sulfur by *O*-acetylserine to form cysteine, or by *O*-acetylhomoserine to produce Hcys [176,245]. Thus, in yeast the reverse transsulfuration is required to allow conversion of Hcys to Cys [246].

Alternatively, Hcys can be remethylated to Met or being transformed into tetrahydrofolate (THF) through the "*methionine cycle"* and the "*folate cycle*", respectively (**Fig. 2.1**). The remethylation occurs by the transfer of a methyl group to Hcys with the help of two different enzymes: (i) the betaine homocysteine methyltransferase (BHMT, methionine cycle) [247] or (ii) the cobalamin (vitamin B_{12}) - dependent methionine synthase (MS, folate cycle) [248] (**Fig. 2.1**). In mammals, the regulatory switch between the remethylation of Hcys and the reverse transsulfuration pathway is S-adenosylmethionine (also known as AdoMet, SAM, or SAMe) [249] (**Figs. 2.1** and **2.2**) AdoMet is formed in the methionine cycle by adenosylation of Met, in a step catalyzed by methionine adenosyltransferase (MAT) [248] (**Fig. 2.2**). In mammals, AdoMet is an allosteric activator in the transsulfuration pathway that binds to CBS, increasing its activity (around 5-fold in humans) [250]. Conversely, AdoMet acts as an allosteric inhibitor in the Hcys remethylation by inhibiting methylenetetrahydrofolate reductase (MTHFR) [251,252] and BHMT [253] (**Fig. 2.2**). Thus, remethylation is favoured at low concentrations of Hcys, whereas at high concentrations, the transsulfuration pathway becomes active in removal of the excess Hcys, which, if accumulated, is toxic. On the other hand, when the concentration of Met and consequently of AdoMet are high in the cell, Met is directed toward Cys synthesis via the reverse transsulfuration pathway. In turn, when Met and/or AdoMet levels are low, the methionine cycle is up-regulated [254].

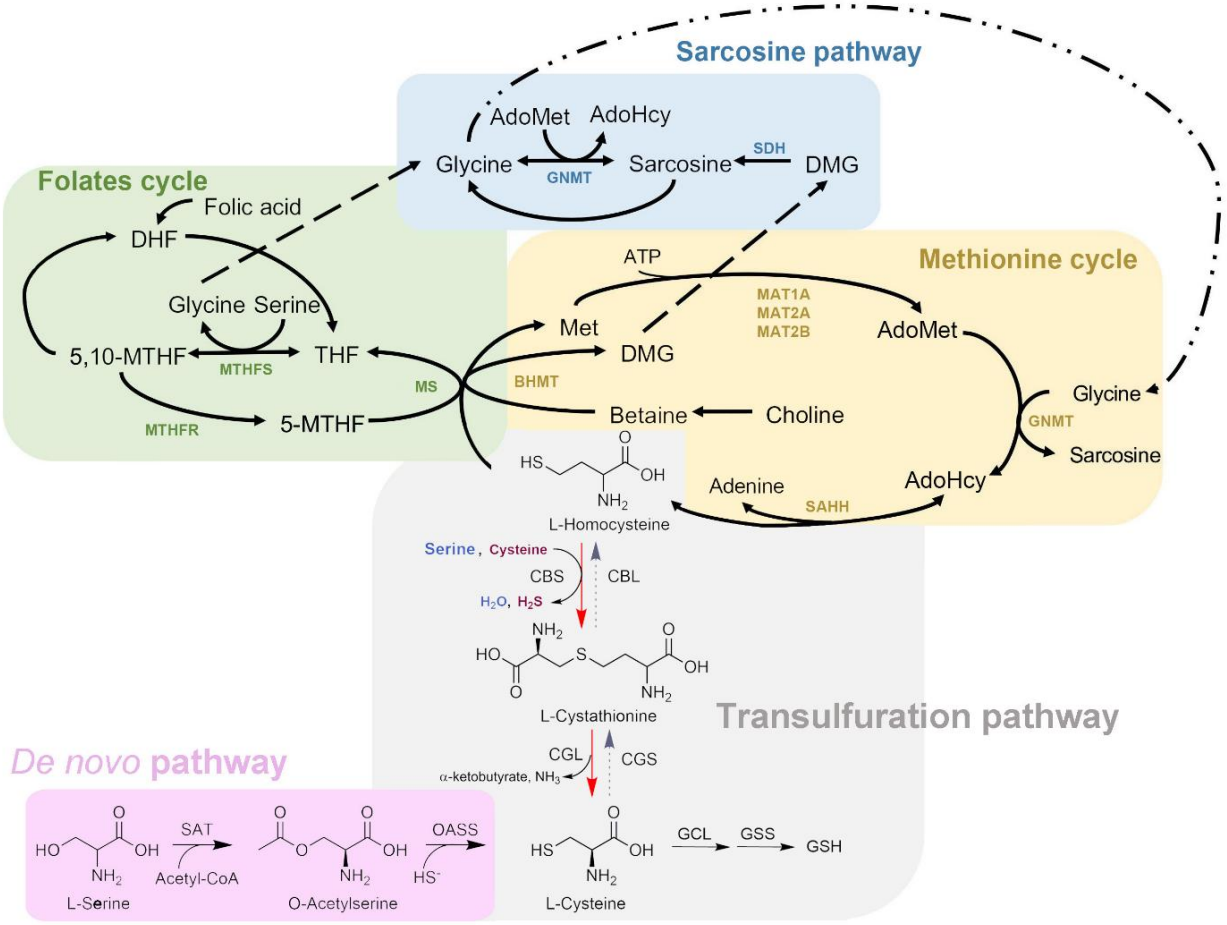

Figure 2.1. Metabolic maps. *Transsulfuration (grey frame) may include two opposite routes that allow the conversion of L-homocysteine (Hcys) into cysteine (Cys) (reverse transsulfuration, red arrows) or viceversa (forward transsulfuration, dotted grey arrows). Transsulfuration is coupled to the folates (green frame) and methionine (yellow frame) cycles, which are coupled to the sarcosine pathway (blue). Some organisms (c.a. bacteria) are able to perform the forward transsulfuration and de-novo cysteine synthesis (pink frame). In mammals, reverse transsulfuration represents the sole source of Cys. Abbreviations: GSH= glutathione; OAS=O-acetylserine; OASS= O-acetylserine sulfhydrylase; GCL=glutamate cysteine ligase; GSS =glutathione synthase; BHMT= betaine homocysteine methyltransferase; MS=methionine synthase; 5-MTHF= 5- methyltetrahydrofolate; THF=tetrahydrofolate; 5,10-MTHF=5,10-methylenetetrahydrofolate; MTHFS=5,10-methylenetetrahydrofolate synthetase; MTHFR=5,10-methylenetetrahydrofolate reductase; CGS=cystathionine γ-synthase; CBL=cystathionine β-lyase; SAT=serine acetyl transferase; Met = methionine; MAT = methionine S-adenosyltransferase; AdoMet= S-adenosyl-L-methionine; GNMT= glycine N-methyltransferase;AdoHcy= S-adenosylhomocysteine; SAHH= S-adenosylhomocysteine hydrolase; CBS = cystathionine β-synthase; CGL= cystathionine γ-lyase; GCLC= glutamate-cysteine ligase; DHF= dihydrofolate; DMG = dimethylglycine; SDH= sarcosine dehydrogenase. Figure adapted from* [255].

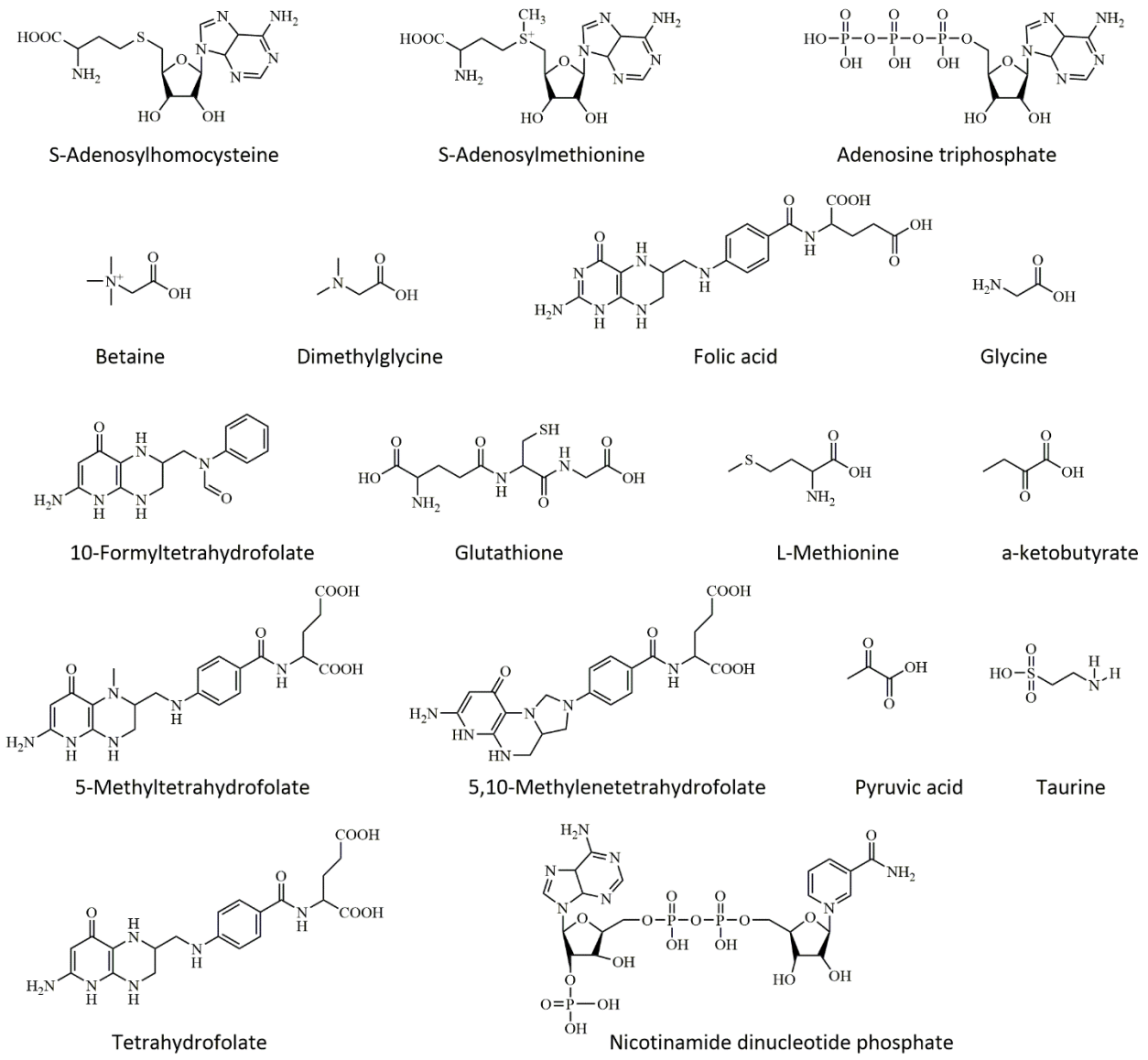

Figure 2.2. *Main metabolites that participate in the Transsulfuration, Folate and Methionine pathways.*

2.1.2. Human diseases related with dysregulation of transsulfuration

An altered transulfuration pathway causes severe diseases in humans. Not only "rare" diseases, like Homocystinuria [256] or Cystathioninuria [257] caused by dysregulation in CBS and CGL, respectively. But also, more prevalent pathologies like neurodegeneration [258], some types of cancer [259], mental disabilities [260] and aging [186].

2.1.2.1. Homocystinuria

Homocystinuria is a group of metabolic inherited diseases that cause disorders in the processing of the essential amino acid methionine. These rare diseases cause mutations or destabilization of enzymes of the transsulfuration pathway, the methionine cycle or the folate cycle, which are responsible for maintaining the correct levels of Hcys in the body. Hcys is an intermediate of methionine which is transformed into important products such as cysteine or glutathione. However, large amounts of Hcys in the blood (hyperhomocysteinemia) or urine (homocystinuria) cause it to become toxic [261–263] (**Fig. 2.3**). Classical homocystinuria is due to a deficiency of CBS activity [256,262]. Type II, III and IV homocystinurias are due to deficiencies in the activity of enzymes involved in Hcys remethylation [263–265].

Classical homocystinuria (HCU) was first described in 1962 by Gerritsen *et al*. [266], and by Carson and Neill [267], when they described a profile of patients with mental retardation due to abnormal urinary amino acid levels. Two years later, the implication of *Hs*CBS in this disease has been [256]. Homocystinuria caused by CBS-deficiency is usually manifest in the first or second decade of life and the clinical features include involvement of the eye (severe myopia and/or ectopia lentis), skeletal system (excessive height, long limbs, and scoliosis and pectus excavatum), vascular system (thromboembolism) and Central Nervous System (CNS) (development delay/ intellectual disability, seizures). The accumulative detection rate of *Cbs* deficiency that have screened over 200 00 newborns is 1 in 344 000 [268,269] varying from 1/1800 (Qatar) [270] to 1/900 000 (Japan) [271] and 1/1 000 000 in Spain [272]. Nowadays, more than 160 different mutations have been described. Some mutations are geographically widespread such as I278T [273]. But others are limited in a specific population; for example G307 mutation (613381.0001) is predominant in patients with Celtic origin [274,275] or T191M (613381.0016) has a high frequency among patients from the Iberian peninsula and several South America Countries [276].

As of now, there are not an effective treatment for HCU, but it is detected that some complications can be prevented by following and strict diet for life low in methionine [277–279] or a therapy including vitamin B6 or supplemented with folate (vitamin B9) or cobalamin (vitamin B12). Therefore, neonatal screening is crucial in the early detection of the disease.

2.1.2.3. Cystathioninuria

Cystathioninuria (CSTNU) (MIM 219500) is an autosomal recessive phenotype characterized by the abnormal accumulation of plasma cystathionine, leading to increase urinary excretion. Due to the inconsistency and wide variety of disease associations, CSTNU is considered to be a benign biochemical anomaly [155,280,281]. For instance, cystathioninuria have been associated with mental retardation and seizures[257,282,283], thrombocytopenia with renal lithiasis [284], diabetes insipidus, encephalomyelopathy [285], cystic fibrosis and celiac disease [286], Down syndrome[287], neuroblastoma [288–290] and hepatoblastoma [291]. In some instances such as cystic fibrosis, cystathioninuria could have developed incidentally [292].

This disease has an estimated prevalence of about 1:14 000 observed in three different populations of newborns [278,292,293]. Four mutations have been identified in cystathioninuric patients [292]. Two are nonsense mutations resulting to early termination, c.a, I403 and S403, and two are missense pathogenic mutations; T67I and Q240E, which show significantly lower activity and PK-content than the wild-type. Among these mutations, there are biochemical differences, such as variable response to B-vitamin treatment, suggesting the possibility of molecular genetic heterogeneity [282,294,295]. Mutation T67I can be fully rescued by exogenous B6-vitamin, on the contrary to Q204E mutation which treatment with PLP is less effective in ameliorating symptoms associated [296].

2.1.2.4. Neurodegeneration diseases.

The transsulfuration pathway is crucial in the synthesis of cysteine from homocysteine. Cysteine not only serves as a building block for protein synthesis, but it is also capable of generating sulphur-containing molecules such as glutathione, taurine, coenzyme A, and lanthionine [297]. The availability of cysteine to act as a limiting factor in the synthesis of glutathione in cells maintains the redox balance. Diversion of cysteine to the synthesis of glutathione is neuroprotective [298]. However, an impaired transsulfuration route leads to elevated blood levels of Hcys (hyperhomocysteinemia), which is a risk factor for the development of cardiovascular and neurodegenerative diseases, including dementia, Alzheimer disease (AD) and Parkinson's disease (PD) [299]. Elevated homocysteine levels has also been associated with epilepsy, neuropsychiatric disorders [300], and brain ageing factors such as an increase in oxidative stress [301–303] or a change in nitric oxide activity [304] (**Fig. 2.3**). Moreover, human Huntington´s disease (HD) patients with more severe clinical manifestations of the disease, show levels of CGL reduced between the 85-90% [305]. In mice, depletion of cystathionine γ-lyase in mice entails the loss of its products, such as cysteine, causing HD neurotoxicity [305].

As mention above, the enzymes of the transsulfuration pathway, CBS and CGL, are main producers of endogenous H_2S. H_2S is an antioxidant that can mitigate mitochondrial dysregulation due to ROS formation [306]. In 1954, association between mitochondrial dysregulation and increased ROS was first established [307–309]. Notably, changes in mytochondrial dynamics, excessive production of ROS and accumulation of misfolded protein all contributed to the onset of neurodegenerative diseases [310] including AD, PD, Huntington´s disease (HD) and amyotrophic lateral sclerosis (ALS). The antioxidant-responses of H_2S are mediated by the activities of glutathionine peroxidase (Gpx), superoxide dismutase (SOD) and catalase (CAT) [311], which neutralize oxidative damage of H_2O_2 and $O_2^{\cdot-}$ [312–314].

2.1.2.5. Impairment of endogenous H_2S production

As mentioned above, CBS and CGL catalyze alternative reactions (**Figs. 2.7** and **2.19**) that led to the formation of hydrogen sulfide. Currently, H_2S is considered a gasotransmitter (gaseous signaling compound) that is as important as nitric oxide (NO) and carbon monoxide (CO) [185,315,316].

The endogenous synthesis of H_2S in different tissues has been linked with various physiological functions and pathologies. Among them are: (i) a vasorelaxation and lowering blood pressure in rats due the direct action of H_2S on smooth muscle cells by activating ATP-K^+ channels [206,208,317–319] (**Fig. 2.4**), (ii) anti-inflammatory properties by downregulating the activity of NF-κB or by upregulating the expression of heme oxygenase 1, which are proinflammatory factors [320–324](**Fig. 2.4**) (iii) cytoprotective, anti-fibrotic, and angiogenesis properties [323,325–328] (**Fig. 2.4**) (iv) cell proliferation regulator, showing pro or anti-apoptotic function by altering the expression of the mitogen activated protein kinase (MAPK) and the extracellular signal-regulated kinase (ERK) [329] (**Fig. 2.4**) (iv) maintenance of insulin secretion [191] and development of diabetes linked to altered H_2S synthesis [215,216,329] (v) regulation of erectile dysfunction through relaxing the corpus cavernosum [330] and (vi) ischemia-reperfusion injury (IRI) and antioxidative stress protection [331]. Among these functions, the role of H_2S as oxidative stress reducer has focused special attention (**Fig. 2.5**). H_2S protects cells against oxidative stress via two different mechanisms: First, it acts as a direct ROS scavenger, and second, it up-regulates antioxidant defense systems such as: (i) Nrf2 a family of nuclear transcription factors which regulate a wide diversity of enzymes that mitigate the oxidative stress [332], (ii) the regulatory factor SR-A, the class A macrophage [333] and (iii) modulation of GSH, the major antioxidant in the cellular defense [334,335] (**Fig. 2.5**). Kimura *et al*. described a mechanism in which H_2S reduces cystine to cysteine in the extracellular space and increases the cysteine levels in the cell to produce GSH [313,334] (**Fig. 2.5**).

Other physiological roles attributed to H_2S are (i) neuromodulator [185], (ii) neurotransmitter by the regulation of the ion calcium concentrations, glutamate receptors and cAMP levels [336–339] and (iii) neuroprotector [340], having beneficial effects on Parkinson's disease [341]. Interestingly AD patients show low levels of H_2S [342,343], whereas in Down syndrome patients, high levels of thiosulfate, catabolite of H_2S, have been found [344–347] (**Fig. 2.4**).

Another studies have been reported the cardioprotection effect of H_2S during myocardial ischaemia/reperfusion injury [348,349] (**Fig. 2.4**). The cardioprotection function have been associated with a wide variety of mechanisms [350], including opening of KATP channels [351,352] stimulating anti-apoptotic signalling [352–354], reducing cellular respiration [355–357], decreasing oxidative stress [358], activating eNOs-mediated Akt phosphorylation [359] and promoting angiogenesis [360] (**Fig. 2.4**).

In cancer, H_2S is considered a double edge sword. Endogenous or relatively low levels of exogenous H_2S may exhibit pro-cancer effects, favoring tumor proliferation and angiogenesis in ovarian cancer [361,362]. Exposure to high concentrations of H_2S over a long period of time can lead to cancer death [363] by triggering uncontrolled intracellular acidification, arresting the cell cycle, and promoting apoptosis [364]. H_2S-inhibitors represent a potential treatment to combat diseases related with the production of this gasotransmitter in animal models and humans [365,366]. For example, Aminooxyacetic acid (AOAA) is a CBS-inhibitor widely used in animals, decreased tumor growth in colorectal [367], breast [368], ovarian [361] and pancreatic [369] cancer. Unfortunately, in humans this treatment causes a dose-dependent toxicity [370].

2.1.2.6. Cancer

Cysteine is an important non-essential amino acid in mammalian cells and its thiol group is the basis for several cellular antioxidant defense mechanisms [371]. During oxidative stress, cysteine utilization is activated for glutathione production and detoxification of reactive oxygen species [372] (**Fig 2.5**). The development of neoplasms requires tumor cells to overcome oxidative stress barriers at various stages [373,374], thus maintaining an adequate supply of cysteine is essential for cancer progression. Thus, deficiencies in the transsulfuration pathway lead to Hcys accumulation and failure in the Cys synthesis, which contributes to tumor development due to elevated ROS and halogen production [259].

Initial investigations describing higher levels of ROS in cancer cells than in normal cells [375], suggested a direct link between ROS and cancer development. The notious effect of ROS was attributed to damage in lipids, proteins, and DNA, that in turn favored tumor progression and genomic instability [376]. More recent

data have also confirmed the role of ROS as signaling molecules involved in processes such as cell survival, angiogenesis, and metastasis [377]. On the other hand, excessive oxidative stress has also been associated with an induction of cancer death [378]. Importantly, high levels of reduced glutathion (GSH) are able to protect cells in bone narrow, breast, colon, larynx and lung cancers, by enhancing their chimioresistance [379], suggesting a relevant and equally complex role of GSH in all these processes . It is well established that GSH is crucial for the removal and detoxification of carcinogens [380].

Likewise, transsulfuration enzymes are directly associated with tumor progression. CBS has been demonstrated to be up-regulated in colon cancer [367]. Accumulating evidence also suggest a pro-cancer role of CBS in ovarian [361] and breast cancers [381]. In the same direction, increased levels of CGL in prostate cancer [221,382], melanoma [383] and gastric cancer [351,384] have been recently reported. Likewise, CGL has also been found to support cell survival in hepatocellular carcinoma [385,386].

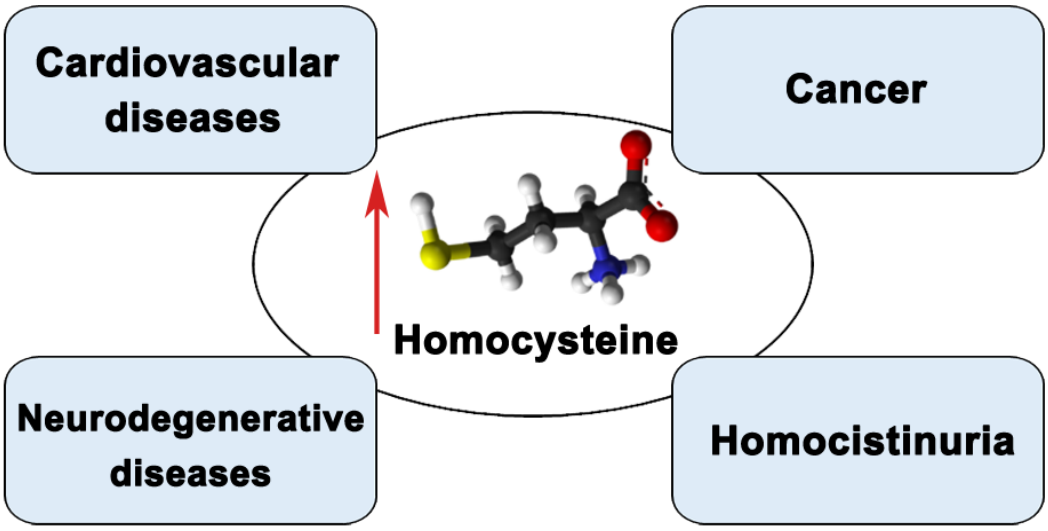

Figure 2.3. Homocysteine in human diseases*. High levels of Hcys are related to cancer, homocistinuria, neurodegenerative diseases such as dementia, AD or PD and cardiovascular diseases (e.g. atherosclerotic vascular disease or arterial and venous thromboembolism [387]).*

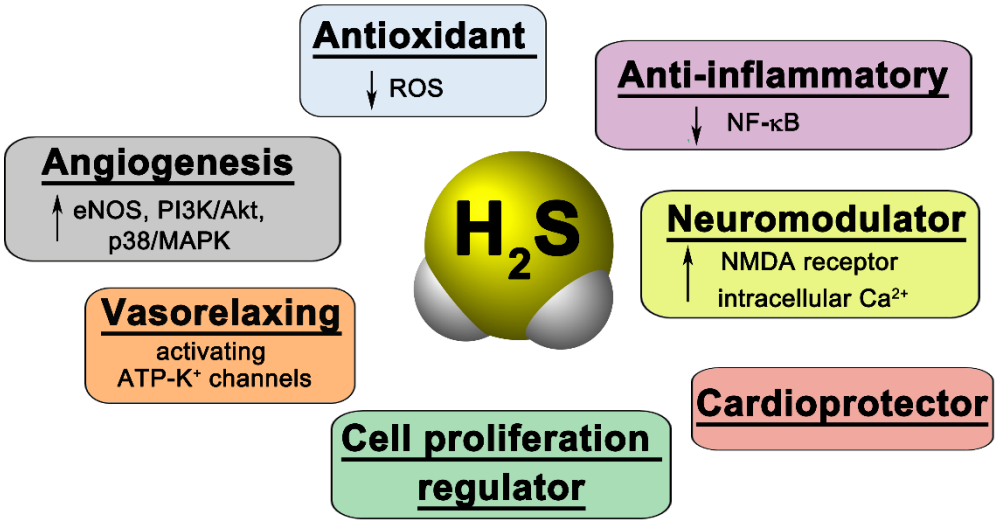

Figure 2.4. *Main physiological roles of H_2S.*

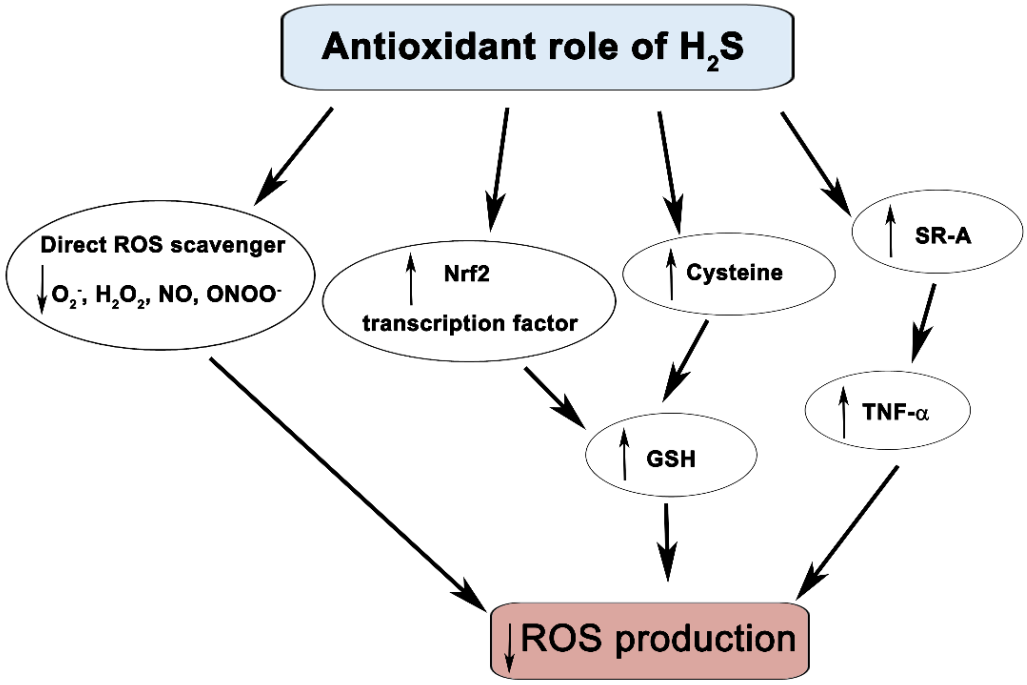

Figure 2.5. Antioxidant general mechanism of H_2S. *ROS= Reactive Oxygen Species, NRf2=NF-E2-related factor 2, GSH= glutathione, SR-A= scavenger receptor, class A, TNF-α= tumor necrosis factor α. Adapted from* [388].

2.1.3. Alteration of the transsulfuration pathway in pathogens

The dysregulation of transsulfuration in different pathogens is known to cause notious effects in their metabolism, likely due to the alteration of the H_2S production. Until recently, the significance of transsulfuration in the pathophysiology of infectious agents such as bacteria and viruses had been explored less than in higher species. According to new research, H_2S produced by bacteria serves as a defense system against antibiotics and oxidative stress [14]. For example, in virus infection, the redox-based activities appear to be affected by H_2S signaling pathway. These studies have led to propose a new strategy to modulate pathogen activity by exploiting endogenous H_2S production as a potential therapeutic target.

2.1.3.1. Hydrogen sulfide in viruses

Viral infections have been associated with induction of ROS/RNS generation and dysregulation of metabolic pathways resulting in several diseases [16,389]. Induction of oxidative stress inside the host is necessary to viral infections. Viral replication needs a favorable environment which depends on the oxidative state of the host cells [390]. In animal models, it has been shown that RNA viruses such as influenza virus, induce oxidative stress and create a redox imbalance by decreasing the levels of the antioxidants GSH and vitamins C and E [391]. Moreover, the role of the oxidative stress in retroviruses as HIV-1 (Human Inmunodeficiency Virus) have been broadly investigated. The replication of HIV-1 leads to ROS activation and decreases the levels of GSH [392,393]. Nuclear factor-erythroid-2 p45 related factor 2-Antioxidant Response Element (Nrf2/ARE) pathway regulates the expression of genes involved in oxidative stress response [394]. In HIV infection Nrf2/ARE is downregulated [389,395]. A supplementation with Sulforaphane (Nrf2 inducer) blocks the HIV-1 infection in primary macrophages [396]. Moreover, in Marburg virus (MARV) and Kaposi sarcoma-associated herpesvirus (KSHV) diseases, Nrf2 activation contributes to the dysregulation of the host antiviral response and generates a favorable environment for the survival and proliferation of infected cells [397,398].

While the link between oxidative stress and viral infections is well established, the role of H_2S remains poorly understood. Recent studies suggest that the missing link between infections and H_2S may be the Nrf2/Keap1 pathway. H_2S inhibits Keap-1 by persulfidation, this fact produces the traslocation of Nrf2 into the cellular nucleus, where it binds to Antioxidant Response Element (ARE) [399,400]. Thus, H_2S protects against oxidative stress via S-sulfhydration of Keap-1 and further activation of Nrf2 [400].

Recent studies have unraveled new links between H_2S and viral infections. For example, it has been shown that Respiratory Syncytial Virus (RSV) (a common respiratory virus that causes upper and lower respiratory tract infection in infants [401], upregulates the expression of several Nf-kB and IRF-3,transcription factors, which in turn activate genes encoding proinflammatory cytokines and chemokines [402]. In addition, RSV infection downregulates the expression of H_2S-producing enzymes [403]. In RSV-infected cells, external addition of H_2S decreases the levels of Nf-kB and IRF-3 [403]. $Cse^{-/-}$ mice enhances RSV viral replication and lung diseases symptoms than the WT [404]. Similarly, exogenous H_2S administration of H_2S donor-GYY4137 *in vitro* and *in vivo* reduces the viral spread and replication by targeting the viral assembly and improves the clinical disease parameters [403,404]. RNA-viruses from Ortho-, Filo- and Bunyavirus families [405] as well as members of the paramyxoviridae family; Nipah virus NiV-B) and human metapneumovirus (hMPV) [404] have also been shown to exert similar effects during infection. GYY4137 treatment reduces viral replication of all mentioned family viruses, confirming that H_2S targets pro-inflammatory transcription factors Nf-κB and IRF-3, as explained earlier [405]. In Coxsackie virus (CVB3), the treatment with H_2S in rats downregulates the proinflammatory Nf-kB reducing the myocardial injury [406].

Over the past two years, the 2019 coronavirus pandemic (COVID -19), due to severe acute respiratory syndrome coronavirus 2 (SARS-CoV-2) infection, has resulted in a public health emergency that has caused more than four million deaths worldwide. COVID -19-related severe respiratory failure is characterized in part by increased neutrophil counts and decreased numbers of lymphocytes (CD4, CD8, and CD19), as well as increased serum IL -6 and serum C-reactive protein (CRP) levels [407,408]. It has been speculated that H_2S may play a protective role against COVID -19-mediated pathology via several mechanisms: (i) altering the function or expression level of angiotensin-converting enzyme 2 (ACE2) and transmembrane serine protease 2 (TMPRSS2) to prevent SARS-CoV-2 from entering host cells. Research has shown that H_2S donors inhibited the expression of ACE in the kidney of hypertensive rats [409], and hypothesized that lower levels of H_2S may lead to increased TMPRSS2 expression in various pathological conditions [410]; (ii) by inhibiting viral replication, the development of inflammation leading to cytokine storm, oxidative stress and organ damage, as seen with other viruses such as RSV or CVB3 [411] and (iii) by suppressing the pulmonary immune response and inflammation [410].

In a study of 74 patients published in 2020, H_2S levels were found to be associated with disease severity [412], with a decrease in H_2S levels being associated with a higher mortality rate. In addition, serum H_2S levels were negatively correlated with IL -6, procalcitonin, and CRP, suggesting that higher H_2S levels are present in patients with a more severe inflammatory response to the disease. However, these results should be

taken with caution due to the sensitivity of serum H_2S measurement techniques. All in all, during viral infection, H_2S modulates Nf-κB transcription factor signaling, which elicits a cytokine-dependent inflammatory response. Although future studies are needed to further investigate the efficacy and applicability of H_2S donors as a good strategy against viral infections, the preliminary results are promising.

2.1.3.2. Hydrogen sulfide in bacteria

In 1877, the first evidence of endogenous H_2S production by bacteria in spoiled chicken eggs was noticed [413,414]. Subsequently, studies reported the production of H_2S by putrefactive organisms associated with soil and feces [415–417]. In the marine sea, H_2S emitted from the deep is an important source of metabolic energy [418]. In the 1960s, the evidence of the protective effect of H_2S was demonstrated. The H_2S produced by *Desullfovibrio desulfuricans* confers to *P. aeruginosa* the ability to resist the toxicity of heavy metals such as mercury [419]. Similarly, hydrogen sulfide generated by *E. coli* protects *S. aureus* from mercuric chloride and merbromin [420]. Although the results were promising, no further examination of the potential protective role of H_2S was attempted. Until 2011, when Shatalin and coworkers highlighted the importance of H_2S in protecting bacteria from antibiotics and oxidative stress [14]. Homologous H_2S-producing enzymes (CBS, CGL and 3-MST) are present in most bacterial species. In *Klebsiella pneumoniae*, *Bacillus anthracis*, *Pseudomonas aeruginosa* and *Staphylococcus aureus* the main source of H_2S are CBS and CGL, while in *E. coli* is 3-MST [14,421].

3-MST overexpression increases the spectinomycin resistance in *E. coli* [14]. As well as inactivation of CBS and CGL in *B. anthracis, P. aeruginosa and S. aureus* and 3-MST in *E. coli* via mutant genetic deletion or chemical inhibitors (PAG and AOAA) reduced the H_2S production rendering these pathogens highly sensitive to gentamycin, ampicillin and nalidixic acid [14].The antibiotic sensitivity of CBS, CGL and 3-MST H_2S-deficient cells was restrain by the H_2S-donor, NaHS [14]. In conclusion, the induction of the ROS production by antibiotics to kill pathogens [422,423] is inhibited by the H_2S. This gasotransmitter provides antibiotic resistance by mitigating the oxidative stress [14].

Several investigations have revealed that antibiotics kill by promoting the formation of harmful hydroxyl radicals via the Fenton reaction [424]. Recent study found that H_2S-endogenous produce by 3-MST protects *E. coli* from DNA damage and oxidative stress via: (i) regulating cysteine levels (toxic above physiological levels) and (ii) quenching the free iron that drives genotoxic Fenton reaction [421] (**Fig 2.6**).

Likewise, a study with *E. coli* and *S. aureus* demonstrates the role of H_2S in bacterial defense against host immunity [425]. The observations confirming this are: firstly, bacterial killing by mouse leukocytes decreases when treated with GYY3743, and secondly the burden is low in H_2S-deficient infected mice [425].

Another research clearly found that $Cbs^{+/-}$ and $cse^{-/-}$ mice have lower Tuberculosis disease [370,426]. In fact that, Mycobacterium tuberculosis (Mtb) infection exploit the H_2S-production in host to growth stimulating the *Mtb* respiration, predominantly via CytBD [426]. The host fight against *Mtb* infection increasing the glycolytic metabolism [427]. Therefore when the production of H_2S is excessive, the host glycolysis is suppressed [370].

Based on this knowledge, H_2S was considered a universal defense mechanism against antibiotics. However, a recent study on *Acetinobacter baumannii* refutes the previously mentioned conception. *A. baumannii* is a multidrug-resistant bacterium that cannot produce H_2S, and its treatment with exogenous H_2S donors (NaHS) makes it sensitive to a variety of antibiotics [428]. Exogenous H_2S creates redox disturbance by affecting Fe^{2+}/Fe^{3+} balance towards Fe^{2+} and increasing Reactive Oxygen Intermediates (ROI) via Fenton Chemistry [428]. (**Fig 2.6**). In conclusion, H_2S can be proposed as an antibiotic-potentiator in bacteria that do not produce it.

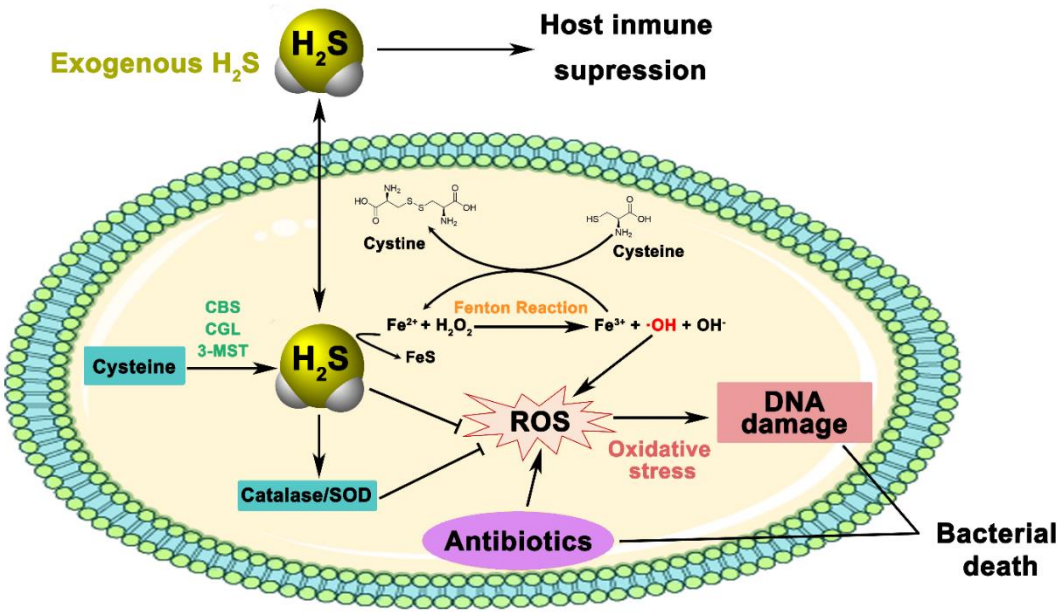

Figure 2.6. H_2S-bacterial protective mechanism against oxidative stress induced by antibiotics and/or host immune response. *H_2S can be endogenously generated or exogenous delivered (NaHS or GYY4137). The protection is accomplished by the increase of the activity of H_2S-producer enzymes, the inhibition of the Fenton reaction producing by the reactivity of H_2S with Fe^{2+}, the high stimulation of the activity of SOD and Catalase mediators and the reduction of the cysteine levels (cysteine produces Fe^{2+} reagent of Fenton reaction). SOD= superoxide dismutase. Figure adapted from [370].*

2.1.4. Enzymes of Reverse Transsulfuration

2.1.4.1. Cystathionine β-synthase (CBS)

2.1.4.1.1. Reactions catalyzed by CBS

Cystathionine β-synthase (CBS), the first enzyme of the reverse transsulfuration pathway, catalyzes the pyridoxal-5´-phosphate (PLP)-dependent β-replacement reaction that condenses serine with homocysteine to yield cystathionine and water (**Figs. 2.7** and **2.8**). Besides this canonical reaction and using cysteine and homocysteine as substrates, CBS can also efficiently produce hydrogen sulfide (H_2S) through alternative β-replacement and α,β-elimination processes (**Fig 2.7**).

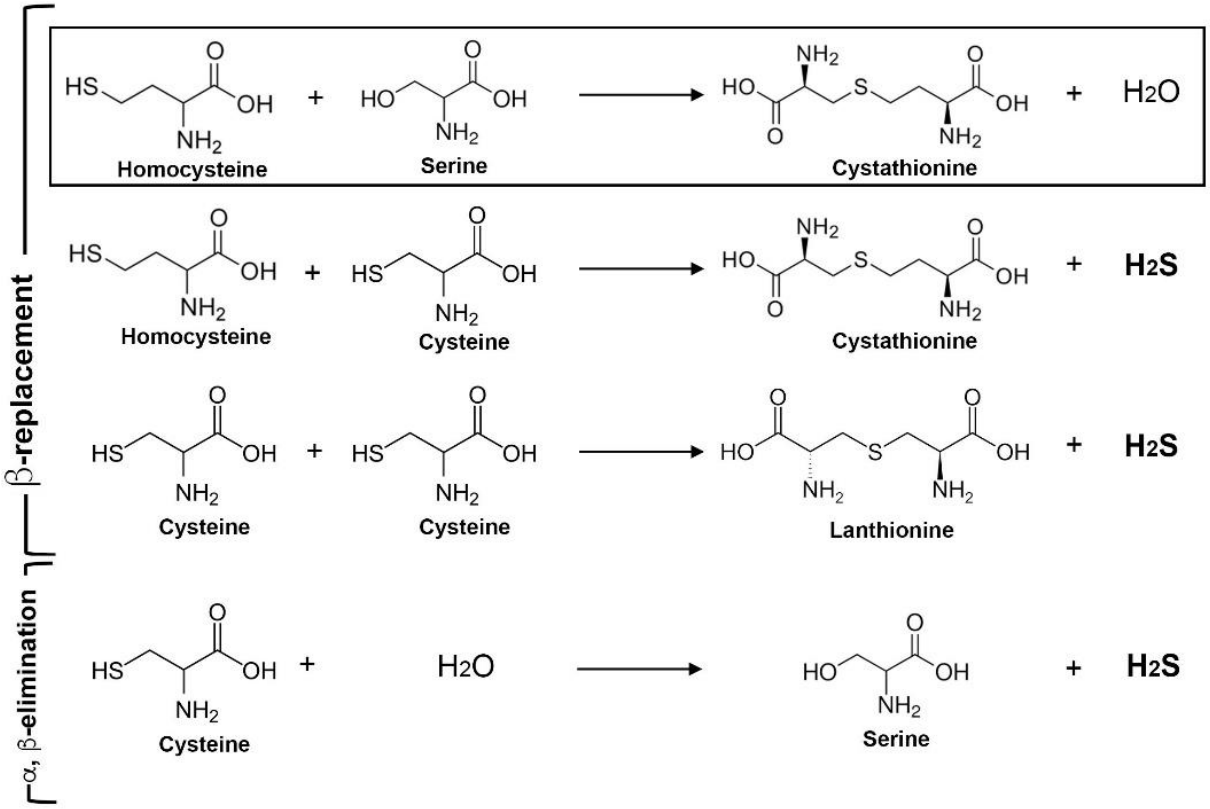

Figure 2.7. *Reactions catalyzed by CBS leading to Cth and hydrogen sulfide (H_2S) generation: The canonical β-replacement reaction in which the thiolate of Hcys replaces the hydroxyl group of Ser to yield Cth and H_2O is framed. Alternative reactions that led to the formation of H_2S. Figure adapted from* [255].

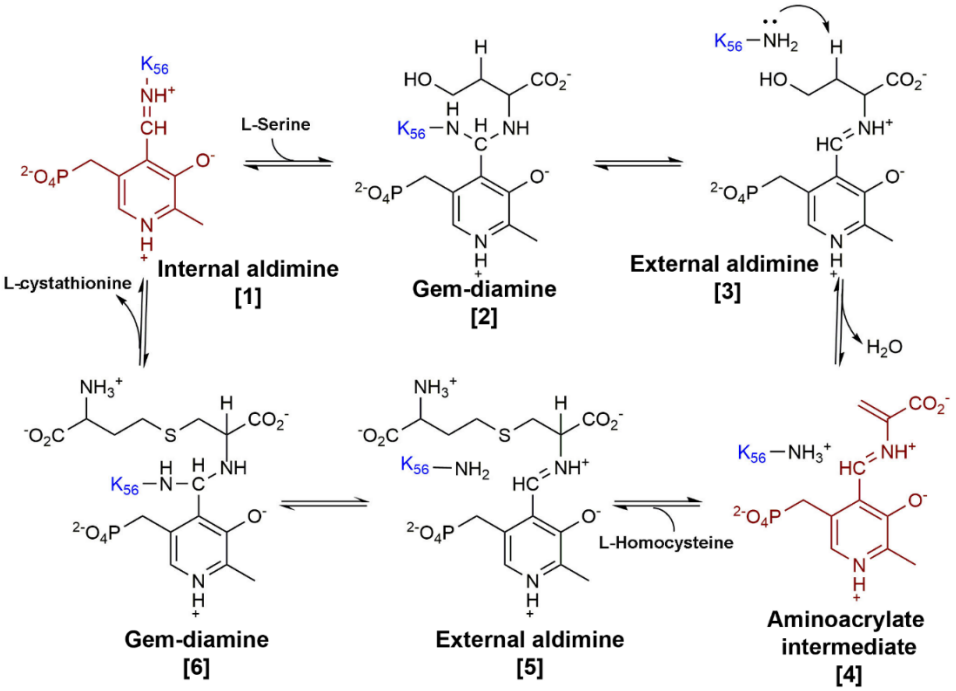

***Figure 2.8**. Ping-pong mechanism of the canonical reaction of CBS.*

2.1.4.1.2. Domain architecture and oligomerization of CBSs.

CBS is a complex modular protein present in a wide variety of organisms from all kingdoms, for which five different domain distributions (herein referred as classes A to E) and two major oligomers (dimers and tetramers) have been described (**Figs. 2.9** and **2.10**) [159]. The simplest architecture, (class A), is found in bacteria and consists of a catalytic domain with the folding of PLP-dependent enzymes of the type II with the cofactor covalently attached to the ε-amino group of a conserved lysine via a Schiff base bond. This type of CBS protomer is the most studied structurally (PDB IDs 6AHI, 5HBG (*Helicobacter pylori*) [242] 5XW3 (*Bacillus anthracis*) [240], 5B1H, 5B1I (*Lactobacillus plantarum*) [241], 4OFX (*Coxiella burnetii*) (**Fig. 2.9**) and self-assembles into active dimers from which reaction intermediates have recently been isolated [240,241]. A rare variant of this CBS, class B, occurs in *Caenorhabditis elegans* (*Ce*CBS) and contains two catalytic domains in tandem arrangement, only one of which binds PLP [159,429]. No structural data is currently available on this CBS type. The next complexity level, class C, occurs in yeast [430] and in some apicomplexan such as *Toxoplasma gondii* [431] (**Fig. 2.9**), but can also be found in Gram negative bacteria such as *Pseudomonas aeruginosa*, whose CBSs retain the catalytic domain and contain an additional C-terminal Bateman module. The Bateman module in turn consists of two so-called CBS motifs (CBS1, CBS2)

whose function is still unknown [126,432]. The crystal structure of a truncated construct containing the catalytic core of *Saccharomyces cerevisiae* CBS bound to some reaction intermediates represents the only structural data available on this class (PDB 6C2Z, 6C4P, 6C2Q, 6C2H) [433]. The next CBS structure type, class D, is found in some insects, e.g., fruit fly [434] (PDB IDs 3PC2, 3PC3, 3PC4) and honeybee [435] (PDB ID 5OHX), and contains an N-terminal heme-binding domain of unclear function that precedes the catalytic domain. The only two crystal structures available from this CBS type [434,435] indicate that the fundamental role of the Bateman module in class D enzymes lies in stabilizing a constitutively activated dimeric assembly without playing any additional role in the regulation or activity of the enzyme. The class D CBSs exist in a sole constitutively active conformation (**Fig. 2.9**). Finally, class E, the most evolved version of the enzyme, is found in mammals, including humans, and has the same domain distribution as flies and bees (**Fig. 2.9**). However, in this case the Bateman module becomes more important and not only determines the degree of oligomerization of the enzyme, which includes dimers, tetramers or even larger aggregates, but also becomes an allosteric module that regulates the degree of enzyme activity upon binding of S-adenosylmethionine (AdoMet) [159,246,436–438] (**Fig. 2.9**). Importantly, class E CBS can adopt two distinct conformations (**Fig. 2.9**). The first is less active and is known as the *basal state*. The second is reached upon binding of AdoMet at the C-terminal regulatory domain and is from 3 to 5 fold more active (**Fig. 2.11**)

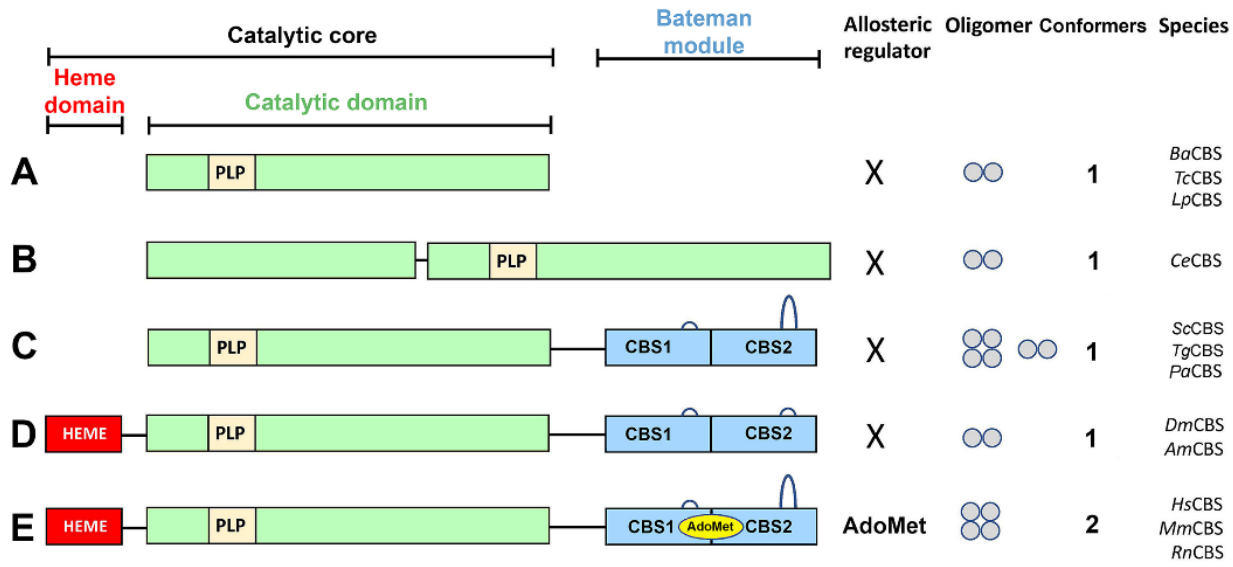

Figure 2.9. CBS architectures. *CBS architectures. Class **A**, found in B. anthracis (BaCBS), L. plantarum (LpCBS) and T. cruzi (TcCBS); Class **B**, found in C. elegans (CeCBS); Class **C,** found in T. gondii (TgCBS), S. cerevisiae (ScCBS) and P. aeruginosa (PaCBS). Class **D,** found in D. melanogaster (DmCBS) and Apis mellifera (AmCBS). All CBSs but class C, usually show a long loop at CBS2. Class **E**, found in mammals, binds AdoMet. The small circles indicate the oligomerization degree. Figure adapted from [255].*

2.1.4.1.3. The three-dimensional structure of CBS.

The current knowledge on the CBSs structure is very scarce and limited to three out of the five known domain organizations (**Fig. 2.10**). Since a truncated construct containing the catalytic core of human CBS was initially solved in early 2000s (PDB IDs 1JBQ, 1M54) [438,439], only four additional structures of full-length CBS proteins containing the regulatory module have been determined. Of these, the first two correspond to the basal (PDB IDs 4L0D, 4L27, 4L28, 4L3V, 4COO) [69,440], and the activated conformations of human CBS (PDB ID 4PCU)[160] (**Fig. 2.11**, A and B, respectively). The other two are the constitutively activated CBS dimers from the fruit fly *Drosophila melanogaster*, both alone (PDB ID 3PC2) and in complex with reaction intermediates (PDB IDs 3PC3, 3PC4) [434], and the wild type honeybee *Apis mellifera* (PDB ID 5OHX) [435], (arrangement D in **Fig. 2.11**). In addition, structures of a truncated construct containing the catalytic core of *Saccharomyces cerevisiae* CBS which naturally lacks the heme cofactor both alone and in complex with different substrates and reaction intermediates have also been elucidated (PDB IDs 6C2H, 6C4P, 6C2Q, 6C2Z) [433]. The list of available structures ends up with the coordinates of the bacterial catalytic core of a closely related *O*-acetylserine-dependent CBS from *Helicobacter pylori* (*Hp*OCBS) (PDB IDs 4L0O, 6AHI, 5HBG, 4L0O), *Lactobacillus plantarum* (PDB IDs 5B1H, 5B1I) [241], *Bacillus anthracis* (PDB ID 5XW3) [240], and *Legionella pneumophila* (PDB ID 6VJU), which naturally lack the regulatory Bateman module (arrangement C in **Fig. 2.11**) an show mixed catalytic features of both CBS and *O*-acetylserine sulfhydrylase (OASS) [239–242].

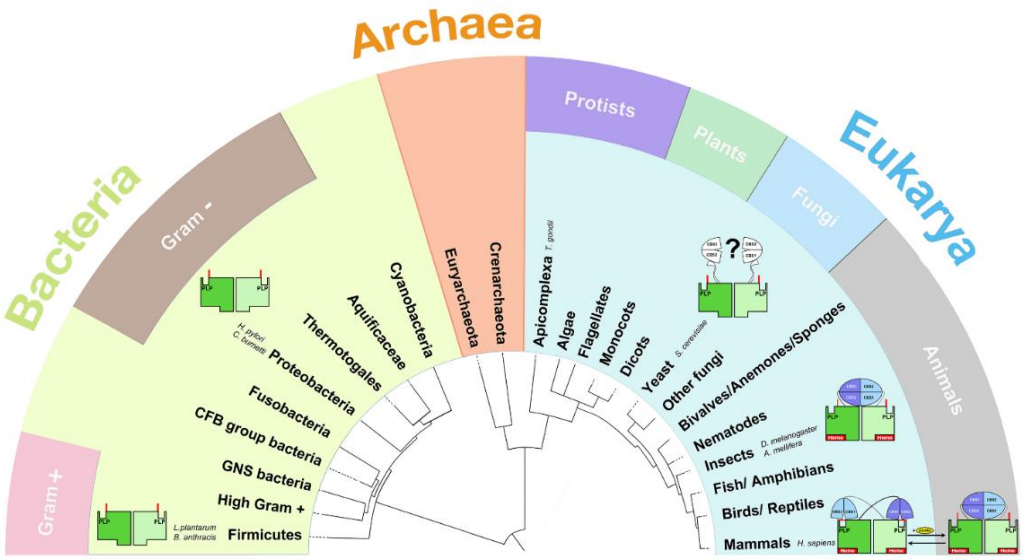

***Figure 2.10. Phylogenetic tree of organisms encoding the CBS enzyme**. The nine available crystal structures of CBSs are indicated. Unsolved domains are in white. Figure adapted from [255].*

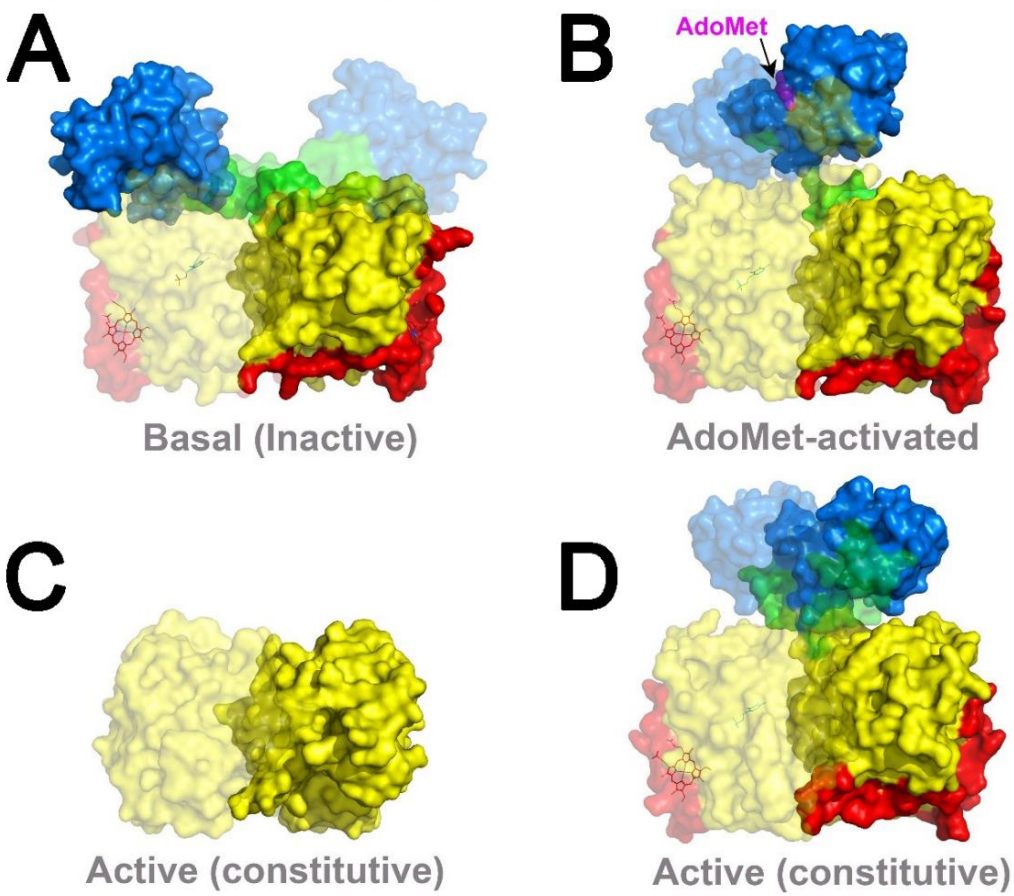

***Figure 2.11. Three-dimensional structures determined for CBS**. Lower part depicts conformations found in CBS enzymes, for which the crystal structures has been determined **(A)** Basal conformation of HsCBSΔ516-525 (engineered dimeric construct) **(B)** AdoMet-bound activated conformation of HsCBSΔ516-525 E201S variant (dimeric construct). **(C)** Active conformation of bacterial CBS. **(D)** Constitutively active conformation of insect CBS. The heme domain, the catalytic domain and the Bateman module are colored in red, yellow and blue, respectively. The interdomain linker is in green. AdoMet is in magenta. The two complementary subunits are represented in opaque and transparent surfaces, respectively. Figure adapted from [161].*

All these data have helped identify the key catalytic residues in catalysis, as well as in AdoMet binding, but are insufficient to predict other relevant features, as for example (i) the actual location of the Bateman module in a particular CBS enzyme and its ability to adopt one or several conformations; (ii) the whole set of residues involved in tetramerization; (iii) potential interactions of the N-terminal domain with the catalytic and/or regulatory domains and (iv) the reaction specificity of a particular CBS. Having this information at hand is key to designing molecules that modulate the catalytic activities of CBS enzymes from different organisms, e.g. human versus bacterial pathogens. The following sections dissect each of the individual domains of CBS in more detail. We have selected the human CBS as template, as it represents the most complex CBS arrangement described so far [161] (**Figs. 2.9** and **2.11**).

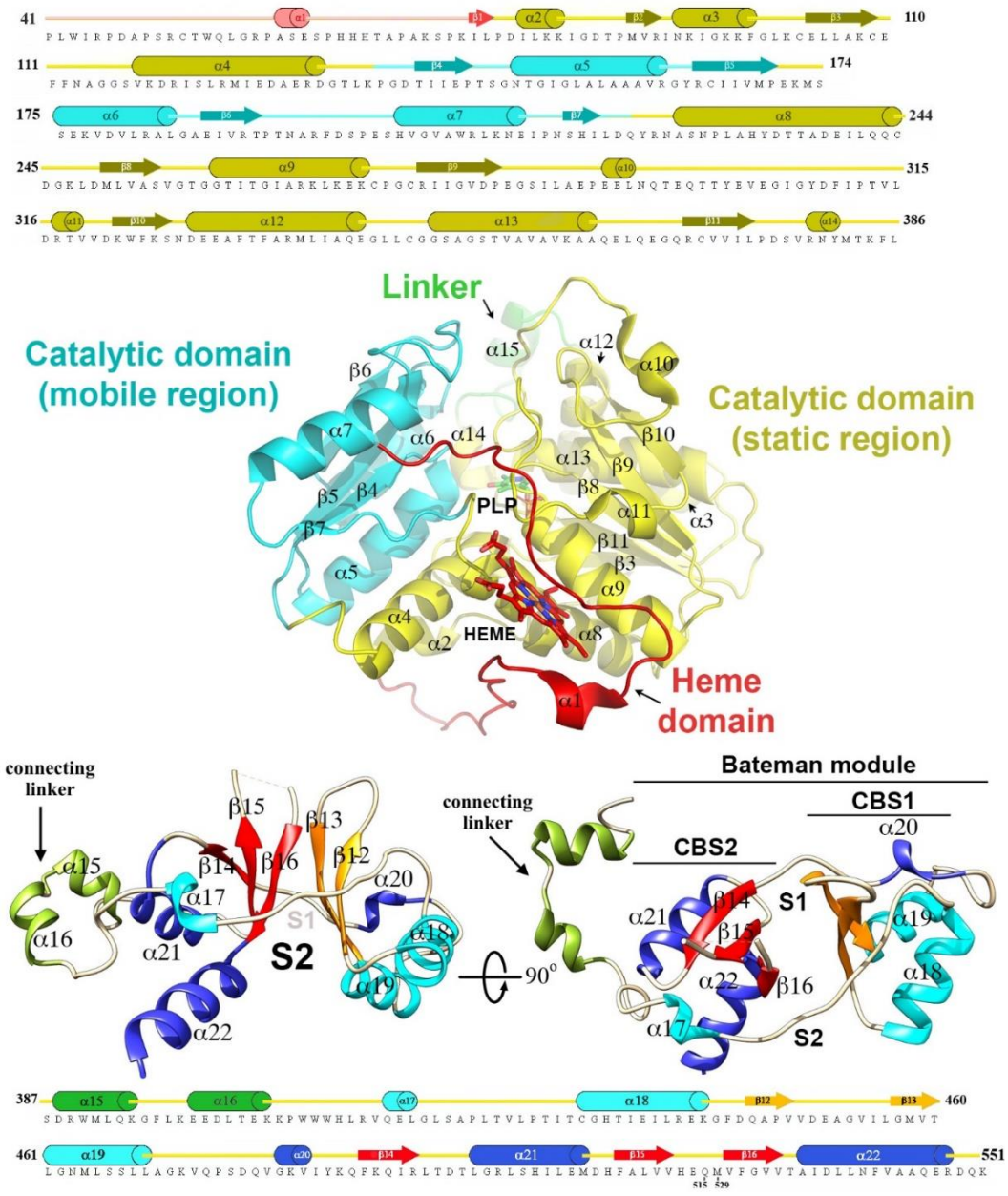

Figure 2.12. Human CBS. *(**top**) Amino acid sequence of the catalytic core of HsCBS. Secondary elements are indicated. The heme binding domain is in red ribbons. Heme is in red sticks. (**middle**) The catalytic domain (in ribbons) is split in two subdomains: static (in yellow) and mobile (in cyan). The linker between the catalytic core and the Bateman module is in green. (**bottom**) The C-terminal regulatory Bateman module consists of two CBS motifs, CBS1, CBS2. Two main cavities, S1 and S2, are formed. S2 represents the AdoMet binding site. Figure adapted from* [161].

2.1.4.1.3.1. The heme-binding domain.

The heme domain is probably the most controversial and less understood region of CBS, which is the only PLP-dependent enzyme containing it [159].This module was incorporated into the enzyme late in evolution [159]. In fact, it is only present in higher eukaryotes like insects [434,435] or mammals [438,439], while other organisms, such as yeast [179], roundworms [429], parasitic protozoans as *Trypanosoma cruzi* [226], lack this domain entirely (**Fig. 2.9**). Interestingly, the heme-domain appears exclusively when the Bateman module is also present (**Fig. 2.9**) suggesting that the function of heme and/or heme-binding domain is interconnected with that of the C-terminal domain. Both, structural [439,441] and regulatory functions have been attributed to the heme cofactor [437], but there is no common consensus about its actual role. Some authors think that it is not essential for catalytic activity, nor for correct protein folding. The main reasoning for this postulate derives from its absence in many CBSs (e.g. yeast) [179]. Interestingly, heme-containing CBSs (e.g. *Dm*CBS or truncated *Hs*CBS) are significantly more resistant towards heat-induced denaturation and unfolding than the heme-independent *Sc*CBS, thus supporting a structural role of heme and heme-binding domain [159]. Other authors, however, proposed a regulatory role for heme, as redox status of heme cofactor affects catalytic activity of the enzyme [346,437].

The heme domain encompasses approximately the first 75 residues. Structurally, it clearly consists of two different regions. The first one comprises the first 40 amino acids and represents an intrinsically disordered region (**Figs. 2.9** and **2.11**). Presumably, this region maintains only scarce or temporal contacts with the rest of the protein, explaining why it is absent in all the crystal structures elucidated so far. A comparative sequence analysis led Kumar *et al*. to hypothesize that this first segment might contain a *non-canonical heme-binding site*, as it presents a conserved cysteine-proline (CP) motif at position 15 followed by two nearby histidines at positions C15+2 (H17) and C15+7 (H22), that is similar to those found in intrinsically disordered regions of other heme-binding proteins [442]. Using NMR techniques, these same authors encountered that the CP motif is indeed involved in transient heme interactions, leading to a hexacoordinated complex with residues C15 and H22. Supporting these findings, mutation of C15 into a serine (C15S) [442], or truncation of the first 39 N-terminal amino acids [443] reduce the CBS activity by approx. 30% [442]. However, the catalytic penalty caused by C15S mutation is questionable as others did not find decreased specific activity of either full-length or truncated *Hs*CBS C15S variants [444,445]. The second stretch of the heme-binding domain comprises the following ~35 residues and forms the *canonical heme-binding site*. In contrast with the first segment, this part is well ordered and visible in all the crystal structures reporting heme-dependent CBS in the literature [69,160,434,435,438–440]. The three-dimensional arrangement of

the canonical heme domain region, was firstly observed in 2001 by Jan P. Kraus and colleagues using a truncated construct (*Hs*CBS45kDa) containing the catalytic core of *Hs*CBS [438](**Fig. 2.12**). Ruma Banerjee´s group reported similar results soon after [439] and confirmed that the prosthetic heme is hexacoordinated and axially liganded to the protein by the residues C52 and H65. Each subunit of *Hs*CBS binds a single heme molecule that is housed in a hydrophobic pocket formed by residues 50-57 of the canonical heme-binding domain, together with helices α8 and α9 and the loop preceding strand β1 and helix α2 of the catalytic domain (nomenclature extracted from [69]) (**Figs. 2.12** and **2.13**). The sulfhydryl group of C52 and the Nε2 atom of H65 axially coordinate the iron of heme [438] (**Fig. 2.13**). Using spectroscopic techniques, it was further demonstrated that despite not being involved in the catalysis, heme plays a relevant regulatory role upon binding to the gaseous molecules CO and NO, which lead to inhibition of the enzyme. CO displaces residue C52, whereas NO displaces H65 and binds 200-fold less tightly than CO [437,439,446]. Importantly, binding of any gaseous molecule or other ligands requires reduction of CBS heme to the ferrous (Fe^{2+}) form, as ferric (Fe^{3+}) form is stable and essentially inert to binding of additional ligands. Moreover, the binding of ligands to ferrous heme is also modulated by pH [447,448]. Thus, the redox status of the tissue was postulated to regulate *Hs*CBS activity, and the inhibitory potential of CO. Moreover, it was found that binding of CO induces a tautomeric shift of the PLP from ketoenamine to enolimine form (**Fig. 2.14**) [437]. The ketoenamine species is key to PLP reactivity because it facilitates the nucleophilic attack by the first substrate (Ser) in the ping pong reaction [437]. As H bond interaction between residue N149 and O4 (PLP) (**Fig. 2.14**) is a stabilizing interaction for the ketoenamine form, the loss of this interaction underlies the tautomer shift to the enolimine (and accordingly, to enzyme inactivation). All these findings were intriguing, as the heme moiety is separated by 20 Å from the PLP at the active site, thus clearly precluding a direct signal transduction from heme to the catalytic cycle or viceversa [434,439]. More importantly, these data placed heme as a key regulator of the mechanisms controlling the endogenous production of H_2S in tissues such as the brain, where it is thought to act as a neuromodulator [449].

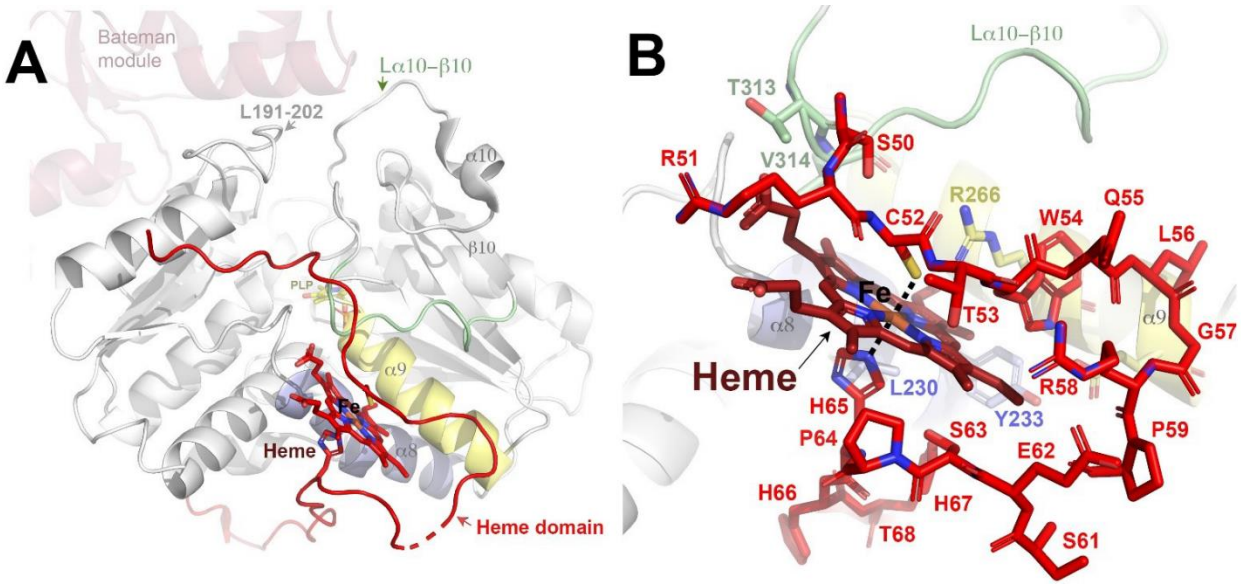

Figure 2.13. Heme-binding domain of HsCBS. *(A) Ribbons representation of the heme binding domain (in red) inserted in the catalytic core, that also contains the catalytic domain (in grey). Helices α8 and α9 from the catalytic domain interact with heme (in sticks). (B) Amino acid residues forming the heme-binding pocket or interacting with heme. Figure adapted from* [161].

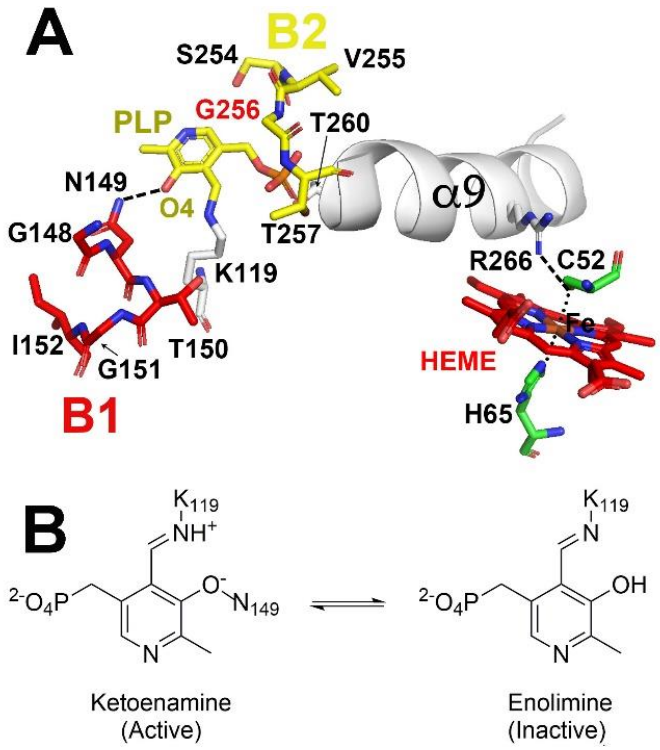

Figure 2.14. Residues connecting heme and PLP. *(**A**) B1 and B2 are two consensus sequences involved in catalysis* [242]*. (**B**) Ketoenamine and enolimine forms of PLP. Figure adapted from* [161].

The three-dimensional structures of the catalytic core of *Hs*CBS [246,438] were key in finding an explanation for the decreased activity observed in CBS upon changes in the heme environment. The crystallographic data revealed that helix α9 (according to nomenclature in [69], extends between the heme and the PLP pockets (**Figs. 2.13** and **2.14**) [450], thus indirectly connecting the two cofactors [451]. More specifically, the PLP is connected to one end of helix α9 by H-bonds to its phosphate group from the side-chains of the helix residues T257 and T260. On the other hand, R266 (located in the middle of helix α9) forms a salt bridge with the heme ligand C52 (**Fig. 2.14**). Weeks *et al*. postulated that

an impairment to this salt bridge could induces a displacement of helix α9, which in turn could disturb the PLP. The N149/O4 H-bond would be broken by this displacement inducing the tautomer shift to the enolimine form, thus inactivating the enzyme [437]. Same authors proposed that binding of CO to heme displaces C52 and causes the loss of the R266/C52 salt bridge. This in turn induces the shift from the ketoenamine to the enolimine form, and inactivates the enzyme. Some years later, Banerjee´s team further demonstrated that the distant communication between the PLP- and heme-binding sites occurring through helix α9 is bidirectional, and that the homocystinuria causing mutation T257M, affecting the conserved threonine residues residing at the N-end of this helix (e.g. T257 and T260) and interacting with the oxygen atoms of the phosphate moiety of PLP, elicited changes in the heme electronic environment and inactivated the enzyme [450]. Interestingly, Yadav *et al*. also found that alteration of the threonine residues not only affected the kinetic properties of the full-length human CBS enzyme with respect to a truncated protein lacking the Bateman module, but it also affected the allosteric regulation by AdoMet. These findings led the authors to suggest that the conserved threonine residues in the so-called *phosphate* binding loop of the catalytic core might be important for transmission of allosteric communication from the regulatory Bateman module [450].

2.1.4.1.3.2. The catalytic domain.

The catalytic domain has been the most studied region of CBSs. Structurally, it presents a conserved fold of the type II family of PLP-dependent enzymes also found in plants and bacteria (**Fig. 2.12**). Unlike the heme domain, that only interacts with the catalytic core of its own subunit, one main feature of the central catalytic domain is that it self-assembles forming compact dimers (**Fig. 2.15**) that are hold together by a mix of hydrophobic and H-bond interaction networks [438,439]. In *Hs*CBS, it includes fourteen α-helices and two β-sheets consisting of four (β4–β7) and six (β2–β3, and β8–β11) strands, respectively (numbering from [69] **Fig. 2.16**). Initially considered mostly as a rigid entity with some few flexible loops involved in the aperture/closure of the catalytic cavity, the availability of the crystal structures of CBSs from human [69,160], fruit fly [434], honeybee [435], and yeast [179,433] both alone and in complex with some of their substrates and reaction intermediates, revealed that this domain is in fact composed by two distinguishable structural blocks (**Figs. 2.15** and **2.16**).

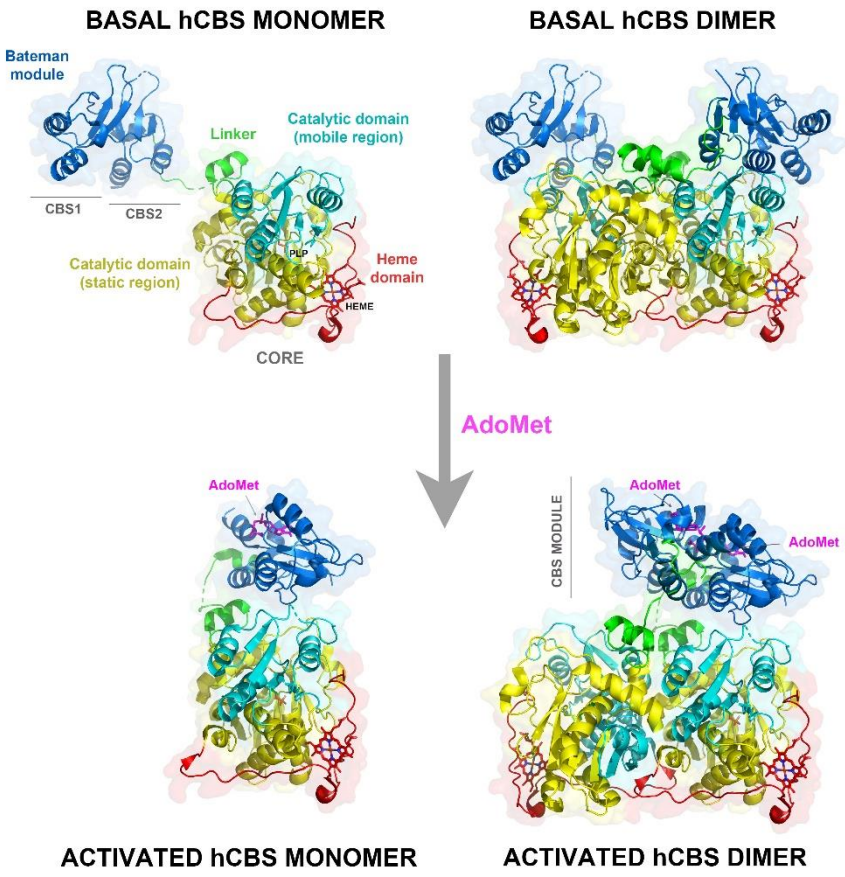

Figure 2.15. Conformations of HsCBS. *Binding of AdoMet to the Bateman module triggers a conformational change that makes HsCBS transition from the basal towards the activated state. The colors of the domains follow the criteria adopted in Figure 2.11. Figure adapted from* [161].

The larger one (amino acid residues ~75-116 and 226-384 in *Hs*CBS), so-called *static subdomain* [435] behaves mostly as a rigid body during the catalysis (**Fig. 2.16**). This subdomain contains two out of the five loops that configure the entrance to the catalytic site (loops B3 and B5, **Fig. 2.16**), as well as four (B2, B3, B4 and B5 in **Fig. 2.16**) out of the five consensus sequences that participate in the interaction with the different CBS substrates (**Fig. 2.16**) [242].On the other hand, the second subdomain, so-called *mobile subdomain* due to its dynamic behavior, is smaller in size (residues 117-225 in *Hs*CBS; **Fig. 2.16**) and is intercalated in the static block, to which is tethered by two flexible loops that connect helix α4 with strand β4, and strand β7 with helix α8, respectively (**Fig. 2.16**). Importantly, the mobile subdomain acts as a lid that regulates the access of substrates into the catalytic cavity (**Fig. 2.16**). There are two circumstances under which the mobile subdomain collapses towards the entrance of the catalytic site and closes it. The first one occurs in the basal state of *Hs*CBS, in which the presence of the Bateman module pushes it towards the static subdomain thus restricting the access to the catalytic center and maintaining the basal activity (**Figs. 2.15** and **2.16**). The second takes place upon binding any of the substrates (**Fig. 2.7**) into the catalytic cavity [242,433,434].The presence of thee small molecules inside implies the formation of new interactions with residues of the protein, including some from the mobile subdomain (B1 block in **Fig. 2.16**), thus promoting the displacement of said subdomain.

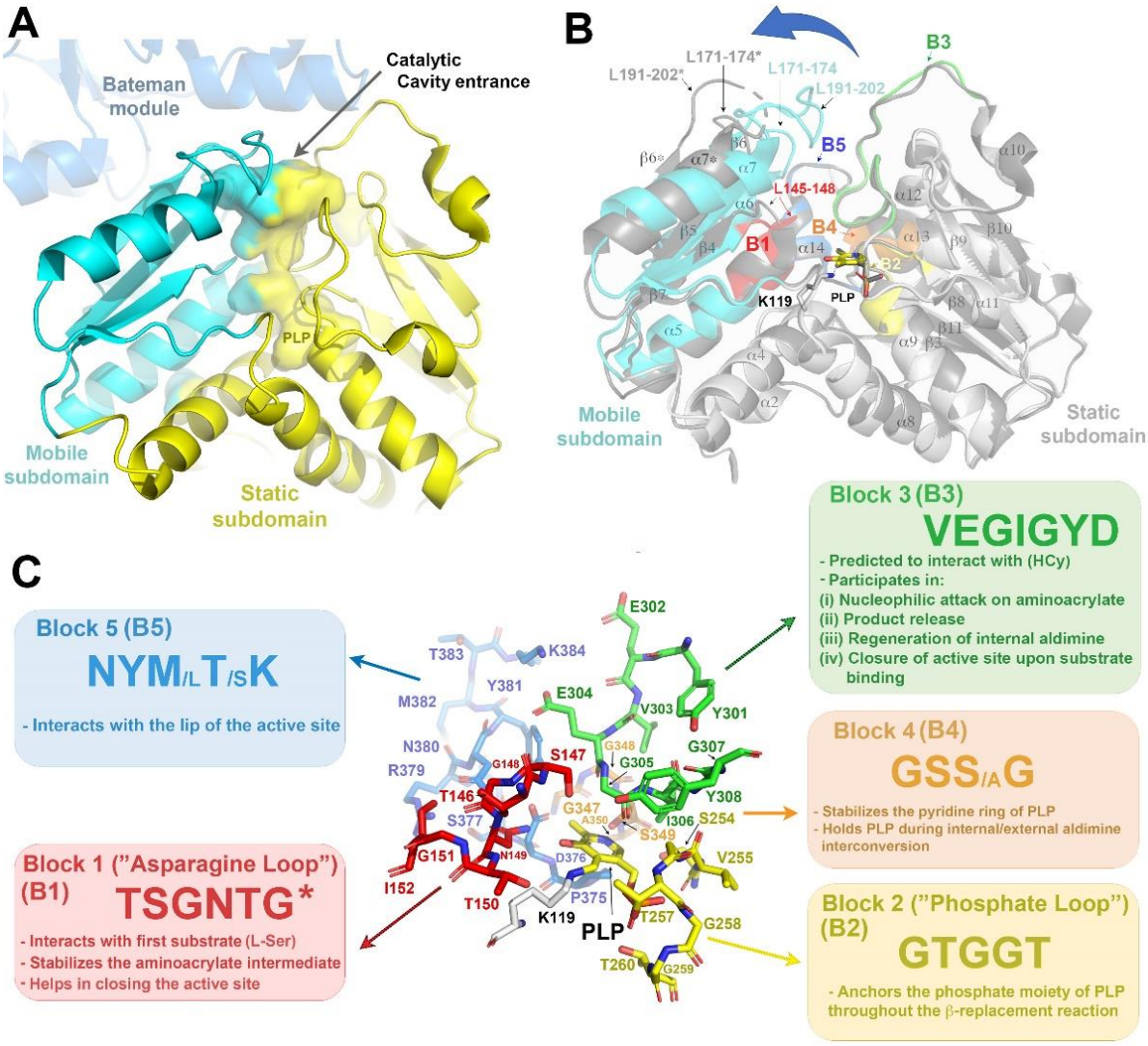

Figure 2.16. Catalytic domain of CBS. (A) *The catalytic domain of HsCBS is formed by two subdomains: static (in yellow) and mobile (cyan). The catalytic cavity hosting PLP (represented as surface) is located between these two blocks. In the basal conformation, the regulatory Bateman module is placed above the mobile subdomain, which is compressed towards the cleft thus impairing the access of substrates to the PLP. (**B**) Superimposition of the catalytic domain in the basal (light grey) and activated (dark grey) states. The mobile subdomain (in cyan) shifts away from the entrance of the cavity in the activated state, allowing the access of substrates to the PLP. (**C**) Consensus sequences (blocks) B1-5 involved in catalysis [242]. Residues (in sticks) are colored according to the block they belong to, following the criteria of panel B. Figure adapted from [161].*

A narrow channel formed between the mobile and static subdomains represents access cavity for the substrates to reach the catalytic PLP located at the bottom of this channel (**Fig. 2.16**). The PLP molecule is covalently attached to the protein via a Schiff bond to the ε-amino group of a conserved lysine (K119 in the case of *Hs*CBS), forming an internal aldimine [452]. Several H-bonds anchor the PLP molecule to the

protein matrix and orient the cofactor appropriately within the cavity. Among them are those formed between the nitrogen of the pyridine and the Oγ of residue S349, and between the 3´-hydroxyl group of PLP and the $N_{\delta 2}$ of residue N139 (**Fig. 2.16**). Importantly, N149 is coplanar with the pyridine ring of PLP and thus allows the appropriate ring tilt upon transaldimination [438]. In the opposite side of PLP, the phosphate moiety interacts with the so-called *phosphate binding loop* (block B2 in **Fig. 2.16**, residues 256-260 in *Hs*CBS), which is located between strand β8 and helix α9 and includes two important threonine residues (T257 and T260) as well as three glycines that form a network of H-bond interactions that ensure the correct orientation of PLP (**Figs. 2.14** and **2.16**). Intriguingly, mutation of the threonines not only causes a loss of CBS activity, but additionally impairs carbonylation of the heme moiety displacing C52 axial ligand in ferrous *Hs*CBS [437].This fact led Banerjee´s team postulate a putative communication between the heme cofactor and the catalytic site through helix α9 [437,450]. An exhaustive comparative sequence analysis of CBSs, OCBSs and OASS enzymes from more than 100 different organisms performed by Devi *et al.* highlighted the presence of five consensus sequences (blocks) near the active site involved in determining catalytic specificity (or rather promiscuity) of CBS enzymes towards the different substrates mentioned in **Fig. 2.7**. The *asparagine-* and *phosphate-binding loops* represent two of these five consensus sequences highlighted by Devi *et al*. [242]. The first block known as the *asparagine loop* (B1, TSGNTG, residues 146-151 in *Hs*CBS, **Fig. 2.16**) is the only one inserted in the mobile subdomain (**Fig. 2.16**). Importantly, block B1 is key in maintaining interactions with the first substrate (Ser) and stabilize the aminoacrylate intermediate during the β-replacement reaction. Moreover, it promotes the displacement of the mobile subdomain that triggers the closure of the active site (**Fig. 2.16**). Block 2 known as the *phosphate binding loop* (B2, GTGGT, residues 256-260 in *Hs*CBS, **Fig. 2.16**) anchors the PLP molecule within the cavity through the β-replacement reaction [240,434]. On the other hand, block 3 (B3, VEGIGYD, residues 303-309 in *Hs*CBS, **Fig. 2.16**) is predicted to interact with the second substrate (Hcys) and also to facilitate the nucleophilic attack on the α–aminoacrylate intermediate and release of the reaction product (Cth), thus restoring the internal aldimine [453]. This postulate needs to be confirmed, as no crystal structure with bound homocysteine is available yet. Similarly to B1, block B3 helps in closing the active site upon substrate binding by establishing interactions with the mobile subdomain through the conserved glutamate of its consensus sequence [240]. Importantly, the conserved tyrosine residue of B3 also interacts with Ser [434]. The fourth block (B4, $GSS/_{A}G$, residues 348-351 of *Hs*CBS, **Fig. 2.16**) helps orienting the PLP through interacting with the nitrogen of the pyridine ring. Finally, block 5 (B5, $NYM/_{L}T/_{s}K$, residues 380-384 in *Hs*CBS, **Fig. 2.16**) contains a conserved lysine residue (K384 in *Hs*CBS) that establishes interactions with residues from the mobile subdomain, thus also contributing to the closure of the active site.

Importantly, the mobile subdomain contains three flexible loops which in the basal state are sandwiched between the core and the Bateman module at the entrance of the catalytic site. These loops contain residues 145-148 (block B1), 171-174 and 191-202 (**Fig. 2.16**) and play a key role in maintaining the active site closed, both in the basal conformation and upon binding of substrates during catalysis.

2.1.4.1.3.3. The regulatory Bateman module.

Finally, the third portion of the CBSs is represented by the C-terminal *Bateman module* (~20 kDa), which was known to exert a regulatory role upon binding of AdoMet for almost two decades [436].In terms of primary structure represents the least conserved region across all CBSs. As mentioned above, this module is not even present in the CBS of some organisms (**Fig. 2.9**), nor it plays the same role in the different CBS enzymes. Structurally, the Bateman module consists of two consecutive CBS motifs (or CBS domains), which include approximately 60 amino acids each (residues 411-551 in *Hs*CBS) and adopt a βαββα fold (**Fig. 2.12**) [69,126,432]. The two CBS motifs are related by a pseudo 2-fold symmetry that confers the Bateman module a characteristic kidney-like shape with two main cavities (named S1 and S2) located at opposite sides of the central axis (**Figs. 2.12** and **2.17**). Each CBS motif is preceded by a flexible peptide segment that includes a short α-helix (α17 and α20, respectively). These linkers not only provide the upper wall of sites S1 and S2 (**Fig. 2.12**), but contribute to hold the two CBS motifs close to each other, during the conformational change triggered by AdoMet that activates the enzyme (see below) [69,160].

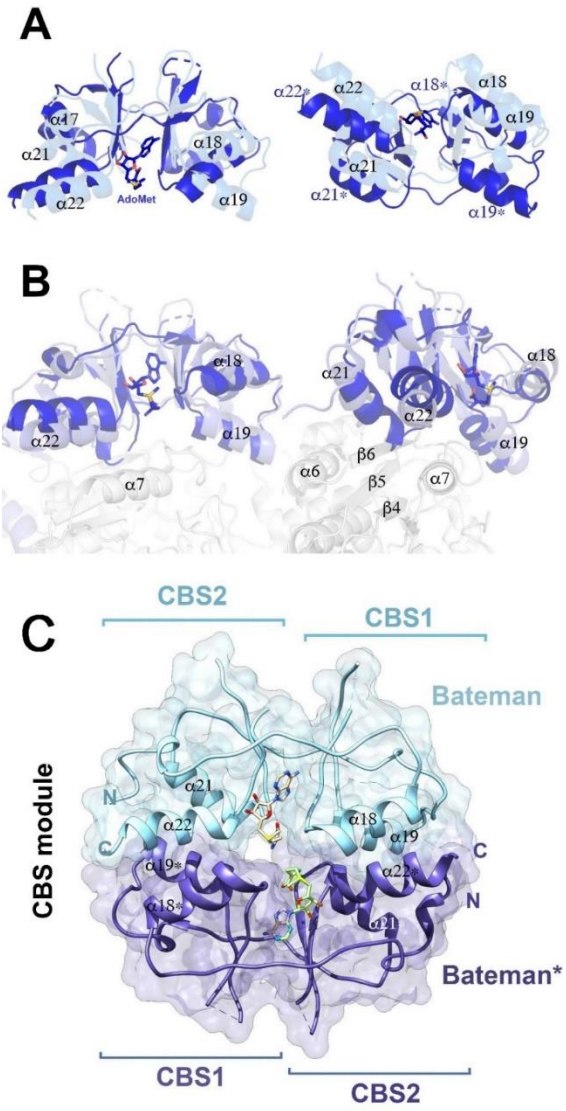

***Figure 2.17. Conformational change triggered by AdoMet**. (**A**) Binding of AdoMet (in sticks) to the site S2 cavity of the Bateman module triggers a conformational change consisting in a relative rotation of the two CBS motifs. Basal and activated conformations are colored in light and dark blue, respectively. (**B**) The orientation of the interfacial helices of the Bateman module changes upon binding of AdoMet, and that weakens their initial interactions with the catalytic core (in grey). (**C**) In the AdoMet-bound form, the Bateman modules form a disc-like structure known as "CBS module". Figure adapted from [161].*

Another relevant feature found in the Bateman module of mammals and yeast CBS enzymes is a long loop that links the last two β-strands (β15-β16) of the CBS2 motif (**Figs. 2.11** and **2.12**) In these organisms this region is significantly larger than in other organisms, and stabilizes the formation of tetramers [69]. Artificial shortening of this region (i.e. by removal of residues 516-525) causes disassembling into dimers [69] and permitted the crystallization of the full-length human CBS in year 2013 [69] after over a decade of unsuccessful attempts with the full-length *Hs*CBS WT. The fruit fly and honeybee CBSs, which exist as dimers, contain a significantly shorter loop [434,435]. Another unique ability acquired by the Bateman module of mammalian CBSs is a conformational change in the relative orientation of its two CBS motifs upon AdoMet binding [160](**Fig. 2.17**). Of the two main cavities of the module, site S2 presents particular features that favor hosting of AdoMet. The first is the presence of a conserved aspartate at the first turn of helix α22 (D538), and a threonine three positions before (T535) that together orient the ribose ring of AdoMet within the cleft. An isoleucine preceding the aspartate (I537) provides the suitable hydrophobic environment for the methyl moiety. At the opposite side of the cavity, a hydrophobic pocket provided by strand β12, helix α19 and the segment connecting helices α17 and α18 anchor the adenine ring of AdoMet [160](**Fig. 2.18**). In contrast, site S1 lacks many of these features and its entrance is occluded by elements of the catalytic domain in the basal conformation. This explains why this cavity is unable to bind AdoMet, even when added at millimolar concentrations.

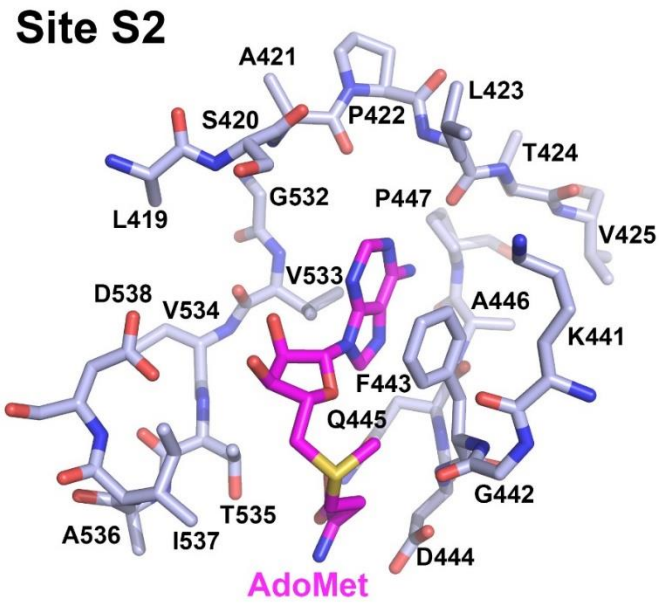

Figure 2.18. AdoMet-binding site of HsCBS. *Sticks representation of residues involved in AdoMet binding at site S2 of the Bateman module. Figure adapted from* [161].

In the absence of AdoMet, the Bateman modules from complementary subunits remain apart from each other, and rests above the entrance of the catalytic cavity of its complementary subunits, thus occluding the access cavity to the catalytic center. Helices α19, α21 and α22 of the Bateman module (**Fig. 2.17**), and loop 191-202, helices α6 and α7 and strand β6 of the mobile subdomain of the catalytic core (**Fig. 2.16**) participate in the interdomain interface. The fourth helix of the Bateman domain, α18, remains exposed to the solvent in the basal state [69,440].

Binding of AdoMet at the S2 cavity of the Bateman module causes a relative rotation of the CBS motifs. Such re-arrangement, in turn, weakens the interaction formerly existing between the Bateman module and the central catalytic domain [160]. Concomitantly, this weaken interaction also resulted in migration of the Bateman module from above the catalytic core of the complementary subunit to its own. At the same time, the relocation of the Bateman modules was stabilized by their assembly in an anti-parallel manner to form a disk-shaped structure known as "CBS module" (**Fig. 2.17**). In this new conformation, the catalytic cavity is exposed and becomes accessible for the substrates. We and others found that such an activated state is permanently maintained in the fruit fly [434] and honeybee CBSs [435], which do not bind and are not regulated by AdoMet [159]. This feature contributes to stabilization of the dimeric state of the enzyme [434,435], which appears to be the only oligomeric state seen in CBSs from these organisms. Interestingly, the Bateman module is also present in yeast [159], amphibians (Uniprot Q7ZXW6), fishes (Uniprot F1QIC0) and birds (Uniprot A0A2I0M5N4). However, relative orientation of the Bateman module with respect to the catalytic core, the degree of its association or its ability to bind AdoMet are currently unknown for these species. Lower eukaryotes such as worm *C. elegans* [429], and bacteria as *Bacillus anthracis* [240] lack the Bateman module. Interestingly, yeast encode an active tetrameric enzyme that binds AdoMet, but is not regulated by this molecule [159].

Microcalorimetric characterization of *Hs*CBS suggested that the *Hs*CBS WT tetramer contains two types of AdoMet binding sites: high (k_D ~10 nM) and low (k_D ~400 nM) affinity site binding two and four AdoMet molecules per tetramer and being responsible for enzyme stabilization and activation, respectively [454]. However, crystal structure of AdoMet-bound *Hs*CBSΔ516-525 E201S dimeric engineered construct showed AdoMet bound only in site S2 yielding stoichiometry of four AdoMet molecules per *Hs*CBS WT and only one type of site. Further microcalorimetric comparison on *Hs*CBS WT and *Hs*CBSΔ516-525 showed that the removal of the loop 516-525 functionally eliminated the high affinity sites [455]. Therefore, it is plausible that these sites are different from the canonical cavities S1 and S2 and are present only in tetramers and higher order oligomers of *Hs*CBS.

2.1.4.2. Cystathionine γ-lyase (CGL, CSE, CTH)

2.1.4.2.1. Reactions catalyzed by CGLs

Cystathionine γ-lyase (CGL or CSE), also known as Cystathionase (CTH), is a PLP-dependent enzyme that catalyzes the α,γ-elimination of cystathionine to give cysteine, α-ketobutyrate and ammonia [456] (**Figs. 2.19** and **2.20**). Alternatively, can also hydrolyze cystathionine acting on atoms at the α and β positions to yield homocysteine (Hcys), pyruvate and ammonia. This latter reaction is known as the α,β-elimination or β-lyase activity of CGL. (**Figs. 2.19** and **2.21**). Alternatively, CGL can also catalyzes hydrogen sulfide (H_2S) producing processes that include cysteine-dependent and homocysteine dependent reactions [457] (**Fig. 2.19**). In general, seven different reactions have been reported as possible by different authors (**Fig. 2.19**), although only few of them (such as α,γ-elimination and α,β-elimination of Cth and α,β-elimination of Cys) have been confirmed for each particular CGL in the organisms studied so far.

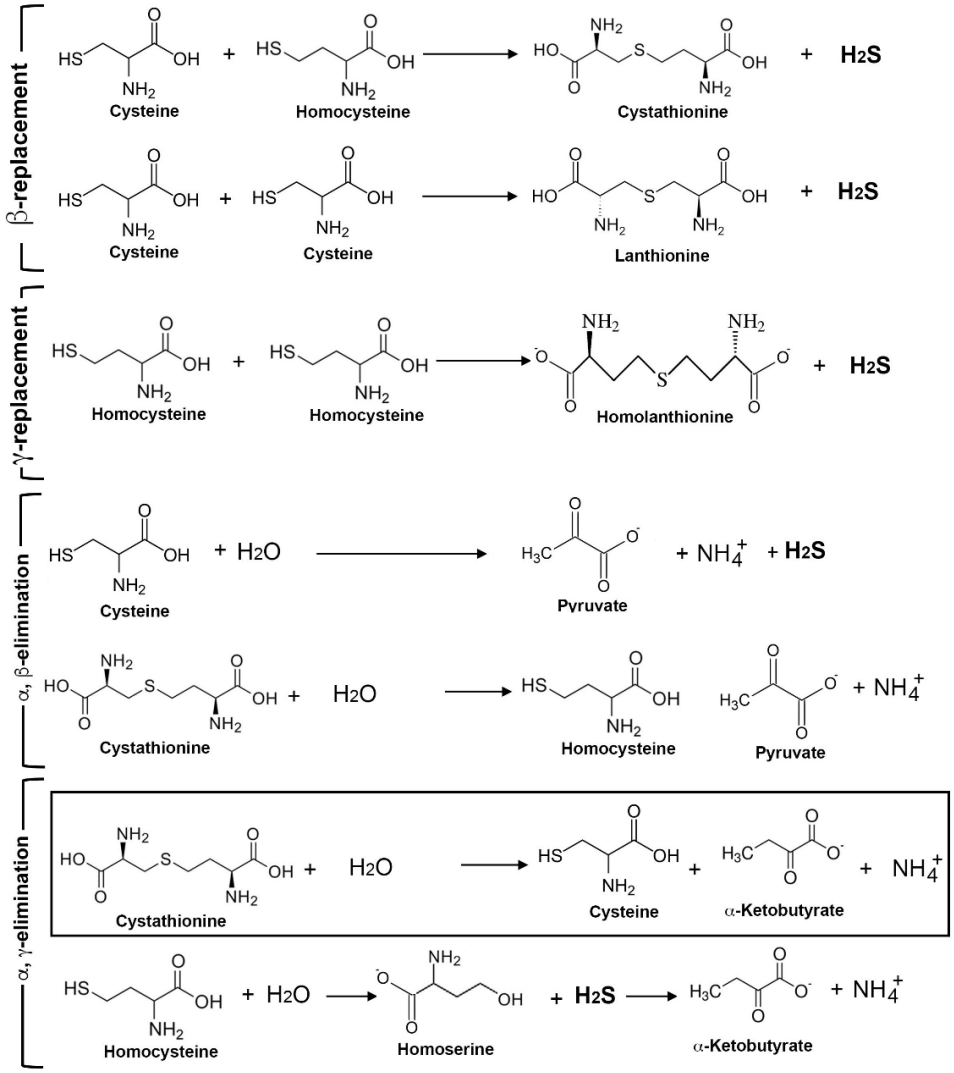

Figure 2.19. Reactions catalyzed by CGL. *Seven catalyzed reactions have been considered in different organisms (the common canonical reaction is framed).*

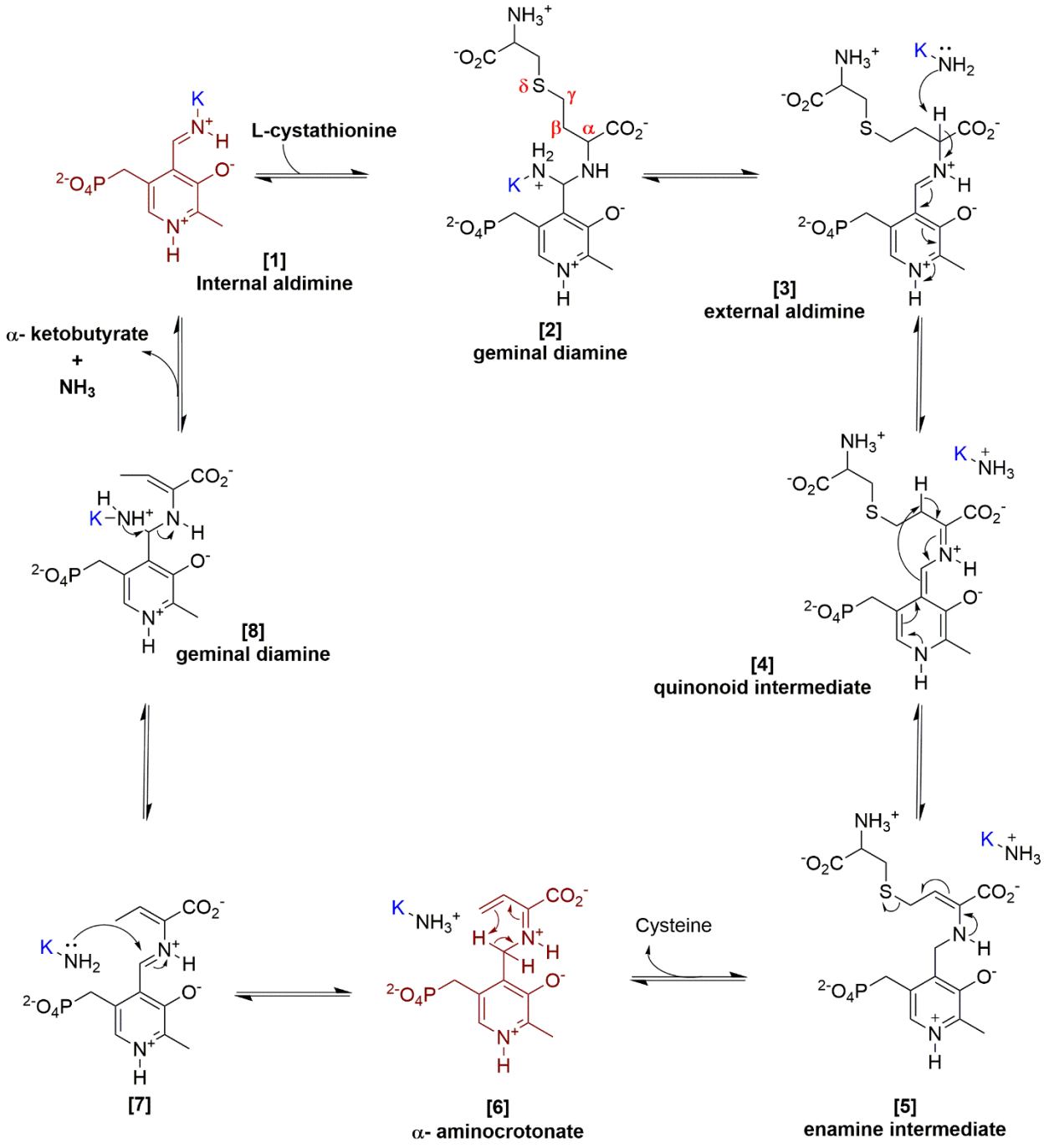

Figure 2.20. *Catalytic mechanism of the canonical α,γ-elimination toward cystathionine catalyzed by CGL* [457–459]*.The positions of atoms at α, β,γ and δ are indicated in red greek letters at intermediate [2].*

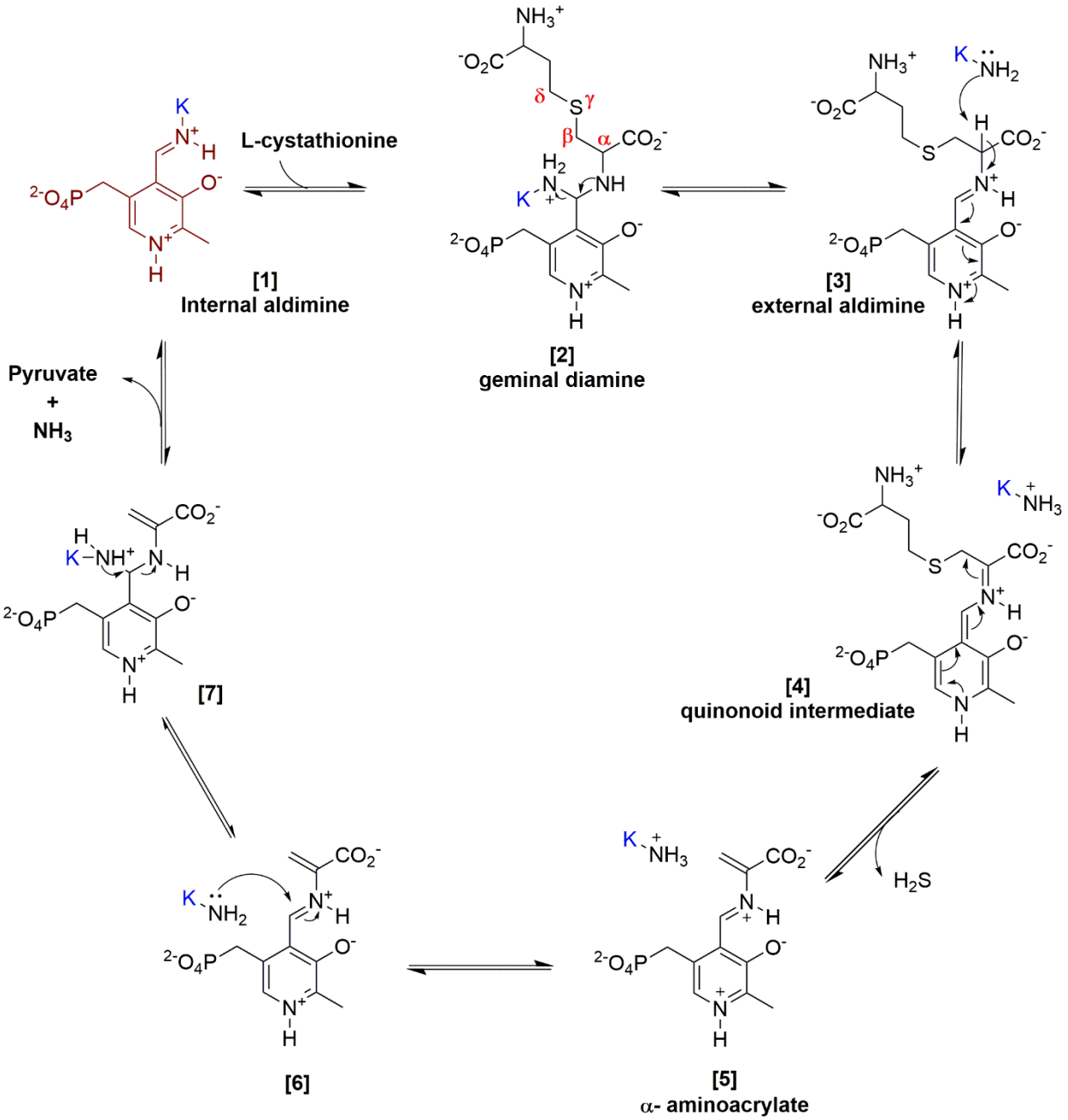

Figure 2.21. *Catalytic mechanism of the alternative reaction α,β-elimination toward cystathionine catalyzed by CGL*[459]*. The positions of atoms at α, β,γ and δ are indicated in red greek letters at intermediate [2].*

2.1.4.2.2. Domain distribution and oligomerization of CGL

Structurally, the Cystathionine γ-lyase enzyme belongs to the family of type I PLP-dependent enzymes. This group also includes cystathionine γ-synthase (CGS) and cystathionine β-lyase (CBL), which are enzymes of the forward transsulfuration pathway [460]. The sole and stable oligomer of this type of enzyme is a homotetramer, in turn formed by two equivalent dimers. The domain architecture of each CGL subunit does not differ among species (**Fig. 2.22**). The N-terminal domain includes approximately 50 residues and contains a very long loop involved in formation of the dimeric entities. This loop is directly followed by the PLP binding domain, which represents the largest region of the protein and contains the most important catalytic residues. The PLP cofactor is covalently bound to the protein, forming an internal aldimine with a well conserved lysine at the active site (**Fig. 2.22**). Finally, the catalytic domain is connected to the smaller C-terminal domain via a long α-helix (a more extensive description of the structure is detailed in the section 2.1.4.2.3.).

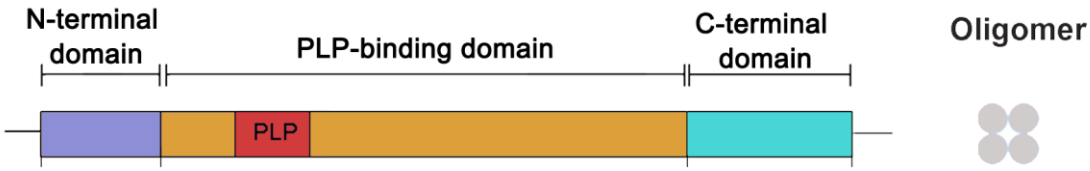

***Figure 2.22. Domain distribution of cystathionine γ-lyase across species**. In purple the N-terminal domain. In orange the PLP-binding-domain and the pyridoxal 5´-phosphate cofactor is in red. The C-terminal domain is in cyan. The grey circles represent the most frequent oligomeric state.*

2.1.4.2.3. Three-dimensional structure of CGL

The three-dimensional structure of CGL was firstly elucidated in the early 2000s from the yeast species (PDB ID 1N8P) [460]. Some years later, the crystal structures of human CGL, alone (PDB ID 2NMP) [461] and in complex with different ligands (PDB IDs 3COG, 6NBA) were reported [461–463]. Several recent manuscripts highlighting the relevance of CGL as a major H_2S producer in bacterial pathogens (H_2S is a gasotransmitter that plays a very important role as a modulator of oxidative stress) [14,15], have encouraged many authors to widen the current knowledge by elucidating new CGL structures from different pathogenic organisms. This includes the crystal structures of CGLs from *Saccharomyces cerevisiae* (PDB 1N8P)[460], *Strenotrophomonas maltophilia* (PDB IDs 6K1M, 6K1N, 6K1O, 6K1L) [464], *Lactobacillus plantarum* (PDB IDs 6LE4, 6LDO) [459], *Bacillus cereus* (PDB 7D7O) [465] and *Staphylococcus aureus* (PDB IDs 6KHQ, 7MCL, 7MCB, 7MCN, 7MCP, 7MCQ, 7MCT, 7MCU, 7MCY, 7MD0, 7MD1, 7MD6, 7MD8, 7MDA, 7MDB) [15,466]. Taking into account the similar domain distribution found in all these enzymes across evolution, we have used the

human CGL as a template model to describe the main overall structural features in the following section (**Fig. 2.23**).

The N-terminal domain of CGL is the smallest in size and consists only of one alpha helix (α1) and one long loop (residues 25-65 in human CGL) (**Fig. 2.23**). This loop interacts with amino acid residues of the active site from a neighboring monomer and is involved in the oligomerization of the enzyme, more concretely in the stabilization of one of the dimers that form the protein homotetramer. The second domain is known as the "PLP-binding domain", and contains most of the active site residues. Within its main cavity, it hosts the PLP cofactor, which is covalently linked to a conserved lysine residue, thus forming an internal aldimine. Structurally, the PLP domain displays an α/β/α fold, where seven β-sheets are flanked by eight α-helices. The central core consists of seven, mostly parallel β-strands, except for β7 which is antiparallel to the rest (β1↑β7↓β6↑β5↑β4↑β2↑β3↑) (**Fig. 2.23**). Some organisms do not present helix α7, and this element appears disordered due to its intrinsic flexibility.

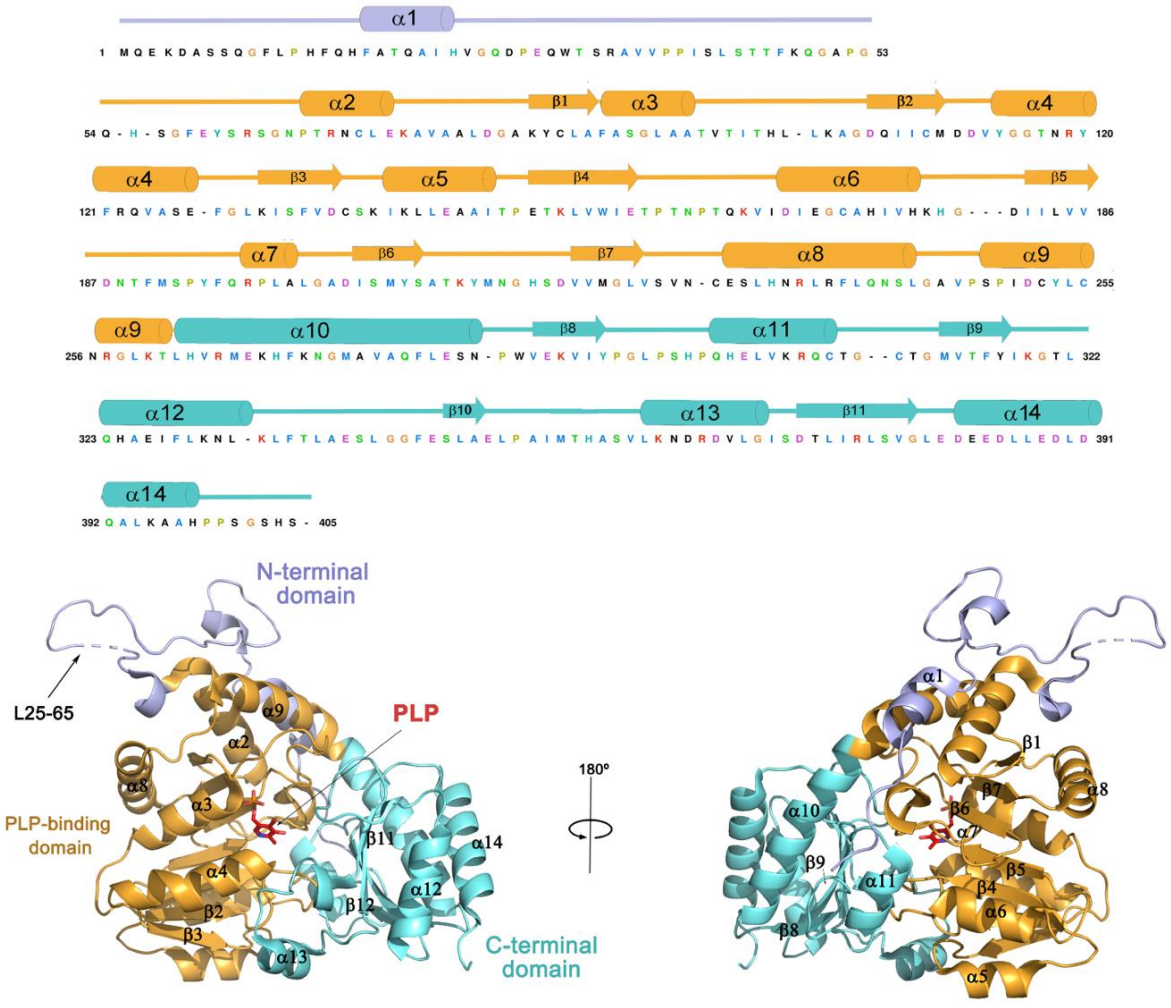

Figure 2.23. Human CGL. *(**top**) Amino acid sequence of the full length HsCGL, colors correspond to the domain distribution. Secondary elements are indicated. (**bottom**) The N-terminal domain is in violet ribbons. The PLP-binding domain is in orange ribbons. PLP is in red sticks. The C-terminal domain is in cyan.*

The active site of CGL is mainly formed by residues from the central seven-stranded β-sheet, and its surrounding α-helices (**Fig. 2.23**). There, PLP is embedded by strong hydrogen bonds between its phosphate moiety and residues G90, L91, S209, T211 of subunit A and Y60*and R62*of the complementary protomer (**Fig. 2.23**). Importantly, the aspartate acid (D187 in *Hs*CGL) is a crucial residue due to its ability to promote the protonation of the nitrogen atom of PLP ring. Such N1-PLP protonation is thought to enhance the "sink effect" of this carbanion intermediate (the electron sink equilibrates the withdrawal of electrons to induce rearrangements and bond cleavage) [467,468] and plays a key role in stabilizing the carbanion intermediate (also known as the quinonoid intermediate) (intermediate [4] in **Fig. 2.20**) [469]. In the human enzyme, PLP is covalently linked to the ε-amino group of lysine K212, thus forming a Schiff-base linkage. On the other hand, residue Y114 exhibits aromatic π-stacking interactions with the pyridine ring of PLP. Interestingly, the substitution of this tyrosine by a phenylalanine in *H. sapiens* and *L. plantarum* (Y114F and Y97F, respectively) showed an increase in the production of H_2S from the β-elimination of Cys (**Fig. 2.19**) [459,470]. A closer look of the side chains of Y114 (in *Hs*CGL-wt) and F114 (in the *Hs*CGL-Y114F artificial variant) provided a reasonable explanation for the reported increase in H_2S levels. The former is more electronic rich than the latter due to the para-hydroxyl group, which increases the electron-donating effect of the tyrosine. Accordingly, the π-stacking interactions between the tyrosine and the cofactor are strong but the electron delocalization into the pyridoxal ring would be less promoted and the α-proton of Cys would be less acidic. In contrast Y114F shows weaker π-interactions with the PLP, which would promotes the electron delocalization of the pyridoxal ring, leading to faster dissociation of the aminoacrylate intermediate in the mutant than the in wild-type enzyme [470]. Another important mutation that affects H_2S production in human CGL is found in the highly conserved E339 residue, which is also located at the catalytic site [470](**Fig. 2.24**). A study in yeast revealed the role of this residue in defining the orientation of the Cth substrate and the specificity for the γ-elimination in catalysis (**Fig. 2.20**) versus the β-elimination [471,472](**Fig. 2.21**). The substitution of E339 in humans to a more hydrophobic residue such as lysine, alanine or tyrosine increased the H_2S production [470]. It has been postulated that an increased hydrophobicity of the residue at this position enhances the catalytic efficiency [470]. Similar studies performed in yeast (E333) to analyze the effect on the catalytic efficiency of β-elimination of Cys, surprisingly showed a decrease in the catalytic efficiency when the equivalent position was occupied by either an alanine, an aspartate or a glutamine, in artificially engineered mutants [472].

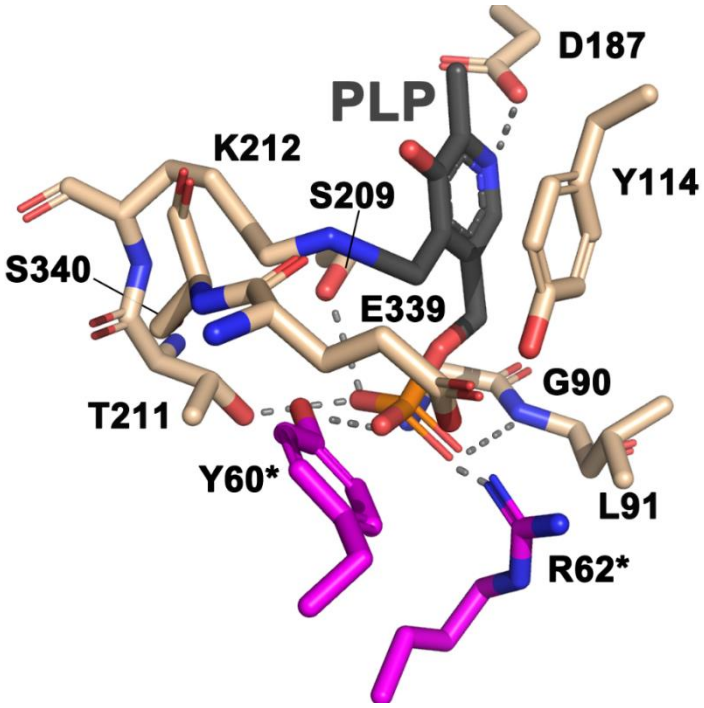

***Figure 2.24. Main residues of the catalytic site of human CGL**. The residues from subunits A and Care colored in wheat and magenta, respectively. The PLP cofactor is in dark grey.*

2.1.4.2.4. Inhibition of CGL

Interestingly, it has been shown that selective inhibition of CGL by molecules such as DL-propargylglycine (PAG) alleviates the cardiovascular and inflammatory symptoms of the CGL-derived disease in animal models [365,473,474]. These observations prompted some authors to address studies on *Hs*CGL-inhibitors complexes to understand how these molecules impair the enzyme activity, and consequently, its H_2S production [461,462]. The mechanism of inhibition of *Hs*CGL by PAG was described in 2008, using the crystal structure of the *Hs*CGL-PAG complex [461]. The structure suggested that the hydroxyl group of Y114 converts the activated allene of PAG into a vinylether (**Fig. 2.25**), and that this residue is involved in the elimination of the reaction product [461,475]. A main conclusion was that both, the entry and the exit of the substrate to the catalytic site is sterically impaired, thus blocking the catalysis of the CGL [461].

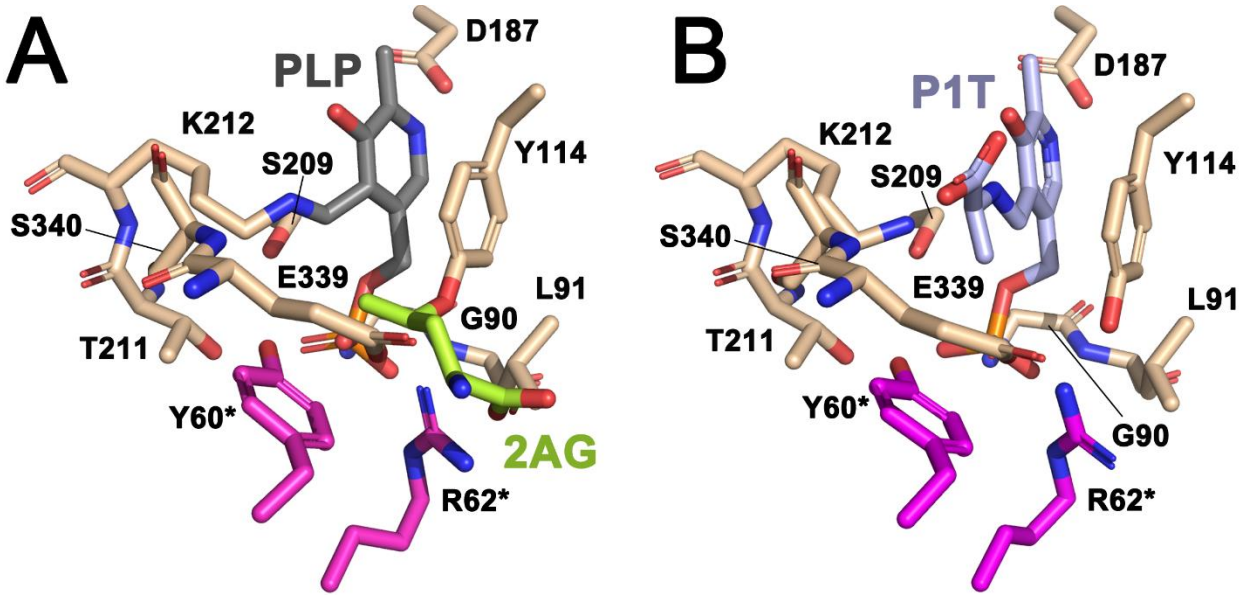

Figure 2.25. Structure of HsCGL in complex with PAG and CPC inhibitors*. (**A**) Stick representation of the residues involved in the binding of PAG in HsCGL (PDB ID 3COG) [461]. The subunits A and C are colored in wheat and magenta, respectively. 2AG (in light green) is the PDB ID for the vinylether formed when the atom Cγ of the inhibitor reacts with the Y114 of the enzyme. (**B**) Residues of the active site of HsCGL that interact with the aminoacrylate intermediate P1T (in light blue) resulting from the reaction of the enzyme with CPC (PDB ID 6NBA) [462].*

Nowadays, a wide variety of compounds is being used for pharmacological inhibition of CGL. Among these, DL-propargylgycine (PAG) is the most commonly used in animal models, acting selectively on CGL in an irreversible manner. Recent studies have shown that concentrations ranging from 1 to 10 mM PAG inhibit >95% of the transsulfuration flux in the presence of cystathionine [462]. Surprisingly, when cysteine is used as a substrate, PAG shows no significant effect, suggesting that cysteine and PAG act competitively, though further evidence is needed [462]. The ability of cysteine in reducing the efficacy of PAG inhibition may have relevant consequences. For example in kidneys, where endogenous cysteine concentration is elevated, cysteine might prevent CGL from PAG inhibition. Very recently, new compounds, structurally analogous to Cth, have shown more optimized inhibitory capabilities. Among them is S-3-carboxpropyl-L-cysteine (CPC), which is a selective and reversible inhibitor of *Hs*CGL that can act on both, cystathionine (K_i 50 ± 3 µM) and cysteine (K_i 180± 15 µM), in the canonical and H_2S production [462]. The co-crystallization of *Hs*CGL with CPC (PDB ID 6NBA) [462] revealed that the mechanism of action is different from that of PAG (**Fig. 2.25**). The structures revealed the formation of an aminoacrylate intermediate that results in the inability of the substrate to bind to PLP for enzymatic catalysis (**Fig. 2.25**). In contrast, the mechanism of inhibition by PAG occurs by blocking the conserved tyrosine at the catalytic site through a covalent bond of this residues with the PAG compound (**Fig. 2.25** and **2.26**).

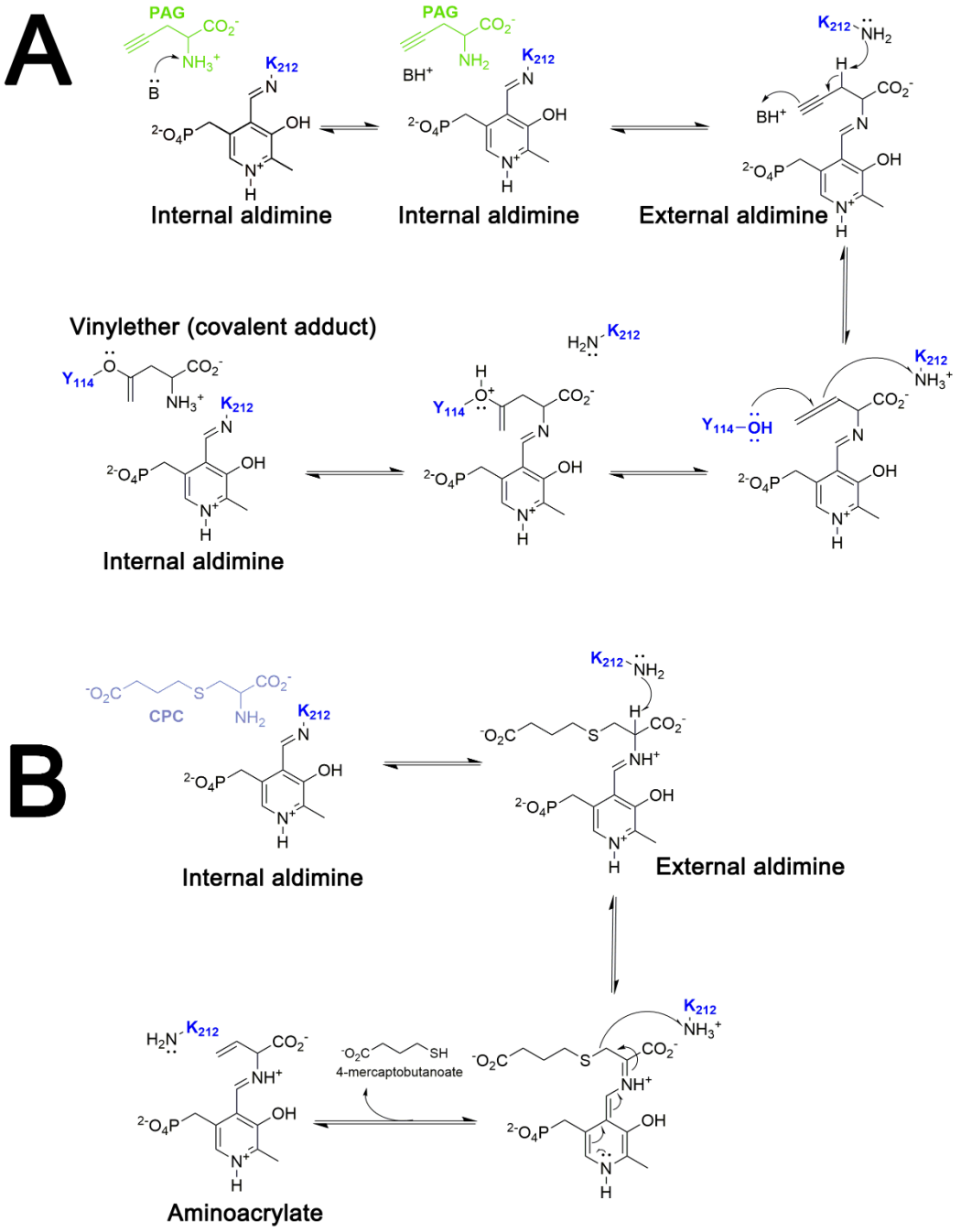

Figure 2.26. *Inhibition mechanisms proposed for the human CGL by PAG* [461] ***(A)*** *and CPC* [462] ***(B)***.

The high similarity existing between the catalytic sites of type I-fold PLP-dependent enzyme family (c.a like CGL, CGS or CBL), from different organisms, implies that the described inhibitors may likely act simultaneously on several targets and several species, thus preventing its general therapeutic use. This situation is problematic when one specific enzyme, encoded by a particular organism (for example a

multidrug resistant bacteria) is pretended to be targeted, without affecting the human host. In this regard, new research has reported novel inhibitor binding sites for the pathogen *Staphylococcus aureus* [15]. These sites are located in a region between helix α4 of the PLP-binding domain and the C-terminal segment. Interestingly, despite the secondary structural elements of this terminal domain are conserved across organisms, the amino acid sequence similarity is poor when compared with the human homolog. For example, the amino acid sequence identity with respect to yeast and *S. aureus* or *Lactobacillus plantarum* is 44%, 42% and 39% identity, respectively in this region. These differences open new windows for therapeutic treatment against concrete pathogens.

2.1.4.2.5. Apo and Holo states of CGLs

A detailed comparison of the structures of the apo (PDB ID 3ELP) and holo (PDB ID 2NMP) forms of human CGL revealed major conformational changes, that were attributed to the absence or presence of the PLP cofactor. The main differences between these two conformers are found in two loops (L110-118 and L210-216), that form the walls of the active site. When the enzyme contains PLP (holo state), these loops fold back towards the cofactor (**Fig. 2.27**). The re-orientation of two residues, K212 and Y114, upon binding of PLP is crucial for the enzymatic catalysis. In the holo state, Y114 is near a two-turn helix (G115-Y120), which unwinds and becomes a loop in the apo state. In turn, K212 is covalently bound to PLP and forms an internal aldimine [461] (**Fig. 2.27**). In contrast, in the absence of PLP, this lysine is moved away from the active site (**Fig. 2.27**), causing that the distance between the K212 of the apo-*Hs*CGL and the PLP of the holo-*Hs*CGL is too large (11Å) for a nucleophilic attack of the lysine. Moreover, in holo-*Hs*CGL the long loop at the N-terminal domain is extended to the complementary monomer and forms part of the adjacent active site [461] (**Fig. 2.27**). However, in the apo conformation, this region is disordered, indicating flexibility due to the lack of stabilizing interactions with the PLP (**Fig. 2.27**). Another region affected by the presence or absence of PLP in the cavity is loop 355-366, which is indirectly stabilized by the cofactor in the *Hs*CGL-PLP complex. In the apo form, the loop 110-118 is shifted slightly upward to occupy the site corresponding to loop 355-366 in the holo conformation. This explains the disorder found for this region in the PLP-free *Hs*CGL.

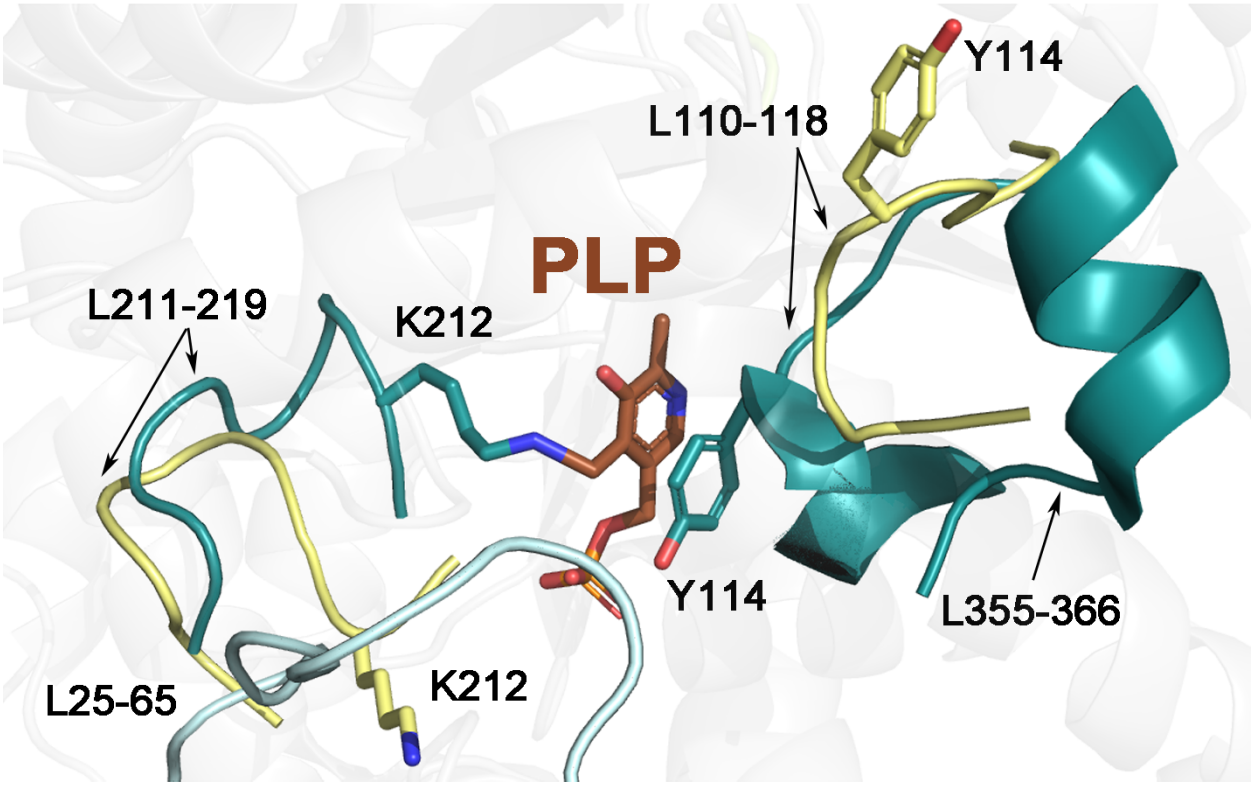

Figure 2.27. Structural comparison of the apo and holo conformations in HsCGL. *Ribbon representation of superimposition of apo-HsCGL (yellow) and holo-HsCGL (blue and green) active site regions. The subunit of the holo-HsCGL enzyme is colored in dark green and the subunit adjacent is colored in light blue. The PLP cofactor is represented by brown sticks. The main loops (L110-118, L211-219 and L65-85) are highlighted. Catalytic lysine is represented by sticks. The orientation of K212 and Y114 in the apo (yellow) and holo (green) states are represented.*

Importantly, the distinct orientation adopted by the above mentioned loops in the absence and in the presence PLP have direct consequences over the overall arrangement of the individual protein subunits in the tetramer assembly (**Fig. 2.28**). For example, the apo-*Hs*CGL shows a more distended arrangement of the monomers within the tetramer ("open conformation" of the tetramer) with respect to the holo-*Hs*CGL form, in which the protein monomers appear more tightly packed ("closed" tetramer) (**Fig. 2.28**). This important difference suggests a weaker interaction between the monomers of the tetramer in the PLP-free enzyme than in the PLP-bound enzyme [461]. Very important salt bridges between R257 and D219 in the A-D and B-C chains help to stabilize the tetrameric assemblies. These residues are largely conserved in this enzyme family [460]. However, in the apo conformation of *Hs*CGL, the interaction of these important tetrameric residues is lost. Remarkably, the open and the closed conformation are observed only in the human enzyme. The crystal structures in the holo and apo states of CGLs from some bacteria such as *Strenotrophomonas maltophilia* [464] (PDB ID code 6K1O and 6K1N apo and holo states, respectively) or

Staphylococcus aureus [15,466] (PDB ID code 6KGZ and 6KHQ apo and holo states, respectively) and another PLP-dependent enzyme, namely threonine synthase from *Aradibopsis thaliana* [476,477] (PDB ID code 15EX and 2C2G apo and holo states, respectively) show no significant conformational changes between states with and without PLP.

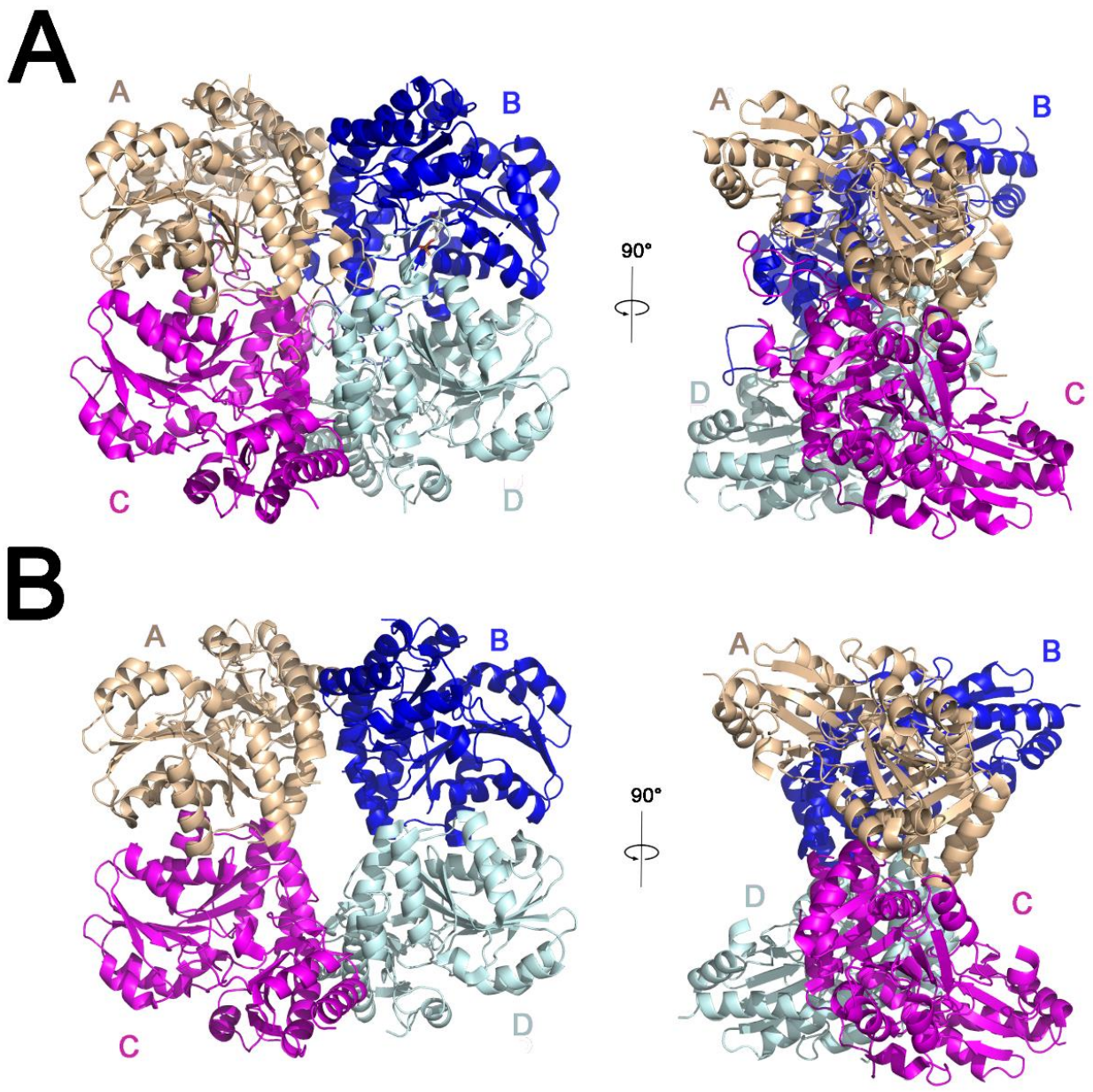

Figure 2.28. Conformational states of HsCGL. *Ribbon representation of three-dimensional structure of HsCGL PLP-bound (A) and HsCGL PLP-free (B). Each subunit is represented with a color. PLP is represented by sticks (grey). The center of HsCGL is opened in the apo conformation.*

2.1.4.3. Cystathionine β-synthase from *T. gondii*

The crystallization of CBS enzymes has historically represented a very challenging task due to the presence of unstructured zones at the ends of their polypeptide chain, the intrinsic mobility of their domains, linked by long flexible loops, and the drastic conformational changes associated with their activity and allosteric regulation. These facts are compounded in some particular cases by a high tendency to form large aggregates (c.a human CBS), and a short half-life when isolated in solution, which causes them to partially or totally lose their three-dimensional folding [454]. The human enzyme has so far been the most extreme case, and involved more than three decades of research until it could finally be elucidated [69,438,440]. Other, somewhat less complex cases, such as some bacterial species which contain just a single catalytic domain [240–242], or the CBSs from insects like the honeybee [435] or the fruit fly [434] that exist in a single constitutively activated conformation and which are not allosterically regulated, provided important clues as to how successfully tackle the crystallographic study of enzymes that are more reluctant to form crystals.

Our collaborators at the University of Verona recently identified that the genome of *T. gondii* (strain ME49) contains a single copy gene for CBS (TGME49_259180), which encodes a multimodular protein (*Tg*CBS) consisting of 514 amino acids (Mw= 55.8 kDa, pI= 7.54) [431]. In solution, *Tg*CBS self associates predominantly in dimers (97 kDa) with some tetramers (234 kDa) [431]. Each monomer presents a domain distribution of class C similar to that found in yeast, Gram-negative bacteria (c.a *P.aeruginosa*) and some apicomplexa (c.a. *T. gondii*) and consisting of: (i) a N-terminal catalytic core (residues 1-323) and (ii) a C-terminal regulatory Bateman module [432] whose function is still unknown. These two main structural domains are connected by a long flexible linker of 29 amino acids (residues 324-353) (**Figs. 2.29** and **2.30**). The catalytic core of *Tg*CBS represents the most conserved region of the protein, showing an amino acid sequence identity of 62%, 56%, and 56% with respect to its human, honeybee, and fly counterparts, respectively. The sequence of the Bateman module is less conserved and shows 8%, 10% and 56% identity with respect to the equivalent region of the human, fly and honeybee enzymes, respectively. As in related proteins, the Bateman module of *Tg*CBS is in turn formed by two consecutive so-called "cystathionine β-synthase domains" (CBS1, residues 354-425; CBS2, residues 426-514), that are linked by two flexible loops and interact mainly through their central β-sheets.

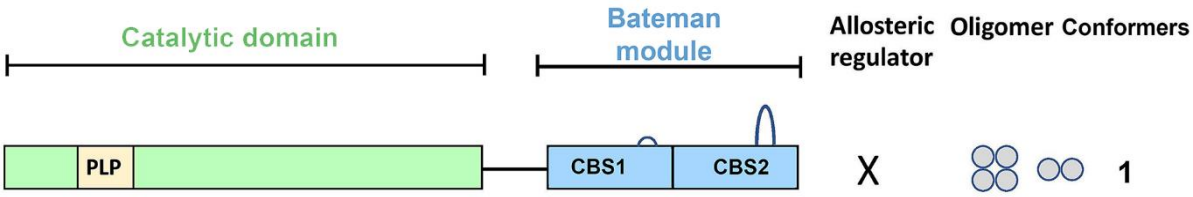

***Figure 2.29. TgCBS architecture**. Class C is found in T. gondii (TgCBS), S. cerevisiae (ScCBS) and P. aeruginosa (PaCBS).*

The *Tg*CBS catalytic activity follows a ping-pong reaction mechanism [431] (**Fig. 2.8**). In its canonical reaction, the enzyme condenses serine with homocysteine (Hcys) to yield cystathionine (Cth) and a molecule of water (**Fig. 2.7**). Similarly to its human counterpart, *Tg*CBS exhibits alternative reactions of decomposition or condensation of Cys that lead to the endogenous production of hydrogen sulfide (H_2S) (**Fig. 2.7**). As it is the case with other protozoan CBSs such as those from *L. major* [225] or *T. cruzi* [478], *Tg*CBS is additionally capable of generating Cth from *O*-acetylserine (OAS) [431]. Two relevant features of *Tg*CBS that relate it to the yeast enzyme are (i) the absence of an N-terminal heme-binding domain preceding the catalytic core and (ii) the inability to bind and be activated by S-adenosylmethionine, AdoMet [159,431]. Similarly to the yeast enzyme [159], *Tg*CBS shows a single thermal denaturation peak (Tm=56 ± 1°C) [431], thus suggesting a single conformation, whose three-dimensional structure remained unknown until this doctoral thesis was developed.

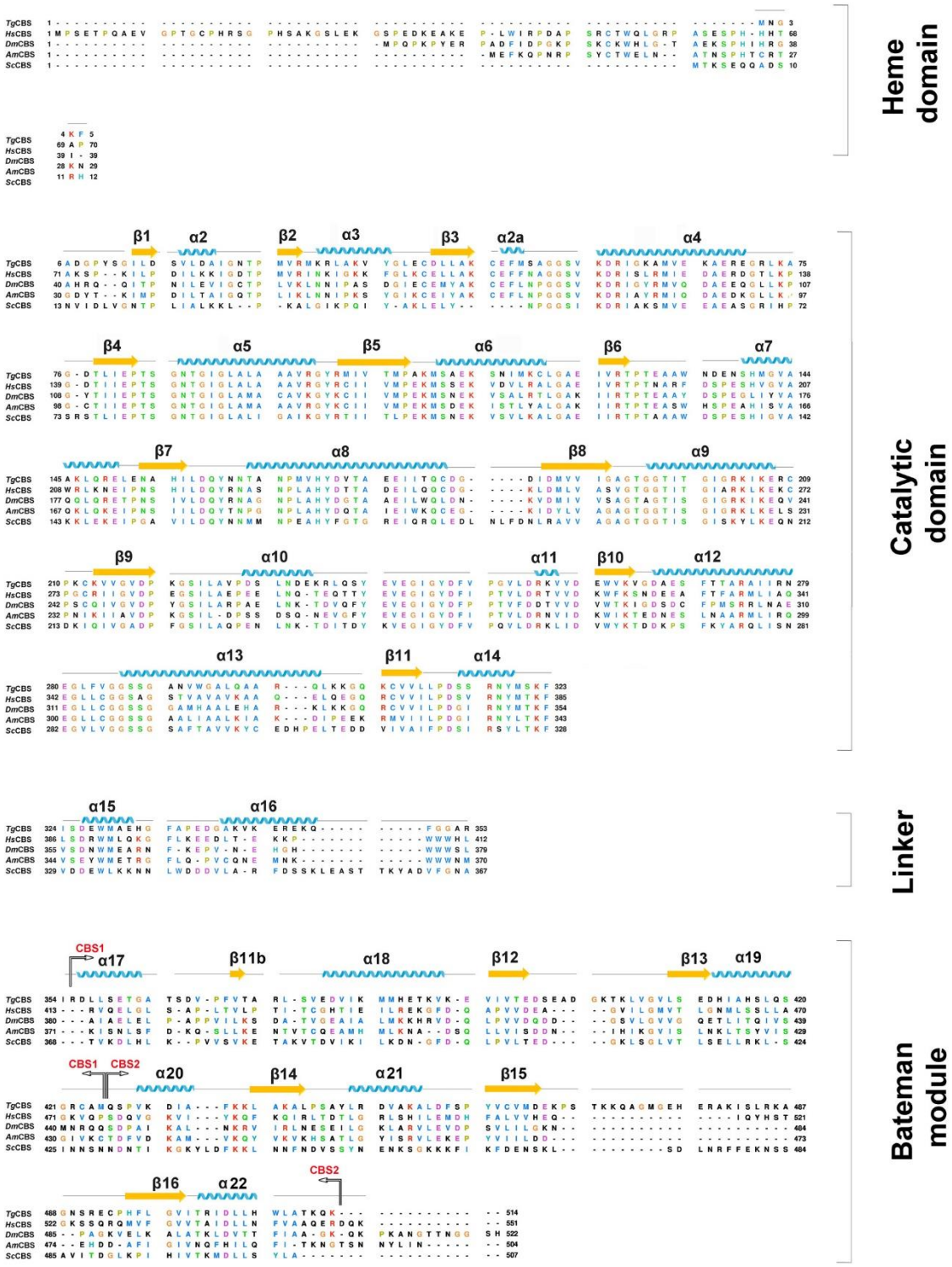

Figure 2.30. CBSs sequence alignment*. Sequence alignment of cystathionine β- synthase from Toxoplasma gondii (TgCBS, UniProt code A0A125YSJ9), Homo sapiens (HsCBS, UniProt code P35520), Drosophila melanogaster (DmCBS, UniProt code Q9VRD9), Apis mellifera (AmCBS, UniProt code Q2V0C9) and Saccharomyces cerevisiae (ScCBS, Uniprot code P32582). The secondary elements of TgCBS are indicated.*

2.2. HYPOTHESIS AND OBJECTIVES

The research developed in this chapter is based on the following hypothesis:

- The CBS enzymes containing a C-terminal Bateman module can exist in active no-allosterically regulated species.
- There may exist active conformations of CBSs, whose three-dimensional structure is distinct from that observed in insects or humans.
- *Toxoplasma gondii* CBS may belong to one of these different structural classes.
- The particular structural features of *Tg*CBS might explain its catalytic diversity.
- *Tg*CBS structure may be used to develop new drugs against toxoplasmosis.

Based on these previous knowledge, we set ourselves the following objectives:

1. Structural determination of cystathionine β-synthase from *T. gondii* (*Tg*CBS) both, alone and in complex with its substrates and products.
2. Elucidation of the mechanisms and conformational changes underlying *Tg*CBS catalytic activity.
3. Elucidation of the mechanisms underlying *Tg*CBS regulation. Role played by the Bateman module.
4. Explanation for the lack of response of *Tg*CBS to AdoMet.
5. Comparative analysis of *Tg*CBS with other CBSs. *Tg*CBS in evolutionary terms.
6. Design of potential strategies for the specific modulation (inhibition) of *Tg*CBS.

2.3. MATERIALS AND METHODS

2.3.1. Protein expression and purification of *Tg*CBSΔ466-491

*Tg*CBS construct lacking the region of the loop of the CBS2 (466-491) was produced by site specific mutagenesis on the pET21a expression vector (InVitrogen Corporation), using the QuickChange site-directed mutagenesis kit (Agilent Technologies). Primers used to insert deletion were: forward (5'-cgtttgtgtgatggacgagaaggaatgcccacatttcctgg) and reverse (5'-ccaggaaatgtgggcattccttctcgtccatcacacaaacg). The correct recombinant plasmid was transformed into Rosetta (DE3) expression *E.coli* host cells (Novagen). The transformed E. coli Rosetta (DE3) cells were picked with a small pipette tip and were grown O/N at 310K in 250 mL Erlenmeyer flask with 125 mL of LB medium supplemented with 25 μg mL^{-1} of chloroamphenicol and 100 μg mL^{-1} of ampicillin. The culture was inoculated in six Erlenmeyer flask (in each flask 20 mL of inoculum were added) containing 2L of LB medium, 25 μg mL^{-1} of chloroamphenicol and 100 μg mL^{-1} of ampicillin and grown to exponential phase at 310K. When the cell density reached OD_{600} ≈ 0.8, the protein expression was induced with 0.5 mM of IPTG and grown for 15 h at 297K.

Cells were pelleted by centrifugation (5 000g for 15 min at 277 K) and resuspended in lysis buffer containing 20 mM sodium phosphate pH 8.5, 150 mM NaCl and 0.1 mM DTT in the presence of protease inhibitor EDTA free. Cells were then disrupted by sonication on ice and centrifugated (30 000g for 30 min at 277 K). The filtered supernatant was loaded on a Ni-sepharose column (Cytiva) previously equilibrated with 20 mM sodium phosphate pH 8.5, 150 mM NaCl, 10 mM imidazole and 0.1 mM DTT. The bound protein was subsequently eluted with the same buffer containing 500 mM imidazole. The buffer of the purified protein was exchanged using Vivaspin concentrators (Sartorius) to remove imidazole with the buffer 20 mM sodium phosphate pH 8.5, 150 mM NaCl and 0.1 mM DTT. The homogeneity and purity of the enzyme was verified by SDS-PAGE to be > 95% (detailed in M&M of Chapter I section 1.3.2.1.). Protein was aliquoted and stored at 193K until use.

2.3.2. *Tg*CBSΔ466-491 activity assay

The activity measurements of the truncated *Tg*CBS enzyme were carried out by the group of Prof. Alessandra Astegno at the University of Verona. The CBS activity in the canonical reactions was determined by a previously described continuous assay for Cth production[431], which employs recombinant

cystathionine β-lyase (CBL) from *C. diphtheriae*, produced in-house [479,480] and lactate dehydrogenase (LDH) from rabbit muscle (Sigma-Aldrich) as coupling enzymes. The activity assay was performed using the dimeric fraction of the enzyme isolated by gel filtration. The kinetic parameters for the β-replacement reaction of *Tg*CBS (condensation of Ser and Hcys, and condensation of OAS and Hcys) were calculated, via global analysis in which both substrates are varied simultaneously, from the fit of the data to the following equation:

$$\frac{v}{E} = \frac{k_{cat} * [SA] * [SB]}{K_m^{SB} * [SA] + K_m^{SA} * [SB] * \left(1 + \frac{[SB]}{K_i^{SB}}\right) + [SA] * [SB]}$$

in which v is the initial velocity, E is the concentration of the enzyme, SA is the concentration of the first substrate, SB the concentration of the second substrate, kcat and Km are the catalytic and the Michaelis–Menten constants, respectively. Substrate inhibition at high concentration of Hcys was observed, thus the equation included a K_iSB value, which represents the inhibition constant for substrate inhibition by Hcys. Kinetic data are presented as the average ± standard error of the mean (SEM) of three to five repetitions using at least three independently purified protein batches. Data fitting was carried out with OriginPro8 (OriginLab) software (Version2008. OriginLab Corporation, MA, USA).

2.3.3. Spectroscopic measurements

The spectroscopic measurements of the truncated *Tg*CBS enzyme were carried out by the group of Prof. Alessandra Astegno at the University of Verona. Absorption spectra were collected on a Jasco-V560 UV-Vis spectrophotometer in 20 mM sodium phosphate pH 8.5. Far-UV CD spectra (250–200 nm) were recorded on a Jasco J-1500 spectropolarimeter as previously described [431,458]. Thermal denaturation profiles were collected by measuring circular dihroism (CD) signal at 222 nm in a temperature range from 20 to 90 °C (scan rate 1.5 °C/min). Protein concentration was 0.2 mg mL^{-1} and measurements were performed using quartz cuvettes with a path length of 0.1 cm in 20 mM sodium phosphate pH 8.5.

2.3.4. Oligomeric state determination

The oligomeric state determination of the truncated *Tg*CBS enzyme were carried out by the group of Prof. Alessandra Astegno at the University of Verona The oligomeric state of *Tg*CBS was investigated via gel filtration on a GE Healthcare Superdex 200 10/30 GL column (GE28-9909-44, Cytiva) in 20 mM sodium phosphate buffer pH 8.5, 150 mM NaCl and 0.1 mM DTT. High molecular weight gel filtration calibration

kit (GE28-4038-41 and GE28-4038-42 from Cytiva) was used to construct a calibration curve, following protocols in [481].

2.3.5. Protein crystallization

The first, one of the principal requirements to obtain suitable protein crystals was to determine the appropriate protein concentration to setup the initial crystallization screens (**Table 2.1**), performing a Pre-Crystallization test (PCT™, HR2-140 from Hampton Research). The initial crystallization process was initiated in the high-throughput crystallization facility at the X-Ray platform of CIC bioGUNE, assisted by liquid handling robots and automatic nanodispensers, which allowed us to examine around 2 500 crystallization conditions. The technique used in this initial screens was the sitting drop vapour diffusion in 96 well MRC plates (MD11-00-100 from Molecular Dimensions). Precipitant solutions were placed in the reservoirs using TECAN Freedom EVO robot (TECAN Group Ltd.) and the protein/precipitant drop was prepared with the automatic nanodispenser MOSQUITO liquid handling robot (TTP Labtech Ltd.) mixing 200 nL of protein solution with 200 nL of reservoir.

Table 2.1. Crystallization screens.

Crystallization Screen	Provider	Catalog number
PCT C Pre-Crystallization test	Hampton Research Corp	HR2-140
PEG/Ion	Hampton Research Corp	HR2-126
PEG/Ion 2	Hampton Research Corp	HR2-098
PEGRx1	Hampton Research Corp	HR2-082
PEGRx2	Hampton Research Corp	HR2-084
Index	Hampton Research Corp	HR2-144
SaltRx1	Hampton Research Corp	HR2-107
SaltRx2	Hampton Research Corp	HR2-109
Crystal Screen Cryo	Hampton Research Corp	HR2-122
Natrix	Hampton Research Corp	HR2-116
PACT premier	Molecular Dimensions Ltd	MD1-36
Morpheus	Molecular Dimensions Ltd	MD1-46
JCSG-plus	Molecular Dimensions Ltd	MD1-37
JCSG Core I Suite	QIAGEN®	130724
JCSG Core II Suite	QIAGEN®	130725
JCSG Core III Suite	QIAGEN®	130726
JCSG Core VI Suite	QIAGEN®	130727

2.3.5.1. Crystallization of *Tg*CBSΔ466-491

For the *Tg*CBSΔ466-491, the suitable concentration is 15 mg mL^{-1} to carry out the subsequent experiments. Once the initial screens were tested, promising conditions were identified around a crystallization condition of the screens PEG ION 1, 2 (HR2-126, HR2-098 from Hampton Research), which yielded small microcrystals. Subsequently, a more specific screening, aimed to optimize the crystallization conditions, was performed. First, the droplet size was significantly increased, and the hanging drop technique was employed in 24-well VDX plates (HR3-171, Hampton Research). The drops contained 1 µL of protein and 1 µL of reservoir. The condition that finally provided the best quality crystals was composed of 8% (w/v) ethylene glycol 3350, and 0.1 M MES pH 5.7 with a protein concentration of 15 mg mL^{-1}. The volume in the reservoir was 500 µL. The plates were incubated at a constant temperature of 291K on the CIC bioGUNE platform. Crystals appeared after 48 hours.

Following a similar protocol, the construct of *Tg*CBS with a deletion in loop L466-491 was crystallized in the presence of L-serine (Sigma-Merck, S4500), cysteine (Sigma-Merck, 168149), cystathionine (Sigma-Merck, C7505- 10 mg), and *O*-acetylserine (Sigma-Merck, CDS020792). To obtain *Tg*CBS crystals with the respective ligands, *Tg*CBS crystals were allowed to grow for 3 days, using the hanging drop technique in 24-well limbro plates. Each drop consisted of 1µL of the study protein and 1µL of precipitant. Subsequently, the corresponding ligand was soaked overnight and stored the next day with 35% (w/v) ethylene glycol until data collection by X-ray diffraction in different European synchrotron facilities (ALBA (Spain) and DIAMOND (UK). The optimum crystallization conditions are described in **Table 2.2**, as well as the concentration of protein and ligand added in each crystallization drop.

***Table 2.2. Optimal crystallization conditions for TgCBSΔ466-491*.**

Protein (concentration)	Crystallization condition	Ligand	Protein-ligand binding method	Concentration of ligand	Cryopotectant
*Tg*CBS*Δ466-491*	8% (w/v) PEG 3350 0.1M MES pH 5.7	-	-	-	30% (v/v) glycerol
*Tg*CBSΔ466-491	7% (w/v) PEG 3350 0.1M MES pH 5.5	Ser	Soaking	10 mM	35% (v/v) ethylene glycol
*Tg*CBSΔ466-491	8%(w/v) PEG 3350 0.1M MES pH 6.1	Cys	Soaking	10 mM	35% (v/v) ethylene glycol
*Tg*CBSΔ466-491	9%(w/v) PEG 3350 0.1M MES pH 6.1	Cth	Soaking	10 mM	35% (v/v) ethylene glycol
*Tg*CBSΔ466-491	8% (w/v) PEG 3350 0.1M MES pH 6.1	OAS	Soaking	10 mM	35% (v/v) ethylene glycol

2.3.6. Structural determination of *Tg*CBSΔ466-491 by X-ray crystallography

The high-energy synchrotron radiation facilities used for our further structural analysis were the beamline MX XALOC-BL13 at ALBA Synchrotron (Barcelona, Spain) and beamlines I03 and I24 at Diamond Light Source (UK) (**Table 2.3**). For data collection, the set of diffraction images was taken in intervals between 0.1 to 0.25° and the distance to the detector was set to reach resolution data between 1.6- 3.8 Å depending on the crystal and according to the quality and intensity of the diffraction determined by test images taken previously. The strategy and characterisation program to determine the number of images and the starting angle to be taken to achieve the 100% of completeness was carried out by EDNA program [482]. For all datasets, a total of 36000 images were collected except for *Tg*CBS-*OAS* which shows crystal decay after 1200 images. A summary of the parameters of the data collection is shown in **Table 2.3**. The diffraction data were indexed, integrated and scaled using XDS [483] and autoPROC [484] programs. The plots of the self-rotation function were calculated with MOLREP [485]. Structure refinement was done with Phenix.Refine[486]. Model was built with Coot [487] Figures were done with Pymol (http://www.pymol.org) and Chimera [106]. Crystallization of the structures of *Tg*CBSΔ466-491 alone and in presence of ligands were determined by Molecular Replacement (MR) [488] with PHASER program [489] from Phenix package. The structure of the truncated 45-kDa *Hs*CBS (PDB ID code 1JBQ) was used as initial search model. After several cycles of refinement using Phenix.Refine the geometric quality of the models were assessed with MolProbity [490] integrated in Phenix program. The atomic coordinates of the *Tg*CBSΔ466-491, *Tg*CBSΔ466-491-*Ser*, *Tg*CBSΔ466-491-*Cys*, *Tg*CBSΔ466-491-*OAS* and *Tg*CBSΔ466-491-*Cth* have been deposited in the Protein Data Bank (PDB) with the ID codes 6XWL, 6XYL, 6ZS7, 6Z3S and 6Y21, respectively.

Table 2.3. Data collection parameters

Parameters	*Tg*CBSΔ466-491	*Tg*CBSΔ466-491 +Ser	*Tg*CBSΔ466-491 +Cys	*Tg*CBSΔ466-491 +Cth	*Tg*CBSΔ466-491 +OAS
No of images	1800	3600	3600	3600	1200
ΔΦ (°/image)	0.2	0.1	0.1	0.1	0.1
Beamline	I03	I24	XALOC-BL13	XALOC-BL13	XALOC-BL13
λ (Å)	0.9800	0.9683	0.9794	0.9794	0.9794
Exposure (sec)	0.01	0.04	0.1	0.1	0.1
Detector	Eiger2 XE16M	Pilatus3-6M	Pilatus 6M-Dectris	Pilatus 6M-Dectris	Pilatus 6M-Dectris
Temperature (K)	100	100	100	100	100

2.4. RESULTS

2.4.1. Construct design

Careful sequence and structural alignments between *Tg*CBS and *Hs*CBS (**Fig. 2.30**) revealed an unusually extended loop (residues 466-491) between the last two β-strands of the CBS2 motif in *Tg*CBS which, as observed in humans, is presumably flexible and may impede crystal growth. Accordingly, we engineered a protein construct (*Tg*CBSΔ466-491) that lacks 25 amino acid residues at the tip of this internal loop.

2.4.2. Overexpression & purification of *Tg*CBSΔ466-491. Properties of truncated *Tg*CBS

In collaboration with Prof. Alessandra Astegno (University of Verona, Italy), *Tg*CBS was cloned into pET21a expression vector with a tag of six Histidines at the N-terminal following the protocol described in [431]. The histidine tail was added to initiate protein purification by nickel affinity chromatography. The purification protocol of the protein is described in detail in section 2.3.1 of M&M.

*Tg*CBSΔ466-491 was overexpressed in *Escherichia coli* and purified as His-tagged protein (located at the N-extreme) to greater than 95% purity as judged by the presence of a single band on SDS-PAGE (**Fig. 2.31, A**). Through absorbance and circular dichroism (CD) studies, our italian collaborators ascertained that the mutant displayed no substantial differences compared to the wild type protein [431] in either the absorbance spectroscopic features (**Fig. 2.31, B**) or protein conformation (secondary structure elements) (**Fig. 2.31, C**). Moreover, thermal stability studies by CD measurements at 222 nm resulted in similar denaturation profiles, indicating that the mutation did not affect the stability of the protein (**Fig. 2.31, D**). The deletion of the region 466-491 did not even alter the oligomeric state of the protein since the *Tg*CBSΔ466-491 variant exists primarily as a dimer with a minor percentage of tetramer as observed for the wild type protein (the percentage of molecules in dimeric and tetrameric form were estimated to be 92% and 8% for *Tg*CBS wild-type, and 82% and 18% for *Tg*CBSΔ466-491, respectively) (**Fig. 2.31, E**). The continuous assay for Cth production (analysis performed at Verona by Astegno *et al*.), employing cystathionine β-lyase (CBL) and lactate dehydrogenase (LDH) as coupling enzymes, was employed to determine the steady-state kinetic parameters of *Tg*CBSΔ466-491 as previously described for the wild type protein [431]. Except for a 1.4-fold difference in K_m^{Ser}, the kinetic parameters of the β-replacement

reaction catalyzed by *Tg*CBSΔ466-491 and wild type proteins are identical, within their experimental error, demonstrating that the removal of the of 25-residue loop does not alter activity (**Table 2.4**). Importantly, no response to AdoMet was observed as for the wild type protein [255] (**Table 2.5**).

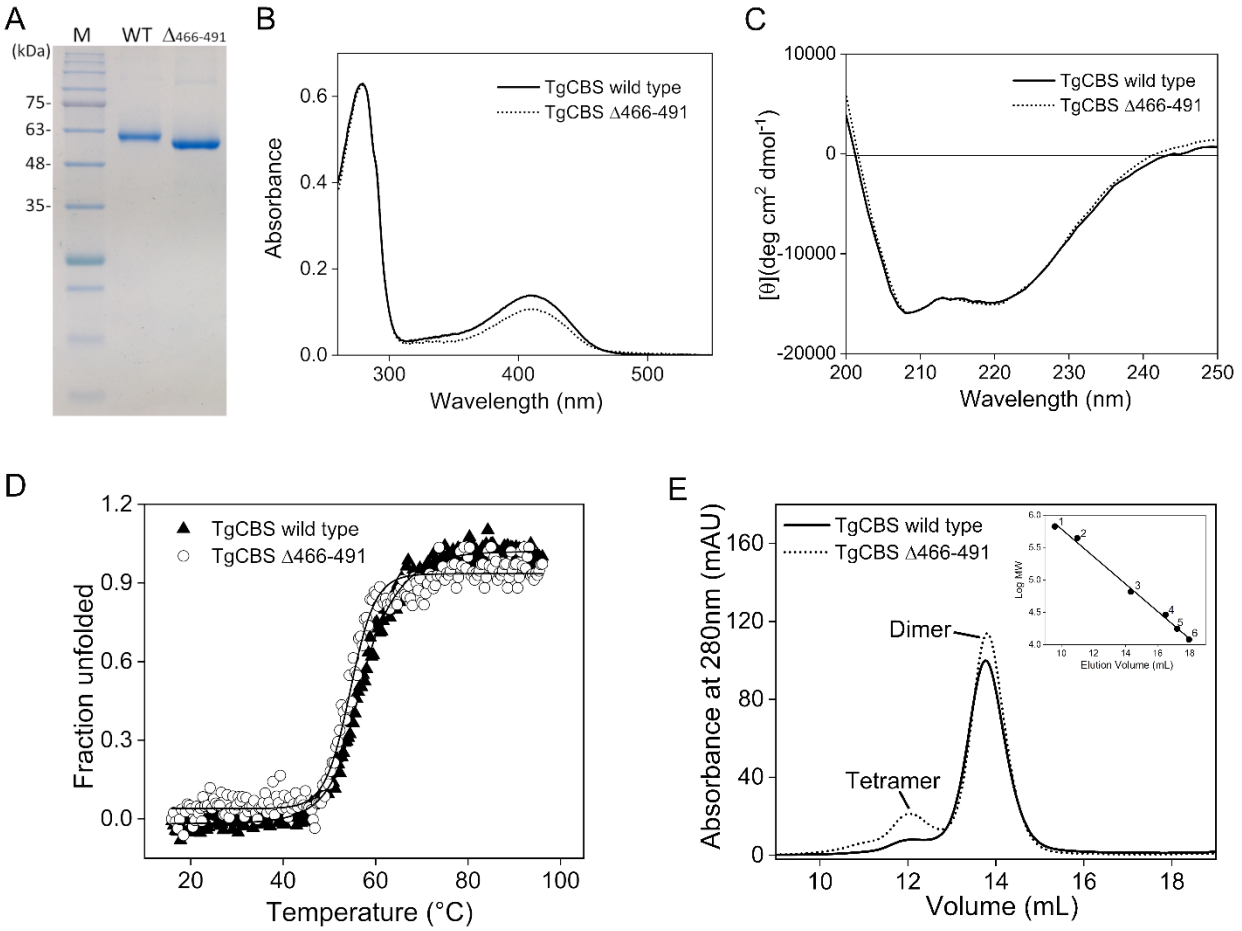

Figure 2.31. Properties of TgCBSΔ466-491. *(**A**) 12% SDS–PAGE analysis of purified recombinant TgCBS wild type and TgCBSΔ466-491. Lane M, protein marker. (**B**) UV-visible absorption spectra of 15 μM purified TgCBS wild type (solid line) and TgCBSΔ466-491 (dotted line) recorded in 20 mM sodium phosphate buffer pH 8.5. (**C**) Far-UV CD spectra of TgCBS wild type (solid line) and TgCBSΔ466-491 (dotted line) at 0.2 mg/mL in 20 mM sodium phosphate buffer pH 8.5. (**D**) Thermal denaturation of TgCBS wild type (solid triangles) and TgCBSΔ466-491 (open circles) recorded following ellipticity signal at 222 nm at 0.2 mg/mL protein concentration in 20 mM sodium phosphate buffer pH 8.5. (**E**) Gel filtration chromatography of TgCBS wild type (solid line) and TgCBSΔ466-491 (dotted line) at 1 mg/mL using a Superdex 200 10/300 GL column in 20 mM sodium phosphate, 150 mM NaCl buffer pH 8.5. Inset, calibration curve of logarithm of the molecular weight versus elution volume. The standard proteins used were: 1, thyroglobulin; 2, apoferritin; 3, albumin bovine serum; 4, carbonic anhydrase; 5, myoglobin; 6, cytochrome c. Recovered from* [255].

Table 2.4. Steady-state kinetic parameters of TgCBS variants for canonical reactions[a].

Kinetic parameter	WT	Δ466-491
L-Ser + L-Hcys→L-Cth		
kcat (s^{-1})	6.3 ± 0.4	5.7 ± 0.5
$Km^{L\text{-}ser}$ (mM)	0.42 ± 0.04	0.6 ± 0.1
$K_m^{L\text{-}Hcys}$ (mM)	0.23 ± 0.03	0.21 ± 0.03
kcat/ $Km^{L\text{-}Ser}$ (mM^{-1} s^{-1})	15 ± 2	10 ± 2
$k_{cat}/ K_m^{L\text{-}Hcys}$ (mM^{-1} s^{-1})	27 ± 5	27 ± 6
$K_i^{L\text{-}Hcys}$ (mM)	1.0 ± 0.1	0.9 ± 0.1
L-OAS + L-Hcys→L-Cth		
k_{cat} (s^{-1})	5.5 ± 0.1	5.6 ± 0.3
$K_m^{L\text{-}OAS}$ (mM)	1.3 ± 0.2	1.7 ± 0.4
$K_m^{L\text{-}Hcys}$ (mM)	0.20 ± 0.05	0.23 ± 0.05
$k_{cat}/ K_m^{L\text{-}OAS}$ (mM^{-1} s^{-1})	4.2 ± 0.7	3.3 ± 0.9
$k_{cat}/ K_m^{L\text{-}Hcys}$ (mM^{-1} s^{-1})	28 ± 7	24 ± 7
$K_i^{L\text{-}Hcys}$ (mM)	1.4 ± 0.2	1.4 ± 0.3

[a] Reactions were carried out in 50 mM MOPS, 50 mM bicine, 50 mM proline buffer pH 9 (pH optimum) containing 0.2 mM NADH, 2 μM LDH, 1.5 μM CBL, and 0.1-30 mM mM L-Ser (or 0.5-100 mM OAS), 0.1-10 mM L-Hcys and 0.2-2 μM TgCBS wild type or Δ466-491 at 37°C. Data were fit as described in the Materials and Methods section 2.3.2. Reported values represent means ± S.E.M of three to five repetitions using at least three independently purified protein batches. Taken from [255].

Table 2.5. Steady-state kinetic parameters of TgCBSΔ466-491 for the physiological condensation of Ser and Hcys in the presence of AdoMet[a].

Kinetic parameter	- AdoMet	+ AdoMet 0.5 mM
L-Ser + L-Hcys →L-Cth + H_2O		
k_{cat} (s^{-1})	5.7 ± 0.5	5.8 ± 0.4
$K_m^{L\text{-}Ser}$ (mM)	0.6 ± 0.1	0.5 ± 0.1
$K_m^{L\text{-}Hcys}$(mM)	0.21 ± 0.03	0.19 ± 0.04
$K_i^{L\text{-}Hcys}$ (mM)	0.9 ± 0.1	1.2 ± 0.3

[a] Reactions were carried out in 50 mM MOPS, 50 mM bicine, 50 mM proline buffer pH 9 (pH optimum) containing 0.2 mM NADH, 2 μM LDH, 1.5 μM CBL, and 0.1-30 mM mM L-Ser, 0.1-10 mM L-Hcys and 0.2-2 μM TgCBSΔ466-491 at 37°C. Data were fit as described in the Materials and Methods section 2.3.2. Reported values represent means ± S.E.M of three to five repetitions using at least three independently purified protein batches. Taken from [255].

2.4.3. Protein crystallization of *Tg*CBSΔ466-491. Preliminary crystallographic studies

Initial crystallization trials were carried out using the vapor-diffusion technique in a sitting-drop format in 96-well MRC crystallization plates and with a wide variety of commercial screens (detailed in section 2.3.5. of M&M). High- throughput screenings were performed in the crystallization facility at CIC bioGUNE. Initial crystallization hits of *Tg*CBSΔ466-491 were obtained in 20% (w/v) PEG 3350 and 0.2M succinic acid pH 7 (**Fig. 2.32**). These conditions were further refined to improve the size and diffraction quality of the

crystals, which were finally grown in 8% (w/v) PEG 3350 and 0.1M MES pH 5.7 at a concentration of 15 mg mL^{-1} by the hanging drop vapor-diffusion method (**Fig. 2.32**).

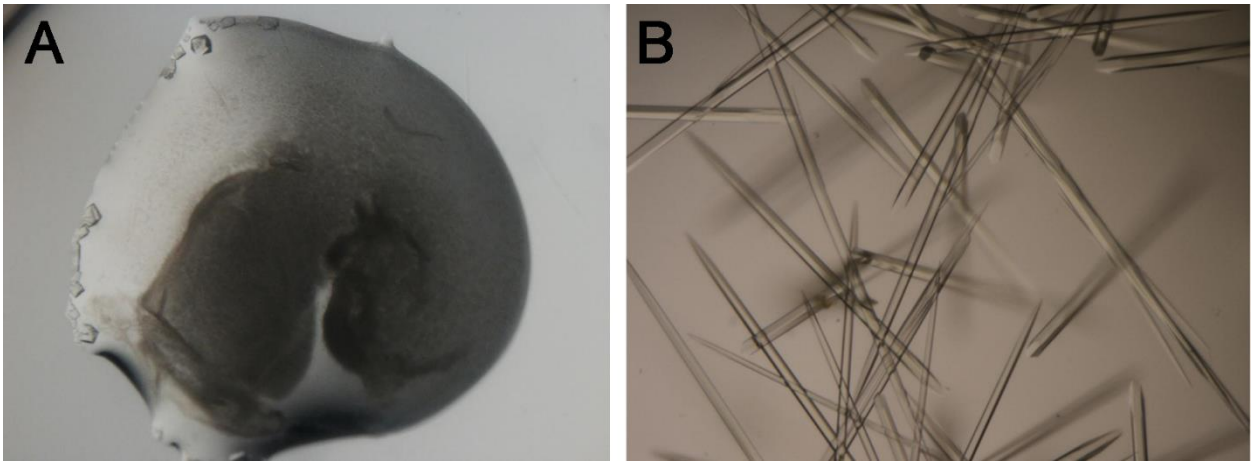

Figure 2.32. Crystals of TgCBS *(A) Preliminary crystals of TgCBSΔ466-491 obtained in 20% (w/v) PEG 3350 and 0.2M succinic acid. (B) Improved Bar-shaped TgCBS crystals obtained in growth in 8% (w/v) PEG 3350 and 0.1M MES pH 5.7. These crystals belong to space group $P3_1$ and diffracted X-rays to 3.2Å. The yellow color reveals the presence of PLP cofactor.*

Data collection was performed at the Diamond Light Source (DLS) synchrotron (Didcot, UK) beamline I03 and yielded about 3600 images with an exposure of 0.1 seconds and an Φ-oscillation of 0.20. Analysis of the diffraction data using the online server "Diffraction Anisotropy Server" of the University of California (UCLA)[491] (https://services.mbi.ucla.edu/anisoscale/), showed strong anisotropy in the diffraction spectrum (spread in values of the three principle components= 47.04 Å2), which required a correction of the intensities according to their characteristics. The data were indexed, integrated and scaled using the XDS [483] and autoPROC programs [484]. The lattice parameters (a=b= 83.23 and c= 420.32; α=β= 90° and γ=120°) were compatible with a trigonal or hexagonal crystalline system. The most probable symmetry was analyzed using the self-rotation function (calculated with the MOLREP5 [485] program of the CCP4 package), from the collected reflections, initially processed in the P3 space group (**Fig. 2.33**). The plot at Chi= 120° indicated the presence of a ternary axis parallel to the c axis. The plot at Chi=180°, on the other hand, indicated the presence of binary axes perpendicular to the c axis, separated by 20° rotations in the XY plane. Among these, the 2-fold axis at 20°, 40° and 80° were interpreted as non-crystallographic axis (**Fig. 2.33**). However, those at 0° and 60° suggested a diffraction pattern consistent with space groups belonging to either (a) the -3m Laue class (c.a P321, P312, $P3_121$, $P3_121$), or (b) Laue class -3 (c.a P3, P31,

P32) hemihedrically twinned. Accordingly, both alternatives were initially taken into account. Further analysis of the reflections with Xtriage [492] led us discard the presence of twinning in our crystals. The best phasing statistics and electron density map were obtained with the P31 space group, on which the final model was refined[486]. The refinement statistics are given in **Table 2.6**.

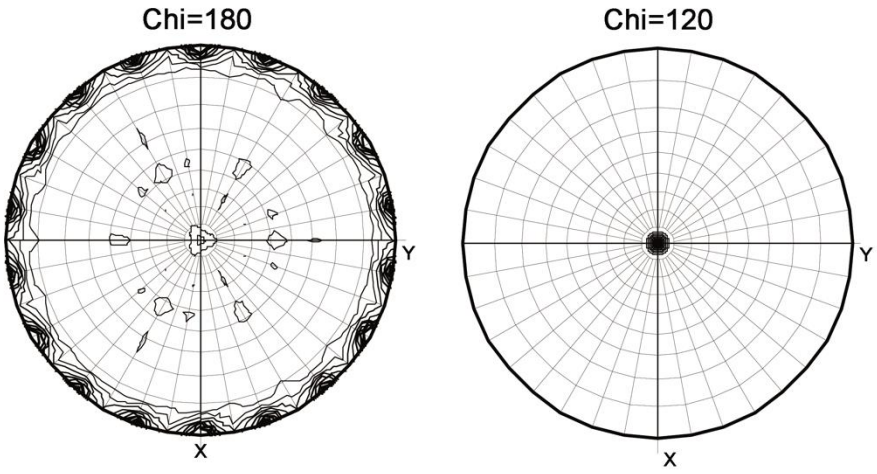

Figure 2.33. *Plot of the self-rotation function of TgCBSΔ466-491 at K= 180° (**left**) and 120° (**right**)*

Table 2.6. Stadistics parameters	***Tg*CBSΔ466-491**	***Tg*CBSΔ466-491+ Ser**	***Tg*CBSΔ466-491+ Cys**	***Tg*CBSΔ466-491+ OAS**	***Tg*CBSΔ466-491+ Cth**
PDB code	6XWL	6XYL	6ZS7	6Z3S	6Y21
Space group	P31	P31	P31	$P3_121$	$P3_121$
Unit cell (a,b,c) (Å)	83.24 83.24 420.31	82.44 82.44 421.25	82.30 82.30 415.98	82.50 82.50 421.80	83.01 83.01 421.37
Resolution (Å)	46.14 – 3.20 (3.30 – 3.20)	41.02 – 3.15(3.20– 3.15)	67.43- 3.50 (3.60 – 3.50)	46.06-3.03 (3.35-3.03)	68.03-3.60 (3.80-3.55)
CC ½ (%)	99.90 (76.10)	98.40 (68.10)	97.70 (57.70)	99.40 (68.40)	99.10 (49.0)
Redundancy	10.30 (9.40)	8.20 (8.40)	10.10 (8.00)	6.10 (5.00)	18.60 (19.10)
Completeness (%) Completeness (spherical) Completeness (ellipsoidal)	 - 91.50 (82.00)	 99.70 (99.70) -	 - 99.40 (90.10)	 - 91.70 (54.30)	 - 90.80 (51.10)
I/σ (I)	12.70 (2.10)	8.70 (2.00)	11.90 (1.60)	6.70 (1.60)	11.40 (1.40)
Wilson B-factor (Å²)	93.40	85.0	64.40	86.05	114.40
R_{merge}[a]	0.111 (0.999)	0.322 (2.136)	0.320 (1.760)	0.190 (0.851)	0.229 (2.695)
R_{meas}[b]	0.117 (1.054)	0.345 (2.277)	0.339 (1.873)	0.208 (0.941)	0.235 (2.769)
R_{pim}[c]	0.036 (0.334)	0.121 (0.783)	0.109 (0.624)	0.083 (0.393)	0.055 (0.630)
Refinement Total reflections Unique reflections Rwork[d]/Rfree[e]	 440638 (20231) 42969 (2145) 0.253/0.277	 454379 (37816) 55218 (4518) 0.274/0.294	 405860 (16005) 40342 (2011) 0.272/0.281	 147075 (6104) 24285 (1214) 0.279/0.288	 327391 (16808) 17599 (882) 0.263/ 0.290
No of atoms Macromolecules Ligand (PLP) Ligand (P1T)	 21306 90 -	 21419 - 63	 21043 - 63	 10560 - 63	 10724 - 63
Average B-factor (Å²) Macromolecules Ligands (PLP) Ligands (P1T)	 89.63 100.36 -	 86.70 - 73.90	 61.35 - 46.00	 78.18 - 59.93	 107.19 - 89.07
Ramachandran plot statistics (%) Res. in most favored regions In additional allowed regions In disallowed regions	 98.00 2.00 0	 97.60 2.40 0	 98.18 1.82 0	 98.19 1.81 0	 98.29 1.71 0
RMSDs Bonds length (Å)/ angle (°)	 0.003/0.54	 0.002/0.56	 0.004/0.75	 0.003/0.70	 0.000/0.52
Rotamers outliers (%)	0.00	0.09	0.09	0.00	0.62
Clashcore	9.30	12.14	13.69	12.04	9.44
MolProbity score [f]	1.49	1.69	1.66	1.59	1.50

One crystal was used for each data set. Values in parentheses are for highest-resolution shell. [a]Rmerge= Σhkl Σi |Ii (hkl)− <I(hkl)>I/Σhkl Σi Ii(hkl) (all I+ and I-); [b]Rmeas = Σhkl Σi |Ii (hkl) − I(hkl)>I/Σhkl Σi Ii(hkl) (all I+ and I-); [c]Rpim= Σhkl Σi |Ii (hkl) − <I(hkl)>I/Σhkl Σi Ii(hkl) (all I+ and I-); [d]Rwork = Σ |Fo – Fc | / ΣFo; [e] Rfree = Σ |Fo – Fc | / ΣFo, calculated using a random 5 % of reflections that were not included throughout refinement. [f]MolProbiscore: 0.426*ln(1+clashcore) + 0.33 *ln(1+max(0;rota_out-1))+ 0.25*ln(1+max(0, rama_iffy-2))) + 0.5

2.4.4. Three-dimensional structure of *Tg*CBSΔ466-491

2.4.4.1. Overall structure

The *Tg*CBSΔ466-491 construct yielded crystals belonging to space groups P31 and $P3_121$, and diffracting X-rays from 3.15 to 3.6 Å resolution (**Table 2.6**). In agreement with its behavior in solution, *Tg*CBSΔ466-491 forms symmetric dimers in the crystals (**Fig. 2.34**). Each protomer is composed of two independent blocks, consisting of a N-terminal catalytic domain (residues 1-323) and a C-terminal Bateman module (residues 353-514), tethered by a long linker (residues 324-352) that contains two α-helices. At first glance, the most striking characteristic is not the intrinsic folding of each of these domains, but their relative orientation, which unexpectedly reproduces the arrangement observed in the *basal conformation* of the human enzyme [437,438] (**Fig. 2.34**). In such conformation the enzyme self-associates in dimers that adopt a basket-shaped domain-swapped symmetrical structure where the catalytic core of each protomer interacts with both the catalytic core and the regulatory domain of the complementary monomer (**Fig. 2.34, A**). Meanwhile, the regulatory domain is strategically positioned above the entrance of the catalytic crevice of the complementary monomer, thus hampering the access of substrates and retaining the enzyme in an apparent inactive state. A priori, we found these findings surprising considering the inability of *Tg*CBS to bind or to be regulated by AdoMet.

Structurally, the catalytic domain of *Tg*CBS presents the overall fold of the β-family of the PLP-dependent enzymes and maintains its secondary elements basically unaltered with respect to the equivalent region in the human [69,246,438](**Fig. 2.34, B** and **D**), fly [434] and honeybee enzymes [435] (**Fig. 2.34,C**). The catalytic domain is composed of fourteen α-helices and two β-sheets consisting of four (β3–β6) and six (β1–β2, and β7–β10) strands, respectively (**Fig. 2.34, A**). An additional β-strand precedes the last α-helix (α14) of the domain. A main difference with the human and insect proteins, but similar to the yeast enzyme is the absence of a heme-binding domain [159,255,431] (**Fig. 2.34** and **2.9**).

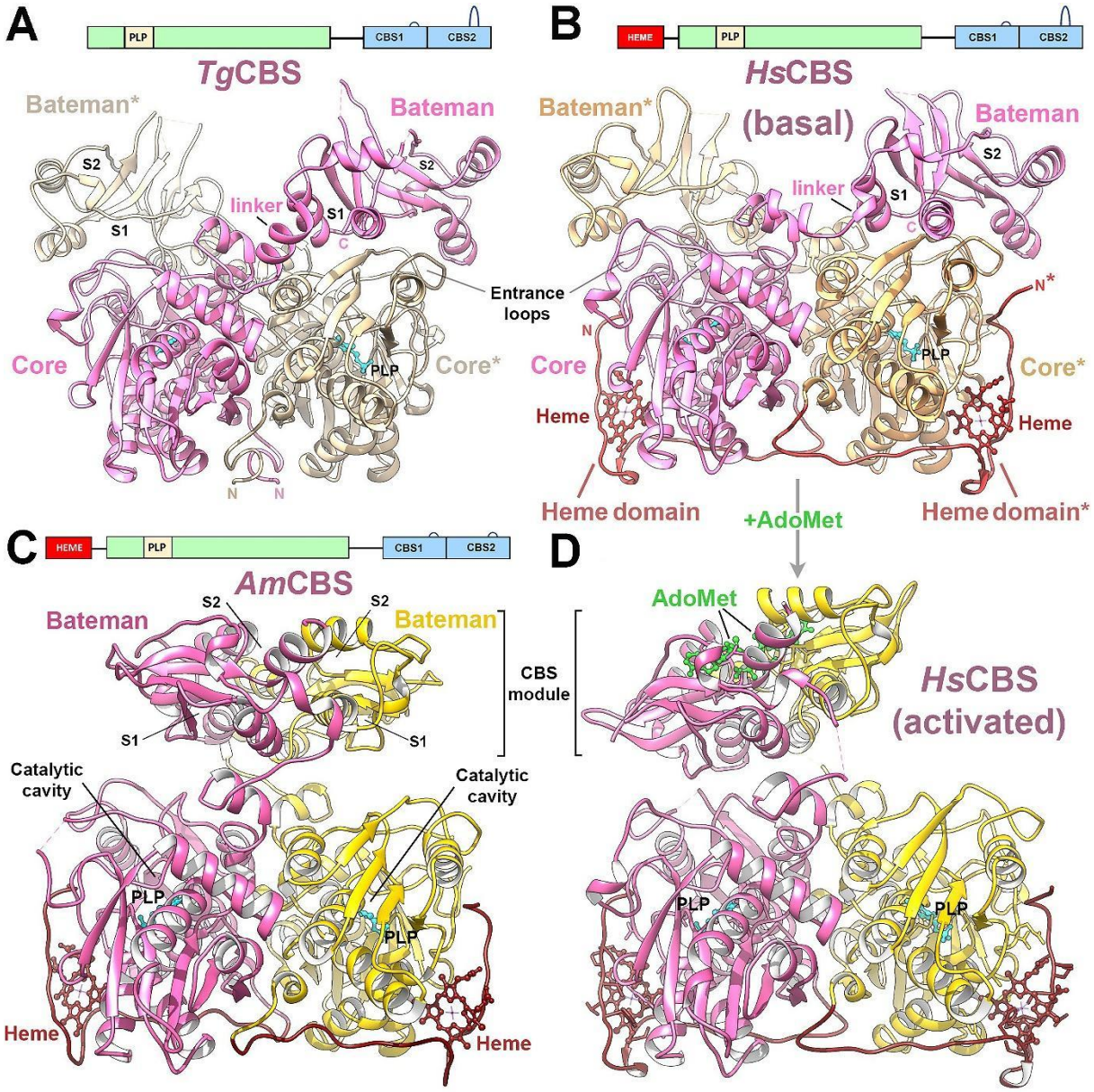

Figure 2.34. Structure of TgCBS. (***A***) *Structure of the basket-shaped TgCBS dimer (PDB ID code 6XWL). The complementary subunits are colored in yellow and pink, respectively. (**B**) Basket-shaped HsCBS dimer (basal state) (PDB ID 4L0D)* [69]*. The heme-binding domain is in red. (**C**) Constitutively activated sea bollard-shaped dimer from Apis mellifera CBS (AmCBS) (PDB ID code 5OHX)*[435]*. (**D**) AdoMet-bound sea bollard-dimer of HsCBS (activated state) (PDB ID 4PCU)*[160]*. The Bateman modules associate forming a disk-like CBS module. Heme, PLP and AdoMet are in red, cyan and green sticks, respectively. Figure recovered from* [255]*.*

2.4.4.1.1. Catalytic core

Two distinct blocks are clearly distinguishable in the catalytic domain (**Fig. 2.35**). The larger one contains two segments of residues distanced in the peptide chain (residues 10-55 and 163-322) and ranges the so-called *static subdomain*. This block behaves as a rigid body during the catalysis in other CBSs and related enzymes, and represents the region that most interacts with other protein domains [435]. In *Tg*CBS, it contributes significantly to maintaining the integrity of the dimer by providing hydrophobic residues (c.a L18, V27, M29, I89, L93, V97, I117, C120, L121, I277, L282, M320, I324) at the interface between complementary subunits. The overall architecture of the static subdomain is mostly conserved when compared with the wild type human enzyme. A least square superposition of the Cα-positions of this region between *Tg*CBS and *Hs*CBS yields a root mean square deviation of only 0.48 Å and 0.58 Å at the monomer and dimer level, respectively. Importantly, this static block configures half the entrance to the catalytic site [433,434] (**Fig. 2.35**) and contains four out of the five consensus sequences that participate in the interaction with the different CBS substrates [242](blocks B2, B3, B4 and B5 in **Fig. 2.35**). The main differences with the human protein are in the region comprising residues 232-238 of block B3 (**Fig. 2.35**), which is more directed towards the catalytic cleft in *Tg*CBS, due to a somewhat longer helix α10 (residues 228-234). The second subdomain of the catalytic core is the *mobile subdomain* [435] which is smaller in size (residues 75-157) and is intercalated in the static block, to which is linked by two loops that connect helix α4 with strand β4, and strand β7 with helix α8, respectively (**Fig. 2.35**). The mobile subdomain provides the second half of the walls of the catalytic cavity, and acts as a cap that limits the access of substrates into the narrow channel where the PLP molecule is covalently attached via a Schiff base bond to the ε-amino group of lysine (K56) [452]. Several H-bonds anchor the PLP molecule to the protein matrix and orient the cofactor appropriately within the cavity. Among them are those formed between the nitrogen of the pyridine and the Oγ of residue S287, and between the 3´-hydroxyl group of PLP and the $N_{\delta 2}$ of residue N86 (**Fig. 2.35**). Importantly, N86 is coplanar with the pyridine ring of PLP to allow the appropriate ring tilt upon transaldimination [438]. On the opposite side of PLP, the phosphate moiety interacts with the so-called *phosphate binding loop* (block B2 in **Fig. 2.35**, residues 193-197), which is located between strand β8 and helix α9. This loop includes two important threonine residues (T194 and T197) as well as three glycines that form a network of H-bond interactions that ensure the correct orientation of PLP. Mutation of the equivalent threonines in *Hs*CBS is known to cause a loss of CBS activity, and impairs carbonylation of the heme moiety [437]. Importantly, in *Tg*CBS the mobile subdomain collapses towards the catalytic cleft pushed by the Bateman module, which is placed just above (**Fig. 2.35**). A similar arrangement is observed in the

basal state of the human enzyme [69,440] (**Fig. 2.34, B**), where the loops L145–148, L171–174, and L191–202, defining the entrance of the catalytic site, are sandwiched between the core and the regulatory module, thus impairing free access of substrates into the PLP site.

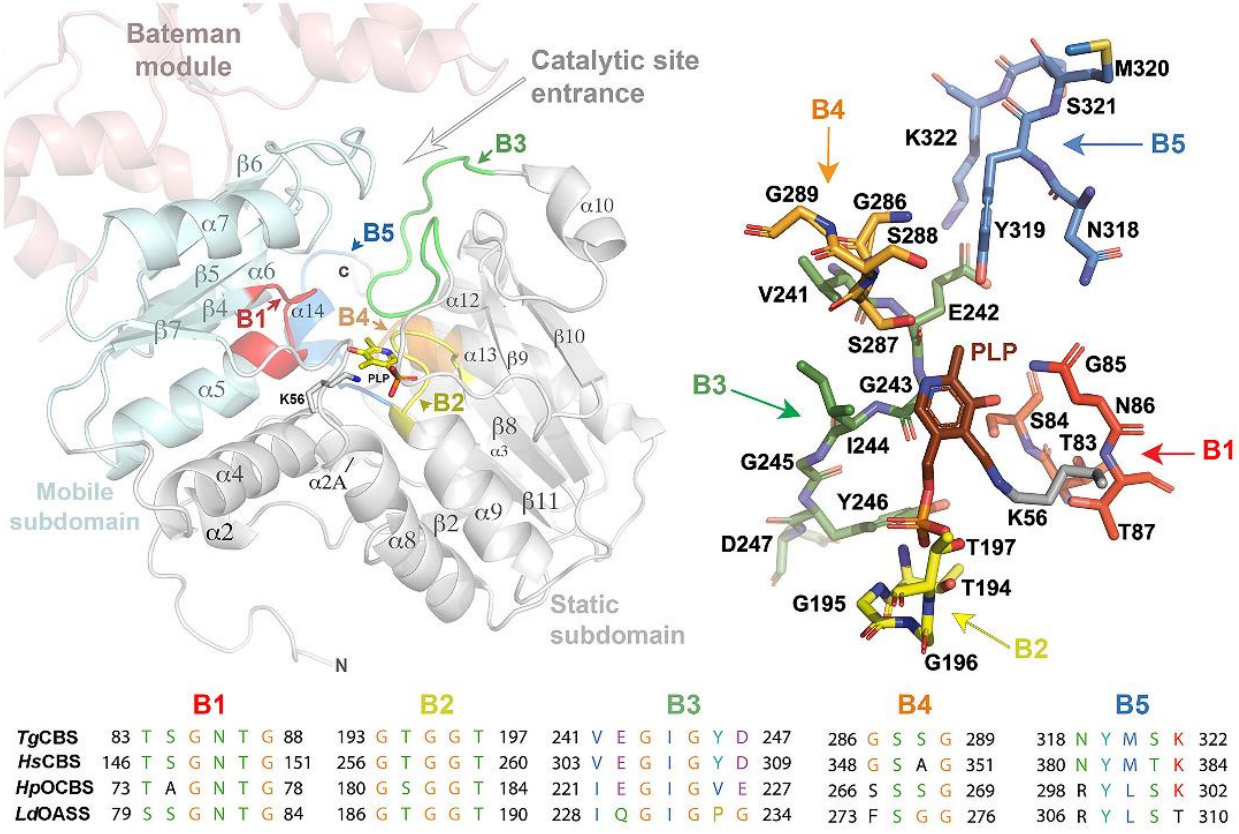

	B1							B2							B3							B4					B5				
*Tg*CBS	83	T	S	G	N	T	G	88	193	G	T	G	G	T	197	241	V	E	G	I	G	Y	D	247	286	G	S	S	G	289	318	N	Y	M	S	K	322
*Hs*CBS	146	T	S	G	N	T	G	151	256	G	T	G	G	T	260	303	V	E	G	I	G	Y	D	309	348	G	S	A	G	351	380	N	Y	M	T	K	384
*Hp*OCBS	73	T	A	G	N	T	G	78	180	G	S	G	G	T	184	221	I	E	G	I	G	V	E	227	266	S	S	S	G	269	298	R	Y	L	S	K	302
*Ld*OASS	79	S	S	G	N	T	G	84	186	G	T	G	G	T	190	228	I	Q	G	I	G	P	G	234	273	F	S	G	G	276	306	R	Y	L	S	T	310

***Figure 2.35. TgCBS catalytic site**. (**Left**) The catalytic domain of TgCBS includes the mobile (cyan) and the static (grey) subdomains. The Bateman module is in light red. (**Right**) Residues configuring the catalytic cavity. PLP (brown) is covalently bound to K56. (**Bottom**) Sequence alignment of blocks configuring the active site. Block B1 (asparagine loop, red), stabilizes the aminoacrylate intermediate and contains a conserved serine (S84) in all CBSs and OASS enzymes. Block B2 (phosphate loop, yellow) anchors the phosphate moiety of PLP. Block B3 (green) is thought to interact with the second substrate, Hcys, and participates in the nucleophilic attack on aminoacrylate, in the regeneration of the internal aldimine, and in the closure of the active site [242]. Block B4 (orange) stabilizes the pyridine ring of PLP. Block B5 (blue) interacts with the lip of the active site. TgCBS= cystathionine β-synthase from T. gondii; HsCBS= cystathionine β-synthase from H.sapiens; HpOCBS= O-acetylserine dependent cystathionine β-synthase from Helicobacter pylori; LdOASS= O-acetylserine sulfhydrylase from Leishmania donovani. Figure recovered from [255].*

2.4.4.1.2. Regulatory domain

Finally, the C-terminal domain of *Tg*CBS comprises a Bateman module (~20 kDa) made up of two CBS motifs (CBS1, residues 354-425; CBS2, residues 426-514) that are connected to each other by a linker of eight amino acid residues (421-428). Both, CBS1 and CBS2 show the canonical βαββα sequence of secondary elements usually found in these types of motif [432], and contact each other via their three-stranded β-sheets. As observed in humans [437,438], the Bateman module of *Tg*CBS presents two symmetrical cavities (S1, S2) (**Fig. 2.36, A**) of which only S2 is exposed to solvent. Site S2 conserves some of the residues that would be necessary to stabilize one AdoMet molecule inside (c.a. T501 and D504 that would interact with the ribose ring of the nucleotide, or I503 and V499 that would help in accommodating the methionyl group of AdoMet), but misses other key features to host AdoMet. Among them is a longer peptide segment comprising residues 361-368 (417-423 in *Hs*CBS, **Fig. 2.36, C**), that stands out preceding the strand β11b, and displaces residue T364 away from the center of the S2 cavity, thus preventing its potential interaction with the ribose ring of AdoMet. The extension of this segment distorts the hydrophobic pocket otherwise required to accommodate and orient the adenine ring of AdoMet inside the cavity [160]. Additionally, a negatively charged glutamate at position 390 invades the position that the AdoMet adenine ring would potentially occupy (**Fig. 2.36, B** and **C**). All these features disable *Tg*CBS from binding AdoMet.

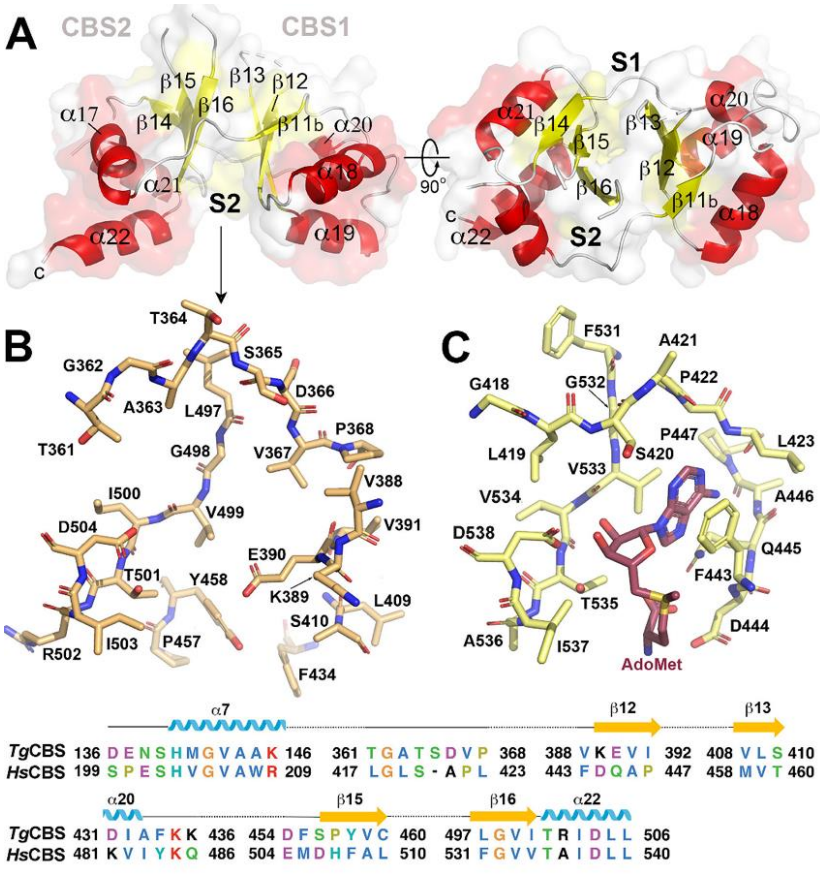

***Figure 2.36. TgCBS regulatory domain**. (**A**) Bateman module of TgCBS. S1 and S2, are the main cavities. (**B**) Residues within cavity S2 in TgCBS; (C) Residues in site S2 of HsCBS. AdoMet is in wine sticks. Bottom: Sequence alignment of residues at cavity S2 in TgCBS and HsCBS. Figure recovered from [255].*

2.4.5. *Tg*CBS exists in a unique basal-like conformation.

A careful comparative analysis of the available CBS three-dimensional data has led us to propose that the basal-type folding of *Tg*CBS represents its sole conformational state. We base our conclusion on three key structural features:

(i) The first one is the inability of *Tg*CBS to bind AdoMet at the site S2 of the Bateman module (**Fig. 2.36, B**), and thus to suffer an AdoMet-induced relative rotation of its two CBS motifs. In allosterically regulated CBS enzymes as *Hs*CBS, such rotation weakens the interactions that maintain the Bateman module anchored to the catalytic core just above the entrance of the catalytic site, and this makes the enzyme progress towards the activated state [160]. It is well established that the migration of the Bateman module allows the free access of substrates into the PLP cleft [160]. Nevertheless, such displacement of the Bateman module can only occur if its contacts with the catalytic core are not too tight. If this were the case, both domains would remain permanently anchored to each other (as it happens in *Tg*CBS).

(ii) The second relevant feature refers to the peptide linker connecting the Bateman module with the catalytic core, which needs to be sufficiently long and flexible as to facilitate the migration of the regulatory domain to its final location in the activated state. Our structures show that, although the length of the *Tg*CBS linker is sufficient, the interactions that it maintains with the Bateman module and with the core are stronger than in *Hs*CBS (**Fig. 2.37, A** and **B**). These contacts significantly enhance the stability of the basket-like conformation vs other possible arrangements, and occur thanks to a specific turn of the interdomain linker in the parasite enzyme, around residues 342-344, that allows positioning helix α16 closer to helices α6, α21 and α22 and to strands β5 and β6, than in the human protein (**Fig. 2.37, B**). This peculiar location of helix α16 in *Tg*CBS results in the formation of a multiple network of salt bridges participated by residues K341, E344 and R345 (α16), K119 (α6), D454 (α21), R502 (α22), R101 (β5), and E124 (β6). These attractive electrostatic interactions complement the effect of the hydrophobic pocket formed by residues F349 from helix α16 and residues L505 and L509 from helix α22, and keep the interdomain linker of *Tg*CBS firmly attached to both the catalytic core and the Bateman module, making the displacement of the latter highly unlikely.

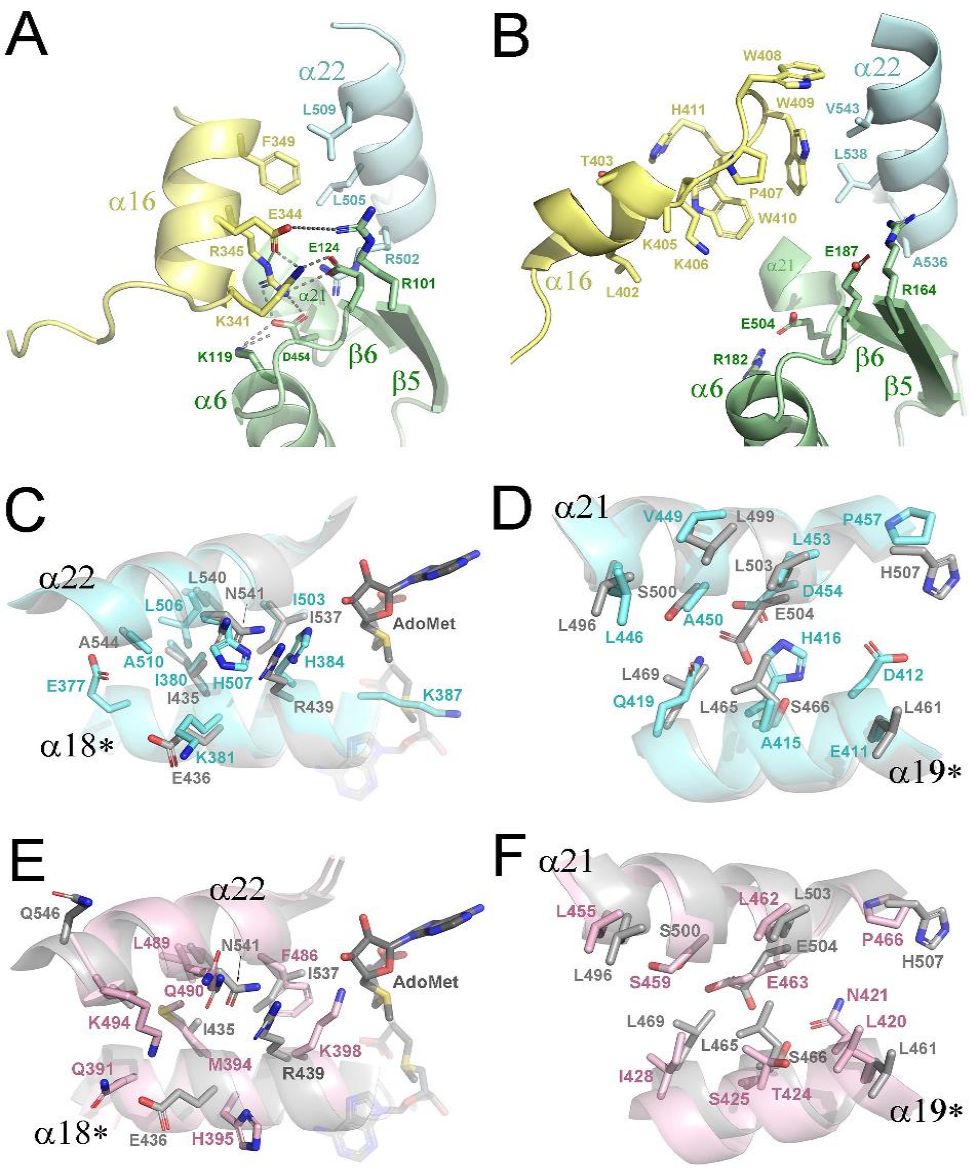

Figure 2.37. *(**A**) Interdomain interactions in TgCBS, HsCBS and AmCBS. Interactions between the interdomain linker (yellow), the catalytic core (green) and the Bateman module (cyan), in TgCBS (**A**) and in HsCBS (**B**). Interface residues in a potential CBS module of TgCBS (cyan) (**C, D**), and AmCBS (pink) (**E, F**) compared to that found in HsCBS (grey)[69]. Figure recovered from [255].*

(iii) Finally, the third requirement in an allosterically regulated CBS enzyme to reach the activated state consists in being able to couple its Bateman module with the equivalent region from the complementary subunit to form a flat disk-shaped structure, known as "*CBS module*". Once formed, this assembly locates far from the entrance of the catalytic cavity, thus allowing free access of all substrates [160](**Fig. 2.38**). The formation of the CBS module necessarily requires the previous rotation of the CBS motifs mentioned above, which only occurs upon binding of one AdoMet molecule to the S2 site [160] (**Fig. 2.34**). The formation of the CBS module also involves establishing new interactions between the interfacial helices of the CBS domains (α18, α19 from CBS1; α21, α22 from CBS2) (**Figs. 2.37, C-F** and **2.38**). It is worth mentioning that in all known CBS enzymes, the CBS module is antiparallel (the two Bateman modules are oriented in a head-to-tail manner) [434,435]. In the said arrangement, the CBS1 of the first subunit interacts with the CBS2 motif of the complementary monomer and vice versa (**Fig. 2.38**). Obviously, if the residues at the interfacial positions do not favor the corresponding interactions, the CBS

module cannot be assembled. Said this, we found that *Tg*CBS does not fulfil the third condition for activation. The independent structural superimposition of the CBS1 and CBS2 domains of *Tg*CBS and *Hs*CBS or *Tg*CBS and *Am*CBS are good (rmsd 0.902 /0.816 and 1.147/0.719, respectively), but significantly worsens when the structural alignment is performed comparing the entire Bateman module of *Tg*CBS with the corresponding region from the AdoMet-bound activated form of the human enzyme (rmsd=1.37) or to the constitutively activated *Am*CBS (rmsd=4.55). In its native conformation, the Bateman module of *Tg*CBS is not compatible with the assembly of a CBS module, as its interfacial helices would not face those of its complementary counterpart (**Fig. 2.38**). Self-assembly of Bateman modules to form a CBS module of *Tg*CBS would cause clashes between some residues (c.a K387) and a bound adenosine derivative (**Fig. 2.37, C**). In such hypothetical CBS module, some favorable hydrophobic interactions could be potentially established between residues of the interfacial helices α18, α19, α21 and α22 of complementary CBS1 and CBS2 motifs (c.a L446, V449, L453 from α21; Q419, A415 from helix α19), but would also be impaired by steric clashes and/or repulsive forces between bulky or charged residues of the complementary subunits (c.a H507/H384) (**Fig. 2.37 C** and **D**).

Put together, all these findings strongly suggest that the basal-like fold of *Tg*CBS represents its unique conformation and that the enzyme does not progress to a second activated form structurally similar to the AdoMet-bound form found in mammals [69] and the constitutively active species of insects [434,435].

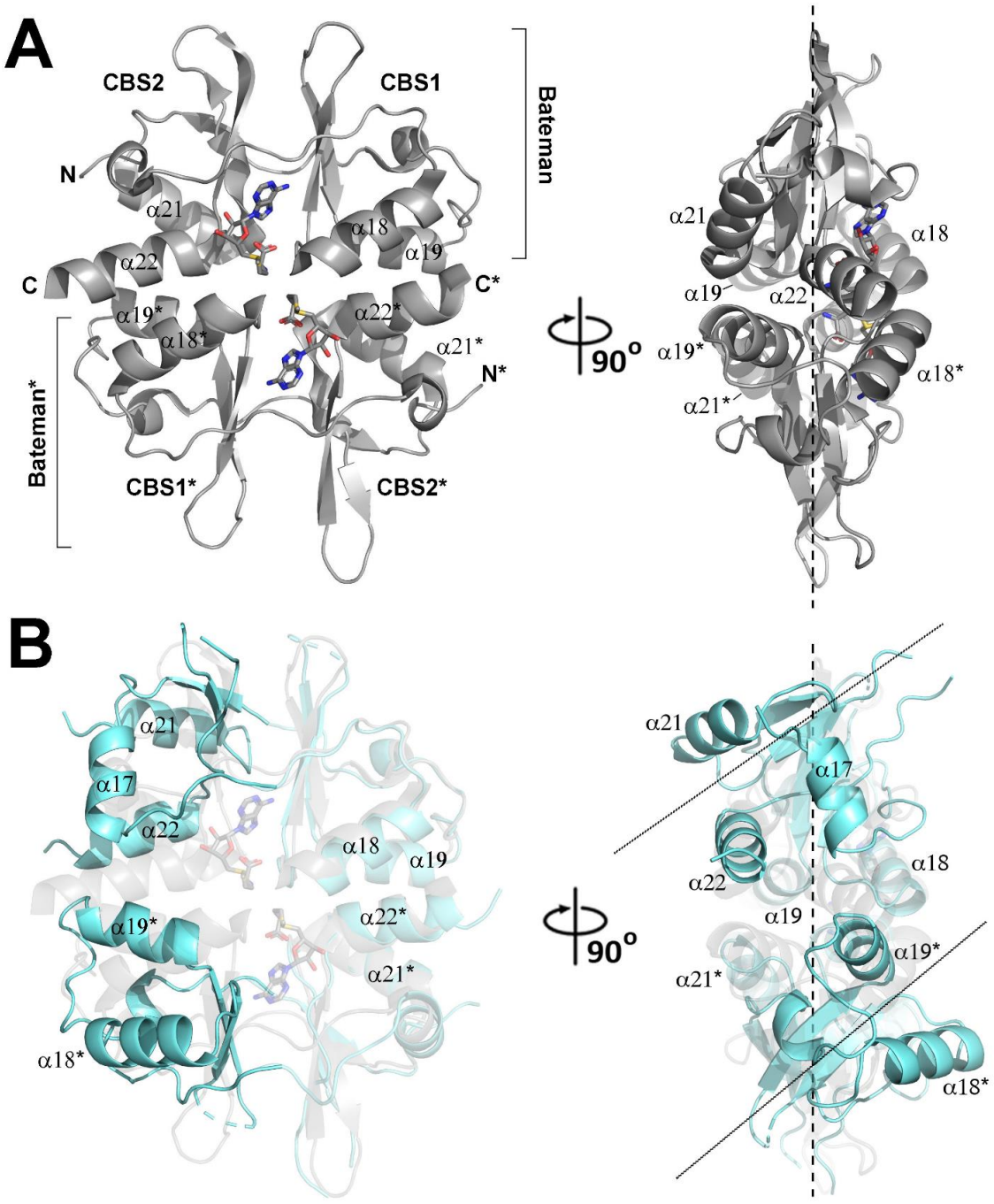

Figure 2.38. The Bateman module of TgCBS is impaired for self-assembly. *(**A**) Disk-shaped CBS module of HsCBS (PDB ID 4PCU) resulting from the assembly of complementary Bateman modules upon binding of AdoMet (in sticks). The asterisk indicates elements from the complementary subunit. The vertical dashed line represents the main plane containing each Bateman module (**B**) Superimposition of the Bateman module of TgCBS (in cyan) on each Bateman module of the human CBS module (in grey). As shown, helices α21 and α22 do not face their equivalent complementary elements in TgCBS due to a rotation of ~50 degrees of its CBS motifs with respect to HsCBS. Dashed and dotted lines represent the main planes containing the CBS motifs located at the back (transparent ribbons) and the front (opaque ribbons), respectively. Figure recovered from* [255].

2.4.6. *Tg*CBS forms large polymer chains

Unexpectedly, the artificial removal of residues 466-491 from the flexible loop that links the last two β-strands of the CBS2 motif in *Tg*CBS did not have the exact same effects formerly found in human CBS [69,160]. It is worth remembering that the shortening of this loop pursued two main objectives: (i) the first was to reduce the flexibility of this region, not involved in the enzyme activity, to favor the crystallization process and increase the diffraction quality of the resulting crystals; (ii) secondly to decrease the heterogeneity of the protein in solution towards a single species, disfavoring the formation of the tetrameric form of the enzyme and/or of large aggregates, thus enriching the sample in a single oligomeric form, the dimer. Contrasting with our initial expectations, only the first objective (obtaining crystals of sufficient quality) seemed to be met. Surprisingly, we did not appreciate significant changes in the oligomeric state of the *Tg*CBS shortened construct with respect to the native enzyme. Thus, large aggregates were still formed, and the tetramer-to-dimer ratio of the *Tg*CBSΔ466-491 construct did not varied much with respect to the *Tg*CBS wild-type protein. In both cases, the dimer was the most abundant species after removal of the large aggregates in the gel filtration step (**Fig. 2.31, E**). This behaviour differs from that observed in the human enzyme, where deletion of the corresponding loop (residues 516-525) drastically impairs the tetramer formation, towards a dimeric species.

A characteristic of human CBS repeatedly described by different authors over the years is the high tendency of this protein to form large aggregates [69,159]. In fact, the recurrent formation of these high molecular weight species in pure protein samples was thought as one of the main causes that prevented the crystallization of the enzyme for decades. It was not until 2010 that our laboratory found a way to decrease the percentage of these large aggregates in solution by artificially shortening a flexible long loop located in the CBS2 domain of the Bateman regulatory module. This strategy allowed the temporal isolation of dimeric entities that could be crystallized, although they presented an intrinsic tendency to re-associate over time, forming aggregates of higher molecular weight (unpublished results).

After an exhaustive analysis of the crystalline molecular packings, our laboratory found that the underlying cause of aggregation appeared to reside in the intrinsic predisposition of the Bateman module, and more concretely on its α-helices, to interact with their complementary subunit counterparts in the basal conformation of the enzyme, where these helices are solvent exposed. Two different types of polymeric chains could be detected in crystals, belonging to the space groups I222 and $C222_1$, respectively [69]. The secondary elements and residues involved were described in detail in 2013 (Supplementary Figure

S3 in [69]), and led to postulate that the large *Hs*CBS aggregates detected in solution, very likely correspond to the long *Hs*CBS polymeric chains present in both type of crystals [69] (**Figs. 2.40** and **2.41**). In the absence of AdoMet, these polymers coexist with the functional biological unit, the tetramer (**Fig. 2.39**), becoming dissassembled into activated "bollard-shaped" dimers upon binding of AdoMet [69].

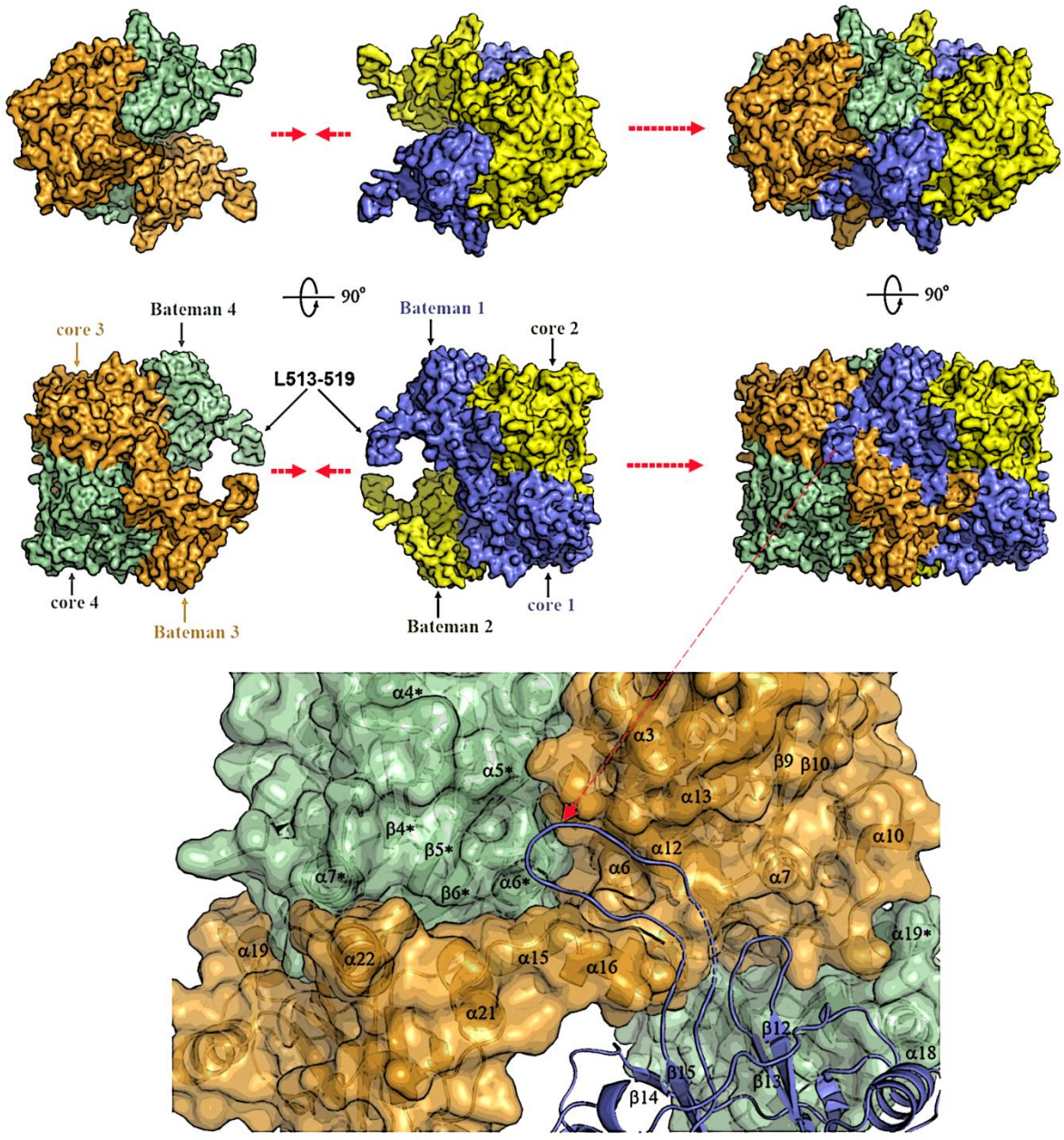

Figure 2.39. The proposed model of the HsCBS tetramer (*adapted from [69]). The HsCBS tetramer is a dimer of dimers sustained by interactions of each Bateman module with the Bateman module and catalytic cores of the complementary dimer. Loop 513-529 serves as a "hook" locking the two dimers together, and the residues located at the cavity formed by the helices α6, α12, α15 and α16 stabilize the overall asssembly.*

Our group found that human CBS presents two regions that favor its self-interaction with nearby molecules. The first of these regions is the flexible loop of its CBS2 domain. The artificial shortening of this loop essentially prevents the formation of the tetrameric form of the enzyme (actually a dimer of dimers), which is thought to be configured from the coupling of two dimers across the central cavity that exists between its Bateman modules (**Fig. 2.39** taken from [69]). In such tetrameric assembly, the loop acts as a buckle that stabilizes the whole assembly, likely by inserting itself into a large lateral cavity that houses the surface of the complementary dimer (**Fig. 2.39**). This is reinforced by the internal symmetry of the assembly, which multiplies the loop-dimer interaction by a factor of four. Importantly, this contributive effect is eliminated by the shortening of the loop, immediately promoting the disassembly of the tetramer into its two component dimers.

The second region that favors and promotes intermolecular contacts in *Hs*CBS corresponds to the α-helices of the Bateman module, whose characteristics award the human enzyme the ability to self-associate and form the so-called "CBS module" upon binding of the allosteric activator AdoMet. This capacity to evolved from a basal, basket-shaped dimer, to an activated "bollard"-like dimer is unique to the mammals CBS enzyme, and is not feasible in Toxoplasma CBS, which neither binds AdoMet nor forms the CBS module. However, this essential and indispensable capacity for the activation of human CBS, also implies a high tendency to aggregation through the same interaction surface (the α-helices of the Bateman module). Such interactions favor the formation of long polymeric chains that are visible not only in the crystals [69] (**Figs. 2.40** and **2.41**), but also in solution (personal unpublished communication by Prof. Tomas Majtan derived from Electron Microscopy studies). Obviously, as interaction occurs mainly through the α-helices of the Bateman module (concretely the helices α18 and α19 of the CBS1 motif), and are not mediated by the extended loop, the shortening of the said loop does not prevent the formation of long polymers and limits itself to disfavor exclusively the assembly of the tetramer. In the basal dimer, the α-helices of the Bateman are fully exposed to the solvent and thus are susceptible of interacting with their counterparts to form these large polymers.

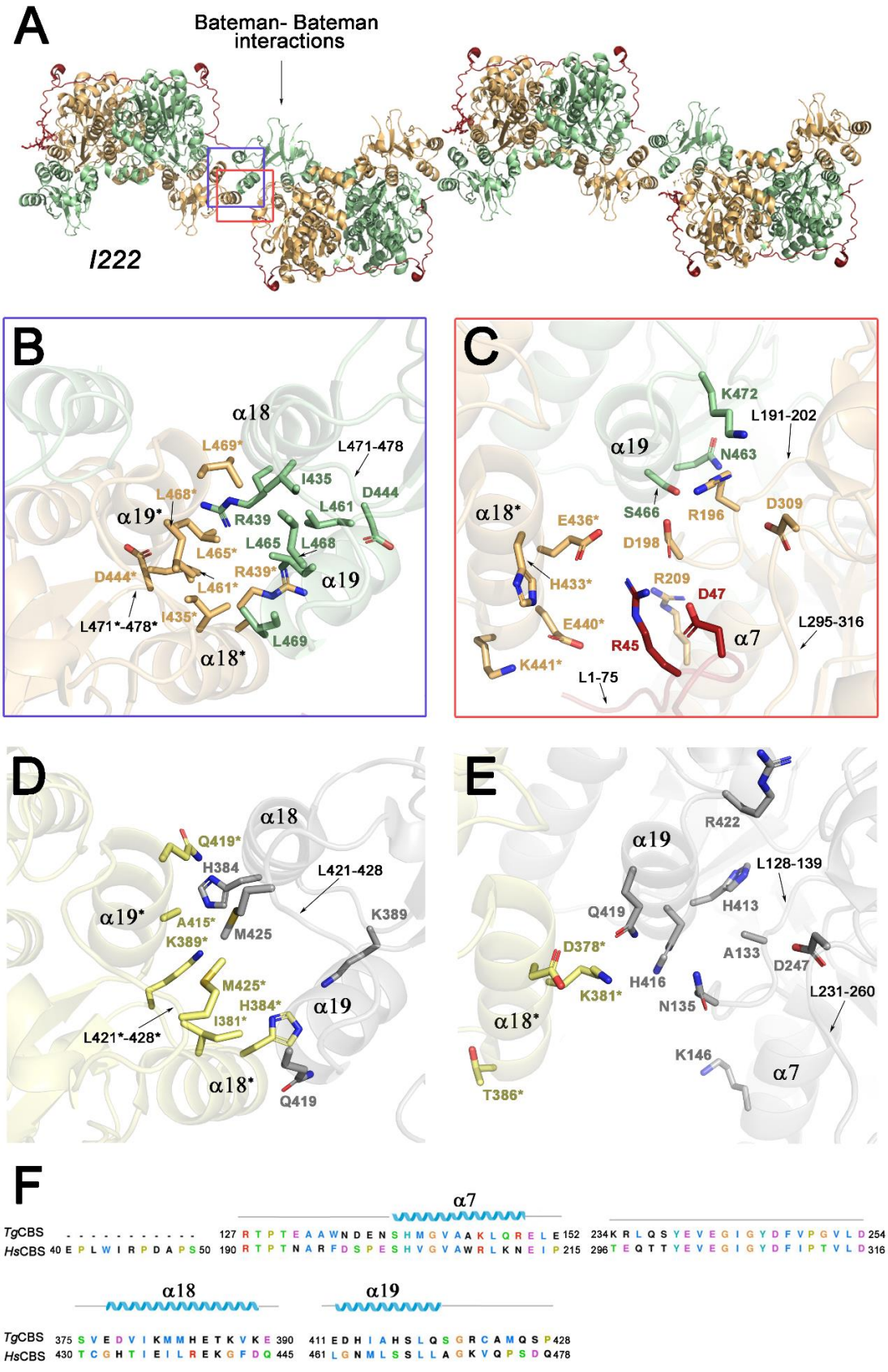
A
Bateman- Bateman interactions
I222
B
α18
L469*
L471-478
I435
L468*
D444
α19*
R439
L461
L465
L468
L465*
D444*
R439*
α19
L461*
I435*
L471*-478*
L469
α18*
C
K472
L191-202
α19
N463
α18*
S466
R196
D309
E436*
D198
H433*
R209
D47
E440*
R45
α7
L295-316
K441*
L1-75
D
α18
Q419*
H384
L421-428
α19*
A415*
K389
K389*
M425
M425*
H384*
α19
I381*
L421*-428*
α18*
Q419
E
R422
α19
L128-139
Q419
H413
D378*
A133
D247
K381*
H416
N135
L231-260
α18*
K146
α7
T386*
F
α7
TgCBS 127 R T P T E A A W N D E N S H M G V A A K L Q R E L E 152 234 K R L Q S Y E V E G I G Y D F V P G V L D 254
HsCBS 40 E P L W I R P D A P S 50 190 R T P T N A R F D S P E S H V G V A W R L K N E I P 215 296 T E Q T T Y E V E G I G Y D F I P T V L D 316
α18
α19
TgCBS 375 S V E D V I K M M H E T K V K E 390 411 E D H I A H S L Q S G R C A M Q S P 428
HsCBS 430 T C G H T I E I L R E K G F D Q 445 461 L G N M L S S L L A G K V Q P S D Q 478

***Figure 2.40. Polymeric chains in crystals I222 of Human CBS**. (**A**) Cartoon representation of polymeric chains of HsCBSΔ516-525 dimers in crystals belonging to space group I222 (PDB ID 4L0D) [69]. The dimers interact through residues of two distinct interfaces of their Bateman modules (framed in blue and red squares). (**B**) Zoom view of the residues involved in the polymerization of the HsCBS corresponding to the region framed in blue. A Bateman module is shown in green and the Bateman module of the complementary dimer is in orange (**C**) Electrostatic interactions between the residues of the heme-binding domain (red), the catalytic core (orange), the helices of the CBS1 motif (green) and the helices of the CBS1 motif (orange) of the adjacent dimer. The zoom view represents the region framed in red. (**D** and **E**) Interface residues of a hypothetical polymeric chain of TgCBS corresponding to the blue and red region in HsCBS, respectively. In section D a CBS1 motif is represented in grey and the CBS1 motif of the complementary dimer is in yellow. In panel E the residues of the catalytic domain are shown in grey and the CBS1 motifs of the dimer and its complementary are represented in grey and yellow, respectively. Residues E411, L418 and E385 in TgCBS (corresponding to residues L461, L468 and E440 in HsCBS, respectively) are absent due to the side chain flexibility. (**F**) Alignment of residues at the interfacial helices in TgCBS and HsCBS.*

Taking into account that *Tg*CBS also assembles into basal-like dimers, we wondered whether the large aggregates observed during the gel filtration purification step, could correspond to elongated polymers, favored by helix-to-helix interactions between the Bateman modules of *Tg*CBS neighbouring molecules. Moreover, we wanted to find out whether such potential polymers reproduced the human pattern, or formed alternative arrangements attributable to the distinct sequence and structural features of *Tg*CBS. To that aim, we first modeled an *in silico Tg*CBS human-like polymer by superimposing the *Tg*CBS dimers on the corresponding counterparts in the human polymers. As shown in Figure 2.42, we found that in a potential human-like *Tg*CBS polymer, the helix-to-helix interfacial contacts would not be favorable. In human CBS, the α-helices (α18 and α 19) of their CBS1 motifs interact through hydrophobic contacts (**Fig. 2.40, B**), and strong electrostatic interactions with the heme domain (R45 and D47) and the catalytic core of the complementary dimer (**Fig. 2.40, C**). In contrast, in *Tg*CBS both the absence of the heme domain, steric clashes (c.a. M425/M425*) (**Fig. 2.40, D**), and/or repulsive forces between charged residues of complementary dimers (e.g., K389/H384 or K381/H416) (**Fig. 2.40, D** and **E**) would weaken the interaction between two subsequent dimers, likely precluding the formation of the large human-like oligomers in the parasite enzyme.

Interestingly, a closer look at the molecular packing of the *Tg*CBS crystals indeed revealed elongated, dextrorotating helical polymers, intertwined with each other, formed by *Tg*CBS dimers connected through the α-helical bundles of both, the Bateman module and the catalytic core (**Figs. 2.42** and **2.43**).

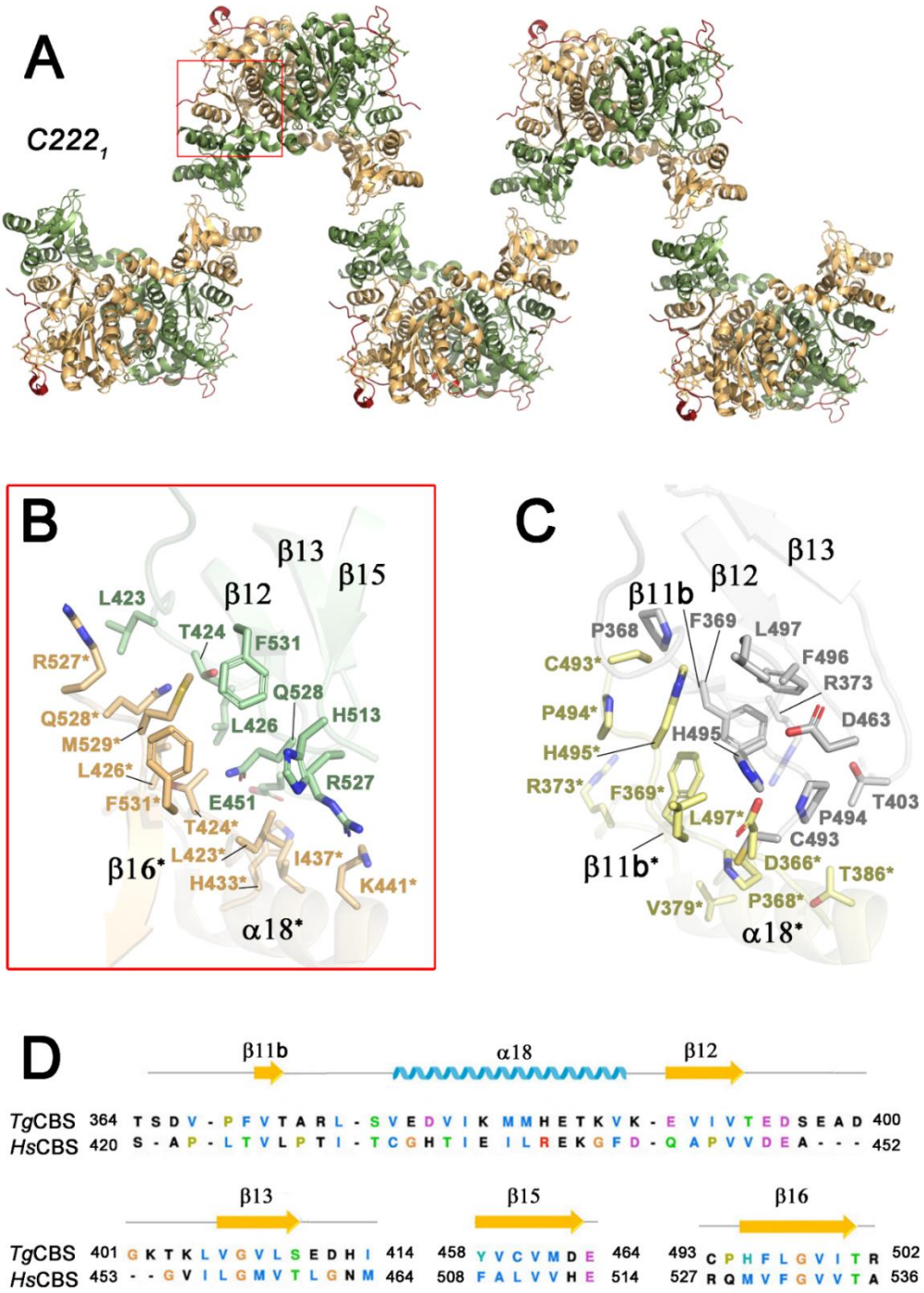

Figure 2.41. Polymeric chains of HsCBS present in crystals C222₁ *(**A**) Representation of polymeric chains of HsCBSΔ516-525 dimers found in crystals belonging to space group C222₁ (PDB ID4L3V)* [69]*. (**B**) Zoom view of the residues involved in the polymerization of HsCBS corresponding to the region framed in red in section A. A Bateman module is shown in green and the complementary Bateman module is in orange. (**C**) Interface residues of a potential polymeric chain of TgCBS in the spacegroup C222₁ corresponding to the red region in HsCBS. Side chains of T371 and M382 are missing in TgCBS (corresponding to residues L426 and I437 in HsCBS). Residue D378 in TgCBS is not represented. (**D**) Sequence alignment of TgCBS and HsCBS in these regions.*

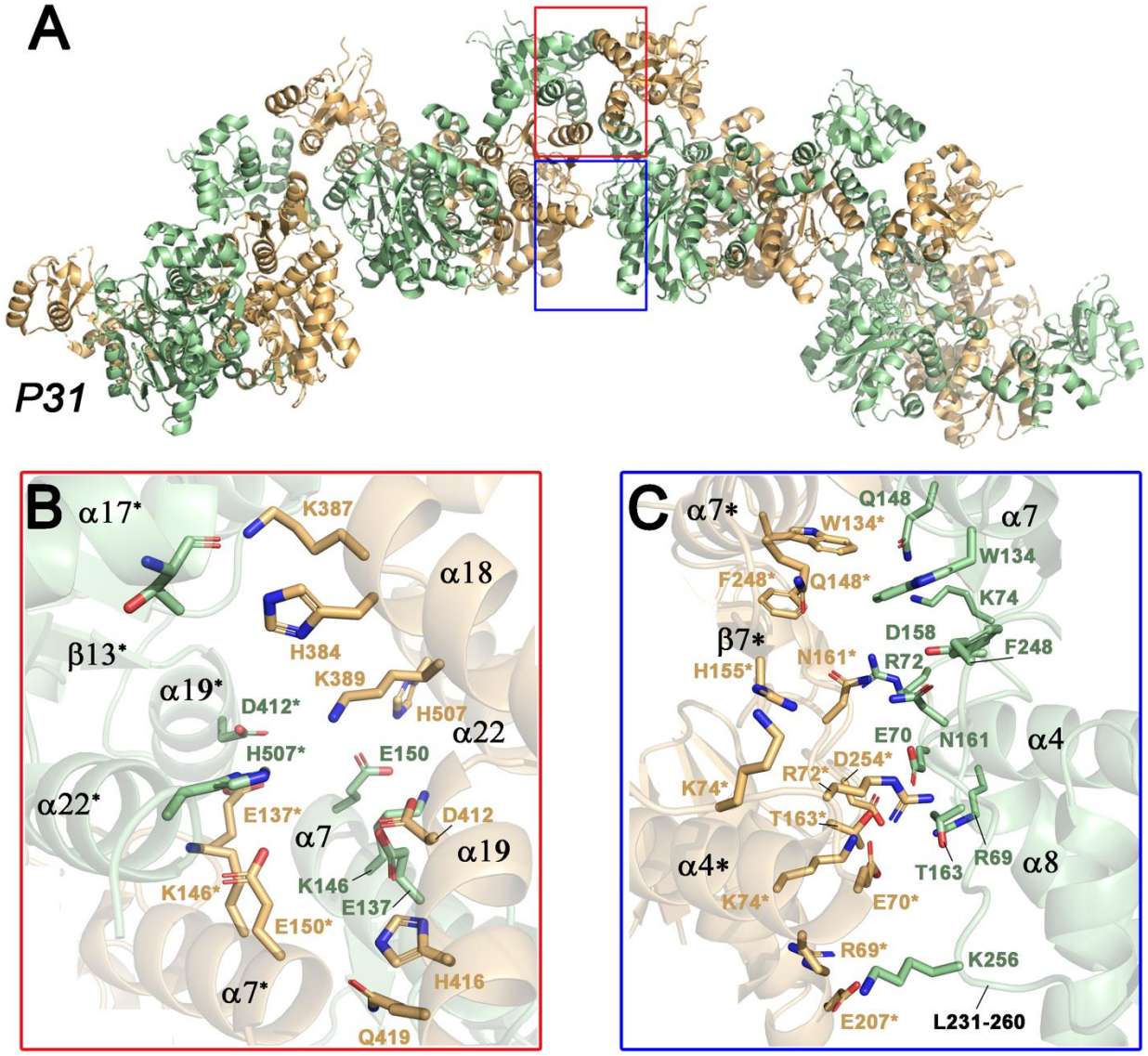

Figure 2.42. TgCBS forms polymeric chains. *(**A**) Small fragment of a TgCBSΔ466-491 helical polymer present in the crystals belonging to the spacegroup $P3_1$ (PDB ID code 6XWL). The two TgCBS subunits of each dimer are colored in green and orange. (**B**) Zoom view of the residues involved in the polymerization (red frame). The interactions occur via the interfacial helices (α17, α18, α19 and α22) of the Bateman module. (**C**) The interface residues in the blue frame belong to the catalytic domains of two consecutive dimers in the polymer.*

The *Tg*CBS helical polymers are structurally distinct from those of the human enzyme, but similarly involve interactions between the α-helices of complementary Bateman modules (α17, α18, α19 and α22) (**Fig. 2.42, B**). Each helix turn has a radius of curvature of approximately 120 Å, and contains nine protein dimers, being the distance between two consecutive turns approximately 421 Å (**Fig. 2.43**). In *Tg*CBS, the dimer-to-dimer interaction also involves contacts between helices from the catalytic domain (α4, α7 and

α8) (**Fig. 2.42, C**). In summary, the *Tg*CBS crystals can be interpreted in terms of an ordered assembly of *Tg*CBS polymeric helical chains. Further studies are due to confirm whether these polymers correspond to the large *Tg*CBS aggregates found in solution.

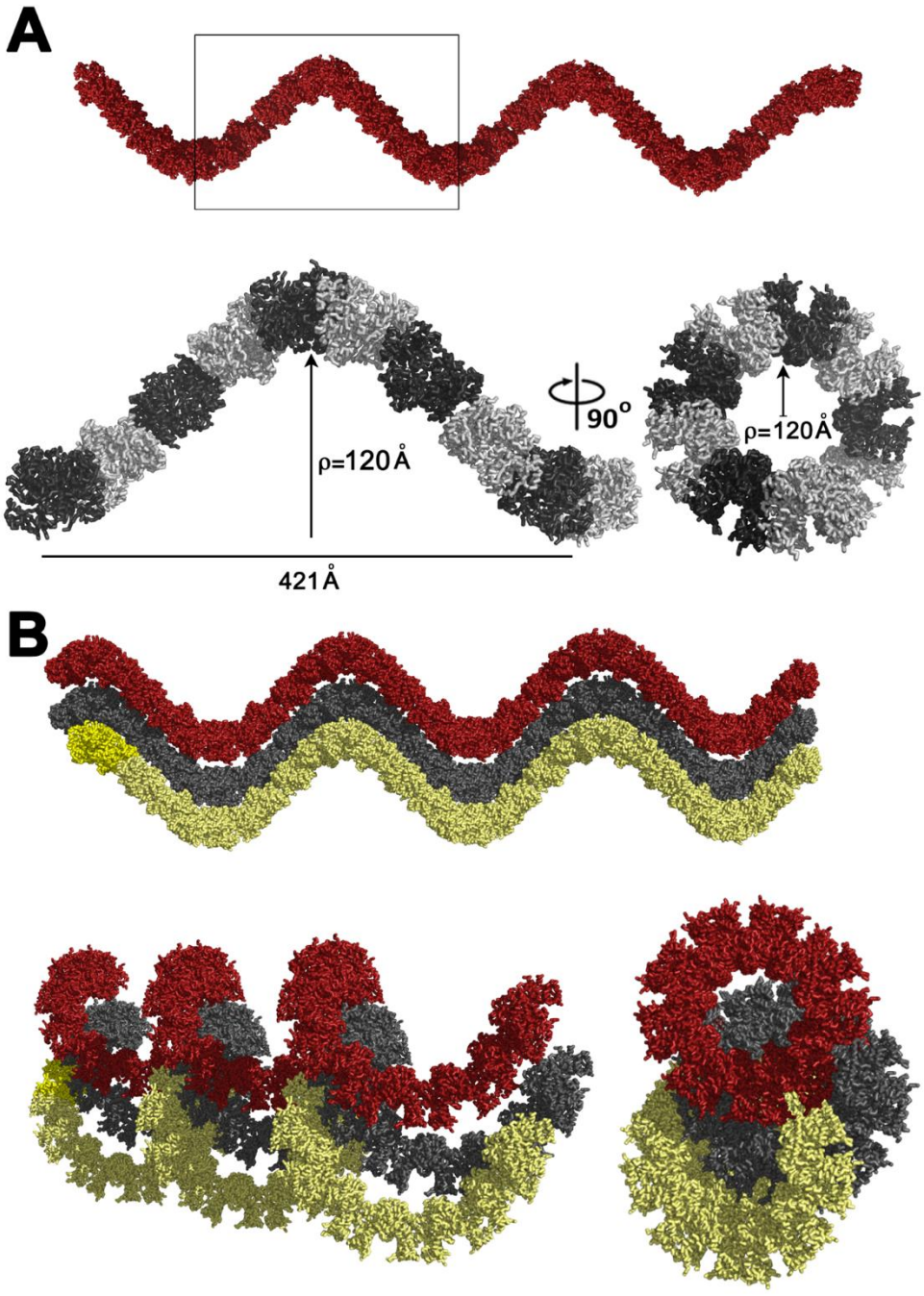

Figure 2.43. TgCBS helical polymers contained in the crystals. *(**A**) TgCBS helix. The framed area is zoom up below. The radius of curvature and the length between consecutive turns along the gyration axis are indicated; (**B**) Representation of three Intertwinned TgCBS helical polymers present in the crystals.*

2.4.7. *Tg*CBS is catalytically active maintaining a basal-like overall fold.

At first sight, the basal-like architecture of the crystallized *Tg*CBS and its closed active site would appear to reflect an inactive or poorly active enzyme. However, detailed 3D-alignments of *Tg*CBS with *Hs*CBS revealed a slight displacement of the complementary Bateman modules towards the central cavity existing between subunits (**Fig. 2.44**). This shift also affects helices α18 and α22, and occurs without significant changes in the catalytic core (**Fig. 2.44**). Interestingly, a similar shift was formerly observed in the pathogenic D444N mutant of *Hs*CBS [160] (**Fig. 2.44**), which shows an approximately two-fold increase in basal activity and impaired response to AdoMet stimulation as compared with the wild type enzyme [451].

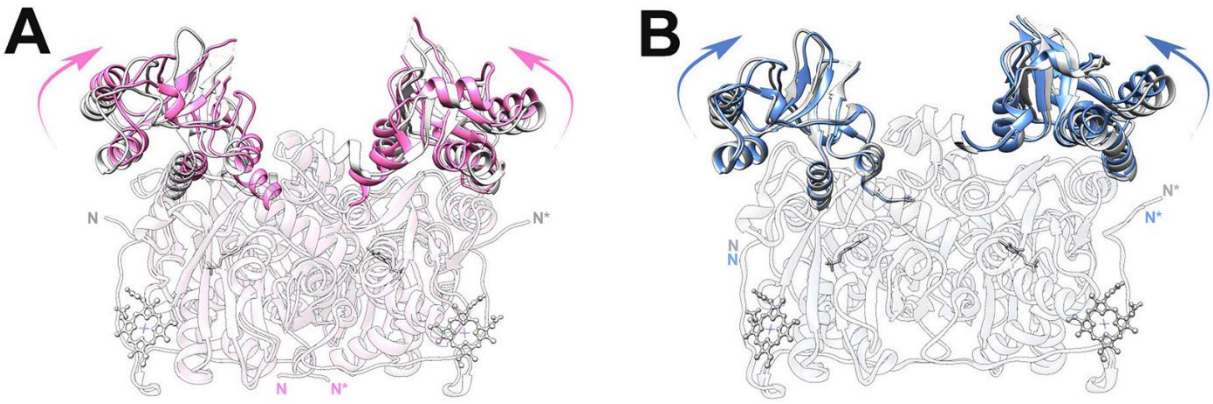

***Figure 2.44. Structural comparison of TgCBS, HsCBS and mutant D444N**. Superimposition of the crystal structures of (A) TgCBS (pink) on basal HsCBS (grey) and (B) of mutant D444N_HsCBS (blue) on basal HsCBS (grey), respectively. The Bateman modules are in opaque ribbons. Heme and PLP are in sticks.*

2.4.7.1. Crystallization of *Tg*CBSΔ466-491 with substrates.

To confirm that the crystallized enzyme is indeed catalytically active, we soaked crystals growth in 10% (w/v) PEG 3350 and 0.1M MES pH 6.1 in buffer containing 10 mM Ser, Cys, OAS and Cth. It should be noted that for both *Tg*CBSΔ466-491 in the presence of Cys and OAS, only one data set of high quality was obtained to elucidate the crystal structure with these ligands. Both data sets were obtained from crystals grown in the presence of one of the heterogeneous nucleating agents engineered at Tekniker (described in Chapter I). In the case of *Tg*CBSΔ466-491+cysteine, crystals were grown in a drop containing 10% (w/v) PEG 3350, 0.1M MES pH 5.9 and the PC-unpatterned tablet (**Fig. 2.45, A**). In the case of OAS, crystals grew in a droplet containing 10% (w/v) PEG 3350, 0.1M MES pH 6.1 and the PC- Laser Ablated Grooves (LA)

tablet (**Fig. 2.45, B**). The Polder omit maps [493] showed additional electron density near the PLP molecule, consistent with the synthesis of the aminoacrylate intermediate (**Fig. 2.46**). Of note, formation of the external aldimine in *Tg*CBS did not result in major distortions in the overall protein fold, and only caused subtle reorientations in the side chain of lysine K56, otherwise associated with PLP in the apoenzyme, and threonine T87, that rotates slightly to avoid clashes with the carboxylate moiety of aminoacrylate (**Fig. 2.46**). These small changes contrast with the behavior of other CBSs, such as the fly enzyme, where three loops (residues 119-122; 144-148 and 165-176) are displaced towards the PLP molecule upon addition of substrates. Formation of the aminoacrylate intermediate in the *Tg*CBS crystals is consistent with the behavior of the protein *in vitro*, where the addition of Ser or OAS results in the disappearance of the 412 nm-peak, representing the internal aldimine in the ketoenamine form, and the appearance of a major band centered at 460 nm in both absorbance and CD spectra, that is attributed indirectly to the aminoacrylate reaction intermediate [431] (**Fig. 2.47**).

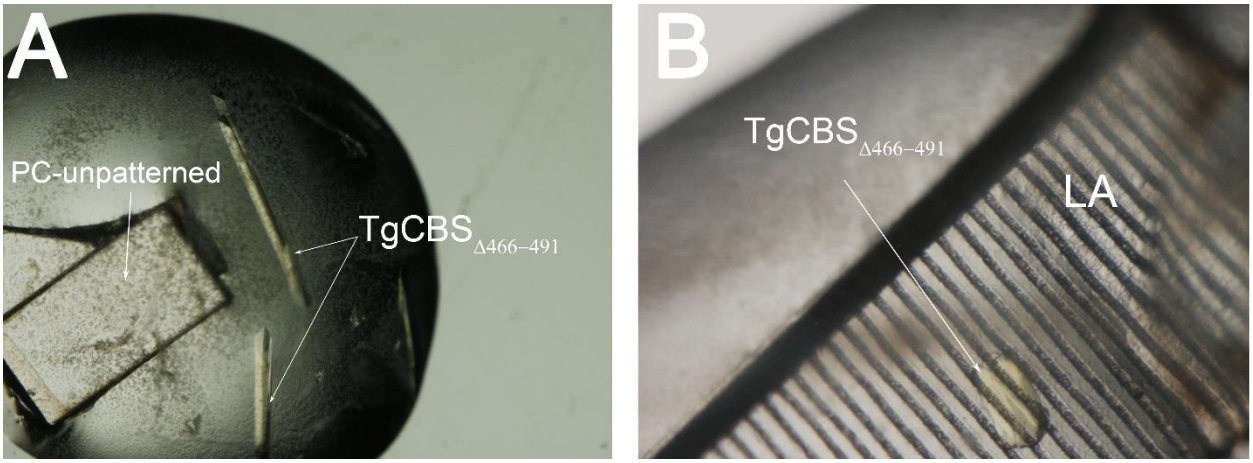

Figure 2.45. *Crystals of TgCBSΔ466-491 soaked with cysteine in drop containing PC-smooth surfaces (developed at CIC bioGUNE &Tekniker) (**A**) and TgCBSΔ466-491 soaked with OAS in presence of PC-Laser Ablated Grooves (CIC bioGUNE & Tekniker) (**B**). All experiments were carried out by using by hanging-drop vapour diffusion methods.*

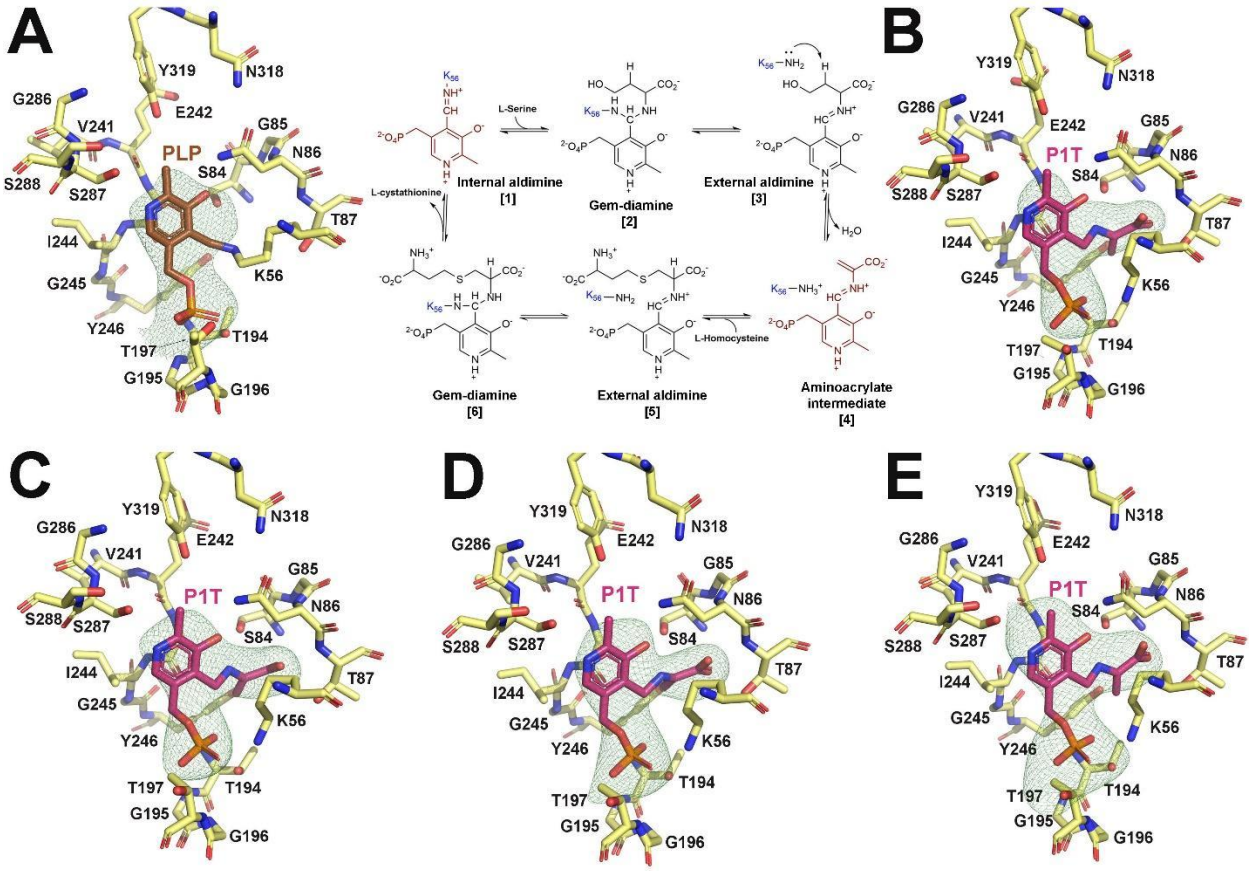

Figure 2.46. TgCBS is active *(A) Fo-Fc Polder omit map around PLP calculated in the absence of substrates. (middle) Mechanism of Cth formation from Ser (or Cys) and Hcys (adapted from [434]). (B, C, D, E,) Zoom views of the TgCBS catalytic site. The Fo-Fc Polder omit maps (contoured at 3σ) represent positive electron density around PLP or P1T for TgCBS (A), and 24h soaked crystals in a buffer containing 10 mM Ser (B), Cys (C), OAS (D) and Cth (E). PLP and P1T are pyridoxal phosphate and aminoacrylate intermediate, respectively.*

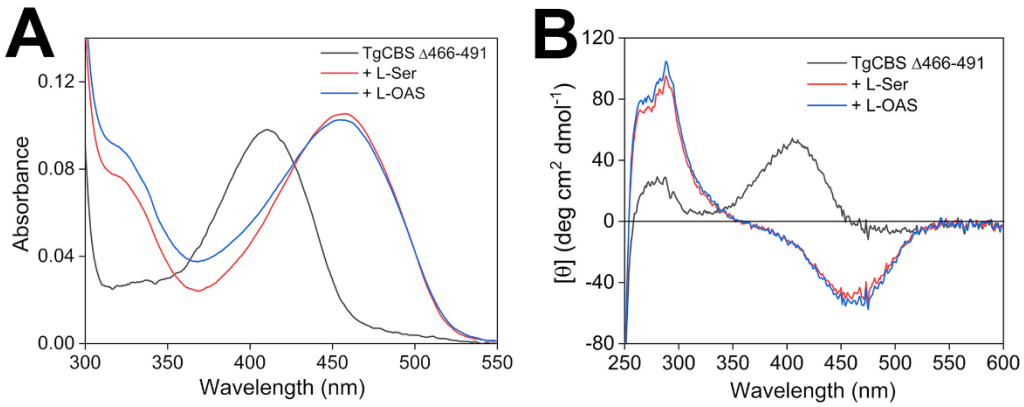

Figure 2.47. Spectra of TgCBSΔ466-491 with substrates. ***(A)*** *Absorbance spectra of 15 µM TgCBSΔ466-491 alone (black line) and upon addition of 10 mM Ser (red line) or 10 mM OAS (blue line).* ***(B)*** *CD spectra of 1 mg/mL TgCBSΔ466-491 alone (black line) and upon addition of 10 mM Ser (red line) or 10 mM OAS (blue line).*

2.4.7.2. Molecular Dynamics Analysis of *Tg*CBSΔ466-491

Taking into account that crystallographic data offer an average spatial-time snapshot of the protein structure captured in a local energy minimum under specific buffered conditions, we found reasonable to postulate that, as formerly observed in the D444N variant [69], the mentioned displacement of the Bateman module provides a greater dynamic freedom to the mobile subdomain of the core domain of *Tg*CBS that facilitates the access of the substrates to the interior of its catalytic site. To evaluate this hypothesis, we explored the conformational behavior of *Tg*CBS, *Hs*CBS and the D444N human variant through microsecond molecular dynamics (μs-MD) simulations. This in silico analysis was performed in close collaboration with Dr. Gonzalo Jiménez Osés and Reyes Nuñez Franco (PhD student) at CIC bioGUNE. To identify the most relevant conformational transitions occurring in each system, the dimensionality reduction technique of principal component analysis (PCA) was applied. The analysis made it possible to decompose the MD trajectory followed by each protein and revealed three distinct structural changes that mostly affect the orientation of the Bateman modules. In the first one, that we have called *longitudinal displacement*, the Bateman module moves along its longest axis, which runs from the CBS1 to the CBS2 domain (**Fig. 2.48**). In the second one, or *lateral displacement*, the shift takes place perpendicularly to the previous movement and occurs along the shortest axis that passes between domains CBS1 and CBS2. Finally, the third change involves a rotation of CBS1 with respect to CBS2 around an imaginary axis that runs parallel to the central β-sheets of the CBS domains and that is perpendicular to the two axis mentioned before (**Fig. 2.48**). Interestingly, the *rotational change* is specific of the human enzyme and is similar to that induced by AdoMet binding at site S2 site in human CBS [160]. These findings suggest that the effect of AdoMet consists essentially in increasing and stabilizing one of the conformational populations already existing in the native protein, thus promoting the activation of the enzyme. The PCA analysis also revealed that each of the three proteins analyzed undergo two main the structural rearrangements, which occur in different percentages (**Fig. 2.48**). The different combination of movements in each protein has well-differentiated effects and determines the number and shape of tunnels that gives access into the corresponding active sites. We found that mutant D444N displays a wider channel cluster than the wild-type protein, and that *Tg*CBS behaves similarly to the D444N mutant (**Fig. 2.48**). Intriguingly, the channel clusters were not symmetrically distributed between the two complementary subunits in any of the analyzed dimers, thus suggesting synergistic behavior between the two active sites. This helps explain the different degree of activity observed for each enzyme in the absence of AdoMet. The dynamic behavior of the Bateman module is also reflected in the degree of

aperture of the entrance loops defining the access to the catalytic cavity in each protein. To define the aperture, we measured the angle between the α-carbons of residues K441, S387 of the first subunit, and K481 of the second subunit of the human enzyme along the MD trajectories. The equivalent angle between residues T386, S325 and D431 of *Tg*CBS was analyzed. As hypothesized, we found that mutant D444N and *Tg*CBS exhibited a significantly wider opening than the wild type human enzyme (**Fig. 2.48**). The impact of conformational dynamics on substrate accessibility to PLP resulted in the appearance of different transient access tunnels along the MD trajectories in each protein (**Fig. 2.48**).

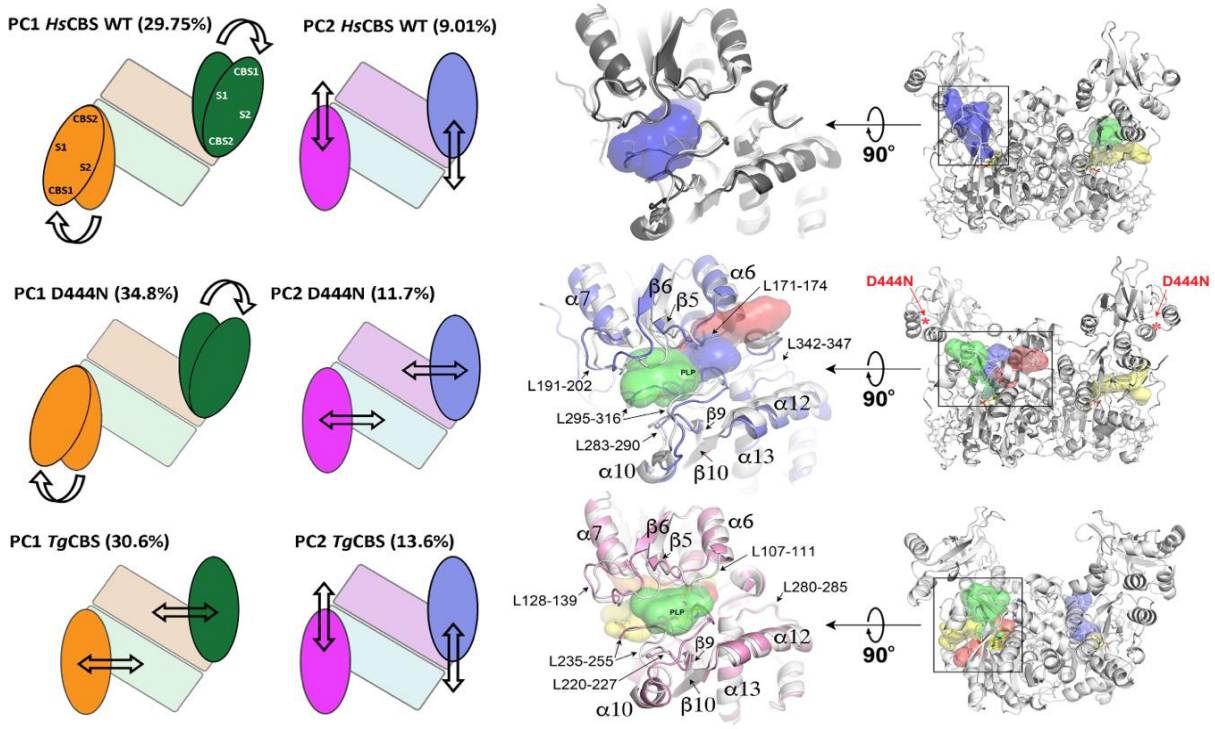

Figure 2.48. MD analysis of TgCBS, HsCBS and mutant D444NHsCBS-Δ516-525. *(**Right**) The Bateman modules are in opaque ribbons. Heme and PLP are in sticks. Structural overlap of the loops defining the entrance of the catalytic site at the narrower (light grey) and the wider amplitude points of the MD simulation in (**up**) basal wild-type HsCBS, (**middle**) mutant D444NHsCBS-Δ516-525 and (**bottom**) TgCBS. HsCBS, D444NHsCBS-Δ516-525 and TgCBS at the wider amplitude are colored in black, marine and pink, respectively. The clusters of tunnels formed along the MD simulation at the corresponding catalytic sites are shown in different colors. (**Left**) Main displacements suffered by the Bateman module of wt-HsCBS (**up**), mutant D444N (**middle**) and TgCBS (**bottom**) detected after PCA analysis of the MD trajectories. The figure schematizes a top view of the enzyme dimer. The Bateman module and the catalytic core are represented as an oval and a rectangle, respectively. Complementary subunits are colored in green/orange in PC1 and in magenta/blue in PC2, respectively. The corresponding displacements are indicated with arrows. Location of CBS1, CBS2, site S1 and site S2 within the Bateman module are also indicated.*

2.5. DISCUSSION

For decades, the limited structural data on the CBS enzyme has hampered the comparative study of its regulatory mechanisms across various species. In fact, the structural information we currently have is still very limited. The main reason for the recalcitrant difficulty in obtaining crystals is attributed to the intrinsic nature of the enzyme, whose half-life in vitro is usually short, as well as to the presence of particularly flexible zones in its polypeptide chain, particularly its regulatory domain. Coexistence of several oligomeric species in equilibrium adds another level of complexity. For example, *Hs*CBS exists as a homotetramer that trends to disassemble into dimers, which, in turn, easily polymerize through the α-helices of their C-terminal domain into higher-order oligomers (octamers, hexadecamers and larger aggregates). This historic lack of knowledge has hampered a detailed comparative analysis of the structural basis that underlies the specific catalytic and regulatory characteristics shown by this complex protein across evolution. Nevertheless, the increasing amount of structural data obtained during the last decade have allowed to achieve several milestones and to answer some of the most relevant questions, which arose from the number of biochemical and biophysical studies since its discovery in the early 1960s. Among these milestones are the identification and description of the AdoMet-binding site at atomic level in mammals, as well as the conformational changes in both the regulatory domain and entire protein triggered by AdoMet in these organisms. In addition, the capture of several reaction intermediates in the crystals of CBSs from bacteria and insects has allowed for identification of the key residues that participate in catalysis and determine specificity for certain substrates including important differences between, for example, *Hs*CBS and its bacterial homologs. This information is thus vital to the development of drugs that modulate the activity of human CBS but also for the structure-based design of potential new class of antimicrobial agents that inhibit the transsulfuration pathway-derived H_2S production required for enhanced survival and/or virulence of certain pathogens.

Among the five distinct domain distributions identified for the enzyme along evolution (**Fig. 2.9**), those containing the C-terminal Bateman module are the ones raising more incognitas. Indeed, such a Bateman module is present in the human enzyme, but also in the CBS of a variety of pathogens (such as *T. gondii* or *P. aeruginosa*), where it exerts different roles that are not yet understood. In mammals, the Bateman module is essential for the allosteric regulation of the enzyme after binding of AdoMet. In contrast, in other organisms such as the fruit fly or honeybee, it appears to have no function other than that of ensuring dimeric assemblies of constitutively activated enzymes. A confident prediction of the role of the

intriguing Bateman domain and its position in overall protein folding is not possible at present, as it represents the least conserved region in all CBSs.

In developmental terms, it seems established that the dimeric assemblies of CBS can exist in two distinct conformations, mostly recognized by the orientation of their Bateman modules. The first is a basket-shaped, and less active conformation (basal conformation), (**Fig. 2.34, B**) while the second is a marine mooring bollard-shaped (please see **Fig. 2.34, A**) and significantly more active conformation (activated conformation) (**Fig. 2.34, D**). The presence of the two conformations has been documented only in human CBS, where the transition from the first to the second conformation necessarily requires binding of the allosteric effector AdoMet at site S2 of the Bateman module. In less evolved organisms, for example the fruit fly or the honeybee, only a single constitutively activated type has been distinguished class D in **Fig. 2.9**), (**Fig. 2.34, C**) [434,435]. This activated fold is structurally equivalent to the AdoMet-bound CBS form of mammals [160]. Intriguingly, the basket-like conformation had not been seen before in any other organism, and its presence in *Tg*CBS as a unique active species was completely unexpected (**Fig. 2.34, A**).

Our structural and biochemical data showing the formation of a stable aminoacrylate intermediate upon addition of either Ser or Cys to the crystals, as expected for a PLP-catalyzed β-replacement reaction, confirms that the crystallized *Tg*CBS conformation corresponds to an active form of the enzyme (**Fig. 2.46**), and have enabled the identification of key distinguishing features that constitutively hold *Tg*CBS in a basket type fold and likewise, the features that would impede, or alternatively promote, the progression of other CBSs towards bollard-shaped activated states. These features comprise (i) the capacity (or inability) of the Bateman module to host AdoMet at site S2 [160] (**Fig. 2.34**); (ii) the arrangement of interaction networks between the interdomain linker and the Bateman module that hinder (or not) the displacement of the latter (**Fig. 2.37**); and (iii) the capacity (or incapacity) of the Bateman module to frame an antiparallel CBS module (**Fig. 2.38**).

These results, by addressing the first proof of a basket-shaped conformation in the CBS enzyme of a lower eukaryote, reveal important structural details of class C CBSs, shared by Apicomplexa and yeast, therefore expanding the structural knowledge on CBS enzymes as well as their structure-activity relationship. In particular, in light of our new information, we propose that CBSs containing a Bateman module can be grouped into at least three categories:

(i) "Basket-shaped"constitutively active basal-like species (c.a *Tg*CBS) without the capacity to develop conformationally to higher activity bollard-like states; [255](**Fig. 2.49, *up***)

(ii) "Bollard-shaped" constitutively active and non-allosterically regulated CBS enzymes, similar to those found in *D. melanogaster* and *A. mellifera* [434,435] (**Fig. 2.49, *middle***)

(iii) allosterically activated enzymes (ca. *Hs*CBS), the most advanced CBSs that can embrace two different conformations, one in which the enzyme is essentially less active (basal) and a second one (activated) with high activity that must be reached with the assistance of an allosteric molecule, for example, AdoMet, which briefly advances the change [69,160] (**Figs. 2.34**), (**Fig. 2.49, *bottom***)

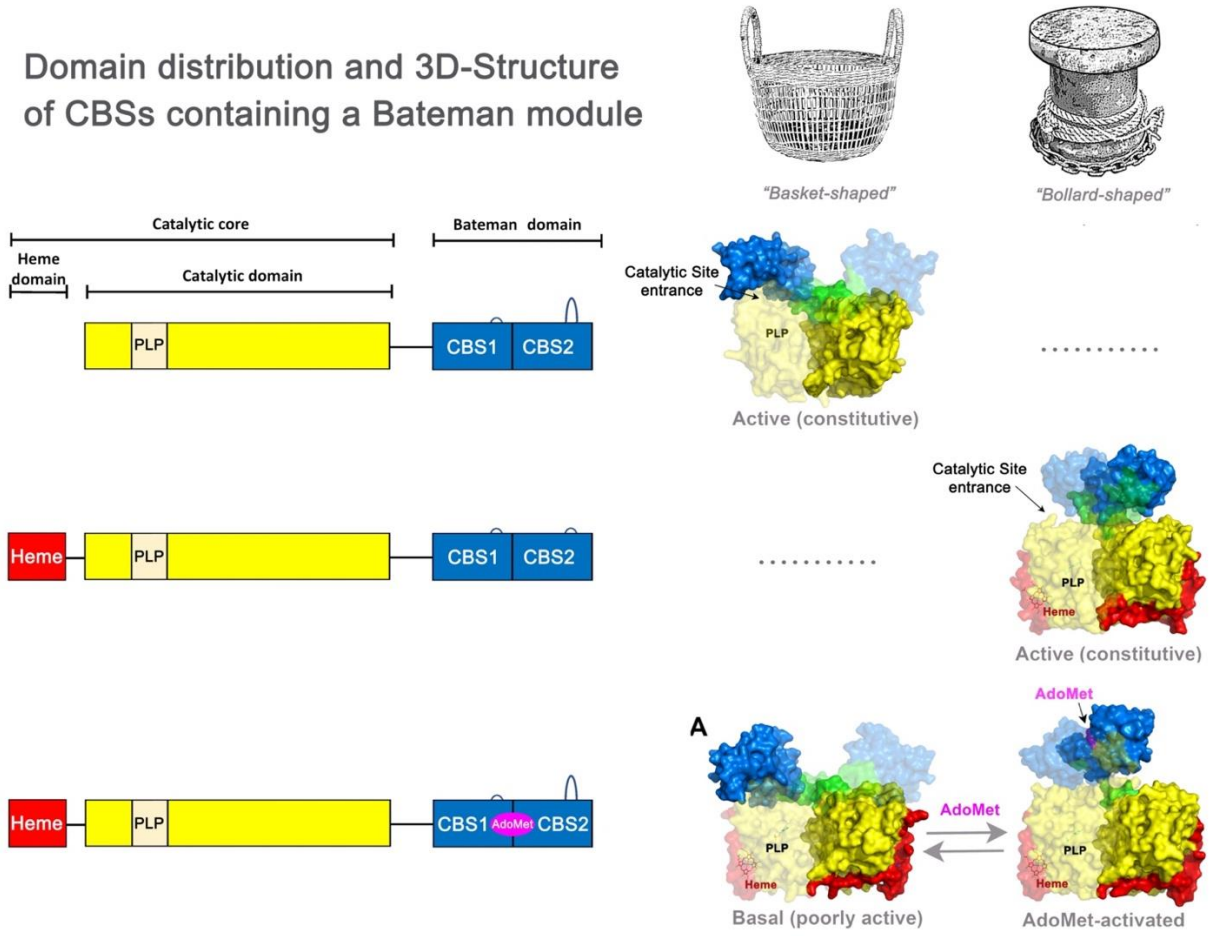

Figure 2.49. New scenario of the 3D-Structure of Cystathionine β-Synthases containing a C-terminal Bateman module. *The figure summarizes the new structural scenario on the CBSs containing a C-terminal Bateman module, based on the work performed in this PhD thesis. (**up**) (Class C CBSs) "Basket-like constitutively activated fold of CBS from Toxoplasma gondii (also found in yeast S. cerevisiae): each protein subunit lacks the heme-binding domain and is not allosterically regulated by AdoMet. The Bateman module (in blue) is located above the entrance of the catalytic cavity of the complementary subunit. The loop of the*

*CBS2 motif is similarly long as in mammals and the enzyme forms tetramers and dimers (the latter are described in this PhD thesis). (**Middle**) (Class D CBSs) "Bollard"-like constitutively activated CBS from fruit fly (Drosophila melanogaster, DmCBS) or honeybee (Apis mellifera, AmCBS) contains the same domain architecture found in the CBS of mammals but is not regulated by AdoMet. The length of the loop of the CBS2 domain is short. The enzyme adopts a unique activated conformation in which the catalytic cavity is exposed. The complementary Bateman modules associate in a disk-like arrangement known as "CBS module" that configures the head of the bollard formed by the protein dimer. (**Bottom**) (Class E CBSs) Mammalian CBS enzymes (e.g. Homo sapiens HsCBS, Mus musculus MmCBS, Rattus norvegicus RnCBS) contain the N-terminal heme-binding domain (red), a central catalytic domain that hosts PLP (yellow) and the C-terminal Bateman regulatory domain (blue) that binds the allosteric activator AdoMet (magenta). The CBS2 motif contains a long loop that participates in protein tetramerization. The protein dimer can adopt two conformations: (i) AdoMet-free basal (Basket-like, low activity) and (ii) AdoMet-bound activated (Bollard-like, high activity). The heme domain, the catalytic domain and the Bateman module are coloured in red, yellow and blue, respectively. The interdomain linker is in green. AdoMet is in magenta. The two complementary subunits of the protein dimers are represented in opaque and transparent surfaces, respectively.*

Importantly, the comparative MD and subsequent PCA of *Tg*CBS, *Hs*CBS and the pathogenic mutant D444N help unravel what features determine the accessibility of substrate into the catalytic site, and provide clues on the ability of each enzyme to prioritize the wide variety of reactions described so far. The access into the catalytic site is not straightforwardly seen in the static, low-energy, and highly packed crystallographic structures, where in some cases the entrance loops may appear dumped towards the catalytic cavity, as observed in *Hs*CBS and *Tg*CBS crystals. The entrance tunnels are disclosed when thermal motions and solvent effects are simulated with μs-MD (**Fig. 2.48**)**.** Our MD investigation clarifies the catalytic activity shown by *Tg*CBS and reveals that inconspicuous rotations and translations of the Bateman module are adequate to make fleeting passages that associate the catalytic cavity with the outside. The MD analysis has likewise uncovered the dynamics of these enzymes and gives a reasoning to the basal activity of wild type *Hs*CBS in the absence of AdoMet [159], which was not very much clarified from the proteins crystallized so far, that showed completely shut active sites, clearly conflicting with such basal activity. Of note, the size and the quantity of these passages are wider in *Tg*CBS and in the homocystinuria causing mutant D444N [69,160] than in wild type *Hs*CBS, thus explaining their higher activity levels. Moreover, the absence of the N-terminal heme-binding domain provides an additional passage access to the catalytic site in the parasite enzyme that is not observed in the human counterpart. This tunnel is framed by helices α8 and α9 and loops β7-α8 and α10-α11, and opens a door for therapeutic intervention through the design of molecules that specifically inhibit *Tg*CBS without affecting the human host. Moreover, our MD and PCA of the *Hs*CBS dimer strongly suggest that the main role of AdoMet as allosteric activator consists essentially in stabilizing one of the conformational populations already existing in the native protein, more concretely that resulting from the arrangement described in PC1 in Fig. 2.48. We postulate that such population is more prompt to evolve towards the final activated state [160]. Our PCA analysis also revealed that *Tg*CBS, *Hs*CBS and mutant D444N undergo two principal structural rearrangements identified, which

occur in different percentages in each protein (**Fig. 2.48**). The combination of the PCA analysis with the reported activity values of the analyzed enzymes in the absence of AdoMet, reveal a different contribution of the identified structural changes in the catalytic activity. The lower basal activity of *Hs*CBS with respect to the D444N variant is likely due to the longitudinal displacement of the Bateman module in *Hs*CBS. On the contrary, the lateral displacement is more efficient in favoring the aperture of the active site in D444N. Interestingly, the rotational displacement of the CBS domains appears to be exclusive of the human protein, suggesting that this structural transformation is key to progress from the basal towards the activated conformational state in the mammalian CBS. Instead, the lateral displacement of the Bateman module is observed in *Tg*CBS and in the D444N mutant, but not in wild type *Hs*CBS (**Fig. 2.48**). Finally, we have found that the different combinations of movements in the analyzed proteins have well-differentiated effects in the number and shape of tunnels that give access to the corresponding active sites. Our MD analysis shows that *Tg*CBS and mutant D444N display a wider channel cluster than wild-type *Hs*CBS. Intriguingly, the channel clusters are not symmetrically distributed between the two complementary subunits in any of the analyzed dimers. This suggests a synergistic behavior between the two active sites.

Taking everything into account, our structures of *Tg*CBS have disentangled the unique domain organization of this pivotal enzyme in the metabolism of sulfur amino acids in *T. gondii*. Because CBS represents an exceptionally important therapeutic target, this new information paves the way for the rational design of drugs that can modulate the activity of CBS and establishes the framework for a therapeutic intervention through the transsulfuration pathway in different organisms (c.a bacterial pathogens) [14,16,426]. Moreover, since Toxoplasma is an early branching eukaryote, the study of CBS enzyme could provide useful information about the early evolution of transsulfuration routes and H_2S signaling.

The new structural information revealed in this work allows us to draw a new scenario on the structural evolution of the enzyme cystathionine β-synthase. The data available so far suggested that the folding of the basal basket-shaped conformation corresponded to a highly evolved folding, such as mammals. Under that scenario, the enzyme seemed to have evolved gradually from a simple form containing only the catalytic domain, to others that incorporated complementary domains such as the Bateman module, and later the heme-binding domain. The function of the Bateman module appeared to be limited to the simple stabilization of the dimeric form (e.g. in insects). Later in evolution, it developed the ability to bind AdoMet and vary its relative position with respect to the catalytic protein core. In this thesis we have shown that the basal basket folding is in fact a very old folding, present in parasites such as *Toxoplasma gondii*, and

that it might also be present in yeast and in some bacteria such as *Pseudomonas aeruginosa*, which share the same domain distribution in their equivalent CBS enzymes. We have also shown that this type of folding is constitutively active, and does not possess allosteric regulatory capacity.

Based on our new data, we postulate that the CBS enzyme may have evolved from at least two different structural lineages (**Fig. 2.50**), and that the basket-shaped form appears to be evolutionarily older than the bollard-shaped species found in insects and mammals. These findings have important implications for the design and development of specific drugs to regulate the activity of the CBS enzyme, and hence the transsulfuration pathway, in specific organisms such as multidrug resistant pathogens.

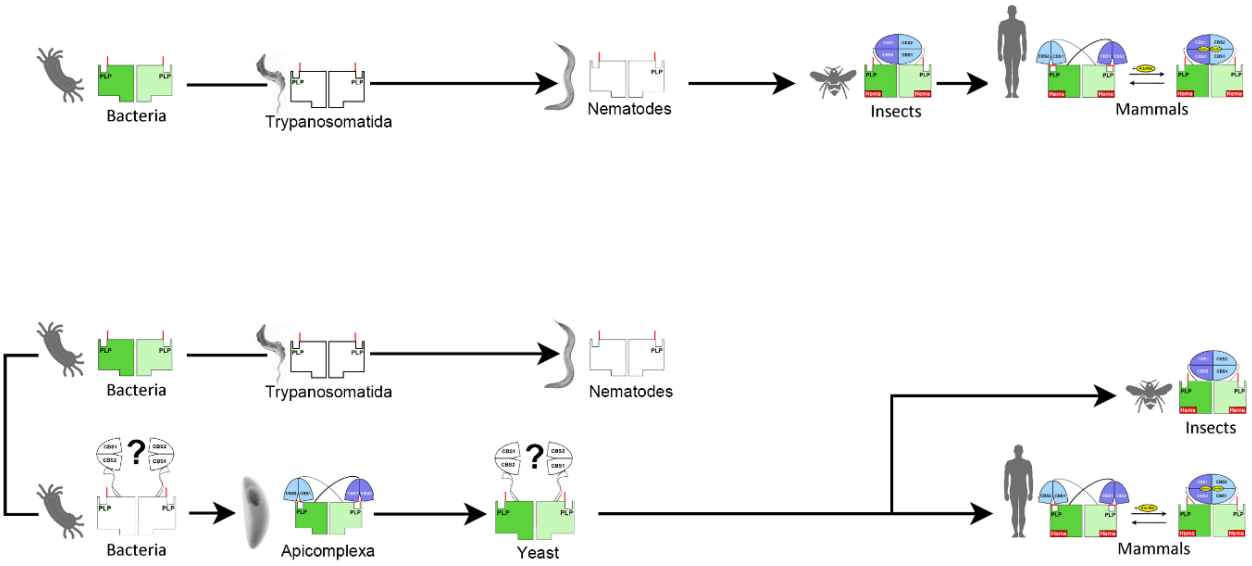

Figure 2.50. Structural Evolution of Cystathionine β-Synthase. *The figure summarizes the structural evolution of CBS in different organisms acoording to the available data (**up**) before this Ph.D thesis and (**down**) after this Ph.D thesis (partially reported in [255]). Blocks in white correspond to known domain distributions whose 3D-structure remain unknown. Colored blocks indicate confirmed crystal structures. The allosteric molecule Adomet is in yellow and makes the mammals enzyme evolve from the poorly active basket basal-like form to the active bollard-like species. The insects enzyme remains always in the bollard-like constitutively active conformation.*

There are still many unknowns, which need to be addressed in upcoming years. For example, determining the exact path followed by the Bateman module during the basal-to-activated state transformation as well as the role played by the interdomain linker in this process and the atomic interactions involved. The location and characteristics of the second AdoMet-binding site identified by calorimetric techniques in tetrameric *Hs*CBS WT also remain unclear. In addition, the role of the Bateman module in CBS enzymes lacking allosteric regulation, such as the fruit fly, the honeybee, or the herein

described *Toxoplasma gondii*, is unknown. Additional structural information is needed to understand catalytic specificity and preferential use alternative substrates, which is important to elucidate the exact role of CBS in H_2S biogenesis. Interaction of CBS with other proteins is yet another area which needs to be addressed to understand regulation and function of CBS in various metabolic processes and physiological signalling. The development of techniques that allow the modulation of the enzyme in selected target organs, where its expression or inhibition offers therapeutic potential is of importance. In the same direction, the identification of molecules that act as potential AdoMet analogues and might stabilise and/or activate the enzyme needs to be resolved hand in hand with understanding of molecular details related to impairment of *Hs*CBS functions by the presence of pathogenic missense mutations causing homocystinuria. Availability of this new information will offer an attractive scenario for the development of personalised medicine for homocystinuric patients, and for the development of specific inhibitors of the transsulfuration pathway to treat multidrug resistant (MDR) pathogens in the near future.

2.6. CONCLUSIONS

1. *Tg*CBS exists as unique dimeric species that is structurally similar to that found in the "Basal" (poorly active) state of human CBS in the absence of AdoMet. Our data provide a missing piece in the structural universe of the CBS enzyme, by revealing the overall fold of the first Class C CBS elucidated so far. Importantly, the class C CBS is encoded by organisms like *S. cerevisiae* or the multidrug resistant bacteria *P. aeruginosa*.

2. Despite its basal-like appearance, *Tg*CBS is constitutively active. The basis for its activity is found in the particular orientation of its Bateman module, which is similar to that found in the homcystinuria causing D444N variant of human CBS. In contrast with the wt-*Hs*CBS enzyme, both *Tg*CBS and the D444N variant form wider tunnels at the entrance of the catalytic cavity that allow easier access of substrates into the PLP cavity.

3. The *Tg*CBS dimers are impaired to bind and/or being allosterically regulated by AdoMet. The structural basis for such inability is detailed along this Thesis chapter.

4. Our new data has led us to postulate that in evolutionary terms, the CBS enzymes may have evolved from at least two different structural lineages, and that the basket-shaped form is likely older than the bollard-shaped active species found in insects and mammals.

5. The crystal structure of *Tg*CBS reveals the particular features of the catalytic site, as well as the main amino acid residues involved in the catalysis, thus explaining the catalytic preferences of *Tg*CBS for its canonical reaction vs its non-canonical activity.

6. Our data sets the basis for the structure-based design of specific drugs that modulate the activity of CBSs in different pathogen

CHAPTER III

Structural Characterization of Cystathionine γ-lyase from *Toxoplasma gondii*

3.1. Cystathionine γ-lyase from *Toxoplasma gondii*

The cystathionine γ-lyase enzyme from *Toxoplasma gondii* (*Tg*CGL), which is encoded by a single gene (UniProtKB A0A125YN40), is a 46kDa cytoplasmic protein monomer consisting of: (i) a N-terminal region (residues 1-84); (ii) a central PLP-binding catalytic domain (residues 85-281) that hosts the PLP cofactor, and (iii) a C-terminal domain (residues 282-417) (**Fig. 3.1**). At the sequence level, *Tg*CGL shares high amino acid identity with CGLs from Trypanosomes and Leishmania parasites (58% homology), but is less similar to the human and yeast counterparts (40% and 37% for *H. sapiens* and *S. cerevisiae*, respectively).

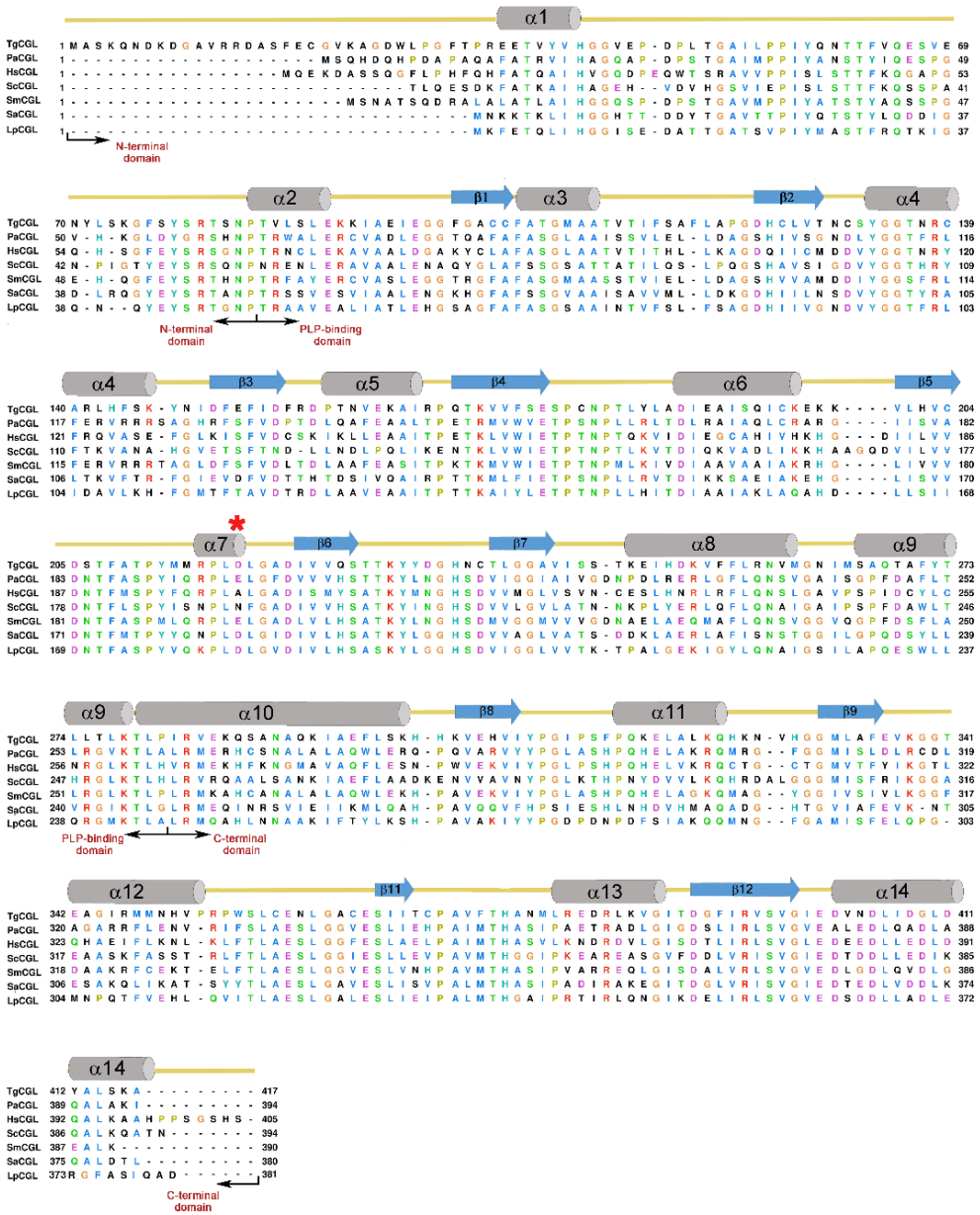

***Figure 3.1. Sequence alignment of cystathionine γ-lyase** from T. gondii (TgCGL), Pseudomonas aeruginosa (PaCGL), Homo sapiens (HsCGL), Saccharomyces cerevisiae (ScCGL), Stenotrophomonas maltophilia (SmCGL), Staphylococcus aureus (SaCGL) and Lactobacillus plantarum (LpCGL). The Uniprot codes of TgCGL, PaCGL, HsCGL, CsCGL, SmCGL, SaCGL and LpCGL are A0A125YN40, A0A2R31X25, P32929, P31373, B4SII9, X5E0F1 and F9UT53, respectively. The secondary elements above the sequences are based on the human enzyme. The red asterisk indicates the absence of helix α7 in TgCGL.*

Reactions catalyzed by *Tg*CGL. Among the seven general reactions proposed to be potentially catalyzed by CGLs (**Fig. 2.19** at the introduction section of Chapter II) [457], *Tg*CGL participates only in one canonical process, which is the α, γ-elimination of Cth to yield Cys, α-ketobutyrate and ammonia (**Fig. 3.2, B**) [456]. This enzymatic ability is commonly shared by many other CGLs, including the human [461,494], *Lactobacillus plantarum* [459], yeast [472] and *Trypanosoma cruzi* enzymes [226]. *Tg*CGL is not able to perform the hydrolysis of cysteine to yield H_2S, pyruvate and ammonia (**Fig. 3.2, A**), and is characterized by a substrate (cysteine) inhibition [458]. The underlying mechanism of such inhibition is poorly understood. Some authors have proposed that it is caused by the cysteine-induced loss of the PLP cofactor within the active site cavity [461,470,495,496]. Others instead, have proposed that it derives from the formation of an external aldimine between cysteine and the PLP molecule, as described for the human and yeast CGLs [470,495] and for other PLP-dependent enzymes [497]. The external aldimine evolves towards a thiazolidine adduct that inhibits the reaction [458,470,495].

"**Humanization of *Tg*CGL". Production of S77E and N360S *Tg*CGL variants.** In addition to the α, γ-elimination reaction, human and yeast CGLs are also capable to perform an α,β-elimination in which Cys reacts with H_2O to generate H_2S, pyruvate and ammonia [461,471,472] (**Fig. 3.2, A**). Aimed to understand why this reaction is not feasible for *Tg*CGL, and in collaboration with Prof. Alessandra Astegno at Verona University, a detailed aminoacid sequence alignment focused on the aminoacids configuring the corresponding catalytic sites was performed. Interestingly, two residues (S77 and N360) were identified at *Tg*CGL, whose position is occupied by a glutamate (E59) and a serine (S340) in human CGL, respectively (**Fig 3.1**). Such glutamate and serine are highly conserved in many other organisms, including yeast and bacteria (c.a *P. aeruginosa*, *L. plantarum*, *S. aureus* and *S. maltophilia*). To investigate the leading role (if any) of these residues in the catalytic specificity of the enzyme, two "humanized" *Tg*CGL variants, baptized as *Tg*CGLS77E and *Tg*CGLN360S, were engineered and subject to crystallographic analyses. The study was carried out both, in the presence and in the absence of substrates and products. Our collaborators found that the N360S mutation barely altered the biophysical characteristics of *Tg*CGL[458]; the absorbance spectrum displayed a peak at 421 nm indicating that the predominant tautomer in the active site is an internal aldimine formed between the pyridoxal phosphate (PLP) cofactor and a lysine residue at position 230 of the polypeptide chain [498], and the conformation from far-UV CD remained unchanged [458]. In contrast, the catalytic specificity of *Tg*CGLN360S was affected by the mutation, displaying wider activity in the variant. Interestingly, while native *Tg*CGL was limited to the α,γ-elimination towards cystathionine

(reaction B, **Fig. 3.2**), the N360S variant was able to accomplish both, the α,γ-elimination and also an α,β-elimination of Cth (the latter process is also known as Cth β-lyase activity) (reaction C in **Fig. 3.2**).

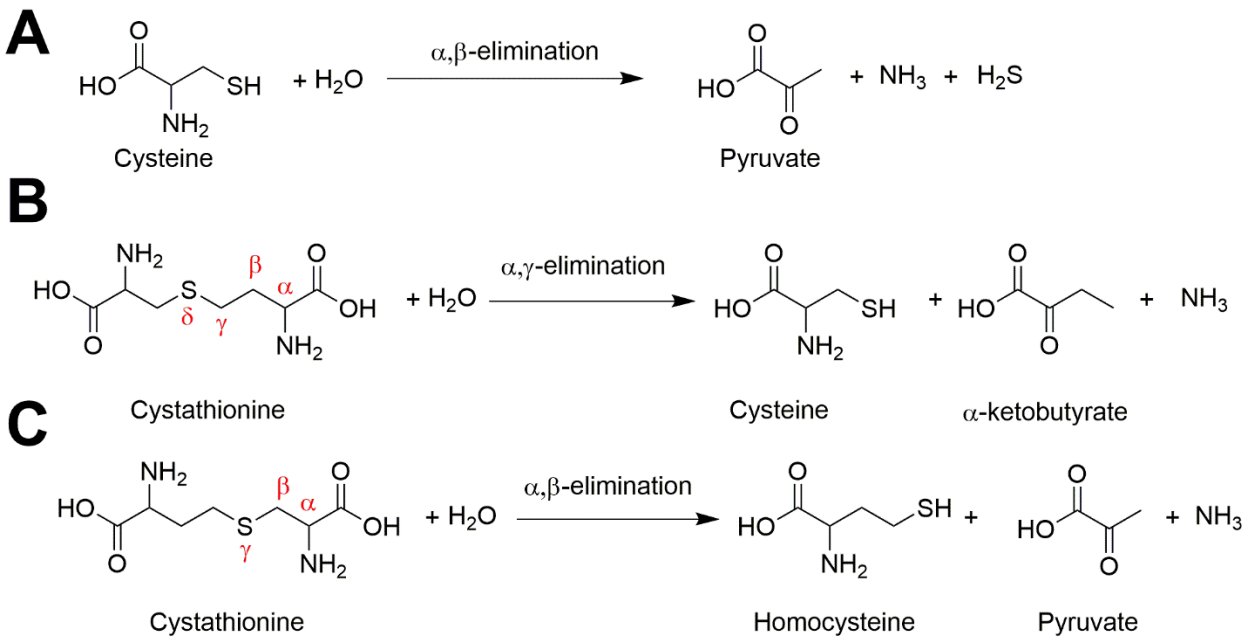

***Figure 3.2**. Reaction scheme of (**A**) α,β-elimination of cysteine, (**B**) α,γ-elimination and (**C**) α,β-elimination reaction of cystathionine catalyzed by CGLs. The relative position of the sulfur atom for each reaction is highlighted in red. The orientation of the Cth molecule is inversedly oriented in panels (**A**) and (**B**). Figure adapted from [458].*

Some authors have formerly proposed that the reaction specificity (α,γ- or alternatively α,β-elimination) of CGLs over Cth depends on the particular orientation adopted by Cth within the catalytic cavity [460]. Concretely, it has been postulated that to form the external aldimine (first step of the catalysis) in the β-elimination process, the Cth molecule needs to be oriented with its sulfur atom in the γ position with respect to the PLP cofactor [459] (**Fig. 3.2, C**). Instead, the γ-elimination requires the S atom to be in the δ position with respect to PLP [460] (**Fig. 3.2, B**) Interestingly, some organisms such as *L. plantarum* [459], *Streptomyces phaechromogenes* [499] and yeast [472] are capable to perform both, γ- and β- carbon split showing CBL-like activity, thus suggesting wider available space for Cth to adopt either orientation. In relation to these findings, Prof. Astegno *et al.* at the Verona, recently demonstrated that substitution of S77 into Glu in *Tg*CGL, causes an activity loss of the enzyme towards Cth. Moreover, such amino acid replacement exerts further effects, and appears to affect the protein stability of *Tg*CGL, disrupting the interaction between the two functional dimers composing the tetrameric structure [458].

To understand the structural differences leading to the catalytic variability observed between *Tg*CGL and its counterparts, we initiated structural studies of *Tg*CGL in its native and mutant forms both, in the presence and in the absence of their different substrates. A comparative analysis with the available CGL structures, including that from human CGL centered our efforts. Unfortunately, and despite an enormous experimental effort, variant *Tg*CGL*S77E* did not yield crystals, in agreement with a potential instability of the protein. In contrast, variant *Tg*CGLN360S could be crystallized and solved by X-rays crystallographic methods.

3.2. HYPOTHESIS AND OBJECTIVES

The research developed in this chapter is based on the following hypothesis:

- The three dimensional structure of *Tg*CGL may show distinct features from its human homolog.
- These differences are expected to be mainly located at the active site, thus affecting the affinity of the enzyme for different substrates.
- The particular structural features of *Tg*CGL might explain its catalytic diversity.
- Similarly to human CGL, *Tg*CGL may be inhibited by small molecules such as DL-propargylglycine.
- *Tg*CGL is an attractive target to develop new drugs against toxoplasmosis.

We proposed to address the following objectives:

1. Crystal structure of the wild-type cystathionine γ-lyase from *T. gondii* (*Tg*CGL) both, alone and in complex with its substrates and the inhibitor DL-propargylglycine.

2. Crystal structure of mutant *Tg*CGLN360S both, alone and in complex with its substrates and the inhibitor DL-propargylglycine.

3. Elucidation of the molecular mechanism underlying the catalytic activity of native and mutant *Tg*CGL.

4. Comparative structural analysis of wt-*Tg*CGL and *Tg*CGLN360S to understand their catalytic variability.

5. Elucidation of the mechanism underlying *Tg*CGL inhibition.

3.3. MATERIALS AND METHODS

3.3.1. Protein expression and purification of *Tg*CGL

The complete cDNA of *Tg*CGL (accession number: XM_002364464) in pMA-T vector was obtained from Invitrogen Corporation with a tag of six His at the N-terminal. The gene was cloned into pET21a vector and transformed into *E.coli* Rosetta (DE3) cells and induced overnight with 0.5 mM isopropyl-β-D-1-thiogalactopyranoside (IPTG) at 297K. Cells were isolated by centrifugation (5000g for 15 min), in lysis buffer 20 mM sodium phosphate pH 8, 150 mM NaCl and 0.1 mM DTT buffer with 1×protease inhibitor EDTA free (Sigma-Aldrich, S8830, Milano, Italy) and sonicated (12 cycles of 10 s ON /20 s OFF on ice water). After centrifugation at 30 000 g for 30 min at 277 K, the supernatant was loaded onto a Ni-affinity column previously equilibrated with 20 mM sodium phosphate at pH 8, 150 mM NaCl, 10 mM imidazole, and 0.1 mM DTT. The column was washed with the equilibration buffer for at least five column volumes and then *Tg*CGL was eluted from the column by applying an imidazole gradient of 10 to 500 mM. After addition of 100µM PLP, fractions containing *Tg*CGL were concentrated and washed with 20 mM sodium phosphate pH 8 and 0.1 mM DTT using Vivaspin concentrators (Sartorius, Goettingen, Germany) to remove imidazole and unbound PLP. The extinction coefficient was used to calculate the monomer concentration of the purified protein (ε_{280nm}= 30745 M^{-1}-cm^{-1}; http://web.expasy.org/protparam/) (described in more detail in Section 1.3.2.2. of Chapter I). The PLP content of the holoenzyme was determined by adding 0.1 M NaOH and using ε_{388nm}= 6600 M^{-1} cm^{-1} as described.

The *Tg*CGLN360S variant was produced by site-directed mutagenesis on the pET21a-*Tg*CGL construct using the QuikChange®site-directed mutagenesis kit (Agilent Technologies, Santa Clara, CA, USA). The primer sequences used are 5´-GGTCTTTGTGTGAAAGCCTGGGAGCGTGCG-3´ (forward) and 5´-CGCACGCTCCCAGGCTTTCACACAAAGACC-3´ (reverse). The mutant sequence was confirmed by DNA sequence analysis. Expression and purification of the mutant *Tg*CGL were performed as described for wild-type enzyme. The homogeneity and purity of the enzyme (95%) was confirmed by SDS-PAGE. The molecular size of the recombinant protein (~46 kDa) obtained in the band of electrophoresis gel corresponds well to the predicted mass of the protein.

3.3.2. Crystallization

3.3.2.1. Crystallization of the *wt*-TgCGL

The ideal concentration for starting the *Tg*CGL crystallization experiments was determined by a pre-crystallization screen (PCT, Hampton Research). The appropriate concentration was determined to be 20 mg mL^{-1}. Following a protocol similar to that described for the crystallization of *Tg*CBSΔ466-491, the search for initial conditions was performed with the screens available on the crystallization platform of the center (**Table 2.1** at Section 2.3.5. of Chapter II). Droplets were arranged in 96-well plates containing 200 nL of protein and 200 nL of precipitant. Once a promising condition was obtained in the PEG ION 1, 2 screens, the next step was to optimize the crystallization conditions by varying different parameters such as the concentration and type of precipitant and salt, the volume of the droplet, the addition of detergents and/or additives (salts, metal ions…) or the use of the microseeding technique with crystals obtained from the same protein in the 96-well sitting drop plate. After a hard optimization process, crystals were grown in hanging drop in 12 % (w/v) PEG 3350, 0.1M sodium citrate pH 4.6 and using either CYMAL-3, CYMAL-4, n-nonyl-β-D-maltoside or n-octyl-β-D-thiomaltoside from the detergents screen of Hampton Research at a protein concentration of 20 mg mL^{-1}, a constant temperature of 291K and an approximate time of 72 h. The drops contained 1 µL of protein, 0.8 µL of precipitant and 0.2 µL of detergent. The crystals were collected with nylon loops and frozen after prior immersion in a solution containing 12 % (w/v) PEG 3350, 0.1M sodium citrate pH 4.6 and 26% (v/v) glycerol as cryoprotective agent (**Table 3.1**).

This protein was also crystallized in the presence of cysteine (Sigma.Merck, 168149- 2.5g), cystathionine (Sigma-Merck, C7505- 10 mg) and DL-propargylglycine (PAG) (Sigma-Merck, P7888- 250mg). Initially, grown protein crystals were exposed to a solution of 10 mM of cysteine. Protein crystals (at a concentration of 22 mg. mL^{-1}) were grown in 12% (w/v) PEG 3350, 0.1M sodium citrate pH 4.6 and CYMAL-3 as a detergent in a 24-well limbro plate. Drops consisted of 1 µL of protein, 0.8 µL of reservoir and 0.2 µL of detergent. The soaking with cysteine was maintained for 1 hr and then the crystals were collected and stored in liquid nitrogen with a previously prepared cryoprotectant solution containing 26% (v/v) glycerol (**Table 3.1**). Unfortunately, the soaked crystals did not diffract X-rays at sufficient resolution for structure determination. Therefore, the next step consisted in co-crystallizing the enzyme with cystathionine (Sigma-Merck, C7505- 10 mg), cysteine (Sigma-Merck, 168149- 2.5g) and PAG (Sigma-Merck, P7888- 250mg). In all cases, the *Tg*CGL was aliquoted and independently incubated with ligands in a ratio (1:100) that ensured full occupancy of ligands in the catalytic site of the protein. Crystals of ligand-

protein complex appeared after 3 days at 291K by hanging drop vapour diffusion in 24-well plates, except for the *Tg*CGL-Cys complex for which no crystals were obtained. The reservoir solution contained 12% (w/v) PEG 3350, 0.1M sodium citrate pH 4.6, and CYMAL-4 as a detergent (for both ligands). Drops were composed by 1 µL of protein solution (15 mg mL^{-1}) incubated with 24 mM and 30 mM of cystathionine and PAG respectively, 0.8 µL of precipitant and 0.2 µL of detergent. Single crystals were transferred to a cryoprotection solution (crystallization buffer with 27% (v/v) glycerol) and flash frozen in liquid N_2.

3.3.2.2. Crystallization of *Tg*CGLN360S

To determine the structure of the *Toxoplasma gondii* enzyme bearing the N360S mutation, we followed a similar protocol to that described for the wild type enzyme. Crystals were obtained by using the hanging-drop technique, in 24-well VDX plates after 1-2 days at 291K (Hampton Research). Drops consisted of 1µL of protein solution (10 mg mL^{-1}) mixed, 0.8 µL of reservoir solution (12% (w/v) PEG 3350 and 0.1 M sodium citrate pH 4.6) and 0.2 µL of CYMAL-4 detergent (Hampton Research). Single crystals of *Tg*CGLN360S were transferred into a cryoprotection solution containing the crystallization buffer with 26% (v/v) glycerol, and flash frozen in liquid N_2 (**Table 3.1**).

For the crystallization of the mutant enzyme with ligands, we followed a protocol similar to the wild type enzyme. First, a solution of 10 mM cysteine and cystathionine were soaked, independently, in crystals of *Tg*CGLN360S (10 mg mL^{-1}) grown in reservoir solution of 12% (w/v) PEG 3350 and 0.1 M sodium citrate pH 4.6 and n-nonyl-β-D-maltoside or n-octyl-β-D-thiomaltoside, respectively (**Table 3.1**). After 4h of soaking, single crystals were inmersed into a cryoprotectant solution, and stored at 193K (**Table 3.1**). However, the *Tg*CGLN360S crystals did not diffract when soaked in Cth. On the other hand, crystals soaked with Cys have poor diffraction quality (≈15Å). Thus, we performed co-crystallization experiments. DL-propargylglycine (PAG) was also co-crystallized in the presence of the mutant. A concentration of 10 mg mL^{-1} was considered suitable to carry out subsequent experiments. The *Tg*CGLN360S was incubated with Cys, Cth and PAG, separately, in a protein-ligand ratio 1:100 to ensure full occupancy of the ligand at the catalytic site. Crystals appeared after 2-3 days at 291K by hanging-drop diffusion technique in 24-well plates. The volume of the reservoir was 500 µL and was composed by 12% (w/v) PEG 3350, 0.1 M sodium citrate pH 4.6 and CYMAL-3 (when Cys and Cth were used as a ligand) or CYMAL-4 (in the case of PAG) as a detergent. Drops contained 1 µL of the protein-ligand solution, 0.8 µL of reservoir and 0.2 µL of detergent. Single crystals were transferred to a cryoprotection solution (buffer of crystallization and 26% (v/v) glycerol) (**Table 3.1**).

Table 3.1. Optimal crystallization conditions and cryoprotectants.

Protein (concentration)	Crystallization condition	Ligand	Protein-ligand binding method	Concentration of ligand	Cryoprotectant
*Tg*CGL (20 mg mL^{-1})	12% (w/v) PEG 3350 0.1M sodium citrate pH 4.6 n-octyl-β-D-thiomaltoside	-	-	-	26% (v/v) glycerol
*Tg*CGL (22 mg mL^{-1})	12% (w/v) PEG 3350 0.1M sodium citrate pH 4.6 CYMAL-3	cysteine	Soaking	10 mM	26% (v/v) glycerol
*Tg*CGL (15 mg mL^{-1})	12% (w/v) PEG 3350 0.1M sodium citrate pH 4.6 CYMAL-4	cystathionine	Co-crystallization	24mM	27% (v/v) glycerol
*Tg*CGL (15 mg mL^{-1})	12% (w/v) PEG 3350 0.1M sodium citrate pH 4.6 CYMAL-4	DL-propargylglycine	Co-crystallization	30mM	27% (v/v) glycerol
*Tg*CGL N360S (10 mg mL^{-1})	12% (w/v) PEG 3350 0.1M sodium citrate pH 4.6 CYMAL-4	-	-	-	26% (v/v) glycerol
*Tg*CGLN360S (10 mg mL^{-1})	12% (w/v) PEG 3350 0.1M sodium citrate pH 4.6 nonyl-β-D-maltoside	cysteine	Soaking	10 mM	26% (v/v) glycerol
*Tg*CGLN360S (10 mg mL^{-1})	12% (w/v) PEG 3350 0.1M sodium citrate pH 4.6 n-octyl-β-D-thiomaltoside	cystathionine	Soaking	10 mM	26% (v/v) glycerol
*Tg*CGLN360S (10 mg mL^{-1})	12% (w/v) PEG 3350 0.1M sodium citrate pH 4.6 CYMAL-3	cysteine	Co-crystallization	20 mM	26% (v/v) glycerol
*Tg*CGLN360S (10 mg mL^{-1})	12% (w/v) PEG 3350 0.1M sodium citrate pH 4.6 CYMAL-3	cystathionine	Co-crystallization	24mM	26% (v/v) glycerol
*Tg*CGLN360S (10 mg mL^{-1})	12% (w/v) PEG 3350 0.1M sodium citrate pH 4.6 CYMAL-4	DL-propargylglycine	Co-crystallization	30mM	26% (v/v) glycerol

3.3.3. Structural determination of CGL native and mutant from *T. gondii* by X-ray crystallography

The high-energy synchrotron radiation facilities used for our structural analysis were the beamline MX XALOC-BL13 at ALBA Synchrotron (Barcelona, Spain), and beamline I24 at Diamond Light Source (UK) (**Table 3.2**). For data collection, the set of diffraction images was taken in intervals between 0.1 to 0.25° and the distance to the detector was set to reach resolution data between 1.6- 3.8Å depending on the crystal and according to the quality and intensity of the diffraction determined by test images taken previously. The strategy and characterization program to determine the number of images and the starting angle to be taken to achieve the 100% of completeness was carried out by EDNA program [482]. A summary of the parameters of the data collection is shown in Table 3.2. The diffraction data were indexed, integrated and scaled using XDS [483] and autoPROC [484] programs. The plots of the self-rotation function were calculated with MOLREP[485]. The three-dimensional structure of *Tg*CGL wild-type and mutant alone and in presence of ligands were determined by MR method [488] with the Phaser-MR program [489] from Phenix Suite [500], using the initial search model the structure of *Hs*CGL holoenzyme (PDB ID 2NMP)[461]. After several cycles of refinement using Phenix.refine program [486] the geometric quality of the models were assessed with MolProbity [490] integrated in Phenix suite.

Ligands geometry restraints builder and optimization was generated with elBOW [501]. Model was built with Coot[487]. Figures were done with Pymol (http://www.pymol.org) and Chimera [106].

Table 3.2. Data collection parameters

Parameters	*Tg*CGL	*Tg*CGL +Cth set1	*Tg*CGL +Cth set2	*Tg*CGLN360S	*Tg*CGLN360S +Cys	*Tg*CGLN360S +Cth	*Tg*CGLN360S +PAG
Number of images	3600	3600	3600	3600	3600	3600	3600
ΔΦ (°/image)	0.15	0.1	0.1	0.15	0.1	0.1	0.1
Beamline	ALBA MX XALOC-BL13	ALBA MX XALOC-BL13	ALBA MX XALOC-BL13	ALBA MX XALOC-BL13	ALBA MX XALOC-BL13	ALBA MX XALOC-BL13	ALBA MX XALOC-BL13
λ (Å)	0.9792	0.9797	0.9797	0.9792	0.9792	0.9791	0.9791
Exposure (sec)	0.1	0.1	0.1	0.1	0.1	0.1	0.1
Detector	Dectris PILATUS 6M	Dectris PILATUS 6M	Dectris PILATUS 6M	Dectris PILATUS 6M	Dectris PILATUS 6M	Dectris PILATUS 6M	Dectris PILATUS 6M
Temperature (K)	100	100	100	100	100	100	100

3.4. RESULTS

3.4.1. Cloning, overexpression and purification of *Tg*CGL

*Tg*CGL was cloned into the pET21a vector with a six-histidine tag (6xHis) at the N-terminus. The cloning and purification protocols of the protein were performed by our collaborators at the University of Verona, who formerly reported the procedures in [458]. Nevertheless, the production steps are also described in detail in Section 3.3.1 of Materials and Methods of this thesis document. Briefly, wt-*Tg*CGL was purified in two subsequent steps, consisting in a Ni^{2+} affinity chromatography followed by a fine-tuning size exclusion chromatography. This last procedure pretends to eliminate rests of aggregates formed during thawing of the sample and ensures a homogeneous protein sample species for further crystallization procedures (Fig. 3.3).

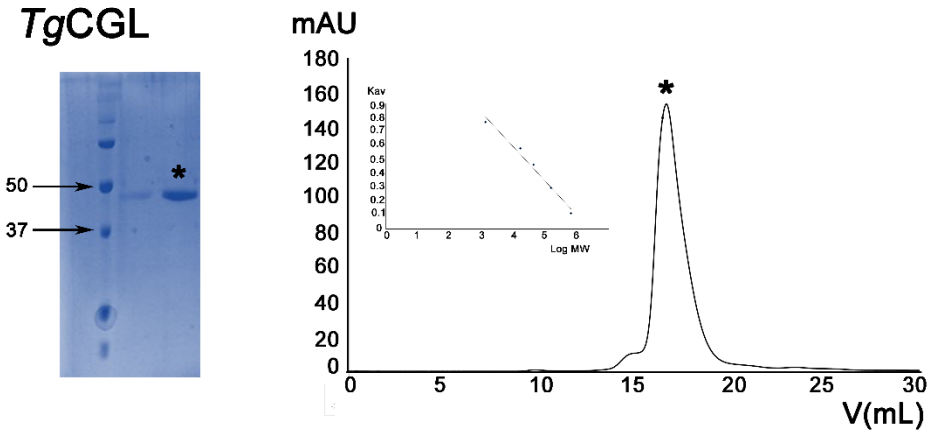

Figure 3.3. *(**Left**) SDS-PAGE of the Size Exclusion Chromatography of TgCGL-wt. The protein was separated on a 12% SDS-PAGE gel and stained using ProBlue Safe Stain (Giotto Biotech). The first lane correspond to the Molecular Weight marker (Biorad). The lane marked with an asterisk is the purified protein TgCGL. (**Right**) TgCGL elution profile of the molecular exclusion chromatography Superdex 200 10/300. The peak corresponding to TgCGL is highlighted with an asterisk. To the left of the peak the calibration curve of the molecular exclusion column is shown.*

3.4.2. Protein crystallization. Preliminary crystallographic studies.

The crystallization experiments began with a high-throughput screening using all commercially available solutions at the X-ray crystallography platform of CIC bioGUNE. Approximately 2000 different buffered solutions were tested, with variations in precipitant type (salts, polyethylene glycols, amines, and alcohols), additives (inorganic and organic salts), and detergents, as well as buffers at different pH (detailed description in section 3.3.2 of Materials and Methods). A constant temperature of 291 K was

maintained during the study. The high number of screening conditions required automated support from liquid handling robots (TECAN EVO) and nanodispensers (Mosquito, SPT Labtech) to speed up the process. Both robots are available at the X-ray platform of CIC bioGUNE. The first crystallization experiments were performed using the sitting-drop vapour diffusion technique in 96-well MRC plates. Initial hits were obtained in two of the 96 conditions offered by Hampton Research's commercial PEG ION 1 and 2 screens (**Fig. 3.4**). Further optimization and scaled up were performed in 24-well plates using the hanging-drop technique, varying protein and precipitant concentration (from 400 to 10K g mol^{-1}), pH (from pH values of 4 to 8), ionic strength of salt solutions, and addition of additives and detergents (Hampton Research screens). Finally, the best crystals were fine-tuned using either CYMAL-3, CYMAL-4, n-nonyl-β-D-maltoside or n-octyl-β-D-thiomaltoside from the detergents screen of Hampton Research, in 12% (w/v) PEG 3350, 0.1M sodium citrate, at a protein concentration of 20 mg mL^{-1} (**Fig. 3.4**). The protein solution volume in the droplet was set to 1 µL, which was mixed with 0.8 µL of the reservoir and 0.2 µL of the additive. Single crystals were flash frozen in liquid N_2 using 26% (v/v) glycerol as cryoprotectant. Three data sets of suitable quality were obtained from crystals diffracting X-rays to a resolution ranging between 1.8 and 2.2 Å.

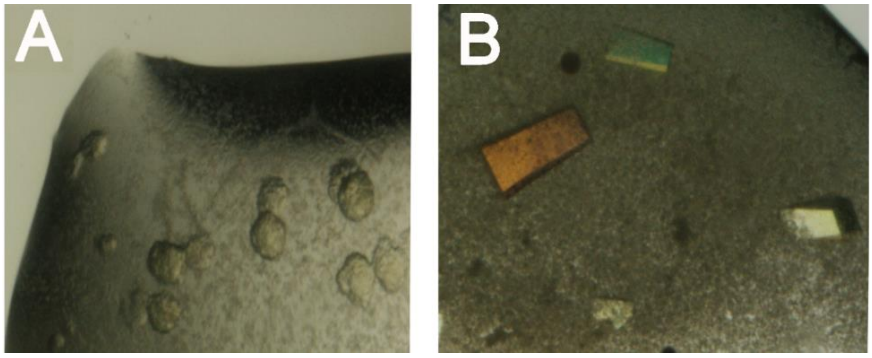

Figure 3.4. Crystals of recombinant TgCGL. *(**A**) Initial crystals of TgCGL grown in 2% (v/v) Tacsimate pH 5, 0.1M sodium citrate tribasic dihydrate pH 5.6 and 16% PEG 3350. (**B**) Crystals of TgCGL grown in 12% PEG 3350, 0.1 M sodium citrate pH 4.6 and CYMAL-3.*

Diffraction data were collected on beamline XALOC-BL13 at Synchrotron ALBA (Barcelona, Spain). The data were indexed, integrated and scaled with the XDS and autoPROC programs. The lattice parameters (a=126.53, b= 138.99 and c= 472.99; α=β=γ=90°) (**Table 3.3**) are compatible with an orthorhombic crystalline system. The preliminary assignment of the crystal symmetry was decided by analyzing the self-rotation function (calculated with the MOLREP5 program integrated in the CCP4 Suite)[485] (**Fig. 3.5**), which revealed three twofold axes parallel to the a, b and c axes in the Chi=180 plot, that were consistent with

the Laue class 222. Two additional 2-fold axes at 45° were observed, likely corresponding to binary non-crystallography (NCS) symmetry axis.

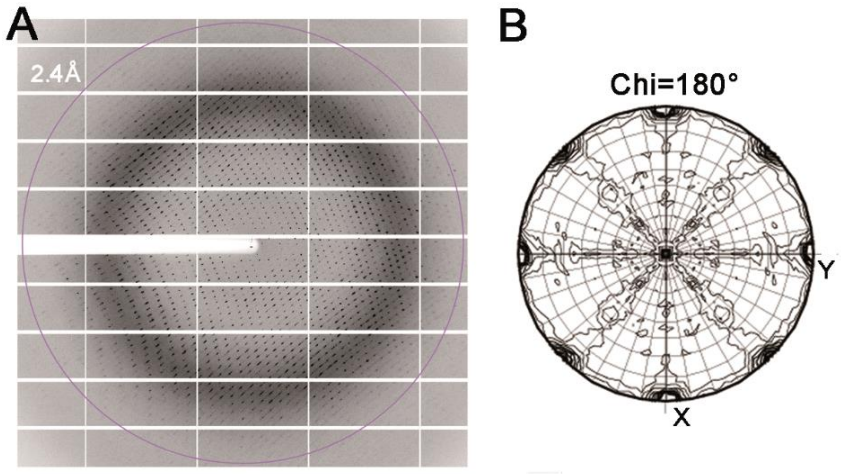

Figure 3.5. *(**A**) Representative X-ray diffraction data frame from the TgCGL, recorded on the ALBA beamline XALOC BL13. The crystals were exposed for 0.1 s per image over 0.15° simple rotation range. Resolution circle is included for clarity. (**B**) Plot of self-rotation function at k=180° of the C222 TgCGL crystals.*

Analysis of the Matthews coefficient (https://www.ruppweb.org/mattprob/default.html), yielded a value of 2.79, 2.23, and 1.86 $Å^{-3}$ Da^{-1} for eight, ten, or twelve molecules within the asymmetric unit (a.u.), respectively, corresponding to a solvent content of 56, 45, and 34%, respectively. Considering the fragility of the crystals, we estimated that eight molecules per a.u. was the most likely value.

3.4.3. Structure determination and refinement.

The crystal structure of *Tg*CGL was elucidated using the Molecular Replacement (MR) technique, taking advantage of the high amino acid sequence homology (94%) existing between the parasite and the human cystathionine γ-lyase, whose crystal structure was known (PDB ID 2NMP). The MR technique allows to obtain initial phases by performing a comparative analysis of the experimental Patterson map obtained from the diffraction pattern, and the theoretical Patterson map calculated from a known structural model. Our preliminary analysis of the diffraction data was consistent with the presence of eight molecules in the asymmetric unit, likely corresponding to two protein tetramers. The program used in the MR resolution process was PHASER-MR [489] integrated in the PHENIX software. The phases were obtained considering any of the possible space groups (*P*222, *P*222$_1$, *P*2$_1$2$_1$2, *P*2$_1$2$_1$2$_1$, *C*222, *C*222$_1$, *F*222, *I*222, *I*2$_1$2$_1$2$_1$) compatible with Laue class 222. Final refinement of the model determined that the correct space group was *C*222$_1$. The molecular modeling procedure and the refinement of the final model were performed with COOT [487] and PHENIX REFINE programs[489]. The statistical parameters of diffraction and refinement are shown in **Table 3.3** and **3.4**.

Table 3.3. Statistics for data collection and refinement for TgCGL	***Tg*CGL**	***Tg*CGL+ PAG**	***Tg*CGL + Cystathionine**	***Tg*CGL + Cystathionine2**
Space group	$C222_1$	P321	P321	P321
Unit cell (a,b,c) (Å)	126.53 138.99 472.99	157.45 157.45 93.20	157.92 157.92 93.60	157.74 157.74 93.40
Resolution (Å)	48.45 - 2.33 (2.41 - 2.33)	45.1 - 2.26 (2.35 - 2.26)	55.22 - 2.21 (2.29 - 2.21)	60.26 - 1.9 (1.96 - 1.9)
CC ½ (%)	99.90 (76.10)	99.50 (64.10)	98.4 (52.7)	99.20 (46.10)
Redundancy	10.30 (9.40)	8.20 (8.40)	10.10 (8.00)	19.90 (20.70)
Completeness (%)	99.90 (80.80)	99.50 (86.50)	100 (100)	100 (100)
I/σ (I)	19.90 (20.4)	14.20 (2.90)	12.7 (4.7)	16.0 (4.40)
Wilson B-factor (Å²)	43.70	29.80	22.70	22.00
R_{merge}[a]	0.153 (1.192)	0.251 (1.257)	0.487 (2.196)	0.435 (2.508)
R_{meas}[b]	0.157 (1.223)	0.256 (1.296)	0.500 (2.251)	0.446 (2.572)
R_{pim}[c]	0.036 (0.272)	0.049 (0.301)	0.112 (0.493)	0.100 (0.566)
Refinement Total reflections Unique reflections Rwork[d]/Rfree[e]	 3461898 (178726) 177123 (8754) 0.174/0.210	 1642693 (47066) 61247 (2656) 0.162/0.186	 1343959 (69207) 67491 (3322) 0.203/0.242	 1343959 (69207) 67491 (3322) 0.154/0.178
No of atoms Macromolecules Ligand (PLP) Ligand (KTB or PAG)	 25451 120 -	 6321 30 17	 6200 30 13	 6156 30 13
Average B-factor (Å²) Macromolecules Ligands (PLP) Ligands (KTB or PAG)	 48.44 41.46 -	 34.26 34.84 51.34(PAG)	 61.00 19.25 40.71 (KTB)	 24.74 20.57 36.14 (KTB)
Ramachandran plot statistics (%) Res. in most favored regions In additional allowed regions In disallowed regions	 96.44 3.53 0.03	 95.00 4.87 0.13	 95.57 4.43 0	 96.25 3.75 0.00
RMSDs Bonds length (Å)/ angle (°)	 0.012/1.48	 0.010/0.65	 0.007/0.92	 0.014/0.83
Rotamers outliers (%)	0.38	0.00	0.15	0.00
Clashcore	4.23	3.98	4.32	10.06
MolProbity score [f]	1.49	1.53	1.52	1.78

One crystal was used for each data set. Values in parentheses are for highest-resolution shell. [a]Rmerge= Σhkl Σi |Ii (hkl)− <I(hkl)>I/Σhkl Σi Ii(hkl) (all I+ and I-); [b]Rmeas = Σhkl Σi |Ii (hkl) − I(hkl)>I/Σhkl Σi Ii(hkl) (all I+ and I-); [c]Rpim= Σhkl Σi |Ii (hkl) − <I(hkl)>I/Σhkl Σi Ii(hkl) (all I+ and I-); [d]Rwork = Σ |Fo – Fc | / ΣFo; [e] Rfree = Σ |Fo – Fc | / ΣFo, calculated using a random 5 % of reflections that were not included throughout refinement. [f]MolProbity score: 0.426*ln(1+clashcore) + 0.33 *ln(1+max(0;rota_out-1))+ 0.25*ln(1+max(0, rama_iffy-2))) + 0.5

Table 3.4. Statistics for data collection and refinement for TgCGLN360S	***Tg*CGLN360S**	***Tg*CGLN360S+ PAG**	***Tg*CGLN360S + Cystathionine**	***Tg*CGLN360S + Cysteine**
Space group	P321	P321	P321	P321
Unit cell (a,b,c) (Å)	157.74 157.74 93.33	158.03 158.03 93.60	158.43 158.43 93.83	158.35 158.35 94.21
Resolution (Å)	77.06 - 2.22 (2.30 - 2.22)	77.26 - 1.98 (2.05 - 1.98)	55.38 - 1.59 (1.64 - 1.59)	45.41 - 1.89 (1.95 - 1.89)
CC ½ (%)	99.70 (88.80)	99.90 (54.40)	99.90 (57.60)	99.90 (89.20)
Redundancy	30.0 (30.3)	17.40 (7.60)	16.70 (7.20)	20.0 (20.70)
Completeness (%)	100 (100)	99.40 (92.30)	97.70 (80.90)	100 (100)
I/σ (I)	12.90 (3.90)	21.90 (1.70)	22.30 (1.30)	28.40 (5.60)
Wilson B-factor (Å²)	22.0	28.4	23.0	24.10
R_{merge}[a]	0.737 (2.972)	0.117 (1.171)	0.076 (1.190)	0.106 (0.877)
R_{meas}[b]	0.749 (3.022)	0.121 (1.256)	0.078 (1.284)	0.109 (0.899)
R_{pim}[c]	0.136 (0.547)	0.028 (0.437)	0.018 (0.468)	0.024 (0.196)
Refinement Total reflections Unique reflections Rwork[d]/Rfree[e]	 1976130 (98457) 65911 (3250) 0.194/0.212	 1615394 (32592) 92916 (4268) 0.175/0.199	 2964409 (52316) 177039 (7304) 0.172/0.190	 2170390 (110939) 108481 (5370) 0.171/0.186
No of atoms Macromolecules Ligand (PLP) Ligand (PAG HCYS or CYS)	 6419 30 -	 6245 30 34	 6532 30 17	 6527 30 28
Average B-factor (Å²) Macromolecules Ligands (PLP) Ligands (PAG/HCYS/CYS)	 29.24 21.46 -	 32.89 27.76 50.22(PAG)	 29.94 18.23 58.00(HCYS)	 26.87 16.48 48.78(CYS)
Ramachandran plot statistics (%) Res. in most favored regions In additional allowed regions In disallowed regions	 95.95 4.05 0.00	 96.46 3.54 0.00	 96.95 3.05 0.00	 96.92 3.08 0.00
RMSDs Bonds length (Å)/ angle (°)	 0.010/1.65	 0.017/1.49	 0.020/1.38	 0.010/0.94
Rotamers outliers (%)	0.44	0.31	0.15	0.00
Clashcore	3.98	4.44	4.73	2.72
MolProbity score [f]	1.46	1.45	1.36	1.24

One crystal was used for each data set. Values in parentheses are for highest-resolution shell. R_{merge} [a] = $\Sigma_{hkl}\ \Sigma_i\ |I_i\ (hkl) - \langle I(hkl)\rangle I/\Sigma_{hkl}\ \Sigma_i\ I_i(hkl)$ (all I+ and I-); R_{meas} [b] = $\Sigma_{hkl}\ \Sigma_i\ |I_i\ (hkl) - \langle I(hkl)\rangle I/\Sigma_{hkl}\ \Sigma_i\ I_i(hkl)$ (all I+ and I-); [c] $R_{pim} = \Sigma_{hkl}\ \Sigma_i\ |I_i\ (hkl) - \langle I(hkl)\rangle I/\Sigma_{hkl}\ \Sigma_i\ I_i(hkl)$ (all I+ and I-); [d] $R_{work} = \Sigma\ |Fo - Fc\ |\ /\ \Sigma Fo$; [e] $R_{free} = \Sigma\ |Fo - Fc\ |\ /\ \Sigma Fo$, calculated using a random 5 % of reflections that were notincluded throughout refinement. [f] MolProbity score: 0.426 *ln(1+clashscore) + 0.33 *ln(1+max(0, rota_out|-1)) + 0.25 *ln(1+max(0, rama_iffy|-2)) + 0.5

3.4.4. Three-dimensional structure of *Tg*CGL

3.4.4.1. Overall structure

Structurally, the CGL from *T. gondii* (*Tg*CGL) shows the overall fold (type α/β/α) of the type I family of PLP-dependent enzymes. Accordingly, it follows the overall architecture of the CGLs from yeast, human and bacteria (c.a. *S. aureus*, *L. plantarum* and *S. maltophilia*) among others. *Tg*CGL exists as an homotetramer, both in solution (**Fig. 3.3**) and in the crystalline state (**Fig. 3.6**), with overall 222 symmetry. The tetramer can be described as an assembly of two dimers related by a 2-fold axis. Each of these dimers, formed by subunits A-C and B-D, respectively, represents a functional unit that contains two catalytic cavities (thus, four in the tetramer). The monomeric subunits consist of three distinct regions (**Fig. 3.6**): (i) The N-terminal domain (residues 1-84), is composed of one helix (α1) and a long unstructured loop (residues 1-54) that interacts with the active site of its neighboring subunit in the dimer (c.a loop from subunit A, interacts with the PLP domain of subunit C). The first twenty residues of the N-domain are very flexible and barely interact with the bulk protein, explaining why it is not visible in most CGL structures deposited in the databases. (ii) The second protein region is known as the "PLP-binding domain" (residues 85- 281), and represents the largest segment of *Tg*CGL. Remarkably, this module contains many of the relevant catalytic residues, including the conserved lysine (K230) that covalently links the PLP to the active site.

The PLP domain is built up of a mainly parallel seven stranded β-sheet, that follows the sequence ↑β1↓β7↑β6↑β5↑β4↑β2↑β3, with strand β7 running antiparallel to the rest of strands. Notably, the β-sheet is sandwiched between two helical bundles, and is bent around helix α3. The first helical bundle includes four helices (α2, α5, α6 and α9), of which α5 and α6 are completely exposed to the solvent, whereas the other two, α2 and α9, play a key role in the dimer integrity by interacting with the short helix (α1) of the N-terminal domain and helix α9 from the adjacent subunit. In contrast with other organisms (c.a yeast), *Tg*CGL lacks a fifth helix (α7) inserted between α2 and α6, being this element more lax, and appearing as a loop that retains certain helicity between amino acid residues 216-221 (**Fig. 3.6**). At the opposite face of the β-sheet, the second bundle formed by helices α3, α4, and α8, is involved in the interactions with the complementary dimer (**Fig. 3.6**). (iii) Finally, the C-terminal domain (residues 282-417) is smaller in size and connects to the PLP domain through the long helix α10. This domain includes

five α-helices (α10-α14) located on one side of a five-stranded β-sheet with the strands sequence (↑β8↓β9↑β11↑β12), of which β10 is not visible in our *Tg*CGL structure.

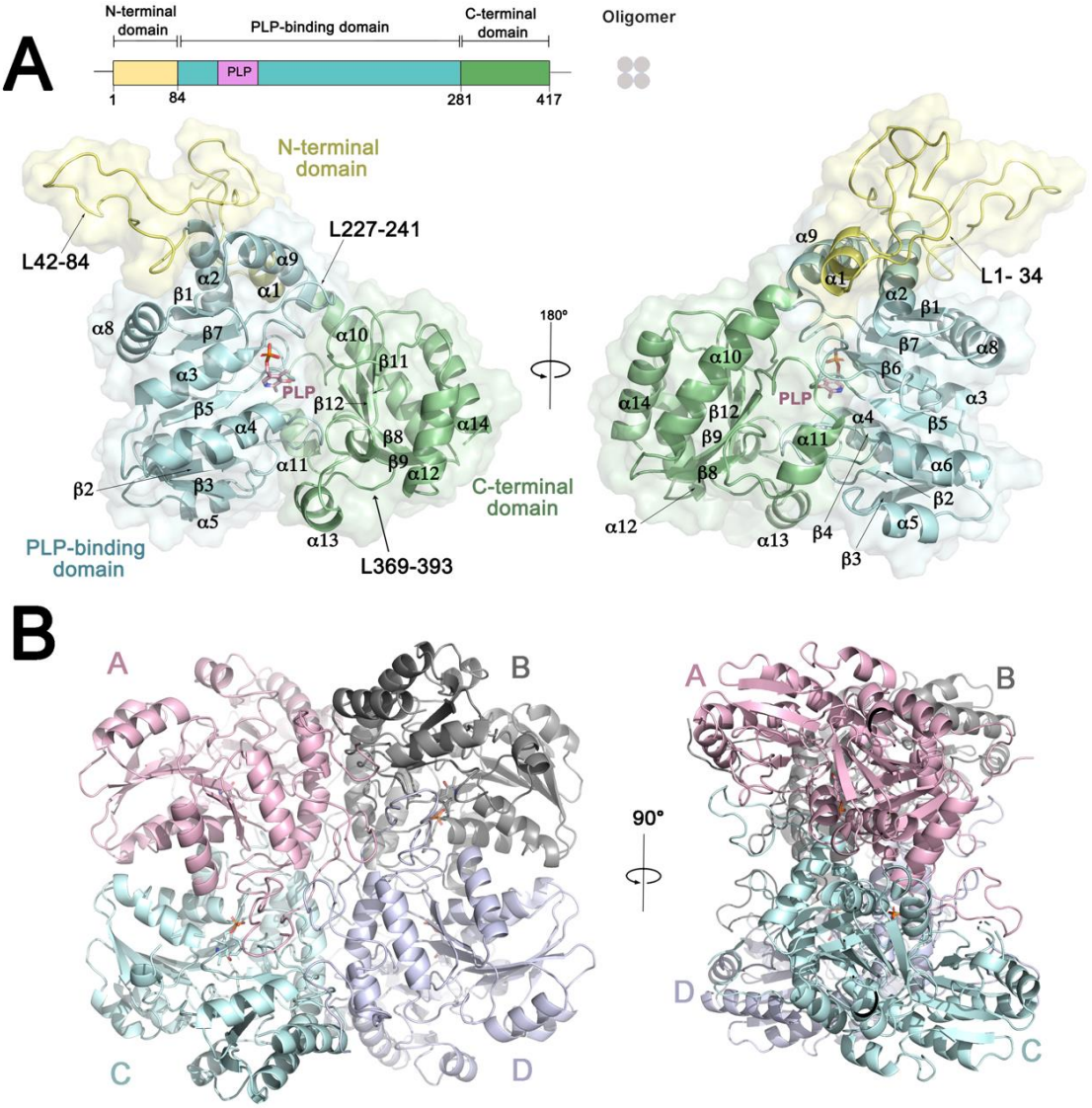

Figure 3.6. Crystal Structure of TgCGL*. (**A**) TgCGL has a modular architecture consisting of three distinct domains): (i) N-terminal domain (yellow), (ii) PLP-binding domain (blue), and (iii) C-terminal domain (green). (left) Ribbon representation of the TgCGL monomer (secondary structure elements are labeled). Each color corresponds to the domain distribution described previously. (**B**) Tetrameric TgCGL. The assembly can be structurally interpreted as two active dimers (dimer 1: subunits A-C; dimer 2: subunits B-D) related by a two-fold axis. The overall symmetry of the tetramer is 222, and harbors four identical active sites, each of which harbors one PLP molecule (in sticks).*

As mentioned above, monomeric *Tg*CGL shares the fold to the holo-form of human and yeast CGLs (*rmsd*= 0.818 and 1.372, of the monomeric form, respectively). As observed in these two proteins, helix α13 is part of a flexible region whose electron density is doubtful in some monomers of the asymmetric unit , but appears stabilized in other *Tg*CGL subunits with visible residues from the N-terminal loop (V66-P84) (**Fig. 3.6**). The structural alignment of monomeric *Tg*CGL with both, apo- and holo-human CGL (*rmsd*= 1.523; *rmsd*=0.818) shows clear differences in the loops containing residues H41-P84, T129-N137 and T228-Y232 (numbering of *Tg*CGL) (**Figs. 3.8** and **3.9**), suggesting that our crystallized *Tg*CGL enzyme displays the holo conformation.

As described earlier, *Tg*CGL exists as a homotetramer in solution [458] (**Fig. 3.4**) and in the crystalline state (**Fig. 3.6**). The approximate dimensions of the monomer and the tetramer are 59x73x42 Å and 88x89x55 Å, respectively. The tetramer can be structurally described as a dimer of dimers related by a 2-fold symmetry axis. The most compact association between neighboring molecules (analyzed using the PISA server (http://www.ccp4.ac.uk/pisa/sessions/OY-814-TF/index.html)) is that formed between monomers A-C and B-D (**Fig. 3.6**). The Buried Surface Area (BSA) for the A-C and B-D dimeric assemblies are 2405Å^2 and 2466Å^2, respectively. The interface between the A-C (or B-D) subunits is stabilized by hydrogen bonds, hydrophobic interactions and intermolecular interactions (**Fig. 3.7**). The N-terminal domain from each subunit plays a key role in maintaining the integrity of each structural dimer, by forming intermolecular hydrogen bonds, like those existing between the phosphate moiety of PLP and residues Y78 and R80 of the complementary monomer (**Fig. 3.7, A**). The latter residue of protomer C (or D, respectively) bonds to the conserved residue Y133 of subunit A (or subunit B, respectively). Likewise, residues E69 and S67 of subunit C interplay with N349 (α12) of the C-terminal domain of subunit A. Polar interactions are detected between the lateral chains of H143 and K146 (α7) of monomer A and the backbone of S117 and L120 (α3) of monomer C. Moreover, side chains of T114 and N263 help reinforce the A-C and B-D dimer assemblies by forming H-bond interactions with the main chain of M261. Finally, hydrophobic interactions keep helices α3, α4 and α8 of subunit A in contact with with α3 and α8 from subunit C.

In turn, assemblies A-C and B-D interact with each other through their α1, α9, α10 and α14 helices thus stabilizing the tetrameric species (**Fig. 3.7**). In yeast, humans, and bacteria (c.a *P. aeruginosa*, *L. plantarum*, and *S. aureus*) there are fully conserved residues that are key in the tetramer formation. These residues

form salt bridges involving the side chains of arginine and asparagine residues (D219 and R257 in *Hs*CGL). Instead, in *T. gondii*, these residues are cysteine and leucine residues (L275 and C237 in *Tg*CGL). Remarkably, multiple network of salt bridges participated by R34, E36 and T37 (α1) of subunit A and K286 (α10), D402, D405 and D408 (α14) of subunit B enhance the stability of the *Tg*CGL tetramer (**Fig. 3.7**). Moreover, the oligomeric state of the enzyme is further reinforced by π-stacking and electrostatic interactions between residues from helices α9 from complementary subunits (α9*) (e.g., F271, Y272 and Q268 (α9) and F271*, Y272* and Q268* (α9*) and K278 (α9) and E365* (α9*)) (**Fig. 3.7**).

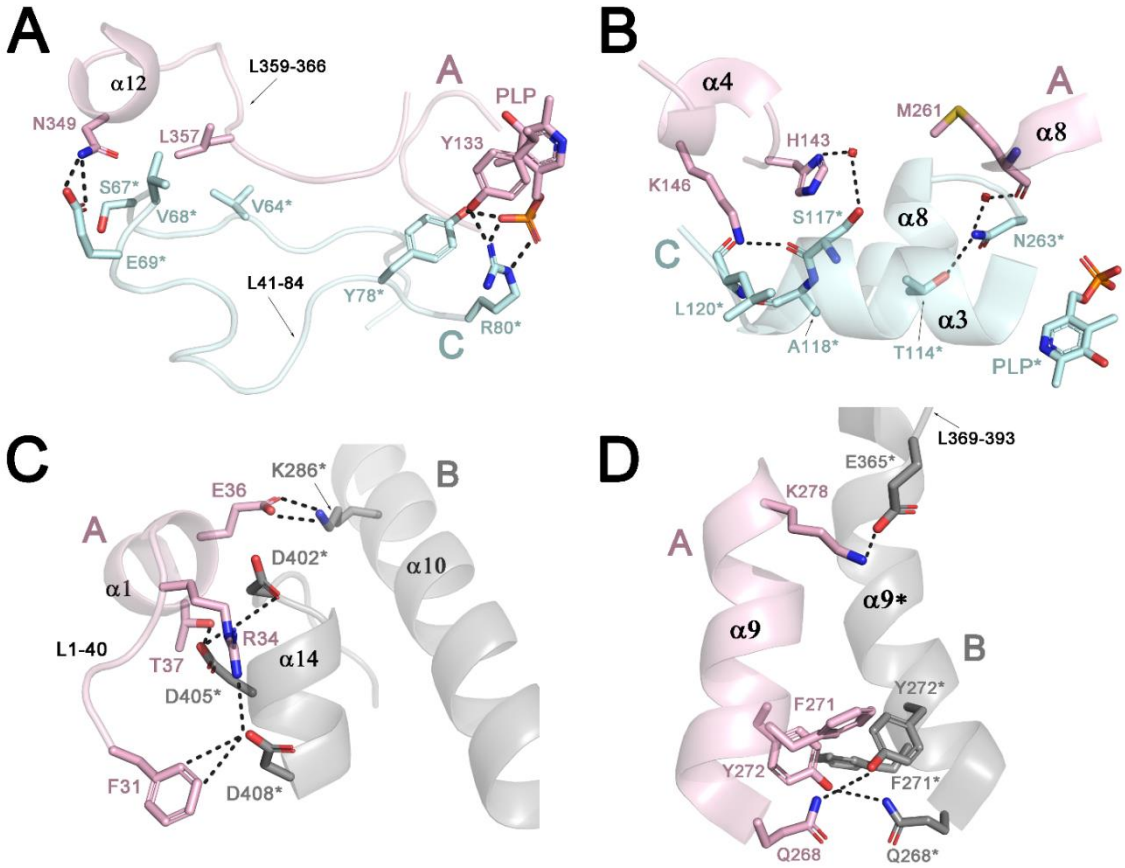

***Figure 3.7*. Interdomain interactions in TgCGL**. (**A, B**) Interactions between monomers A (pink) and C (blue) forming the active dimer. (**C, D**) Interfacial residues of monomers B (grey) and A (pink) stabilizing the tetrameric oligomerization. The monomer nomenclature is based on the tetramer represented in the **Fig 3.6, B**.*

3.4.4.2. Conformational state

The superimposition of the A-C *Tg*CGL assembly with the human counterpart in the apo state, revealed that the active site of apo-*Hs*CGL is considerably more expanded than that of *Tg*CGL (*rmsd* = 2.968) (**Figs. 3.8, A** and **3.9**). Detailed comparison of *Tg*CGL with apo-*Hs*CGL and with holo-*Hs*CGl disclosed the key changes between the apo form and the PLP-bound enzyme. The most significant differences reside in the α9, α10 and α12 helices, and in the three loops H41-P84, T129- N137 and T228-Y232 (numbers correspond the *Tg*CGL) (**Figs. 3.8** and **3.9**). These loops are part of the walls of the catalytic site that harbors the PLP cofactor. When PLP is present in the catalytic cavity of human CGL, these loops point towards the catalytic site establishing effective interactions with the cofactor. The largest displacements observed in *Tg*CGL correspond to the side chains of the catalytic residues Y133 and K230 (*Tg*CGL numbering), shifted over 9 Å and 7Å, respectively, with respect to their homolog residues in apo-*Hs*CGL (**Fig. 3.8**).

In PLP-bound enzymes, the cofactor is covalently bound via a conserved lysine in the active site. However, in the apo form, this lysine is far from the cofactor, preventing nucleophilic attack and the subsequent internal aldimine formation. Finally, the CGL enzymes usually present a helix with two turns (residues 127-139 in *Tg*CGL and 111-120 in *Hs*CGL) that unwinds and becomes a loop in apo-*Hs*CGL (**Fig. 3.8, A**). Thus, *Tg*CGL shares the structural features of holo-*Hs*CGL. In particular, helices α12 and α14 are appreciably more shifted in *Tg*CGL (grey arrow in **Fig. 3.9, F**) than in the apo-*Hs*CGL adopting a closed conformation.

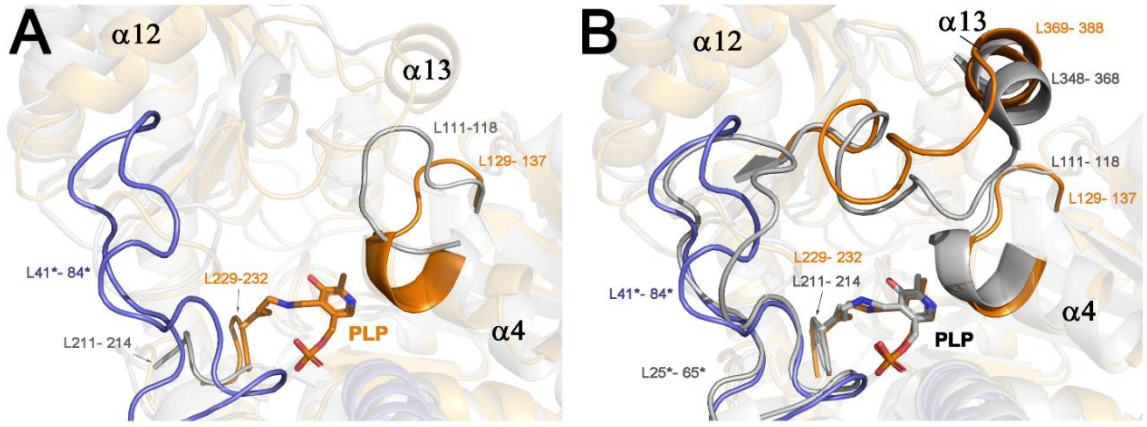

***Figure 3.8**: Structural comparison of apo- and holo-HsCGL with TgCGL. Superimposition of TgCGL (subunit A, orange; subunit B, blue) with (**A**) apo-HsCGL (no PLP) (grey) and (**B**) holo-HsCGL (with bound PLP) (grey). The main loops involved in the conformational change (L129-137, L229- 232, L369-388, and L41*-84* of TgCGL and L211-215, L111-116, L348-368, and L25*-65* of HsCGL) are highlighted in opaque ribbons. PLP and TgCGL residue K230 are in sticks.*

Structural comparison of tetrameric *Tg*CGL with the apo- and holo-human CGL tetramers, revealed a higher similarity with holo-*Hs*CGL (**Fig. 3.9, A-C**).

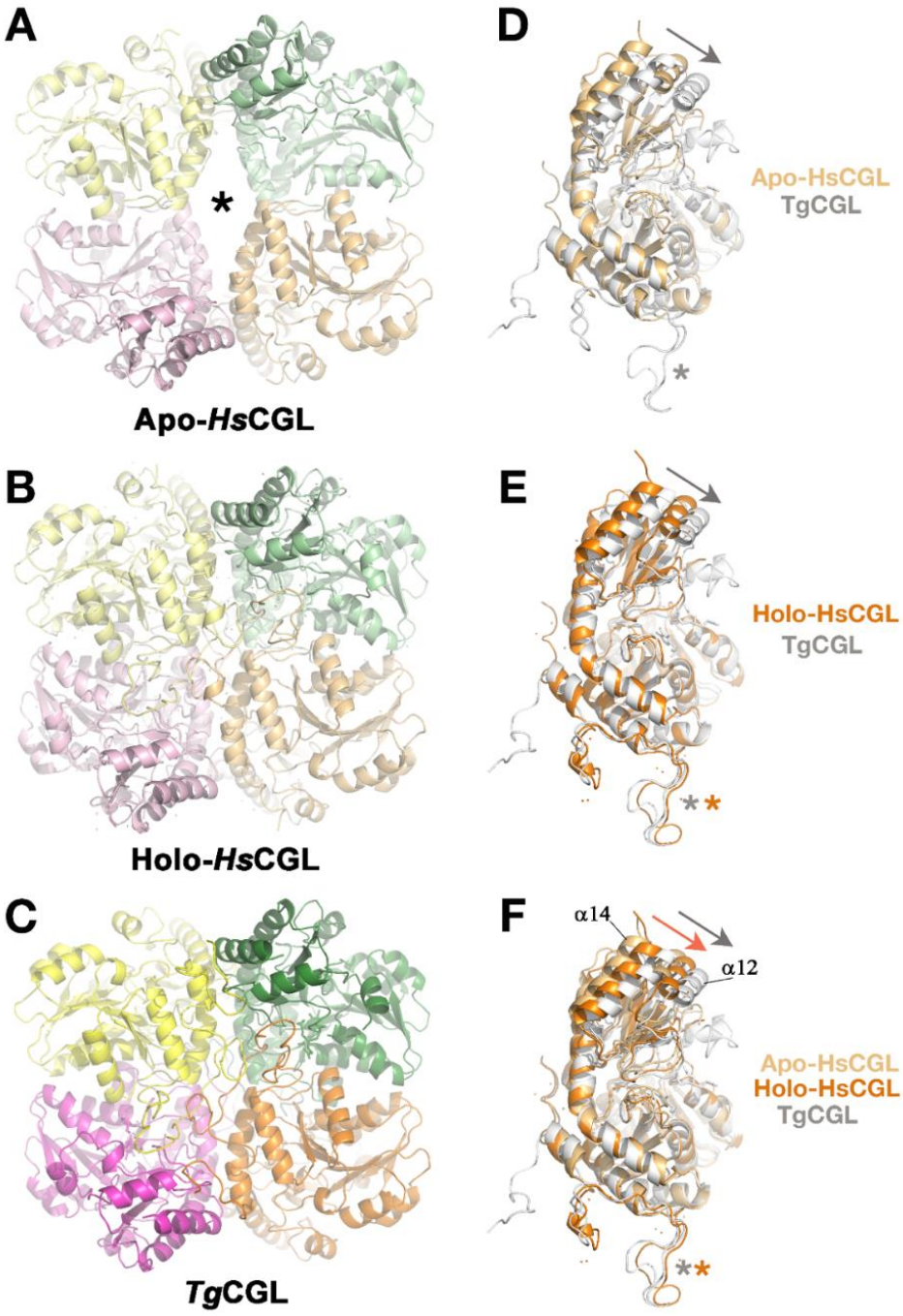

***Figure 3.9. TgCGL shows a holo-like conformation**. (**A**) Tetrameric apo-HsCGL; (**B**) tetrameric holo-HsCGL; (**C**) TgCGL; Superimposition of monomeric TgCGL (grey) with (**D**) apo-HsCGL (light orange); (**E**) Holo-HsCGL (orange), and (**F**) Apo- and holo-HsCGL. The helices α12 and α14 are highlighted. The arrows show the movement of these helices in TgCGL (grey arrow) and holo-HsCGL (orange arrow) compared to apo-HsCGL.*

3.4.4.3. Structure of *Tg*CGLN360S enzyme variant

In 2003, Messerschmidt and coworkers proposed that the reaction specificity for the α, γ- versus α, β-elimination depends on the orientation taken by Cth molecule within the catalytic site [460]. Our collaborators at Verona proposed that substitution of the asparagine at position 360 by serine, favors a Cth conformation that is suitable to undergo both, γ- or β-eliminations [458]. To unravel this duality on the catalytic activity (**Fig. 3.10**), we engineered a "humanized" variant *Tg*CGLN360S and determined its crystal structure. In addition, we performed co-crystallization experiments of the mutant enzyme with different substrates (Cth, Cys) and with the DL-propargylglycine (PAG) inhibitor (**Table 3.1**). *Tg*CGLN360S yielded crystals under the same conditions used for the native enzyme. The crystals belong to space group P321 and diffracted X-rays to 2.22 Å resolution (**Fig. 3.10**).

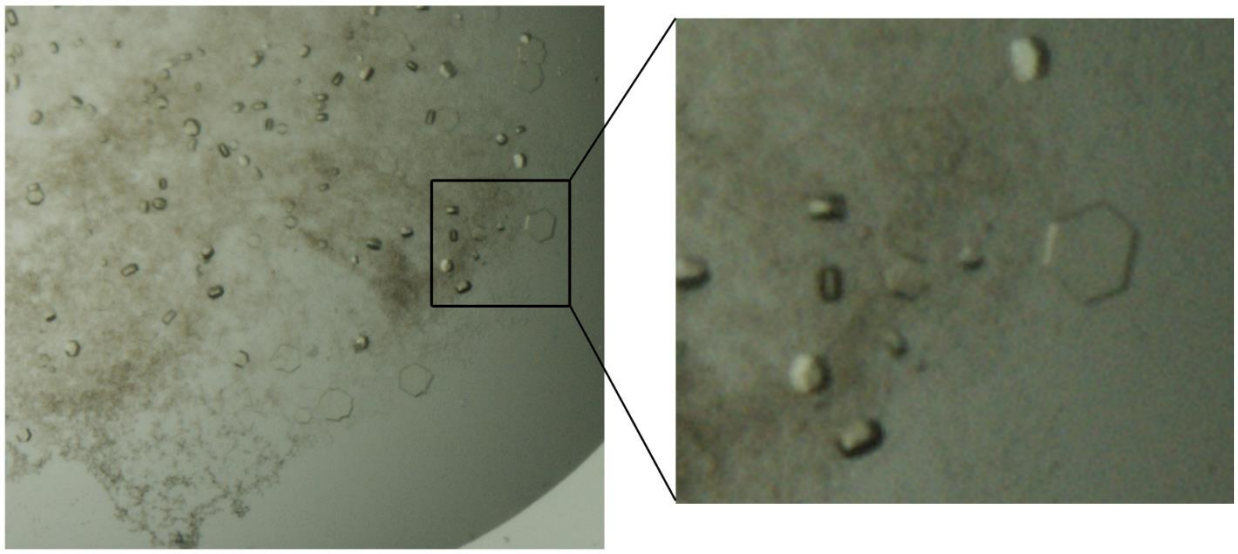

Figure 3.10. *Crystals of the TgCGLN360S variant. Crystals were grown in 12%PEG 3350, 0.1M sodium citrate pH 4.6 and CYMAL-4. The yellow color of the crystals reveals the presence of the bound PLP cofactor.*

The *Tg*CGLN360S crystals contain two molecules in the asymmetric unit (monomers A-C), that are related by a 2-fold crystallographic axis with an equivalent dimeric assembly, thus forming the tetrameric biological unit (**Fig. 3.6**). The overall fold of *Tg*CGLN360S barely changes with respect to the native enzyme. Superimposition of *Tg*CGLN360S with the *Tg*CGL monomer (*rmsd*=0.220) and dimer (*rmsd*=0.249) revealed some differences in the V351-F393 loop (**Fig. 3.11**), which appeared slightly open in the mutant enzyme, shifted in its central part towards helix α4. The largest displacement of the main chain is observed

at the level of residue N378, which is shifted by approximately 4 Å in the mutant. The maximum distance between this loop (residues 351-393) and helix α4, measured between residues N137 and H376 is 11.91 Å in the native protein, whereas 9.72Å in the N360S mutant (**Fig. 3.12**).

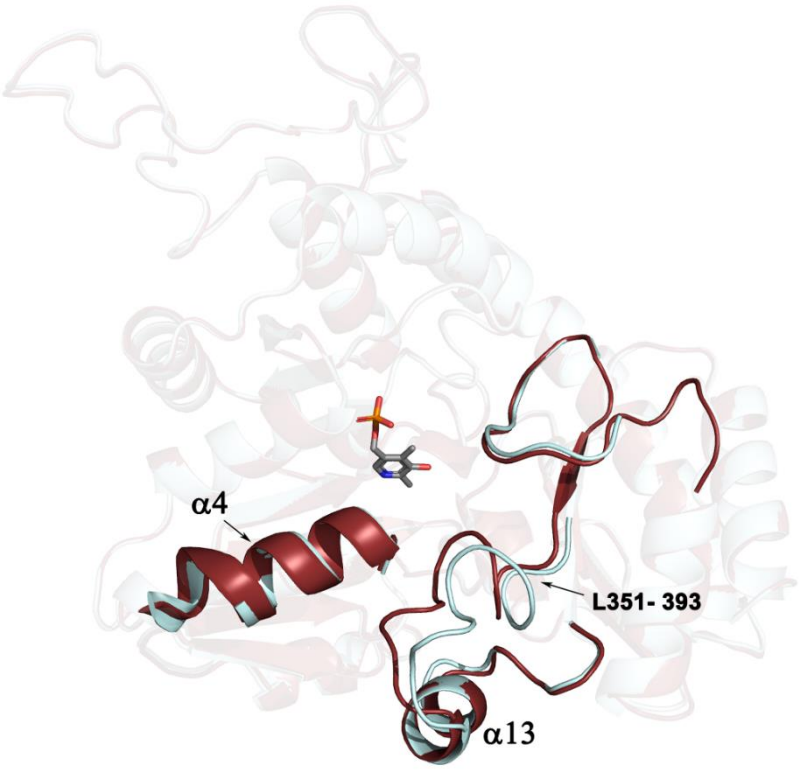

Figure 3.11. Conformational differences in loop L351-393 in the N360S variant*. Superimposition of the wt-TgCGL (blue) and mutant N360S (red) monomers. PLP is in sticks.*

The mutation facilitates the formation of new interactions that approximate loop L351-393 to helix α4 (**Fig. 3.12**). In native *Tg*CGL, the distance N360-N236 is 2.54 Å, whereas in the mutant the equivalent distance S360-N236 grows up to 5 Å (**Fig. 3.12**). During the last steps of the refinement, we noticed the presence of residual electron density in the catalytic site of the N360S variant. A polder omit map revealed the presence of a glycerol molecule, provenient from the cryoprotectant solution used in the freezing process. The glycerol interacts via its hydroxyl moiety O2 with the main chain nitrogen atom of residue S360 (**Fig. 3.12**). Additionally, the hydroxyl group of T375 and Y133 are within hydrogen bond distance (2.80 Å and 2.58 Å, respectively) to glycerol. As mentioned above, the loop L351-393 is located farther away from the α4 helix in the native enzyme (**Figs. 3.11** and **3.12**). As found in the protein variant, the polder omit map revealed the presence of residual electron density (bulkier in this case) in the catalytic cavity of the native protein. Several runs of refinement led us attribute this density to a molecule of TCEP (tris(2-carboxyethyl)phosphine), used as a reducing agent during the purification protocol. The TCEP molecule establishes additional interactions

with the protein. Firstly, the short distance between residues N360 and N236 (2.54 Å) shortens the distance between TCEP and the main chain nitrogen of N360 (2.49 Å). This shorter distance triggers a weakening of the hydrogen bonds between the substrate and residues Y133 and T375 (3 Å and 3.2 Å, respectively). Importantly, this displacement leads to a widening of the pocket in the wt enzyme to accommodate TCEP. In the mutant, such pocket is narrower, thus explaining why a smaller molecule such as glycerol, and not TCEP (also present in the solution) occupy the cavity. Taken together, these findings suggest that mutation N360S induces a conformational displacement of one of the main loops in *Tg*CGL (residues 351- 393).

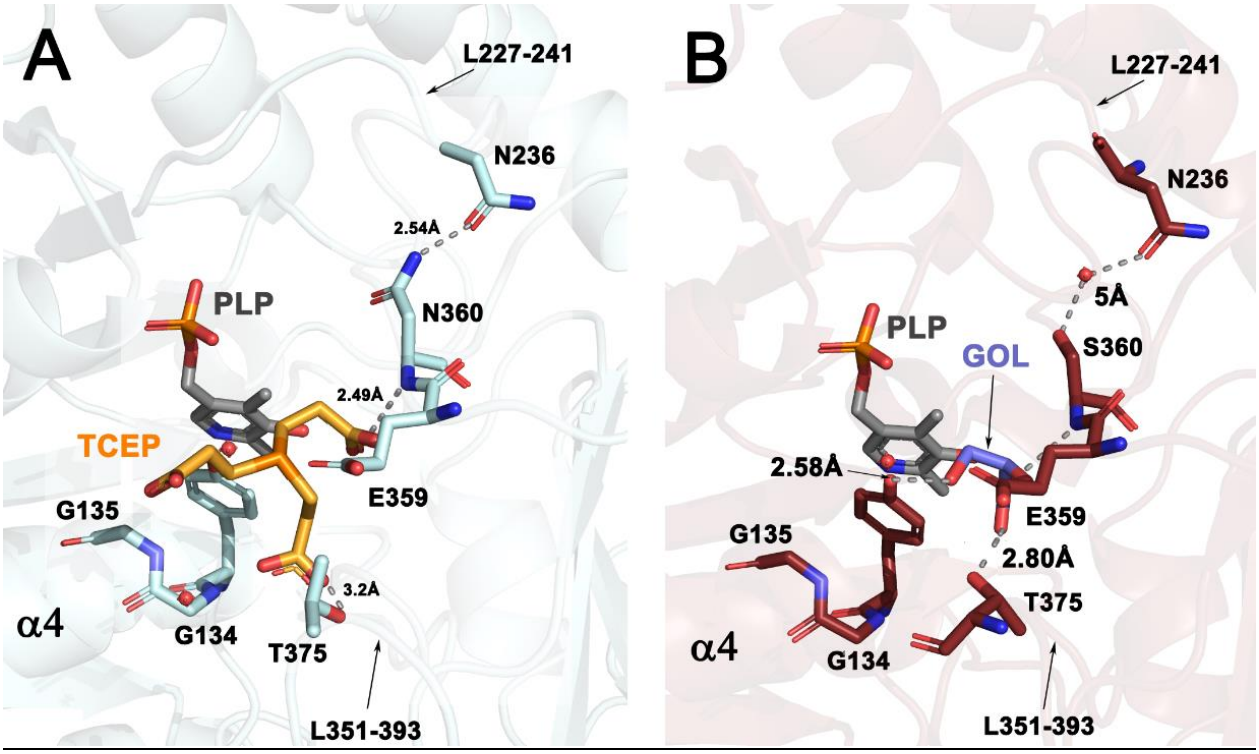

Figure 3.12. Mutation N360S weakens some interactions at the catalytic site*. Main hydrogen bonds formed between residues of the catalytic site in native (A) and mutant (B) TgCGL. Substitution of N360S increases the distance between S360 and residue N236, leading to an approximation of L351-393 to the helix α4.*

3.4.4.4. Catalytic site

As mentioned above, *Tg*CGL exists as a homtetramer, formed by two symmetric dimers, each containing two equivalent catalytic sites. The walls of the catalytic site are made up of residues donated by the PLP-binding domain and the C-terminal segment of subunit A, and the N-terminal domain of subunit C. The PLP is embedded by part of helix α3, strands of the PLP-binding domain (β5-β7) and from the C-terminal segment (β9, β11 and β12), and the connecting loops T129-G134, D205-P216, S227-G241, V351-I367 and Y58-P84 (the latter belongs to the complementary subunit of the structural dimer). The pyridine N1 nitrogen of PLP is stabilized by residue D205, and its pyridine ring is coplanar to the phenolic ring of Y133, which forms π-stacking interactions with PLP (**Fig. 3.13**).

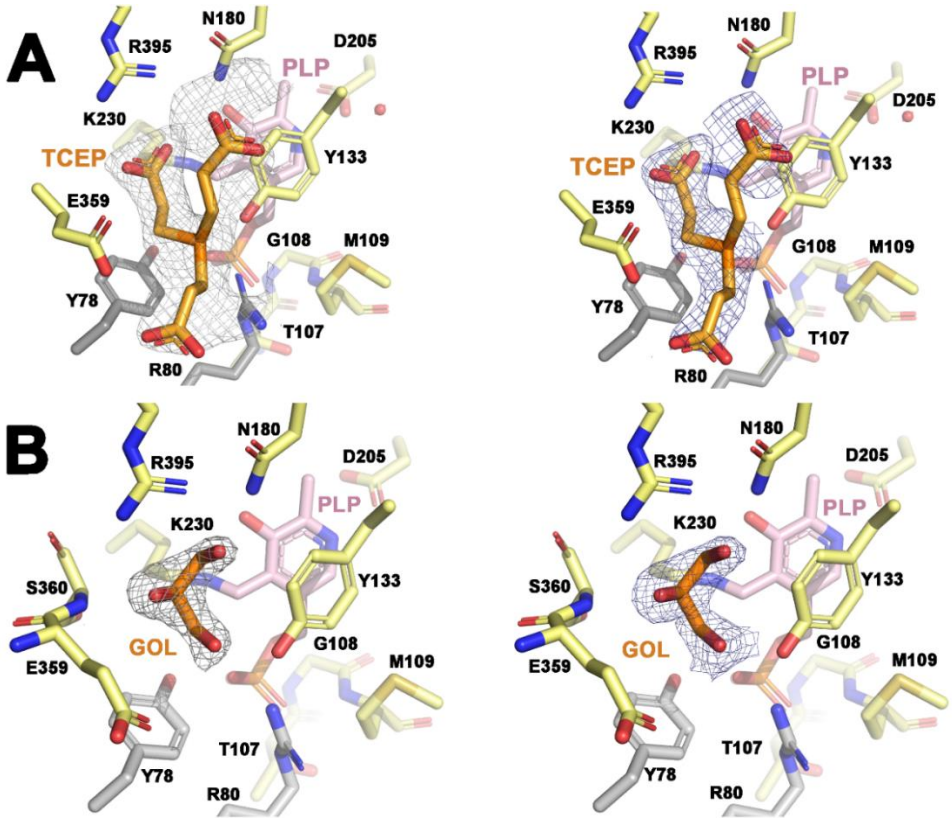

***Figure 3.13. Active site of TgCGL**. (Left) Polder omit map of native TgCGL (**A**) and mutant N360S (**B**), calculated around the bound molecules (glycerol and TCEP, in orange). The residues involved in the stabilization of PLP are represented in sticks (subunit A in yellow; subunit B in grey). (Right) Main residues at the catalytic site of native (**A**) and mutant N360S (**B**), and 2Fo-Fc map around the bound molecules, after model refinement. GOL (in orange) is glycerol.*

Residues T107, G108, M109 and T229, anchor the PLP molecule through hydrogen bond interactions with the phosphate moiety of the cofactor. Additionally, the complementary subunit is involved in a total of three hydrogen bonds between atoms OP2 and OP3 of PLP, and protein residues Y78* and R80*. The amino group of N180 is within hydrogen bond distance to OH3´-hydroxyl group of PLP (3.12Å). The aldehyde portion of PLP at position 4 is implicated in the formation of a Schiff base with the ε-amino group of lysine 230. This stable PLP-enzyme complex is commonly observed in the majority of PLP-dependent enzymes [502].

Moreover, a polder omit map calculated for the *Tg*CGL-wt around the PLP molecule revealed residual electron density consistent with the presence of an additional small molecule in the active site. Since no ligands were added to the crystallization drop, we interpreted that this density likely corresponded to a small molecule dragged during the purification protocol, or alternatively to any of the chemicals present in the crystallization buffer. Several runs of refinements led us attribute this residual density to a TCEP molecule, added as reducing agent along the purification protocol. Interestingly, TCEP occupies part of the substrate binding site, being stabilized through interactions between its carboxyl groups and the side chains of residues R395, T375 and R138, as well as with the main chain nitrogen atom of residue N360 (**Fig. 3.13**).

Similarly, a polder omit map calculated for the N360S mutant in the same area, displayed residual electronic density around the center of the catalytic site. In this case, the density was consistent in shape and size with the presence of a glycerol molecule, likely derived from the cryoprotectant used to flash freeze the crystal. The refined model revealed that glycerol mediates a series of interactions that cause an approach of loop L351-366 to helix α4, that does not take place in the native enzyme. The O1 and O2 hydroxyl groups of glycerol are anchored by hydrogen bond interactions with the guanidine moiety of R395 (2.70Å and 2.90 Å, respectively). Additionally, the O2 atom from glycerol interacts with the amino group of (i) side chain of N180 and (ii) protein backbone of S360. Finally, the hydroxyl group of Y133 is involved in the stabilization of glycerol within the cavity by the interacting with its O3-atom.

3.4.5. Structure of *Tg*CGL - ligands complexes.

Kinetic data reported in previous studies [458], revealed that the catalysis of wild-type TgCGL on cystathionine is limited to the α,γ-elimination reaction, which yields Cys, α-ketobutyrate (KTB) and ammonia ($NH4^+$) as final products (**Fig. 3.14**)

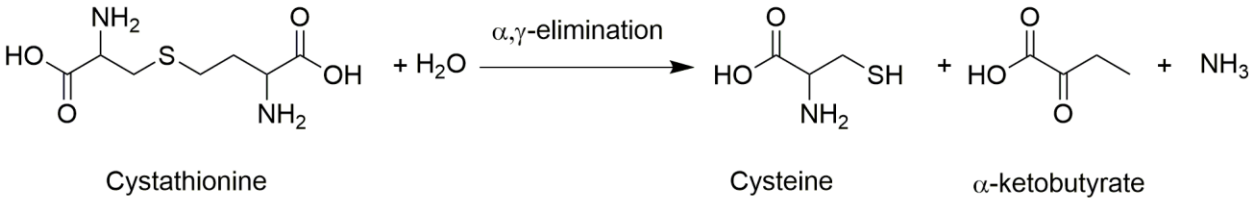

Figure 3.14. Canonical reaction of CGL. *The cystathionine is hydrolyzed at the α and γ positions to perform cysteine, α-ketobutyrate and ammonia.*

Besides the former reaction, the N360S *Tg*CGL mutant is additionally able to catalyze an α, β-elimination reaction on cystathionine, which yields homocysteine, pyruvate and ammonia as products (**Fig. 3.15**)

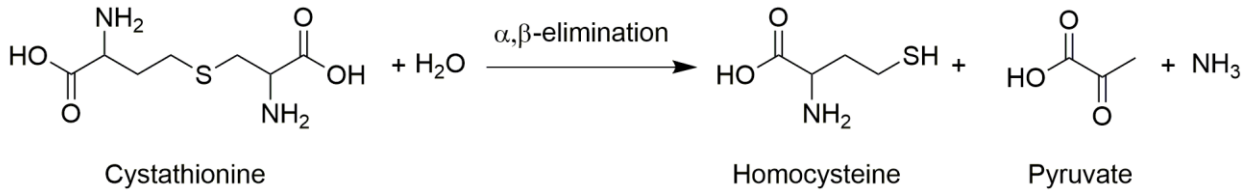

Figure 3.15. α, β-elimination of Cth catalyzed by CGL. *The cystathionine is hydrolyzed at the α and β positions to perform homocysteine, pyruvate and ammonia*

As mentioned earlier, the reason for these different catalytic abilities are thought to be due to a distinct orientation of the substrate (Cth) within the catalytic cavity, but the actual mechanism of catalysis is poorly understood. With the intention of helping to unravel this intricate puzzle, we decided to grow

crystals of both proteins in the presence of their potential ligands (cystathionine (Cth), cysteine (Cys) and the inhibitor DL-propargylglycine (PAG)), to analyze the resulting reaction intermediates and/or products. In addition, we pursued to confirm, if possible, the distinct orientation of Cth within the active site cavity in each particular protein. Third, we wanted to understand why cysteine inhibits *Tg*CGL [458]. Initially the soaking technique was used to obtain protein-ligand complex crystal since no conformational changes were expected upon addition of the ligand. However, after unsuccessful attempts with such technique, the co-crystallization technique was used to obtain the crystals for this study. To ensure complete occupancy of all binding sites, an excess of the corresponding substrate (molar ratio 1:100) was added independently to the protein solutions subjected to crystallization. The successful crystallization mix consisted of 12% (w/v) PEG 3350 and 0.1M sodium citrate pH 4.6, and using CYMAL-4 or CYMAL-3 as an additive (from the detergent screen of Hampton Research), in all cases. The protein concentration ranged between 15 to 25 mg mL^{-1}. The X-rays diffraction data were collected at the BL13-XALOC beamline of the ALBA synchrotron in Barcelona.

3.4.5.1. *Tg*CGL crystallized in presence of cystathionine

With the exception of the loop described in the previous section (slightly shifted in the mutant), the structural superimposition of the native and the N360S variant obtained in the presence of cystathionine, barely exhibited major differences. However, different molecules were detected within the corresponding catalytic cavities.

In the case of native *Tg*CGL, two different datasets were collected (*Tg*CGL+Cth1 and *Tg*CGL+Cth2). The intensity statistics for the dataset with the best resolution (*Tg*CGL+Cth2, **Table 3.3**) indicated the presence of hemihedral twinning, that was corrected by applying the appropriate twin operator (-h, -k, l) in the data processing and the refinement (**Table 3.3**). In any case, the conclusions obtained from the twinned and the untwinned datasets were equivalent.

Since cysteine and ketobutyrate are structurally very similar, two independent refinement protocols considering the presence of either molecule were performed. In one, a cysteine molecule was introduced into the catalytic site. In the other, a α-ketobutyrate (KTB) molecule was considered at the same position. After several runs of refinement, we concluded that the molecule that best matched the electron density in the two native datasets was KTB (**Fig. 3.16, A**). The final average thermal B-factors for KTB were 40 $Å^2$,

whereas a value of 60 Å^2 was obtained if cysteine was introduced as the bound molecule. These data were in agreement with the sole α,γ-elimination capacity of the native enzyme reported by other authors [458]. A careful analysis of the active site showed that the carboxylate group of KTB forms a salt bridge with the guanidine group of R395 and H-bonds the main chain N atom of residue N360, as well as the amino group of the side chain of N180 (**Fig. 3.16, A**). The carbonyl moiety of KTB is oriented towards the internal aldimine formed by K230 and PLP, and in turn interacts via a hydrogen bond with the hydroxyl group of Y133. The methyl group of KTB is exposed to the wider pocket of the catalytic site **Fig. 3.16, A**). Of note, the loop containing T375 (L373-381) is disordered in the native enzyme, indicating the flexibility of this region.

Interestingly, the results obtained with the mutant enzyme were different. As mentioned earlier, the N360S mutation leads to a change in the catalysis of the enzyme and allows the α,β-elimination of cystathionine in addition to the α,γ-elimination. Thus, in principle, a reverse orientation of Cth within the cavity would be expected. If certain, the amino group of the cysteine segment of Cth (Cth results from the condensation of Cys with Hcys) (**Fig. 3.15**) would be placed near the aldehyde position of PLP, thus near the covalent bond that links K230 with the cofactor forming the internal aldimine. As in the case of the native protein, addition of cystathionine to the crystallization drop, resulted in residual electron density within the catalytic site. However the shape and size of this density suggested the presence of a larger molecule, such as homocysteine (**Fig. 3.16, B**). Based on these findings, we proceeded with three different refinement protocols, in which either Cys, KTB or homocysteine were incorporated into the cavity independently.

After careful analysis of all refinement outcomes, we concluded that Hcys, containing an additional methylene (-CH2) and a sulfhydryl group, was the substrate that best suited the residual electron density found in the catalytic cavity (**Fig. 3.16, B**). Thus, a product of the α,β-elimination was detected in our N360S crystals. Hcys forms a salt link with R395 through its carboxylate group, and interacts with the side chain of N180 and T375, and with the main chain of S360. The amino group of Hcys is oriented towards the amino atom of K230, which is covalently linked to PLP forming an internal aldimine. The amino group of Hcys is also at hydrogen-bond distance (2.8 Å) of the hydroxyl of Y133. Finally, the thiol of Hcys participates in H-bonds with E359, Y133, and R80 of the adjacent monomer (**Fig. 3.16, B**).

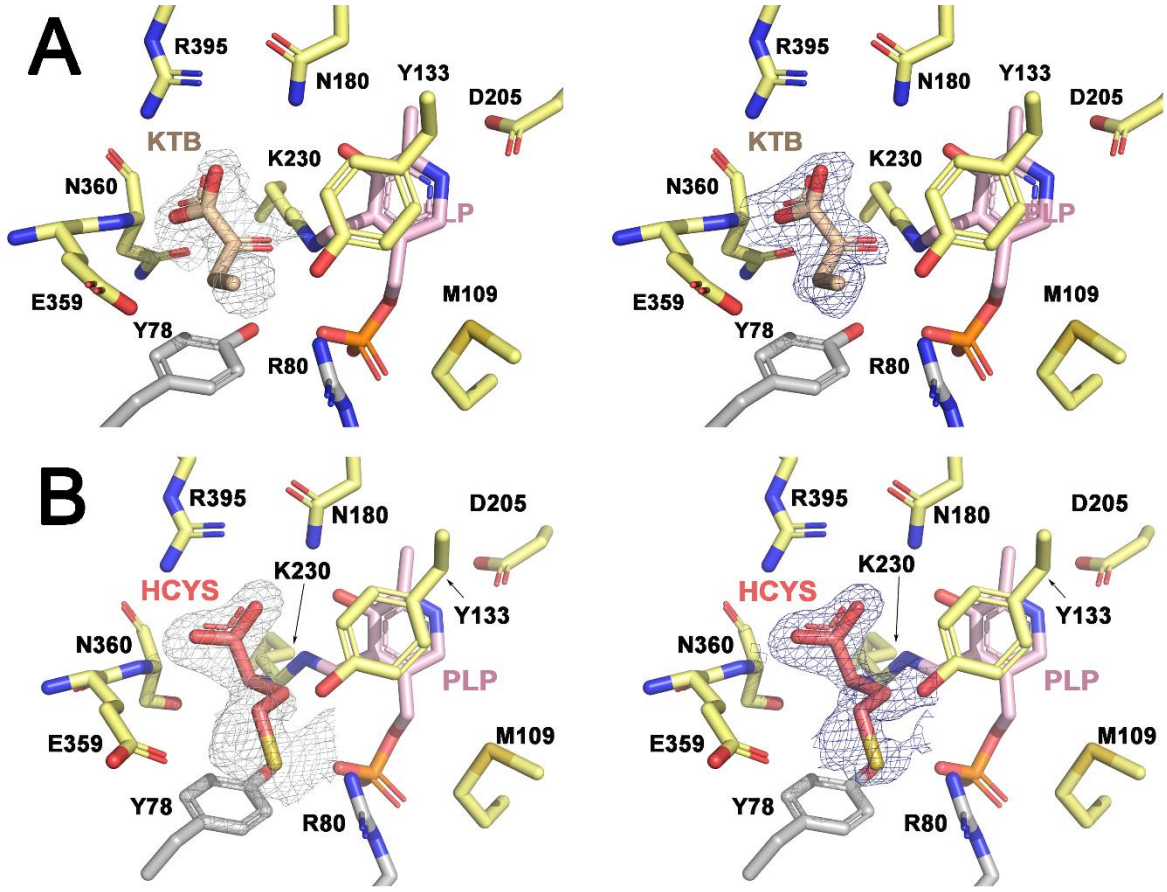

***Figure 3.16**. **TgCGL catalytic site refined from crystals grown in the presence of Cth**. (**A**, left) Main residues of the catalytic site of native TgCGL. The electron density corresponds to a Polder omit map calculated around PLP. The molecule represented in orange sticks is KTB. (**A**, right) 2Fo-Fc map around the KTB molecule resulting from the model refinement. (**B**,left). Polder omit map calculated around PLP in the N360S TgCGL mutant. The molecule represented in salmon sticks is homocysteine (HCYS). (**B**,right). 2Fo-Fc map centered on the HCYS molecule after the model refinement.*

3.4.5.2. *Tg*CGL-Cysteine complex

Cysteine is a substrate of CGL enzymes that allows the release of ammonium, pyruvate, and H_2S through an α, β-elimination reaction (**Fig. 3.17**).

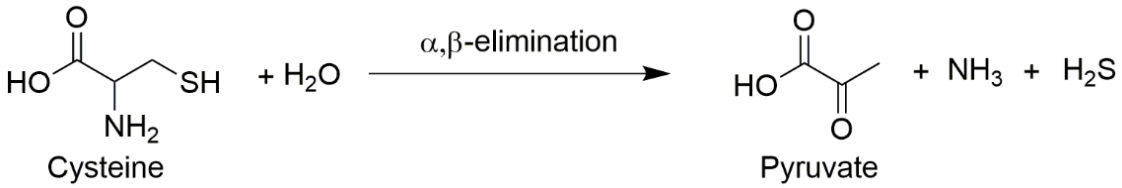

Figure 3.17. Reaction of H_2S production catalyzed by CGL. *β- elimination of cysteine to produce pyruvate, ammonia and H_2S.*

Previous studies have reported that Cys exerts an inhibitory effect on most CGL-enzymes, but the underlying mechanism remains unknown. Different hypothesis have been proposed, among which are the formation of a thiazolidine intermediate with the PLP cofactor, or the cysteine-induced dissociation of PLP to generate the apoenzyme [458,461,470,495,496].

In this section we describe the first crystal structure of a CGL enzyme complexed with cysteine. To obtain the enzyme-substrate complex, both, wild-type and N360S variant from *T. gondii* were subjected to an excess of cysteine (1:100 ratio) during the co-crystallization process. Despite numerous attempts, only crystals of the *Tg*CGLN360S+Cys complex could be obtained. The final crystallization conditions were 12% (w/v) PEG 3350, 0.1M sodium citrate and CYMAL-3 (**Table 3.1**). Data collection represented an enormous experimental effort, an above 50 crystals were tested, after which only one dataset diffracting X-rays at 1.9 Å resolution, was suitable for structure determination. The crystal belongs to space group P321, and contains two molecules in the asymmetric unit. These molecules form a dimer that is related by 2-fold crystallographic symmetry with the other half of the actual biological unit, a tetramer with internal symmetry 222.

As discussed below, our structure does not reproduce previous findings perform on the human CGL enzyme showing that incubation of *Hs*CGL with physiologically relevant concentrations of cysteine (10 mM) generates the apo enzyme (no electron density for PLP was observed in the crystal structure of the human (PDB ID 3ELP)) [461]. In contrast with these results, our structural analysis clearly demonstrated the

presence of bound PLP. Additionally, the Polder omit map showed an additional density in the catalytic cavity (**Fig. 3.18**), that was consistent with an Cys molecule in both asymmetric unit molecules. As shown in Fig. 3.18, the carboxylate group of Cys (easily recognized in the electron density maps) forms a salt bridge with R395, and an H-bond with the amide group of N180. The sulfhydryl group of Cys is anchored by an H-bond interaction with E359. Moreover, and as observed for the KTB and homocysteine products described above, the amino group bound to the Cα carbon of Cys, is oriented towards lysine 230. Surprisingly, binding of cysteine does not appear to alter the overall conformation of the enzyme.

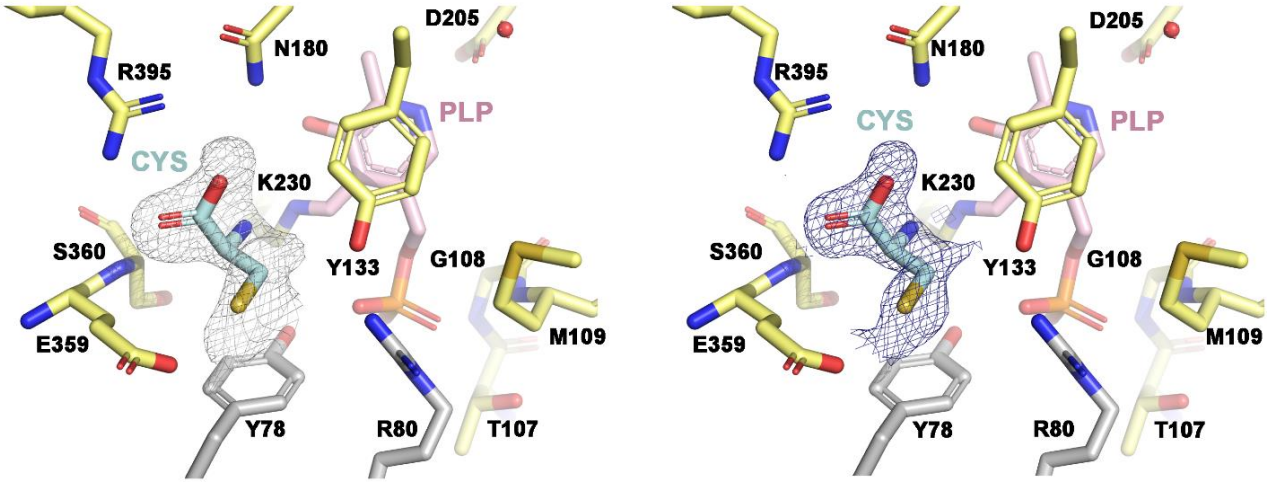

Figure 3.18. Catalytic site of N360STgCGL co-crystallized with cysteine*. Polder omit map (left) and 2Fo-Fc electron density map (right) calculated around the location of the cysteine molecule.*

3.4.5.3. *Tg*CGL-PAG complex

DL -Propargylglycine (PAG) is one of the most commonly used agents to inhibit H_2S production. Concretely, PAG is claimed to be a specific inhibitor of cystathionine γ-lyase [503]. The interaction between the enzyme and the inhibitor has so far only been described by the structure of human CGL [461]. To explore whether of PAG could act on *Tg*GCL, and to determine possible binding and mechanistic differences with respect to the human enzyme, we elucidated the crystal structure of the *Tg*CGL-PAG complex, both for the native and the mutant protein constructs. Briefly, both the crystals of the native and mutant enzymes in complex with PAG were growth in 12% (w/v) PEG 3350, 0.1M sodium citrate and CYMAL-4. After testing the diffraction quality of above 20-30 crystals from both proteins, we obtained one data set for each

protein at resolution 2.26 Å and 1.9 Å for the native and mutant enzymes, respectively. Both crystals belong to space group P321 and contain two molecules (a symmetric dimer) in the asymmetric unit. Application of the crystallographic symmetry permits the visualization of the actual biological unit, a tetramer with internal symmetry 222.

Once the refinement of the wild-type protein model was complete, a polder omit map calculated around the PLP molecule showed additional electron density that could not be attributed to the protein chain, thus suggesting the presence of a molecule within the catalytic site. Such density was observable only in one of the two molecules of the asymmetric unit (thus, two per tetramer), and was consistent with a PAG molecule that was subsequently included in the next refinement steps. Based on the literature [461], we first considered the formation of a vinylether in the PAG molecule, and an interaction with the protein through a covalent bond between its Cγ atom and residue Y133. In these first set of refinements the Cδ atom of PAG was oriented towards the amino group of the internal aldimine formed by K230 and PLP. However, after numerous refinements, the geometry of the PAG molecule and the electron density for this orientation were not consistent with the electron density. Alternatively, we tried different orientations of PAG within the cavity, finding that a rotation by 180° of the PAG molecule, with the Cα ofthe substrate pointing towards the internal aldimine, yielded a much better fit and final statistical parameters. With the PAG molecule in this orientation, two scenarios were considered for subsequent refinement steps. In the first one, the triple bond between the Cγ and Cδ atoms of PAG were preserved. In the second, the reduction of the triple bond to form a vinylether (as observed in *Hs*CGL) was considered (**Fig. 3.19, A**). In the final model, residue K230 remains covalently bound to PLP, and the side chains of R395 and N180 interact with the carboxylate group of the inhibitor. Interestingly, the double bond points to residue E359, leading the Cβ of PAG to bind covalently to the hydroxyl group of Y133. Moreover, the amino group of PAG is near (2.7 Å) and oriented towards the internal aldimine formed by K230 and PLP (**Fig. 3.19, A**).

Unexpectedly, the crystal structure of the N360S*Tg*CGL+PAG complex showed a different orientation of the inhibitor within the cavity (**Fig. 3.19, B**). In this case, the polder omit map around PLP revealed that the two molecules of the asymmetric unit harbored a substrate at the catalytic site. In the final model the Cβ atom of PAG appears close to Y133, suggesting a putative bond, while PAG again seems to form a vinylether (**Fig. 3.19, B**). In contrast to the native enzyme, in the mutant the double bound of PAG is clearly

oriented to residue R80 of the adjacent monomer. The side chains of R395 and N180, and the backbone of S360 are hydrogen-bonded to the carboxylate group of PAG. Finally, the amino group linked to the Cα atom of PAG appears to be interacting with the internal aldimine of the enzyme (**Fig. 3.19, B**).

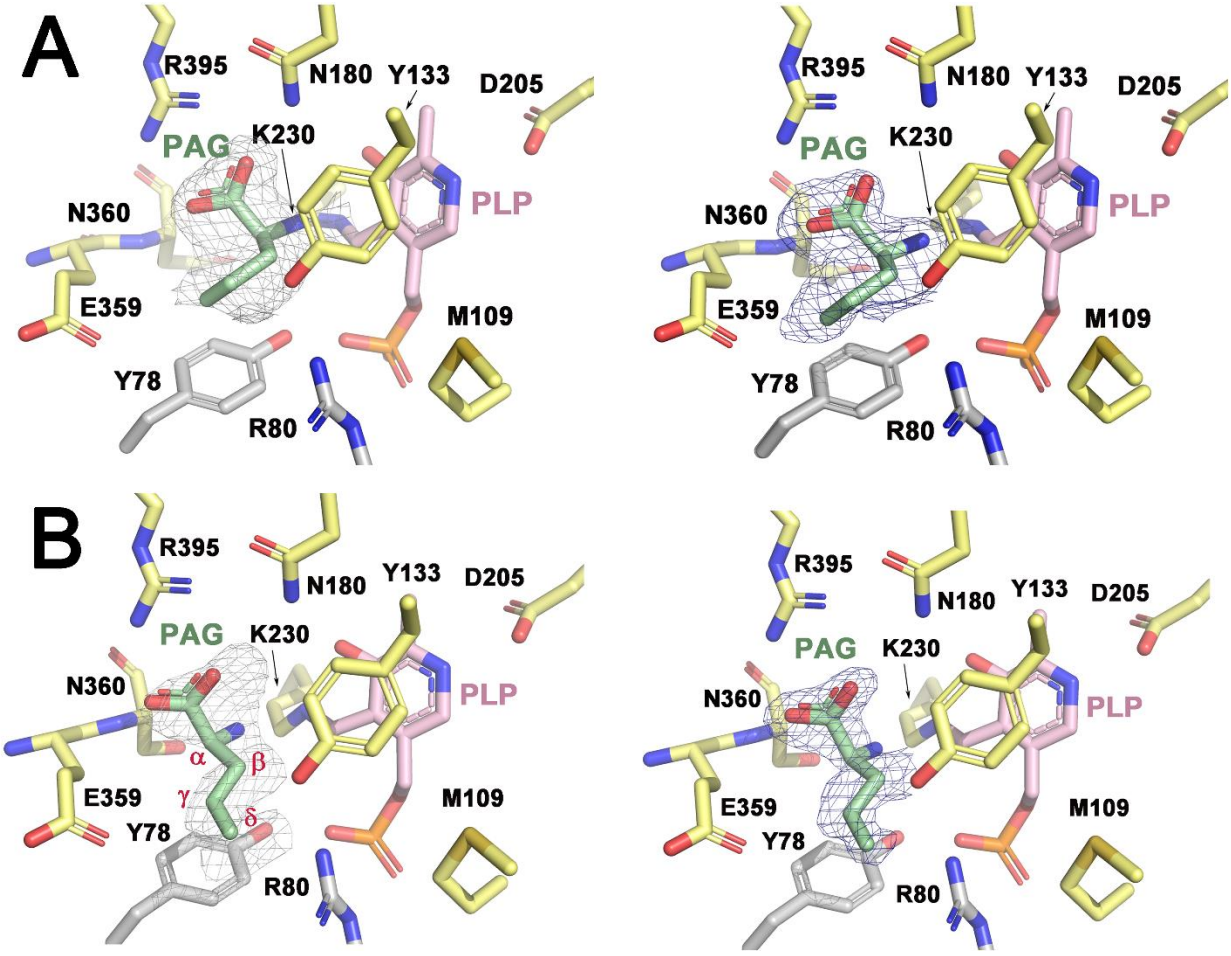

***Figure 3.19. Catalytic site of TgCGL co-crystallized with DL-propargylglycine**. (**A**) Polder omit map (left) and 2Fo-Fc map (right) consistent with the presence of a PAG molecule in the native enzyme. Note: the PAG code in PDB data base is 2AG. (**B**) Main residues within the catalytic site of TgCGLN360S. The PAG molecule is in green sticks, the polder omit map is represented on the left and the 2Fo-Fc map on the right. The position of the atoms in PAG are highlighted in red.*

3.5. DISCUSSION

It is widely accepted that transsulfuration plays a key role in reducing the oxidative stress in many bacteria, and therefore in ensuring the survival of these microorganisms in adverse environments. Two breakthrough studies by Shatalin *et al.* highlighted the therapeutic potential of inhibiting the cystathionine β-synthase and cystathionine γ-lyase enzymes in *S. aureus* and *P. aeruginosa* [14,15]. The authors provided a detailed structural characterization of the cystathionine γ-lyase from *S. aureus* complexed to several inhibitors, and revealed particular features that differentiate the bacterial enzyme from its human counterpart [15]. This elegant work has opened the door to new therapeutic strategies to fight persistent bacteria, whose multiresistence to current antibiotics represents a difficult challenge to treat recurrent infections in hospitals nowadays. In connection with these findings, this chapter of the doctoral thesis expands the structural knowledge on the cystathionine γ-lyase from two human pathogens: the parasite *Toxoplasma gondii*, and the multidrug resistant bacteria *Pseudomonas aeruginosa*.

The catalytic specificity of CGL: The canonical reaction par excellence of the CGL enzyme is the α,γ-hydrolysis of Cth to produce cysteine, α-ketobutyrate and ammonia (**Fig. 3.2, B**). However, in organisms such as *T. gondii, T. cruzi, L. plantarum or S. cerevisiae*, the enzyme shows a lower catalytic efficiency for this reaction (≈ 2 mM^{-1} s^{-1}) [226,458,459,472], than the observed in the human enzyme (15 mM^{-1} s^{-1})[461] and is able to catalyze alternative (non-canonical) processes with significant efficiency. These alternative processes may coexist with the canonical activity, or become the principal catalytic event. For example, *Tg*CGL cleaves Cth almost exclusively through the Cγ-S bond, as it occurs in *T. cruzi* [226] and humans [461,494], whereas the CGL from *S. cerevisiae* [460,472] and *L. plantarum* [459] show a pronounced cystationine β-lyase (CBL) -like activity, and are able to hydrolyze Cth at both, the Cγ-S and the Cβ-S bonds (**Fig. 3.2**).

Some authors have proposed that an important factor underlying these differences, is the protonation of the N1-PLP atom that stabilizes the carbanion-PLP intermediate. Obviously, the tendency to protonation varies depending on the most favorable, or less favorable amino acid environment surrounding the carbanion in each particular protein [467,468] (intermediate 4 of **Fig. 2.20** at the introduction section of the Chapter II). It appears that, the longer is the distance between the conserved aspartate in the catalytic site (D187, D205 and D183, in human, Toxoplasma and Pseudomonas, respectively) and the

N1 atom of the PLP cofactor, the lower is the possibility of protonating the N atom, and the less efficient is the catalytic reaction [472]. Accordingly, the longer aspartate-N1 distances found in yeast, *L. plantarum* and *T. gondii* CGLs (3.6 Å, 2.8 Å and 2.75 Å, respectively) with respect to the human enzyme (2.6 Å), might explain the poorer catalytic efficiency of the three former enzymes.

Intriguingly, we found that substitution of the asparagine at position 360 by a serine in *Tg*CGL affects the reaction preference in the mutated enzyme, that now acquires Cth β-lyase (CBL) ability [458]. Our crystal structures of *Tg*CGLN360S obtained in the presence of Cth, have provided the first structural evidence confirming this reaction by proving the presence of the homocysteine product at the catalytic site, and confirming the duality of *Tg*CGLN360S versus native *Tg*CGL.

Based on these findings, we wondered what structural features underlie the catalytic duality exhibited by *Tg*CGLN360S versus native *Tg*CGL. Or, in other words, what features impede in native *Tg*CGL to perform the β-lyase (CBL) catalysis. Previous modeling studies on *Tg*CGL hypothesized that the long side chain of asparagine 360 might interfere with an appropriate orientation of the sulfur atom at the γ-position with respect to the PLP molecule to perform the β-cleavage of Cth [458]. However, in apparent contradiction with this hypothesis, our structures of native and *Tg*CGLN360S have shown that the side chain of both N360 (in the native enzyme), or its S360 equivalent (in the variant), are not oriented towards the protein substrate site, making steric hindrance between the sulfur atom of Cth and the amide group of the asparagine (or the hydroxyl group of serine), unlikely.

Our new structural data led us think that an alternative explanation for the *Tg*CGL selectivity might be encountered by a reduction in the volume of the catalytic cavity (from 287 $Å^3$ in the native enzyme to 152 $Å^3$ in the N360S variant), caused by a conformational displacement of loop L351-393 towards helix α4 in the mutant (**Fig. 3.11**). However, in the light of this argument, it is paradoxical that despite a reduction in volume, the N360S mutant still retains the ability to perform the α,γ-elimination reaction. On the other hand, the maintenance of such capacity is in apparent conflict with the observations by Lee *et al*., claiming that CGL enzymes performing the γ-elimination of Cth require a wider and more flexible catalytic cavity, capable to allow a change in the hybridization of the N atom of the catalytic lysine (K230 in *Tg*CGL) from a sp^2 to a sp^3 state[466] (intermediates 4 and 5 **Fig. 2.20** at the section 2.1.4.2.1. of the Chapter II). Such requirement does not need to be met in the β-elimination process (intermediates 4 and 5 of **Fig. 2.21** at the introduction section of Chapter II), thus justifying why enzymes performing majorly the β-elimination

present less bulky crevices. A detailed comparison of the catalytic cavities (performed with CASTp server [504]) of the CGLs whose structure is known, with enzymes that exclusively perform the β-elimination reaction (c.a *Escherichia coli* CBL), led us conclude that the volume of the catalytic cavity of *Tg*CGLN360S (capable of cleaving both the CγS bond and the CβS bond of Cth) is in the range of the *E. coli* CBL enzyme (152 $Å^3$ in both cases). Likewise, we found that the CGL enzymes from *L. plantarum* and yeast (which also catalyze γ- and β-cleavage [459,472]), exhibit a similar available volume (146 $Å^3$ and 148 $Å^3$, respectively). Briefly, we concluded that 150 $Å^3$ appears to be a characteristic volume of CGL enzymes with dual γ- and the β-cleavage capability. According to this approximation one would expect that both, native *Tg*CGL and *Hs*CGL, that only perform γ-cleavage [458,461,494], would display larger catalytic sites. Native *Tg*CGL accomplishes this hypothesis, (288 $Å^3$), but not *Hs*CGL, wich shows a reduced volume of only 87 $Å^3$.

Searching for alternative explanations to the different catalytic profile of CGLs, other authors have proposed that the specificity of the reaction (α,γ- vs α,β-elimination) depends on a pair of highly conserved glutamate residues (E59-E339 in human, and E48-E333 in yeast CGL, respectively) [460,505], which are located at the entrance of the active site and coordinate the cysteinyl moiety of Cth, providing a negatively charged surface. In particular, mutational analysis of E333 in yeast CGL led to postulate that this residue is key in defining the orientation of the substrate. The authors found that the electrostatic repulsion exerted over the S atom in the γ-position, likely directs Cth it in the favorable position to undergo β-elimination [472]. In addition, this glutamate would interact with the distal amino group of Cth, stabilizing the appropriate orientation of the substrate within the catalytic pocket [472]. This would explain why substitution of these glutamates in yeast CGL disfavors the β-elimination of Cth [472]. Interestingly, the equivalent glutamate in *Tg*CGL (E359) is conserved , and stabilizes the thiol group of the Hcys product obtained after β-elimination of Cth, as shown in our crystal structure of *Tg*CGLN360S (**Fig. 3.16, B**). Our findings suggest that, as observed in yeast, the glutamate at position 359 is key in determining the orientation of the sulfur atom of Cth within the catalytic cavity of *Tg*CGL. As mentioned above, residue E48 residue also plays a very important role in the active site of the yeast enzyme. In toxoplasma, however, the equivalent glutamate is replaced by serine 77. Unfortunately, and despite a significant experimental effort, we failed to crystallize the *Tg*CGL S77E mutant. One possible explanation for this failure is the potentially destabilization of the overall structure caused by the mutation. Alignment of *Tg*CGL against its homologs demonstrates that the Y71 residue is found exclusively in the protozoan, and is not conserved in other organisms. For example, in *Tg*CGL, Y71 interacts with S77 of the same chain and with E359 of a

complementary monomer. Our structures suggest that, as postulated by Maresi *et al.* in 2018; the S77E mutation likely causes clashes between the mentioned residues due to the longer length of the glutamate side chain, probably perturbing the interaction between the two chains composing the dimer, and destabilizing the overall three-dimensional structure, what would explain the difficulties to grow crystals of this mutant.

Using the yeast enzyme, Hopwood *et al.* proposed another interesting hypothesis to explain the different specificity of CGLs. In this case, the authors suggested that residues E333 and L335 flanking serine S334, had a relevant role in fixing the final orientation of the catalytic lysine (K203) that binds PLP. According to their model, the specificity of the CGL reactions is mediated by interactions that optimize the relative positions of the substrate, the cofactor (PLP) and the catalytic base (lysine) [472]. In this regard, a mutational study on *E. coli* CGS, an enzyme belonging to the fold type I family of PLP-dependent enzymes (like CGL and CBL), revealed that substitutions at S326 (N360 in *T. gondii*) has a key role in guiding the ε-amino group of catalytic lysine (K198) [506]. Our *Tg*CGL structures show that the N360S mutation increases the distance between the nitrogen of K230 and the oxygen of the asparagine and serine side chain, respectively (from 4.6 Å to 5.2 Å). This difference might modulate the electronic properties of PLP, allowing or restricting the access of the catalytic base to the C4'and Cβ positions of the cofactor and substrate, respectively.

Other authors have highlighted the presence of a highly conserved set of residues that participate in a hydrogen-bond network that involves a sequence of serine-water-serine-glutamate residues in all CGLs. Due to their location within the catalytic site, catalytic-based properties have been attributed to this group of residues in the γ-elimination reaction, similar to the catalytic serine-histidine-aspartate triad found in serine proteases [466]. However, the amino acid sequence of *Tg*CGL does not conform to this pattern, as serines are replaced by asparagines, resulting in a netwotk N360-N236-E365. Despite not being conserved, *Tg*CGL is able to catalyze the γ-elimination of Cth. Thus, it appears that the presence of two asparagines instead of serines does not affect the enzymatic activity. Of note, the N360S mutation artificial introduces a S360-N236-E365 triad that interacts with a water molecule located between residues S360 and N236. The exact function of this network in *Tg*CGLN360S remains unknown, but it might play a relevant role in the catalytic specificity differences observed in the mutant. On the other hand, the presence of an asparagine at position 360 (instead of a serine) neither influences the enzymatic reaction.

Inhibition of TgCGL by cysteine: As mentioned previously, cysteine exerts a substrate inhibitory effect on both, native *Tg*CGL and the *Tg*CGLN360S mutant. This effect has been widely reported in other CGLs, whose activity decreases gradually as the concentration of cysteine increases in the solution. The actual mechanism of inhibition remains unknown, but two different hypothesis have been postulated [461,472,494,495]. In humans, the addition of cysteine concentrations greater than 10 mM results in the detach of the PLP cofactor from the enzyme [461]. This loss is detected spectroscopically by the concomitant disappearance of the absorption peak at 427 nm corresponding to the holoenzyme, and the appearance of a peak at 388 nm characteristic of the apoenzyme. This situation can be reversed upon addition of PLP. Of note, the inhibition by high concentrations of cysteine, does not prevent the human enzyme from synthesizing H_2S through the β-elimination reaction of cysteine [461] (**Fig. 3.17**).

Research conducted by Yamagata *et al.* and Maresi *et al.* in 2002 and 2018, showed that Cys interacts with the enzyme, forming a cyclic thiazolidine complex [458,495]. In contrast to these observations, our crystals of *Tg*CGLN360S grown in the presence of an excess of cysteine (20 mM), showed neither loss of the PLP cofactor nor the formation of the cyclic thiazolidine intermediate. In contrast, we found a stable holoenzyme-substrate complex, in which the cysteine molecule, without being covalently linked to the cofactor, is placed nearby the catalytic lysine (K230) that in turn maintains the internal aldimine with PLP (**Fig. 3.18**). Our findings suggest that inhibition by cysteine originates from the competitive occupation of the site to which other reactive molecules need to gain access for catalysis to continue. Interestingly, the crystal structure of *Lactobacillus plantarum* CGL (*Lp*CGL) complexed with serine (structural analog of cysteine), suggested that the formation of a hydrogen bond between the hydroxyl group of residue Y97 (Y133 in *Tg*CGL) and the Oγ atom of serine (Sγ in the case of cysteine) is key in orienting the serine appropriately for the β-elimination reaction [459]. Based on these data, it is reasonable to think that an equivalent tyrosine, conserved in the catalytic site of all CGLs, might act as an acid to protonate the first leaving group of the β-cleavage reaction, thus yielding the aminoacrylate intermediate (β-lyase reaction), or the aminocrotonate (γ-elimination reaction) (**Figs. 2.21** and **2.20** at the introduction section of Chaper 2, respectively). By a similar rationale, it would be expected that, to perform the β-elimination of cysteine, the thiol group of cysteine should interact with residue Y133 in *Tg*CGL. If this hypothesis is correct, this interaction would promote the formation of an aminoacrylate intermediate. However, in our crystals, cysteine adopts an orientation that a priori is not suitable for the β-elimination reaction, due to the

presence of residue E359 that alternatively interacts with the -SH group of cysteine and inhibits the aforementioned contact between the thiol group of the substrate and Y133 (**Fig. 3.18**).

Two independent studies have confirmed the relevance of glutamate (E339) in the β-elimination of Cys by human CGL [463,470]. The substitution of this residue by more hydrophobic amino acids (lysine, alanine or tyrosine) leads to an increase in H_2S production [470]. On the other hand, kinetic and structural analysis have shown that the E339V substitution increases the hydrophobicity of the catalytic site of *Hs*CGL and enhances the binding of Cys within the cavity (PDB ID 5EIG) [463]. The structural comparison of *Tg*CGLN360S with *Hs*CGL-E339V has allowed us to confirm that the orientation of Cys within the catalytic site is very similar (**Fig. 3.20**). Intriguingly, cysteine forms an external aldimine in the human enzyme, whereas is not covalently linked to neither the cofactor nor the protein in the *Tg*CGLN360S crystals (**Fig. 3.20**).

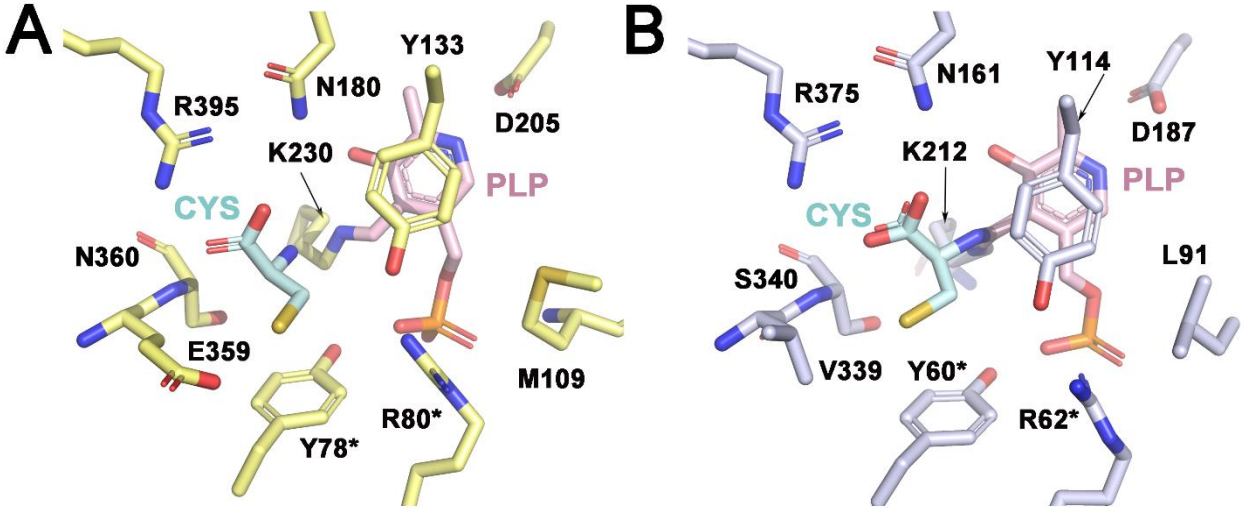

Figure 3.20. Cysteine location at the catalytic site *Aminoacid residues surrounding cysteine at the catalytic site of (**A**) TgCGLN360S and (**B**) HsCGL-E339V.*

Inhibition of TgCGL by DL-propargylglycine (PAG): PAG is the most widely used inhibitor of the H_2S production, and has shown high efficacy in animal models [365]. This molecule inactivates *Hs*CGL irreversibly and selectively [504]. The structural basis of PAG binding to the human CGL enzyme was unraveled in 2008 , and served to propose a putative mechanism of inhibition [461] (**Fig. 2.26**, at the introduction of Chapter II, section 2.1.4.2.4.)

Three crystal structures of PAG-protein complexes had been reported prior to the writing of this thesis. The first corresponds to the methionine gamma-lyase (MGL) from *Trichomonas vaginalis* (PDB ID 1E5E). The second is the CsdB lyase from *E. coli*, a pyridoxal 5'-phosphate (PLP)-dependent enzyme that catalyzes both cysteine desulfuration and selenocysteine deselenation (PDB ID 1I29)[507]. Finally, the third is represented by the *Hs*CGL-PAG complex (PDB ID 3COG)[461]. These three proteins share with *Tg*CGL the characteristic folding of the type I folding-dependent PLP family of enzymes, and thus have a very similar architecture in their catalytic site. The location of PAG within the active site of these enzymes is very similar in all cases (except in *Hs*CGL), and basically coincides with the site found in our *Tg*CGL and *Tg*CGLN360S crystals (**Fig. 3.19**). In MGL and CsdB, PAG is covalently link to the PLP cofactor through its amino group and the C4' atom of PLP, thus forming an external aldimine (**Fig. 3.21**). Instead, in *Tg*CGL, the electron density clearly shows the formation of an internal aldimine between the conserved lysine (K230) and the cofactor, and the PAG molecule though is located nearby, does not covalently link to the catalytic lysine (**Fig. 3.19**). Remarkably, the orientation of PAG is significantly different in *Hs*CGL (PDB ID 3COG) with respect to MGL and CsdB, and is rotated by 180°, with its carboxylate and amino groups pointing towards residue R62 (R80 in *T. gondii*) [461](**Fig. 3.21**).

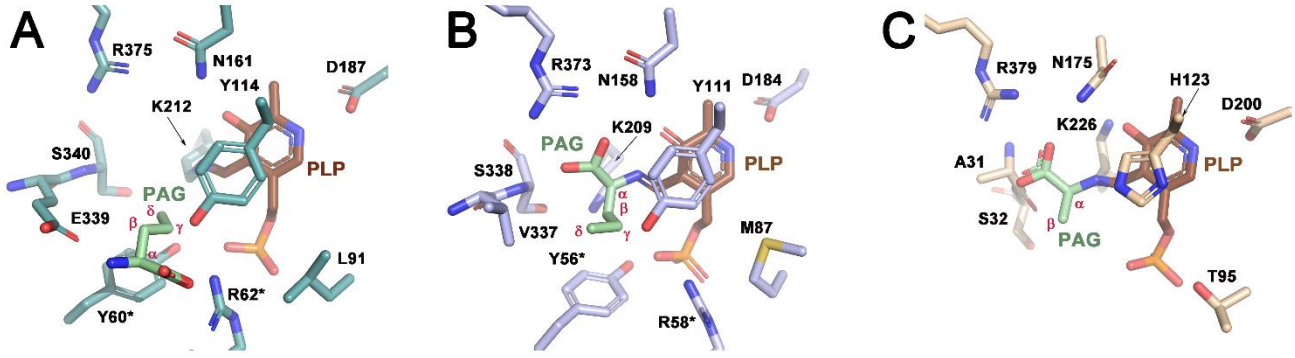

Figure 3.21. PAG binding mode *in (**A**) HsCGL, (**B**) MGL and (**C**) CsdB. PAG is colored in green following the color code used in Fig. 3.19. PLP is represented in brown. The residues of an adjacent subunit are shown with an asterisk. The position of the atoms of PAG are highlighted in red greek letters.*

In the structures of MGL and *Hs*CGL, the PAG molecule is covalently bound through its Cγ atom to the conserved tyrosine of the catalytic site (Y111 in MGL and Y114 in *Hs*CGL) (**Fig. 3.21**). In contrast, in CsdB H123 (equivalent to Y111/Y114) is not covalently linked to PAG. Although H123 occupies the same position of the tyrosine and could attack the Cγ of PAG, the side chain of H123 is far away from the substrate (the

Cγ-Cδ bond is disordered in the crystal structure). Surprisingly, the structure of the complexes of PAG with native and mutant *Tg*CGL show a single covalent bond between the Cβ atom of the inhibitor and Y133 (**Fig. 3.19**). Equivalent distances between the hydroxyl of Tyr and Cβ in MGL and *Hs*CGL (2.62Å and 2.47Å, respectively) suggest that these atoms might also be favorable for a nucleophilic attack. However, in the parasite the carbon atom in the beta position is clearly more accessible than the carbon in the gamma position (**Fig. 3.19**).

The crystal structures of native and N360S mutant *T. gondii* CGL has allowed us to identify eight residues that interact with PAG; R395, Y133, N/S360, K230, N180, R80 (of the adjacent subunit) and E359 (**Fig. 19**). This last residue is key in the native enzyme, attracting the PAG double bond towards itself, contrary to what is observed in the mutant enzyme where the double bond is positioned towards R80 of the adjacent monomer (**Fig. 3.19**). Likewise, this residue is not present in MGL or CsdB. Thus, in agreement with what Sun postulated in 2008, E359 may be of critical importance for the design of specific inhibitors, since it is conserved only in CGL proteins[461].

Previous kinetic studies [461,494] and the results obtained from the crystal structures of the *Tg*CGL-PAG and *Tg*CGLN360S-PAG complexes have allowed us to postulate an alternative mechanism of *Tg*CGL inhibition by PAG, distinct from that proposed for the human enzyme (**Fig. 2.26**, at the introduction of Chapter II, section 2.1.4.2.4.) (**Fig. 3.22**). First, for transaldimination to occur (step 2 of **Fig. 3.22**) the amino group of PAG is deprotonated by a basic residue. Next, the beta position of the alkyne is deprotonated by K230 to generate the allene intermediate (step 3 of **Fig. 3.22**). Finally, the alternative step proposed in this work is the attack of Y133 on the innermost carbon of the allene forming the vinylether (step 4 of **Fig. 3.22**).

The basic amino acid proposed for deprotonation of the incoming PAG (step 1 of **Fig. 3.22**) and protonation of the alkyne (step 3 of **Fig. 3.22**) is R80 of the adjacent monomer. R80 is located at the inhibitor/substrate binding site entrance and is in a favorable position to deprotonate the incoming substrate/inhibitor. In addition, the side chain of R80 is at a distance that facilitates the protonation of the alkyne at the gamma position (4.3 and 3.8 A for the native and mutant *Tg*CGL, respectively) (step 3 of **Fig. 3.22**), Next, Y133 acts as a base converting the allene to the vinylether and forming a covalent bond with the Cβ. The allenes have a very special reactivity and all three carbon atoms can be attacked being in all cases kinetically and thermodynamically favorable processes[508]. In this work the crystal structures

show that the innermost carbon (Cβ) is placed in a more favorable position for nucleophilic attack originating a covalent bond between Cβ and Y133.

The binding of PAG occupies the substrate binding space, thus inhibiting CGL by blocking accessibility to the catalytic site. In addition, the release of the substrate is prevented due to the covalent bond of PAG to Y133, a key residue in the catalytic process [459,475].

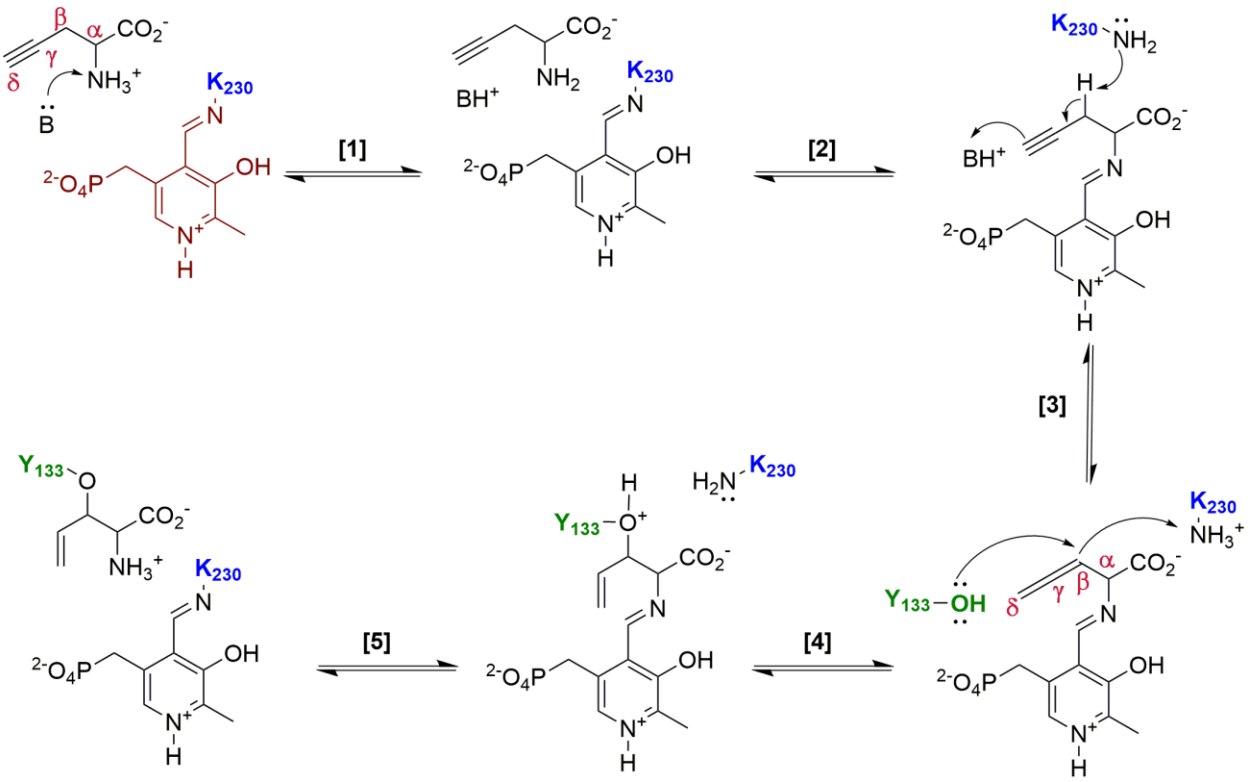

Figure 3.22. Mechanism of inhibition of TgCGL by PAG*. The PAG is deprotonated by the R80 of the adjacent monomer (Step 1) for transaldimination to occur (Step 2). Residue K230 attracts the proton at β-position of alkyne to form the alene intermediate (step 3). The hydroxyl group of Y133 attacks the β-position of the allene to generate the vinyl ether (step 4). The internal aldimine is regenerated and Y133 is covalently bound to vinylether of PAG.Figure adapted from [461].*

3.6. CONCLUSIONS

1. We have elucidated the crystal structure of cystathionine γ-lyase from *Toxoplasma gondii*, the causative agent of toxoplasmosis, from an engineered construct that includes the full-length aminoacid sequence of the native enzyme.

2. A second similar construct (*Tg*CGLN360S) including a subtle modification that "humanizes" the catalytic site by including the mutation N360S, has also been solved by the same X-rays crystallographic techniques.

3. The N360S mutation triggers a cascade change of interactions within the catalytic site that results in a conformational displacement of one of its constitutive loops (L351-393)**.** This change consists in approximating L351-393 to helix α4, thus resulting in a narrowing of the catalytic cavity in the mutant with respect to the native enzyme.

4. Co-crystallization of the *Tg*CGLN360S crystals in a solution containing the cystathionine substrate, results in a *Tg*CGLN360S+homocysteine complex, consistent with its ability to perform the β-elimination reaction of Cth.

5. Co-crystallization of *Tg*CGLN360S crystals in a solution containing cysteine, results in the corresponding *Tg*CGLN360S+Cysteine complex, explaining why cysteine, by occupying the substrate binding position, inhibits the enzyme. Interestingly, the orientation of Cys within the cavity is not favorable to perform the β-elimination reaction to produce H_2S, pyruvate and ammonia.

6. Co-crystallization of the wt- and *Tg*CGLN360S crystals in a solution containing the DL-propargylglycine (PAG) inhibitor, results in the corresponding complexes with PAG. Noteworthy, PAG occupies the substrate binding site and prevents the access to the catalytic site. The formation of a covalent bond between the inhibitor and the enzyme blocks the release of the ligand.

7. The crystal structure of the native and mutant enzyme in the presence of PAG has led us propose a new mechanism of inhibition not previously observed for any other enzyme of the type I family of PLP-dependent enzymes.

8. The data presented in this section provides the first three-dimensional template available of CGL from *T. gondii*, thus paving the way for the rational design of inhibitors to modulate the activity of the enzyme.

9. Our data provides information to analyze the structural evolution of the enzyme across different organisms.

10. Finally, our structures of *Tg*CGL have revealed the main differences existing between the pathogen and the human enzyme, thus helping to understand the distinct catalytic abilities performed by CGLs in different organisms.

CHAPTER IV

Structural Characterization of Cystathionine γ-lyase from *Pseudomonas aeruginosa*

4.1. Cystathionine γ-lyase from *Pseudomonas aeruginosa*

It has recently been demonstrated that several inhibitors of human CGL, have a different effect, or simply lack any effect, on homolog bacterial enzymes encoded by different pathogens. For example DL-propargylglycine (PAG), β-cyano-L-alanine (BCA), hydroxylamine (HA), aminooxyacetic acid (AOAA**)** and L-aminoethoxyvinylglycine (AVG), impair *Hs*CGL activity, while only three of them (AOAA, AVG and HA) are able to inactivate bacterial homologs at low micromolar doses in both, *in vitro* and *in vivo* [15]. Not less importantly, the efficient dose concentrations are significantly higher in the pathogens than in humans [15]. This suggests that there are likely particular structural and physico-chemical differences for each CGL enzyme that could be exploited to develop new antibiotics and/or adjuvants to treat recurrent infections caused by concrete pathogens. In line with these findings, recent studies revealed the presence of the *Cse* gene encoding for the CGL enzyme in the multidrug resistant bacteria of *Pseudomonas aeruginosa*. *PaCse* is arranged in a single operon that is responsible for H_2S production in normal media or under antibiotic stress [14,15]. Interestingly, the absence of *Pa*CGL reduces H_2S production in clinical strains of *P. aeruginosa*. More importantly, knocking down of the gene or alternatively chemical inhibition of the *Pa*CGL enzyme, sensitizes the microorganism to low doses of classical antibiotics such as gentamycin (Gm), norfloxacin (Nor), and ampicillin (Amp), thus opening the door to novel therapeutic strategies to combat resistant infections and extending the life of such antibiotics [14,15].

The structure of *Pa*CGL as 3D-template for drug design

These exciting observations encouraged us to elucidate the still unknown crystal structure of *Pa*CGL, to serve as a three-dimensional template on which to develop specific inhibitors. *Pa*CGL (also known as *Pa*CSE), is composed by 394 amino acids (≈43kDa), and shows a domain distribution similar to that of *Tg*CGL (**Fig. 2.22** at the introduction section of Chapter II). To our knowledge, after *S. aureus* [15], the crystal structure of CGL from *P. aeruginosa* described in this thesis, represents the second three-dimensional structure reported for a CGL enzyme from an organism classified as a critical priority pathogen by the World Health Organization (WHO, https://www.who.int/health-topics/antimicrobial-resistance) (**Fig. 4.1**). This new structural knowledge paves the way for rational drug design against this "superbug" and its relatives, and may have an impact on global health in the near future.

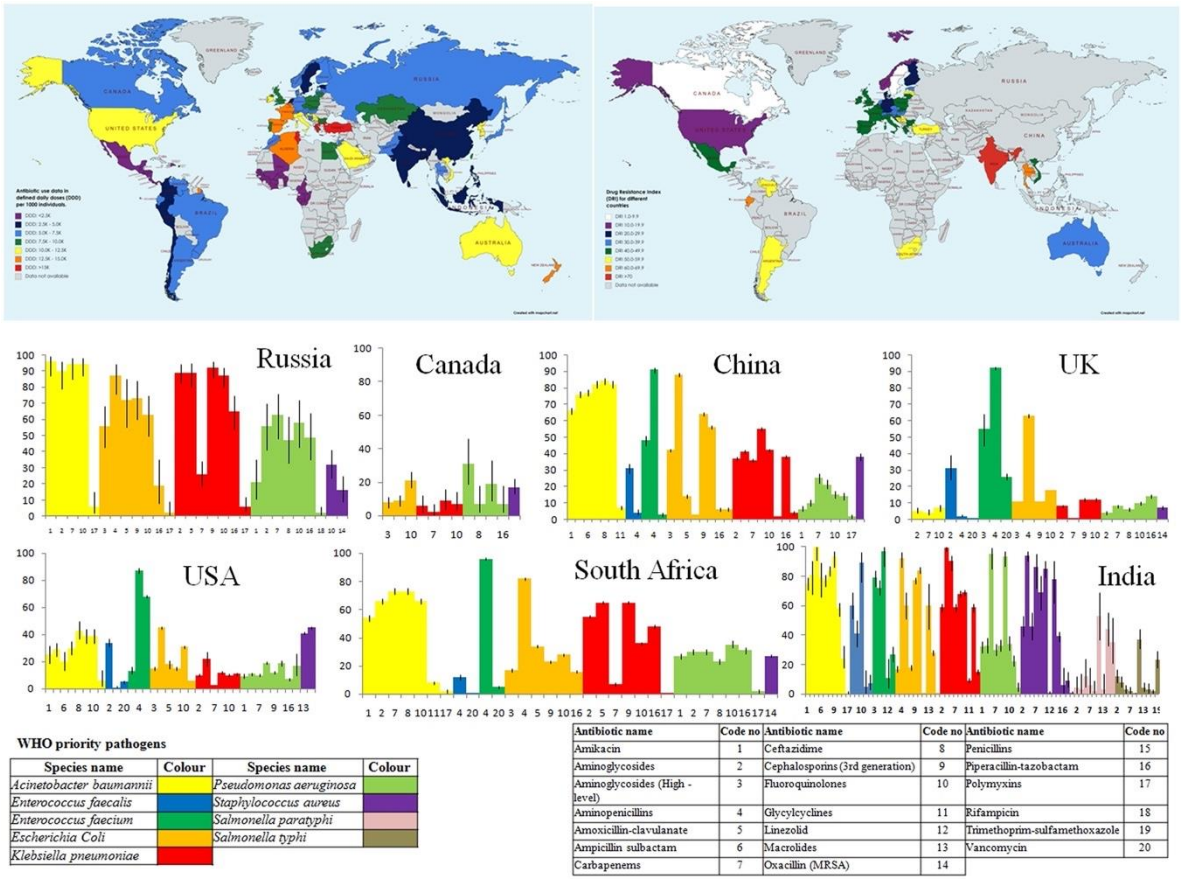

WHO priority pathogens

Species name	Colour	Species name	Colour
Acinetobacter baumannii		*Pseudomonas aeruginosa*	
Enterococcus faecalis		*Staphylococcus aureus*	
Enterococcus faecium		*Salmonella paratyphi*	
Escherichia Coli		*Salmonella typhi*	
Klebsiella pneumoniae			

Antibiotic name	Code no	Antibiotic name	Code no	Antibiotic name	Code no
Amikacin	1	Ceftazidime	8	Penicillins	15
Aminoglycosides	2	Cephalosporins (3rd generation)	9	Piperacillin-tazobactam	16
Aminoglycosides (High - level)	3	Fluoroquinolones	10	Polymyxins	17
Aminopenicillins	4	Glycylcyclines	11	Rifampicin	18
Amoxicillin-clavulanate	5	Linezolid	12	Trimethoprim-sulfamethoxazole	19
Ampicillin sulbactam	6	Macrolides	13	Vancomycin	20
Carbapenems	7	Oxacillin (MRSA)	14		

Figure 4.1. Antibiotic consumption rate in the world. *(**left**) Daily doses (DD) per 1000 individuals and (**right**) Drug Resistance Index (DRI) and antibiotics resistance in some selected countries. Data retrieved from The Center for Disease Dynamics, Economics and Policy. Drug Resistance Index map has been created from the date provided by [509]. Figure replicated from [510].*

4.2. HYPOTHESIS AND OBJECTIVES

The research developed in this chapter is based on the following hypothesis:

- The three dimensional structure of *Pa*CGL may show distinct features from its human homolog.
- These differences are expected to be mainly located at the active site, thus affecting the affinity of the enzyme for different substrates.
- The particular structural features of *Pa*CGL might explain its catalytic diversity.
- Similarly to human CGL, *Pa*CGL may be inhibited by small molecules different from those used to inhibit human CGL.
- *Pa*CGL is an attractive target to develop new antibiotics against multiresistant bacteria such as *Pseudomonas aeruginosa*.

The main objectives in this study were the following:

1. Elucidation of the crystal structure of cystathionine γ-lyase from *P. aeruginosa.*
2. Identification of the key catalytic residues in *Pa*CGL.
3. Comparative structural analysis of *Pa*CGL with other CGLs.
4. Identification of potential sites for specific inhibition of *Pa*CGL.

4.3. MATERIALS AND METHODS

4.3.1. Crystallization of *Pa*CGL

The *Pa*CGL protein was kindly expressed and purified by Prof. Tomas Majtan at the University of Colorado. Preliminary crystallization trials were carried out by the vapor diffusion technique in a sitting-drop format with 96-well MRC crystallization plates, using a variety of commercially screens available on the crystallization platform of the center (**Table 2.1** at section 2.3.5 of Chapter II). Screening plates were set-up in the high-throughput crystallization facility at CIC bioGUNE, and incubated at a constant temperature of 293 K. Drops consisted of 200 nL protein solution mixed with 200 nL precipitant solution and the reservoir volume was 50 µl; the protein concentration was 20 mg ml^{-1}. The successful condition was scaled-up in a hanging-drop format using 24-well VDX plates (Hampton Research) in a reservoir with drops consisting of 0.5 µl protein (protein concentration of 20 mg ml^{-1}) with 0.5 µl precipitant solution. This reservoir was composed by 9% v/v Polyethylene glycol 4000 and 0.1M sodium acetate pH 4.6 with a volume of 0.5 ml. The crystals were transferred to a crystallization buffer containing 9% (w/v) PEG 4000, 0.1M Sodium acetate pH 4.6, and 20% glycerol for a few seconds before being flash-cooled by directly immersing into the liquid nitrogen at 93 K.

4.3.2. Structural determination of *Pa*CGL by X-ray crystallography

The diffraction properties of the crystals were examined at beamlines ID29 of ESRF (Grenoble) and XALOC BL13 of Alba (Barcelona). Crystals were mounted for X-ray data collection using either Cryoloops (Hampton Research) or MicroMounts loops (MiTeGen). Datasets were collected over a range of 0.1- 0.25 ° and the distance to the detector was set to reach resolution data between 1.6-3.8Å depending on the crystal, and according to the diffraction parameters previously determined by several test images. Several data set were collected but only one allowed the structural determination of *Pa*CGL (**Table 4.1**). Diffraction data were processed using HKL2000 [511] or XDS [483] programs. The three-dimensional structure of *Pa*CGL was determined by MR method [488] with the Phaser-MR program[489] from Phenix Suite [500] using the coordinates of *Hs*CGL holoenzyme (PDB ID 2NMP) as initial search model [461]. After several cycles of refinement using Phenix.refine program [486] the geometric quality of the models was assessed with MolProbity [490] integrated in Phenix suite.

Model was built with Coot [487]. Figures were done with Pymol (http://www.pymol.org) and Chimera [106].

Table 4.1. Data collection parameters of PaCGL

Number of images	ΔΦ (°/image)	Beamline	λ (Å)	Exposure (sec)	Detector	Temperature (K)
3600	0.1	ALBA MX XALOC-BL13	1.1074	0.5	Dectris PILATUS 6M	100

4.4. RESULTS

4.4.1. Protein crystallization. Preliminary crystallographic studies

Crystallization of the C-*Pa*CGL protein (consisting of a histidine tail at the C-terminal end) was performed according to the protocol previously described in the Materials and Methods section 4.3.1. Briefly, the protein crystallized at a concentration of 20 $mg.mL^{-1}$ in 9% v/v polyethylene glycol 4000 and 0.1M sodium acetate pH 4.6, using a 1:1 ratio of protein dilution to reservoir dilution, with 0.5 µL protein and 0.5 µL precipitant. The C-*Pa*CGL crystals were soaked in a solution identical to the crystallization buffer but containing 20% glycerol as cryoprotectant, and then were flash frozen in liquid N_2. X-rays diffraction data were collected at lines ID29 from ESRF (Grenoble, France) and XALOC BL23 from Alba Syncrotron (Barcelona, Spain). The best dataset used to refine the final model showed a resolution of 2.0Å. The diffraction data were processed using HKL2000 [511] and XDS [483]. The lattice parameters (a=b= 79.30 and c=446.66; α=β=90° and γ=120°) are compatible with a trigonal crystal system. A preliminary analysis of the data sets was performed using the program CCP4 [512]. The plot of the self-rotation function was calculated using MOLREP[485]. At Chi=180° and Chi=120°, and shows two binary axes parallel to the a and b axes, and a ternary axis parallel to the c axis, respectively, consistent with a Laue -3m class (**Fig. 4.2**).

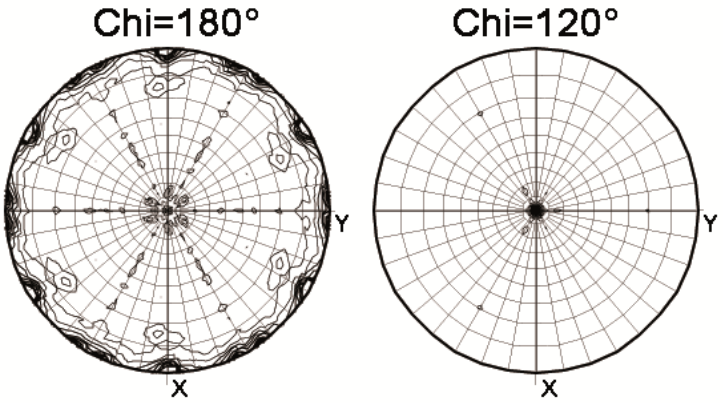

***Figure 4.2**. Plot of self-rotation function at Chi=180° and Chi=120° of the $P3_121$ PaCGL crystals.*

The crystal structure was determined by the molecular replacement (MR) technique, using the human CGL coordinates (PDB ID 2NMP) as the search model. Preliminary analysis of the diffraction data suggested the presence of four molecules in the asymmetric unit, likely corresponded to the functional biological unit (a dimer of dimers). The program used for the structural resolution was PHASER-MR, which is integrated into the PHENIX package[489]. The phases were obtained considering

as possible any of the spacegroups compatible with the Laue -3m class: P321, P312, $P3_121$, $P3_112$, $P3_221$ and $P3_212$. Refinement of the final model revealed that the correct space group was $P3_121$. The statistics of the data collection are summarized in **Table 4.2**.

Table 4.2. Statistics for data collection	***Pa*CGL**
PDB code	7BA4
Space group	$P3_121$
Unit cell (Å) (a, b, c)	79.30 79.30 446.67
Resolution (Å)(a, b, c)	54.45 – 1.99 (2.03 - 1.99)
CC ½ (%)	99.50 (77.50)
Redundancy	18.30 (10.60)
Completeness (%)	99.90 (98.80)
I/σ (I)	13.90 (2.90)
Wilson B-factor (Å²)	30.70
R_{merge}[a]	0.158 (0.780)
R_{meas}[b]	0.162 (0.820)
R_{pim}[c]	0.037 (0.247)
Refinement Total reflections Unique reflections R_{work}[d]/R_{free}[e]	 2060939 (58513) 112386 (5512) 0.160/0.205
No of non-hydrogen atoms Macromolecules Ligand (PLP)	 12573 15
Average B-factor (Å²) Macromolecules Ligands	 40.00 37.19
Ramachandran plot statistics (%) Res. in most favored regions In additional allowed regions In disallowed regions	 98.07 1.72 0.21
RMSDs Bonds length (Å)/ angle (°)	0.010/0.99
Rotamers outliers (%)	0.00
Clashcore	4.32
MolProbity score [f]	1.21

One crystal was used for each data set. Values in parentheses are for highest-resolution shell. R_{merge} [a] = $\Sigma_{hkl} \Sigma_i |I_i(hkl) - \langle I(hkl)\rangle| / \Sigma_{hkl} \Sigma_i I_i(hkl)$ (all I+ and I-); [b] $R_{meas} = \Sigma_{hkl} \Sigma_i |I_i(hkl) - \langle I(hkl)\rangle| / \Sigma_{hkl} \Sigma_i I_i(hkl)$ (all I+ and I-); [c] $R_{pim} = \Sigma_{hkl} \Sigma_i |I_i(hkl) - \langle I(hkl)\rangle| / \Sigma_{hkl} \Sigma_i I_i(hkl)$ (all I+ and I-); [d] $R_{work} = \Sigma ||Fo| - |Fc|| / \Sigma |Fo|$; [e] $R_{free} = \Sigma ||Fo| - |Fc|| / \Sigma |Fo|$, calculated using a random 5 % of reflections that were not included throughout refinement. [f] MolProbity score: 0.426 *ln(1+clashscore) + 0.33 *ln(1+max(0, rota_out|-1)) + 0.25 *ln(1+max(0, rama_iffy|-2)) + 0.5

4.4.2. Three- dimensional structure of *Pa*CGL

4.4.2.1. Overall structure

The final refined model of *Pa*CGL is consistent with folding of type I PLP-dependent enzymes, also found in other CGLs (human, yeast, bacteria), and enzymes like cystathionine γ-lyase (CGS), or cystathionine β-lyase (CBL) [513]. Each *Pa*CGL monomer consists of 394 amino acids distributed in three blocks: (i) an N-terminal domain (residues 1-62), (ii) a PLP-binding domain (residues 63-260), and (iii) a C-terminal domain (residues 261-394) (**Fig. 4.3**). The N-terminal domain consists of a small helix (α1, residues 15-21) and a long loop that interacts with the complementary subunit and is involved in oligomerization of the enzyme. As observed in *Tg*CGL, the PLP-binding domain is built up of a seven-stranded, mostly parallel, β-sheet (↑β1↓β7↑β6↑β5↑β4↑β2↑β3), with strand β7 antiparallel to the rest. This domain additionally contains eight α-helices (α 1 to 9) that flank the central β-sheet core. Importantly, this protein module hosts the catalytic PLP cofactor inside (**Fig. 4.3**). Lysine 208 covalently anchors PLP to the enzyme forming an internal aldimine (**Fig. 2.20** at the introduction section of the Chapter II). On the other hand, the C-terminal domain is organized into a four-stranded antiparallel β-sheet, that follows the sequence (↑β8↓β9↓β11↑β12), (numbering assigned according to human CGL), decorated with five α-helices (α10-14). One distinct feature of *Pa*CGL with respect to other CGLs (c.a *Hs*CGL, *Sc*CGL, *Sa*CGL, and *Tg*CGL) resides in the unwinding of helix α13 (residues 346-370) into an unusually unstructured extended loop (**Fig. 4.3**).

Similarly to all previously characterized CGLs, *Pa*CGL self assembles into a homotetramer [15,459–461,466] that is in fact, a dimer of dimers, formed by two equivalent 2-fold symmetric assemblies formed by subunits A-C and B-D, respectively. The four subunits are in turn very similar (*rmsd*= 0.132), and the two dimers are also related by a 2-fold axis. Thus, the tetramer shows an overall internal symmetry 222, and represents the functional biological unit (**Fig. 4.3, B**). In the tetramer, each subunit interacts with its neighbors through more than 10% of its surface area. Protomer A (with a solvent accessible area of 16626 Å^2) shares surface interactions of 1529 Å^2 (10%) and 2127 Å^2 (13%) with protomers B and C, respectively. Remarkably, an extended loop of the N-terminal region including residues 21-61, is key in stabilizing the tetrameric assembly. Subunit A interacts with subunit D through such extended loop L21-61 (**Fig. 4.4, C**) and is connected with promoter B through it, and also through helices α1, α9, α10 and α14 (**Fig. 4.4, A** and **B**). Likewise, protomer B

interacts with protomer D (and equivalently, A with C) to constitute the two structural dimers mentioned above.

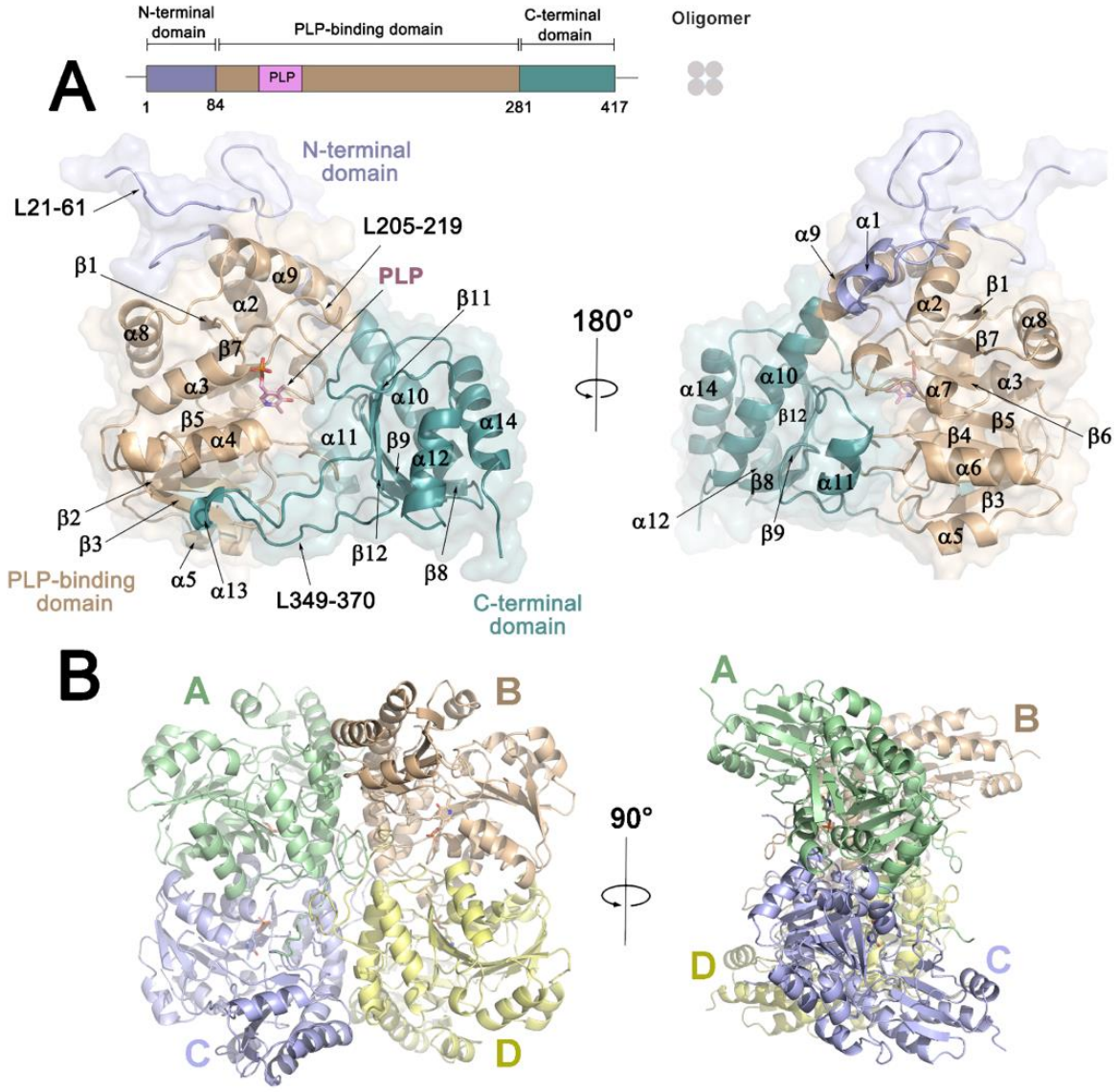

***Figure 4.3. Structure of PaCGL**. (**A**) Domain architecture and folding of the PaCGL monomer. The N-terminal domain (residues 1-62), the PLP-binding domain (residues 63-260), and the C-terminal module (residues 261-394), are colored in violet, brown, and dark green, respectively. PLP is in pink sticks. Grey circles represent the tetrameric state of PaCGL. (**B**) PaCGL tetramer.*

In summary, the *Pa*CGL dimers are stabilized by contacts mediated by the extended loop (L 21-61), and by helices α3, α4, and α8 (**Fig. 4.4, D** and **E**). In contrast with the CGLs from human, *T. gondii*, *S. maltophilia*, *S. aureus* and *L. plantarum*, residue Y56 does not interact with the phosphate moiety of PLP, but rather establishes an H-bond with the N-terminal residue Q45. This particular contact is possible thanks to the flexibility provided by residue G57 to the polypeptide main chain. Residue G57 of *Pa*CGL is usually substituted by a conserved serine in other CGLs (**Fig. 4.4, E**). A salt bridge between residues R254 and D215* from complementary monomers, helps to connect the A-B subunits (or the equivalent C-D protomers) (**Fig. 4.4, A** and **B**). This electrostatic contact is highly conserved in all CGLs enzymes and helps to sustain the tetrameric assembly. *Tg*CGL is an exception and shows hydrophobic interactions (residues L275 and C237, respectively) that play a similar stabilizing role. In addition, the CGLs tetramer is usually stabilized by complementary hydrophobic contacts located at the central part of the assembly. For example, in human CGL, this core involves residuesI41, L43, I250, Y253 and L254, whereas in *Pa*CGL is participated by residues I37, A39, F247, F250 and L251, donated from all monomers. Similar hydrophobic amino acids are present *S. cerevisiae* (residues I29, L31, F241, W244 and L245) or *Stenotrophonomas maltophilia* (residues I35, A37, F245, F248 and L249) CGLs [460,464]. Strikingly, the *Toxoplasma* enzyme (*Tg*CGL), behaves differently, and shows a more hydrophylic tetramer core (Y272 and Q268 occupy the equivalent position of L251 and F247 in *Pa*CGL, respectively).

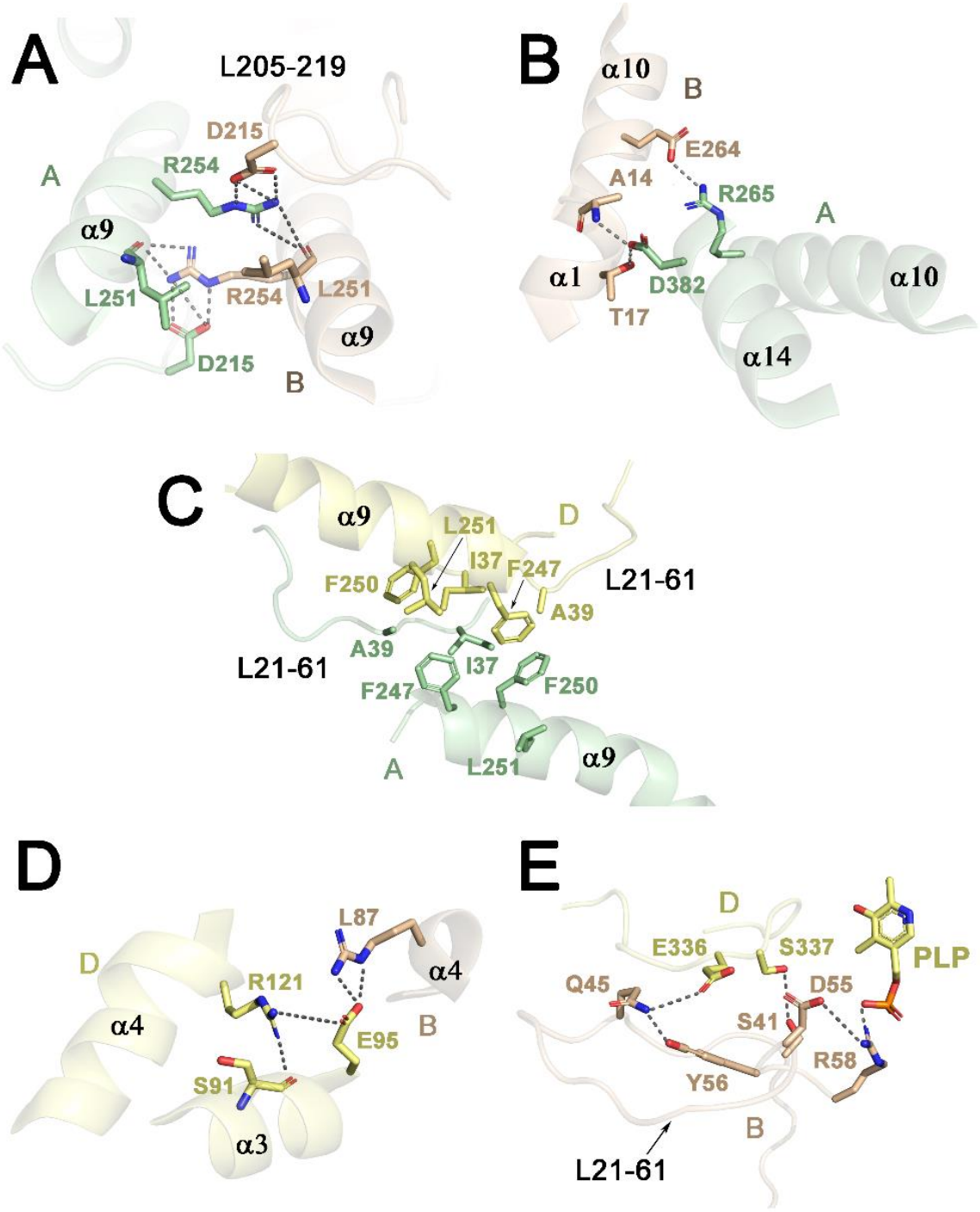

Figure 4.4. Interface interactions between PaCGL subunits. *(**A, B**) Main interactions between the interfacial helices of protomers A and B. (**C**) Hydrophobic interactions between subunits A and D located in the center of the tetramer. (**D, E**) Interfacial interactions between protomers B and D. The residues involved in each interaction are represented by sticks. Dotted lines highlight electrostatic interactions.*

4.4.2.2. Conformational state of *Pa*CGL

The structural alignment of *Pa*CGL assembly A-C (or B-D) with its equivalent from the apo state of human CGL in (*rmsd*= 2.76) shows that the active site is slightly more close in *Pa*CGL (**Fig. 4.5, A**). The superimposition of *Pa*CGL with the holo and apo states of the human enzyme showed that our crystallized *Pa*CGL corresponds to a holo-like conformation. As mentioned in the *Tg*CGL section, in general the main differences between apo- and holo-states reside in the orientation of helices α9, α10 and α12, as well as in loops L21-61, L108-113 and L206-215 (numbers corresponds to PaCGL) (**Fig. 4.5**). When the enzyme harbors the cofactor within the active site, these loops are collapse towards the PLP molecule, establishing electrostatic interactions that stabilize the orientation of the cofactor. In the PLP-free human enzyme, the N-terminal loop containing residues 24-65 appears mostly disordered, indicating the flexibility of this segment in the absence of PLP. Similarly, the most significant shifts in *Pa*CGL are observed at the level of residues Y110 and K208, whose location with respect to the HsCGL residues are separated by a distance of 7Å and 11Å, respectively. In general, PLP-binding enzymes have a conserved lysine that binds covalently to PLP. In *Pa*CGL, such lysine is K208 (**Fig. 4.5**). Finally, *Pa*CGL loop L108-113 in (L112-117 in *Hs*CGL) contains a helix that unwinds into a loop in *Hs*CGL when PLP is absent.

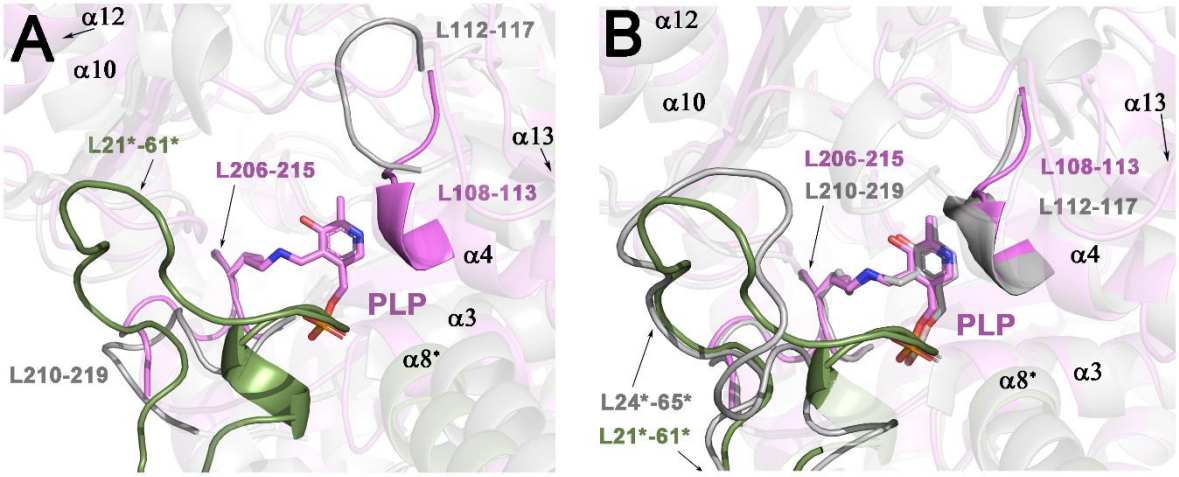

***Figure 4.5. Structural comparison of the holo and apo conformation of the human enzyme to PaCGL**. Superimposition of PaCGL (subunit A in pink and subunit B in green) and (**A**) human apo- enzyme (grey) or (**B**) human in the holo-state (grey). The loops involved in the conformational change are L21*-61*, L108-113 and L206-21of PaCGL and L24*-65*, L112-117 and L210-219 of HsCGL, highlighted in their respective colors. PLP and K212 (number refer to P.aeruginosa enzyme) are shown in sticks.*

A structural comparison of the tetrameric assemblies shows that *Pa*CGL and holo-*Hs*CGL have a more closed conformation than apo-*Hs*CGL (**Fig. 4.6, A-C**). In the PLP-free enzyme, the N-terminal loop (residues 21-61 in *Pa*CGL and 24-65 in *Hs*CGL) appears mostly disordered, and the hydrogen bond contacts between the four monomers are significantly reduced.

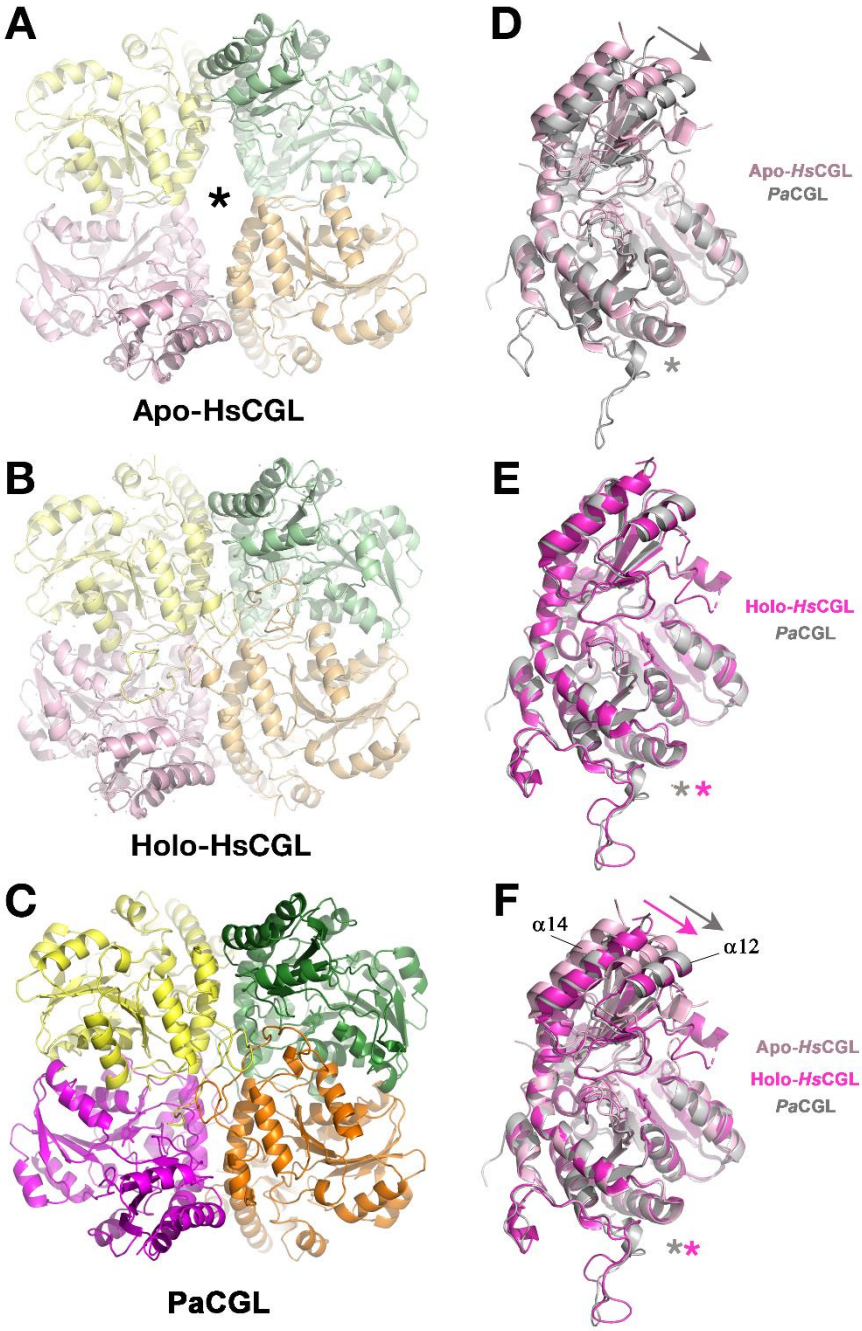

Figure 4.6. Tetrameric comparison of PaCGL with apo- and holo-HsCGL. *(**A**) Cartoon representation of tetrameric apo-HsCGL (no bound PLP), (**B**) holo-HsCGL (with PLP) and (**C**) PaCGL (with PLP). The asterisk represents the opening of the apo-enzyme at the center of apo-HsCGL. The protomers are represented in different colors. At the right of each panel is (**D**) the superimposition of monomeric PaCGL (grey) with apo-HsCGL (light pink); (**E**) PaCGL (grey) vs holo-HsCGL (dark pink) and (**F**) PaCGL (grey) vs holo- (dark pink) and apo-HsCGL (light pink). As depicted PaCGL basically reproduces the fold of holo-HsCGL.*

4.4.2.3. Catalytic site

PLP is a critical cofactor employed by the cystathionine γ-lyase family. In fact, former studies have shown that inhibition of PLP-dependent enzymes by the mentioned above molecules (PAG, AOO, etc) occurs mainly via interferences between the protein and the PLP cofactor, .The PLP-interacting residues are conserved across all CGLs and in *Pa*CGL are represented by Y110, R372, K208, S337 (substituted by N360 in *T. gondii*) and S205. Lysine K208 is covalently bound to PLP through its ε-amino group, and forms a Schiff- base linkage in the C4A position of PLP (**Fig. 4.7**). On the other hand, the orientation of PLP is fixed by H-bond interactions between its phosphate group and the main chains nitrogens of residues G86 and L87. The hydroxyl group of aminoacids S205 and T207 also stabilize the PLP phosphate moiety. Interestingly, the complementary subunit, additionally, interacts with O2P and O3P of PLP via the guanidine group of R58. Most CGLs also show interactions between the PLP and the conserved tyrosine of the neighbouring subunit. As earlier mentioned, in *Pa*CGL, this tyrosine (Y56) changes its orientation, losing its contact with the phosphate moiety (**Fig. 4.7**). Finally, the pyridoxal ring of PLP is stacked with the phenol ring of Y110. The N-atom of the pyridine ring H-bonds residue the carboxylate group of residue D183. R372, mediated by water molecules, forms an H-bond network with the hydroxyl C3 group of pyridoxal 5'-phosphate.

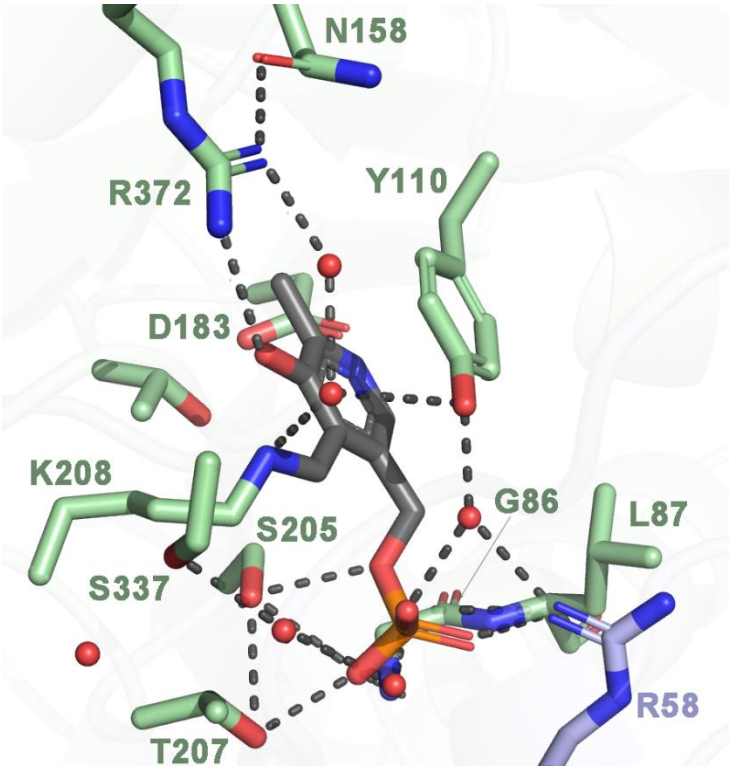

Figure 4.7. Active site of PaCGL. *Stick representation of residues which interacts with the PLP. Subunit A is in green and subunit B is in light blue. Interactions are represented in dashed lines. PLP is represented in grey. For clarity, the H-bond between D183 and PLP is not represented.*

4.4.2.4. Potential drug-binding sites

Our crystal structure of *Pa*CGL provides the first three-dimensional template of the enzyme. Once deciphered, we first wondered whether *Pa*CGL differs sufficiently from other CGLs as to be targeted independently with specific inhibitors. A preliminary analysis of the main surface cavities present in *Pa*CGL and in all CGL structures available in the Protein Database (PDB), indeed showed marked differences (**Fig. 4.8**). Interestingly, we found that the number and size of cavities was significantly different in each target protein. Moreover, the access to the identified clefts was characterized by amino acid residues with different physico-chemical properties (hydrophobicity, electrostatic profile, etc), as well as by distinct conformation of some secondary elements. For example, apo-*Hs*CGL clearly presented the largest entrance to the catalytic site, whereas *Tg*CGL, *Pa*CGL, *Bc*CGL or *Sc*CGL showed less accesibility. In addition, the PLP site was accessible from at least two different paths in some of the enzymes, like *Hs*CGL, *Sa*CGL, or *Sc*CGL, whereas a sole entrance was apparently present in other species such as *Pa*CGL or *Bc*CGL (CGL from *Bacillus cereus*, [465]). Among all these cavities (**Fig. 4.9**), we paid special attention on two clefts in particular that were recently identified in the CGL from *Staphylococcuss aureus* [15]. Both crevices, baptized as Area-1 and Area-2 by Shatalin and colleagues, present suitable dimensions to allow a small organic molecule to pass through. The Area-1 coincides with the catalytic site and is widely exposed to the solvent to facilitate the access of substrates. However, despite its relevance for the enzyme activity, this area has not been considered a suitable inhibition site to nullify the CGL of infectious pathogens. The underlying reason is that humans encode many non-functionally related PLP-dependent enzymes with very similar catalytic sites that could also exhibit affinity for a molecule designed against this zone. An unspecific drug-induced inhibition of these proteins would likely cause unwanted collateral effects, including the impairment of relevant metabolic and signaling pathways.

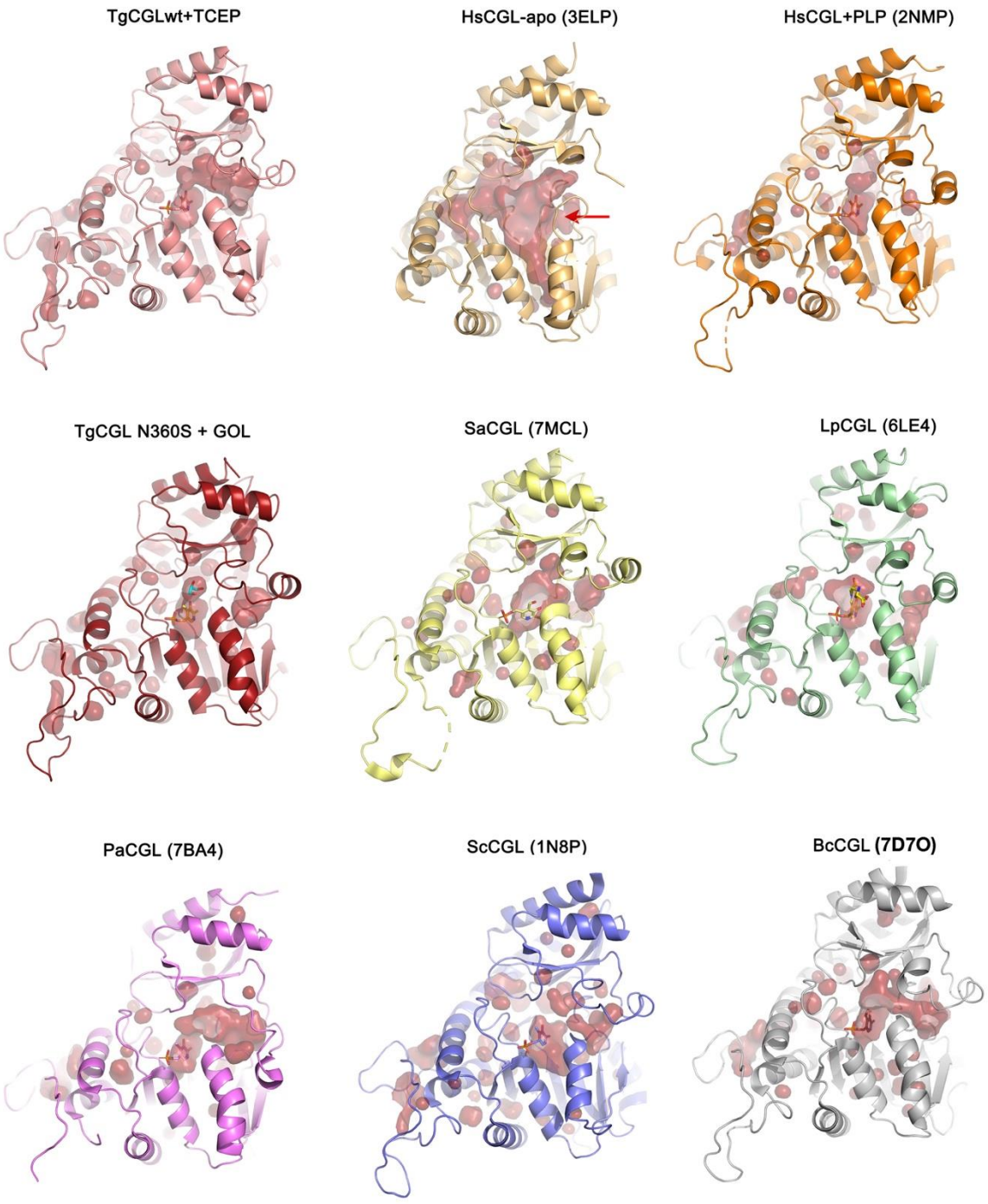

Fig. 4.8. Main surface cavities identified in CGLs whose 3D-structure is available *(by November, 2021). The figure shows the interior volume of the main clefts, coloured in red. Importantly, the number of cavities, their size and accessibility, are different in each enzyme, thus potentially offering the possibility of a specific targeting. The cavity detection radius and the cavity detection cut-off used to build this figure were 7 Å and 5 solvent radii, respectively (*http://www.pymol.org*).*

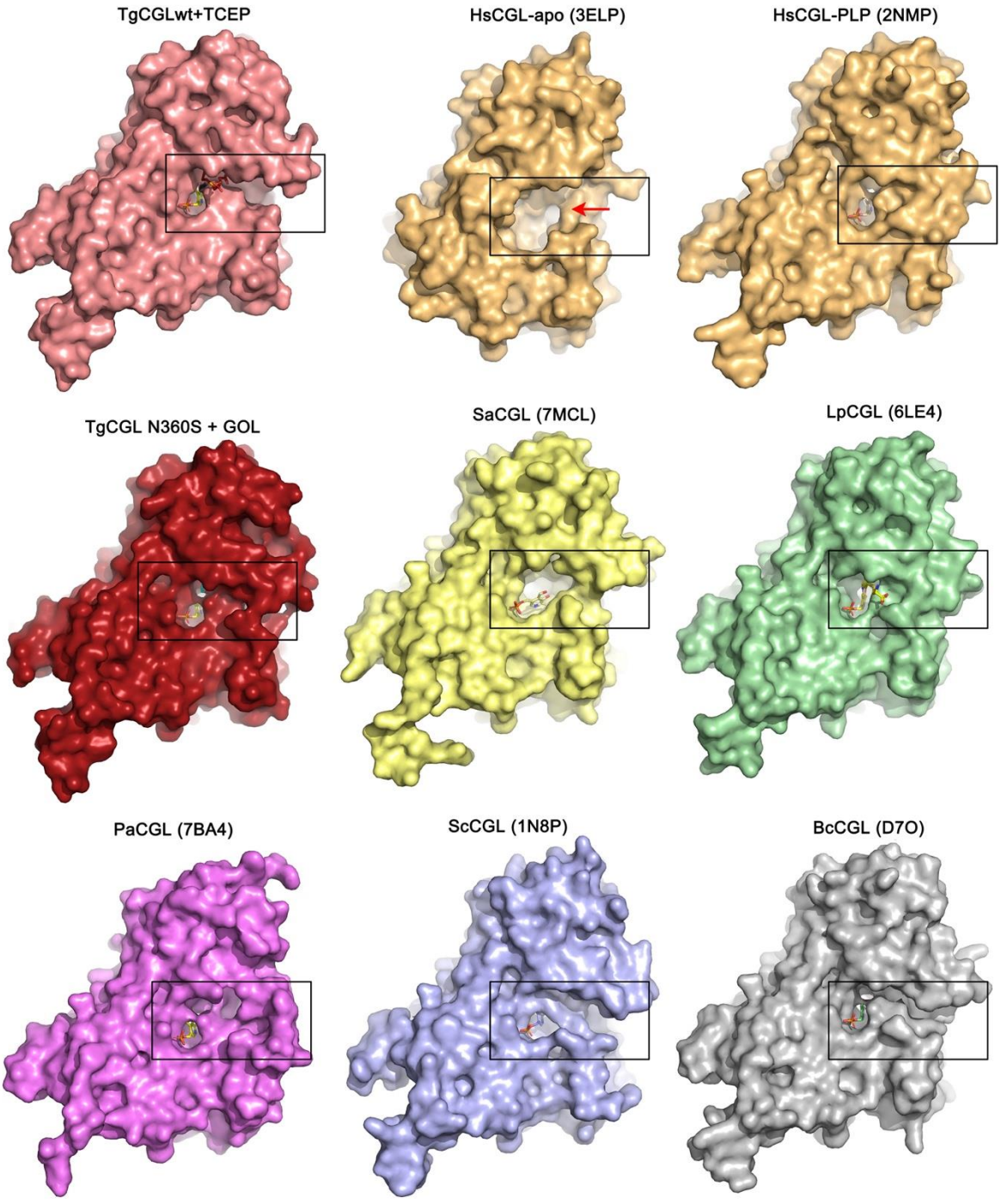

***Fig. 4.9. Main cavities found in CGLs**. External surface representation of all CGLs whose 3D-structure is available (by November, 2021). The catalytic cavity containing the PLP molecule (in sticks), and the Area-2 cleft (whose entrance is indicated with a red arrow) are framed.*

In turn, Area-2, is less voluminous and reachable through a channel whose access is usually limited by a bulky tyrosine residue (Y103 in *Sa*CGL; Y102 in *Bc*CGL). Some CGL enzymes lack this tyrosine, which is substituted by either another bulky hydrophobic residue (c.a. F114 in *Pa*CGL; F101 in *Lp*CGL), or alternatively a conserved asparagine (N137 in *Tg*CGL; N118 in *Hs*CGL). The presence of one residue or the other, not only determines the general characteristics of the entrance channel to Area-2 (volume, size, steric hindrance) but modulates the type of molecule (c.a an inhibitor) that can (or cannot) get into the Area-2 cavity, and consequently infer (or not) an inactivating effect on the corresponding enzyme.

On the other hand, two additional amino acids located at the bottom of the cavity, define the connecting gate between Area-2 and the catalytic site (Area-1): the first is a conserved histidine (H339 in *Sa*CGL; H356 in *Hs*CGL; H338 in *Bc*CGL; H337 in *Lp*CGL; H353 in *Pa*CGL; and H376 in *Tg*CGL) (**Fig. 4.10**), and the second is a conserved tyrosine that packs against the pyridine ring of PLP and helps to orient the cofactor (Y99 in *Sa*CGL; Y114 in *Hs*CGL; Y98 in *Bc*CGL; Y97 in *Lp*CGL; Y110 in *Pa*CGL; and Y133 in *Tg*CGL, respectively). As shown below in Fig. 4.10, the volume and access of Area-2 differs significantly in *Sa*CGL, *Pa*CGL and *Tg*CGL and (**Figs. 4.11, 4.12** and **4.13**). In apo-*Hs*CGL (no PLP cofactor present), this tyrosine (Y114) appears displaced towards the bottom of the Area-2 cavity, due to a partial unwinding of the last turn of helix α4. Upon binding of PLP (holo state of the enzyme), the last turn of this same helix recovers its helicity and reorients the tyrosine towards the interior of the catalytic Area-1 cavity. This conformational change is thought to function as an access gate from Area-2 to the catalytic site [15].

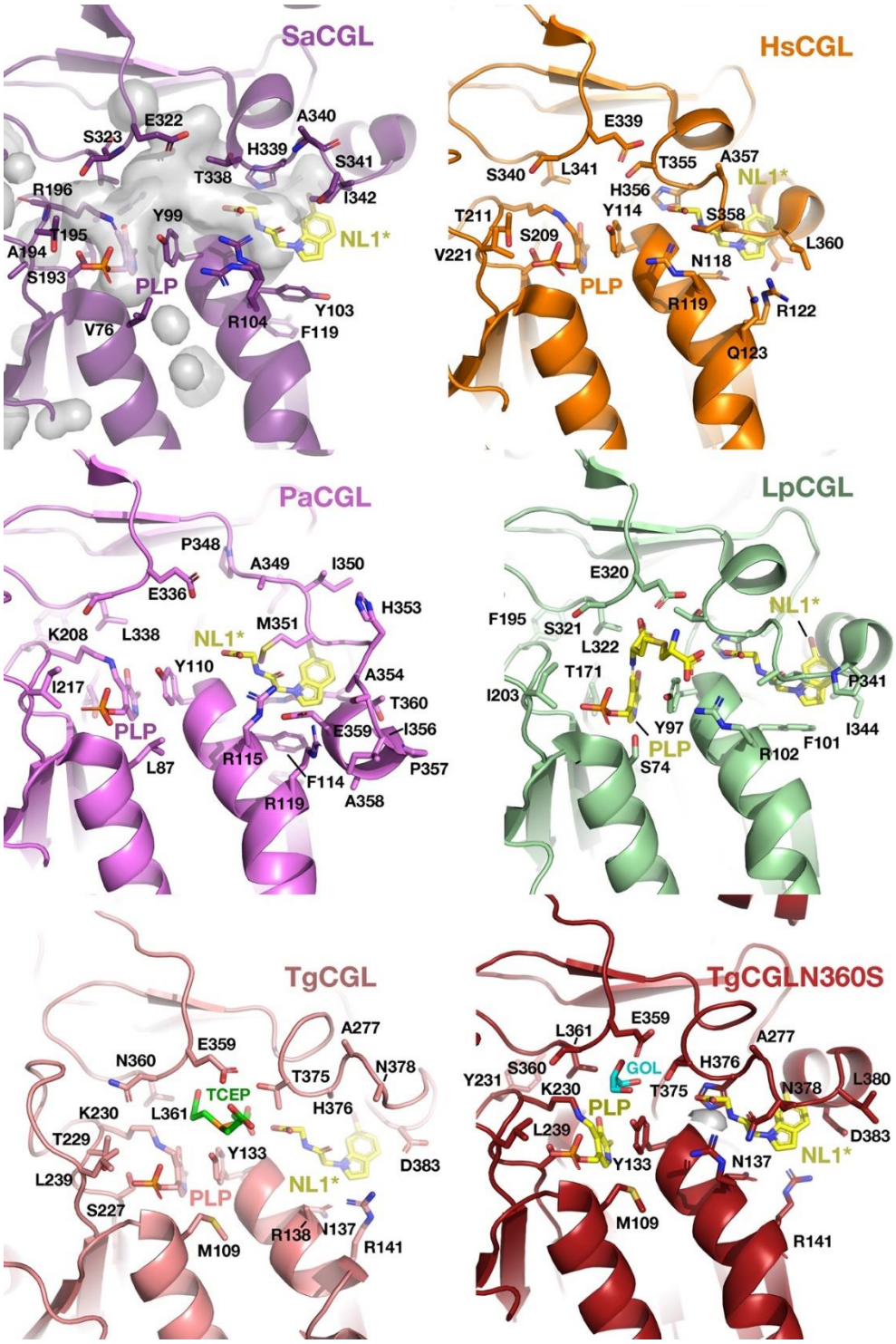

Figure 4.10. Interaction of NL1 with known CGLs*. The picture shows the potential location of NL1 inhibitor within the Area-2 cavity of all known CGLs. The position of the molecule is derived from the detail superimposition of the SaCGL-NL1 complex* [15] *with the corresponding proteins. Note the steric hindrance potentially exerted over the inhibitor by some residues in several enzymes (c.a. PaCGL M351; TgCGL-N378; LpCGL-P341-I344)*

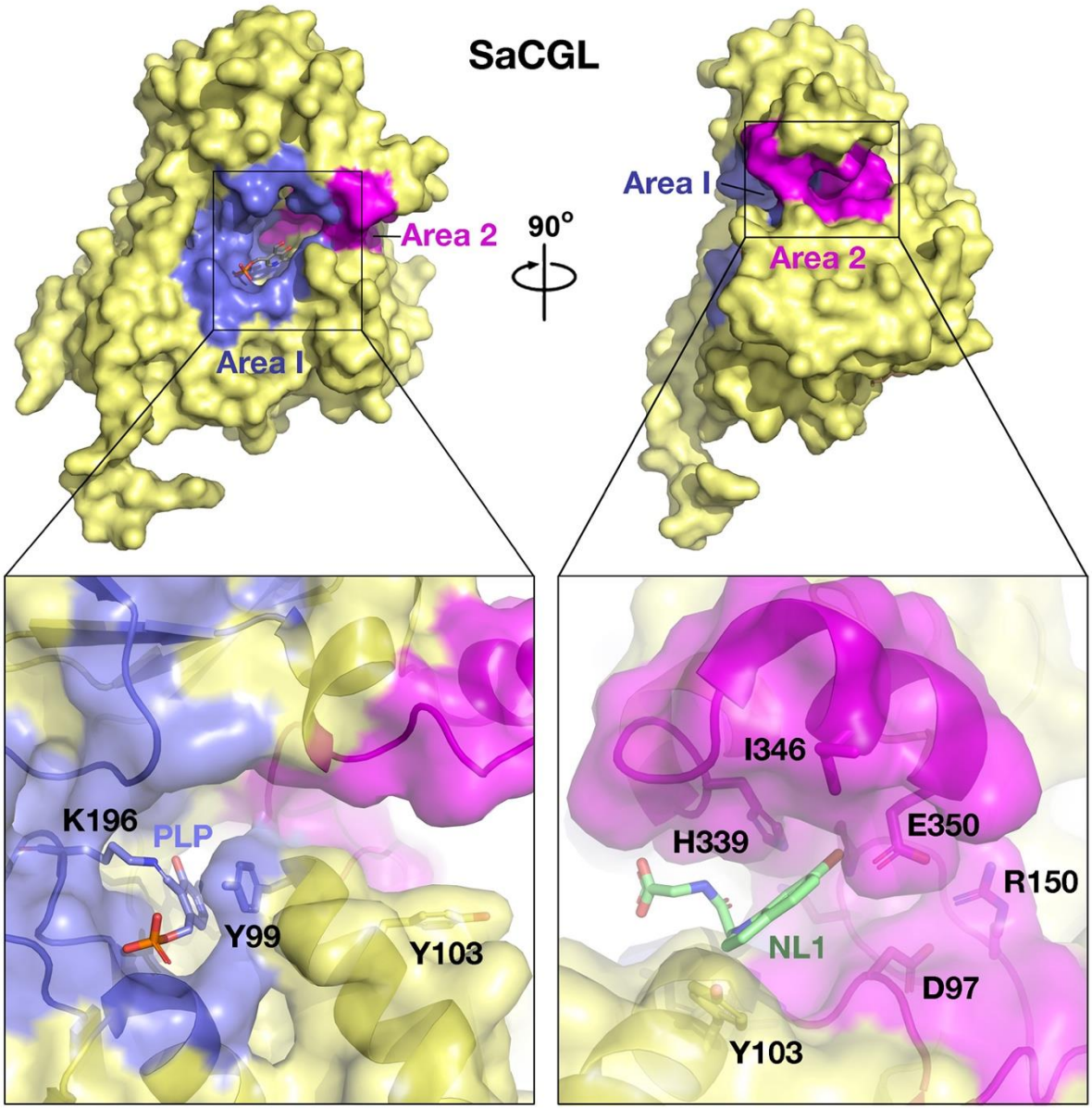

Figure 4.11. Areas -1 and -2 in SaCGL*. (**up**) Surface representation of the SaCGL monomer. Areas 1- and 2- are colored in blue and magenta, respectively. (**down**) Main amino acid residues within the cavities. PLP is in sticks.*

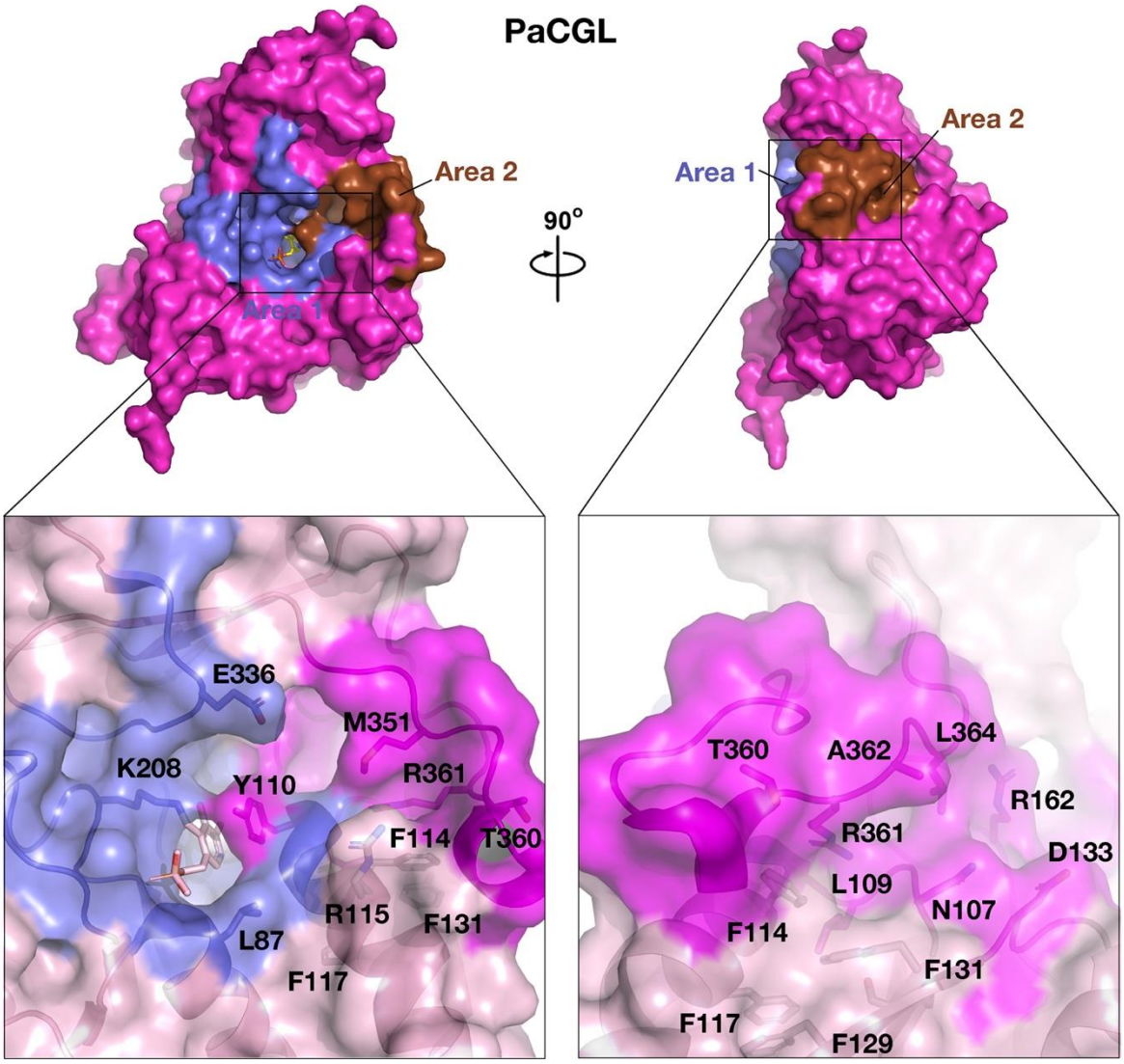

Figure 4.12. Areas -1 and -2 in PaCGL*. (**up**) Surface representation of the PaCGL monomer. Areas 1- and 2- are colored in blue and magenta, respectively. (**down**) Main amino acid residues within the cavities. PLP is in sticks.*

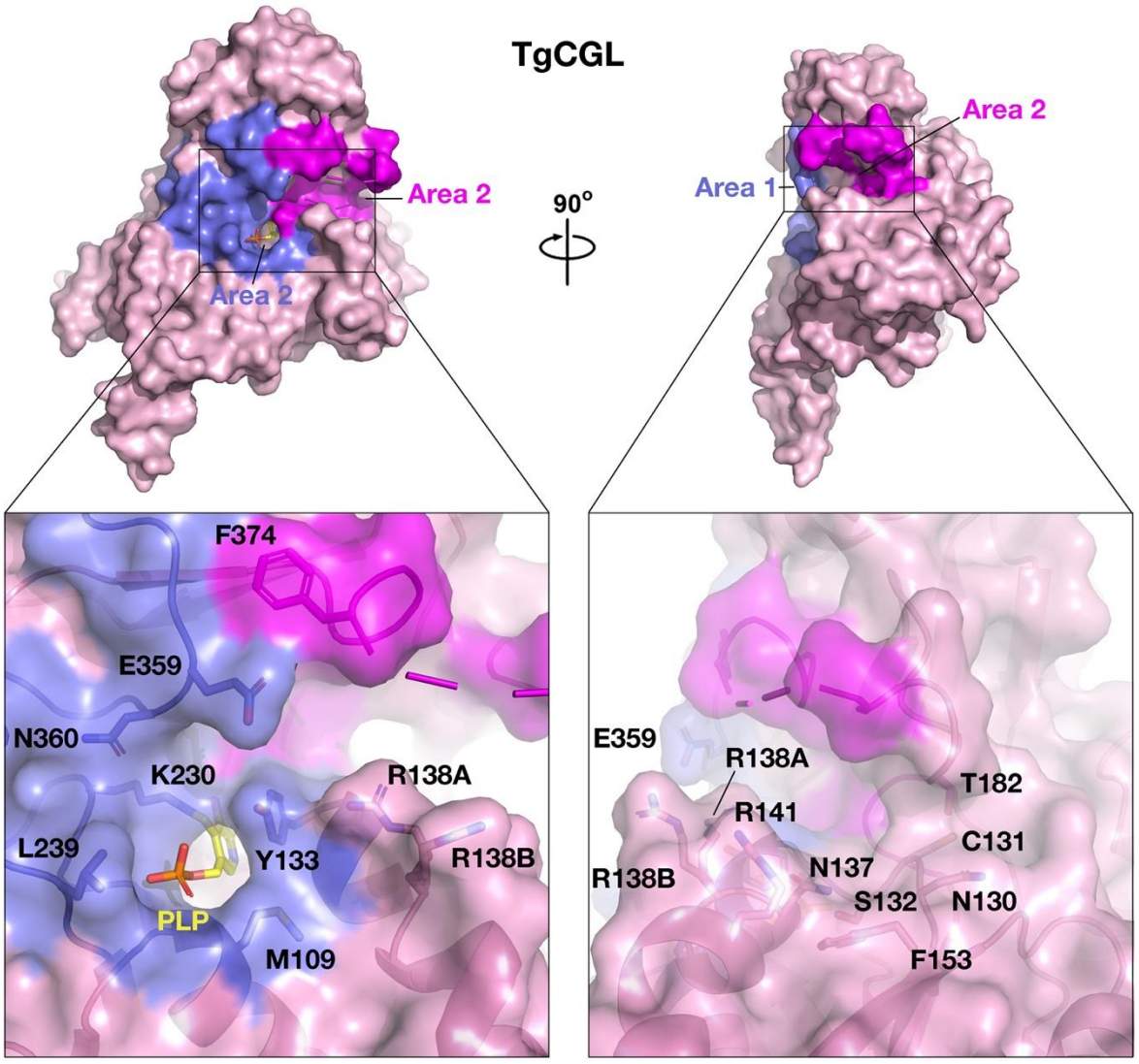

Figure 4.13. Areas -1 and -2 in TgCGL*. (**up**) Surface representation of the TgCGL monomer. Areas 1- and 2- are coloured in blue and magenta, respectively. (**down**) Main amino acid residues within the cavities. PLP is in sticks.*

As mentioned above, Area-2 was recently postulated as a promising druggable site to host small hydrophobic molecules. This fact was indeed confirmed by Shatalin *et al.*, by determining the crystal structure of *Sa*CGL in complex with three independent compounds (named as NL1, NL2 and NL3). Despite chemical and conformational differences, all three drugs were found to bind to the same site (Area-2) and inhibit *Sa*CGL similarly. The drugs bind sandwiched between two important aromatic residues: a histidine (H339) and a tyrosine (Y103 (α4)) (**Fig. 4.14, A**). The latter is crucial in stabilizing the inhibitor within the cavity through a π-stacking interaction. Of note, it was found that the interactions between the inhibitor, the histidine and the tyrosine, block the conformational rearrangement of Y99 (numbers corresponding to *Sa*CGL), an indispensable residue for enzymatic catalysis (**Fig. 4.14, A**). Moreover, Shatalin *et al*. also reported that compounds NL1, NL2, and NL3 impair the H_2S production in live *P. aeruginosa* PA14 [15].

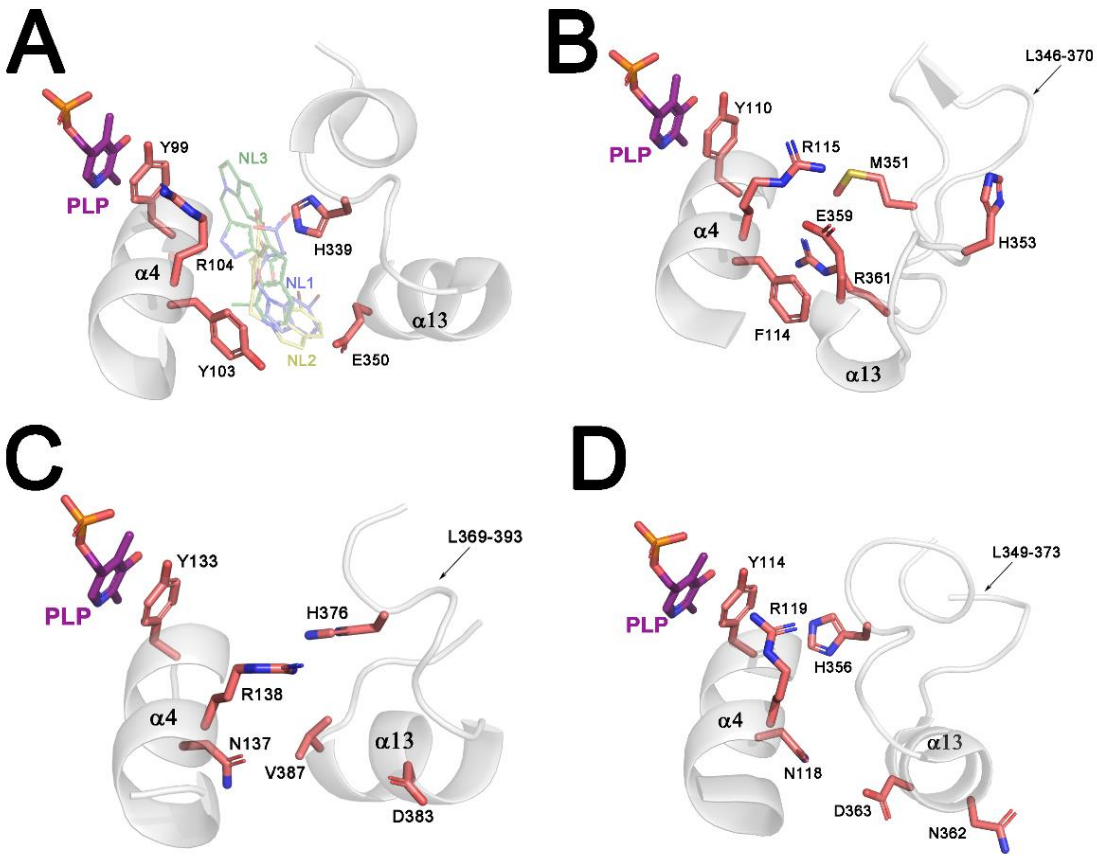

Figure 4.14. Interactions at the drug binding-site *in SaCGL (**A**), PaCGL (**B**), TgCGL (**C**) and HsCGL (**D**). Stick representation of residues involved in the binding with NL1 (blue), NL2 (yellow) and NL3 inhibitors in SaCGL (**A**). Residues involved in a potential drug binding-site of PaCGL (**B**), TgCGL (**C**) and HsCGL (**D**).*

In apparent conflict with the ability to be inactivated by the NL compounds, our crystal structure of *Pa*CGL reveals that the long flexible loop containing the equivalent histidine (H353), adopts a different conformation than in *S. aureus* (**Fig. 4.14, B**). The direct consequence of this structural change is a reorientation of residues M351, E359 and R361 in *Pa*CGL, which point towards the interior of the Area-2 cavity, there where the inhibitor would be potentially located. In principle, this distinct orientation of H353 would disfavour the stabilization of NL1, NL2 or NL3 within the cavity in *Pa*CGL. In contrast, the aromatic properties of Y103 in *Sa*CGL are preserved by its homolog F114 in *Pa*CGL (**Fig. 4.14, B**). These seemingly opposing structural characteristics of *Pa*CGL to accommodate NL molecules in Area-2, suggest the need of a structural rearrangement of several residues within the cavity to avoid the otherwise steric hindrance exerted by these residues and explain the proven inhibition ability of the molecules. On the other hand, the structural comparison of the bacterial enzymes with human CGL, revealed a fundamental difference, consisting in the presence of an asparagine (N118) in humans instead of the mentioned aromatic amino acid (F114 in *Pa*CGL and Y103 in *Sa*CGL). The immediate consequence is the disruption of the π-stacking interaction maintained between the pathogen enzymes and the inhibitor. In principle, these differences would explain the lower effect exerted by NLs in in mammals (**Fig. 4.14, D**). Remarkably, a detailed superimposition of the Area-2 sites of all 3D-structures known of CGLs (**Fig. 4.10**), with the herein presented *Pa*CGL and *Tg*CGL, led us found that the homolog asparagine present in humans is conserved in *T. gondii* (N137), suggesting that *Tg*CGL is likely unable to bind this type of compounds (**Fig. 4.14, C**). In other words, neither the endogenous synthesis of H_2S, nor the intracellular oxidative stress, would be altered by NLs in the causative agent of toxoplasmosis, suggesting the need of further investigation focused in alternative cavities or compounds.

4.5. DISCUSSION

The development of adjuvant drugs that increase oxidative stress in pathogenic organisms [14,15], has recently re-emerged as an effective strategy for the treatment of persistent bacterial infections. The unjustified abuse of common antibiotics for decades has allowed numerous bacteria to become "superbugs", with multiresistance abilities, thus complicating or completely causing treatments of infections to fail. This unfortunate situation forces us to urgently search for novel therapeutic alternatives, to avoid millions of deaths in an immediate future [514]. Among these superbacterias is the Gram-negative bacteria *Pseudomonas aeruginosa*, which nowadays is considered one of the main causative agents of complicate hospital infections. As discussed in previous sections, *P.aeruginosa* encodes the two enzymes of the reverse transsulfuration pathway, which is a principal route used by this, and many other pathogens to endogenously produce H_2S and reduce its intracellular oxidative stress.

Of the two enzymes (*Pa*CBS and *Pa*CGL), PaCGL is able to perform γ-elimination of cystathionine and release cysteine, α-ketobutyrate and pyruvate. At the moment, it is unknown whether it is additionally able to perform β-elimination of Cth as has been described for other CGLs, such as *Lp*CGL, *Sc*CGL or the artificial humanized mutant *Tg*CGLN360S that we have also described in this thesis. The crystal structure that we have elucidated of *Pa*CGL has allowed us to compare relevant areas of this enzyme with the equivalent zones of its bacterial counterparts, as well as with the human enzyme, and has unveiled structural features that differentiate it, and potentially offer the possibility of drugging it in the near future.

One of these differences, for example, concerns the variable volume of the catalytic cavity, which is larger in some enzymes (*Pa*CGL (223 $Å^3$); *Sa*CGL (220 $Å^3$) or *Tg*CGL (280 $Å^3$) than in others (CGLs from yeast, *L. plantarum* or the *Tg*CGLN360S mutant (with a value ~145 $Å^3$). Interestingly, some authors have observed that CGLs catalyzing the γ-elimination of Cth require a larger space in the active center than those performing the β-elimination of this substrate. The underlying reason is the formation of a bulkier reaction intermediate in the first process [466]. Based on this criterion, the *Pa*CGL enzyme should show similar catalytic activities to those of *T. gondii* CGL (experiments still in progress).

Our study has also revealed that, despite being very similar in amino acid sequence and overall three-dimensional structure (c.a sequence identity *Pa*CGL-*Hs*CGL= 45%), *Pa*CGL shows unique peculiarities that are not present in any other CGL enzyme whose crystal structure is known. For example, the L346-370 loop is disordered and more widespread in *Pa*CGL than in any other CGL (**Fig. 4.3, A**). This feature has also been described in other functionally unrelated PLP-dependent enzymes of type I, such as cystathionine γ-synthase from *E. coli* (*e*CGS; PDB ID 1CS1), in which this unusually long loop (residues 336-358) causes a narrowing of the active site [475]. In *e*CGS, this steric effect affects both, substrate binding and product release [475]. *Pa*CGL shows an even more extended loop than *e*CGS, making this region of the catalytic site much narrower. At such narrowed zone, *Pa*CGL does not contain catalytically important residues or amino acids directly involved in substrate binding, but rather influences the overall shape and electrostatic environment of the catalytic site.

Another intriguing difference that we have detected in *Pa*CGL is the orientation of the Y56 tyrosine. In all CGLs except *P. aeruginosa*, the tyrosine in the equivalent position forms a hydrogen bond with one of the PLP phosphates. Instead, in *Pa*CGL, Y56 is oriented towards the inside of the N-terminal loop (residues 21-61), possibly favored by the presence of a glycine (G57), not found in any other CGL that allows a turn in that region of the loop. Also upstream of this tyrosine is aspartate D55 (E59 in human). Surprisingly, this residue is usually a glutamate in all CGLs, with the exception of *T. gondii* (S77) and *P. aeruginosa* (D55). *e*CGS, also has an aspartate at the equivalent position (D45). A mutational analysis in *e*CGS reported that substitution of this residue leads to slight kinetic differences, showing lower transamination activity [506]. This suggests that this residue does not directly participate in substrate binding, but does contribute to the catalytic site architecture and substrate positioning [506]. In yeast and humans, the glutamate located at the position corresponding to D55 of *Pa*CGL (E59 in humans and E48 in yeast), together with another glutamate (E339 or E333 in humans and yeast, respectively) coordinates the cysteinyl moiety of Cth, forming a negatively charged area [460,505]. Substitutions at E48 in yeast CGL do not influence the specificity of the reaction or substrate binding, as all mutations exhibit near native-like kinetic parameters [472]. In *Pa*CGL, the shorter side chain of D55, next to the conserved residue E336 (E333 in yeast; E339 in humans), helps to maintain the negative charge in this area of the catalytic cavity. Future experiments will be necessary to determine how this residue influences enzymatic catalysis of *Pa*CGL using Cth as a substrate. Nevertheless, measurements performed on native *Pa*CGL, have shown that H_2S levels are

not affected despite the presence of an aspartate at this position, suggesting that residue D55 does not influence the β-elimination reaction of Cysteine [15].

As discussed above, previous studies have demonstrated the pivotal role of CGL in H_2S biogenesis in *P. aeruginosa* and *S. aureus* [14,15]. Likewise, the effect of three promising CGL inhibitors that potentiated the effect of existing antibiotics on these bacteria has been reported [15]. The three-dimensional structure of cocrystallized *Sa*CGL in the presence of the three inhibitors (NL1, NL2 and NL3) revealed the binding site of the inhibitors (**Fig. 4.14**). This binding site, Area-2, showed the presence of two key residues in the stabilization of these compounds, Y103 and H376. Particularly, the Y103A mutation, or even the humanized Y103N variant abolished *Sa*CGL activity, demonstrating the critical role of possessing an aromatic amino acid at position 103 [15]. The crystal structure of these *Sa*CGL mutants (Y103A, Y103N) in the presence of NL1 and NL2 revealed weak or no interaction of the inhibitors with the protein [15]. Strikingly, mutant *Sa*CGL H339A shared the same H_2S production ability than the native enzyme and NL3 inhibited this variant similarly to the *wt*-protein [15], suggesting a less relevant role of this histidine residue. Our crystal structure of *Pa*CGL has allowed us to know the exact location of residue F114, which occupies the conserved equivalent position of residue Y103 in *Sa*CGL. Intriguingly, the conserved histidine H353 of *Pa*CGL is oriented differently from the equivalent histidine residue of *Sa*CGL (**Figs. 4.10** and **4.14**). Although the use of these inhibitors in *Pa*CGL has been shown to reduce the production of endogenous H_2S levels in *Pseudomonas* strain PA14, structural features found at the inhibitor binding site may provide a possible explanation as to why *Pa*CGL exhibits an IC50 with NL3 of 1.2 uM versus 0.7 uM in *Sa*CGL [15]. On the other hand, the presence of an asparagine in *T. gondii* at position 137 (conserved in human) suggests that the inhibition of the protozoan would be less efficient, since it lacks an aromatic residue in that region (as it occurs in the human enzyme) (**Figs. 4.10** and **4.14**).

In summary, the results reported in this chapter have allowed us to unveil the main structural features of the *P. aeruginosa* CGL enzyme. Its recent involvement in H_2S production in the pathogen has made it a pharmacological target of great interest. The knowledge of its structural characteristics opens the window to the development of new inhibitors that sensitize this superbacterium against the action of antibiotics. Likewise, the mechanism of inhibition of the drugs already discovered against this enzyme, can now be improved.

4.6. CONCLUSIONS

1. We have elucidated the crystal structure of full-length cystathionine γ-lyase from the Gram-negative bacteria *Pseudomonas aeruginosa,* a multidrug resistant bacteria classified as a critical priority pathogen by the World Health Organization.

2. Similarly to other CGLs, *Pa*CGL is built up of three distinguishable structural domains. The central one constitutes the catalytic module and shows subtle features with respect to its homologs.

3. *Pa*CGL self-associates forming a dimer of dimers with internal symmetry 222. The overall assembly found in our crystals corresponds to the "closed" assembly characteristic of the holo-(PLP-bound) state of human CGL.

4. A comparative analysis of *Pa*CGL with its relatives has helped us to explain the distinct effects exerted by three inhibitors (NL compounds) with respect to the human and the *S. aureus* CGLs.

5. Our *Pa*CGL structures pave the way for the structure-guided design of new antibiotics, or adyuvants of antibiotics, to treat recurrent infections caused by *Psedomonas aeruginosa* or related pathogens, that caused millions of deaths worldwide.

BIBLIOGRAPHY

BIBLIOGRAPHY

(1) Infectious Diseases Kill over 17 Million People a Year: WHO Warns of Global Crisis. *Indian Pediatr.* **1996**, *33* (7), 617-23.

(2) Nikaido, H. Multidrug Resistance in Bacteria. *Annu. Rev. Biochem.* **2009**, *78* (1), 119–146. https://doi.org/10.1146/annurev.biochem.78.082907.145923.

(3) van Duin, D.; Paterson, D. L. Multidrug-Resistant Bacteria in the Community. *Infect. Dis. Clin. North Am.* **2016**, *30* (2), 377–390. https://doi.org/10.1016/j.idc.2016.02.004.

(4) McArthur, D. B. Emerging Infectious Diseases. *Nurs. Clin. North Am.* **2019**, *54* (2), 297–311. https://doi.org/10.1016/j.cnur.2019.02.006.

(5) Weber, D. J.; Rutala, W. A.; Fischer, W. A.; Kanamori, H.; Sickbert-Bennett, E. E. Emerging infectious diseases: Focus on infection control issues for novel coronaviruses (Severe Acute Respiratory Syndrome-CoV and Middle East Respiratory Syndrome-CoV), hemorrhagic fever viruses (Lassa and Ebola), and highly pathogenic avian influenza viruses, A(H5N1) and A(H7N9). *Am. J. Infect. Control.* **2016**, *44* (5), e91- e100. https:// doi: 10.1016/j.ajic.2015.11.018

(6) Scallan, E.; Hoekstra, R. M.; Angulo, F. J.; Tauxe, R. V.; Widdowson, M. A.; Roy, S. L.; Jones, J. L.; Griffin, P. M. Foodborne Illness Acquired in the United States-Major Pathogens. *Emerg. Infect. Dis.* **2011**, *17* (1), 7–15. https://doi.org/10.3201/eid1701.P11101.

(7) Tack, D. M.; Ray, L.; Griffin, P. M.; Cieslak, P. R.; Dunn, J.; Rissman, T.; Jervis, R.; Lathrop, S.; Muse, A.; Duwell, M.; *et al*. Preliminary Incidence and Trends of Infections with Pathogens Transmitted Commonly Through Food — Foodborne Diseases Active Surveillance Network, 10 U.S. Sites, 2016–2019. *Morb. Mortal. Wkly. Rep.* **2020**, *69* (17), 509-514. https://doi.org/10.15585/mmwr.mm6917a1.

(8) Jones, J. L.; Parise, M. E.; Fiore, A. E. Neglected Parasitic Infections in the United States: Toxoplasmosis. *Am. J. Trop. Med. Hyg.* **2014**, *90* (5), 794–799. https://doi.org/10.4269/ajtmh.13-0722.

(9) Aguirre, A. A.; Longcore, T.; Barbieri, M.; Dabritz, H.; Hill, D.; Klein, P. N.; Lepczyk, C.; Lilly, E. L.; McLeod, R.; Milcarsky, J.; *et al*. The One Health Approach to Toxoplasmosis: Epidemiology, Control, and Prevention Strategies. *Ecohealth* **2019**, *16* (2), 378–390. https://doi.org/10.1007/s10393-019-01405-7.

(10) Wang, Z. D.; Liu, H. H.; Ma, Z. X.; Ma, H. Y.; Li, Z. Y.; Yang, Z. Bin; Zhu, X. Q.; Xu, B.; Wei, F.; Liu, Q. Toxoplasma Gondii Infection in Immunocompromised Patients: A Systematic Review and Meta-Analysis. *Front. Microbiol.* **2017,** *8*, 389. https://doi.org/10.3389/fmicb.2017.00389.

(11) Flegr, J.; Horáček, J. Negative Effects of Latent Toxoplasmosis on Mental Health. *Front. Psychiatry.* **2020,** *10*, 1012. https://doi.org/10.3389/fpsyt.2019.01012.

(12) CDC. Antibiotic Resistance Threats in the United States, 2019. Atlanta, GA: U.S. Department

of Health and Human Services, CDC; 2019.

(13) Pang, Z.; Raudonis, R.; Glick, B. R.; Lin, T. J.; Cheng, Z. Antibiotic Resistance in Pseudomonas Aeruginosa: Mechanisms and Alternative Therapeutic Strategies. *Biotechnol. Adv.* **2019**, *37* (1), 177–192. https://doi.org/10.1016/j.biotechadv.2018.11.013.

(14) Shatalin, K.; Shatalina, E.; Mironov, A.; Nudler, E. H2S: A Universal Defense against Antibiotics in Bacteria. *Science.* **2011,** *334* (6058), 986-90. https://doi.org/10.1126/science.1209855.

(15) Shatalin, K.; Nuthanakanti, A.; Kaushik, A.; Shishov, D.; Peselis, A.; Shamovsky, I.; Pani, B.; Lechpammer, M.; Vasilyev, N.; Shatalina, E.; *et al*. Inhibitors of Bacterial H2S Biogenesis Targeting Antibiotic Resistance and Tolerance. *Science.* **2021**, *372* (6540), 1169–1175. https://doi.org/10.1126/SCIENCE.ABJ0434.

(16) Pal, V. K.; Bandyopadhyay, P.; Singh, A. Hydrogen Sulfide in Physiology and Pathogenesis of Bacteria and Viruses. *IUBMB Life.* **2018**, *70* (5), 393–410. https://doi.org/10.1002/iub.1740.

(17) Kimura, H. Signaling Molecules: Hydrogen Sulfide and Polysulfide. *Antioxid. Redox Signal.* **2015**, *22* (5), 362–376. https://doi.org/10.1089/ars.2014.5869.

(18) Pechkova, E.; Nicolini, C. From Art to Science in Protein Crystallization by Means of Thin-Film Nanotechnology. *Nanotechnology.* **2002**, *13* (4), 460. https://doi.org/10.1088/0957-4484/13/4/304.

(19) Chayen, N. E. Turning Protein Crystallisation from an Art into a Science. *Curr Opin Struct Biol*. **2004**, *14* (5), 577-83. https://doi.org/10.1016/j.sbi.2004.08.002.

(20) Tosi, G.; Fermani, S.; Falini, G.; Gavira, J. A.; Ruiz, J. M. G. Hetero-vs Homogeneous Nucleation of Protein Crystals Discriminated by Supersaturation. *Cryst. Growth Des.* **2011**, *11* (5), 1542-1548. https://doi.org/10.1021/cg101460z.

(21) Fermani, S.; Vettraino, C.; Bonacini, I.; Marcaccio, M.; Falini, G.; Gavira, J. A.; Garcia Ruiz, J. M. Heterogeneous Crystallization of Proteins: Is It a Prenucleation Clusters Mediated Process? *Cryst. Growth Des.* **2013**, *13* (7), 3110-3115. https://doi.org/10.1021/cg400501f.

(22) Bergfors, T. Seeds to Crystals. *J. Struct. Biol.* **2003**, *142* (1), 66-76. https://doi.org/10.1016/S1047-8477(03)00039-X.

(23) D'Arcy, A.; Villard, F.; Marsh, M. An Automated Microseed Matrix-Screening Method for Protein Crystallization. *Acta Crystallogr. Sect. D Biol. Crystallogr.* **2007**, *63* (Pt4), 550-4. https://doi.org/10.1107/S0907444907007652.

(24) Van Meel, J. A.; Sear, R. P.; Frenkel, D. Design Principles for Broad-Spectrum Protein-Crystal Nucleants with Nanoscale Pits. *Phys. Rev. Lett.* **2010**, *105* (20), 1–4. https://doi.org/10.1103/PhysRevLett.105.205501.

(25) Lutsko, J. F. How Crystals Form: A Theory of Nucleation Pathways. *Sci. Adv.* **2019**, *5* (4), eaav7399. https://doi.org/10.1126/sciadv.aav7399.

(26) Nanev, C. N. Protein Crystal Nucleation: Recent Notions. *Cryst. Res. Technol.* **2007**, *42* (1), 4–12. https://doi.org/10.1002/crat.200610761.

(27) Botsaris, G. D. SECONDARY NUCLEATION-A REVIEW. In *Industrial Crystallization*; Mullin J.W., Ed.; Springer: Boston, 1976; pp 3-22.

(28) Xu, Y.; Shen, Y.; Tao, J.; Lu, Y.; Chen, H.; Hou, W.; Jiang, B. Selective Nucleation of Ice Crystals Depending on the Inclination Angle of Nanostructures. *Phys. Chem. Chem. Phys.* **2020**, *22* (3), 1168-1173. https://doi.org/10.1039/c9cp05449a.

(29) Shah, U. V.; Williams, D. R.; Heng, J. Y. Y. Selective Crystallization of Proteins Using Engineered Nanonucleants. *Cryst. Growth Des.* **2012**, *12* (3), 1362–1369. https://doi.org/10.1021/cg201443s.

(30) Govada, L.; Leese, H. S.; Saridakis, E.; Kassen, S.; Chain, B.; Khurshid, S.; Menzel, R.; Hu, S.; Shaffer, M. S. P.; Chayen, N. E. Exploring Carbon Nanomaterial Diversity for Nucleation of Protein Crystals. *Sci. Rep.* **2016**, *6* , 20053. https://doi.org/10.1038/srep20053.

(31) Chayen, N. E.; Saridakis, E.; Sear, R. P. Experiment and Theory for Heterogeneous Nucleation of Protein Crystals in a Porous Medium. *Proc. Natl. Acad. Sci. U. S. A.* **2006**, *103* (3), 597–601. https://doi.org/10.1073/pnas.0504860102.

(32) Khurshid, S.; Saridakis, E.; Govada, L.; Chayen, N. E. Porous Nucleating Agents for Protein Crystallization. *Nat. Protoc.* **2014**, *9* (7), 1621–1633. https://doi.org/10.1038/nprot.2014.109.

(33) Diao, Y.; Harada, T.; Myerson, A. S.; Alan Hatton, T.; Trout, B. L. The Role of Nanopore Shape in Surface-Induced Crystallization. *Nat. Mater.* **2011**, *10* (11), 867–871. https://doi.org/10.1038/nmat3117.

(34) Sengupta Ghatak, A.; Ghatak, A. Disordered Nanowrinkle Substrates for Inducing Crystallization over a Wide Range of Concentration of Protein and Precipitant. *Langmuir.* **2013**, *29* (13), 4373–4380. https://doi.org/10.1021/la305135y.

(35) Poncin-Epaillard, F.; Vrlinic, T.; Debarnot, D.; Mozetic, M.; Coudreuse, A.; Legeay, G.; El Moualij, B.; Zorzi, W. Surface Treatment of Polymeric Materials Controlling the Adhesion of Biomolecules. *J. Funct. Biomater.* **2012**, *3* (3), 528-43. https://doi.org/10.3390/jfb3030528.

(36) Chen, W.; Li, X.; Guo, M.; Link, F. J.; Ramli, S. S.; Ouyang, J.; Rosbottom, I.; Heng, J. Y. Y. Biopurification of Monoclonal Antibody (MAb) through Crystallisation. *Separation and Purification Technology*. **2021**, *263*, 118358. https://doi.org/10.1016/j.seppur.2021.118358.

(37) Sanjoh, A.; Tsukihara, T. Spatiotemporal Protein Crystal Growth Studies Using Microfluidic Silicon Devices. *J. Cryst. Growth.* **1999**, *196* (2–4), 691–702. https://doi.org/10.1016/S0022-0248(98)00821-5.

(38) Rong, L.; Komatsu, H.; Yoda, S. Control of Heterogeneous Nucleation of Lysozyme Crystals by Using Poly-L-Lysine Modified Substrate. *J. Cryst. Growth.* **2002**, *235* (1–4), 489–493. https://doi.org/10.1016/S0022-0248(01)01792-4.

(39) Tsekova, D.; Popova, S.; Nanev, C. Nucleation Rate Determination by a Concentration Pulse Technique: Application on Ferritin Crystals to Show the Effect of Surface Treatment of a Substrate. *Acta Crystallogr. Sect. D Biol. Crystallogr.* **2002**, *58* (10 II), 1588–1592. https://doi.org/10.1107/S0907444902014452.

(40) Fermani, S.; Falini, G.; Minnucci, M.; Ripamonti, A. Protein Crystallization on Polymeric Film Surfaces. *J. Cryst. Growth.* **2001**, *224* (3–4), 327–334. https://doi.org/10.1016/S0022-0248(01)00797-7.

(41) Falini, G.; Fermani, S.; Conforti, G.; Ripamonti, A. Protein Crystallisation on Chemically Modified Mica Surfaces. *Acta Crystallogr. Sect. D Biol. Crystallogr.* **2002**, *58* (10 II), 1649–1652. https://doi.org/10.1107/S0907444902012763.

(42) Georgieva, D. G.; Kuil, M. E.; Oosterkamp, T. H.; Zandbergen, H. W.; Abrahams, J. P. Heterogeneous Nucleation of Three-Dimensional Protein Nanocrystals. *Acta Crystallogr. Sect. D Biol. Crystallogr.* **2007**, *63* (5), 564–570. https://doi.org/10.1107/S0907444907007810.

(43) Tosi, G.; Fermani, S.; Falini, G.; Gavira Gallardo, J. A.; García Ruiz, J. M. Crystallization of Proteins on Functionalized Surfaces. *Acta Crystallogr. Sect. D Biol. Crystallogr.* **2008**, *64* (10), 1054–1061. https://doi.org/10.1107/S0907444908025079.

(44) Saridakis, E.; Khurshid, S.; Govada, L.; Phan, Q.; Hawkins, D.; Crichlow, G. V.; Lolis, E.; Reddy, S. M.; Chayen, N. E. Protein Crystallization Facilitated by Molecularly Imprinted Polymers. *Proc. Natl. Acad. Sci. U.S.A.* **2011**, *108* (27), 11081-6. https://doi.org/10.1073/pnas.1116413108.

(45) Asanithi, P.; Saridakis, E.; Govada, L.; Jurewicz, I.; Brunner, E. W.; Ponnusamy, R.; Cleaver, J. A. S.; Dalton, A. B.; Chayen, N. E.; Sear, R. P. Carbon-Nanotube-Based Materials for Protein Crystallization. *ACS Appl. Mater. Interfaces.* **2009**, *1* (6), 1203–1210. https://doi.org/10.1021/am9000858.

(46) Diao, Y.; Myerson, A. S.; Hatton, T. A.; Trout, B. L. Surface Design for Controlled Crystallization: The Role of Surface Chemistry and Nanoscale Pores in Heterogeneous Nucleation. *Langmuir.* **2011**, *27* (9), 5324–5334. https://doi.org/10.1021/la104351k.

(47) Eral, H. B.; López-Mejías, V.; O'Mahony, M.; Trout, B. L.; Myerson, A. S.; Doyle, P. S. Biocompatible Alginate Microgel Particles as Heteronucleants and Encapsulating Vehicles for Hydrophilic and Hydrophobic Drugs. *Cryst. Growth Des.* **2014**, *14* (4), 2073-2082. https://doi.org/10.1021/cg500250e.

(48) Profio, G. Di; Polino, M.; Nicoletta, F. P.; Belviso, B. D.; Caliandro, R.; Fontananova, E.; De Filpo, G.; Curcio, E.; Drioli, E. Tailored Hydrogel Membranes for Efficient Protein Crystallization. *Adv. Funct. Mater.* **2014**, *24* (11), 1582–1590. https://doi.org/10.1002/adfm.201302240.

(49) D'Arcy, A.; Mac Sweeney, A.; Haber, A. Using Natural Seeding Material to Generate Nucleation in Protein Crystallization Experiments. *Acta Crystallogr. - Sect. D Biol. Crystallogr.* **2003**, *59* (Pt 7), 1343-6. https://doi.org/10.1107/S0907444903009430.

(50) Thakur, A. S.; Robin, G.; Guncar, G.; Saunders, N. F. W.; Newman, J.; Martin, J. L.; Kobe, B. Improved Success of Sparse Matrix Protein Crystallization Screening with Heterogeneous Nucleating Agents. *PLoS One.* **2007**, *2* (10), e1091. https://doi.org/10.1371/journal.pone.0001091.

(51) Chayen, N. E.; Saridakis, E.; El-Bahar, R.; Nemirovsky, Y. Porous Silicon: An Effective Nucleation-Inducing Material for Protein Crystallization. *J. Mol. Biol.* **2001**, *312* (4), 591–595. https://doi.org/10.1006/jmbi.2001.4995.

(52) Saridakis, E.; Chayen, N. E. Towards a "universal" Nucleant for Protein Crystallization. *Trends Biotechnol.* **2009**, *27* (2), 99–106. https://doi.org/10.1016/j.tibtech.2008.10.008.

(53) Page, A. J.; Sear, R. P. Heterogeneous Nucleation in and out of Pores. *Phys. Rev. Lett.* **2006**, *97* (6), 1–4. https://doi.org/10.1103/PhysRevLett.97.065701.

(54) Sugahara, M.; Asada, Y.; Morikawa, Y.; Kageyama, Y.; Kunishima, N. Nucleant-Mediated Protein Crystallization with the Application of Microporous Synthetic Zeolites. *Acta Crystallogr. Sect. D Biol. Crystallogr.* **2008**, *64* (6), 686–695. doi: 10.1107/S0907444908009980

(55) Curcio, E.; Curcio, V.; Di Profi, G.; Fontananova, E.; Drioli, E. Energetics of Protein Nucleation on Rough Polymeric Surfaces. *J. Phys. Chem. B.* **2010**, *114* (43), 13650–13655. https://doi.org/10.1021/jp106349d.

(56) Nanev, C. N.; Saridakis, E.; Chayen, N. E. Protein Crystal Nucleation in Pores. *Sci. Rep.* **2017**, *7* , 35821. https://doi.org/10.1038/srep35821.

(57) Stolyarova, S.; Saridakis, E.; Chayen, N. E.; Nemirovsky, Y. A Model for Enhanced Nucleation of Protein Crystals on a Fractal Porous Substrate. *Biophys. J.* **2006**, *91* (10), 3857–3863. https://doi.org/10.1529/biophysj.106.082545.

(58) Gully, B. S.; Zou, J.; Cadby, G.; Passon, D. M.; Iyer, K. S.; Bond, C. S. Colloidal Graphenes as Heterogeneous Additives to Enhance Protein Crystal Yield. *Nanoscale.* **2012**, *4* (17), 5321–5324. https://doi.org/10.1039/c2nr31150j.

(59) Curcio, E.; Fontananova, E.; Di Profio, G.; Drioli, E. Influence of the Structural Properties of Poly(Vinylidene Fluoride) Membranes on the Heterogeneous Nucleation Rate of Protein Crystals. *J. Phys. Chem. B.* **2006**, *110* (25), 12438–12445. https://doi.org/10.1021/jp061531y.

(60) Liu, Y. X.; Wang, X. J.; Lu, J.; Ching, C. B. Influence of the Roughness, Topography, and Physicochemical Properties of Chemically Modified Surfaces on the Heterogeneous Nucleation of Protein Crystals. *J. Phys. Chem. B.* **2007**, *111* (50), 13971–13978. https://doi.org/10.1021/jp0741612.

(61) Rechendorff, K.; Hovgaard, M. B.; Foss, M.; Zhdanov, V. P.; Besenbacher, F. Enhancement of Protein Adsorption Induced by Surface Roughness. *Langmuir.* **2006**, *22* (26), 10885-8. https://doi.org/10.1021/la0621923.

(62) Grosfils, P.; Lutsko, J. F. Impact of Surface Roughness on Crystal Nucleation. *Crystals.* **2021**,

11 (1), 1–20. https://doi.org/10.3390/cryst11010004.

(63) Nanev, C.; Govada, L.; Chayen, N. E. Theoretical and Experimental Investigation of Protein Crystal Nucleation in Pores and Crevices. *IUCrJ.* **2021**, *8* (Pt 2), 270-280. https://doi.org/10.1107/S2052252521000269.

(64) De Poel, W.; Münninghoff, J. A. W.; Elemans, J. A. A. W.; Van Enckevort, W. J. P.; Rowan, A. E.; Vlieg, E. Surfaces with Controllable Topography and Chemistry Used as a Template for Protein Crystallization. *Cryst. Growth Des.* **2018**, *18* (2), 763–769. https://doi.org/10.1021/acs.cgd.7b01174.

(65) Di Profio, G.; Fontananova, E.; Curcio, E.; Drioli, E. From Tailored Supports to Controlled Nucleation: Exploring Material Chemistry, Surface Nanostructure, and Wetting Regime Effects in Heterogeneous Nucleation of Organic Molecules. *Cryst. Growth Des.* **2012**, *12* (7), 3749-3757. https://doi.org/10.1021/cg3005568.

(66) Ye, Z. Y.; Broströmer, E.; Nan, J.; Cao, X. fang; Liu, X.; Qiao, L.; Liu, Z. J.; Su, X. D. Protein Crystallization Benefits from the Rough Well Surface of a 48-Well Polystyrene Microplate. *J. Cryst. Growth.* **2020**, *532* (1-2), 125425. https://doi.org/10.1016/j.jcrysgro.2019.125425.

(67) Polino, M.; Carvalho, A. L.; Juknaite, L.; Portugal, C. A. M.; Coelhoso, I. M.; Romão, M. J.; Crespo, J. G. Ion-Exchange Membranes for Stable Derivatization of Protein Crystals. *Cryst. Growth Des.* **2017**, *17* (9), 4563-4572. https://doi.org/10.1021/acs.cgd.7b00315.

(68) Polino, M.; Portugal, C. A. M.; Le The, H.; Tiggelaar, R.; Eijkel, J.; Crespo, J. G.; Coelhoso, I. M.; Pina, M. P.; Mallada, R. Enhanced Protein Crystallization on Nafion Membranes Modified by Low-Cost Surface Patterning Techniques. *Cryst. Growth Des.* **2020**, *20* (4), 2174–2186. https://doi.org/10.1021/acs.cgd.9b00969.

(69) Ereno-Orbea, J.; Majtan, T.; Oyenarte, I.; Kraus, J. P.; Martinez-Cruz, L. A. Structural Basis of Regulation and Oligomerization of Human Cystathionine -Synthase, the Central Enzyme of Transsulfuration. *Proc. Natl. Acad. Sci.* **2013**, *110* (40), E3790–E3799. https://doi.org/10.1073/pnas.1313683110.

(70) Mcpherson, A.; Shlichta, P. Heterogeneous and Epitaxial Nucleation of Protein Crystals on Mineral Surfaces. *Science*. **1988**, *239* (4838), 385-7. https:// doi: 10.1126/science.239.4838.385.

(71) Kertis, F.; Khurshid, S.; Okman, O.; Kysar, J. W.; Govada, L.; Chayen, N.; Erlebacher, J. Heterogeneous Nucleation of Protein Crystals Using Nanoporous Gold Nucleants. *J. Mater. Chem.* **2012**, *22* (41), 21928–21934. https://doi.org/10.1039/c2jm34527g.

(72) Foroughi, L. M.; Kang, Y. N.; Matzger, A. J. Polymer-Induced Heteronucleation for Protein Single Crystal Growth: Structural Elucidation of Bovine Liver Catalase and Concanavalin a Forms. *Cryst. Growth Des.* **2011**, *11* (4), 1294–1298. https://doi.org/10.1021/cg101518f.

(73) Alexander, C.; Andersson, H. S.; Andersson, L. I.; Ansell, R. J.; Kirsch, N.; Nicholls, I. A.; O'Mahony, J.; Whitcombe, M. J. Molecular Imprinting Science and Technology: A Survey of the Literature for the Years up to and Including 2003. *J Mol Recognit*. **2006**, *19* (2), 106-80.

https://doi.org/10.1002/jmr.760.

(74) Takeuchi, T.; Goto, D.; Shinmori, H. Protein Profiling by Protein Imprinted Polymer Array. *Analyst.* **2007**, *132* (2), 101-3. https://doi.org/10.1039/b614532a.

(75) Fernández, J.; Etxeberria, A.; Sarasua, J. R. Synthesis, Structure and Properties of Poly(L-Lactide-Co-ε-Caprolactone) Statistical Copolymers. *J. Mech. Behav. Biomed. Mater.* **2012**, *9,* 100-12. https://doi.org/10.1016/j.jmbbm.2012.01.003.

(76) Nair, L. S.; Laurencin, C. T. Polymers as Biomaterials for Tissue Engineering and Controlled Drug Delivery. *Ad Biochem Eng /Biotech.* **2006**, *102*, 47-90. https://doi.org/10.1007/b137240.

(77) Grumezescu, V.; Grumezescu, A. M. *Materials for Biomedical Engineering : Thermoset and Hermoplastic Polymers*; Elsevier: 2019. https://doi.org/10.1016/C2017-0-04394-X.

(78) da Costa, A. P.; Botelho, E. C.; Costa, M. L.; Narita, N. E.; Tarpani, J. R. A Review of Welding Technologies for Thermoplastic Composites in Aerospace Applications. *Journal of Aerospace Technology and Management*. **2012**, *13* (8), 1208. https://doi.org/10.5028/jatm.2012.04033912.

(79) Coiai, S.; Passaglia, E.; Pucci, A.; Ruggeri, G. Nanocomposites Based on Thermoplastic Polymers and Functional Nanofiller for Sensor Applications. *Materials (Basel).* **2015**, *8* (6), 3377-3427. https://doi.org/10.3390/ma8063377.

(80) Polino, M.; Portugal, C. A. M.; Di Profio, G.; Coelhoso, I. M.; Crespo, J. G. Protein Crystallization by Membrane-Assisted Technology. *Cryst. Growth Des.* **2019**, *19* (8), 4871–4883. https://doi.org/10.1021/acs.cgd.9b00223.

(81) Kooy, N.; Mohamed, K.; Pin, L. T.; Guan, O. S. A Review of Roll-to-Roll Nanoimprint Lithography. *Nanoscale Res. Lett.* **2014**, *9* (1), 1–13. https://doi.org/10.1186/1556-276X-9-320.

(82) Chou, S. Y.; Krauss, P. R.; Renstrom, P. J. Imprint of Sub-25 Nm Vias and Trenches in Polymers. *Appl. Phys. Lett.* **1995**, *67* (21), 3114-3116. https://doi.org/10.1063/1.114851.

(83) Wen-Wen, L.; Zhen-Ling, C.; Xing-Yu, J. Methods for Cell Micropatterning on Two-Dimensional Surfaces and Their Applications in Biology. *Fenxi Huaxue/ Chinese J. Anal. Chem.* **2009**, *37* (7), 943–949. https://doi.org/10.1016/S1872-2040(08)60113-9.

(84) Torabi, K.; Farjood, E.; Hamedani, S. Rapid Prototyping Technologies and Their Applications in Prosthodontics, a Review of Literature. *J. Dent. (Shiraz, Iran)* **2015**, *16* (1), 1-9.

(85) Serafetinides, A. A.; Makropoulou, M. I.; Skordoulis, C. D.; Kar, A. K. Ultra-Short Pulsed Laser Ablation of Polymers. *Appl. Surf. Sci.* **2001**, *180* (1–2), 42–56. https://doi.org/10.1016/S0169-4332(01)00324-5.

(86) Ortiz Márquez, R. Ultrashort-Pulsed Laser Ablation of Poly-L-Lactide (PLLA) for Cell and Tissue Engineering Applications. Thesis, Basque Country University, 2017.

(87) Ravi-Kumar, S.; Lies, B.; Zhang, X.; Lyu, H.; Qin, H. Laser Ablation of Polymers: A Review. *Polym. Int.* **2019**, *68* (8), 1391–1401. https://doi.org/10.1002/pi.5834.

(88) Urech, L.; Lippert, T. Photoablation of Polymer Materials. In *Photochemistry and Photophysics of Polymer Materials;* Allen, S. N., Eds.; John Willey & Sons Inc.*:* 2010; pp. 541-568. https://doi.org/10.1002/9780470594179.ch14.

(89) Ortiz, R.; Quintana, I.; Etxarri, J.; Lejardi, A.; Sarasua, J. R. Picosecond Laser Ablation of Poly-L-Lactide: Effect of Crystallinity on the Material Response. *J. Appl. Phys.* **2011**, *110* (9), 094902. https://doi.org/10.1063/1.3653964.

(90) Ortiz, R.; Moreno-Flores, S.; Quintana, I.; Vivanco, M. M.; Sarasua, J. R.; Toca-Herrera, J. L. Ultra-Fast Laser Microprocessing of Medical Polymers for Cell Engineering Applications. *Mater. Sci. Eng. C.* **2014**, *37* (1), 241-50. https://doi.org/10.1016/j.msec.2013.12.039.

(91) Ortiz, R.; Aurrekoetxea-Rodríguez, I.; Rommel, M.; Quintana, I.; Vivanco, M. M.; Toca-Herrera, J. L. Laser Surface Microstructuring of a Bio-Resorbable Polymer to Anchor Stem Cells, Control Adipocyte Morphology, and Promote Osteogenesis. *Polymers (Basel).* **2018**, *10* (12), 1337. https://doi.org/10.3390/polym10121337.

(92) Pacharra, S.; Ortiz, R.; McMahon, S.; Wang, W.; Viebahn, R.; Salber, J.; Quintana, I. Surface Patterning of a Novel PEG-Functionalized Poly-l-Lactide Polymer to Improve Its Biocompatibility: Applications to Bioresorbable Vascular Stents. *J. Biomed. Mater. Res. - Part B Appl. Biomater.* **2019**, *107* (3), 624–634. https://doi.org/10.1002/jbm.b.34155.

(93) Otsuka, H. Micropatterning of Cell Aggregate in Three Dimension for in Vivo Mimicking Cell Culture. In *Colloid and Interface Science in Pharmaceutical Research and Development*. Ohshima, H., Makino, K., Eds.; Elsevier: 2014; pp 223-241. https://doi.org/10.1016/B978-0-444-62614-1.00011-9.

(94) Gurr, M.; Mülhaupt, R. Rapid Prototyping. In *Polymer science: a comprehensive reference.* Moeller, M., Matyjaszewski, K., Eds.; Elsevier: Amsterdam, 2012; pp 77–99.

(95) Fiedor, P.; Ortyl, J. A New Approach to Micromachining: High-Precision and Innovative Additive Manufacturing Solutions Based on Photopolymerization Technology. *Materials (Basel).* **2020**, *13* (13), 1–25. https://doi.org/10.3390/ma13132951.

(96) Machining with Long Pulse Lasers, Machining with Ultrafast Laser Pulses. http://www.cmxr.com/Education/Long.html (accesed September, 2021).

(97) Galkin, O.; Vekilov, P. G. Are Nucleation Kinetics of Protein Crystals Similar to Those of Liquid Droplets? *J. Am. Chem. Soc.* **2000**, *122* (1), 156–163. https://doi.org/10.1021/ja9930869.

(98) Vekilov, P. G. Dense Liquid Precursor for the Nucleation of Ordered Solid Phases from Solution. *Cryst. Growth Des.* **2004**, *4* (4), 671–685. https://doi.org/10.1021/cg049977w.

(99) Filobelo, L. F.; Galkin, O.; Vekilov, P. G. Spinodal for the Solution-to-Crystal Phase Transformation. *J. Chem. Phys.* **2005**, *123* (1), 014904. https://doi.org/10.1063/1.1943413

(100) Pan, W.; Kolomeisky, A. B.; Vekilov, P. G. Nucleation of Ordered Solid Phases of Proteins via a Disordered High-Density State: Phenomenological Approach. *J. Chem. Phys.* **2005**, *122* (17), 174905. https://doi.org/10.1063/1.1887168.

(101) Vekilov, P. G. The Two-Step Mechanism of Nucleation of Crystals in Solution. *Nanoscale.* **2010**, *2* (11), 2346-57. https://doi.org/10.1039/c0nr00628a.

(102) Erdemir, D.; Lee, A. Y.; Myerson, A. S. Nucleation of Crystals from Solution: Classical and Two-Step Models. *Acc. Chem. Res.* **2009**, *42* (5), 621–629. https://doi.org/10.1021/ar800217x.

(103) Corral-Rodríguez, M. Á.; Stuiver, M.; Abascal-Palacios, G.; Diercks, T.; Oyenarte, I.; Ereño-Orbea, J.; De Opakua, A. I.; Blanco, F. J.; Encinar, J. A.; Spiwok, V.; *et al*. Nucleotide Binding Triggers a Conformational Change of the CBS Module of the Magnesium Transporter CNNM2 from a Twisted towards a Flat Structure. *Biochem. J.* **2014**, *464* (1), 23-34. https://doi.org/10.1042/BJ20140409.

(104) Oyenarte, I.; Majtan, T.; Ereño, J.; Corral-Rodríguez, M. A.; Kraus, J. P.; Martínez-Cruz, L. A. Purification, Crystallization and Preliminary Crystallographic Analysis of Human Cystathionine β-Synthase. *Acta Crystallogr. Sect. F Struct. Biol. Cryst. Commun.* **2012**, *68* (11), 1318–1322. https://doi.org/10.1107/S1744309112037219.

(105) Artimo, P.; Jonnalagedda, M.; Arnold, K.; Baratin, D.; Csardi, G.; De Castro, E.; Duvaud, S.; Flegel, V.; Fortier, A.; Gasteiger, E.; *et al*. ExPASy: SIB Bioinformatics Resource Portal. *Nucleic Acids Res.* **2004**, *40* (Web Server issue), W597-603. https://doi.org/10.1093/nar/gks400.

(106) Pettersen, E. F.; Goddard, T. D.; Huang, C. C.; Couch, G. S.; Greenblatt, D. M.; Meng, E. C.; Ferrin, T. E. UCSF Chimera - A Visualization System for Exploratory Research and Analysis. *J. Comput. Chem.* **2004**, *25* (13), 1605-12. https://doi.org/10.1002/jcc.20084.

(107) Gómez García, I.; Oyenarte, I.; Martínez-Cruz, L. A. Purification, Crystallization and Preliminary Crystallographic Analysis of the CBS Pair of the Human Metal Transporter CNNM4. *Acta Crystallogr. Sect. F Struct. Biol. Cryst. Commun.* **2011**, *67* (3), 349-53. https://doi.org/10.1107/S1744309110053856.

(108) Oyenarte, I.; Lucas, M.; Gómez García, I.; Martínez-Cruz, L. A. Purification, Crystallization and Preliminary Crystallographic Analysis of the CBS-Domain Protein MJ1004 from Methanocaldococcus Jannaschii. *Acta Crystallogr. Sect. F Struct. Biol. Cryst. Commun.* **2011**, *67* (3), 318–324. https://doi.org/10.1107/S1744309110053479.

(109) Retolaza, A.; Juarros, A.; Ramiro, J.; Merino, S. Thermal Roll to Roll Nanoimprint Lithography for Micropillars Fabrication on Thermoplastics. *Microelectron. Eng.* **2018**, *193*, 54–61. https://doi.org/10.1016/j.mee.2018.02.026

(110) Shirk, M. D.; Molian, P. A. A Review of Ultrashort Pulsed Laser Ablation of Materials. *Jla.Aip.Org.* **1998**, *10* (1), 18–28. https://doi.org/10.2351/1.521827

(111) Shirk, M. D.; Molian, P. A.; Malshe, A. P. Ultrashort Pulsed Laser Ablation of Diamond. *J. Laser Appl.* **1998**, *10* (2), 64–70. https://doi.org/10.2351/1.521822

(112) Mezera, M.; Richter, A.; Krüger, J.; Bonse, J.; Schwibbert, K. Bacterial Adhesion on Femtosecond Laser-Induced Periodic Surface Structures. In *Future Tech week*, Sept 21-25, 2020.

(113) Zou, H.; Zhang, Y.; Guo, L.; Wang, P.; He, X.; Dai, G.; Zheng, H.; Chen, C.; Wang, A. C.; Xu, C.; *et al*. Quantifying the Triboelectric Series. *Nat. Commun.* **2019**, *10* (1), 1–9. https://doi.org/10.1038/s41467-019-09461-x.

(114) Agrawal, G.; Negi, Y. S.; Pradhan, S.; Dash, M.; Samal, S. K. Wettability and Contact Angle of Polymeric Biomaterials. In *Characterization of Polymeric Biomaterials.*Tanzi, M. C., Fare, S., Eds.; Woodhead Publishing: 2017; pp 57-81. https://doi.org/10.1016/B978-0-08-100737-2.00003-0.

(115) Giridhar, G.; Manepalli, R. K. N. R.; Apparao, G. Contact Angle Measurement Techniques for Nanomaterials. In T*hermal and Rheological Measurement Techniques for Nanomaterials Characterization*. Collyer, A. A., Eds.; Springer: 2017; pp 173-195. https://doi.org/10.1016/B978-0-323-46139-9.00008-6.

(116) Yuan, Y.; Lee, T. R. Contact Angle and Wetting Properties. *Springer Ser. Surf. Sci.* **2013**, *51* (1), 3-34. https://doi.org/10.1007/978-3-642-34243-1_1.

(117) Yeo, J.; Kim, D. S. The Effect of the Aspect Ratio on the Hydrophobicity of Microstructured Polydimethylsiloxane (PDMS) Robust Surfaces. *Microsyst. Technol.* **2010**, *16* (8–9), 1457–1463. https://doi.org/10.1007/s00542-010-1101-1.

(118) Sun, J.; Wang, X.; Wu, J.; Jiang, C.; Shen, J.; Cooper, M. A.; Zheng, X.; Liu, Y.; Yang, Z.; Wu, D. Biomimetic Moth-Eye Nanofabrication: Enhanced Antireflection with Superior Self-Cleaning Characteristic. *Sci. Rep.* **2018**, *8* (1), 5438. https://doi.org/10.1038/s41598-018-23771-y.

(119) Raguin, D. H.; Morris, G. M. Antireflection Structured Surfaces for the Infrared Spectral Region. *Appl. Opt.* **1993**, *32* (7), 1154-67. https://doi.org/10.1364/ao.32.001154.

(120) Steel, M. J.; White, T. P.; Martijn de Sterke, C.; McPhedran, R. C.; Botten, L. C. Symmetry and Degeneracy in Microstructured Optical Fibers. *Opt. Lett.* **2001**, *26* (8), 488-490. https://doi.org/10.1364/ol.26.000488.

(121) Weiblen, R. J.; Menyuk, C. R.; Busse, L. E.; Shaw, L. B.; Sanghera, J. S.; Aggarwal, I. D. Optimized Moth-Eye Anti-Reflective Structures for As_2S_3 Chalcogenide Optical Fibers. *Opt. Express.* **2016**, *24* (10), 10172-10187. https://doi.org/10.1364/oe.24.010172.

(122) Vijayan, P. P.; Puglia, D. Biomimetic Multifunctional Materials: A Review. *Emergent Mater.* **2019**, *2* (4), 391–415.https://doi.org/10.1007/s42247-019-00051-7.

(123) Krauss, I. R.; Merlino, A.; Vergara, A.; Sica, F. An Overview of Biological Macromolecule Crystallization. *Int. J. Mol. Sci.* **2013**, *14* (6), 11643–11691. https://doi.org/10.3390/ijms140611643.

(124) McPherson, A.; Gavira, J. A. Introduction to Protein Crystallization. *Acta Crystallogr Sect F Struct Biol Commun*. **2014**, *70* (Pt 1), 2-20. https://doi.org/10.1107/S2053230X13033141.

(125) Giménez-Mascarell, P.; Oyenarte, I.; González-Recio, I.; Fernández-Rodríguez, C.; Corral-Rodríguez, M. Á.; Campos-Zarraga, I.; Simón, J.; Kostantin, E.; Hardy, S.; Quintana, A. D.; *et al*. Structural Insights into the Intracellular Region of the Human Magnesium Transport Mediator CNNM4. *Int. J. Mol. Sci.* **2019,** *20* (24), 6279. https://doi.org/10.3390/ijms20246279.

(126) Baykov, A. A.; Tuominen, H. K.; Lahti, R. The CBS Domain: A Protein Module with an Emerging Prominent Role in Regulation. *ACS Chem Biol*. **2011**, *6* (11), 1156-63. https://doi.org/10.1021/cb200231c.

(127) Wang, C. Y.; Shi, J. Da; Yang, P.; Kumar, P. G.; Li, Q. Z.; Run, Q. G.; Su, Y. C.; Scott, H. S.; Kao, K. J.; She, J. X. Molecular Cloning and Characterization of a Novel Gene Family of Four Ancient Conserved Domain Proteins (ACDP). *Gene.* **2003**, *306*, 37-44. https://doi.org/10.1016/S0378-1119(02)01210-6.

(128) Stuiver, M.; Lainez, S.; Will, C.; Terryn, S.; Günzel, D.; Debaix, H.; Sommer, K.; Kopplin, K.; Thumfart, J.; Kampik, N. B.; *et al.* CNNM2, Encoding a Basolateral Protein Required for Renal Mg2+ Handling, Is Mutated in Dominant Hypomagnesemia. *Am. J. Hum. Genet.* **2011**, *88* (3), 333-43. https://doi.org/10.1016/j.ajhg.2011.02.005.

(129) Giménez-Mascarell, P.; Oyenarte, I.; Hardy, S.; Breiderhoff, T.; Stuiver, M.; Kostantin, E.; Diercks, T.; Pey, A. L.; Ereño-Orbea, J.; Martínez-Chantar, M. L.; *et al.* Structural Basis of the Oncogenic Interaction of Phosphatase PRL-1 with the Magnesium Transporter CNNM2. *J. Biol. Chem.* **2017**, *292* (3), 786-801. https://doi.org/10.1074/jbc.M116.759944.

(130) De Baaij, J. H. F.; Stuiver, M.; Meij, I. C.; Lainez, S.; Kopplin, K.; Venselaar, H.; Müller, D.; Bindels, R. J. M.; Hoenderop, J. G. J. Membrane Topology and Intracellular Processing of Cyclin M2 (CNNM2). *J. Biol. Chem.* **2012**, *287* (17), 13644-55. https://doi.org/10.1074/jbc.M112.342204.

(131) Kolisek, M.; Sponder, G.; Pilchova, I.; Cibulka, M.; Tatarkova, Z.; Werner, T.; Racay, P. Magnesium Extravaganza: A Critical Compendium of Current Research into Cellular Mg2+ Transporters Other than TRPM6/7. *Reviews of Physiology, Biochemistry and Pharmacology*. **2019**, *176*, 65-105. https://doi.org/10.1007/112_2018_15.

(132) Arjona, F. J.; de Baaij, J. H. F. CrossTalk Opposing View: CNNM Proteins Are Not Na + /Mg 2+ Exchangers but Mg 2+ Transport Regulators Playing a Central Role in Transepithelial Mg 2+ (Re)Absorption. *J. Physiol*. **2018**, *596* (5), 747-750. https://doi.org/10.1113/JP275249.

(133) Funato, Y.; Furutani, K.; Kurachi, Y.; Miki, H. CrossTalk Proposal: CNNM Proteins Are Na+/Mg2+ Exchangers Playing a Central Role in Transepithelial Mg2+ (Re) Absorption. *J. Physiol.* **2018**, *596* (5), 743–746.https:// doi: 10.1113/JP275248.

(134) Schäffers, O. J. M.; Hoenderop, J. G. J.; Bindels, R. J. M.; de Baaij, J. H. F. The Rise and Fall of Novel Renal Magnesium Transporters. *Am J Physiol Renal Physiol*. **2018**, *314* (6), F1027-F1033. https://doi.org/10.1152/ajprenal.00634.2017.

(135) Yamazaki, D.; Funato, Y.; Miura, J.; Sato, S.; Toyosawa, S.; Furutani, K.; Kurachi, Y.; Omori, Y.; Furukawa, T.; Tsuda, T.; *et al*. Basolateral Mg2+ Extrusion via CNNM4 Mediates Transcellular

Mg2+ Transport across Epithelia: A Mouse Model. *PLoS Genet.* **2013**, *9* (12), e1003983. https://doi.org/10.1371/journal.pgen.1003983.

(136) Sponder, G.; Mastrototaro, L.; Kurth, K.; Merolle, L.; Zhang, Z.; Abdulhanan, N.; Smorodchenko, A.; Wolf, K.; Fleig, A.; Penner, R.; *et al.* Human CNNM2 Is Not a Mg2+ Transporter per Se. *Pflugers Arch. Eur. J. Physiol.* **2016**, *468* (7), 1223-1240. https://doi.org/10.1007/s00424-016-1816-7.

(137) Parry, D. A.; Mighell, A. J.; El-Sayed, W.; Shore, R. C.; Jalili, I. K.; Dollfus, H.; Bloch-Zupan, A.; Carlos, R.; Carr, I. M.; Downey, L. M.; *et al.* Mutations in CNNM4 Cause Jalili Syndrome, Consisting of Autosomal-Recessive Cone-Rod Dystrophy and Amelogenesis Imperfecta. *Am. J. Hum. Genet.* **2008**, *84* (2), 266-73. https://doi.org/10.1016/j.ajhg.2009.01.009.

(138) Polok, B.; Escher, P.; Ambresin, A.; Chouery, E.; Bolay, S.; Meunier, I.; Nan, F.; Hamel, C.; Munier, F. L.; Thilo, B.; *et al.* Mutations in CNNM4 Cause Recessive Cone-Rod Dystrophy with Amelogenesis Imperfecta. *Am. J. Hum. Genet.* **2008**, *84* (2), 259-65. https://doi.org/10.1016/j.ajhg.2009.01.006.

(139) Luder, H. U.; Gerth-Kahlert, C.; Ostertag-Benzinger, S.; Schorderet, D. F. Dental Phenotype in Jalili Syndrome Due to a c.1312 DupC Homozygous Mutation in the CNNM4 Gene. *PLoS One.* **2013**, *8* (10), e78529. https://doi.org/10.1371/journal.pone.0078529.

(140) Cherkaoui Jaouad, I.; Lyahyai, J.; Guaoua, S.; El Alloussi, M.; Zrhidri, A.; Doubaj, Y.; Boulanouar, A.; Sefiani, A. Novel Splice Site Mutation in CNNM4 Gene in a Family with Jalili Syndrome. *Eur. J. Med. Genet.* **2017**, *60* (5), 239-244. https://doi.org/10.1016/j.ejmg.2017.02.004.

(141) Topçu, V.; Alp, M. Y.; Alp, C. K.; Bakır, A.; Geylan, D.; Yılmazoğlu, M. Ö. A New Familial Case of Jalili Syndrome Caused by a Novel Mutation in CNNM4. *Ophthalmic Genet.* **2017**, *38* (2), 161-166. https://doi.org/10.3109/13816810.2016.1164192.

(142) Hirji, N.; Bradley, P. D.; Li, S.; Vincent, A.; Pennesi, M. E.; Thomas, A. S.; Heon, E.; Bhan, A.; Mahroo, O. A.; Robson, A.; *et al.* Jalili Syndrome: Cross-Sectional and Longitudinal Features of Seven Patients With Cone-Rod Dystrophy and Amelogenesis Imperfecta. *Am. J. Ophthalmol.* **2018**, *188,* 123-120. https://doi.org/10.1016/j.ajo.2018.01.029.

(143) Maia, C. M. F.; Machado, R. A.; Gil-da-Silva-Lopes, V. L.; Lustosa-Mendes, E.; Rim, P. H. H.; Dias, V. O.; Martelli, D. R. B.; Nasser, L. S.; Coletta, R. D.; Martelli-Júnior, H. Report of Two Unrelated Families with Jalili Syndrome and a Novel Nonsense Heterozygous Mutation in CNNM4 Gene. *Eur. J. Med. Genet.* **2018**, *61* (7), 384-387. https://doi.org/10.1016/j.ejmg.2018.02.003.

(144) Yamazaki, D.; Miyata, H.; Funato, Y.; Fujihara, Y.; Ikawa, M.; Miki, H. The Mg2+ Transporter CNNM4 Regulates Sperm Ca2+ Homeostasis and Is Essential for Reproduction. *J. Cell Sci.* **2016**, *129* (9), 1940-9. https://doi.org/10.1242/jcs.182220.

(145) Rezende, F. M.; Dietsch, G. O.; Peñagaricano, F. Genetic Dissection of Bull Fertility in US Jersey Dairy Cattle. *Anim. Genet.* **2018**, *49* (5), 393-402. https://doi.org/10.1111/age.12710.

(146) Accogli, A.; Scala, M.; Calcagno, A.; Napoli, F.; Di Iorgi, N.; Arrigo, S.; Mancardi, M. M.; Prato, G.; Pisciotta, L.; Nagel, M.; *et al.* CNNM2 Homozygous Mutations Cause Severe Refractory Hypomagnesemia, Epileptic Encephalopathy and Brain Malformations. *Eur. J. Med. Genet.* **2019**, *62* (3), 198-203. https://doi.org/10.1016/j.ejmg.2018.07.014.

(147) Rose, E. J.; Hargreaves, A.; Morris, D.; Fahey, C.; Tropea, D.; Cummings, E.; Caltagirone, C.; Bossù, P.; Chiapponi, C.; Piras, F.; *et al.* Effects of a Novel Schizophrenia Risk Variant Rs7914558 at CNNM2 on Brain Structure and Attributional Style. *Br. J. Psychiatry.* **2014**, *204* (2), 115-21. https://doi.org/10.1192/bjp.bp.113.131359.

(148) Ohi, K. Influences of Schizophrenia Risk Variant Rs7914558 at CNNM2 on Brain Structure. *Br J Psychiatry*. **2015**, *206* (4), 343-4. https://doi.org/10.1192/bjp.206.4.343b.

(149) Guan, F.; Zhang, T.; Li, L.; Fu, D.; Lin, H.; Chen, G.; Chen, T. Two-Stage Replication of Previous Genome-Wide Association Studies of AS3MT-CNNM2-NT5C2 Gene Cluster Region in a Large Schizophrenia Case–Control Sample from Han Chinese Population. *Schizophr. Res.* **2016**, *176* (2–3), 125-130. https://doi.org/10.1016/j.schres.2016.07.004.

(150) Paparelli, A.; Iwata, K.; Wakuda, T.; Iyegbe, C.; Murray, R. M.; Takei, N. Perinatal Asphyxia in Rat Alters Expression of Novel Schizophrenia Risk Genes. *Front. Mol. Neurosci.* **2017**, *10,* 341. https://doi.org/10.3389/fnmol.2017.00341.

(151) Funato, Y.; Yamazaki, D.; Miki, H. Renal Function of Cyclin M2 Mg2+ Transporter Maintains Blood Pressure. *J. Hypertens.* **2017**, *35* (3), 585-592. https://doi.org/10.1097/HJH.0000000000001211.

(152) Hardy, S.; Uetani, N.; Wong, N.; Kostantin, E.; Labbé, D. P.; Bégin, L. R.; Mes-Masson, A.; Miranda-Saavedra, D.; Tremblay, M. L. The Protein Tyrosine Phosphatase PRL-2 Interacts with the Magnesium Transporter CNNM3 to Promote Oncogenesis. *Oncogene.* **2015**, *34* (8), 986-95. https://doi.org/10.1038/onc.2014.33.

(153) Gulerez, I.; Funato, Y.; Wu, H.; Yang, M.; Kozlov, G.; Miki, H.; Gehring, K. Phosphocysteine in the PRL-CNNM Pathway Mediates Magnesium Homeostasis. *EMBO Rep.* **2016**, *17* (12), 1890-1900. https://doi.org/10.15252/embr.201643393.

(154) Simón, J.; Goikoetxea-Usandizaga, N.; Serrano-Maciá, M.; Fernández-Ramos, D.; Sáenz de Urturi, D.; Gruskos, J. J.; Fernández-Tussy, P.; Lachiondo-Ortega, S.; González-Recio, I.; Rodríguez-Agudo, R.; *et al.* Magnesium Accumulation upon Cyclin M4 Silencing Activates Microsomal Triglyceride Transfer Protein Improving NASH. *J. Hepatol.* **2021,** *75* (1), 34-45. https://doi.org/10.1016/j.jhep.2021.01.043.

(155) Mudd, S. H.; Levy, H. H. L.; Kraus, J. P. J. Disorders of Transsulfuration. In *The Metabolic and Molecular Bases of Inherited Disease*. Valle, D.L., Eds.; McGraw-Hill Education/Medical: 2001. https:// DOI: 10.1036/ommbid.401.

(156) Kim, J.; Hong, S. J.; Park, J. H.; Park, S. Y.; Kim, S. W.; Cho, E. Y.; Do, I.-G.; Joh, J.-W.; Kim, D. S. Expression of Cystathionine β-Synthase Is Downregulated in Hepatocellular Carcinoma and Associated with Poor Prognosis. *Oncol. Rep.* **2009**, *21* (6), 1449–1454. https://doi:

10.3892/or_00000373.

(157) Hellmich, M. R.; Szabo, C. Hydrogen Sulfide and Cancer. *Chem. Biochem. Pharmacol. Hydrog. Sulfide.* **2015**, *230*, 233–241. https:// doi: 10.1007/978-3-319-18144-8_12.

(158) Golimbet, V.; Korovaitseva, G.; Abramova, L.; Kaleda, V. The 844ins68 Polymorphism of the Cystathionine Beta-Synthase Gene Is Associated with Schizophrenia. *Psychiatry Res.* **2009**, *170* (2–3), 168–171. https:// doi: 10.1016/j.psychres.2008.07.007.

(159) Majtan, T.; Pey, A. L.; Fernández, R.; Fernández, J. A.; Martínez-Cruz, L. A.; Kraus, J. P. Domain Organization, Catalysis and Regulation of Eukaryotic Cystathionine Beta-Synthases. *PLoS One.* **2014**, *9* (8), e105290. https://doi.org/10.1371/journal.pone.0105290.

(160) Ereño-Orbea, J.; Majtan, T.; Oyenarte, I.; Kraus, J. P.; Martínez-Cruz, L. A. Structural Insight into the Molecular Mechanism of Allosteric Activation of Human Cystathionine β-Synthase by S -Adenosylmethionine. *Proc. Natl. Acad. Sci.* **2014**, *111* (37), E3845–E3852. https://doi.org/10.1073/pnas.1414545111.

(161) González-Recio, I.; Fernández-Rodríguez, C.; Simón, J.; Goikoetxea-Usandizaga, N.; Martínez-Chantar, M. L.; Astegno, A.; Majtan, T.; Martinez-Cruz, L. A. Current Structural Knowledge on Cystathionine B-Synthase, a Pivotal Enzyme in the Transsulfuration Pathway. *eLS.* **2020**, *1*, 453-468. https://doi.org/10.1002/9780470015902.a0028966.

(162) Wei, M. K.; Yang, H. Cumulative Heat Effect in Excimer Laser Ablation of Polymer PC and ABS. *Int. J. Adv. Manuf. Technol.* **2003**, *21* (12), 1029–1034. https://doi.org/10.1007/s00170-002-1431-y.

(163) Lee, J. J.; Park, S. Y.; Choi, K. B.; Kim, G. H. Nano-Scale Patterning Using the Roll Typed UV-Nanoimprint Lithography Tool. *Microelectron. Eng.* **2008**, *85* (5–6), 861–865. https://doi.org/10.1016/j.mee.2007.12.059.

(164) Glassford, S.; Chan, K. L. A.; Byrne, B.; Kazarian, S. G. Chemical Imaging of Protein Adsorption and Crystallization on a Wettability Gradient Surface. *Langmuir.* **2012**, *28* (6), 3174–3179. https://doi.org/10.1021/la204524w.

(165) Price, C. P.; Grzesiak, A. L.; Matzger, A. J. Crystalline Polymorph Selection and Discovery with Polymer Heteronuclei. *J. Am. Chem. Soc.* **2005**, *127* (15), 5512–5517. https:// doi: 10.1021/ja042561m.

(166) Delmas, T.; Roberts, M. M.; Heng, J. Y. Y. Nucleation and Crystallization of Lysozyme: Role of Substrate Surface Chemistry and Topography. *J. Adhes. Sci. Technol.* **2011**, *25* (4–5), 357–366. https://doi.org/10.1163/016942410X525614.

(167) Page, A. J.; Sear, R. P. Crystallization Controlled by the Geometry of a Surface. *J. Am. Chem. Soc.* **2009**, *131* (48), 17550–17551. https://doi.org/10.1021/ja9085512.

(168) Zhou, R. Bin; Cao, H. L.; Zhang, C. Y.; Yin, D. C. A Review on Recent Advances for Nucleants and Nucleation in Protein Crystallization. *Cryst Eng Comm.* **2017**, *19* (8), 1143–1155. https://doi.org/10.1039/c6ce02562e.

(169) Chayen, N. E., Hench, L. *Mesoporous Glass as Nucleant for Macromolecule Crystallisation*. WO2004041847A1, May 21, **2004**.

(170) Cooper, A. J. L. Biochemistry of Sulfur-Containing Amino Acids. *Annu. rev. of biochem.* **1983**, *52* (1), 187-222. https:// doi: 10.1146/annurev.bi.52.070183.001155.

(171) Griffith, O. W. Mammalian Sulfur Amino Acid Metabolism: An Overview. *Methods Enzymol.* **1987**, *143*, 366-76. https://doi.org/10.1016/0076-6879(87)43065-6.

(172) Brosnan, J. T.; Brosnan, M. E. The Sulfur-Containing Amino Acids: An Overview. *J. Nutr.* **2006**, *136* (6), 1636S-1640S. https://doi.org/10.1093/jn/136.6.1636S.

(173) Oda, H. Functions of Sulfur-Containing Amino Acids in Lipid Metabolism. *J. Nutr.* **2006**, *136* (6 Suppl), 1666S-1669S. https://doi.org/10.1093/jn/136.6.1666s.

(174) Ostrakhovitch, E. A.; Tabibzadeh, S. Homocysteine in Chronic Kidney Disease. *Adv. Clin. Chem*. **2015**, *72*, 77-106. https://doi.org/10.1016/bs.acc.2015.07.002.

(175) Laster, L.; Mudd, S. H.; Finkelstein, J. D.; Irreverre, F. Homocystinuria Due to Cystathionine Synthase Deficiency: The Metabolism of L-Methionine. *J. Clin. Invest.* **1965**, *44* (10), 1708–1719. https://doi.org/10.1172/JCI105278.

(176) Charmel, R.; Jacobsen, D. W. *Homocysteine in Health and Disease*; Cambridge University Press: New York, 2001. https://doi.org/10.1093/clinchem/48.6.966b.

(177) Kredich, N. M.; Tomkins, G. M. The Enzymic Synthesis of L-Cysteine in Escherichia Coli and Salmonella Typhimurium. *J. Biol. Chem.* **1966**, *241* (21), 4955-65. https://doi.org/10.1016/s0021-9258(18)99657-2.

(178) Macnicol, P. K.; Datko, A. H.; Giovanelli, J.; Mudd, S. H. Homocysteine Biosynthesis in Green Plants: Physiological Importance of the Transsulfuration Pathway in Lemna Paucicostata. *Plant Physiol.* **1981**, *68* (3), 619–625. https://doi.org/10.1104/pp.68.3.619.

(179) MacLean, K. N.; Janošík, M.; Oliveriusová, J.; Kery, V.; Kraus, J. P. Transsulfuration in Saccharomyces Cerevisiae Is Not Dependent on Heme: Purification and Characterization of Recombinant Yeast Cystathionine β-Synthase. *J. Inorg. Biochem.* **2000**, *81* (3), 161-71. https://doi.org/10.1016/S0162-0134(00)00100-8.

(180) Brzovic, P.; Holbrook, E. L.; Greene, R. C.; Dunn, M. F.; Brzovic, P.; Holbrook, E. L.; Greene, R. C.; Dunn, M. F.; Brzovic, P.; Greene, R. C.; *et al.* Reaction Mechanism of Escherichia Coli Cystathionine γ-Synthase: Direct Evidence for a Pyridoxamine Derivative of Vinylglyoxylate as a Key Intermediate in Pyridoxal Phosphate Dependent γ-Elimination and γ-Replacement Reactions. *Biochemistry.* **1990**, *29* (2), 442-51. https://doi.org/10.1021/bi00454a020.

(181) Clausen, T.; Huber, R.; Laber, B.; Pohlenz, H. D.; Messerschmidt, A. Crystal Structure of the Pyridoxal-5'-Phosphate Dependent Cystathionine β-Lyase from Escherichia Coli at 1.83 Å. *J. Mol. Biol.* **1996**, *262* (2), 202–224. https://doi.org/10.1006/jmbi.1996.0508.

(182) Mudd, S. H.; Finkelstein, J. D.; Irreverre, F.; Laster, L. Transsulfuration in Mammals.

Microassays and Tissue Distributions of Three Enzymes of the Pathway. *J. Biol. Chem.* **1965**, *240* (11), 4382–4392.

(183) Dicker-Brown, A.; Fonseca, V. A.; Fink, L. M.; Kern, P. A. The Effect of Glucose and Insulin on the Activity of Methylene Tetrahydrofolate Reductase and Cystathionine-β-Synthase: Studies in Hepatocytes. *Atherosclerosis.* **2001**, *158* (2), 297-301. https://doi.org/10.1016/S0021-9150(01)00442-7.

(184) Damba, T.; Zhang, M.; Buist-Homan, M.; van Goor, H.; Faber, K. N.; Moshage, H. Hydrogen Sulfide Stimulates Activation of Hepatic Stellate Cells through Increased Cellular Bio-Energetics. *Nitric Oxide - Biol. Chem.* **2019**, *92,* 26-33. https://doi.org/10.1016/j.niox.2019.08.004.

(185) Abe, K.; Kimura, H. The Possible Role of Hydrogen Sulfide as an Endogenous Neuromodulator. *J. Neurosci.* **1996**, *16* (3), 1066-71. https://doi.org/10.1523/jneurosci.16-03-01066.1996.

(186) Zhang, Y.; Tang, Z.-H.; Ren, Z.; Qu, S.-L.; Liu, M.-H.; Liu, L.-S.; Jiang, Z.-S. Hydrogen Sulfide, the Next Potent Preventive and Therapeutic Agent in Aging and Age-Associated Diseases. *Mol. Cell. Biol.* **2013**, *33* (6), 1104-13. https://doi.org/10.1128/mcb.01215-12.

(187) Robert, K.; Vialard, F.; Thiery, E.; Toyama, K.; Sinet, P. M.; Janel, N.; London, J. Expression of the Cystathionine β Synthase (CBS) Gene during Mouse Development and Immunolocalization in Adult Brain. *J. Histochem. Cytochem.* **2003**, *51* (3), 363-71. https://doi.org/10.1177/002215540305100311.

(188) Enokido, Y.; Suzuki, E.; Iwasawa, K.; Namekata, K.; Okazawa, H.; Kimura, H. Cystathionine B-synthase, a Key Enzyme for Homocysteine Metabolism, Is Preferentially Expressed in the Radial Glia/Astrocyte Lineage of Developing Mouse CNS. *FASEB J.* **2005**, *19* (13), 1854-6. https://doi.org/10.1096/fj.05-3724fje.

(189) Huang, S.; Li, H.; Ge, J. A Cardioprotective Insight of the Cystathionine γ-Lyase/Hydrogen Sulfide Pathway. *IJC Hear. Vasc.* **2015**, *7,* 51-57. https://doi.org/10.1016/j.ijcha.2015.01.010.

(190) Yuan, X.; Zhang, J.; Xie, F.; Tan, W.; Wang, S.; Huang, L.; Tao, L.; Xing, Q.; Yuan, Q. Loss of the Protein Cystathionine β-Synthase during Kidney Injury Promotes Renal Tubulointerstitial Fibrosis. *Kidney Blood Press. Res.* **2017**, *42* (3), 428-443. https://doi.org/10.1159/000479295.

(191) Kaneko, Y.; Kimura, Y.; Kimura, H.; Niki, I. L-Cysteine Inhibits Insulin Release from the Pancreatic β-Cell: Possible Involvement of Metabolic Production of Hydrogen Sulfide, a Novel Gasotransmitter. *Diabetes.* **2006**, *55* (5), 1391-7. https://doi.org/10.2337/db05-1082.

(192) Kaneko, Y.; Kimura, T.; Taniguchi, S.; Souma, M.; Kojima, Y.; Kimura, Y.; Kimura, H.; Niki, I. Glucose-Induced Production of Hydrogen Sulfide May Protect the Pancreatic Beta-Cells from Apoptotic Cell Death by High Glucose. *FEBS Lett.* **2009**, *583* (2), 377-82. https://doi.org/10.1016/j.febslet.2008.12.026.

(193) Tamizhselvi, R.; Moore, P. K.; Bhatia, M. Hydrogen Sulfide Acts as a Mediator of Inflammation Inacute Pancreatitis: In Vitro Studies Using Isolated Mouse Pancreatic Acinar Cells. *J. Cell.*

Mol. Med. **2007**, *11* (2), 315-26. https://doi.org/10.1111/j.1582-4934.2007.00024.x.

(194) Wang, C. N.; Liu, Y. J.; Duan, G. L.; Zhao, W.; Li, X. H.; Zhu, X. Y.; Ni, X. CBS and CSE Are Critical for Maintenance of Mitochondrial Function and Glucocorticoid Production in Adrenal Cortex. *Antiox. Redox Signal.* **2014**, *21* (16), 2192-207. https://doi.org/10.1089/ars.2013.5682.

(195) Turbat-Herrera, E. A.; Kilpatrick, M. J.; Chen, J.; Meram, A. T.; Cotelingam, J.; Ghali, G.; Kevil, C. G.; Coppola, D.; Shackelford, R. E. Cystathione β-Synthase Is Increased in Thyroid Malignancies. *Anticancer Res.* **2018**, *38* (11), 6085-6090. https://doi.org/10.21873/anticanres.12958.

(196) Magierowski, M.; Magierowska, K.; Hubalewska-Mazgaj, M.; Sliwowski, Z.; Pajdo, R.; Ginter, G.; Kwiecien, S.; Brzozowski, T.; Nagahara, N.; Wrobel, M. Exogenous and Endogenous Hydrogen Sulfide Protects Gastric Mucosa against the Formation and Time-Dependent Development of Ischemia/Reperfusion-Induced Acute Lesions Progressing into Deeper Ulcerations. *Molecules.* **2017**, *22* (2), 295. https://doi.org/10.3390/molecules22020295.

(197) Tomuschat, C.; O'Donnell, A. M.; Coyle, D.; Puri, P. Reduction of Hydrogen Sulfide Synthesis Enzymes Cystathionine-β-Synthase and Cystathionine-γ-Lyase in the Colon of Patients with Hirschsprungs Disease. *J. Pediatr. Surg.* **2018**, *53* (3), 525-530. https://doi.org/10.1016/j.jpedsurg.2017.06.011.

(198) Saghazadeh-Dezfuli, M.; Fanaei, H.; Gharib-Naseri, M. K.; Nasri, S.; Mard, S. A. Antidiarrheal Effect of Sodium Hydrosulfide in Diabetic Rats: In Vitro and in Vivo Studies. *Neurogastroenterol. Motil.* **2018**, *30* (10), e13273. https://doi.org/10.1111/nmo.13273.

(199) Han, W.; Dong, Z.; Dimitropoulou, C.; Su, Y. Hydrogen Sulfide Ameliorates Tobacco Smoke-Induced Oxidative Stress and Emphysema in Mice. *Antiox. Redox Signal.* **2011**, *15* (8), 2121-34. https://doi.org/10.1089/ars.2010.3821.

(200) Talaei, F.; Bouma, H. R.; Hylkema, M. N.; Strijkstra, A. M.; Boerema, A. S.; Schmidt, M.; Henning, R. H. The Role of Endogenous H2S Formation in Reversible Remodeling of Lung Tissue during Hibernation in the Syrian Hamster. *J. Exp. Biol.* **2012**, *215* (16), 2912-9. https://doi.org/10.1242/jeb.067363.

(201) Rashid, S.; Heer, J. K.; Garle, M. J.; Alexander, S. P. H.; Roberts, R. E. Hydrogen Sulphide-Induced Relaxation of Porcine Peripheral Bronchioles. *Br. J. Pharmacol.* **2013**, *168* (8), 1902-10. https://doi.org/10.1111/bph.12084.

(202) Luo, H.; Liu, L. B.; Feng, A. P.; Gao, Y.; Liao, G. Y.; Qiu, M. Q. Expressions of Cystathionine-Beta-Synthase and Cystathionine-Gamma-Lyase in the Corpus Cavernosum Smooth Muscle of Castrated Rats. *Zhonghua Nan Ke Xue.* **2013**, *19* (7), 599-603.

(203) Donovan, J.; Wong, P. S.; Garle, M. J.; Alexander, S. P. H.; Dunn, W. R.; Ralevic, V. Coronary Artery Hypoxic Vasorelaxation Is Augmented by Perivascular Adipose Tissue through a Mechanism Involving Hydrogen Sulphide and Cystathionine-β-Synthase. *Acta Physiol.* **2018**, *224* (4), e13126. https://doi.org/10.1111/apha.13126.

(204) Miles, E. W.; Kraus, J. P. Cystathionine β-Synthase: Structure, Function, Regulation, and

Location of Homocystinuria-Causing Mutations. *J. Biol. Chem.* **2004**, *279* (29), 29871–29874. https://doi.org/10.1074/jbc.R400005200.

(205) Zhu, H.; Blake, S.; Chan, K. T.; Pearson, R. B.; Kang, J. Cystathionine β -Synthase in Physiology and Cancer. *Biomed Res. Int.* **2018**, *2018,* 3205125. https://doi.org/10.1155/2018/3205125.

(206) Yang, G.; Wu, L.; Jiang, B.; Yang, W.; Qi, J.; Cao, K.; Meng, Q.; Mustafa, A. K.; Mu, W.; Zhang, S.; *et al.* H2S as a Physiologic Vasorelaxant : hypertension in mice with deletion of Cystathionine gamma -Lyase. *Science.* **2008**, *322* (5901), 587-90. https:// doi: 10.1126/science.1162667.

(207) Mustafa, A. K.; Gadalla, M. M.; Sen, N.; Kim, S.; Mu, W.; Gazi, S. K.; Barrow, R. K.; Yang, G.; Wang, R.; Snyder, S. H. H2S Signals through Protein S-Sulfhydration. *Sci. Signal.* **2009**, *2* (96), ra72. https://doi.org/10.1126/scisignal.2000464.

(208) Zhao, W.; Zhang, J.; Lu, Y.; Wang, R. The Vasorelaxant Effect of H2S as a Novel Endogenous Gaseous KATP Channel Opener. *EMBO J.* **2001**, *20* (21), 6008-16. https://doi.org/10.1093/emboj/20.21.6008.

(209) Mani, S.; Li, H.; Untereiner, A.; Wu, L.; Yang, G.; Austin, R. C.; Dickhout, J. G.; Lhoták, Š.; Meng, Q. H.; Wang, R. Decreased Endogenous Production of Hydrogen Sulfide Accelerates Atherosclerosis. *Circulation.* **2013**, *127* (25), 2523-34. https://doi.org/10.1161/CIRCULATIONAHA.113.002208.

(210) Ishii, I.; Akahoshi, N.; Yu, X. N.; Kobayashi, Y.; Namekata, K.; Komaki, G.; Kimura, H. Murine Cystathionine γ-Lyase: Complete CDNA and Genomic Sequences, Promoter Activity, Tissue Distribution and Developmental Expression. *Biochem. J.* **2004**, *381* (1), 113-23. https://doi.org/10.1042/BJ20040243.

(211) Mani, S.; Cao, W.; Wu, L.; Wang, R. Hydrogen Sulfide and the Liver. *Nitric Oxide - Biol. Chem.* **2014**, *41*, 62–71. https://doi.org/10.1016/j.niox.2014.02.006.

(212) Untereiner, A. A.; Dhar, A.; Liu, J.; Wu, L. Increased Renal Methylglyoxal Formation with Down-Regulation of PGC-1α-FBPase Pathway in Cystathionine γ-Lyase Knockout Mice. *PLoS One.* **2011**, *6* (12), e29592. https://doi.org/10.1371/journal.pone.0029592.

(213) Tripatara, P.; Patel, N. S. A.; Brancaleone, V.; Renshaw, D.; Rocha, J.; Sepodes, B.; Mota-Filipe, H.; Perretti, M.; Thiemermann, C. Characterisation of Cystathionine Gamma-Lyase/Hydrogen Sulphide Pathway in Ischaemia/Reperfusion Injury of the Mouse Kidney: An in Vivo Study. *Eur. J. Pharmacol.* **2009**, *606* (1–3), 205-9. https://doi.org/10.1016/j.ejphar.2009.01.041.

(214) Bos, E. M.; Wang, R.; Snijder, P. M.; Boersema, M.; Damman, J.; Fu, M.; Moser, J.; Hillebrands, J. L.; Ploeg, R. J.; Yang, G.; *et al.* Cystathionine γ-Lyase Protects against Renal Ischemia/Reperfusion by Modulating Oxidative Stress. *J. Am. Soc. Nephrol.* **2013**, *24* (5), 759-70. https://doi.org/10.1681/ASN.2012030268.

(215) Wu, L.; Yang, W.; Jia, X.; Yang, G.; Duridanova, D.; Cao, K.; Wang, R. Pancreatic Islet Overproduction of H2S and Suppressed Insulin Release in Zucker Diabetic Rats. *Lab. Investig.* **2009**, *89* (1), 59-67. https://doi.org/10.1038/labinvest.2008.109.

(216) Yang, G.; Tang, G.; Zhang, L.; Wu, L.; Wang, R. The Pathogenic Role of Cystathionine γ-Lyase/Hydrogen Sulfide in Streptozotocin-Induced Diabetes in Mice. *Am. J. Pathol.* **2011**, *179* (2), 869-79. https://doi.org/10.1016/j.ajpath.2011.04.028.

(217) Chang, T.; Untereiner, A.; Liu, J.; Wu, L. Interaction of Methylglyoxal and Hydrogen Sulfide in Rat Vascular Smooth Muscle Cells. *Antiox. Redox Signal.* **2010**, *12* (9), 1093-100. https://doi.org/10.1089/ars.2009.2918.

(218) Yang, G.; Sun, X.; Wang, R. Hydrogen Sulfide-induced Apoptosis of Human Aorta Smooth Muscle Cells via the Activation of Mitogen-activated Protein Kinases and Caspase-3. *FASEB J.* **2004**, *18* (14), 1782-4. https://doi.org/10.1096/fj.04-2279fje.

(219) Chen, Y.-H.; Wu, R.; Geng, B.; Qi, Y.-F.; Wang, P.-P.; Yao, W.-Z.; Tang, C.-S. Endogenous Hydrogen Sulfide Reduces Airway Inflammation and Remodeling in a Rat Model of Asthma. *Cytokine.* **2009**, *45* (2), 117–123.https:// doi: 10.1016/j.cyto.2008.11.009.

(220) Wang, P.; Zhang, G.; Wondimu, T.; Ross, B.; Wang, R. Hydrogen Sulfide and Asthma. *Experimental Physiology*. **2011**, *96* (9), 847-52. https://doi.org/10.1113/expphysiol.2011.057448.

(221) Pei, Y.; Wu, B.; Cao, Q.; Wu, L.; Yang, G. Hydrogen Sulfide Mediates the Anti-Survival Effect of Sulforaphane on Human Prostate Cancer Cells. *Toxicol. Appl. Pharmacol.* **2011**, *257* (3), 420-8. https://doi.org/10.1016/j.taap.2011.09.026.

(222) Mustafa, A. K.; Sikka, G.; Gazi, S. K.; Steppan, J.; Jung, S. M.; Bhunia, A. K.; Barodka, V. M.; Gazi, F. K.; Barrow, R. K.; Wang, R.; *et al.* Hydrogen Sulfide as Endothelium-Derived Hyperpolarizing Factor Sulfhydrates Potassium Channels. *Circ. Res.* **2011**, *109* (11), 1259-68. https://doi.org/10.1161/CIRCRESAHA.111.240242.

(223) Dharavath, S.; Raj, I.; Gourinath, S. Structure-Based Mutational Studies of O-Acetylserine Sulfhydrylase Reveal the Reason for the Loss of Cysteine Synthase Complex Formation in Brucella Abortus. *Biochem. J.* **2017**, *474* (7), 1221–1239. https://doi.org/10.1042/BCJ20161062.

(224) Schnell, R.; Oehlmann, W.; Singh, M.; Schneider, G. Structural Insights into Catalysis and Inhibition of O-Acetylserine Sulfhydrylase from Mycobacterium Tuberculosis: Crystal Structures of the Enzyme α-Aminoacrylate Intermediate and an Enzyme-Inhibitor Complex. *J. Biol. Chem.* **2007**, *282* (32), 23473–23481. https://doi.org/10.1074/jbc.M703518200.

(225) Williams, R. A. M.; Westrop, G. D.; Coombs, G. H. Two Pathways for Cysteine Biosynthesis in Leishmania Major. *Biochem. J.* **2009**, *420* (3), 451–462. https://doi.org/10.1042/BJ20082441.

(226) Marciano, D.; Santana, M.; Nowicki, C. Functional Characterization of Enzymes Involved in Cysteine Biosynthesis and H2S Production in Trypanosoma Cruzi. *Mol. Biochem. Parasitol.* **2012**, *185* (2), 114–120. https://doi.org/10.1016/j.molbiopara.2012.07.009.

(227) Raj, I.; Kumar, S.; Gourinath, S. The Narrow Active-Site Cleft of O-Acetylserine Sulfhydrylase from Leishmania Donovani Allows Complex Formation with Serine Acetyltransferases with a Range of C-Terminal Sequences. *Acta Crystallogr. Sect. D Biol. Crystallogr.* **2012**, *68* (8), 909–

919. https://doi.org/10.1107/S0907444912016459.

(228) Mori, M.; Jeelani, G.; Masuda, Y.; Sakai, K.; Tsukui, K.; Waluyo, D.; Tarwadi; Watanabe, Y.; Nonaka, K.; Matsumoto, A.; *et al.* Identification of Natural Inhibitors of Entamoeba Histolytica Cysteine Synthase from Microbial Secondary Metabolites. *Front. Microbiol.* **2015**, *6*, 962. https://doi.org/10.3389/fmicb.2015.00962.

(229) Jeelani, G.; Nozaki, T. Metabolomic Analysis of Entamoeba: Applications and Implications. *Curr. Opin. Microbiol*. **2014**, *20*, 118-24. https://doi.org/10.1016/j.mib.2014.05.016.

(230) Bonner, E. R.; Cahoon, R. E.; Knapke, S. M.; Jez, J. M. Molecular Basis of Cysteine Biosynthesis in Plants: Structural and Functional Analysis of O-Acetylserine Sulfhydrylase from Arabidopsis Thaliana. *J. Biol. Chem.* **2005**, *280* (46), 38803–38813. https://doi.org/10.1074/jbc.M505313200.

(231) Romero, L. C.; Aroca, M. Á.; Laureano-Marín, A. M.; Moreno, I.; García, I.; Gotor, C. Cysteine and Cysteine-Related Signaling Pathways in Arabidopsis Thaliana. *Molecular Plant*. **2014**, *7* (2), 264-76. https://doi.org/10.1093/mp/sst168.

(232) Campanini, B.; Benoni, R.; Bettati, S.; Beck, C. M.; Hayes, C. S.; Mozzarelli, A. Moonlighting O-Acetylserine Sulfhydrylase: New Functions for an Old Protein. *Biochim. Biophys.* **2015**, *1854* (9), 1184–1193. https://doi.org/10.1016/j.bbapap.2015.02.013.

(233) Rabeh, W. M.; Cook, P. F. Structure and Mechanism of O-Acetylserine Sulfhydrylase. *Journal of Biological Chemistry*. **2004**, *279* (26), 26803-6. https://doi.org/10.1074/jbc.R400001200.

(234) Raboni, S.; Spyrakis, F.; Campanini, B.; Amadasi, A.; Bettati, S.; Peracchi, A.; Mozzarelli, A.; Contestabile, R. Pyridoxal 5-Phosphate-Dependent Enzymes: Catalysis, Conformation, and Genomics. *Compr. Nat. Prod. II Chem. Biol.* **2010**, *7*, 273–315. https://doi.org/10.1016/b978-008045382-8.00140-4.

(235) Berkowitz, O.; Wirtz, M.; Wolf, A.; Kuhlmann, J.; Hell, R. Use of Biomolecular Interaction Analysis to Elucidate the Regulatory Mechanism of the Cysteine Synthase Complex from Arabidopsis Thaliana. *J. Biol. Chem.* **2002**, *277* (34), 30629-34. https://doi.org/10.1074/jbc.M111632200.

(236) Wirtz, M.; Hell, R. Functional Analysis of the Cysteine Synthase Protein Complex from Plants: Structural, Biochemical and Regulatory Properties. *J. Plant Physiol.* **2006**, *163* (3), 273-86. https://doi.org/10.1016/j.jplph.2005.11.013.

(237) Kredich, N. M.; Becker, M. A.; Tomkins, G. M. Purification and Characterization of Cysteine Synthetase, a Bifunctional Protein Complex, from Salmonella Typhimurium. *J. Biol. Chem.* **1969**, *244* (9), 2428-39. https://doi.org/10.1016/s0021-9258(19)78241-6.

(238) Pye, V. E.; Tingey, A. P.; Robson, R. L.; Moody, P. C. E. The Structure and Mechanism of Serine Acetyltransferase from Escherichia Coli. *J. Biol. Chem.* **2004**, *279* (39), 40729–40736. https://doi.org/10.1074/jbc.M403751200.

(239) Hullo, M. F.; Auger, S.; Soutourina, O.; Barzu, O.; Yvon, M.; Danchin, A.; Martin-Verstraete, I.

Conversion of Methionine to Cysteine in Bacillus Subtilis and Its Regulation. *J. Bacteriol.* **2007**, *189* (1), 187–197. https://doi.org/10.1128/JB.01273-06.

(240) Devi, S.; Abdul Rehman, S. A.; Tarique, K. F.; Gourinath, S. Structural Characterization and Functional Analysis of Cystathionine β-Synthase: An Enzyme Involved in the Reverse Transsulfuration Pathway of Bacillus Anthracis. *FEBS J.* **2017**, *284* (22), 3862–3880. https://doi.org/10.1111/febs.14273.

(241) Matoba, Y.; Yoshida, T.; Izuhara-Kihara, H.; Noda, M.; Sugiyama, M. Crystallographic and Mutational Analyses of Cystathionine β-Synthase in the H2S-Synthetic Gene Cluster in Lactobacillus Plantarum. *Protein Sci.* **2017,** *26* (4), 763-783. https://doi.org/10.1002/pro.3123.

(242) Devi, S.; Tarique, K. F.; Ali, M. F.; Abdul Rehman, S. A.; Gourinath, S. Identification and Characterization of Helicobacter Pylori O-acetylserine-dependent Cystathionine B-synthase, a Distinct Member of the PLP-II Family. *Mol. Microbiol.* **2019**, *112* (2), 718–739. https://doi.org/10.1111/mmi.14315.

(243) Rege, V. D.; Kredich, N. M.; Tai, C. H.; Karsten, W. E.; Schnackerz, K. D.; Cook, P. F. A Change in the Internal Aldimine Lysine (K42) in O-Acetylserine Sulfhydrylase to Alanine Indicates Its Importance in Transimination and as a General Base Catalyst. *Biochemistry.* **1996**, *35* (41), 13485-93. https://doi.org/10.1021/bi961517j.

(244) Kredich, N. M. The Molecular Basis for Positive Regulation of Cys Promoters in Salmonella Typhimurium and Escherichia Coli. *Mol. Microbiol.* **1992**, *6* (19), 2747–2753. https://doi.org/10.1111/j.1365-2958.1992.tb01453.x.

(245) Cherest, H.; Surdin-Kerjan, Y. Genetic Analysis of a New Mutation Conferring Cysteine Auxotrophy in Saccharomyces Cerevisiae: Updating of the Sulfur Metabolism Pathway. *Genetics.* **1992**, *130* (1), 51–58.https:// doi: 10.1093/genetics/130.1.51.

(246) Taoka, S.; Lepore, B. W.; Kabil, Ö.; Ojha, S.; Ringe, D.; Banerjee, R. Human Cystathionine β-Synthase Is a Heme Sensor Protein. Evidence That the Redox Sensor Is Heme and Not the Vicinal Cysteines in the CXXC Motif Seen in the Crystal Structure of the Truncated Enzyme. *Biochemistry.* **2002,** *41* (33), 10454-61. https://doi.org/10.1021/bi026052d.

(247) Finkelstein, J. D.; Harris, B. J.; Kyle, W. E. Methionine Metabolism in Mammals: Kinetic Study of Betaine-Homocysteine Methyltransferase. *Arch. Biochem. Biophys.* **1972**, *153* (1), 320-4. https://doi.org/10.1016/0003-9861(72)90451-1.

(248) Finkelstein, J. D.; Martin, J. J. Methionine Metabolism in Mammals. Adaptation to Methionine Excess. *J. Biol. Chem.* **1986**, *261* (4), 1582-7. https://doi.org/10.1016/s0021-9258(17)35979-3.

(249) Cantoni, G. L. The Nature of the Active Methyl Donor Formed Enzymatically from L-Methionine and Adenosinetriphosphate. *Journal of the American Chemical Society*. **1952**, *74* (11), 2942-2943. https://doi.org/10.1021/ja01131a519.

(250) Finkelstein, J. D.; Kyle, W. E.; Martin, J. J.; Pick, A. M. Activation of Cystathionine Synthase by

Adenosylmethionine and Adenosylethionine. *Biochem. Biophys. Res. Commun.* **1975**, *66* (1), 81-7. https://doi.org/10.1016/S0006-291X(75)80297-X.

(251) Kutzbach, C.; Stokstad, E. L. R. Mammalian Methylenetetrahydrofolate Reductase Partial Purification, Properties, and Inhibition by S-Adenosylmethionine. *BBA - Enzymol.* **1971**, *250* (3), 459-77. https://doi.org/10.1016/0005-2744(71)90247-6.

(252) Kutzbach, C.; Stokstad, E. L. R. Feedback Inhibition of Methylene-Tetrahydrofolate Reductase in Rat Liver by S-Adenosylmethionine. *BBA - Enzymol.* **1967**, *139* (1), 217-20. https://doi.org/10.1016/0005-2744(67)90140-4.

(253) Finkelstein, J. D.; Martin, J. J. Methionine Metabolism in Mammals. Distribution of Homocysteine between Competing Pathways. *J. Biol. Chem.* **1984**, *259* (15), 9508-13. https://doi.org/10.1016/s0021-9258(17)42728-1.

(254) Martinov, M. V.; Vitvitsky, V. M.; Mosharov, E. V.; Banerjee, R.; Ataullakhanov, F. I. A Substrate Switch: A New Mode of Regulation in the Methionine Metabolic Pathway. *J. Theor. Biol.* **2000**, *204* (4), 521-32. https://doi.org/10.1006/jtbi.2000.2035.

(255) Fernández-Rodríguez, C.; Oyenarte, I.; Conter, C.; González-Recio, I.; Núñez-Franco, R.; Gil-Pitarch, C.; Quintana, I.; Jiménez-Osés, G.; Dominici, P.; Martinez-Chantar, M. L.; *et al.* Structural Insight into the Unique Conformation of Cystathionine β-Synthase from Toxoplasma Gondii. *Comput. Struct. Biotechnol. J.* **2021**, *19*, 3542–3555. https://doi.org/10.1016/j.csbj.2021.05.052.

(256) Mudd, S.H.; Finkelstein, J. D.; Irreverre, F.; Laster, L. Homocystinuria: An Enzymatic Defect. *Science.* **1964**, *143* (3613), 1443-5. https://doi.org/10.1126/science.143.3613.1443.

(257) HARRIS, H.; PENROSE, L. S.; THOMAS, D. H. H. CYSTATHIONINURIA. *Ann. Hum. Genet.* **1959**, *23* (4). https://doi.org/10.1111/j.1469-1809.1959.tb01485.x.

(258) Sachdev, P. S. Homocysteine and Brain Atrophy. *Progress in Neuro-Psychopharmacology and Biological Psychiatry*. **2005**, *29* (7), 1152-61. https://doi.org/10.1016/j.pnpbp.2005.06.026.

(259) Rosado, J. O.; Salvador, M.; Bonatto, D. Importance of the Trans-Sulfuration Pathway in Cancer Prevention and Promotion. *Molecular and Cellular Biochemistry*. **2007**, *301* (1-2), 1-12. https://doi.org/10.1007/s11010-006-9389-y.

(260) Régnier, V.; Billard, J. M.; Gupta, S.; Potier, B.; Woerner, S.; Paly, E.; Ledru, A.; David, S.; Luilier, S.; Bizot, J. C.; *et al.* Brain Phenotype of Transgenic Mice Overexpressing Cystathionine β-Synthase. *PLoS One.* **2012**, *7* (1), e29056. https://doi.org/10.1371/journal.pone.0029056.

(261) Castro, R.; Rivera, I.; Blom, H. J.; Jakobs, C.; Tavares de Almeida, I. Homocysteine Metabolism, Hyperhomocysteinaemia and Vascular Disease: An Overview. *Journal of Inherited Metabolic Disease*. **2006**, *29*(1), 3-20. https://doi.org/10.1007/s10545-006-0106-5.

(262) Mudd, S. H.; Skovby, F.; Levy, H. L. The Natural History of Homocystinura Due to Cystathionine β-Synthase Deficiency. *American Journal of Human Genetics*. **1985**, *37* (1), 1-31. https:// doi: 10.1016/j.ymgme.2009.09.009.

(263) Murray, R. K.; Granner, D. K.; Mayes, P. A.; Rodwell, V. W. *Harper's Illustrated Biochemistry (31st Edition)*; McGraw Hill: New York, 2018; Vol 32.

(264) Sulochana, K. N.; Amirthalakshmi, S.; Vasanthi, S. B.; Tamilselvi, R.; Ramakrishnan, S. Homocystinuria with Congenital/Developmental Cataract. *Indian J. Pediatr.* **2000**, *67* (10), 725-8. https://doi.org/10.1007/BF02723928.

(265) Watkins, D.; Ru, M.; Hwang, H. Y.; Kim, C. D.; Murray, A.; Philip, N. S.; Kim, W.; Legakis, H.; Wai, T.; Hilton, J. F.; *et al.* Hyperhomocysteinemia Due to Methionine Synthase Deficiency, CblG: Structure of the MTR Gene, Genotype Diversity, and Recognition of a Common Mutation, P1173L. *Am. J. Hum. Genet.* **2002**, *71* (1), 143-54. https://doi.org/10.1086/341354.

(266) Gerritsen, T.; Vaughn, J. G.; Waisman, H. A. The Identification of Homocystine in the Urine. *Biochem. Biophys. Res. Commun.* **1962**, *9* (6), 493-6. https://doi.org/10.1016/0006-291X(62)90114-6.

(267) Carson, N. A. J.; Neill, D. W. Metabolic Abnormalities Detected in a Survey of Mentally Backward Individuals in Northern Ireland. *Arch. Dis. Child.* **1962**, *37* (195), 505-13. https://doi.org/10.1136/adc.37.195.505.

(268) De Franchis, R.; Sperandeo, M. P.; Sebastio, G.; Andria, G. Clinical Aspects of Cystathionine Beta-Synthase Deficiency: How Wide Is the Spectrum? The Italian Collaborative Study Group on Homocystinuria. *Eur. J. Pediatr.* **1998**, *157 Suppl 2, S67-70*. https://doi.org/10.1007/pl00014309.

(269) Naughten, E. R. Newborn Screening for Homocystinuria: Irish and World Experience. *Eur. J. Pediatr. Suppl.* **1998**, *157* (2), S84-7. https://doi.org/10.1007/pl00014310.

(270) Zschocke, J.; Kebbewar, M.; Gan-Schreier, H.; Fischer, C.; Fang-Hoffmann, J.; Wilrich, J.; Abdoh, G.; Ben-Omran, T.; Shahbek, N.; Lindner, M.; *et al*. Molecular Neonatal Screening for Homocystinuria in the Qatari Population. *Hum. Mutat.* **2009**, *30* (6), 1021-2. https://doi.org/10.1002/humu.20994.

(271) Tada, K.; Tateda, H.; Arashima, S.; Sakai, K.; Kitagawa, T.; Aoki, K.; Suwa, S.; Kawamura, M.; Oura, T.; Takesada, M.; *et al*. Follow-up Study of a Nation-Wide Neonatal Metabolic Screening Program in Japan - A Collaborative Study Group of Neonatal Screening for Inborn Errors of Metabolism in Japan. *Eur. J. Pediatr.* **1984**, *142* (3), 204-7. https://doi.org/10.1007/BF00442450.

(272) García-Jiménez, M. C.; Baldellou, A.; García-Silva, M. T.; Dalmau-Serra, J.; García-Cazorla, A.; Gómez-López, L.; Pedrón Giner, C.; Alonso Luengo, O.; Peña Quintana, L.; Luz Couce, M.; *et al*. Epidemiological Study of the Metabolic Diseases with Homocystinuria in Spain. *An. Pediatría Publicación Of. la Asoc. Española Pediatría (AEP).* **2012**, *76* (3), 133-9. https://doi.org/10.1016/j.anpedi.2011.08.008.

(273) Kraus, J. P.; Janosĭk, M.; Kožich, V.; Mandell, R.; Shih, V.; Sperandeo, M. P.; Sebastio, G.; De Franchis, R.; Andria, G.; Kluijtmans, L. A. J.; *et al*. Cystathionine β-Synthase Mutations in Homocystinuria. *Hum. Mutat.* **1999**, *13* (5), 362-75. https://doi.org/10.1002/(SICI)1098-1004(1999)13:5<362::AID-HUMU4>3.0.CO;2-K.

(274) Kraus, J. P. Komrower Lecture. Molecular Basis of Phenotype Expression in Homocystinuria. *J. Inherit. Metab. Dis.* **1994**, *17* (4), 383–390. https://doi.org/10.1007/BF00711354.

(275) Gallagher, D. T.; Gilliland, G. L.; Xiao, G.; Zondlo, J.; Fisher, K. E.; Chinchilla, D.; Eisenstein, E. Structure and Control of Pyridoxal Phosphate Dependent Allosteric Threonine Deaminase. *Structure.* **1998**, *6* (4), 465-75. https://doi.org/10.1016/S0969-2126(98)00048-3.

(276) Urreizti, R.; Asteggiano, C.; Bermudez, M.; Córdoba, A.; Szlago, M.; Grosso, C.; De Kremer, R. D.; Vilarinho, L.; D'Almeida, V.; Martínez-Pardo, M.; *et al*. The p.T191M Mutation of the CBS Gene Is Highly Prevalent among Homocystinuric Patients from Spain, Portugal and South America. *J. Hum. Genet.* **2006**, *51* (4), 305-313. https://doi.org/10.1007/s10038-006-0362-0.

(277) Yap, S.; Naughten, E. Homocystinuria Due to Cystathionine β-Synthase Deficiency in Ireland: 25 Years' Experience of a Newborn Screened and Treated Population with Reference to Clinical Outcome and Biochemical Control. *J. Inherit. Metab. Dis.* **1998**, *21* (7), 738–747. https://doi.org/10.1023/A:1005445132327.

(278) Wilcken, D. E. L.; Wilcken, B. The Natural History of Vascular Disease in Homocystinuria and the Effects of Treatment. In *Journal of Inherited Metabolic Disease*. Green, A., Eds.; Springer: 1992; Vol. 20 (2), pp 295-300. https://doi.org/10.1023/A:1005373209964.

(279) Yap, S.; Barry-Kinsella, C.; Naughten, E. R. Maternal Pyridoxine Non-Responsive Homocystinuria: The Role of Dietary Treatment and Anticoagulation. *Br. J. Obstet. Gynaecol.* **2001**, *108* (4), 425-8. https://doi.org/10.1016/S0306-5456(00)00086-3.

(280) Perry, T. L.; Hardwick, D. F.; Hansen, S.; Love, D. L.; Israels, S. Cystathioninuria in Two Healthy Siblings. *N. Engl. J. Med.* **1968**, *278* (11), 590–592.https:// doi: 10.1056/NEJM196803142781104.

(281) Vargas, J. E.; Mudd, S. H.; Waisbren, S. E.; Levy, H. L. Maternal γ-Cystathionase Deficiency: Absence of Both Teratogenic Effects and Pregnancy Complications. *Am. J. Obstet. Gynecol.* **1999**, *181* (3), 753-5. https://doi.org/10.1016/S0002-9378(99)70525-9.

(282) Schneiderman, L. J. Latent Cystathioninuria. *J. Med. Genet.* **1967**, *4* (4), 260-3. https://doi.org/10.1136/jmg.4.4.260.

(283) Espinós, C.; García-Cazorla, A.; Martínez-Rubio, D.; Martínez-Martínez, E.; Vilaseca, M. A.; Pérez-Dueñas, B.; Kožich, V.; Palau, F.; Artuch, R. Ancient Origin of the CTH Alelle Carrying the c.200C>T (p.T67I) Variant in Patients with Cystathioninuria. *Clin. Genet.* **2010**, *78* (6), 554-9. https://doi.org/10.1111/j.1399-0004.2010.01431.x.

(284) Mongeau, J. G.; Hilgartner, M.; Worthen, H. G.; Frimpter, G. W. Cystathioninuria: Study of an Infant With normal Mentality, Thrombocytopenia, and Renal Calculi. *J. Pediatr.* **1966**, *69* (6), 1113-1120. https://doi.org/10.1016/S0022-3476(66)80303-7.

(285) Weil, M. L.; Shaw, K. N.; Menkes, J. Cystathioninuria Accompanying Necrotizing Encephalomyelopathy of Childhood. *Neurology* **1968**, *18* (3), 301.

(286) Endres, W.; Wuttge, B. Occurrence of Secondary Cystathioninuria in Children with Inherited

Metabolic Disorders, Liver Diseases, Neoplasms, Cystic Fibrosis and Celiac Disease. *Eur. J. Pediatr.* **1978**, *129* (1), 29-35. https://doi.org/10.1007/BF00441371.

(287) HESTNES, A.; BORUD, O.; LUNDE, H.; GJESSING, L. Cystathioninuria in Down's Syndrome. *J. Intellect. Disabil. Res.* **1989**, *33* (3), 261-5. https://doi.org/10.1111/j.1365-2788.1989.tb01474.x.

(288) Klein, C. E.; Roberts, B.; Glode, L. M.; Holcenberg, J. Cystathionine Metabolism in Neuroblastoma. *Cancer.* **1988**, *62* (2), 291-8. https://doi.org/10.1002/1097-0142(19880715)62:2<291::AID-CNCR2820620211>3.0.CO;2-Q.

(289) Rajnherc, J. R.; van Gennip, A. H.; Abeling, N. G. G. M.; van der Zee, J. M.; Voŭte, P. A. Cystathioninuria in Patients with Neuroblastoma. *Med. Pediatr. Oncol.* **1984**, *12* (2), 81-4. https://doi.org/10.1002/mpo.2950120203.

(290) Shin, Y. S.; Rasshofer, R.; Friedrich, B.; Endres, W. Pyridoxal-5'-Phosphate Determination by a Sensitive Micromethod in Human Blood, Urine and Tissues; Its Relation to Cystathioninuria in Neuroblastoma and Biliary Atresia. *Clin. Chim. Acta.* **1983**, *127* (1), 77-85. https://doi.org/10.1016/0009-8981(83)90077-3.

(291) Geiser, C. F.; Shih, V. E. Cystathioninuria and Its Origin in Children with Hepatoblastoma. *J. Pediatr.* **1980**, *96* (1), 72-5. https://doi.org/10.1016/S0022-3476(80)80333-7.

(292) Wang, J.; Hegele, R. A. Genomic Basis of Cystathioninuria (MIM 219500) Revealed by Multiple Mutations in Cystathionine Gamma-Lyase (CTH). *Hum. Genet.* **2003**, *112* (4), 404-8. https://doi.org/10.1007/s00439-003-0906-8.

(293) Wong, L. T. K.; Hardwick, D. F.; Applegarth, D. A.; Davidson, A. G. F. Review of Metabolic Screening Program of Children's Hospital, Vancouver, British Columbia. 1971-1977. *Clin. Biochem.* **1979**, *12* (5), 167-72. https://doi.org/10.1016/S0009-9120(79)80083-1.

(294) Pascal, T. A.; Gaull, G. E.; Beratis, N. G.; Gillam, B. M.; Tallan, H. H. Cystathionase Deficiency: Evidence for Genetic Heterogeneity in Primary Cystathioninuria. *Pediatr. Res.* **1978**, *12* (2), 125-33. https://doi.org/10.1203/00006450-197802000-00012.

(295) Tada, K.; Yoshida, T.; Yokoyama, Y.; Sato, T.; Nakagawa, H.; Arakawa, T. Cystathioninuria Not Associated with Vitamin B6 Dependency: A Probably New Type of Cystathioninuria. *Tohoku J. Exp. Med.* **1968**, *95* (3), 235-42. https://doi.org/10.1620/tjem.95.235.

(296) Zhu, W.; Lin, A.; Banerjee, R. Kinetic Properties of Polymorphic Variants and Pathogenic Mutants in Human Cystathionine γ-Lyase. *Biochemistry.* **2008**, *47* (23), 6226-32. https://doi.org/10.1021/bi800351a.

(297) Paul, B. D.; Sbodio, J. I.; Snyder, S. H. Cysteine Metabolism in Neuronal Redox Homeostasis. *Trends in Pharmacological Sciences*. **2018**, *39* (5), 513-524. https://doi.org/10.1016/j.tips.2018.02.007.

(298) Ratan, R. R.; Murphy, T. H.; Baraban, J. M. Macromolecular Synthesis Inhibitors Prevent Oxidative Stress-Induced Apoptosis in Embryonic Cortical Neurons by Shunting Cysteine from

Protein Synthesis to Glutathione. *J. Neurosci.* **1994**, *14* (7), 4385-92. https://doi.org/10.1523/jneurosci.14-07-04385.1994.

(299) Seshadri, S.; Beiser, A.; Selhub, J.; Jacques, P. F.; Rosenberg, I. H.; D'Agostino, R. B.; Wilson, P. W. F.; Wolf, P. A. Plasma Homocysteine as a Risk Factor for Dementia and Alzheimer's Disease. *N. Engl. J. Med.* **2002**, *346* (7), 476-83. https://doi.org/10.1056/nejmoa011613.

(300) Ansari, R.; Mahta, A.; Mallack, E.; Luo, J. J. Hyperhomocysteinemia and Neurologic Disorders: A Review. *J Clin Neurol*. **2014**, *10* (4), 281-8. https://doi.org/10.3988/jcn.2014.10.4.281.

(301) Starkebaum, G.; Harlan, J. M. Endothelial Cell Injury Due to Copper-Catalyzed Hydrogen Peroxide Generation from Homocysteine. *J. Clin. Invest.* **1986**, *77* (4), 1370-6. https://doi.org/10.1172/JCI112442.

(302) Beal, M. F. Aging, Energy, and Oxidative Stress in Neurodegenerative Diseases. *Ann. Neurol.* **1995**, *38* (3), 357-66. https://doi.org/10.1002/ana.410380304.

(303) Mccann, S. M. The Nitric Oxide Hypothesis of Brain Aging. *Exp.Gerontol.* **1997**, *32* (4-5), 431-40. https://doi.org/10.1016/S0531-5565(96)00154-4.

(304) Chao, C. L.; Kuo, T. L.; Lee, Y. T. Effects of Methionine-Induced Hyperhomocysteinemia on Endothelium- Dependent Vasodilation and Oxidative Status in Healthy Adults. *Circulation.* **2000**, *101* (5), 485-90. https://doi.org/10.1161/01.CIR.101.5.485.

(305) Paul, B. D.; Snyder, S. H. Neurodegeneration in Huntington's Disease Involves Loss of Cystathionine γ-Lyase. *Cell Cycle.* **2014**, *13* (16), 2491–2493. https://doi.org/10.4161/15384101.2014.950538.

(306) Tabassum, R.; Jeong, N. Y. Potential for Therapeutic Use of Hydrogen Sulfide in Oxidative Stress-Induced Neurodegenerative Diseases. *Int. J. Med. Sci*. **2019**, *16* (10), 1386-1396. https://doi.org/10.7150/ijms.36516.

(307) Commoner, B.; Townsend, J.; Pake, G. E. Free Radicals in Biological Materials. *Nature.* **1954**, *174* (4432), 689-91. https://doi.org/10.1038/174689a0.

(308) Newsholme, P.; Cruzat, V. F.; Keane, K. N.; Carlessi, R.; De Bittencourt, P. I. H. Molecular Mechanisms of ROS Production and Oxidative Stress in Diabetes. *Biochem. J*. **2016**, *473* (24), 4527-4550. https://doi.org/10.1042/BCJ20160503C.

(309) Ahmad, W.; Ijaz, B.; Shabbiri, K.; Ahmed, F.; Rehman, S. Oxidative Toxicity in Diabetes and Alzheimer's Disease: Mechanisms behind ROS/ RNS Generation. *J. Biomed. Sci*. **2017**, *24* (1), 76. https://doi.org/10.1186/s12929-017-0379-z.

(310) Cenini, G.; Lloret, A.; Cascella, R. Oxidative Stress and Mitochondrial Damage in Neurodegenerative Diseases: From Molecular Mechanisms to Targeted Therapies. *Oxid. Med. Cell. Longev*. **2020**, *2020*, 1270256. https://doi.org/10.1155/2020/1270256.

(311) Birben, E.; Sahiner, U. M.; Sackesen, C.; Erzurum, S.; Kalayci, O. Oxidative Stress and Antioxidant Defense. *World Allergy Org. J*. **2012**, *5* (1), 9-19.

https://doi.org/10.1097/WOX.0b013e3182439613.

(312) Perron, N. R.; Hodges, J. N.; Jenkins, M.; Brumaghim, J. L. Predicting How Polyphenol Antioxidants Prevent DNA Damage by Binding to Iron. *Inorg. Chem.* **2008**, *47* (14), 6153-61. https://doi.org/10.1021/ic7022727.

(313) Xie, Z. Z.; Liu, Y.; Bian, J. S. Hydrogen Sulfide and Cellular Redox Homeostasis. *Oxid. Med. Cell. Longev.* **2016**, *2016,* 6043038. https://doi.org/10.1155/2016/6043038.

(314) Fukai, T.; Ushio-Fukai, M. Superoxide Dismutases: Role in Redox Signaling, Vascular Function, and Diseases. *Antiox. Redox Signal*. **2011**, *15* (6), 1583-606. https://doi.org/10.1089/ars.2011.3999.

(315) Wang, R. Gasotransmitters: Growing Pains and Joys. *Trends Biochem.l Sci*. **2014**, *39* (5), 227-32. https://doi.org/10.1016/j.tibs.2014.03.003.

(316) Olas, B. Gasomediators (·NO, CO, and H2S) and Their Role in Hemostasis and Thrombosis. *Clin. Chim. Acta*. **2015**, *445*, 115-21. https://doi.org/10.1016/j.cca.2015.03.027.

(317) Hosoki, R.; Matsuki, N.; Kimura, H. The Possible Role of Hydrogen Sulfide as an Endogenous Smooth Muscle Relaxant in Synergy with Nitric Oxide. *Biochem. Biophys. Res. Commun.* **1997**, *237* (3), 527-31. https://doi.org/10.1006/bbrc.1997.6878.

(318) Yang, G.; Wu, L.; Jiang, B.; Yang, W.; Qi, J.; Cao, K.; Meng, Q.; Mustafa, A. K.; Mu, W.; Zhang, S.; *et al*. H2S as a Physiologic Vasorelaxant: Hypertension in Mice with Deletion of Cystathionine γ-Lyase. *Science.* **2008**, *322* (5901), 587-90. https://doi.org/10.1126/science.1162667.

(319) Cheng, Y.; Ndisang, J. F.; Tang, G.; Cao, K.; Wang, R. Hydrogen Sulfide-Induced Relaxation of Resistance Mesenteric Artery Beds of Rats. *Am. J. Physiol. - Hear. Circ. Physiol.* **2004**, *287* (5), H2316-23. https://doi.org/10.1152/ajpheart.00331.2004.

(320) Hu, L. F.; Wong, P. T. H.; Moore, P. K.; Bian, J. S. Hydrogen Sulfide Attenuates Lipopolysaccharide-Induced Inflammation by Inhibition of P38 Mitogen-Activated Protein Kinase in Microglia. *J. Neurochem.* **2007**, *100* (4), 1121-8. https://doi.org/10.1111/j.1471-4159.2006.04283.x.

(321) Kim, K. M.; Pae, H. O.; Zhung, M.; Ha, H. Y.; Ha, Y. A.; Chai, K. Y.; Cheong, Y. K.; Kim, J. M.; Chung, H. T. Involvement of Anti-Inflammatory Heme Oxygenase-1 in the Inhibitory Effect of Curcumin on the Expression of pro-Inflammatory Inducible Nitric Oxide Synthase in RAW264.7 Macrophages. *Biomed. Pharmacother.* **2008**, *62* (9), 630-6. https://doi.org/10.1016/j.biopha.2008.01.008.

(322) Oh, G. S.; Pae, H. O.; Lee, B. S.; Kim, B. N.; Kim, J. M.; Kim, H. R.; Jeon, S. B.; Jeon, W. K.; Chae, H. J.; Chung, H. T. Hydrogen Sulfide Inhibits Nitric Oxide Production and Nuclear Factor-KB via Heme Oxygenase-1 Expression in RAW264.7 Macrophages Stimulated with Lipopolysaccharide. *Free Radic. Biol. Med.* **2006**, *41* (1), 106-19. https://doi.org/10.1016/j.freeradbiomed.2006.03.021.

(323) Wang, M.-J.; Cai, W.-J.; Zhu, Y.-C. Mechanisms of Angiogenesis: Role of Hydrogen Sulphide. *Clin. Exp. Pharmacol. Physiol.* **2010**, *37* (7), 764-71. https://doi.org/10.1111/j.1440-1681.2010.05371.x.

(324) Pan, L. L.; Liu, X. H.; Gong, Q. H.; Wu, D.; Zhu, Y. Z. Hydrogen Sulfide Attenuated Tumor Necrosis Factor-α-Induced Inflammatory Signaling and Dysfunction in Vascular Endothelial Cells. *PLoS One.* **2011**, *6* (5), e19766. https://doi.org/10.1371/journal.pone.0019766.

(325) Calvert, J. W.; Coetzee, W. A.; Lefer, D. J. Novel Insights into Hydrogen Sulfide-Mediated Cytoprotection. *Antiox. Redox Signal*. **2010**, *12* (10), 1203-17. https://doi.org/10.1089/ars.2009.2882.

(326) Sen, N.; Paul, B. D.; Gadalla, M. M.; Mustafa, A. K.; Sen, T.; Xu, R.; Kim, S.; Snyder, S. H. Hydrogen Sulfide-Linked Sulfhydration of NF-KB Mediates Its Antiapoptotic Actions. *Mol. Cell.* **2012**, *45* (1), 13-24. https://doi.org/10.1016/j.molcel.2011.10.021.

(327) Tan, G.; Pan, S.; Li, J.; Dong, X.; Kang, K.; Zhao, M.; Jiang, X.; Kanwar, J. R.; Qiao, H.; Jiang, H.; *et al*. Hydrogen Sulfide Attenuates Carbon Tetrachloride-Induced Hepatotoxicity, Liver Cirrhosis and Portal Hypertension in Rats. *PLoS One.* **2011**, *6* (10), e25943. https://doi.org/10.1371/journal.pone.0025943.

(328) Cheng, Z.; Kishore, R. Potential Role of Hydrogen Sulfide in Diabetes-Impaired Angiogenesis and Ischemic Tissue Repair. *Redox Biol.* **2020**, *37*, 101704. https://doi.org/10.1016/j.redox.2020.101704.

(329) Yang, G.; Yang, W.; Wu, L.; Wang, R. H2S, Endoplasmic Reticulum Stress, and Apoptosis of Insulin-Secreting Beta Cells. *J. Biol. Chem.* **2007**, *282* (22), 16567-76. https://doi.org/10.1074/jbc.M700605200.

(330) Di Villa Bianca, R. D. E.; Sorrentino, R.; Maffia, P.; Mirone, V.; Imbimbo, C.; Fusco, F.; De Palma, R.; Ignarro, L. J.; Cirino, G. Hydrogen Sulfide as a Mediator of Human Corpus Cavernosum Smooth-Muscle Relaxation. *Proc. Natl. Acad. Sci. U. S. A.* **2009**, *106* (11), 4513-8. https://doi.org/10.1073/pnas.0807974105.

(331) Zheng, D.; Dong, S.; Li, T.; Yang, F.; Yu, X.; Wu, J.; Zhong, X.; Zhao, Y.; Wang, L.; Xu, C.; *et al.* Exogenous Hydrogen Sulfide Attenuates Cardiac Fibrosis Through Reactive Oxygen Species Signal Pathways in Experimental Diabetes Mellitus Models. *Cell. Physiol. Biochem.* **2015**, *36* (3), 917-29. https://doi.org/10.1159/000430266.

(332) Fisher, C. D.; Augustine, L. M.; Maher, J. M.; Nelson, D. M.; Slitt, A. L.; Klaassen, C. D.; Lehman-McKeeman, L. D.; Cherrington, N. J. Induction of Drug-Metabolizing Enzymes by Garlic and Allyl Sulfide Compounds via Activation of Constitutive Androstane Receptor and Nuclear Factor E2-Related Factor 2. *Drug Metab. Dispos.* **2007**, *35* (6), 995-1000. https://doi.org/10.1124/dmd.106.014340.

(333) Huang, H.; Li, X.; Zhuang, Y.; Li, N.; Zhu, X.; Hu, J.; Ben, J.; Yang, Q.; Bai, H.; Chen, Q. Class a Scavenger Receptor Activation Inhibits Endoplasmic Reticulum Stress-Induced Autophagy in Macrophage. *J. Biomed. Res.* **2014**, *28* (3), 213-21. https://doi.org/10.7555/JBR.28.20130105.

(334) Kimura, Y.; Goto, Y. I.; Kimura, H. Hydrogen Sulfide Increases Glutathione Production and Suppresses Oxidative Stress in Mitochondria. *Antiox. Redox Signal.* **2010**, *12* (1), 1–13. https://doi.org/10.1089/ars.2008.2282.

(335) Kimura, Y.; Dargusch, R.; Schubert, D.; Kimura, H. Hydrogen Sulfide Protects HT22 Neuronal Cells from Oxidative Stress. *Antiox. Redox Signal.* **2006**, *8* (3–4), 661-70. https://doi.org/10.1089/ars.2006.8.661.

(336) Kimura, H. Hydrogen Sulfide Induces Cyclic AMP and Modulates the NMDA Receptor. *Biochem. Biophys. Res. Commun.* **2000**, *267* (1), 129-33. https://doi.org/10.1006/bbrc.1999.1915.

(337) Lu, S. C. Regulation of Glutathione Synthesis. *Mol. Aspects Med.* **2009**, *30* (1–2), 42–59. https://doi.org/10.1016/j.mam.2008.05.005.

(338) Kamat, P. K.; Kalani, A.; Tyagi, N. Role of Hydrogen Sulfide in Brain Synaptic Remodeling. *Methods Enzymol.* **2015**, *555*, 207-29. https://doi.org/10.1016/bs.mie.2014.11.025.

(339) Deng, J.; Lei, C.; Chen, Y.; Fang, Z.; Yang, Q.; Zhang, H.; Cai, M.; Shi, L.; Dong, H.; Xiong, L. Neuroprotective Gases - Fantasy or Reality for Clinical Use? *Progress in Neurobiology*. **2014**, *115*, 210-45. https://doi.org/10.1016/j.pneurobio.2014.01.001.

(340) Lee, S. W.; Hu, Y. S.; Hu, L. F.; Lu, Q.; Dawe, G. S.; Moore, P. K.; Wong, P. T. H.; Bian, J. S. Hydrogen Sulphide Regulates Calcium Homeostasis in Microglial Cells. *Glia.* **2006**, *54* (2), 116-24. https://doi.org/10.1002/glia.20362.

(341) Kida, K.; Yamada, M.; Tokuda, K.; Marutani, E.; Kakinohana, M.; Kaneki, M.; Ichinose, F. Inhaled Hydrogen Sulfide Prevents Neurodegeneration and Movement Disorder in a Mouse Model of Parkinson's Disease. *Antiox. Redox Signal.* **2011**, *15* (2), 343-52. https://doi.org/10.1089/ars.2010.3671.

(342) Eto, K.; Asada, T.; Arima, K.; Makifuchi, T.; Kimura, H. Brain Hydrogen Sulfide Is Severely Decreased in Alzheimer's Disease. *Biochem. Biophys. Res. Commun.* **2002**, *293* (5), 1485-8. https://doi.org/10.1016/S0006-291X(02)00422-9.

(343) Berry, T.; Abohamza, E.; Moustafa, A. A. A Disease-Modifying Treatment for Alzheimer ' s Disease : Focus on the Trans-Sulfuration Pathway. *Rev. Neurosci*. **2020**, *31* (3), 1–16.https:// doi: 10.1515/revneuro-2019-0076.

(344) Kamoun, P. Endogenous Production of Hydrogen Sulfide in Mammals. *Amino Acids* **2004**, *26* (3), 243-54. https://doi.org/10.1007/s00726-004-0072-x.

(345) Kamoun, P. Mental Retardation in Down Syndrome: A Hydrogen Sulfide Hypothesis. *Med. Hypotheses.* **2001**, *57* (3), 389-92. https://doi.org/10.1054/mehy.2001.1377.

(346) Kabil, O.; Banerjee, R. Redox Biochemistry of Hydrogen Sulfide. *J. Biol. Chem*. **2010**, *285* (29), 21903-7. https://doi.org/10.1074/jbc.R110.128363.

(347) Belardinelli, M. C.; Chabli, A.; Chadefaux-Vekemans, B.; Kamoun, P. Urinary Sulfur

Compounds in down Syndrome. *Clin. Chem*. **2001**, *47* (8), 1500-1. https://doi.org/10.1093/clinchem/47.8.1500.

(348) Sivarajah, A.; McDonald, M. C.; Thiemermann, C. The Production of Hydrogen Sulfide Limits Myocardial Ischemia and Reperfusion Injury and Contributes to the Cardioprotective Effects of Preconditioning with Endotoxin, but Not Ischemia in the Rat. *Shock.* **2006**, *26* (2), 154-61. https://doi.org/10.1097/01.shk.0000225722.56681.64.

(349) Geng, B.; Yang, J.; Qi, Y.; Zhao, J.; Pang, Y.; Du, J.; Tang, C. H2S Generated by Heart in Rat and Its Effects on Cardiac Function. *Biochem. Biophys. Res. Commun.* **2004**, *313* (2), 362-8. https://doi.org/10.1016/j.bbrc.2003.11.130.

(350) Lavu, M.; Bhushan, S.; Lefer, D. J. Hydrogen Sulfide-Mediated Cardioprotection: Mechanisms and Therapeutic Potential. *Clin. Sci*. **2011**, *120* (6), 219-29. https://doi.org/10.1042/CS20100462.

(351) Zhang, Z.; Huang, H.; Liu, P.; Tang, C.; Wang, J. Hydrogen Sulfide Contributes to Cardioprotection during Ischemia-Reperfusion Injury by Opening K ATP Channels. *Can. J. Physiol. Pharmacol.* **2007**, *85* (12), 1248-53. https://doi.org/10.1139/Y07-120.

(352) Sivarajah, A.; Collino, M.; Yasin, M.; Benetti, E.; Gallicchio, M.; Mazzon, E.; Cuzzocrea, S.; Fantozzi, R.; Thiemermann, C. Anti-Apoptotic and Anti-Inflammatory Effects of Hydrogen Sulfide in a Rat Model of Regional Myocardial I/R. *Shock.* **2009**, *31* (3), 267–274. https://doi.org/10.1097/SHK.0b013e318180ff89.

(353) Jha, S.; Calvert, J. W.; Duranski, M. R.; Ramachandran, A.; Lefer, D. J. Hydrogen Sulfide Attenuates Hepatic Ischemia-Reperfusion Injury: Role of Antioxidant and Antiapoptotic Signaling. *Am. J. Physiol. - Hear. Circ. Physiol.* **2008**, *295* (2), H801-6. https://doi.org/10.1152/ajpheart.00377.2008.

(354) Osipov, R. M.; Robich, M. P.; Feng, J.; Liu, Y.; Clements, R. T.; Glazer, H. P.; Sodha, N. R.; Szabo, C.; Bianchi, C.; Sellke, F. W. Effect of Hydrogen Sulfide in a Porcine Model of Myocardial Ischemia-Reperfusion: Comparison of Different Administration Regimens and Characterization of the Cellular Mechanisms of Protection. *J. Cardiovasc. Pharmacol.* **2009**, *54* (4), 287-97. https://doi.org/10.1097/FJC.0b013e3181b2b72b.

(355) Forgan, L. G.; Forster, M. E. Oxygen Consumption, Ventilation Frequency and Cytochrome c Oxidase Activity in Blue Cod (Parapercis Colias) Exposed to Hydrogen Sulphide or Isoeugenol. *Comp. Biochem. Physiol. - C Toxicol. Pharmacol.* **2010**, *151* (1), 57-65. https://doi.org/10.1016/j.cbpc.2009.08.008.

(356) Cooper, C. E.; Brown, G. C. The Inhibition of Mitochondrial Cytochrome Oxidase by the Gases Carbon Monoxide, Nitric Oxide, Hydrogen Cyanide and Hydrogen Sulfide: Chemical Mechanism and Physiological Significance. *J. of Bioenerg. Biomembr*. **2008**, *40* (5), 533-9. https://doi.org/10.1007/s10863-008-9166-6.

(357) Volpato, G. P.; Searles, R.; Yu, B.; Scherrer-Crosbie, M.; Bloch, K. D.; Ichinose, F.; Zapol, W. M. Inhaled Hydrogen Sulfide: A Rapidly Reversible Inhibitor of Cardiac and Metabolic Function in the Mouse. *Anesthesiology.* **2008**, *108* (4), 659-68.

https://doi.org/10.1097/ALN.0b013e318167af0d.

(358) Calvert, J. W.; Jha, S.; Gundewar, S.; Elrod, J. W.; Ramachandran, A.; Pattillo, C. B.; Kevil, C. G.; Lefer, D. J. Hydrogen Sulfide Mediates Cardioprotection through Nrf2 Signaling. *Circ. Res.* **2009**, *105* (4), 365-74. https://doi.org/10.1161/CIRCRESAHA.109.199919.

(359) Yong, Q. C.; Lee, S. W.; Foo, C. S.; Neo, K. L.; Chen, X.; Bian, J. S. Endogenous Hydrogen Sulphide Mediates the Cardioprotection Induced by Ischemic Postconditioning. *Am. J. Physiol. - Hear. Circ. Physiol.* **2008**, *295* (3), H1330-H1340. https://doi.org/10.1152/ajpheart.00244.2008.

(360) Cai, W. J.; Wang, M. J.; Moore, P. K.; Jin, H. M.; Yao, T.; Zhu, Y. C. The Novel Proangiogenic Effect of Hydrogen Sulfide Is Dependent on Akt Phosphorylation. *Cardiovasc. Res.* **2007**, *76* (1), 29-40. https://doi.org/10.1016/j.cardiores.2007.05.026.

(361) Bhattacharyya, S.; Saha, S.; Giri, K.; Lanza, I. R.; Nair, K. S.; Jennings, N. B.; Rodriguez-Aguayo, C.; Lopez-Berestein, G.; Basal, E.; Weaver, A. L.; *et al*. Cystathionine Beta-Synthase (CBS) Contributes to Advanced Ovarian Cancer Progression and Drug Resistance. *PLoS One.* **2013**, *8* (11), e79167. https://doi.org/10.1371/journal.pone.0079167.

(362) Chakraborty, P. K.; Xiong, X.; Mustafi, S. B.; Saha, S.; Dhanasekaran, D.; Mandal, N. A.; McMeekin, S.; Bhattacharya, R.; Mukherjee, P. Role of Cystathionine Beta Synthase in Lipid Metabolism in Ovarian Cancer. *Oncotarget.* **2015**, *6* (35), 37367-84. https://doi.org/10.18632/oncotarget.5424.

(363) Cao, X.; Ding, L.; Xie, Z. Z.; Yang, Y.; Whiteman, M.; Moore, P. K.; Bian, J. S. A Review of Hydrogen Sulfide Synthesis, Metabolism, and Measurement: Is Modulation of Hydrogen Sulfide a Novel Therapeutic for Cancer? *Antiox. Redox Signal.* **2019**, *31* (1), 1–107. https://doi.org/10.1089/ars.2017.7058.

(364) Lee, Z. W.; Teo, X. Y.; Tay, E. Y. W.; Tan, C. H.; Hagen, T.; Moore, P. K.; Deng, L. W. Utilizing Hydrogen Sulfide as a Novel Anti-Cancer Agent by Targeting Cancer Glycolysis and PH Imbalance. *Br. J. Pharmacol.* **2014**, *171* (18), 4322-36. https://doi.org/10.1111/bph.12773.

(365) Szabõ, C. Hydrogen Sulphide and Its Therapeutic Potential. *Nat. Rev. Drug. Discov.* **2007**, *6* (11), 917-35. https://doi.org/10.1038/nrd2425.

(366) Vandiver, M. S.; Snyder, S. H. Hydrogen Sulfide: A Gasotransmitter of Clinical Relevance. *J. Mol. Med.* **2012**, *90* (3), 255-63. https://doi.org/10.1007/s00109-012-0873-4.

(367) Szabo, C.; Coletta, C.; Chao, C.; Módis, K.; Szczesny, B.; Papapetropoulos, A.; Hellmich, M. R. Tumor-Derived Hydrogen Sulfide, Produced by Cystathionine-β-Synthase, Stimulates Bioenergetics, Cell Proliferation, and Angiogenesis in Colon Cancer. *Proc. Natl. Acad. Sci. U. S. A.* **2013**, *110* (30), 12474-9. https://doi.org/10.1073/pnas.1306241110.

(368) Thornburg, J. M.; Nelson, K. K.; Clem, B. F.; Lane, A. N.; Arumugam, S.; Simmons, A.; Eaton, J. W.; Telang, S.; Chesney, J. Targeting Aspartate Aminotransferase in Breast Cancer. *Breast Cancer Res.* **2008**, *10* (5), R84. https://doi.org/10.1186/bcr2154.

(369) Son, J.; Lyssiotis, C. A.; Ying, H.; Wang, X.; Hua, S.; Ligorio, M.; Perera, R. M.; Ferrone, C. R.; Mullarky, E.; Shyh-Chang, N.; *et al*. Glutamine Supports Pancreatic Cancer Growth through a KRAS-Regulated Metabolic Pathway. *Nature.* **2013**, *496* (7443), 101-5. https://doi.org/10.1038/nature12040.

(370) Rahman, M. A.; Glasgow, J. N.; Nadeem, S.; Reddy, V. P.; Sevalkar, R. R.; Lancaster, J. R.; Steyn, A. J. C. The Role of Host-Generated H2S in Microbial Pathogenesis: New Perspectives on Tuberculosis. *Front. Cell. Infect. Microbiol.* **2020**, *10* (November), 1–33. https://doi.org/10.3389/fcimb.2020.586923.

(371) Jones, D. P.; Sies, H. The Redox Code. *Antiox. Redox Signaling*. **2015**, *23* (9), 734-46. https://doi.org/10.1089/ars.2015.6247.

(372) Rojo de la Vega, M.; Chapman, E.; Zhang, D. D. NRF2 and the Hallmarks of Cancer. *Cancer Cell*. **2018**, 34 (1), 21-43. https://doi.org/10.1016/j.ccell.2018.03.022.

(373) Harris, I. S.; Treloar, A. E.; Inoue, S.; Sasaki, M.; Gorrini, C.; Lee, K. C.; Yung, K. Y.; Brenner, D.; Knobbe-Thomsen, C. B.; Cox, M. A.; *et al*. Glutathione and Thioredoxin Antioxidant Pathways Synergize to Drive Cancer Initiation and Progression. *Cancer Cell.* **2015**, *27* (2), 211-22. https://doi.org/10.1016/j.ccell.2014.11.019.

(374) Piskounova, E.; Agathocleous, M.; Murphy, M. M.; Hu, Z.; Huddlestun, S. E.; Zhao, Z.; Leitch, A. M.; Johnson, T. M.; DeBerardinis, R. J.; Morrison, S. J. Oxidative Stress Inhibits Distant Metastasis by Human Melanoma Cells. *Nature.* **2015**, *527* (7577), 186-91. https://doi.org/10.1038/nature15726.

(375) Szatrowski, T. P.; Nathan, C. F. Production of Large Amounts of Hydrogen Peroxide by Human Tumor Cells. *Cancer Res.* **1991**, *51* (3), 794-8.

(376) Ames, B. N.; Shigenaga, M. K.; Hagen, T. M. Oxidants, Antioxidants, and the Degenerative Diseases of Aging. *Proceedings of the National Academy of Sciences of the United States of America*. **1993**, *90* (17), 7915-22. https://doi.org/10.1073/pnas.90.17.7915.

(377) Sabharwal, S. S.; Schumacker, P. T. Mitochondrial ROS in Cancer: Initiators, Amplifiers or an Achilles' Heel? *Nature Reviews Cancer*. **2014**, *14* (11), 709-21. https://doi.org/10.1038/nrc3803.

(378) Nogueira, V.; Park, Y.; Chen, C. C.; Xu, P. Z.; Chen, M. L.; Tonic, I.; Unterman, T.; Hay, N. Akt Determines Replicative Senescence and Oxidative or Oncogenic Premature Senescence and Sensitizes Cells to Oxidative Apoptosis. *Cancer Cell.* **2008**, *14* (6), 458-70. https://doi.org/10.1016/j.ccr.2008.11.003.

(379) Wu, G.; Fang, Y.-Z.; Yang, S.; Lupton, J. R.; Turner, N. D. Glutathione Metabolism and Its Implications for Health. *J. Nutr.* **2004**, *134* (3), 489–492.https:// doi: 10.1093/jn/134.3.489.

(380) Bansal, A.; Celeste Simon, M. Glutathione Metabolism in Cancer Progression and Treatment Resistance. *J. Cell Biol.* **2018**, *217* (7), 2291–2298. https://doi.org/10.1083/jcb.201804161.

(381) Sen, S.; Kawahara, B.; Gupta, D.; Tsai, R.; Khachatryan, M.; Roy-Chowdhuri, S.; Bose, S.; Yoon,

A.; Faull, K.; Farias-Eisner, R.; *et al*. Role of Cystathionine β-Synthase in Human Breast Cancer. *Free Radic. Biol. Med.* **2015**, *86,* 228-38. https://doi.org/10.1016/j.freeradbiomed.2015.05.024.

(382) Guo, Z.; Chen, G.; Zeng, G.; Li, Z.; Chen, A.; Wang, J.; Jiang, L. Fluorescence Chemosensors for Hydrogen Sulfide Detection in Biological Systems. *Analyst.* **2015**, *140* (6), 1772-86. https://doi.org/10.1039/c4an01909a.

(383) Panza, E.; De Cicco, P.; Armogida, C.; Scognamiglio, G.; Gigantino, V.; Botti, G.; Germano, D.; Napolitano, M.; Papapetropoulos, A.; Bucci, M.; *et al*. Role of the Cystathionine γ Lyase/Hydrogen Sulfide Pathway in Human Melanoma Progression. *Pigment Cell Melanoma Res.* **2015**, *28* (1), 61-72. https://doi.org/10.1111/pcmr.12312.

(384) MA, K.; Liu, Y.; Zhu, Q.; Liu, C. hua; Duan, J. L.; Tan, B. K. H.; Zhu, Y. Z. H2S Donor, S-Propargyl-Cysteine, Increases CSE in SGC-7901 and Cancer-Induced Mice: Evidence for a Novel Anti-Cancer Effect of Endogenous H2S? *PLoS One.* **2011**, *6* (6), e20525. https://doi.org/10.1371/journal.pone.0020525.

(385) Pan, Y.; Ye, S.; Yuan, D.; Zhang, J.; Bai, Y.; Shao, C. Hydrogen Sulfide (H2S)/Cystathionine γ-Lyase (CSE) Pathway Contributes to the Proliferation of Hepatoma Cells. *Mutat. Res. - Fundam. Mol. Mech. Mutagen.* **2014**, *763–764*. https://doi.org/10.1016/j.mrfmmm.2014.03.002.

(386) Yin, P.; Zhao, C.; Li, Z.; Mei, C.; Yao, W.; Liu, Y.; Li, N.; Qi, J.; Wang, L.; Shi, Y.; *et al*. Sp1 Is Involved in Regulation of Cystathionine γ-Lyase Gene Expression and Biological Function by PI3K/Akt Pathway in Human Hepatocellular Carcinoma Cell Lines. *Cell. Signal.* **2012**, *24* (6), 1229-40. https://doi.org/10.1016/j.cellsig.2012.02.003.

(387) Refsum, H.; Ueland, P. M.; Nygård, O.; Vollset, S. E. Homocysteine and Cardiovascular Disease. *Annu. Rev. Med.* **1998**, *49* (1), 31–62.https:// doi: 10.1146/annurev.med.49.1.31.

(388) Xiao, Q.; Ying, J.; Xiang, L.; Zhang, C. The Biologic Effect of Hydrogen Sulfide and Its Function in Various Diseases. *Med. (United States).* **2018**, *97* (44), e13065. https://doi.org/10.1097/MD.0000000000013065.

(389) Ivanov, A. V.; Valuev-Elliston, V. T.; Ivanova, O. N.; Kochetkov, S. N.; Starodubova, E. S.; Bartosch, B.; Isaguliants, M. G. Oxidative Stress during HIV Infection: Mechanisms and Consequences. *Oxid. Med. Cell. Longev.* **2016**, *2016*, 8910396. https://doi.org/10.1155/2016/8910396.

(390) Peterhans, E.; Grob, M.; Burge, T.; Zanoni, R. Virus-Induced Formation of Reactive Oxygen Intermediates in Phagocytic Cells. *Free Radic. Res.* **1987**, *3* (1–5), 39–46. https://doi.org/10.3109/10715768709069768.

(391) Hennet, T.; Peterhans, E.; Stocker, R. Alterations in Antioxidant Defences in Lung and Liver of Mice Infected with Influenza A Virus. *J. Gen. Virol.* **1992**, *73* (1), 39-46. https://doi.org/10.1099/0022-1317-73-1-39.

(392) Perl, A.; Banki, K. Genetic and Metabolic Control of the Mitochondrial Transmembrane

Potential and Reactive Oxygen Intermediate Production in HIV Disease. *Antiox. Redox Signaling*. **2000**, *2* (3), 551-73. https://doi.org/10.1089/15230860050192323.

(393) Müller, F. Reactive Oxygen Intermediates and Human Immunodeficiency Virus (HIV) Infection. *Free Radic. Biol. Med.* **1992**, *13* (6), 651-7. https://doi.org/10.1016/0891-5849(92)90039-J.

(394) He, F.; Ru, X.; Wen, T. NRF2, a Transcription Factor for Stress Response and Beyond. *International Journal of Molecular Sciences*. **2020**, *21* (13), 4777. https://doi.org/10.3390/ijms21134777.

(395) Staitieh, B. S.; Ding, L.; Neveu, W. A.; Spearman, P.; Guidot, D. M.; Fan, X. HIV-1 Decreases Nrf2/ARE Activity and Phagocytic Function in Alveolar Macrophages. *J. Leukoc. Biol.* **2017**, *102* (2), 517-525. https://doi.org/10.1189/jlb.4a0616-282rr.

(396) Furuya, A. K. M.; Sharifi, H. J.; Jellinger, R. M.; Cristofano, P.; Shi, B.; de Noronha, C. M. C. Sulforaphane Inhibits HIV Infection of Macrophages through Nrf2. *PLoS Pathog.* **2016**, *12* (4), e1005581. https://doi.org/10.1371/journal.ppat.1005581.

(397) Page, A.; Volchkova, V. A.; Reid, S. P.; Mateo, M.; Bagnaud-Baule, A.; Nemirov, K.; Shurtleff, A. C.; Lawrence, P.; Reynard, O.; Ottmann, M.; *et al*. Marburgvirus Hijacks Nrf2-Dependent Pathway by Targeting Nrf2-Negative Regulator Keap1. *Cell Rep.* **2014**, *6* (6), 1026-1036. https://doi.org/10.1016/j.celrep.2014.02.027.

(398) Gjyshi, O.; Bottero, V.; Veettil, M. V.; Dutta, S.; Singh, V. V.; Chikoti, L.; Chandran, B. Kaposi's Sarcoma-Associated Herpesvirus Induces Nrf2 during De Novo Infection of Endothelial Cells to Create a Microenvironment Conducive to Infection. *PLoS Pathog.* **2014**, *10* (10), e1004460. https://doi.org/10.1371/journal.ppat.1004460.

(399) Hourihan, J. M.; Kenna, J. G.; Hayes, J. D. The Gasotransmitter Hydrogen Sulfide Induces Nrf2-Target Genes by Inactivating the Keap1 Ubiquitin Ligase Substrate Adaptor through Formation of a Disulfide Bond between Cys-226 and Cys-613. *Antiox. Redox Signal.* **2013**, *19* (5), 465-81. https://doi.org/10.1089/ars.2012.4944.

(400) Yang, G.; Zhao, K.; Ju, Y.; Mani, S.; Cao, Q.; Puukila, S.; Khaper, N.; Wu, L.; Wang, R. Hydrogen Sulfide Protects against Cellular Senescence via S-Sulfhydration of Keap1 and Activation of Nrf2. *Antiox. Redox Signal.* **2013**, *18* (15), 1906-19. https://doi.org/10.1089/ars.2012.4645.

(401) Schmidt, M. E.; Varga, S. M. Modulation of the Host Immune Response by Respiratory Syncytial Virus Proteins. *J. Microbiol*. **2017**, *55* (3), 161-171. https://doi.org/10.1007/s12275-017-7045-8.

(402) Garofalo, R. P.; Haeberle, H. Epithelial Regulation of Innate Immunity to Respiratory Syncytial Virus. *Am. J. Respir. Cell. Mol. Biol*. **2000**, *23* (5), 581-5. https://doi.org/10.1165/ajrcmb.23.5.f204.

(403) Li, H.; Ma, Y.; Escaffre, O.; Ivanciuc, T.; Komaravelli, N.; Kelley, J. P.; Coletta, C.; Szabo, C.; Rockx, B.; Garofalo, R. P.; *et al*. Role of Hydrogen Sulfide in Paramyxovirus Infections. *J. Virol.* **2015**, *89* (10), 5557–5568. https://doi.org/10.1128/jvi.00264-15.

(404) Ivanciuc, T.; Sbrana, E.; Ansar, M.; Bazhanov, N.; Szabo, C.; Casola, A.; Garofalo, R. P. Hydrogen Sulfide Is an Antiviral and Antiinflammatory Endogenous Gasotransmitter in the Airways Role in Respiratory Syncytial Virus Infection. *Am. J. Respir. Cell Mol. Biol.* **2016**, *55* (5), 684-696. https://doi.org/10.1165/rcmb.2015-0385OC.

(405) Bazhanov, N.; Ansar, M.; Ivanciuc, T.; Garofalo, R. P.; Casola, A. Hydrogen Sulfide: A Novel Player in Airway Development, Pathophysiology of Respiratory Diseases, and Antiviral Defenses. *Am. J. Respir. Cell Mol. Biol.* **2017**, *57* (4), 403–410. https://doi.org/10.1165/rcmb.2017-0114TR.

(406) Wu, Z.; Peng, H.; Du, Q.; Lin, W.; Liu, Y. GYY4137, a Hydrogen Sulfide-Releasing Molecule, Inhibits the Inflammatory Response by Suppressing the Activation of Nuclear Factor-Kappa B and Mitogen-Activated Protein Kinases in Coxsackie Virus B3-Infected Rat Cardiomyocytes. *Mol. Med. Rep.* **2015**, *11* (3), 1837-44. https://doi.org/10.3892/mmr.2014.2901.

(407) Giamarellos-Bourboulis, E. J.; Netea, M. G.; Rovina, N.; Akinosoglou, K.; Antoniadou, A.; Antonakos, N.; Damoraki, G.; Gkavogianni, T.; Adami, M. E.; Katsaounou, P.; *et al*. Complex Immune Dysregulation in COVID-19 Patients with Severe Respiratory Failure. *Cell Host Microbe.* **2020**, *27* (6), 992-1000. https://doi.org/10.1016/j.chom.2020.04.009.

(408) Zhou, P.; Yang, X. Lou; Wang, X. G.; Hu, B.; Zhang, L.; Zhang, W.; Si, H. R.; Zhu, Y.; Li, B.; Huang, C. L.; *et al*. A Pneumonia Outbreak Associated with a New Coronavirus of Probable Bat Origin. *Nature.* **2020**, *579* (7798), 270-273. https://doi.org/10.1038/s41586-020-2012-7.

(409) Tain, Y. L.; Hsu, C. N.; Lu, P. C. Early Short-Term Treatment with Exogenous Hydrogen Sulfide Postpones the Transition from Prehypertension to Hypertension in Spontaneously Hypertensive Rat. *Clin. Exp. Hypertens.* **2018**, *40* (1), 58-64. https://doi.org/10.1080/10641963.2017.1313847.

(410) Yang, G. H2S as a Potential Defense against COVID-19? *Am. J. Physiol. - Cell Physiol.* **2020**, *319* (2), C244–C249. https://doi.org/10.1152/ajpcell.00187.2020.

(411) Bourgonje, A. R.; Offringa, A. K.; van Eijk, L. E.; Abdulle, A. E.; Hillebrands, J.-L.; van der Voort, P. H. J.; van Goor, H.; van Hezik, E. J. N-Acetylcysteine and Hydrogen Sulfide in Coronavirus Disease 2019. *Antioxid. Redox Signal.* **2021**, *35* (14), 1207-1225. https://doi.org/10.1089/ars.2020.8247.

(412) Renieris, G.; Katrini, K.; Damoulari, C.; Akinosoglou, K.; Psarrakis, C.; Kyriakopoulou, M.; Dimopoulos, G.; Lada, M.; Koufargyris, P.; Giamarellos-Bourboulis, E. J. Serum Hydrogen Sulfide and Outcome Association in Pneumonia by the SARS-CoV-2 Coronavirus. *Shock.* **2020**, *54* (5), 633-637. https://doi.org/10.1097/SHK.0000000000001562.

(413) Gayon, M. U. Note Presentee Par M. Pasteur. Sur Les Alterations Des Oeufs, a l'occasion d'une Note de MM. A. Bechamp et G. Eustache. *Ann. Ec. Norm. Super. S6r.* **1877**, *2*.

(414) Szabo, C. A Timeline of Hydrogen Sulfide (H2S) Research: From Environmental Toxin to Biological Mediator. *Biochem. Pharmacol.* **2018**, *149*, 5–19. https://doi.org/10.1016/j.bcp.2017.09.010.

(415) Durham, H. E. A Simple Method for Demonstrating the Production of Gas by Bacteria. *Br. Med. J.* **1898**, *1* (1952), 1387. https://doi.org/10.1136/bmj.1.1952.1387.

(416) Beijerinck, M. W. Über Spirillum Desulfuricans Als Ursache von Sulfatreduktion. *Zentralblatt Bakteriol* **1895**, *1*, 1–9.

(417) Schardinger, F. Beitrag Zur Hygienischen Beurteilung Des Trinkwassers. *Zentralblatt für Bakteriol. Parasitenkd. und Infekt.* **1894**, *16*, 853–859.

(418) Olson, K. R.; Straub, K. D. The Role of Hydrogen Sulfide in Evolution and the Evolution of Hydrogen Sulfide in Metabolism and Signaling. *Physiology.* **2016**, *31* (1), 60–72. https://doi.org/10.1152/physiol.00024.2015.

(419) Bachenheimer, A. G.; Bennett, E. O. The Sensitivity of Mixed Populations of Bacteria to Inhibitors - I. The Mechanism by Which Desulfovibrio Desulfuricans Protects PS. Aeruginosa from the Toxicity of Mercurials. *Antonie Van Leeuwenhoek.* **1961**, *27*, 180-8. https://doi.org/10.1007/BF02538438.

(420) Stutzenberger, F. J.; Bennett, E. O. Sensitivity of Mixed Populations of Staphylococcus Aureus and Escherichia Coli to Mercurials . *Appl. Microbiol.* **1965**, *13* (4), 570-4. https://doi.org/10.1128/am.13.4.570-574.1965.

(421) Mironov, A.; Seregina, T.; Nagornykh, M.; Luhachack, L. G.; Korolkova, N.; Lopes, L. E.; Kotova, V.; Zavilgelsky, G.; Shakulov, R.; Shatalin, K.; *et al*. Mechanism of H2S-Mediated Protection against Oxidative Stress in Escherichia Coli. *Proc. Natl. Acad. Sci. U. S. A.* **2017**, *114* (23), 6022–6027. https://doi.org/10.1073/pnas.1703576114.

(422) Dwyer, D. J.; Belenky, P. A.; Yang, J. H.; Cody MacDonald, I.; Martell, J. D.; Takahashi, N.; Chan, C. T. Y.; Lobritz, M. A.; Braff, D.; Schwarz, E. G.; *et al*. Antibiotics Induce Redox-Related Physiological alterations as part of their lethality. *Proc. Natl. Acad. Sci. U. S. A.* **2014**, *111* (20), E2100-9. https://doi.org/10.1073/pnas.1401876111.

(423) Kohanski, M. A.; Dwyer, D. J.; Hayete, B.; Lawrence, C. A.; Collins, J. J. A Common Mechanism of Cellular Death Induced by Bactericidal Antibiotics. *Cell.* **2007**, *130* (5), 797-810. https://doi.org/10.1016/j.cell.2007.06.049.

(424) Imlay, J. A. The Molecular Mechanisms and Physiological Consequences of Oxidative Stress: Lessons from a Model Bacterium. *Nature Rev. Microbiol*. **2013**, *11* (7), 443-54. https://doi.org/10.1038/nrmicro3032.

(425) Toliver-Kinsky, T.; Cui, W.; Törö, G.; Lee, S. J.; Shatalin, K.; Nudler, E.; Szaboa, C. H 2 S, a Bacterial Defense Mechanism against the Host Immune Response. *Infect. Immun.* **2019**, *87* (1), e00272-18. https://doi.org/10.1128/IAI.00272-18.

(426) Saini, V.; Chinta, K. C.; Reddy, V. P.; Glasgow, J. N.; Stein, A.; Lamprecht, D. A.; Rahman, M. A.; Mackenzie, J. S.; Truebody, B. E.; Adamson, J. H.; *et al*. Hydrogen Sulfide Stimulates Mycobacterium Tuberculosis Respiration, Growth and Pathogenesis. *Nat. Commun.* **2020**, *11* (1), 1–17. https://doi.org/10.1038/s41467-019-14132-y.

(427) Hackett, E. E.; Charles-Messance, H.; O'Leary, S. M.; Gleeson, L. E.; Muñoz-Wolf, N.; Case, S.; Wedderburn, A.; Johnston, D. G. W.; Williams, M. A.; Smyth, A.; *et al.* Mycobacterium Tuberculosis Limits Host Glycolysis and IL-1β by Restriction of PFK-M via MicroRNA-21. *Cell Rep.* **2020**, *30* (1), 124-136.e4. https://doi.org/10.1016/j.celrep.2019.12.015.

(428) Ng, S. Y.; Ong, K. X.; Surendran, S. T.; Sinha, A.; Lai, J. J. H.; Chen, J.; Liang, J.; Tay, L. K. S.; Cui, L.; Loo, H. L.; *et al*. Hydrogen Sulfide Sensitizes Acinetobacter Baumannii to Killing by Antibiotics. *Front. Microbiol.* **2020**, *11*, 1875, 1–9. https://doi.org/10.3389/fmicb.2020.01875.

(429) Vozdek, R.; Hnízda, A.; Krijt, J.; Kostrouchová, M.; Kožich, V. Novel Structural Arrangement of Nematode Cystathionine β-Synthases: Characterization of Caenorhabditis Elegans CBS-1. *Biochem. J.* **2012**, *443* (2), 535–547. https://doi.org/10.1042/BJ20111478.

(430) Jhee, K. H.; Niks, D.; McPhie, P.; Dunn, M. F.; Miles, E. W. The Reaction of Yeast Cystathionine β-Synthase Is Rate-Limited by the Conversion of Aminoacrylate to Cystathionine. *Biochemistry.* **2001**, *40* (36), 10873–10880. https://doi.org/10.1021/bi011087j.

(431) Conter, C.; Fruncillo, S.; Fernández-Rodríguez, C.; Martínez-Cruz, L. A.; Dominici, P.; Astegno, A. Cystathionine β-Synthase Is Involved in Cysteine Biosynthesis and H2S Generation in Toxoplasma Gondii. *Sci. Rep.* **2020**, *10* (1), 14657. https://doi.org/10.1038/s41598-020-71469-x.

(432) Bateman, A. The Structure of a Domain Common to Archaebacteria and the Homocystinuria Disease Protein. *Trends Biochem. Sci.* **1997**, *22* (1), 12–13. https://doi.org/10.1016/S0968-0004(96)30046-7.

(433) Tu, Y.; Kreinbring, C. A.; Hill, M.; Liu, C.; Petsko, G. A.; McCune, C. D.; Berkowitz, D. B.; Liu, D.; Ringe, D. Crystal Structures of Cystathionine β-Synthase from Saccharomyces Cerevisiae : One Enzymatic Step at a Time. *Biochemistry.* **2018**, *57* (22), 3134–3145. https://doi.org/10.1021/acs.biochem.8b00092.

(434) Koutmos, M.; Kabil, O.; Smith, J. L.; Banerjee, R. Structural Basis for Substrate Activation and Regulation by Cystathionine Beta-Synthase (CBS) Domains in Cystathionine -Synthase. *Proc. Natl. Acad. Sci.* **2010**, *107* (49), 20958–20963. https://doi.org/10.1073/pnas.1011448107.

(435) Giménez-Mascarell, P.; Majtan, T.; Oyenarte, I.; Ereño-Orbea, J.; Majtan, J.; Klaudiny, J.; Kraus, J. P.; Martínez-Cruz, L. A. Crystal Structure of Cystathionine β-Synthase from Honeybee Apis Mellifera. *J. Struct. Biol.* **2018**, *202* (1), 82–93. https://doi.org/10.1016/j.jsb.2017.12.008.

(436) Janošík, M.; Kery, V.; Gaustadnes, M.; Maclean, K. N.; Kraus, J. P. Regulation of Human Cystathionine β-Synthase by S-Adenosyl-L-Methionine: Evidence for Two Catalytically Active Conformations Involving an Autoinhibitory Domain in the C-Terminal Region. *Biochemistry.* **2001**, *40* (35), 10625–10633. https://doi.org/10.1021/bi010711p.

(437) Weeks, C. L.; Singh, S.; Madzelan, P.; Banerjee, R.; Spiro, T. G. Heme Regulation of Human Cystathionine β-Synthase Activity: Insights from Fluorescence and Raman Spectroscopy. *J. Am. Chem. Soc.* **2009**, *131* (35), 12809–12816. https://doi.org/10.1021/ja904468w.

(438) Meier, M. Structure of Human Cystathionine Beta-Synthase: A Unique Pyridoxal 5'-Phosphate-Dependent Heme Protein. *EMBO J.* **2001**, *20* (15), 3910–3916. https://doi.org/10.1093/emboj/20.15.3910.

(439) Taoka, S.; Banerjee, R. Stopped-Flow Kinetic Analysis of the Reaction Catalyzed by the Full-Length Yeast Cystathionine β-Synthase. *J. Biol. Chem.* **2002**, *277* (25), 22421-5. https://doi.org/10.1074/jbc.M202513200.

(440) McCorvie, T. J.; Kopec, J.; Hyung, S.-J.; Fitzpatrick, F.; Feng, X.; Termine, D.; Strain-Damerell, C.; Vollmar, M.; Fleming, J.; Janz, J. M.; *et al*. Inter-Domain Communication of Human Cystathionine β-Synthase. *J. Biol. Chem.* **2014**, *289* (52), 36018–36030. https://doi.org/10.1074/jbc.M114.610782.

(441) Janošík, M.; Oliveriusová, J.; Janošíková, B.; Sokolová, J.; Kraus, E.; Kraus, J. P.; Kožich, V. Impaired Heme Binding and Aggregation of Mutant Cystathionine β-Synthase Subunits in Homocystinuria. *Am. J. Hum. Genet.* **2001**, *68* (6), 1506–1513. https://doi.org/10.1086/320597.

(442) Kumar, A.; Wißbrock, A.; Goradia, N.; Bellstedt, P.; Ramachandran, R.; Imhof, D.; Ohlenschläger, O. Heme Interaction of the Intrinsically Disordered N-Terminal Peptide Segment of Human Cystathionine-β-Synthase. *Sci. Rep.* **2018**, *8* (1), 2474. https://doi.org/10.1038/s41598-018-20841-z.

(443) Oliveriusová, J.; Kery, V.; Maclean, K. N.; Kraus, J. P. Deletion Mutagenesis of Human Cystathionine β-Synthase: Impact on Activity, Oligomeric Status, Ands-Adenosylmethionine Regulation. *J. Biol. Chem.* **2002**, *277* (50), 48386–48394.https:// doi: 10.1074/jbc.M207087200

(444) Frank, N.; Kery, V.; Maclean, K. N.; Kraus, J. P. Solvent-Accessible Cysteines in Human Cystathionine β-Synthase: Crucial Role of Cysteine 431 in S-Adenosyl-L-Methionine Binding. *Biochemistry.* **2006**, *45* (36), 11021-9. https://doi.org/10.1021/bi060737m.

(445) Bublil, E. M.; Majtan, T.; Park, I.; Carrillo, R. S.; Hůlková, H.; Krijt, J.; Kožich, V.; Kraus, J. P. Enzyme Replacement with PEGylated Cystathionine β-Synthase Ameliorates Homocystinuria in Murine Model. *J. Clin. Invest.* **2016**, *126* (6), 2372-84. https://doi.org/10.1172/JCI85396.

(446) Vicente, J. B.; Colaço, H. G.; Sarti, P.; Leandro, P.; Giuffrè, A. S-Adenosyl-L-Methionine Modulates CO and NO· Binding to the Human H2S-Generating Enzyme Cystathionine β-Synthase. *J. Biol. Chem.* **2016**, *291* (2), 572-81. https://doi.org/10.1074/jbc.M115.681221.

(447) Pazicni, S.; Lukat-Rodgers, G. S.; Oliveriusová, J.; Rees, K. A.; Parks, R. B.; Clark, R. W.; Rodgers, K. R.; Kraus, J. P.; Burstyn, J. N. The Redox Behavior of the Heme in Cystathionine β-Synthase Is Sensitive to pH. *Biochemistr.* **2004**, *43* (46), 14684-95. https://doi.org/10.1021/bi0488496.

(448) Cherney, M. M.; Pazicni, S.; Frank, N.; Marvin, K. A.; Kraus, J. P.; Burstyn, J. N. Ferrous Human Cystathionine β-Synthase Loses Activity during Enzyme Assay Due to a Ligand Switch Process. *Biochemistry.* **2007**, *46* (45), 13199-210. https://doi.org/10.1021/bi701159y.

(449) Eto, K.; Ogasawara, M.; Umemura, K.; Nagai, Y.; Kimura, H. Hydrogen Sulfide Is Produced in

Response to Neuronal Excitation. *J. Neurosci.* **2002**, *22* (9), 3386–3391. https://doi.org/10.1523/JNEUROSCI.22-09-03386.2002.

(450) Yadav, P. K.; Banerjee, R. Detection of Reaction Intermediates during Human Cystathionine β-Synthase-Monitored Turnover and H2S Production. *J. Biol. Chem.* **2012**, *287* (52), 43464–43471. https://doi.org/10.1074/jbc.M112.414722.

(451) Evande, R.; Blom, H.; Boers, G. H. J.; Banerjee, R. Alleviation of Intrasteric Inhibition by the Pathogenic Activation Domain Mutation, D444N, in Human Cystathionine β-Synthase. *Biochemistry.* **2002**, *41* (39), 11832–11837. https://doi.org/10.1021/bi026248d.

(452) Christen, P.; Mehta, P. K. From Cofactor to Enzymes. The Molecular Evolution of Pyridoxal-5?-Phosphate-Dependent Enzymes. *Chem. Rec.* **2001**, *1* (6), 436–447. https://doi.org/10.1002/tcr.10005.

(453) Lodha, P. H.; Jaworski, A. F.; Aitken, S. M. Characterization of Site-directed Mutants of Residues R58, R59, D116, W340 and R372 in the Active Site of E. Coli Cystathionine beta-lyase. *Protein Sci.* **2010**, *19* (3), 383–391.https:// doi: 10.1002/pro.308

(454) Pey, A. L.; Majtan, T.; Kraus, J. P. The Role of Surface Electrostatics on the Stability, Function and Regulation of Human Cystathionine β-Synthase, a Complex Multidomain and Oligomeric Protein. *Biochim. Biophys. Acta - Proteins Proteom.* **2014**, *1844* (9), 1453-62. https://doi.org/10.1016/j.bbapap.2014.04.015.

(455) Pey, A. L.; Martínez-Cruz, L. A.; Kraus, J. P.; Majtan, T. Oligomeric Status of Human Cystathionine Beta-Synthase Modulates AdoMet Binding. *FEBS Lett.* **2016**, *590* (24), 4461–4471. https://doi.org/10.1002/1873-3468.12488.

(456) Aitken, S. M.; Lodha, P. H.; Morneau, D. J. K. The Enzymes of the Transsulfuration Pathways: Active-Site Characterizations. *Biochim. Biophys. Acta (BBA)-Proteins Proteom.* **2011**, *1814* (11), 1511–1517.https:// doi: 10.1016/j.bbapap.2011.03.006.

(457) Chiku, T.; Padovani, D.; Zhu, W.; Singh, S.; Vitvitsky, V.; Banerjee, R. H2S Biogenesis by Human Cystathionine γ-Lyase Leads to the Novel Sulfur Metabolites Lanthionine and Homolanthionine and Is Responsive to the Grade of Hyperhomocysteinemia. *J. Biol. Chem.* **2009**, *284* (17), 11601–11612. https://doi.org/10.1074/jbc.M808026200.

(458) Maresi, E.; Janson, G.; Fruncillo, S.; Paiardini, A.; Vallone, R.; Dominici, P.; Astegno, A. Functional Characterization and Structure-Guided Mutational Analysis of the Transsulfuration Enzyme Cystathionine γ-Lyase from Toxoplasma Gondii. *Int. J. Mol. Sci.* **2018**, *19* (7), 2111. https://doi.org/10.3390/ijms19072111.

(459) Matoba, Y.; Noda, M.; Yoshida, T.; Oda, K.; Ezumi, Y.; Yasutake, C.; Izuhara-Kihara, H.; Danshiitsoodol, N.; Kumagai, T.; Sugiyama, M. Catalytic Specificity of the Lactobacillus Plantarum Cystathionine γ-Lyase Presumed by the Crystallographic Analysis. *Sci. Rep.* **2020**, *10* (1), 1–16. https://doi.org/10.1038/s41598-020-71756-7.

(460) Messerschmidt, A.; Worbs, M.; Steegborn, C.; Wahl, M. C.; Huber, R.; Laber, B.; Clausen, T. Determinants of Enzymatic Specificity in the Cys-Met-Metabolism PLP-Dependent Enzymes

Family: Crystal Structure of Cystathionine γ-Lyase from Yeast and Intrafamiliar Structure Comparison. *Biol. Chem.* **2003**, *384* (3), 373–386. https://doi.org/10.1515/BC.2003.043.

(461) Sun, Q.; Collins, R.; Huang, S.; Holmberg-Schiavone, L.; Anand, G. S.; Tan, C. H.; Van-den-Berg, S.; Deng, L. W.; Moore, P. K.; Karlberg, T.; *et al*. Structural Basis for the Inhibition Mechanism of Human Cystathionine γ-Lyase, an Enzyme Responsible for the Production of H2S. *J. Biol. Chem.* **2009**, *284* (5), 3076–3085. https://doi.org/10.1074/jbc.M805459200.

(462) Yadav, P. K.; Vitvitsky, V.; Kim, H.; White, A.; Cho, U. S.; Banerjee, R. S-3-Carboxypropyl-L-Cysteine Specifically Inhibits Cystathionine -Lyase–Dependent Hydrogen Sulfide Synthesis. *J. Biol. Chem.* **2019**, *294* (28), 11011–11022. https://doi.org/10.1074/jbc.RA119.009047.

(463) Cramer, S. L.; Saha, A.; Liu, J.; Tadi, S.; Tiziani, S.; Yan, W.; Triplett, K.; Lamb, C.; Alters, S. E.; Rowlinson, S.; *et al*. Systemic Depletion of L-Cyst(e)Ine with Cyst(e)Inase Increases Reactive Oxygen Species and Suppresses Tumor Growth. *Nat. Med.* **2017**, *23* (1), 120–127. https://doi.org/10.1038/nm.4232.

(464) Wang, Y.; Chen, H.; Huang, Z.; Yang, M.; Yu, H.; Peng, M.; Yang, Z.; Chen, S. Structural Characterization of Cystathionine γ-Lyase SmCSE Enables Aqueous Metal Quantum Dot Biosynthesis. *Int. J. Biol. Macromol.* **2021**, *174*, 42–51. https://doi.org/10.1016/j.ijbiomac.2021.01.141.

(465) Sagong, H. Y.; Kim, B.; Joo, S.; Kim, K. J. Structural and Functional Characterization of Cystathionine γ-Lyase from Bacillus Cereus ATCC 14579. *J. Agric. Food Chem.* **2020**, *68* (51), 15267–15274. https://doi.org/10.1021/acs.jafc.0c06503.

(466) Lee, D.; Jeong, S.; Ahn, J.; Ha, N. C.; Kwon, A. R. Crystal Structure of Bacterial Cystathionine γ-Lyase in the Cysteine Biosynthesis Pathway of Staphylococcus Aureus. *Crystals.* **2019**, *9* (12), 656. https://doi.org/10.3390/cryst9120656.

(467) Mueser, T. C.; Drago, V.; Kovalevsky, A.; Dajnowicz, S. Pyridoxal 5'-Phosphate Dependent Reactions: Analyzing the Mechanism of Aspartate Aminotransferase. *Methods Enzymol.* **2020**, *634*, 333–359.https:// doi: 10.1016/bs.mie.2020.01.009.

(468) Dajnowicz, S.; Johnston, R. C.; Parks, J. M.; Blakeley, M. P.; Keen, D. A.; Weiss, K. L.; Gerlits, O.; Kovalevsky, A.; Mueser, T. C. Direct Visualization of Critical Hydrogen Atoms in a Pyridoxal 5'-Phosphate Enzyme. *Nat. Commun.* **2017**, *8* (1), 955. https://doi.org/10.1038/s41467-017-01060-y.

(469) Toney, M. D. Controlling Reaction Specificity in Pyridoxal Phosphate Enzymes. *Biochim. Biophys. Acta.* **2011**, *1814* (11), 1407–1418.https:// doi: 10.1016/j.bbapap.2011.05.019.

(470) Huang, S.; Chua, J. H.; Yew, W. S.; Sivaraman, J.; Moore, P. K.; Tan, C. H.; Deng, L. W. Site-Directed Mutagenesis on Human Cystathionine-γ-Lyase Reveals Insights into the Modulation of H2S Production. *J. Mol. Biol.* **2010**, *396* (3), 708–718. https://doi.org/10.1016/j.jmb.2009.11.058.

(471) Farsi, A.; Lodha, P. H.; Skanes, J. E.; Los, H.; Kalidindi, N.; Aitken, S. M. Interconversion of a Pair of Active-Site Residues in Escherichia Coli Cystathionine β-Synthase, E. Coli Cystathionine

β-Lyase, and Saccharomyces Cerevisiae Cystathionine γ-Lyase and Development of Tools for the Investigation of Their Mechanisms and Reacti. *Biochem. Cell Biol.* **2009**, *87* (2), 445–457. https://doi.org/10.1139/O08-144.

(472) Hopwood, E. M. S.; Ahmed, D.; Aitken, S. M. A Role for Glutamate-333 of Saccharomyces Cerevisiae Cystathionine γ-Lyase as a Determinant of Specificity. *Biochim. Biophys. Acta - Proteins Proteom.* **2014**, *1844* (2), 465–472. https://doi.org/10.1016/j.bbapap.2013.11.012.

(473) Collin, M.; Anuar, F. B. M.; Murch, O.; Bhatia, M.; Moore, P. K.; Thiemermann, C. Inhibition of Endogenous Hydrogen Sulfide Formation Reduces the Organ Injury Caused by Endotoxemia. *Br. J. Pharmacol.* **2005**, *146* (4), 498–505.https:// doi: 10.1038/sj.bjp.0706367.

(474) Zhang, H.; Zhi, L.; Moore, P. K.; Bhatia, M. Role of Hydrogen Sulfide in Cecal Ligation and Puncture-Induced Sepsis in the Mouse. *Am. J. Physiol. Cell. Mol. Physiol.* **2006**, *290* (6), L1193–L1201.https:// doi: 10.1152/ajplung.00489.2005.

(475) Clausen, T.; Huber, R.; Prade, L.; Wahl, M. C.; Messerschmidt, A. Crystal Structure of Escherichia Coli Cystathionine γ-Synthase at 1.5 Å Resolution. *EMBO J.* **1998**, *17* (23), 6827–6838. https://doi.org/10.1093/emboj/17.23.6827.

(476) Thomazeau, K.; Curien, G.; Dumas, R.; Biou, V. Crystal Structure of Threonine Synthase from Arabidopsis Thaliana. *Protein Sci.* **2001**, *10* (3), 638–648. https:// doi: 10.1110/ps.44301.

(477) Mas-Droux, C.; Curien, G.; Robert-Genthon, M.; Laurencin, M.; Ferrer, J.-L.; Dumas, R. A Novel Organization of ACT Domains in Allosteric Enzymes Revealed by the Crystal Structure of Arabidopsis Aspartate Kinase. *Plant Cell.* **2006**, *18* (7), 1681–1692.https:// doi: 10.1105/tpc.105.040451.

(478) Nozaki, T.; Shigeta, Y.; Saito-Nakano, Y.; Imada, M.; Kruger, W. D. Characterization of Transsulfuration and Cysteine Biosynthetic Pathways in the Protozoan Hemoflagellate, Trypanosoma Cruzi: Isolation and Molecular Characterization of Cystathionine β-Synthase and Serine Acetyltransferase from Trypanosoma. *J. Biol. Chem.* **2001**, *276* (9), 6516–6523. https://doi.org/10.1074/jbc.M009774200.

(479) Astegno, A.; Giorgetti, A.; Allegrini, A.; Cellini, B.; Dominici, P. Characterization of C-S Lyase from C. Diphtheriae: A Possible Target for New Antimicrobial Drugs. *Biomed Res. Int.* **2013,** *2013,* 701536. https://doi.org/10.1155/2013/701536.

(480) Astegno, A.; Allegrini, A.; Piccoli, S.; Giorgetti, A.; Dominici, P. Role of Active-Site Residues Tyr55 and Tyr114 in Catalysis and Substrate Specificity of Corynebacterium Diphtheriae C-S Lyase. *Proteins Struct. Funct. Bioinforma.* **2015,** *83* (1), 78-90. https://doi.org/10.1002/prot.24707.

(481) Astegno, A.; Capitani, G.; Dominici, P. Functional Roles of the Hexamer Organization of Plant Glutamate Decarboxylase. *Biochim. Biophys. Acta - Proteins Proteom.* **2015**, *1854* (9), 1229–1237. https://doi.org/10.1016/j.bbapap.2015.01.001.

(482) Incardona, M. F.; Bourenkov, G. P.; Levik, K.; Pieritz, R. A.; Popov, A. N.; Svensson, O. EDNA: A Framework for Plugin-Based Applications Applied to X-Ray Experiment Online Data

Analysis. *J. Synchrotron Radiat.* **2009**, *16* (Pt 6), 872-9. https://doi.org/10.1107/S0909049509036681.

(483) Kabsch, W. XDS. *Acta Crystallogr. Sect. D Biol. Crystallogr.* **2010,** *66* (Pt2), 125-32. doi: 10.1107/S0907444909047337

(484) Vonrhein, C.; Flensburg, C.; Keller, P.; Sharff, A.; Smart, O.; Paciorek, W.; Womack, T.; Bricogne, G. Data Processing and Analysis with the AutoPROC Toolbox. *Acta Crystallogr. Sect. D Biol. Crystallogr.* **2011**, *67* (4), 293–302. https://doi.org/10.1107/S0907444911007773.

(485) Vagin, A.; Teplyakov, A. Molecular Replacement with MOLREP. *Acta Crystallogr. Sect. D Biol. Crystallogr.* **2010**, *66* (1), 22-5. https://doi.org/10.1107/S0907444909042589.

(486) Adams, P. D.; Afonine, P. V.; Bunkóczi, G.; Chen, V. B.; Echols, N.; Headd, J. J.; Hung, L.-W.; Jain, S.; Kapral, G. J.; Grosse Kunstleve, R. W.; *et al*. The Phenix Software for Automated Determination of Macromolecular Structures. *Methods.* **2011**, *55* (1), 94–106. https://doi.org/10.1016/j.ymeth.2011.07.005.

(487) Emsley, P.; Lohkamp, B.; Scott, W. G.; Cowtan, K. Features and Development of Coot. *Acta Crystallogr. Sect. D Biol. Crystallogr.* **2010**, *66* (4), 486–501. https://doi.org/10.1107/S0907444910007493.

(488) Drenth, J.; Mesters, J. *Principles of Protein X-Ray Crystallography: Third Edition;* Springer*:* 2007; Vol 9780387333342. https://doi.org/10.1007/0-387-33746-6.

(489) McCoy, A. J.; Grosse-Kunstleve, R. W.; Adams, P. D.; Winn, M. D.; Storoni, L. C.; Read, R. J. Phaser Crystallographic Software. *J. Appl. Crystallogr.* **2007,** *40* (Pt4), 658-674. https://doi.org/10.1107/S0021889807021206.

(490) Chen, V. B.; Arendall, W. B.; Headd, J. J.; Keedy, D. A.; Immormino, R. M.; Kapral, G. J.; Murray, L. W.; Richardson, J. S.; Richardson, D. C. MolProbity: All-Atom Structure Validation for Macromolecular Crystallography. *Acta Crystallogr. Sect. D Biol. Crystallogr.* **2010**, *66* (1), 12-21. https://doi.org/10.1107/S0907444909042073.

(491) Strong, M.; Sawaya, M. R.; Wang, S.; Phillips, M.; Cascio, D.; Eisenberg, D. Toward the Structural Genomics of Complexes: Crystal Structure of a PE/PPE Protein Complex from Mycobacterium Tuberculosis. *Proc. Natl. Acad. Sci. U. S. A.* **2006**, *103* (21), 8060–8065. https://doi.org/10.1073/pnas.0602606103.

(492) Zwart, P. H., Grosse-Kunstleve, R. W., Adams, P. D. Xtriage and Fest: Automatic Assessment of X-Ray Data and Substructure Structure Factor Estimation. *CCP4 Newsl.* **2005**, *43*.

(493) Liebschner, D.; Afonine, P. V.; Moriarty, N. W.; Poon, B. K.; Sobolev, O. V.; Terwilliger, T. C.; Adams, P. D. Polder Maps: Improving OMIT Maps by Excluding Bulk Solvent. *Acta Crystallogr. Sect. D Struct. Biol.* **2017**, *73* (2), 148–157. https://doi.org/10.1107/S2059798316018210.

(494) Steegborn, C.; Clausen, T.; Sondermann, P.; Jacob, U.; Worbs, M.; Marinkovic, S.; Huber, R.; Wahl, M. C. Kinetics and Inhibition of Recombinant Human Cystathionine γ-Lyase: Toward the Rational Control of Transsulfuration. *J. Biol. Chem.* **1999**, *274* (18), 12675–12684.

https://doi.org/10.1074/jbc.274.18.12675.

(495) Yamagata, S.; Isaji, M.; Yamane, T.; Iwama, T. Substrate Inhibition of L-Cysteine α,β-Elimination Reaction Catalyzed by L-Cystathionine γ-Lyase of Saccharomyce Cerevisiae. *Biosci. Biotechnol. Biochem.* **2002**, *66* (12), 2706–2709. https://doi.org/10.1271/bbb.66.2706.

(496) Cherest, H.; Thomas, D.; Surdin-Kerjan, Y. Cysteine Biosynthesis in Saccharomyces Cerevisiae Occurs through the Transsulfuration Pathway Which Has Been Built up by Enzyme Recruitment. *J. Bacteriol.* **1993**, *175* (17), 5366–5374. https://doi.org/10.1128/JB.175.17.5366-5374.1993.

(497) Kobylarz, M. J.; Grigg, J. C.; Liu, Y.; Lee, M. S. F.; Heinrichs, D. E.; Murphy, M. E. P. Deciphering the Substrate Specificity of SbnA, the Enzyme Catalyzing the First Step in Staphyloferrin B Biosynthesis. *Biochemistry* **2016**, *55* (6), 927–939. https://doi.org/10.1021/acs.biochem.5b01045.

(498) Cook, P. F.; Wedding, R. T. A Reaction Mechanism from Steady State Kinetic Studies for O Acetylserine Sulfhydrylase from Salmonella Typhimurium LT 2. *J. Biol. Chem.* **1976**, *251* (7), 2023-9. https://doi.org/10.1016/s0021-9258(17)33649-9.

(499) Nagasawa, T.; Kanzaki, H.; Yamada, H. Cystathionine γ-Lyase of Streptomyces Phaeochromogenes. The Occurrence of Cystathionine γ-Lyase in Filamentous Bacteria and Its Purification and Characterization. *J. Biol. Chem.* **1984**, *259* (16), 10393–10403. https://doi.org/10.1016/s0021-9258(18)90978-6.

(500) Liebschner, D.; Afonine, P. V.; Baker, M. L.; Bunkoczi, G.; Chen, V. B.; Croll, T. I.; Hintze, B.; Hung, L. W.; Jain, S.; McCoy, A. J.; *et al*. Macromolecular Structure Determination Using X-Rays, Neutrons and Electrons: Recent Developments in Phenix. *Acta Crystallogr. Sect. D Struct. Biol.* **2019**, *75* (Pt10), 861-877. https://doi.org/10.1107/S2059798319011471.

(501) Moriarty, N. W.; Grosse-Kunstleve, R. W.; Adams, P. D. Electronic Ligand Builder and Optimization Workbench (ELBOW): A Tool for Ligand Coordinate and Restraint Generation. *Acta Crystallogr. Sect. D Biol. Crystallogr.* **2009**, *65* (10), 1074-80. https://doi.org/10.1107/S0907444909029436.

(502) Oliveira, E. F.; Cerqueira, N. M. F. S. A.; Fernandes, P. A.; Ramos, M. J. Mechanism of Formation of the Internal Aldimine in Pyridoxal 5'-Phosphate-Dependent Enzymes. *J. Am. Chem. Soc.* **2011**, *133* (39), 15496-505. https://doi.org/10.1021/ja204229m.

(503) Asimakopoulou, A.; Panopoulos, P.; Chasapis, C. T.; Coletta, C.; Zhou, Z.; Cirino, G.; Giannis, A.; Szabo, C.; Spyroulias, G. A.; Papapetropoulos, A. Selectivity of Commonly Used Pharmacological Inhibitors for Cystathionine β Synthase (CBS) and Cystathionine γ Lyase (CSE). *Br. J. Pharmacol.* **2013**, *169* (4), 922–932. https://doi.org/10.1111/bph.12171.

(504) Tian, W.; Chen, C.; Lei, X.; Zhao, J.; Liang, J. CASTp 3.0: Computed Atlas of Surface Topography of Proteins. *Nucleic Acids Res.* **2018**, *46* (W1), W363-W367. https://doi.org/10.1093/nar/gky473.

(505) Yan, W.; Stone, E.; Zhang, Y. J. Structural Snapshots of an Engineered Cystathionine-γ-Lyase Reveal the Critical Role of Electrostatic Interactions in the Active Site. *Biochemistry.* **2017**, *56* (6), 876–885. https://doi.org/10.1021/acs.biochem.6b01172.

(506) Jaworski, A. F.; Lodha, P. H.; Manders, A. L.; Aitken, S. M. Exploration of the Active Site of Escherichia Coli Cystathionine γ-Synthase. *Protein Sci.* **2012**, *21* (11), 1662-71. https://doi.org/10.1002/pro.2135.

(507) Mihara, H.; Fujii, T.; Kato, S. ichiro; Kurihara, T.; Hata, Y.; Esaki, N. Structure of External Aldimine of Escherichia Coli CsdB, an IscS/NifS Homolog: Implications for Its Specificity toward Selenocysteine. *J. Biochem.* **2002**, *131* (5), 679–685. https://doi.org/10.1093/oxfordjournals.jbchem.a003151.

(508) Vitkovskaya, N. M.; Kobychev, V. B.; Bobkov, A. S.; Orel, V. B.; Schmidt, E. Y.; Trofimov, B. A. Nucleophilic Addition of Ketones to Acetylenes and Allenes: A Quantum-Chemical Insight. *J. Org. Chem.* **2017**, *82* (23), 12467-12476. https://doi.org/10.1021/acs.joc.7b02263.

(509) Klein, E. Y.; Tseng, K. K.; Pant, S.; Laxminarayan, R. Tracking Global Trends in the Effectiveness of Antibiotic Therapy Using the Drug Resistance Index. *BMJ Glob. Heal.* **2019**, *4* (2), e001315. https://doi.org/10.1136/bmjgh-2018-001315.

(510) Kumar, M.; Sarma, D. K.; Shubham, S.; Kumawat, M.; Verma, V.; Nina, P. B.; JP, D.; Kumar, S.; Singh, B.; Tiwari, R. R. Futuristic Non-Antibiotic Therapies to Combat Antibiotic Resistance: A Review. *Frontiers in Microbiology*. **2021**, *12*, 609459. https://doi.org/10.3389/fmicb.2021.609459.

(511) Minor, W.; Cymborowski, M.; Otwinowski, Z.; Chruszcz, M. HKL-3000: The Integration of Data Reduction and Structure Solution - From Diffraction Images to an Initial Model in Minutes. *Acta Crystallogr. Sect. D Biol. Crystallogr.* **2006**, *62* (8), 859-66. https://doi.org/10.1107/S0907444906019949.

(512) Winn, M. D.; Ballard, C. C.; Cowtan, K. D.; Dodson, E. J.; Emsley, P.; Evans, P. R.; Keegan, R. M.; Krissinel, E. B.; Leslie, A. G. W.; McCoy, A.; *et al.* Overview of the CCP4 Suite and Current Developments. *Acta Crystallogr. Sect. D Biol. Crystallogr.* **2011**, *67* (4), 235–242. https://doi.org/10.1107/S0907444910045749.

(513) Liang, J.; Han, Q.; Tan, Y.; Ding, H.; Li, J. Current Advances on Structure-Function Relationships of Pyridoxal 5'-Phosphate-Dependent Enzymes. *Frontiers in Molecular Biosciences*. **2019**, *6*, 4. https://doi.org/10.3389/fmolb.2019.00004.

(514) Kaldalu, N.; Hauryliuk, V.; Turnbull, K. J.; La Mensa, A.; Putrinš, M.; Tenson, T. In Vitro Studies of Persister Cells. *Microbiol. Mol. Biol. Rev.* **2020**, *84* (4), e00070-20. https://doi.org/10.1128/mmbr.00070-20.

PUBLICATIONS

Publications

Part of this thesis has been published in the following articles:

- González-Recio, I.; Fernández-Rodríguez, C.; Simón, J.; Goikoetxea-Usandizaga, N.; Martínez-Chantar, M. L.; Astegno, A.; Majtan, T.; Martinez-Cruz, L. A. Current Structural Knowledge on Cystathionine B-Synthase, a Pivotal Enzyme in the Transsulfuration Pathway. In *eLS.* **2020**, *1*, 453-468. https://doi.org/10.1002/9780470015902.a0028966.

- Conter, C.; Fruncillo, S.; Fernández-Rodríguez, C.; Martínez-Cruz, L. A.; Dominici, P.; Astegno, A. Cystathionine β-Synthase Is Involved in Cysteine Biosynthesis and H2S Generation in Toxoplasma Gondii. *Sci. Rep.* **2020**, *10* (1), 14657. https://doi.org/10.1038/s41598-020-71469-x.

- Fernández-Rodríguez, C.; Oyenarte, I.; Conter, C.; González-Recio, I.; Núñez-Franco, R.; Gil-Pitarch, C.; Quintana, I.; Jiménez-Osés, G.; Dominici, P.; Martinez-Chantar, M. L.; *et al*. Structural Insight into the Unique Conformation of Cystathionine β-Synthase from Toxoplasma Gondii. *Comput. Struct. Biotechnol. J.* **2021**, *19*, 3542–3555. https://doi.org/10.1016/j.csbj.2021.05.052.

Other related publications:

- Giménez-Mascarell, P.; González-Recio, I.; Fernández-Rodríguez, C.; Oyenarte, I.; Müller, D.; Martínez-Chantar, M. L.; Martínez-Cruz, L. A. Current Structural Knowledge on the CNNM Family of Magnesium Transport Mediators. *International Journal of Molecular Sciences*. **2019,** *20* (5), 1135. https://doi.org/10.3390/ijms20051135.

- Seker, M.; Fernandez-Rodriguez, C.; Martinez-Cruz, L. A.; Müller, D. Mouse Models of Human Claudin-Associated Disorders: Benefits and Limitations. *International Journal of Molecular Sciences*. **2019**, *20* (21), 5504. https://doi.org/10.3390/ijms20215504.

- Giménez-Mascarell, P.; Oyenarte, I.; González-Recio, I.; Fernández-Rodríguez, C.; Corral-Rodríguez, M. Á.; Campos-Zarraga, I.; Simón, J.; Kostantin, E.; Hardy, S.; Quintana, A. D.; *et al.* Structural Insights into the Intracellular Region of the Human Magnesium Transport Mediator CNNM4. *Int. J. Mol. Sci.* **2019**, *20* (24), 6279. https://doi.org/10.3390/ijms20246279.

- Simón, J.; Goikoetxea-Usandizaga, N.; Serrano-Maciá, M.; Fernández-Ramos, D.; Sáenz de Urturi, D.; Gruskos, J. J.; Fernández-Tussy, P.; Lachiondo-Ortega, S.; González-Recio, I.; Rodríguez-Agudo, R.; *et al.* Magnesium Accumulation upon Cyclin M4 Silencing Activates Microsomal Triglyceride Transfer Protein Improving NASH. *J. Hepatol.* **2021**, *75* (1), 34-45. https://doi.org/10.1016/j.jhep.2021.01.043.